Springer Atmospheric Sciences

Nicole Mölders
Gerhard Kramm

Lectures in Meteorology

Springer

Springer Atmospheric Sciences

For further volumes:
http://www.springer.com/series/10176

Nicole Mölders • Gerhard Kramm

Lectures in Meteorology

Springer

Nicole Mölders
Department of Atmospheric Sciences
College of Natural Science and Mathematics
Geophysical Institute
University of Alaska Fairbanks
Fairbanks, AK, USA

Gerhard Kramm
Geophysical Institute
University of Alaska Fairbanks
Fairbanks, AK, USA

ISSN 2194-5217 ISSN 2194-5225 (electronic)
ISBN 978-3-319-02143-0 ISBN 978-3-319-02144-7 (eBook)
DOI 10.1007/978-3-319-02144-7
Springer Cham Heidelberg New York Dordrecht London

Library of Congress Control Number: 2014941621

Printed on acid-free paper

Springer is part of Springer Science+Business Media (www.springer.com)

To Hermann und Ilse Mölders, Anna and Wilhelm Kramm, and Kasimir E. Erdmann

Preface

Lectures in Meteorology is intended as a comprehensive reference book for meteorologists and environmental scientists to look up material. The basic concept of these lectures is that all equations are derived from the physical and chemical basic equations. This concept well distinguishes these lectures from classical textbooks as it demonstrates how to derive/develop equations, which is essential for model development.

The lectures are written in module form. This means the student/instructor can address Chaps. 2 and 4 in any order. The order of Chap. 5 and 6 can be switched as well. Chapter 7 needs the understanding of Chaps. 2–5. Chapter 3 needs basics from Chap. 2. The lectures can be used at the undergraduate level for the separate classes covered by the chapters or at the graduate level as a one semester comprehensive, intensive course.

Lectures in meteorology comprises the thermodynamics, dynamics and chemistry of the troposphere. The governing conservation (balance) equations for trace constituents, dry air, water substances, total mass (equation of continuity), energy (1st law of thermodynamics), entropy (2nd law of thermodynamics), and momentum (Newton'ś 2nd axiom) are presented and explained. This presentation includes simplifications like the hydrostatic and geostrophic approximations and their application in models. Static and conditional stability criteria are explained too. Phenomena discussed include, for instance, atmospheric waves and their analytical solutions, frontal systems, hurricanes, föhn wind systems (Chinook), classical and non-classical mesoscale circulations, the global circulation and circulation systems (e.g. El Niño Southern Oscillation). Basic principles of climatology and data analysis are introduced as well. Chemical processes taking place in the atmosphere are analyzed based on kinetic processes, but thermodynamic equilibrium is also discussed. The discussion comprises, among other things, photolytic and gas phase oxidation processes, heterogeneous and aqueous chemistry, as well as gas-to-particle conversion. Fundamentals of biogeochemical cycles (e.g., CO_2, water, nitrogen, etc.) and the origin of the ozone layer are pointed out. The role of clouds in cleaning the atmosphere, in the radiation budget, and as consequence of motions, and how atmospheric processes affect the appearance of clouds are elucidated.

Cloud microphysical processes are also covered. The chapter on radiation includes solar and terrestrial radiation, major absorbers, radiation balance, radiative equilibrium, radiative-convective equilibrium, basics of molecular, aerosol, and cloud adsorption and scattering. Satellite imaginary, greenhouse gases (e.g., CO_2, H_2O, CH_4, etc.), and optical phenomena like rainbows, halos etc. are included too. Interactions of the energy, water, and trace gas cycles and their influence on general circulation and their role in climate variability and change are presented. Some aspects of numerical modeling of atmospheric, air quality and hydro-meteorological processes are discussed.

Fairbanks, USA
February 2014

Nicole Mölders
Gerhard Kramm

Contents

Acronyms

ABL	Atmospheric boundary layer
ACRIM	Active cavity radiometer irradiance monitor
AD	Anno domini
AU	Astronomic unit
AVHRR	Advanced very high resolution radiometer
BC	Before Christi
BP	Before present
CAPE	Convective available potential energy
CAT	Clear air turbulence
CCN	Cloud condensation nuclei
CIN	Convective inhibition
CFC	Chlorofluorocarbon
CTM	Chemistry transport model
DEA	Disjunct true eddy accumulation
DMS	Dimethylsulfide
ECMWF	European Centre for Medium-Range Weather Forecasts
ENSO	El Niño-Southern Oscillation
ERBE	Earth Radiation Budget Experiment
ESA	European Space Agency
FOV	Field of view
GCM	Global Circulation Model
GHG	Greenhouse gas
GMT	Greenwich mean time
GPCC	Global Precipitation Climatology Centre
GPS	Global positioning system
H	High
IN	Ice nuclei
IOM	Indian Ocean monsoon
IPCC	Intergovernmental Panel on Climate Change
IPO	Inter-decadal oscillation

IR	Infrared
ISCCP	International Satellite Cloud Climatolgy Project
ITCZ	Inter-tropical convergence zone
LCL	Lifting condensation level
LES	Large eddy simulation
LFC	Level of free convection
lidar	Light detection and ranging
LT	Local time
LTE	Local thermodynamic equilibrium
L	Low
l.h.s	Left hand side
LWC	Liquid water content
MODIS	Moderate resolution imaging spectroradiometer
NAO	North Atlantic Oscillation
NASA	National Aeronautics and Space Administration
NCAR	National Center for Atmospheric Research
NOAA	National Oceanic and Atmospheric Administration
NPO	North Pacific Oscillation
NWP	Numerical weather prediction
NWS	National Weather Service
PDO	Pacific Decadal Oscillation
PL	Prandtl layer
PM	Particulate matter
PSC	Polar stratospheric clouds
QBO	Quasi biannual oscillation
radar	Radio detection and ranging
RASS	Radio acoustic sounding system
REA	Relaxed eddy accumulation
r.h.s.	Right hand side
RTE	Radiative transfer equation
SBL	Surface boundary layer
SI	International system of units
SOA	Secondary organic aerosol
sodar	Sonic detection and ranging
SOI	Southern Oscillation Index
SORCE	Solar radiation and climate experiment
SST	Sea-surface temperature
TIM	Total irradiance monitoring
TNI	Trans-Niño Index
TOA	Top of the atmosphere
UTC	Universal time coordinated
UV	Ultra-violet
US	United States

USGS	United States Geological Survey
VIS	Visible
VOC	Volatile organic compounds
VW	Water vapor
WMO	World Meteorological Organization

Chapter 1
Introduction

Abstract This chapter defines various sub-disciplines within meteorology. It gives a motivation why humans were interested in meteorology. It provides a brief history of the development of meteorology, and illustrates how other disciplines affected the progress in meteorology. It discusses the vertical structure of the atmosphere under different aspects (temperature, pressure, composition, magnetism, ionization).

Keywords Atmospheric structure • Atmospheric composition • History of meteorology • Steps for research • Inert and reactive gases

1.1 Aspects of Meteorology

Primary tasks of meteorology are to understand the processes and phenomena in the atmosphere, explain weather, climate, air quality, climate variability and change, causal relations like water resources and availability, and their spatial and temporal variation. Thus, meteorology applies physical and chemical laws. Understanding of and research in meteorology requires basic knowledge in mathematics, physics, chemistry, statistics, computer science, and modern technologies.

Classically, atmospheric science encompasses **meteorology** (*Greek* meta = beyond, eora = suspension, logos = discourse), **aeronomy** and **climatology** as well as the physical and chemical processes in the atmosphere of other celestial bodies with an atmosphere. Meteorology encompasses **atmospheric chemistry** and **atmospheric physics** with a major focus on weather forecasting and hence modeling. Meteorology deals with the structure, composition and thermodynamic behavior of the atmosphere (Chap. 2), the transfer of electromagnetic and acoustic waves (Chap. 4), the physical processes involved in cloud- and precipitation formation and atmospheric electricity (Chap. 3), and atmospheric motion (Chaps. 6 and 7). Air chemistry encompasses photochemistry, gas phase, aqueous and aerosol chemistry, and deals with the chemical reactions, transport, and removal of atmospheric trace gases as well as air quality questions.

N. Mölders and G. Kramm, *Lectures in Meteorology*, Springer Atmospheric Sciences,
DOI 10.1007/978-3-319-02144-7_1,

Climatology deals with the long-term statistical properties of the atmosphere (e.g. mean values, range of variability, frequency of events) as a function of time and space (e.g. day, month, season, annual cycle, geographical location, altitude) and its natural and anthropogenic changes (Chap. 7). Climatology encompasses **physical climatology**, **climatography**, and **applied climatology**. Physical climatology deals with the underlying reasons for a certain **climate** (*Greek* klima = slope, zone). Climatography provides climate statistics on global, regional, and local scale. It describes which climate exists in a region on Earth. In applied climatology, climatic statistics serve to solve practical problems. Knowledge of maximum precipitation, for instance, permits engineers to construct bridges optimally. Likewise, knowledge of wind statistics allows optimizing the location for wind-energy farms or assessment which coastal areas need protection against erosion.

According to the World Meteorological Organization (WMO) climate refers to the average weather of 30 years. This means meteorological processes on all scales determine climate (Chap. 7). Climate is a time-dependent problem of various interacting processes of the atmosphere, biosphere, cryosphere, hydrosphere, and lithosphere. Therefore, a single collection of statistics from atmospheric variables alone cannot describe the climate.

The distinction between climatology and meteorology results from the long tradition of these fields developing independently. Especially, under the aspect of **climate change**, and climate impact assessment studies this separation and the exclusion of air chemistry will diminish in the future.

Aeronomy studies the upper atmospheric layers of planets, where dissociation and ionization are important. Focus is on atmospheric tides, upper-atmospheric chemistry and lightning discharges, such as red sprites, sprite halos, blue jets, and elves. Research in aeronomy uses balloons, satellites, lidars, sounding rockets, and modeling.

Since the atmosphere varies steadily, no 2 days have exactly the same weather. Consequently, we can neither reproduce experiments in the atmosphere with the exact same conditions, nor experiment with the atmosphere. Therefore, atmospheric scientists have created numerical models to use them like laboratories. Models namely permit us to include/exclude processes, vary the initial and boundary conditions and reproduce experiments.

The main methods to gain knowledge in meteorology are observations, statistical analysis, and development of theoretical concepts, developing and applying models, and defining knowledge deficits to set up new observational designs to close the identified gaps. A major difficulty is the scale problem. Processes occur at different temporal and spatial scales that interact with each other (Fig. 1.1). Furthermore, observations are often at different scales than for which equations are derived and/or valid.

Since many of the processes occurring in the atmospheric system somehow interact with other systems (e.g. ocean, land-surface, glaciers) solution of many atmospheric questions requires interdisciplinary collaboration and understanding of related or auxiliary sciences. Examples are:

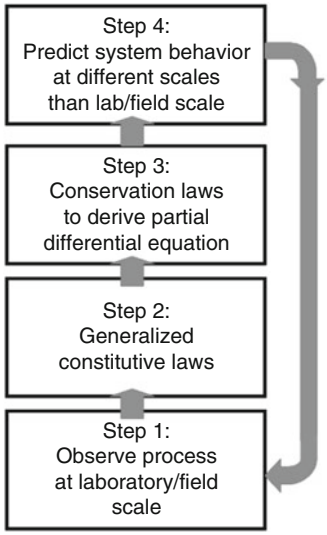

Fig. 1.1 Schematic view of knowledge development and refinement

- Numerical modeling, remote sensing techniques and some measuring techniques need knowledge from computational sciences and mathematics.
- Measuring air pollution requires knowledge of atmospheric and aerosol physics, electronics, computational sciences, and chemistry.
- Climate studies require knowledge on astronomic parameters, oceanography, biology, and glaciology.
- Reconstruction of paleo-climate bases on biological, geological, astro-geophysical knowledge, and application of physical techniques (e.g. C^{14}-method; Chap. 7).

1.2 History of Meteorology

Humans have always been concerned about weather: Sailors and millers needed knowledge on the winds; farmers worried about too few or too much precipitation or the timing of precipitation or flooding. Often laws governing atmospheric processes were not derived with better understanding the atmosphere in mind, but because of other necessities. Findings from other disciplines have been integrated, adopted and/or synthesized for use in meteorology.

1.2.1 First Steps

The concept of a global water cycle dates back at least 3,000 B.P. when King Solomon wrote that "*all rivers run into the sea, yet the sea is not full, unto the*

place from where the rivers come thither they return again" (Ecclesiates 1:7). The first known rainfall measurements by Kautilya of India in 2,400 B.P. served to determine taxes that depended on rain amount. The Babylonians provided some basic mathematics, and defined the four main directions, north, east, south, and west, and the intermediary directions northeast, southeast, southwest, northwest. The Egyptians defined weights and measures, and introduced the 365-day year.

The old Greeks contributed methodically to meteorology. Around 430 B.C, the Greeks made the first wind measurements, however, the first reliable instruments to determine wind direction and speed were not developed before the seventeenth century. About 400 B.C. Hippocrates[1] published *Airs, Waters and Places*, a study of climate and medicine. Some years later, Aristotle[2] wrote *Meteorologica*. Thales of Miletus[3] applied meteorological knowledge to predict an abundant olive crop one summer. He wisely bought all olive presses in his immediate vicinity and became a rich man, as his prediction was right. About 300 B.C. Theophrastus[4] published *On the signs of rain, winds, storms and fair weather*. Seneca[5] discussed various aspects of atmospheric phenomena in *Natural questions* which mainly based on previous works by Greek authors.

In the Middle Age, progress in meteorology stagnated. About 1170 Gerard of Cremona,[6] translated Aristotles *Meteorologica*, which finally was first printed in 1474. In 1543, Copernicus[7] published his *De revolutionibus orbium coelestium* in which he showed that the Earth is part of a vast solar system.

1.2.2 Instrument Development

The invention of meteorological instruments and introduction of meteorological observations laid the foundation of modern meteorology. Torricelli[8] built the first mercury-filled barometer in 1644. Von Guericke[9] constructed the first water-filled barometer in 1654 at Magdeburg. Based on the **pressure** (defined as the force per unit surface area due to the weight of the atmosphere) decrease measured by his barometer he predicted a strong storm. This event marked the detection of the mid-latitude storms. The aneroid barometer was invented in 1843.

---

[1] Hippocrates, Greek physician, ca. 460–370 B.C.

[2] Aristotle, Greek philosopher, 384–322 B.C.

[3] Thales of Miletus, Greek philosopher, 625–540 B.C.

[4] Theophrastus, Greek philosopher, 371–287 B.C.

[5] Seneca Greek, philosopher, 2–65 A.D.

[6] Gerardo da Cremona or Gerardus Cremonensis, Italian translator, ca. 1114–1187.

[7] Nicolaus Copernicus, German astronomer and mathematician, 1473–1543.

[8] Evangelista Torricelli, Italian mathematician and physicist, 1608–1647.

[9] Otto von Guericke, German engineer and physicist, 1602–1686.

In 1593, Galilei[10] invented the gas thermometer. Torricelli's mercury barometer led to the invention of the liquid-in-glass thermometer in the mid seventeenth century. Fahrenheit[11] and Celsius[12] developed reasonable scales for thermometers.

Hooke[13] developed a pressure-plate anemometer that measured the deflection and force of the wind on a vertically hanging metal sheet. In the seventeenth century, the first cup anemometer was developed in France. It based on the principle of windmills that were used since 644 A.D. in Persia.

Based on ideas of Cryfts[14] da Vinci[15] invented the basic principle of the hygrometer, an instrument to measure humidity.

Assmann[16] invented the aspiration psychrometer that still is widely used to measure water-vapor content. He also introduced rubber balloons to measure wind velocity by following the balloons by theodolite. After WWII the use of radar simplified the tracking of the weather balloons. Today, radiosondes use GPS.

1.2.3 Finding Physical Laws

In 1661, Boyle[17] and Mariotte[18] came up with the first law on the nature of gases. In 1687, Newton[19] formulated the laws of mechanics. In the eighteenth century, Pitot,[20] Bernoulli,[21] Euler,[22] Chézy,[23] and other Europeans considerably advanced the applications of mathematics to fluid mechanics and hydraulics. In 1752, for example, Euler derived the equations of fluid motion.

In 1787, Dalton[24] started a meteorological diary that he continued all his life. His about 200,000 observations are one of the first modern meteorological time series. Routine network measurements of precipitation began before 1800 in Europe and the United States of America and by 1820 in India.

---

[10] Galileo Galilei, Italian mathematician, physicist and astronomer, 1564–1642.

[11] Daniel Gabriel Fahrenheit, German physicist and maker of scientific instruments, 1686–1736.

[12] Andres Celsius, Swedish astronomer, 1701–1744.

[13] Robert Hooke, English natural philosopher and polymath, 1635–1703.

[14] Nicolas Cryfts or Nicholas of Cusa, German cardinal, 1401–1464.

[15] Leonardo da Vinci, Italian artist, 1452–1519.

[16] Richard Aßmann, German meteorologist and physician, 1845–1915.

[17] Sir Robert Boyle, British physicist and chemists, 1776–1856.

[18] Edme Mariotte, French physicist, 1620–1684.

[19] Sir Isaac Newton, British physicist, mathematician and astronomer, 1643–1727.

[20] Henri de Pitot, French inventor and hydraulician, 1695–1771.

[21] Johann Bernoulli, Swiss mathematician, 1667–1748.

[22] Leonhard Euler, Swiss mathematician, physicist and astronomer, 1707–1783.

[23] Antoine de Chézy, French hydraulician, 1717–1798.

[24] John Dalton, British chemist and physicist, 1766–1844.

In the age of steam engines, Poisson,[25] Clausius,[26] Benoit,[27] and Carnot[28] formulated important thermo-dynamical laws. In 1811, Avogadro[29] published the hypothesis that gases containing the same number of molecules occupy the same volumes at the same temperature and pressure.

In 1835, de Coriolis[30] introduced a theory describing the behavior of bodies in motion on a spinning surface. By mathematical calculations, he showed that the path of any object moving on a rotating body curves in relation to the rotating surface. This apparent force is called **Coriolis force**.

Stokes[31] and Navier[32] independently from each other contributed to the progress of dynamics by deriving the friction laws and equation of motion. The Navier-Stokes equations characterize the behavior of flows in Newton[33] fluids and gas mixtures[34] in form of the principle of momentum, i.e. the dependency of velocity and pressure in space and time. Until today, no general solution for these non-linear partial differential equations exists.

Being the captain of HMS Beagle during Charles Darwin's famous voyage FitzRoy[35] made detailed weather observations that later led to the establishment of meteorology as a science discipline.

Buys-Ballot[36] derived and published rules for weather prediction (*Regelen voor de wachten van weerveranderingen* 1860), and developed the first European storm-warning system. In 1905, Ekman[37] brought up the first mathematical solution of a simple atmospheric motion.

Aitken[38] pointed out the role of small particles (**Aitken nuclei**) in cloud droplet condensation.

Boltzmann[39] proved experimentally the electro-magnetic light theory and explained the radiation law found by Stefan.[40] By using probability calculations, he

[25] Simeon Denis Poisson, French mathematician and physicist, 1781–1840.

[26] Rudolf Julius Emanuel Clausius, German physicist, 1822–1888.

[27] Pierre-Emile Benoit, French technician and physicist, 1799–1864.

[28] Nicolas Leonard Sadi Carnot, French engineer and physicist, 1796–1832.

[29] Amedo Lorenzo Romano Avogadro, Italian physicist and chemist, 1776–1856.

[30] Gaspard Gustave de Coriolis, French physicist and engineer, 1792–1843.

[31] Sir George Gabriel Stokes, English mathematician and physicist, 1819–1903.

[32] Claude Louis Marie Henry Navier, French physicist, 1785–1836.

[33] Sir Isaac Newton, English physicist, mathematician, astronomer, natural philosopher, alchemist and theologian, 1643–1727.

[34] Water and air.

[35] Robert FitzRoy, Vice-Admiral, meteorologist, hydrographer, Governor of New Zealand from 1843 to 1845, 1805–1865.

[36] Henricus Didericus Christophorus Buys-Ballot, Dutch meteorologist, 1817–1890.

[37] Valfried Ekman, Swedish oceanographer and physicist, 1861–1930.

[38] John Aitken British, physicist and meteorologist, 1839–1919.

[39] Ludwig Boltzmann, Austrian physicist, 1844–1906.

[40] Josef Stefan, Austria Slovene physicist, mathematician and poet, 1835–1893.

explained the relation between thermodynamics and mechanics and was the first to apply statistical laws to gas molecules.

1.2.4 Towards Modern Meteorology

The first half of the twentieth century brought great advances in turbulence and **atmospheric boundary layer** (ABL) physics (e.g. Prandtl,[41] Heisenberg,[42] Monin, Obukov). Prandtl formulated the ABL and turbulent flow theories with the **Prandtl number** as a parameter. He introduced the wind tunnel for experiments on flows and boundary-layer processes. During his time as a British war prisoner, Heisenberg worked on the theory of statistical and isotropic turbulence. He pointed out that viscosity reduces the degrees of freedom because it damps all motion into small eddies. He showed that turbulence can be described without going into much mechanical detail just by applying similarity theory. Monin and Obukov developed the similarity theory known as Monin-Obukov similarity hypothesis, usually applied in ABL physics (Chap. 6).

In 1884, Köppen[43] published a world climatology that he modified notably in 1918 and 1936. Later, he collaborated with Geiger[44] on improving the classification system that today is known as the **Köppen-Geiger climate classification system** (Chap. 7).

Thornwaite[45] and Penman contributed to understanding climate aspects of evapotranspiration. In 1931, Thornthwaite published a system to classify the world's climates. In the same year, Piccard[46] made the first, but foggy photos on cloud distributions from their stratospheric balloon. In the following year, introducing a red filter led to improved photos.

Charney[47] developed the quasi-geostrophic vorticity equation to describe the large-scale motion of planetary flows. Rossby[48] described large-scale wave characteristic of the circumpolar upper atmospheric flow and found the principles on eddy phenomena and atmospheric turbulence. The theory of Rossby and Charney on planetary waves builds the fundamentals of our understanding of the general circulation and weather forecasting.

---

[41] Ludwig Prandtl, German engineer and physicist, 1875–1953.

[42] Werner Karl Heisenberg, German physicist, 1904–1976.

[43] Wladimir Köppen, Russian climatologist, 1846–1940.

[44] Rudolf Geiger, German climatologist, 1894–1981.

[45] Charles Warren Thornthwaite, American geographer, 1899–1963.

[46] Auguste Piccard, Swiss physicist, 1884–1962.

[47] Jule Gregory Charney, American meteorologist, 1917–1981.

[48] Carl-Gustaf Rossby, Swedish-American meteorologist, 1898–1957.

After the Great War, Bjerknes[49] and his co-workers formulated the frontal theories and developed synoptic meteorology. He developed the idea of weather forecasting based on the laws of physics, but did not believe that prognostic meteorological equations could be solved analytically. Thus, he developed the graphical calculus technique that was operated on observations to forecast the weather.

Richardson[50] developed a different technique between 1913 and 1919 wherein equations were simplified before solving them numerically by hand. He published his work in a book (*Weather Prediction by Numerical Processes, London, Cambridge University Press, 1922*). At that time, his work was ignored until 1946 because of the computational effort. Then von Neumann[51] who was involved in the development of the first electronic computer, made weather forecasting its main application. Finally, in 1950, the first computer-based weather prediction was made. In 1956, Phillips performed the first successful numerical simulation of the general circulation of the atmosphere. Since then General Circulation Models (GCM) and later climate models have been developed. More and more aspects of the Earth System have recently been added to better describe and understand the interactions between the various systems and climate, climate variability and climate change.

Around 1960, satellites become available for monitoring of weather and short-term weather forecasting. Since the monitoring of weather from satellites, no tropical storm keeps undetected. Satellites improved the short-term weather prediction (**nowcasting**) and the knowledge on climatology.

1.2.5 Air Pollution

Natural pollution stems from wildfires, volcanic eruptions, meteorite impacts and strong winds. Anthropogenic pollution existed already early in history in any urban area due to combustion. Before the twentieth century, air pollution was rather treated as a regulatory problem than science. In Great Britain, the emissions of steam engines and furnaces led to the Public Health Act in 1848, and the emission of hydrogen chloride in the soap producing process to the Alkali Act in 1863. Any regulation reduced marginally the pollution, but led to the development of instruments to control the pollution and models to examine regulatory strategies numerically.

[49] Vilhelm Bjerknes, Norwegian meteorologist and physicist, 1862–1951.

[50] Lewis Fry Richardson, British physicist and chemist, 1881–1953.

[51] John von Neumann, American mathematician, 1903–1957.

The term **smog** was coined in 1905 by Des Voeux[52] to describe the mixture of fog and smoke he observed in British cities. Later this term was applied to the air pollution in cities like Los Angeles. However, this smog stems from ozone formation (Chap. 5). Due to the different origin of these smog types, we today speak of **London-type smog** and **Los Angeles-type smog**.

Between 1950 and 1970, first air quality models were developed. In the 1970s, three-dimensional Chemistry Transport Models (CTM) or photochemical air-quality models became available to predict the gas chemistry, transport, and deposition using meteorological observation and emissions as input data (Chap. 5). In the 1980s, numerical weather prediction (NWP) models were used as preprocessors to drive the CTMs. Heterogeneous and aerosol chemistry as well as wet deposition were introduced. The amount of trace gases considered increased the initialization problem. For application in Europe, a main problem was the reliability of emission data from the Eastern Block countries at the time of the Cold War. In the late 1990s, first fully integrated CTM that simultaneously simulate the meteorological and chemical conditions were developed. Not before the Millennium, the available computers permitted real time air-quality forecasts.

1.3 Atmospheric Composition

Planets having enough gravity can hold an atmosphere, i.e. a gaseous envelope surrounding the planet. Atmospheres have a central role in the transfers of energy between the Sun and the planet's surface and from one region to another. These transfers maintain equilibrium and determine the planet's climate (Chap. 7).

The Earth's atmosphere consists of a mixture of gases, and suspended liquid and solid particles (e.g. drops, ice crystals, aerosols). The main constituents of the Earth's atmosphere are nitrogen (N_2), oxygen (O_2), Argon (Ar), water vapor (H_2O), and carbon dioxide (CO_2) whose concentration except water vapor hardly vary.

It is common to use only the main constituents of **dry air** (N_2, O_2, Ar, and CO_2) that make up a volume of nearly 1 (Table 1.1). **Trace gases** (e.g. CH_4, NO_2, NO, O_3) correspond to a volume fraction of $3 \cdot 10^{-5}$ (cf. Table 1.1). Their concentrations differ in space and time (e.g. Fig. 1.2) depending on their various sources and sinks. Despite of their low concentrations trace gases are important for atmospheric chemistry, the thermodynamic structure of the atmosphere, and life. The radiatively active constituents, CO_2, CH_4, N_2O, CO, H_2O (liquid water, ice, water vapor) are often addressed as **greenhouse gases** (Chap. 4). Radiatively active trace gases absorb and re-radiate the long-wave infrared (terrestrial) radiation back to the Earth (Chap. 4), i.e. they are energetically relevant. Thus, radiatively active constituents affect climate, when their concentration changes. It also means that any emission-control measures also affect climate (Chaps. 5 and 7).

[52] Harold Antoine Des Voeux, French, 1834–1909.

Table 1.1 Composition of the Earth's atmosphere below 100 km. The letter v and quotation marks indicate varying concentrations depending on distance to sources and sinks, and unknown lifetime, respectively. p_i/p indicates the ratio of partial pressure to pressure (Chap. 2)

Constituent	Molecular mass (10^{-3}kg mol^{-1})	Content/concentration	Lifetime
Dry air	28.97	1	$1.6 \cdot 10^7$ year
Nitrogen (N_2)	28.01	0.7808 p_i/p	∼10,000 year
Oxygen (O_2)	32	0.2095 p_i/p	3,000–10,000 year
Argon (Ar)	39.95	0.0093 p_i/p	?
Carbon-dioxide (CO_2)	44.01	0.0004 p_i/p	3–4 year
Hydroxyl radical (OH)	17.01	Very low	∼s
Nitrate (NO_3)	62.0049	Very low at day	∼10 s at day
Hydroperoxyl[a] (HO_2)	33.01	Low	∼100 s
Methyldioxy radical (CH_3O_2)	47.03348	Low	∼min
Isoprene (C_5H_8)	68.11702	v	∼h
Nitrogen oxide	30.01	v	∼days
$NO_x = NO + NO_2$	46.0055		
Hydrogen peroxide (H_2O_2)	34.0147	v	days
Sulfur dioxide (SO_2)	64.066	v	days
Water vapor H_2O	18.02	0-0.04 p_i/p	8–10 days
Aerosols	v	v	1–2 months
Carbon-monoxide (CO)	28.01	$9.0 \cdot 10^{-8}$ p_i/p	∼60 days
Ozone (O_3)	48.00	$4.0 \cdot 10^{-8}$ p_i/p	100 days
Bromomethane[b] (CH_3Br)	94.9387	v	∼1 year
Methane (CH_4)	16.04	$1.7 \cdot 10^{-6}$ p_i/p	9 year
Methyl chloroform (CH_3CCl_3)	133.40	v	years
Nitrous oxide (N_2O)	44.013	v	>10 year
CFC	120.91	v	>80 year
Neon (Ne)	20.18	$1.8 \cdot 10^{-5}$ p_i/p	?
Helium (He)	4.003	$5.2 \cdot 10^{-6}$ p_i/p	10^6 year
Krypton (Kr)	83.80	$1.1 \cdot 10^{-7}$ p_i/p	?
Hydrogen (H_2)	2.02	$5 \cdot 10^{-7}$ p_i/p	∼253 year
Xenon (Xe)	131.30	$8.7 \cdot 10^{-8}$ p_p/p	∼107 year

[a] Hydroperoxylis also known as perhydroxyl radical

[b] Bromomethane is also known as methyl bromide. It was used in pesticides, but phased out in 2000

1.3.1 Gases with Quasi-constant Concentration

1.3.1.1 Nitrogen

Gas-phase molecular nitrogen is produced biologically in the soil (Chap. 5). In anerobic soils, nitrogen denitrification leads to N_2 formation. Since N_2 undergoes no significant chemical reactions in the atmosphere, and because its removal process is marginally slower than the production, its concentration has built up over time.

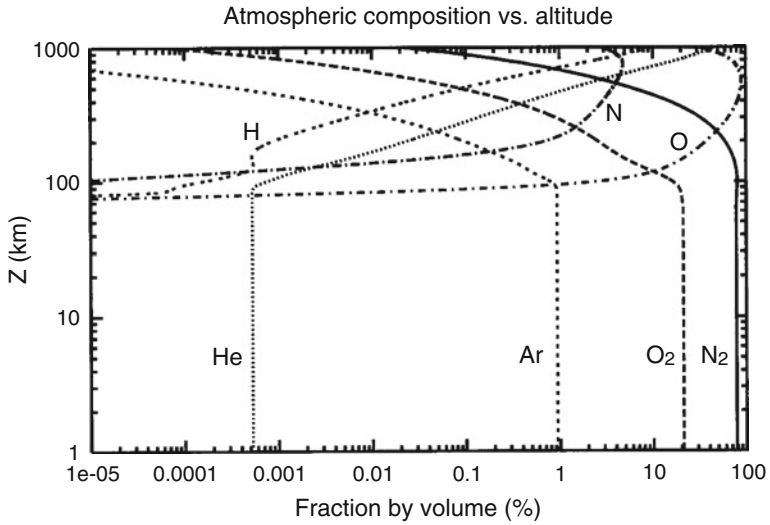

Fig. 1.2 Vertical distribution of various atmospheric gases (From Petty (2008))

The vertical distribution of nitrogen is homogeneous and vertical mixing is the controlling process.

1.3.1.2 Oxygen

Vegetation produces oxygen by photosynthesis. Since the great oxidation event occurred, O_2 concentrations built up over time. The vertical distribution of oxygen is homogeneous and controlled by vertical mixing. According to estimates the entire atmospheric O_2-content undergoes photosynthesis in about 10,000 years. Oxygen is important for life as it enables the formation of the ozone layer (Chap. 5).

1.3.2 Gases with Variable Concentrations

In contrast to the noble gases like argon, neon (Ne), helium (He), krypton (Kr), and xenon (Xe) that do not react chemically, the concentrations of many atmospheric chemically reactive gases vary in time and space.

1.3.2.1 Carbon Dioxide, Carbon Monoxide, and Hydrocarbons

Carbon dioxide (CO_2) results from combustion, soil processes, oceanic evaporation, and various organic processes. Plants continuously consume CO_2 through photosynthesis, and the oceans can dissolve considerable amounts of CO_2. Since

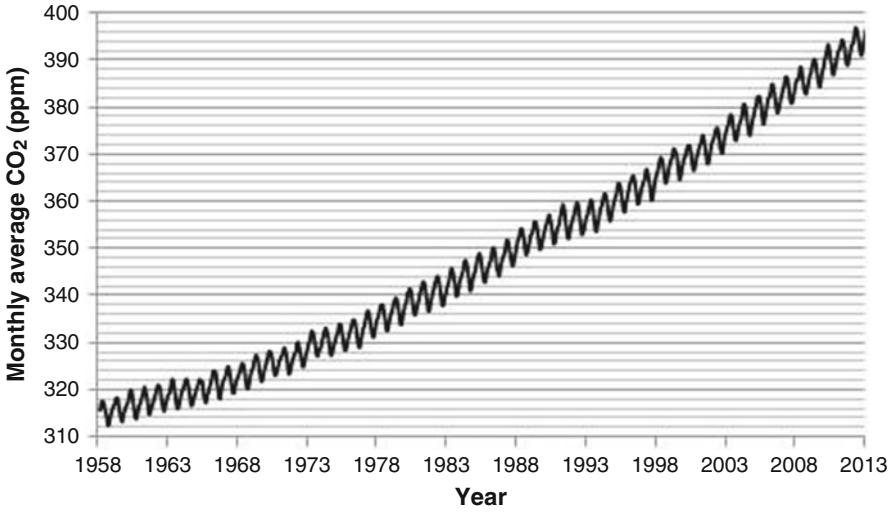

Fig. 1.3 Increase of monthly mean CO_2 concentrations at Mauna Loa Observatory in Hawaii (Data from http://co2now.org/images/stories/data/co2-atmospheric-mlo-monthly-scripps.xls (2014))

1900, the CO_2 concentration has increased by about 25 % from 296 to 393 ppm in 2012 (Fig. 1.3).

Hydrocarbons, including those released from vegetation, are oxidized through pathways involving carbon monoxide (CO) oxidation (Chap. 5; Fig. 5.9). Consequently, high carbon monoxide and ozone concentrations may exist over forested regions. Concentrations of CO are higher in the northern hemisphere, presumably due to the greater land-mass and the stronger anthropogenic activity (e.g. industrial combustion, biomass burning) than in the southern hemisphere. Due to its moderate lifetime CO is often used as a tracer for wildfire smog propagation. CO plays a role in the oxidation of methane.

1.3.2.2 Ozone

Ozone (O_3) varies strongly in space and time (Fig. 1.4) due to chemical, radiative, and dynamic processes. At a height between 16 and 25 km, light of wavelengths less than 190 nm breaks the bonds between the atoms of O_2. The free oxygen atoms collide and bind with normal oxygen molecules to form ozone. The speed of formation increases by a neutral molecule M, usually nitrogen, that acts as a catalyst (Chap. 5).

Although the photochemical production of ozone is the greatest at the equator, the density of the ozone layer is the thickest at the poles (Fig. 1.4) due to transport processes (Chap. 6). Since the 1980s, measurements showed a significant decrease

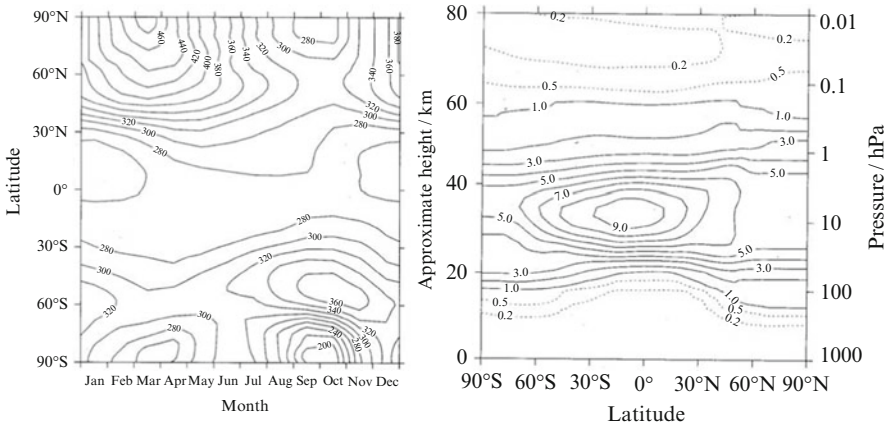

Fig. 1.4 Ozone-concentration distribution (*left*) column integrated (in $Dobson$) annual cycle based on a 5-year climatology and (*right*) zonal mean volume mixing (ppm) as a vertical cross section for January based on the same climatology (Permission Andrews (2010))

of the stratospheric ozone layer at the poles. Here **chlorofluorocarbons** (CFC) and reaction with NO destroy ozone (Chap. 5). The decline of O_3 results in an increased flux of UV-radiation to the Earth's surface and lowers stratospheric temperatures. The former may harm life, while the latter may alter the global energy balance.

Below 10 km or so, some ozone originates from downward transport by a dynamic process called **tropospause folding** or downward mixing due to high-reaching thunderstorm clouds. Below this height, most ozone forms in conurbations by photochemical reactions. Since lower in the atmosphere, less UV-light is available (Chap. 4), ozone production is slower than above 10 km.

Ozone O_3 and hydroxyl radicals OH make up the primary species that oxidize many trace gases to CO_2, HNO_3, and H_2SO_4 which are removed from the atmosphere as dissolved constituents by rainfall (Chap. 5). OH plays a key role in eliminating some greenhouse gases (GHG), e.g. methane, ozone. Since ozone is highly reactive, it destroys macro-molecules and is harmful to health.

1.3.2.3 Nitrogen Compounds

Oxides of nitrogen like NO_2 (nitrogen dioxide) and NO (nitrogen oxide) are relevant for ozone photochemistry. Anthropogenic sources for $NO_x = NO + NO_2$ are traffic, heating, and industrial processes. Natural sources of NO_x are wildfires and lightning discharges. Aircraft exhaust also releases NO. The lifetime of NO_2 is about 0.5–2 days. Since NO is highly reactive, only a small amount of the released NO reaches heights where it can contribute to destruct the ozone shield by catalytic processes (Chap. 5).

Nitrogen oxide N_2O is primarily produced by soil bacteria and emitted from soils. Combustion of fossil fuels and use of fertilizers emit N_2O, a radiatively active

trace gas. N_2O is homogeneously distributed below 10 km or so. Above that height, it decreases due to dissociation. The lifetime is about 150 years (Table 1.1).

Domestic animals and calcareous desert soils emit ammonia, NH_3. Its major sinks are heterogeneous reactions and removal by rain (Chap. 5). Since NH_3 is very water soluble, its atmospheric concentration varies with relative humidity.

1.3.2.4 Methane and Chlorofluorocarbons

Cattle, coalmines, oil dwells, gas pipelines, thawing of permafrost and bacterial activity in rice fields emit methane. In the last decades, CH_4 concentrations have increased by about 0.01 ppm year^{-1}. Methane effectively absorbs thermal radiation (Chap. 4). Oxidation of CH_4 produces H_2O.

Chlorofluorocarbon (freons, CFC) is an organic compound containing carbon, chlorine, and fluorine. It is produced as a volatile derivative of ethane and methane as aerosol propellants, solvents, and refrigerant. Two types of CFC exist, $CFC-12$ (CF_2Cl_2) and $CFC-11$ ($CFCl_3$) with atmospheric residence times of more than 80 years and about 80 years, respectively, in the troposphere. In the stratosphere, decomposition of CFCs by photochemical reactions produces chlorine (Cl) that catalytically destroys ozone (Chap. 5).

1.3.2.5 Water Vapor, Water, and Ice

Atmospheric water vapor results from evaporation of water from oceans and continents and transpiration by plants. Water in all phases cycles between the ocean and the various atmospheric and terrestrial reservoirs. On average, water vapor resides 8–10 days in the atmosphere. Near-surface water-vapor content ranges from less than 1 % per volume of the atmosphere over desert and polar regions to about 4 % in the Tropics (Table 1.1). Water-vapor concentration usually decreases rapidly with altitude and most water vapor exists below 5 km.

When the atmosphere becomes saturated, the excess water vapor condenses and/or deposits to form cloud droplets and/or ice crystals. During phase transitions, latent heat of condensation/deposition is released that warms the atmosphere. Evaporation, melting, and sublimation consume energy and cool the atmosphere (Chaps. 2 and 3). Due to the release of latent heat and consumption of heat during phase transition processes and the related change in temperature, water vapor is energetically relevant.[53] All phases of water affect atmospheric radiation (Chap. 4). Cloud water, rainwater and solid precipitation may remove pollutants from the atmosphere. This means the atmospheric water-, energy-, and trace-gas cycles are linked (Chaps. 4 and 5).

[53] Chemical reactions among trace gases are not energetically relevant (Chap. 5).

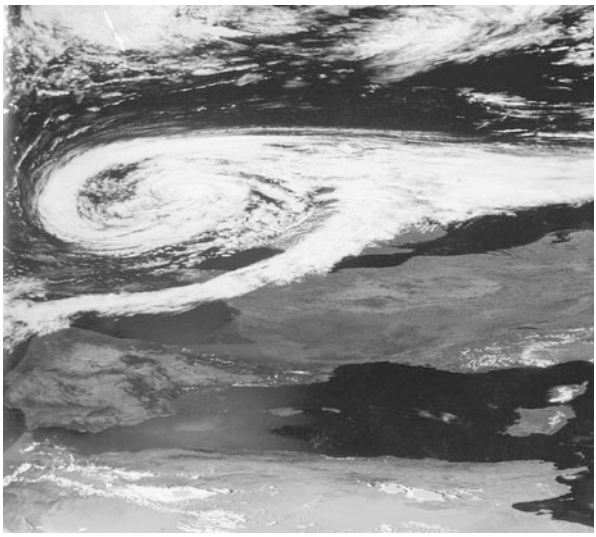

Fig. 1.5 Saharan dust over the Mediterranean Sea north off Africa as captured by the Advanced Very High Resolution Radiometer (AVHRR) (Data processed by N. Mölders)

1.3.2.6 Aerosols

The term **aerosol** refers to solid and liquid particles suspended in the atmosphere. Aerosols are atmospheric particles with sizes ranging from thousands of a micron to several hundred microns, and cover the nucleation, accumulation and coarse-particle mode (Chap. 5). The terms **nucleation mode** and **accumulation mode** denote the mechanical and chemical processes respectively that produce particles in these two size ranges. In the nucleation mode, the particles are the smallest. The largest mass and number of particles occur in the accumulation or coarse-particle mode due to the lack of efficient removal mechanisms for these particles.

Natural aerosols stem from sea spray, uptake of silicates, wildfires and from organic or volcanic sources (Fig. 7.38). Anthropogenic aerosols result from combustion. They can be directly emitted, build in the air by **gas-to-particle conversion** (Sect. 5.4), or result from evaporation of cloud droplets. Gas-to-particle conversion denotes physio-chemical reactions involving among other precursors (Chap. 5). Aerosols in this coarse-particle mode typically stem from mineral dust and ash fly from biomass burning.

The different sources for aerosols result in different spectra and kinds of aerosols over the continents and oceans. The mean aerosol concentration amounts to $10^7-10^8\,m^{-3}$ at a saturation of 0.1–10 % over the oceans, while it is an order of magnitude greater ($10^8-10^9\,m^{-3}$) over the continents. Even over the oceans or continents, strong variations in the aerosol distribution exist in space and time. Aerosol concentrations are high in the lee-side of conurbations because of the industrial sources. Wind may take up desert sand (Fig. 1.5), for which in their downwind, silicates are the major contributors to the total aerosol. Aerosols can be transported over long-distances. In March, Alaska often experiences layers composed of aerosol of North European, Siberian or Asian origin.

Aerosols affect the atmospheric energy and water balance (Chap. 4) as well as cloud and precipitation formation (Fig. 3.4; Chap. 3). Due to their different origins aerosols differ in hydroscopic properties. Suspension of liquid and solid particles is relevant to chemical, radiative and cloud physical processes. Aerosols can act as **cloud condensation nuclei** (CCN), and **ice nuclei** (IN) play a role in heterogeneous chemistry when multiple phases are involved. Aerosols scatter solar radiation at visible (VIS) wavelengths and absorb infrared (IR) radiation emitted by the Earth's atmosphere and surface. Sporadic increases of aerosols after great volcanic eruptions lead to changes in optical, thermal, and chemical properties of the atmosphere.

1.4 Vertical Structure of the Atmosphere

We can describe the vertical structure of the atmosphere by its composition, thermal state, pressure (force per area), escape velocity, ionization, and the strength of the magnetic field (Fig. 1.6).

1.4.1 Classification by Composition

In the absence of sources and sinks, two competing processes determine the gaseous composition of the atmosphere: **mixing** and **molecular diffusion**. Mixing due to fluid motion is a **macroscopic process** (Chap. 2). Herein interaction among

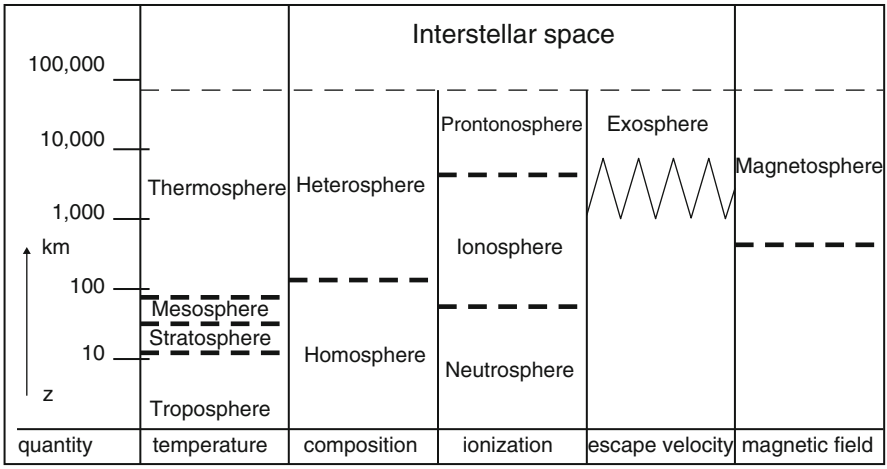

Fig. 1.6 Schematic view of the vertical structure of the atmosphere with respect to its various characteristics

individual gas molecules is negligible, i.e. mixing affects all gases independent of their molecular weight. Diffusion by random molecular motions leads to an atmosphere in which the mean molecular weight of the gas mixture decreases gradually with height. Consequently, each constituent behaves as if it exists alone. Thus, the density of each gas decreases exponentially with height and each gas has its own scale height (Sect. 2.3), which is inversely proportional to the molecular weight.

From the Earth's surface to an altitude of about 100 km mixing predominates. Constituents are well-mixed for which this region is called the **homosphere** (*Greek* homoios = equal, of similar kind).

At about 100 km, mixing and molecular diffusion have nearly the same importance. This level of the transition from mixing and to molecular diffusion dominated is called the **turbopause**.

Above 100 km, molecular diffusion prevails leading to a heterogeneous atmosphere called the **heterosphere**. Here, the gases form four roughly spherical shells of distinct composition around the Earth. In the lowermost layer, molecular nitrogen dominates. In the next layer above about 120 km, atomic oxygen prevails, followed by a layer around 500 km dominated by atomic oxygen, with traces of diatomic nitrogen, helium and hydrogen atoms. The fourth zone located above 1,000 km mainly consists of helium and hydrogen atoms.

1.4.2 Classification by Temperature

Temperature characterizes the thermal condition of the atmosphere and is proportional to the average kinetic energy of the air molecules. In the **troposphere** (*Greek* trepin = turn around), usually temperature decreases with height. The temperature decrease with height is called the **environmental lapse rate** (Chap. 2). The lapse rate[54] is usually derived from radiosonde data. The lapse rate can be highly variable depending on the time of day, fluctuation with weather, season, and location (Chap. 2). The temperature profile is closely related to the absorption and emission of radiation at the Earth's surface, the radiation budget, and the resulting atmospheric fluxes of sensible and latent heat (Chap. 4).

The troposphere is subdivided into the ABL and the **free atmosphere**. In the ABL, temperature varies significantly with the diurnal cycle and depends on the thermal characteristics of the underlying surface and the exchange of energy at the surface-atmosphere interface. The free atmosphere is influenced by the ABL on the longer time scale. In the free atmosphere, typically temperature decreases with height with an average environmental lapse rate of $0.65\,^{\circ}\mathrm{C}\,10^{-2}\,\mathrm{m}^{-1}$ (normal lapse rate). Occasionally **temperature inversions** (Chap. 2) may occur where temperature increases with height over a shallow layer.

[54] The definition of lapse rate yields a positive algebraic sign.

Weather mainly occurs in the troposphere. Strong mixing, cloud- and precipitation formation characterize the troposphere (Chap. 3). On average, the troposphere reaches to about 8, 10, and 16 km height in Polar Regions, mid-latitudes, and the Tropics, respectively (Chap. 7).

The region at which the lapse rate decreases to $2\,\mathrm{K\,km^{-1}}$ or less and does not exceed this value in the next 2 km is defined as **tropopause** (*Greek* pauein = stop, end). This means nearly isothermal conditions characterize the tropopause. The major physical processes at and near the tropopause are radiation, convection, turbulence, advection and vertical convergence. Radiation usually smoothes the temperature profile. So does turbulence unless the fluxes have a certain relationship to hydrostatic stability. Convection is infrequent and unimportant in establishing the tropopause. Observations and the principle of continuity indicate that advection and vertical convergence are not the universal mechanisms for tropopause formation.

In the layer above the tropopause, called the **stratosphere** (*Greek* stratus = layered), temperature increases to about 45 km height where the **stratopause** is located. Low water content, nearly no clouds and high ozone concentration characterize the stratosphere. The temperature maximum at the stratopause results from radiation absorption by ozone. Here, on average, the temperature amounts to −3 °C on global average, −24 °C for the winter pole, and 12 °C for the summer pole.

The following layer of decreasing temperature is called the **mesosphere** (*Greek* for in between). It reaches to the **mesopause** in about 85 km height.

The mesopause is followed by the **thermosphere**. In the thermosphere, temperature increases with height due to absorption of solar radiation in combination with dissociation of diatomic nitrogen and oxygen molecules and stripping of electrons. In the thermosphere, temperature is defined by the mean distance between the molecules because of the low atmospheric **density** (density is the mass per unit volume). Temperature depends on Sun activity (about 600 K for a quite, 2,000 K for an active sun). Temperature reaches about 1,000 K at 400 km height and then remains constant to about 800 km. Atmospheric tides govern the dynamics of the mesosphere and lower thermosphere.

Example. On a spring day an air temperature T_{SL} of 10 °C was observed close to the surface at a station at sea level. Calculate the tropopause height z_T assuming the vertical sounding reveals a nearly constant environmental lapse rate of $0.65\,^{\circ}\mathrm{C}\,10^{-2}\,\mathrm{m^{-1}}$ and the temperature at the tropopause T_T is −55 °C. Discuss your result.

Solution. Phrasing the problem into an equation yields $T_T = T_{SL} - \frac{0.65\,^{\circ}\mathrm{C}}{100\,\mathrm{m}} z_T$ and $-55\,^{\circ}\mathrm{C} = 10\,^{\circ}\mathrm{C} - \frac{0.65\,^{\circ}\mathrm{C}}{100\,\mathrm{m}} z_T$. Rearranging and calculating provide $z_T = 10{,}000\,\mathrm{m}$, which is a typical tropopause height in mid-latitudes.

1.4.3 Classification by Pressure

The atmosphere exerts a downward force on the Earth's surface because of the Earth's gravitational field (Chap. 2). At mean sea-level height, the average pressure[55] is 1,013.25 hPa. Pressure exponentially decreases with height (Sect. 2.3). Fifty percent of the atmosphere is below 5.6 km; at 16 km, 90 % of the atmosphere are traversed. About 99 % of the atmospheric mass exist below 30 km. Above 100 km only 0.00003 % of the atmosphere are located. Here the atmosphere is so thin and its density is low like in the most-perfect artificial vacuum achievable at the surface.

Example. Estimate the mean atmospheric pressure averaged over the globe assuming a total mass of the atmosphere of $M = 5.14 \cdot 10^{18}$ kg, a mean radius of the Earth of $R = 6.37 \cdot 10^{6}$ m and an acceleration of gravity of $g = 9.81\,\mathrm{m\,s^{-2}}$.

Solution. By using the definition of pressure $\frac{M\,g}{4\,\pi R^2}$ we obtain $p = \frac{5.14 \cdot 10^{18}\,kg\,9.81\,\mathrm{m\,s^{-2}}}{4 \cdot 3.14 \cdot (6.37 \cdot 10^{6}\,\mathrm{m})^2} \sim 98{,}938\,\mathrm{Pa}$

Pressure and density more strongly vary in the vertical than in the horizontal direction or in time. Therefore, it is practical to define a **standard atmosphere** (Chap. 2, Table 2.2) that represents the horizontally and temporally averaged vertical profile of the atmosphere. At any height up to 100 km, the atmospheric pressure is typically within 30 % of the corresponding standard atmosphere value.

1.4.4 Classification by Escape Velocity

The Earth's current atmosphere mainly consists of molecules that move too slowly to escape to space. The relation between the velocity of a molecule and temperature can serve to calculate a **probable escape velocity** of any molecular species

$$v_{probable} = \sqrt{\frac{2kT}{Mm}} \tag{1.1}$$

where $k(= 1.38 \cdot 10^{-23}\,\mathrm{J\,K^{-1}})$ is the **Boltzmann constant**, T is the absolute temperature (K), M is the molecular weight, and m is the mass of an atom. Equation (1.1) provides species and height dependent probable escape velocities

[55] An average pressure of 1,000 hPa = 1,000 kg m^{-1} s^2 is often denoted to as 1 atm in atmospheric chemistry.

Fig. 1.7 Aurora borealis with massive green arc and curtain display. Black and white version of Curtis' original photo (The color version can be found at http://www.geo.mtu.edu/weather/aurora/images/aurora/jan.curtis/janc_004.jpg (retrieved 2002). Reproduced by permission of Jan Curtis)

The probable escape velocity may exceed the **escape velocity** ($\approx$11.2 km s^{-1}), i.e. the speed at which a molecule overcomes gravitational attraction.[56] Under conditions of a quite Sun, the probable escape velocity for a hydrogen atom ($m = 1.67 \cdot 10^{-27}$ kg) is about 1,006 km s^{-1}. The term **exosphere** denotes the layer where atoms may escape to space.

1.4.5 Classification by Ionization

Between 80 and 400 km, an electrically charged layer exists, the **ionosphere** (Fig. 1.6). Molecules of nitrogen (N_2) and oxygen (O_2) and oxygen atoms (O) absorb X-ray and ultraviolet radiation from the Sun and ionize (Chaps. 4 and 5). Ionization means that each affected molecule loses one or more of its electrons and becomes a positively charged ion. The electrons are set free to travel as electric current. Gases become excited meaning that the electrons jump to a greater distance from the atom nuclei. When falling back to a lower orbital distance from the nuclei, radiation is emitted visible as aurora (Fig. 1.7).

Since N_2, O_2 and O emit at different colors, auroras come in a variety of colors depending on solar activity. Around 100 km, nitrogen molecules cause reddish

[56] For a molecule to escape from the atmosphere its kinetic energy must exceed the potential energy required to lift the molecule out of the gravitational field. With $F_{gravitational} = \gamma \frac{m_1 \cdot m_2}{R^2}$. Here m_1 and m_2 are the masses of the molecule and the Earth, $\gamma = 6.67 \cdot 10^{-11}$ m^3 kg^{-1} s^{-2} is the gravitational constant, and $R \approx 6{,}371$ km is the Earth radius. With the kinetic energy $E_{kin} = \frac{1}{2} m_1 v^2$ we obtain after rearranging $v_{escape} \approx$11.2 km s^{-1}. This means that the escape velocity is independent of the mass of the molecule.

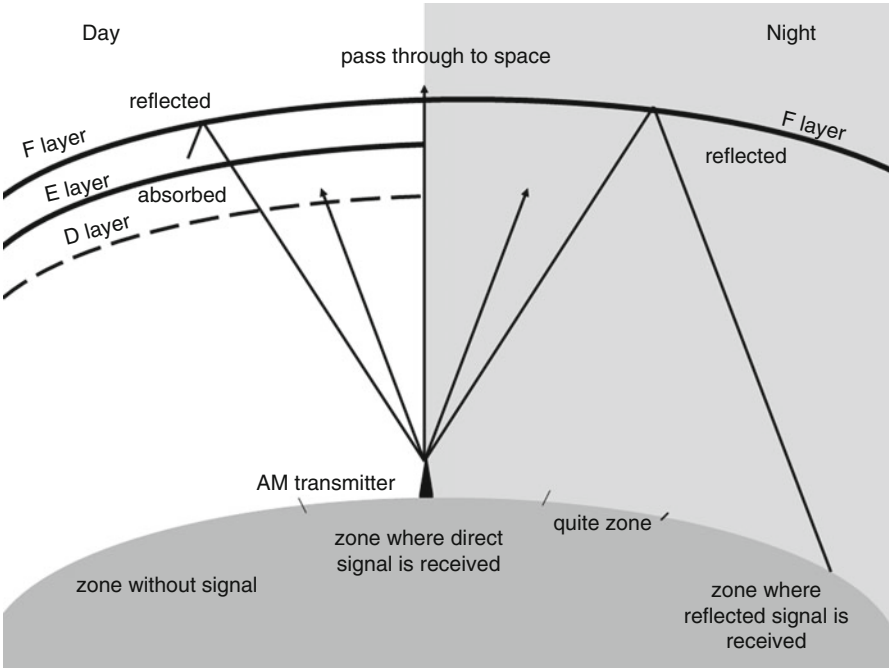

Fig. 1.8 Schematic view of the propagation of radio signals at day and night

fringes on the lower part of aural curtains. Oxygen between 100 and 300 km produces yellowish greenish auroras. At heights above 300 km, where oxygen is the most common atom, emission yields the seldom red aurora. Hydrogen and helium, which dominate higher in the ionosphere, lead to bluish and purplish colors. Besides solar activity, aurora occurrence depends on the Earth's magnetic poles and geographical latitude. In the northern and southern hemisphere, we call these atmospheric phenomena **aurora borealis** (Fig. 1.7) and **aurora australis**, respectively.

Most free electrons exist at levels above 60 km where they occur in sufficient numbers to influence radio-wave propagation. The concentration of free electrons increases monotonically with height from small values below 60 km to a maximum at 300 km. The electrical structure of the ionosphere shows three distinct layers, the **D-**, **E-**, and **F-layer** (Fig. 1.8). Since the ionization depends on daylight, the concentration of charged particles decreases after sunset especially in the D- and E-layer. Large-scale motions in the polar regions called the **sudden warming** also introduce variability within the D-layer. The D-layer absorbs AM radio-waves. During night, these waves reach the F-layer that reflects them. As the Earth's surface reflects them too, AM radio-waves can overcome the Earth's curvature and broadcasts can be received far away from the radio station.

In the E-layer, the mean free path is sufficiently short that the drift of neutral constituents mainly controls the motion of positive ions. Free electrons move along the magnetic field lines. Consequently, whenever the neutral atmosphere within the E-layer crosses the magnetic field lines charge separation occurs, currents flow, and voltage is introduced. These currents cause variations in geomagnetism and structure of the F-layer that exists both day and night. In the F-layer, the diurnal variability of electron density is smaller than the D-layer.

1.4.6 Classification by Magnetic Characteristics

The Earth's magnetic field significantly influences particle motion. Since the **magnetosphere** can hold escaping particles, we consider the **magnetopause** the uppermost border of the Earth's atmosphere. The magnetopause separates the solar wind particles that flow around the magnetosphere from the charged particles in the magnetosphere. Sun eruptions increase the speed and particle density of the solar wind. Clouds of solar particles cause changes in the magnetic field, anomalous currents in the ionosphere and inject high-energy particles in the lower polar ionosphere. The interplanetary magnetic field that rotates with the Sun also affects the magnetosphere.

Problems

Knowledge and Comprehension

1. Which three gases constitute over 98 % of the gas in the Earth's troposphere?
2. What is the difference between trace gases and permanent gases?
3. Why do we consider trace gases despite their low fraction of the atmospheric volume?
4. How do humans, vegetation, or oceans affect the carbon dioxide balance of the atmosphere?
5. Explain the role of vegetation for the atmospheric composition.
6. Explain why ozone is important in the troposphere.
7. What are aerosols?
8. How do the aerosol concentrations differ in magnitude over the land and ocean masses?
9. What distinguishes trace gases from aerosols?
10. What besides enough water vapor is required for condensation?
11. Explain how the trace gas-, energy-, and water cycle interact.
12. What part of the atmosphere shields the Earth from harmful UV radiation?
13. Why is it impossible to define an absolute top of the atmosphere?

14. Describe the vertical structure of the atmosphere by temperature, pressure, and composition.
15. What is the average temperature at the stratopause on the global mean, at the winter and summer pole?
16. Why are temperatures in the thermosphere not comparable with those of the troposphere?
17. Which layer of the Earth's atmosphere contains charged particles, why, and what do they cause?
18. From the color of the aurora we can conclude on the gases of a planet's atmosphere. How should the aurora look like to be a sign for a planet with life?
19. Explain the difference between the escape and probable escape velocity.

Application, Analysis, and Evaluation

1.1. Mercury (Mars) has a gravitational acceleration of $3.8\,\mathrm{m\,s^{-2}}$ ($3.72\,\mathrm{m\,s^{-2}}$) and a radius of about 2,400 km (3,398 km). Determine the escape velocity for Mercury (Mars) and compare it with the escape velocity (in $\mathrm{m\,s^{-1}}$) on the Earth. Discuss your results.

1.2. In Egypt, Alhazen (965–1039) used the duration of twilight to estimate the "top of the atmosphere" by assuming that air density gradually decreases with height, and defining the "top of the atmosphere" as the level where air density is small compared to its density at the surface. Estimate this height using his assumptions that the twilight lasts 36 min, the Earth turns, and the Earth's radius is 6,115 km. Discuss your results in view of the material learned in this chapter.

References

Material, concepts, ideas and problems of the following books and articles inspired this chapter. These sources are recommended for further reading.

Akasofu S-I (1979) Aurora borealis: the amazing northern lights. Alaska Geographic, Fairbanks

Andrews DG (2010) Introduction to atmospheric physics. Cambridge University Press, New York, 237pp

Angevine WM, Ecklund WL (1994) Errors in radio acoustic sounding of temperature. J Atmos Ocean Technol 11:837–842

Bergmann-Schäffer (1997) Lehrbuch der Experimental Physik Erde und Planeten. In: Raith W (ed) de Gruyter, Berlin, 727pp

Broeckner WS (1997) Mountain glaciers: recorders of atmospheric water vapor content. Glob Biogeochem Cycles 11:589–597

Canfield DE (2014) Oxygen – a four billion year history. Princeton University Press, Princeton/ Oxford, 196pp

Foken T (2014) Micrometeorology (trans: Nappo CJ). Springer, Heidelberg, 350pp

Haltiner GJ, Martin FL (1957) Dynamical and physical meteorology. McGraw-Hill, New York/Toronto/London, 470pp
Hobbs PV (2000a) Introduction to atmospheric chemistry. Cambridge University Press, Cambridge, 262pp
Hobbs PV (2000b) Basic physical chemistry for atmospheric sciences. Cambridge University Press, Cambridge, 209pp
Keeling CD, Whorf TP (1998) Atmospheric CO_2 concentrations-Mauna Loa Observatory, Hawaii, $1958 \approx 1997$, ORNL NDP-001. Oak Ridge National Laboratory, Oak Ridge
Kertz W (1969) Einführung in die Geophysik. Band 1. Erdkörper. BI Wissenschaftsverlag, Mannheim/Leipzig/Wien/Zürich, 232pp
Kraus H (2000) Die Atmosphäre der Erde. Eine Einführung in die Meteorologie. Vieweg, Braunschweig/Wiesbaden, 470pp
Li D, Shine KP (1995) A 4-dimensional ozone climatology for UGAMP models. U.K. Universities – Global Atmospheric Modelling Programme internal report no. 35
Lin Y-L (2007) Mesoscale dynamics. Cambridge University Press, Cambridge, 630pp
McKnight (1996) Physical geography, 5th edn. Prentice Hall, Upper Saddle River, 624pp
Mölders N (2011/2012) Land-use and land-cover changes – impact on climate and air quality. Atmospheric and oceanographic sciences library, vol 44. Springer, Dordrecht/ Heidelberg/London/New York. doi:10.1007/978-94-007-1527-1 3
Mölders N, Kramm G (2007) Influence of wildfire induced land-cover changes on clouds and precipitation in interior Alaska – a case study. Atmos Res 84:142–168
Möller F (1973) Einführung in die Meteorologie – Physik der Atmosphäre – Band 1. BI Hochschultaschenbücher, Mannheim, 222pp
Peixto JP, Oort AH (1992) Physics of climate. Springer, New York, 520pp
Petty GW (2008) A first course in atmospheric thermodynamics. Sundog Publishing, Madison, 337pp
Sorbjan Z (1996) Hands-on meteorology: stories, theories, and simple experiments – project atmosphere. American Meteorological Society, Boston
Staley DO (1957) Some comments on physical processes at and near the tropopause. Meteorol Atmos Phys 10:1–19
Standish EM, Williams EM (1992) Orbital ephemerides of the Sun, Moon, and planets. Updated version (unpublished) of Standish EM, Newhall XX, Williams JG, Yeomans DK (eds) Orbital ephemerides of the sun, moon and planets. Explanatory Supplement to the Astronomical Almanac. University Books, Mill Valley, pp 279–374
Tsonis AA (2002) An introduction to atmospheric thermodynamics. Cambridge University Press, New York, 171pp
Twomey S, Wojciechowski TA (1969) Observations of the geographical variation of cloud nuclei. J Atmos Sci 26:648–651
Wallace JM, Hobbs PV (1977) Atmospheric science – an introductory survey. Academic, San Diego/New York/Boston/London/Sydney/Tokyo/Toronto, 467pp
Wallace JM, Hobbs PV (2006) Atmospheric Science – an introductory survey. Academic, San Diego/New York/Boston/London/Sydney/Tokyo/Toronto, 483pp
Wayne RP (1985) Chemistry of atmospheres – an introduction to the chemistry of the atmospheres of Earth, the planets, and their satellites. Clarendon, Oxford, 361pp

Chapter 2
Thermodynamics

Abstract This chapter provides the fundamentals of the thermodynamics of irreversible processes as they are used in meteorology. The discussion includes the laws of thermodynamics, kinetic gas theory, atmospheric stability, and thermodynamics charts. The idea of an air parcel and various thermodynamic systems as they are used in meteorology and climate modeling are introduced as well. Both adiabatic and diabatic processes are discussed. Thermodynamic potentials are introduced for explanation of thermodynamical, dynamical and chemical concepts throughout the book. The chapter covers dry and moist air, phase transition processes and genesis of air masses. In addition, various meteorological concepts important for atmospheric modeling, weather forecasting and analysis of meteorological measurements like the potential temperature, hydrostatic approximation, convective inhibition, convective available potential energy are presented.

Keywords Thermodynamics of irreversible processes • Application of thermodynamical laws to meteorology • Dry and moist air • Phase transition processes • Hydrostatic equation • Use of potentials in meteorology • Atmospheric stability • Genesis and modification of air masses

2.1 Basic Definitions

Introducing meteorological concepts requires discussing basics of thermodynamics. Thermodynamics is an axiomatic science based on fundamental principles that themselves are no longer explainable. This chapter defines the termini of thermodynamics required in meteorology.

N. Mölders and G. Kramm, *Lectures in Meteorology*, Springer Atmospheric Sciences,
DOI 10.1007/978-3-319-02144-7_2,

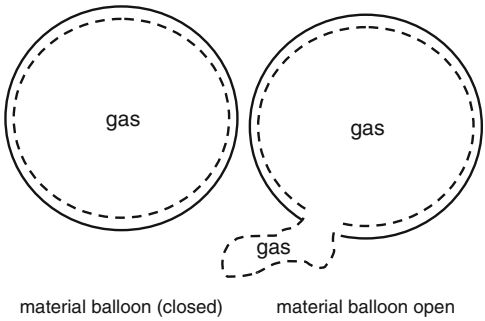

Fig. 2.1 Schematic view of a closed and open system

2.1.1 System

In thermodynamics, we regard a **thermodynamic system** or abbreviated **system**. A system is a specific sample of matter surrounded by material[1] not belonging to the system. In meteorology, the "material" only exists in an idealized view. An **air parcel** in its environment, for instance, can be considered as a system.

Systems may interact with their environment in different ways (Fig. 2.1). An **isolated system** exchanges no material or **energy** with its environment. Energy refers to the ability to do work (unit Joule J). Energy can occur as radiant, electrical, nuclear, and chemical energy. All forms of energy fall into the two categories, kinetic energy (e.g. light and other forms of radiation, heat, motion, electrical power) or potential energy (e.g. water in a reservoir behind a dam, high pressure, battery, gasoline, firewood, explosives, food). Kinetic energy is the energy in use; potential energy is the energy that has not been used.

An **open system** exchanges matter and energy with its surrounding (Fig. 2.1). More or less all atmospheric systems show this behavior. On the time-scale of the Earth, the Earth system looses gases (Chap. 1) and receives material from space by meteors, i.e. exchanges material and therefore is an open system.

A **closed system** exchanges energy, but not mass with the environment, i.e. it is always composed of the same molecules (Fig. 2.1). In meteorology, for simplicity, we usually treat most systems as closed assuming that the interactions associated with open systems can be neglected. On short time-scales and in climate and Earth system modeling, the climate system is considered as a closed system as it receives radiation from the Sun and radiates energy into space (Chap. 4).

2.1.1.1 State Variables

The **state variables** or **state parameters** or **thermodynamic coordinates** denote to any variable that defines the final thermodynamic state of a system. Pressure, p,

[1] e.g. cacao in a cup.

temperature, T, volume, V, mass, m, number of particles, n, or energy, E are examples for state variables. Quantities defined by state variables are state variables themselves (e.g. specific internal energy, specific entropy), i.e. the nth state variable z_n can be determined from any $n-1$ state variables, $z_1, \cdots, z_{n-1}$ by an equation of state of the form $f(z_1, \cdots, z_n) = 0$ or, equivalently $z_n = g(z_1, \cdots, z_{n-1})$. Such equations can be complex if they are to be valid for arbitrarily chosen systems.

We distinguish between the primary (integral, **intensive**) quantities (e.g. temperature, pressure), and the secondary specific (differential, **extensive**), mass-dependent quantities (e.g. volume). Intensive variables characterize a field independent of mass and/or amount. They describe characteristics of a substance (e.g. specific volume, density, temperature). For an intensive variable A the following applies: When $A(n) \neq A(m)$ then mixing leads to a weighted mean $A(n+m) = \frac{m_1 A(n) + m_2 A(m)}{m_1 + m_2}$ where $m_{1,2}$ relate to the mass or amount involved in the mixing of two substances. When $A(n) = A(m)$ then $A(n) = A(m) = A(n+m)$. Consequently, for intensive variables no conservation laws apply. Independent of the motion of a fluid/gas, we can describe its state by two intensive properties. In this sense, a fluid/gas has two thermodynamic **degrees of freedom**.

Extensive variables characterize the amount[2] involved (e.g. energy, mass, volume, number of particles, enthalpy, heat, work, momentum, electric charge, moles). For an extensive variable B, $B(n) = n(B(1))$ and $B(0) = 0$.

2.1.1.2 Marcoscopic System

By saying that air moves or that air has a pressure or density, we relate these properties to air parcels. This **macroscopic** view is the basics of **continuum mechanics** or **continuum hydrodynamics**. It requires that air parcels consist of so many molecules so that wind speed, density, pressure, temperature, etc. are defined in a statistical sense. In addition, the volume of the air parcel has to be small compared to that of the entire system. Thus, we often speak of a point in space. Each point in space owns statistically defined values of the various meteorological variables. These variables and their derivatives are **field quantities** and can be intensive or extensive. Field quantities are continuous functions of space, (x, y, z), and time (t) and describe a four dimensional field $(f(x, y, x, t))$. A gas or liquid considered like this is a **fluid** or **continuum**.

2.1.1.3 Thermodynamic Equilibrium

When the state variables are constant with time, the system is in **thermodynamic equilibrium**, i.e. thermodynamic equilibrium is the final state of an isolated system.

[2] In atmospheric chemistry, the focus is on transformation and reactions. It is required to characterize a fluid by the mass of its constituents and the amount (in mol). The molar mass or molecular/atomic weight (units $\mathrm{kg\,kmol^{-1}}$) allows the conversion from mass to the amount of the constituent. Physical tasks focus on forces and energy and usually prefer mass.

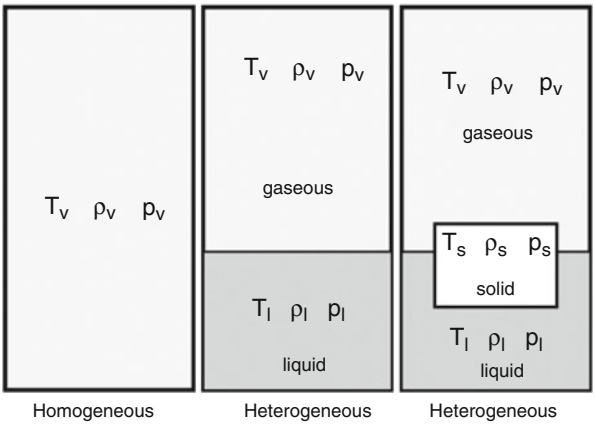

Fig. 2.2 Schematic view of homogeneous and heterogeneous systems. The letters T, p, and ρ denote to temperature, pressure and density; the indices v, l and s refer to the vapor, liquid and solid phase. In thermodynamic equilibrium, $T_v = T_l (= T_s)$, $p_v = p_l (= p_s)$, and $\rho_v \neq \rho_l (\neq \rho_s)$ in the heterogeneous system(s). See text for discussion

When an isolated system is **homogeneous**, for instance a gas, its temperature, pressure, and density are the same everywhere within the system (Fig. 2.2). When an isolated system is **heterogeneous**, it consists of at least two components (e.g. water and air). The temperature and pressure of the combined system are the same everywhere and the density of each homogeneous part is the same everywhere in the respective homogeneous part (Fig. 2.2). Two or more systems can be in a partial equilibrium with each other without equilibrium of the individual systems. Mixed phase clouds (Chap. 3) are examples of heterogeneous systems.

2.2 The Gas Laws

2.2.1 Equation of State

The **ideal gas** refers to a hypothetical gas with molecules of negligible size that exert no intermolecular forces. An ideal gas obeys the general equation of state (2.1). Under terrestrial conditions, atmospheric gases behave nearly like ideal gases. Additionally, atoms or molecules of an ideal gas undergo perfectly elastic collisions. Despite **real gases**[3] lack these exact characteristics in the atmosphere, real gases are often approximated by ideal gases.

[3]Real gases cannot be approximated as ideal gases at high pressures and low temperatures because then intermolecular forces determine the properties of the gas.

$$pV = nR^*T \tag{2.1}$$

where p is pressure, V is volume, $n = m/M$ is the number of kilo moles of the gas with M and m being the atomic/molecular weight[4] and mass of the gas, respectively, and $T = 273.15 + \vartheta$ is the absolute temperature (in K) where ϑ is the temperature[5] in degree Celsius (°C). The **universal gas constant**, $R^* = 8.3144\,\mathrm{J\,K^{-1}\,mol^{-1}}$ is the same for all gases.

The **individual gas constant**, R for 1 kg of gas can be calculated by dividing the universal gas constant by the sum of the atomic weights of all the atoms in a molecule which is the molecular weight M of a respective gas

$$R = \frac{R^*}{M}. \tag{2.2}$$

The individual gas constant of water vapor, for instance, $R_v = \frac{R^*}{M_v}$ is $461.5\,\mathrm{J\,kg^{-1}\,K^{-1}}$ with $M_v = M_H + M_H + M_O = 18.016 \cdot 10^{-3}\,\mathrm{kg\,mol^{-1}}$.

The nearly constant composition of the troposphere and stratosphere (Chap. 1) allows applying a constant molecular weight of dry air, i.e. the individual gas constant for dry air calculated from the mixture of dry air is $R_d = 287.04\,\mathrm{J\,kg^{-1}\,K^{-1}}$. Given the high spatial and temporal variability of atmospheric water vapor, the individual gas constant of moist air varies strongly with water-vapor content.

In meteorological applications, it is more convenient to work with density $\rho = m/V$ than mass or volume. Thus, the equation of state reads

$$p = \rho_d R_d T \tag{2.3}$$

where ρ_d is the density of dry air. In the following the gas constant of air and dry air are denoted R, and R_d, respectively.

2.2.1.1 Other Forms of the Equation of State

The gas constant of one mole of any gas is also a constant called the **Boltzmann's constant** defined as $k = \frac{R^*}{N_A} = 1.3806 \cdot 10^{-23}\,\mathrm{J\,K^{-1}}$ where $N_A = 6.02 \cdot 10^{23}$ is the **Avogadro's**[6] **number**.[7] The Avogardo number is the number of molecules in a

[4] A mole is a unit of mass numerically equal to the molecular weight of a substance.

[5] In this book, ϑ indicates that a temperature value is to be used in degree Celsius.

[6] Lorenzo Romano Amedeo Carlo Avogadro di Quaregna e di Cerreto, Count of Quaregna and Cerreto, Italian savant, 1776–1856.

[7] Note that in German literature, the Avogardo number is often called Loschmidt number after Johann Josef Loschmidt (Austrian chemist, physicist, 1821–1895). He was the first to mention the value of the Avogadro number when he estimated the average diameter of the molecules in air by a method similar to calculating the number of particles in a given volume of gas in 1865.

mole of any gas. **Avogadro's hypothesis** states that a mole of any gas at constant pressure and temperature occupies the same volume. The equation of state (2.1) expressed for a gas with n molecules per unit volume reads $p = nkT$. The number of molecules n is related to the mass, m and molecular weight, M, of any gas by $n = \frac{m}{M}$. Thus, the equation of state (2.1) reads $pV = nR^*T = mRT$.

Example. Determine the relative change in density for dry air being heated from −40 to 20 °C at constant pressure.

Solution. $p = \rho_{cold} R_d 233.15\,\mathrm{K} = \rho_{warm} R_d 293.15\,\mathrm{K}$. Density decreases about 20.5 %.

Example. If the temperature of an air mass increases by 10 K without change in density ($\rho = 1.29\,\mathrm{kg\,m^{-3}}$), how much will its pressure change?

Solution. Using the equation of state, $p = \rho R_d T$, leads to $p + \Delta p = \rho R_d (T + \Delta T)$. Subtracting yields $\Delta p = \rho R_d \Delta T = 3{,}702\,\mathrm{Pa} \approx 37\,\mathrm{hPa}$ as all other values remain constant.

Example. In 1990, the mean CO_2 concentration was 355 ppm (Fig. 1.3). Determine the number of molecules in 1 m³ of air at 1,020 hPa and −10 °C.

Solution. $n_{CO_2} = \frac{p}{kT} = \frac{102{,}000\,\mathrm{N\,m^{-2}}}{1.3806 \cdot 10^{-23}\,\mathrm{J\,K^{-1}} 263.15\,\mathrm{K}} \approx 2.809 \cdot 10^{25}\,\mathrm{m^3}$. At same temperature and pressure, the number of molecules in a gas and the volume, which they occupy, are proportional to $\frac{V_{CO_2}}{V_{air}} = \frac{n_{CO_2}}{n_{air}}$. Rearranging yields $355 \cdot 10^{-6}$ molecules $\mathrm{m^{-3}} \cdot 2.809 \cdot 10^{25}\,\mathrm{m^3} = 9.97 \cdot 10^{21}$ molecules.

2.2.1.2 Special Cases

Several empirical laws were found prior to the equation of state (2.1) and are special cases thereof. The first law by **Gay-Lussac**[8] states that at constant pressure the volume increase is proportional to the increase in temperature ϑ measured in the Celsius scale ($V = V_o(1 + \alpha\vartheta)$). Herein α is the volume coefficient of thermal expansion at constant pressure. His second law states, $p = p_0(1 + \beta\vartheta)$ that an increase by 1 K at constant volume increases pressure by $\beta = 1/273\,\mathrm{K^{-1}}$ of

[8]Joseph Louis Gay-Lussac, also Louis Joseph Gay-Lussac, French chemist and physicist, 1778–1850.

the pressure p_0 the gas had at 0 °C. The **Boyle-Mariotte law** states that for an isothermal process $pV = constant$. Changes in the physical state of a gas that occur under constant temperature are denoted **isothermal**, under constant pressure **isobar**, and under constant volume **isochoric**.

Charles'[9] **first law** states that the volume of a gas is directly proportional to its absolute temperature at constant pressure and mass. **Charles' second law** says that for a fixed mass of gas held in a fixed volume the pressure of the gas is proportional to its absolute temperature.

2.2.1.3 Discussion of the Gas Laws

Since the equation of state relates three state variables, one has to be careful in interpreting changes of one variable. To elucidate the behavior, we differentiate the equation of state (2.1) and obtain $dp = R_d T d\rho_d + R_d \rho_d dT$, i.e. if $dp > 0$ and $dV \geq 0$ then $dT > 0$, and if $dp > 0$ and $dV < 0$, $|Vdp| > |dV|$ then $dT > 0$. When pressure increases, temperature increases only if the density (volume) decreases (increases) or remains constant, or increases (decreases) by a smaller amount as compared with pressure. Cold air is denser than warm air only when pressure remains constant or its changes do not offset the temperature change.

2.2.2 Dalton's Law

In a volume of air, V, all i constituents of mass, m_i, and molecular weight, M_i, are equally distributed, and have the same temperature, T, but different pressures

$$p_i = n_i R^* T = \frac{M_i}{m_i} R^* T = \frac{m_i R_i T}{V} \tag{2.4}$$

The **partial pressure**, p_i, of each component of a mixture of ideal gases is independent of the presence of other gases. The total pressure of the mixture is the sum of the partial pressures of the single components that would be exerted by each single component alone when it occupied the entire volume at that temperature alone

$$p = \sum_{i=1}^{n} p_i \tag{2.5}$$

with $\frac{p_i}{p} = \frac{V_i}{V} = \frac{m_i}{M_i}$. Air chemists often quantify chemical concentrations by the partial pressure.

[9] Jacques Alexandre César Charles, French inventor, scientist, mathematician, and balloonist, 1746–1823.

For a mixture of gases, such as air, the molecular weight is an apparent molecular weight made up from the mass-weighted sum of its i constituents

$$M = \frac{\sum_{i=1}^{n} m_i}{\sum_{i=1}^{n} (\frac{m_i}{M_i})}. \tag{2.6}$$

Here the $i = 1$ must be below the sum sign and the n must be above the sum sign

Dalton's[10] law yields that the individual gas constant of moist air depends on water-vapor content.

Example. Determine the gas constant of dry air by Dalton's law and Table 1.1.

Solution. The mol mass of dry air reads $M_d = M_{N_2} \frac{p_{N_2}}{p} + M_{O_2} \frac{p_{O_2}}{p} + M_{Ar} \frac{p_{Ar}}{p} + M_{CO_2} \frac{p_{CO_2}}{p}$. Thus, we obtain $M_d = (28.013 \cdot 0.7808 + 31.999 \cdot 0.2095 + 39.948 \cdot 0.0093 + 44.010 \cdot 0.0004) \cdot 10^{-3}\,\mathrm{kg\,mol^{-1}} = 28.965 \cdot 10^{-3}\,\mathrm{kg\,mol^{-1}}$, and $R^* = 8.3144\,\mathrm{J\,mol^{-1}\,K^{-1}}$. The individual gas constant of dry air is given by $R_d = \frac{R^*}{M_d} = 287\,\mathrm{J\,kg^{-1}\,K^{-1}}$.

Example. An air parcel of $1\,\mathrm{m}^3$ and $T = 273.15\,\mathrm{K}$ contains N_2, O_2, Ar, and CO_2 with partial pressures of 79,114, 21,227, 942, and 42 Pa. Determine the pressure of the air sample.

Solution. Inserting the values in Eq. (2.5) yields 1,013.25 hPa for the pressure of the air sample.

2.3 Hydrostatic Equation

Although the atmosphere is in motion all times, **Newton's law**[11] requires that the upward force acting on a thin layer of air from the decrease of pressure with height is generally closely balanced by the downward force due **gravity** (Fig. 2.3).

According to **Archimedes' principle**, at a distance z from the surface, pressure is given as $p = g\rho z$ where g is the acceleration of gravity[12] and ρ is air density.

[10] John Dalton, English chemist, meteorologist and physicist, 1766–1844.

[11] Actio = reactio, *Latin* for action = reaction.

[12] The acceleration of gravity is great as compared to nearly all accelerations occurring in the atmosphere. If the Earth's interior were uniform, acceleration of gravity would just depend

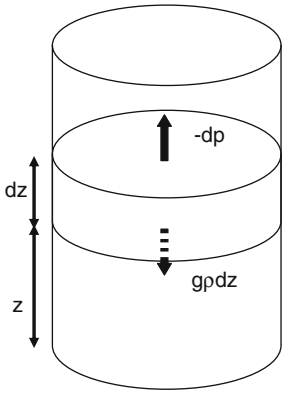

Fig. 2.3 Schematic view of a layer of air in hydrostatic equilibrium. Balance of the upward directed vertical pressure gradient force and downward directed gravity force (*thick arrows*) with no vertical acceleration

Pressure p changes by the amount Δp when going from height z to $z + \Delta z$. At height z, the force acting on the column due to the weight of air amounts to $g\rho\Delta z$. As pressure decreases with height, Δp must be negative, and the net vertical force resulting from the vertical pressure gradient points upwards (Fig. 2.3). The change in pressure for a given layer thickness depends on density. The $\lim_{\Delta z \to 0} \frac{\Delta p}{\Delta z}$ yields the **hydrostatic equation**

$$\frac{\partial p}{\partial z} = -g\rho \tag{2.7}$$

that applies to any fluid/gas in a gravity field. Separation of the variables and integration provide after rearranging

$$p(z) = -\int_{p(z)}^{p(\infty)=0} dp = \int_{z}^{\infty} g(z)\rho(z)dz. \tag{2.8}$$

Since the acceleration of gravity can be approximated as being constant with height, only density depends on height in equation (2.8).

Under the assumption of a uniform distribution of the Earth's atmosphere, the pressure at sea level amounts 1,013.25 hPa. This value is called the **normal pressure**.

In equation (2.8), the ∂-sign indicates that only the change of p with respect to z is meant. The **quasi-static assumption** describes the change in pressure by $\frac{dp}{dz}$. This equation is exact for a static geo-fluid and approximates a fluid in motion well.

---

on geographical latitude, φ, and the distance from the surface, z. The variation caused by the inhomogeneity of the Earth's interior is neglected in meteorological applications using $g(\varphi, z) = 9.80665(1 - 0.0026373\cos\varphi + 0.0000059\cos^2\varphi)(1 - 3.14 \cdot 10^{-7}z)\,\mathrm{m\,s^{-2}}$. This equation leads to an acceleration at sea level of 9.83257, 9.80665, 9.78084 $\mathrm{m\,s^{-2}}$ at the poles, 45° latitude, and the equator, respectively.

Typically, deviations from the **hydrostatic approach** occur locally, e.g. in up- and downdrafts or when the air hits a small obstacle (Chap. 6). In contrast to the hydrostatic approach, then an air particle undergoes acceleration

$$\frac{dw}{dt} = -\frac{1}{\rho}\frac{dp}{dz} - g. \tag{2.9}$$

Combination of the hydrostatic equation[13] (2.7) and equation of state (2.1) yields

$$g\,dz = -\frac{1}{\rho}dp = -RT\frac{dp}{p} =: d\Phi. \tag{2.10}$$

We now can define the potential energy of a body/fluid/gas in the gravitational field as the geopotential

$$\Phi(z) := \int_0^z g\,dz \tag{2.11}$$

with the units $\mathrm{J\,kg^{-1}}$ or $\mathrm{m^2\,s^{-2}}$. The **geopotential height** is given by $Z = \frac{\Phi(z)}{\overline{g}}$ where $\overline{g}$ is the averaged acceleration ($9.8\,\mathrm{m\,s^{-2}}$) in the troposphere. The geopotential height represents the actual height of a pressure surface above mean sea level (Fig. 2.4). Surfaces of equal geopotential height are called the **geopotential surfaces**.[14] The mean sea-level surface is an example of a geopotential surface (Fig. 2.4). The geopotential heights permit us to locate troughs and ridges that are the upper level counterparts of surface cyclones and anticyclones (Figs. 2.5 and 6.49).

Applications of Eq. (2.8) and Related Equations

- Determination of pressure change
- Use of pressure as a vertical coordinate[15]
- Use of pressure as a mass coordinate; for $p(\infty) = 0$, the surface pressure is proportional to the total mass of air in the atmospheric column with a unit surface area
- Geopotential as vertical coordinate
- Formulation of hydrostatic numerical weather prediction and climate models
- Definition of idealized atmospheres for simple estimates

Equation (2.8) is difficult to integrate as the density depends on pressure and temperature, which both vary with height. Thus, different cases are distinguished.

[13] See Chap. 6 for a derivation from the vertical equation of motion.

[14] On the 500 hPa level map, contours of geopotential height are typically spaced at 60 m.

[15] In mountainous regions, pressure coordinates are disadvantageous as they intersect with the terrain.

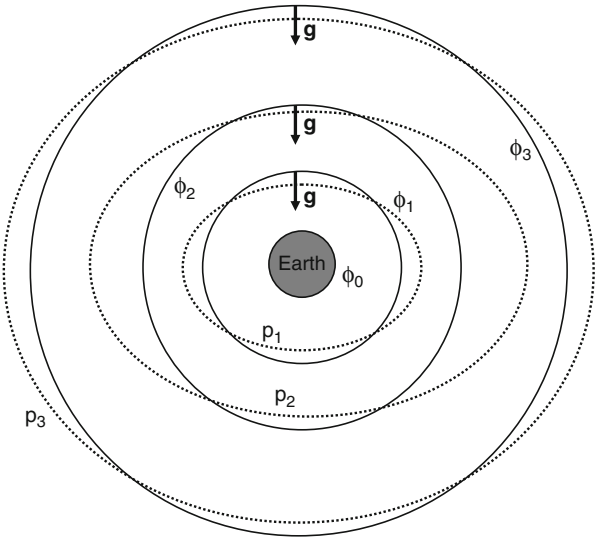

Fig. 2.4 Schematic view of layers of equal geopotential around the Earth. Surfaces of pressure p and geopotential Φ may intersect as illustrated here

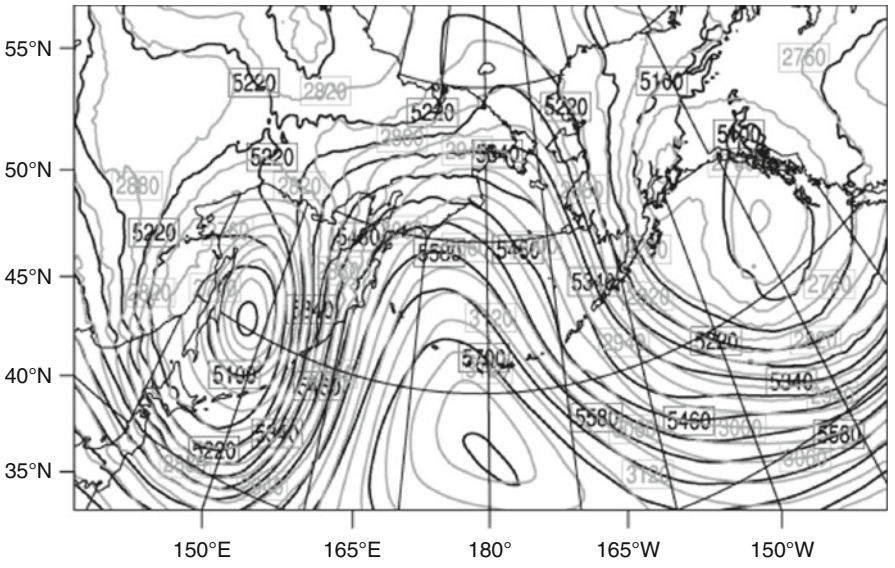

Fig. 2.5 Geopotential heights at 700 (*gray*) and 500 hPa (*Black*) as for January 11, 2000 at 1200 UTC

2.3.1 Isothermal Atmosphere

Assuming no change of temperature with height provides an **isothermal atmosphere**.[16] The isothermal atmosphere is a good first approximation because tropospheric temperature only varies by about 20 %. For an isothermal atmosphere, the integration of

$$\int_{p_0}^{p} \frac{dp}{p} = -\rho g \int_{z_0}^{z} dz = -\frac{g}{RT} \int_{z_0}^{z} dz \tag{2.12}$$

provides $\ln(\frac{p}{p_0}) = -\frac{g(z-z_0)}{RT}$. Taking the antilog yields the **barometric equation**

$$p = p_0 \exp\left(-\frac{g(z-z_0)}{RT}\right) \tag{2.13}$$

The decrease in pressure from z_0 to z is exponential to the ratio between the potential energy or difference in the geopotential height ($g(z-z_0)$) and the **thermal energy** (RT). In most applications, $z_0 = 0$ and p_0 refers to the height and pressure at the surface.

When we define the **scale height**

$$H = \frac{RT}{g} \tag{2.14}$$

we obtain $z = H \ln(\frac{p_o}{p})$ with z being the geometric height above ground. The scale height is 8,430 m for a surface temperature of 288.15 K.

When the difference in height is set successively equal to $0, H, 2H, 3H, \ldots$, the pressure ratios, e.g. $\frac{p_1}{p_2}$ etc., are equal to 1, $\exp(-1)$, $\exp(-2)$, $\exp(-3)$, ..., i.e. the pressure decreases by a factor of $e(= 2.718)$ or about 37 % of its original value for each increase by H in geopotential height. Thus, the isothermal atmosphere has an infinity vertical extension. Inserting the scale height into Eq. (2.13) provides $p = p_o \exp(\frac{-z}{H})$. The exponential decrease of pressure and density with height mentioned in Chap. 1 is now explainable.

The atmosphere is well-mixed below the turbopause because pressure and density of individual gases decrease with height at the same rate and with a scale height related to the apparent molecular weight of air. According to Eq. (2.14), scale height is proportional to the gas constant for a unit mass of gas, i.e. inversely proportional to the molecular weight of the gas. Above the turbopause, molecular diffusion controls the vertical distribution of gases (Chap. 1). Pressure and density of lighter gases fall off less rapidly above the turbopause than heavier gases, and individual scale heights can be defined here.

[16] In an isothermal atmosphere, adiabatic sound-wave speed c_s is independent of height.

Table 2.1 Mean temperature between various isobar levels

p (hPa)	T (K)
1,000–850	295.6
850–700	284.1
700–500	269.1
500–400	253.9
400–300	242.0
300–200	228.1
200–150	213.6
150–100	198.8
100–50	203.4
50–20	220.5
20–10	239.1

Assume for the pressure levels p_1, p_2 and heights z_1, z_2 that $p_1 > p_2$, $z_1 < z_2$ (Fig. 2.3). By rearranging and integration of Eq. (2.12) we yield $z_2 - z_1 = -\frac{R}{g}\int_{p_1}^{p_2} T d(\ln p)$ or the **hypsometric equation**

$$\Delta z = z_2 - z_1 = \frac{R\overline{T}}{g}\ln(\frac{p_1}{p_2}). \tag{2.15}$$

The hypsometric equation can assess the thickness of a layer when temperature is known as a function of pressure from weather balloons or satellite-borne instruments. To get reasonable results we have to use the mean temperature between the two heights given by

$$\overline{T} = \frac{\int_{p_2}^{p_1} T d(\ln p)}{\int_{p_2}^{p_1} d(\ln p)}. \tag{2.16}$$

The above equation means that the atmosphere acts as a thermometer and measuring $\Delta\Phi$ corresponds to a temperature measurement. Table 2.1 lists mean temperatures for the atmosphere between various pressure levels.

Example. In a lab class, a student measures air pressure to be 1,025 and 1,020 hPa at the entrance and on the roof of the institute. Air temperature is 20 °C at both locations. Determine the height of the building assuming dry air.

Solution. $102{,}000\,\text{Pa} = 102{,}500\,\text{Pa}\exp(-\frac{9.81\,\text{m s}^{-2}(z_{roof}-z_0)}{287\,\text{J kg}^{-1}\text{K}^{-1}\cdot 293.15\,\text{K}})\,\text{Pa}$. Rearranging leads to $z_{roof} = -\frac{287\,\text{kg m}^2\,\text{s}^{-2}\,\text{kg}^{-1}\text{K}^{-1}293.15\,\text{K}}{9.81\,\text{m s}^{-2}}\ln(\frac{102{,}000\,\text{Pa}}{102{,}500\,\text{Pa}}) \sim 42\,\text{m}$.

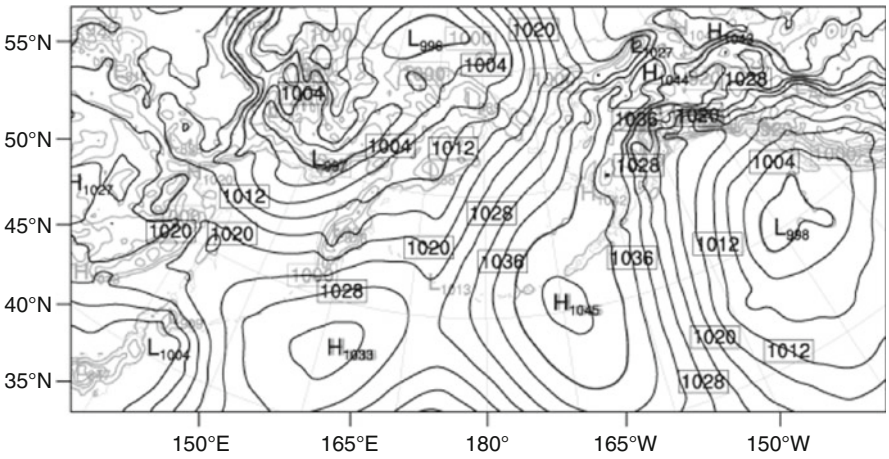

Fig. 2.6 Illustration of application of the barometric equation (2.13) to convert surface pressure (*gray contours*) to sea level pressure (*black contours*) as obtained for 13 January 2000, 1000 UTC

Atmospheric applications for an isothermal atmosphere, Eq. (2.13) or its derivatives are:

- In synoptic (Chap. 6), the thickness of a layer between two pressure levels (Fig. 2.5; Eq. (2.15)) may be used to interpret advection of heat and moisture[17] (Table 2.1). In the upper troposphere, troughs tend to be filled by positive thickness anomalies, while ridges tend to flatten in the case of negative thickness anomalies. A common rule of thumb for forecasting the rain/snow boundary for a precipitation event is that snow usually falls where thickness of the 1,000 to 500 hPa layer is less than 5,400 m thick, whereas the opposite is true for rain.
- In an isothermal atmosphere, at constant geopotential height (e.g. Φ = 5,000 gpm), the following basic law applies: In a warm air mass, pressure decreases slower with height than in cold air mass.
- In synoptic, the barometric equation serves to reduce measured pressure to mean sea-level height to be able to distinguish synoptic, weather-relevant changes in pressure from pressure variation related to terrain elevation (Fig. 2.6). Otherwise, maps with contours of equal pressure would mainly follow the terrain elevation.

[17]The thickness is proportional to the virtual temperature (Sect. 2.7.6) in the lower and mid-troposphere.

Example. Calculate the thickness of the layer between 1,000 and 850 hPa for dry air with a mean temperature of 22.5 °C.

Solution. $\Delta z = \frac{R_d \overline{T}}{g} \ln(\frac{1{,}000\,\text{hPa}}{850\,\text{hPa}}) = \frac{287\,\text{J kg}^{-1}\,\text{K}^{-1} \cdot 293.15\,\text{K}}{9.81\,\text{m s}^{-2}} \ln(\frac{1{,}000\,\text{hPa}}{850\,\text{hPa}}) \approx 1{,}405.7\,\text{m}$.

2.3.2 Homogeneous Atmosphere

By assuming that density is independent from height ($\rho = constant$), we obtain the model of a **homogeneous atmosphere**.[18] In a homogeneous atmosphere, pressure decreases linearly with height. Since pressure cannot be negative a finite altitude H exists where the top of the atmosphere (fluid) is reached and pressure goes to zero, i.e. the homogeneous atmosphere has a finite vertical extension. Integration of the hydrostatic equation (2.7) and $p = 0\,\text{Pa}$ at $z = H$ and $z = 0\,\text{m}$ at surface pressure p yields $p = g\rho H$ where H is the vertical extension or scale height of the homogeneous atmosphere. By using $p = g\rho H$ and the equation of state (2.1), we can determine a scale height of a fictive homogeneous atmosphere for any actual atmosphere with given air temperature at sea level. For an average global temperature, $T = 288.15\,\text{K}$, for instance, a homogeneous atmosphere extends 8,430 m.

Let us investigate how a homogeneous atmosphere would look like. An atmosphere could only behave like this if it were totally **incompressible**.[19] Differentiating the equation of state for dry air (2.3) and assuming a homogeneous atmosphere yield

$$\frac{\partial p}{\partial z} = R\rho \frac{\partial T}{\partial z} = -g\rho. \tag{2.17}$$

Rearranging provides the vertical temperature gradient of the homogeneous atmosphere as

$$\frac{\partial T}{\partial z} = -\frac{g}{R} = -3.416\,\text{K}10^{-2}\,\text{m}^{-1} \tag{2.18}$$

which is called the **auto-convective lapse rate**. In the homogeneous atmosphere, temperature decreases with height about six times faster than observed in the troposphere. As will be shown in Sect. 2.10, such an atmospheric stratification would be unstable.

[18] The assumption of constant density is a far better approximation for the ocean than the atmosphere because of the sharp upper boundary and because the density of seawater is independent of pressure.

[19] Water is nearly incompressible.

Fig. 2.7 Mirage as seen from the University of Alaska Fairbanks campus over the Alaska Range (Photo courtesy to Shaw (2002))

The real world lesson from the homogeneous atmosphere is that when the actual lapse rate exceeds $-3.416\,\mathrm{K10^{-2}\,m^{-1}}$ density increases with height leading to a **density inversion**. Overturning will inevitably occur in the affected layer. Warmer air will spontaneously rise, cooler aloft will sink. An auto-convective lapse rate never exists for deep layers, but often occurs close to the surface on sunny days with intense surface heating. When the surface heating is strong enough to create a sharp temperature gradient despite overturning, the density inversion yields to upward refraction of light beams resulting in **mirages**. This phenomenon often occurs on roads on hot summer days or in spring and fall over mountain ranges (Fig. 2.7).

2.3.3 Polytropic Atmosphere

Assuming an isothermal or homogeneous atmosphere simplifies the integration, but fails to reflect that on average, temperature decreases with height by about $0.65\,\mathrm{K10^{-2}\,m^{-1}}$ in the troposphere.

Usually, the temperature gradient γ is constant at least over a small layer. Such a layer or atmosphere is called **polytropic**. Let us assume that temperature linearly decreases with height according to $T(z) = T_0 - \gamma(z - z_0)$ which can be expressed by $\gamma = -\frac{\partial T}{\partial z}$. Here $T(z_0) = T_0$ is the temperature at the bottom of the polytropic atmospheric layer (z_0). Inserting this relation into the hydrostatic equation (2.7)

$$\frac{dp}{p} = -\frac{g}{R_d}\frac{dz}{T_0 - \gamma z} \tag{2.19}$$

and integration from p_0 to the top of the polytropic layer provide

$$\ln\frac{p}{p_0} = \frac{1}{\gamma}\frac{g}{R_d}\ln(T_0 - \gamma z) + const \tag{2.20}$$

with $p = p_0$ and $z = z_0 \ln \frac{p}{p_0} = 0$ which yields for the constant $-\frac{g}{R_d \gamma} \ln(T_0 - \gamma z_0)$. Thus, $\ln(\frac{p}{p_0}) = \frac{g}{R_d \gamma} \ln \frac{T_0 - \gamma z}{T_0 - \gamma z_0}$ or $p = p_0 (\frac{T_0 - \gamma z}{T_0 - \gamma z_0})^{\frac{g}{R_d \gamma}}$. Solving for height yields

$$z = z_0 + \frac{T_0}{\gamma}(1 - (\frac{p}{p_0})^{\frac{R_d \gamma}{g}}). \tag{2.21}$$

Herein the relation of the temperature gradient of the homogeneous atmosphere g/R_d and the actual atmosphere γ stand in the exponent. A typical value for the exponent is 0.19. The equations describing the isothermal and homogeneous atmospheres are special cases of Eq. (2.21). Equation (2.21) serves for altitude measurements in small aircrafts by measuring the hydrostatic pressure on board, and calculating the height by using quantities of γ, z_0, p_0 and T_0 from the **standard atmosphere** (Table 2.2).

2.3.4 U.S. Standard Atmosphere

The U.S. standard atmosphere (Table 2.2) gives the average pressure, temperature and air density at different heights. Its values base on the mathematical formulas introduced above. To apply easily the barometric equation the vertical profile is approximated by various polytropic layers.

The hydrostatic and thermal vertical structure of the actual atmosphere deviates only slightly from the idealized structure of the standard atmosphere. Many applications (e.g. altimeter calibration, atmospheric correction in satellite meteorology) make use of the standard atmosphere. In weather, climate variability, and climate change applications, however, the deviations from the standard atmosphere are relevant.

2.4 Zeroth Law of Thermodynamics

The **zeroth law of thermodynamics** postulates the existence of a state variable named temperature. It being equal is the necessity of the **thermodynamic equilibrium** of two systems or two parts of the same system. This definition gives a directive for measuring temperature by establishing thermal equilibrium between the thermometer and object.[20]

In other words: Assume two systems with temperatures T_1 and T_2 in which all variables change with time, but the difference in temperature is always zero. In this case, $T_1 = T_2$ is the thermodynamic equilibrium. When dT is a total differential summarizing of dT on every path provides zero, i.e. $\oint dT = 0$.

[20]This procedure is how to measure fever, by establishing an equilibrium between the body and the thermometer.

Table 2.2 U.S. standard atmosphere

Height (m)	Temperature (°C)	Pressure (hPa)	Density (kg m^{-3})
35,000	−36.1	5.6	0.0082
34,000	−38.9	6.5	0.0096
33,000	−41.7	7.5	0.011
32,000	−44.5	8.7	0.013
31,000	−45.5	10	0.015
30,000	−46.5	12	0.018
29,000	−47.5	14	0.021
28,000	−48.5	16	0.025
27,000	−49.5	18	0.029
26,000	−50.5	22	0.034
25,000	−51.5	25	0.039
24,000	−52.5	29	0.046
23,000	−53.5	34	0.054
22,000	−54.5	40	0.064
21,000	−55.5	47	0.075
20,000	−56.5	55	0.088
19,000	−56.5	65	0.10
18,000	−56.5	75	0.12
17,000	−56.5	90	0.14
16,000	−56.5	100	0.17
15,000	−56.5	120	0.19
14,000	−56.5	140	0.23
13,000	−56.5	170	0.27
12,000	−56.5	190	0.31
11,000	−56.5	230	0.36
10,000	−50.0	260	0.41
9,000	−43.5	310	0.47
8,000	−37.0	360	0.53
7,000	−30.5	410	0.59
6,000	−24.0	470	0.66
5,000	−17.5	540	0.74
4,000	−11.0	620	0.82
3,000	−4.5	700	0.91
2,000	2.0	800	1.0
1,000	8.5	900	1.1
0000	15.0	1,013	1.2

2.5 First Law of Thermodynamics

The **first law of thermodynamics** states that *the net energy flow across the boundaries of a system equals the net change in the system's energy*. It postulates for each thermodynamic system a characteristic state variable called the specific **internal energy**, u. The physical unit of energy is J. Internal energy grows according

to the heat introduced to the system, decreases according to the work[21] provided by the system to its environment, and changes by chemical transitions within the system and particle exchange with the environment

$$du = \delta q - \delta w + \sum_i \mu_i dn_i. \tag{2.22}$$

This formulation of energy conservation means that the total energy remains constant in a closed system, i.e. energy cannot be created or destroyed. The small letters mean that the quantities are **mass-specific**, i.e. per mass unit. Thus, q is the specific heat, w is the specific work done by the system, and $\sum_i \mu_i dn_i$ stands for all possible forms of particle exchange or chemical transitions.

The δ-sign means that δw and δq are **inexact differentials**, i.e. neither total (d) nor partial (∂) differentials. The amount of heat/work depends on the path of the processes. Therefore, q and w are no state variables. However, we can define a quantity $ds = \delta q/T$ that is a total differential and a state variable called the specific **entropy**.

In the above equation, dn_i is the fraction. It indicates the impact that adding of mass has on energy, and μ is the **chemical potential**. The chemical potential[22] is the amount by which the energy of a system changes when additional particles were added at constant volume and entropy, i.e. the partial molar **Gibbs**[23] **energy**.

2.5.1 Equivalence of Heat and Work Done

Assume two samples of water at temperatures T_1. Two mechanisms can be applied to rise their temperature to T_2 with $T_1 < T_2$: heating and friction. Inserting a rotating paddle rises temperature mechanically via friction. Both systems reach temperature T_2, but on different paths. When the principle of energy conservation holds, heating is a non-mechanical form of energy transfer, while the rotating paddle provides mechanical work. Consequently, heat and mechanical work are equivalent and two different aspects of the same thing: energy. The energy required to heat one gram of water from 14.5 to 15.5 °C is defined equal to 1 cal = 4.185 J. This value is the **mechanical equivalent of heat**.

---

[21] Work is force times path, i.e. $\mathbf{F} \cdot d\mathbf{r} = F \cos\theta dr$ with θ being the angle between the vectors $\mathbf{F}$ and $\mathbf{r}$.

[22] Chemical potentials differ among species. When, for instance, 1 kg water is added to a system, doing so changes the system's energy by a smaller value than adding hydrogen despite both substances consist of the same atoms in the same number. However, the chemical potential of hydrogen exceeds that of water.

[23] Josiah Willard Gibbs, American mathematical-engineer, theoretical physicist, and chemist, 1839–1903. He is famous for his 1876 publication of *On the Equilibrium of Heterogeneous Substances* that graphically analyzes multi-phase chemical systems.

Table 2.3 Important forms of energy in the atmosphere and typical values. After Peixto and Oort (1992)

Form of energy	Typical value	
	Mass specific ($10^4\,\mathrm{J\,kg^{-1}}$)	Planetary atmosphere ($10^6\,\mathrm{J\,m^2}$)
Kinetic energy ($E_{kin} = \frac{1}{2}mv^2$, e.g. $v \approx 100\,\mathrm{km\,h^{-1}}$)	0.05	1
Potential energy ($\Phi = gh$, e.g. for $h = 5\,\mathrm{km}$)	4.9	693
Thermal energy (c_pT, e.g. for $T = 250\,\mathrm{K}$)	25.0	2,496
Chemical energy (L_vq, e.g. $q \approx 10\,\mathrm{g\,kg^{-1}}$)	2.5	64

2.5.2 *Application of the First Law of Thermodynamics to Meteorology*

The most important forms of energy in meteorology are the (internal) kinetic energy of random molecular motion and kinetic energy of the mean motion, i.e. the kinetic energy $\frac{m\mathbf{v}^2}{2}$ of the motion of the center of mass of the system, heat, and potential energy associated with the gravitational field. Heat input can be radiation (Chap. 4), or molecular conduction. Work provided by the atmosphere or air parcel can be compression (pdV), surface tension, or friction (Chap. 6). Thus, the first law of thermodynamics reads for a unit mass ($m = 1\,\mathrm{kg}$)

$$dE_{total} = dU + d(\frac{v^2}{2}) + d\Phi + \delta Q. \tag{2.23}$$

The potential and kinetic energy of the mean motion are called **mechanical energy**. Table 2.3 compares typical values of energy in the atmosphere.

2.5.2.1 Gravitational Field

Consider the balance between the potential and internal energy only.[24] The gravitational force $\mathbf{F} = -m\mathbf{g}$ has only a component in the z-direction. Thus, $dU = -\mathbf{F}dz$ where z is the vertical coordinate (counted positive upward). Combination leads to $dU = m\mathbf{g}dz = md\Phi$, i.e. potential energy increases with height in the gravitational field (Fig. 2.4).

2.5.2.2 Velocity Field

Let us consider the balance between the kinetic and internal energy only. A weather balloon of mass m drifts with velocity $\mathbf{v}$ with the kinetic energy $U = m\frac{\mathbf{v}^2}{2}$. Since mass cannot change for an intact balloon, kinetic energy changes only when the velocity changes. Such a change corresponds to an acceleration $\frac{d\mathbf{v}}{dt}$ and results

[24] All other components of the first law of thermodynamics are assumed to be zero in this example.

in a force $\mathbf{F} = -m\frac{d\mathbf{v}}{dt}$ that the system opposes to the acceleration. We obtain $d\mathbf{U} = m\frac{d\mathbf{v}}{dt}d\mathbf{r} = md\mathbf{v}\frac{d\mathbf{r}}{dt}$. Since $\frac{d\mathbf{r}}{dt} = \mathbf{v}$, $md\mathbf{v} = d\mathbf{P}$ is the vector of **momentum**. Differentiating $U = m\frac{\mathbf{v}^2}{2}$ provides the same result.

Example. Creating renewable energy[25] from wind uses the kinetic energy of the atmosphere. Assume a change in kinetic energy caused by a change in velocity $\Delta v = 1\,\mathrm{m\,s^{-1}}$ for wind of $v_{weak} = 3\,\mathrm{m\,s^{-1}}$ and $v_{strong} = 15\,\mathrm{m\,s^{-1}}$. Calculate the change in specific kinetic energy assuming a unit mass of air $m = 1\,\mathrm{kg}$. Comment on the result.

Solution. $U = \frac{m\mathbf{v}^2}{2}$ and $U + \Delta U = \frac{m(\mathbf{v}+\Delta\mathbf{v})^2}{2}$. Rearranging and plugging in the values leads to $U_{weak} = 4.5\,\mathrm{kg\,m^2\,s^{-2}}$, $U_{strong} = 112.5\,\mathrm{kg\,m^2\,s^{-2}}$, $U + \Delta U_{weak} = 8\,\mathrm{kg\,m^2\,s^{-2}}$, $U + \Delta U_{strong} = 128\,\mathrm{kg\,m^2\,s^{-2}}$, $\Delta U_{weak} = 3.5\,\mathrm{kg\,m^2\,s^{-2}}$, and $\Delta U_{strong} = 15.5\,\mathrm{kg\,m^2\,s^{-2}}$. The same increase in speed increases kinetic energy more than four times in this case.

2.5.2.3 Expansion and Contraction

When an air parcel ascends, it is cut off from the heat supply from the surface. When the air parcel does not mix with its environment, its pressure rises under conservation of energy, as the pressure in its surrounding decreases as the height of the parcel increases. The force related to the pressure change forces the parcel to adjust to achieve equilibrium with its new environmental conditions to achieve the same pressure, i.e. it expands. The expansion means the parcel performs work on its environment from its internal energy for which its temperature decreases. During descend work performed by the environment on the air parcel leads to contraction, for which internal energy and temperature increase.

Example. Show for an air parcel of dry air, which ascends to a level and then descend back to its original level that δW is not a total differential.

Solution. Applied to this problem the first law of thermodynamics reads $du(T) = \delta q - \delta w = \delta q - pdv$. When we assume a cycle process for constant volume and pressure (Fig. 2.8), the provided work is $\oint \delta W = \oint pdV = p_2(V_2 - V_1) + p_1(V_1 - V_2)$ i.e. the air parcel provides work on the path from V_1 to V_2 at constant p_2 ($dV > 0$) and gains work ($dV < 0$) on the path from

(continued)

[25]The term 'renewable energy' is technically incorrect from a thermodynamic point of view. Actually, kinetic energy, in case of wind energy, or solar energy, in the cases of bio-fuels or solar panels, are used and taken from the system.

(continued)

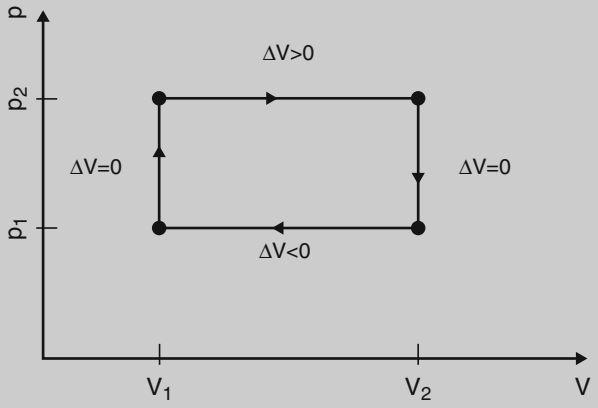

Fig. 2.8 Example for a cycle process to illustrate that the work provided by $\delta W = pdV$ is not a state variable. At the corner (p_2, V_1), the process begins and ends

V_2 to V_1 at constant p_1, and $\oint \delta W = (p_2 - p_1)\Delta V$ with $\Delta V = V_2 - V_1$. The total positive work is non-zero and depends on the path. Work due to compression defined by $pdV = \delta W$ is not a state variable. q.e.d.

2.5.3 *Kinetic Theory of Heat*

The temperature of an ideal gas depends on three variables related by the equation of state for an ideal gas. According to the **kinetic theory of heat**, all atoms or molecules (hereafter referred to as mass points) of a gas move randomly in all directions (**Brownian motion**) obeying the law of equal distribution. Because of the randomness of Brownian motion, the individual mass points have different internal energies that change with temperature. Due to conservation of energy, the mean energy of the system remains the same. The kinetic theory of heat accepts that the mean internal energy is proportional to the absolute temperature of the system ($U = constant \cdot T$). Thus, we can understand the temperature of a gas as the mean kinetic energy of the gas molecules. At the absolute zero point, $T = 0\,\mathrm{K}$ and $p = 0\,\mathrm{Pa}$, i.e. the absolute zero point is defined by $\overline{v^2} = 0\,\mathrm{m^2\,s^{-2}}$ where $\bar{v}$ is the average velocity. This means it is impossible to deduce further energy of motion from that gas. The overbar means that this definition is only valid for the collective average. It makes no sense for an individual molecule.

Each gas has at least three degrees of translation (Fig. 2.9) as an atom has three directions to move. Monoatomic gases have only these **degrees of freedom**. The thermodynamic degree of freedom defines the number of independent variables required to describe the energy of the system's point masses completely. Due to the law of equal distribution each degree of freedom of a molecule at absolute

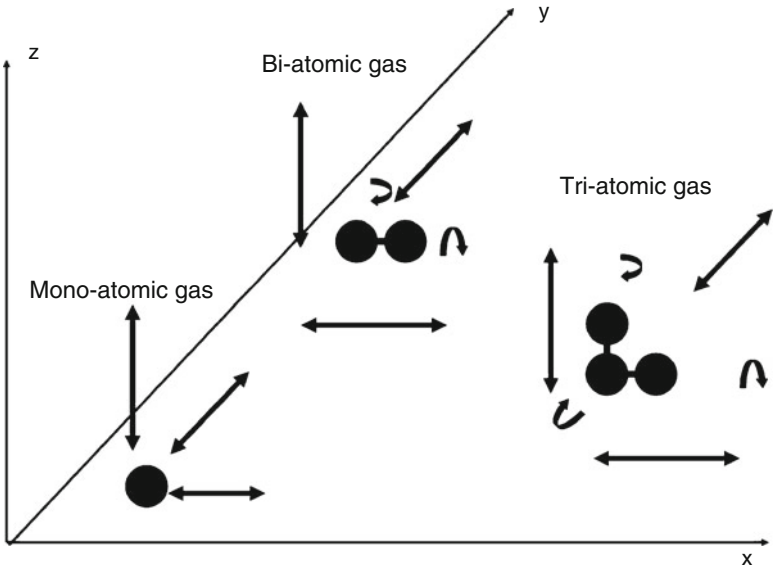

Fig. 2.9 Schematic view of degrees of freedom of an atom and a molecule

temperature T has the same energy on the temporal and spatial average, $\overline{U} = \frac{kT}{2}$ with $k = 1.3806 \cdot 10^{-23}\,\mathrm{J\,K^{-1}}$ being Boltzmann's constant. The mean kinetic translation energy, $\overline{U}$, of a monoatomic gas of mass, m and temperature, T are related by

$$\overline{U} = \frac{m\overline{v^2}}{2} = \frac{3}{2}kT. \tag{2.24}$$

Gases of molecules with two atoms in addition have two degrees of rotation. Molecules with three or more atoms that are not aligned like a stick have three degrees of rotation (Fig. 2.9).

A gas with f degrees of freedom of n molecules has the energy

$$\overline{U} = \frac{1}{2}fnR^*T = \frac{f}{2}kT. \tag{2.25}$$

Recall that the temperature of the thermosphere is determined from kinetic theory of heat (Chap. 1).

Example. Determine the mean energy and temperature of a monoatomic gas with unit mass having an average velocity of $2.5 \cdot 10^{-10}\,\mathrm{m\,s^{-1}}$.

Solution. The mean energy amounts to $\overline{U} = \frac{m\overline{v^2}}{2} = \frac{1\,\mathrm{kg}\overline{(2.5\cdot 10^{-10}\,\mathrm{m\,s^{-1}})^2}}{2} \approx 3.125 \cdot 10^{-20}\,\mathrm{J}$. Rearranging $\overline{U} = \frac{3}{2}kT$ for temperature provides $T = \frac{\overline{U}2}{3k} = \frac{3.125\cdot 10^{-20}\,\mathrm{J}2}{3\cdot 1.3806\cdot 10^{-23}\,\mathrm{J\,K^{-1}}} \approx 1{,}509\,\mathrm{K}$.

2.5.4 Specific Heat

The **specific heat** is the heat input required to increase the temperature of an unit mass of a system by one temperature unit, i.e. the heat input per mass and temperature unit ($\mathrm{J\,kg^{-1}\,K^{-1}}$). Despite its slight temperature-dependency[26], the specific heat is considered as a material constant for gases, liquids, and solids. For some gases the provided work depends on the path in the p, v-diagram. The transition can occur at constant volume (**isochoric**)

$$c_v := \frac{\delta q}{dT}|_v = \frac{Tds}{dT}|_v \tag{2.26}$$

or pressure (**isobaric**)

$$c_p := \frac{\delta q}{dT}|_p = \frac{Tds}{dT}|_p \tag{2.27}$$

By using the internal energy we obtain for an isochoric process

$$\delta q = Tds = du + pdv \Rightarrow du = c_v dT. \tag{2.28}$$

During an isochoric process, the physical and chemical states of the parcel remain unchanged, temperature changes proportional to the heat absorbed/released. According to the first law of thermodynamics when $du = 0$, u only depends on T.

We obtain for an isobaric process

$$Tds = dh - vdp \Rightarrow dh = c_p dT \tag{2.29}$$

where $h = u + pv$ is a state variable, the specific **enthalpy** and v is specific volume. Enthalpy $H = U + pV$ accounts for the gain in internal energy plus mechanical work required for expansion. During an isobaric process, enthalpy changes according to the change of absorbed/released heat, $dH = dU + pdV = \delta Q$. Consequently, by adding x units of heat at constant pressure to a dry air parcel, the parcel gains x units of enthalpy. When an air parcel in contact with the surface is heated/cooled isobarically by conduction, the exchange of heat at the surface-atmosphere interface equals the change in enthalpy of the air parcel and is called the **sensible heat**.

Since the quantities determined by Eqs. (2.28) and (2.29) are constants in first approximation, we can integrate these equations from 0 to T and obtain

$$u = c_v T \tag{2.30}$$

$$h = c_p T \tag{2.31}$$

[26] $c_p = 1{,}005.45 + 0.033T$ for $-100\,^\circ\mathrm{C} \leq T \leq 60\,^\circ\mathrm{C}$.

The take home message is that specific heat at constant pressure, c_p, measures the rate at which enthalpy increases with temperature during an isobaric process; the specific heat at constant volume, c_v, measures the rate at which internal energy increases with temperature during isochoric processes. Their relationship is

$$Tds = c_v dT + pdv = c_v dT + d(pv) - vdp \tag{2.32}$$

Using the equation of state (2.1) yields

$$c_v dT + d(pv) - vdp = c_v dT + RdT - vdp = (c_v + R)dT - vdp \tag{2.33}$$

Comparison with $Tds = c_p dT - vdp$ results in (Eq. 2.29)

$$c_p - c_v = R \tag{2.34}$$

where R is a placeholder for the individual gas constant of any gas. Inserting the individual gas constant for dry air $R_d = \frac{R^*}{M_d}$ provides $c_p = 1{,}004\,\mathrm{J\,kg^{-1}\,K^{-1}}$, $c_v = 717\,\mathrm{J\,kg^{-1}\,K^{-1}}$, and $R_d = 287\,\mathrm{J\,kg^{-1}\,K^{-1}}$. The ratio $\frac{c_p - c_v}{c_p} = \frac{R_d}{c_p} = \kappa = 0.286$ is the **Poisson-constant**.[27] The ratio $c_p/c_v = 1.4$ results from the kinetic gas theory as a function of the number of degrees of freedom of the gas.

Example. Assess the specific heat capacity at constant volume and pressure for a mono-atomic gas with individual gas constant R.

Solution. Applying the theorem of equal distribution and the fact that a mono-atomic gas has three degrees of freedom yield for the internal energy of a mono-atomic gas $U = \frac{1}{2}m\mathbf{v}^2 = \frac{3}{2}nkT$ where n is the number of molecules. Thus, $C_v = \frac{dU}{dT} = \frac{3}{2}nk = \frac{3}{2}mR$ or $c_v = \frac{3}{2}R$. Analogously, $C_p = \frac{dH}{dT} = \frac{dU}{dT} + mR = \frac{5}{2}mR$ or $c_p = \frac{5}{2}R$.

Example. Assume wind of $15\,\mathrm{m\,s^{-1}}$ blowing from the ocean onto forest-covered land. Due to frictional dissipation, 75 % of the kinetic energy are converted into heat. Calculate the maximum possible increase of air temperature that may result of an isobaric process. Assume unit mass ($m = 1\,\mathrm{kg}$).

Solution. $m\frac{v^2}{2} = c_p dT$. Thus, $\Delta T_{max} = \frac{(15\,\mathrm{m\,s^{-1}})^2}{2 \cdot 1{,}004\,\mathrm{J\,kg^{-1}\,K^{-1}}} 0.75 = 0.08\,\mathrm{K}$.

[27] Simon Denis Poisson, French mathematician and physicist, 1781–1840.

2.5.5 Potential Temperature

Assume a dry air parcel that ascends without exchange of heat with its environment ($\delta Q = Tds = 0$), i.e. adiabatically (*Greek* unpassable). Mixing with the surrounding air is excluded because the air-parcel concept assumes a closed system. During upward motion the parcel experiences a decrease in pressure, expanses ($dv > 0$) and performs the work pdv. The first law of thermodynamics yields that du and dT are negative. We can use this law to derive equations that describe the change in T with height/pressure for an vertically moving air parcel

$$c_p dT = \frac{1}{\rho} dp. \tag{2.35}$$

Inserting the equation of state rearranged for density $\rho = \frac{p}{R_d T}$ yields

$$c_p dT = \frac{R_d T}{p} dp. \tag{2.36}$$

Separation of the variables and rearranging results in

$$c_p \frac{dT}{T} - \frac{R_d dp}{p} = 0 \tag{2.37}$$

or

$$c_p d(\ln T) - R_d d(\ln p) = 0. \tag{2.38}$$

Integration provides

$$c_p \ln T - R_d \ln p = c_p \ln T_o - R_d \ln p_o = constant \tag{2.39}$$

and after rearranging we obtain the **Poisson equation**.

$$\ln \frac{T_o}{T} = \frac{R_d}{c_p} \ln \frac{p_o}{p}. \tag{2.40}$$

We now take the antilog and define the **potential temperature** at pressure $p_o = 1{,}000\,\text{hPa}$ as $\theta := T_o$,

$$\theta = T(\frac{p_o}{p})^{\frac{R_d}{c_p}}. \tag{2.41}$$

When an air parcel has a given potential temperature, Eq. (2.41) gives its temperature as a function of pressure and vice versa. The potential temperature is the final temperature a parcel has when it is expanded/compressed adiabatically from

any state (T, p) to the 1,000 hPa-level. During any adiabatic ascend/descend the temperature of the air parcel decreases/increases to such extend that its potential temperature remains constant.

Example. The potential temperature is related to specific entropy by $ds = c_p \frac{d\theta}{\theta}$. Use the specific entropy and the definition of potential temperature to show that except for an additional constant the specific entropy of an air parcel is given by the logarithm of potential temperature.

Solution. $\theta = T(\frac{1{,}000}{p})^{\frac{R_d}{c_p}}$
$\ln \theta = \ln T + \frac{R_d}{c_p} \ln 1{,}000 - \frac{R_d}{c_p} \ln p$
$c_p \ln \theta = c_p \ln T + R_d \ln 1{,}000 - R_d \ln p$
$ds = c_p \frac{dT}{T} - R_d \frac{dp}{p}$
$ds = c_p d \ln \theta$
Integration leads to $s = c_p \ln \theta + constant$, q.e.d.

2.5.5.1 Applications of Potential Temperature

Conservation of Potential Temperature under Adiabatic Motion

During an adiabatic motion, an air parcel exchanges no heat with its environment, $(\delta Q = 0)$. The temperature of a moving air parcel decreases, as it ascends and moves to lower pressure and vice versa. The thermodynamic equation reduces to $\frac{d\theta}{dz} = 0$, i.e. potential temperature is conserved. Thus, an air parcel initially being on an **isentropic** surface ($\theta = constant$) remains on that surface.

Tracking Tracers

As long as the motion of a parcel can be considered as adiabatic, the parcel travels on isentropic surfaces. Isentropic surfaces are material surfaces under adiabatic conditions. Air chemists use isentropic surfaces to determine the source areas of chemically inert pollutants or aerosols. Since many non-adiabatic (diabatic) processes occur in the atmosphere, estimates of the origin of inert air pollutants and aerosols that are determined by backward trajectories on isentropic surfaces, only provide a broad idea of the source region, rather than the exact point or area source.

Characterizing Air Masses

Isentropic compression to pressure p_0 means that the air parcel still has the same potential temperature. Consequently, θ is more suitable for characterizing air masses than T as θ is invariant to pressure changes.

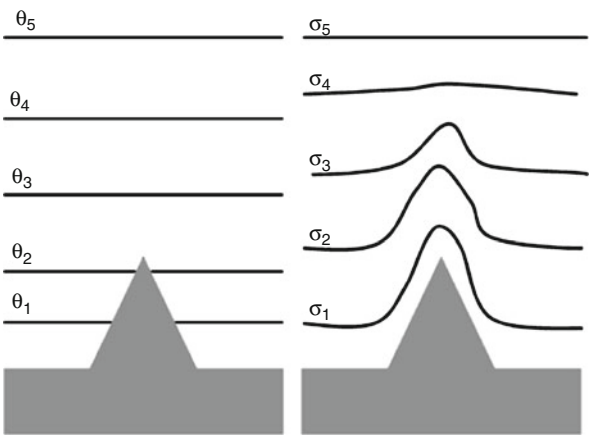

Fig. 2.10 Schematic views of the isentropic coordinates (*left*) and terrain following σ-coordinates (*right*). Note that $\sigma = (p - p_{top})/(p_s - p_{top})$

Isentropic Coordinates

Using isentropic coordinates in numerical models at upper levels is advantageous as isentropic coordinates reduce vertical transport through coordinate surfaces. This type of coordinate system is called a hybrid coordinate system. It is frequently applied in General Circulation Models (GCM), climate models, and Earth system models. The lateral mixing occurs on isentropic surfaces instead of across them, i.e. unwanted cross-isentropic mixing is avoided. In climate models without this feature, the growth of entropy leads to a cold bias. Applying isentropic coordinates throughout the entire domain has the disadvantage that in mountainous terrain, isentropic coordinates may intersect with the terrain, which requires special numerical procedures to ensure realistic results (Fig. 2.10).

2.5.5.2 Dry Adiabatic Lapse Rate

The differential $d\theta$ can be determined by differentiating the Poisson-equation (2.41) with $\kappa = R_d/c_p$ and the equation of state (2.3)

$$d\theta = \frac{\theta}{T}(dT - \frac{1}{\rho c_p}dp). \tag{2.42}$$

Rearranging and $ds = c_p d\theta/\theta$ provide

$$c_p d\theta = \frac{\theta}{T}(c_p dT - \frac{1}{\rho}dp) = \frac{\theta}{T}T\,ds. \tag{2.43}$$

Division by θ and replacing dp/ρ by the hydrostatic equation (2.7) yield

$$c_p \frac{dT}{T} + \frac{g}{T_e} dz = 0 \tag{2.44}$$

where T_e stands for the air in the immediate vicinity, i.e. $dp_e = -\rho_e g dz$ with $p_e = \rho_e R_d T_e$ and $p_e = p$. Rearranging provides

$$\frac{dT}{dz} = -\frac{g}{c_p} \frac{T}{T_e}. \tag{2.45}$$

Since $T_e \approx T$ and $g/c_p = 0.98\,\mathrm{K10^{-2}\,m^{-1}}$ we obtain

$$\frac{dT}{dz} =: -\Gamma_d = -\frac{g}{c_p} \approx -\frac{0.98\,\mathrm{K}}{100\,\mathrm{m}}. \tag{2.46}$$

Here $-\Gamma_d$ is the **dry adiabatic temperature gradient** or **dry adiabatic lapse rate**, at which the temperature of a dry adiabatically ascending air parcel decreases with increasing height.

Example. At the surface, the temperatures of the gas in a balloon and the ambient air are 10 °C. At 100 and 200 m, the temperature sensor measures an environmental temperature of 9.4 and 8.7 °C, respectively. Determine the temperature in the balloon for these heights. Think about your result.

Solution. Since the balloon is a closed system, its enclosed air behaves adiabatically. At 100 and 200 m, the balloon air temperature is $10\,^\circ\mathrm{C} - \frac{0.98\,^\circ\mathrm{C}}{100\,\mathrm{m}} 100\,\mathrm{m} \approx 9$ and 8 °C, respectively. The balloon would not ascend if it contained air.

Forecasting Subsidence Inversions

In high pressure systems, entire layers of the atmosphere sink (subside) adiabatically and can cause **temperature inversions**. Pressure increases during the process, which often results in **subsidence inversion** lower in the troposphere. By assuming that the subsiding layer preserves its total mass and sinks adiabatically, we can determine the vertical temperature gradient within the layer when we know the potential temperature of the top and bottom of the layer at their original heights. The level at which the subsiding layer becomes isothermal gives us the inversion height (Fig. 2.11).

Fig. 2.11 Inversions over Fairbanks. The high buoyancy of the two plumes allows them to break through the surface inversion. The higher buoyancy of the plume to the right permits it to break through another inversion. The plumes show well the different wind directions (Photo: Kramm 2004)

2.5.5.3 Dry Static Energy

With $h = u + pv = c_p T$, we can express the vertical temperature gradient as an enthalpy change

$$\frac{dh}{dz} = -g \tag{2.47}$$

The sum of enthalpy and potential energy $h + gz$ is defined as the **dry static energy**. This relationship means that (1) for a dry adiabatically moving air parcel $c_p\theta$ is the constant sum of enthalpy and potential energy, (2) enthalpy of an adiabatically ascending/descending air parcel decreases/increases because it performs gravitational work, and (3) the static energy is conserved in an adiabatic motion, i.e. $\frac{d(h+gz)}{dz} = 0$. Thus, we can consider enthalpy as the specific internal energy plus the work done by the parcel on its environment. This characteristic of the air parcel does not change during vertical motions, i.e. $\frac{d\theta}{dz} = 0$.

2.5.5.4 Diabatic Heating

In the atmosphere, absorption of radiation energy (Chap. 4) or release of latent heat or consumption of heat during phase transition processes (Sect. 2.7, Chap. 3) change θ by adding/reducing entropy. Under such **diabatic** conditions, the system interacts with its environment mechanically by turbulent mixing and thermally by conduction, radiative transfer, consumption of heat or release of latent heat. Potential temperature changes proportional to the heat transferred to the air parcel ($\delta Q \neq 0$) and is no longer conserved ($d\theta/dz \neq 0$). The parcel drifts across isentropic surfaces proportional to the net heat exchange. Taking the logarithm of Eq. (2.41) gives the difference relations among θ, T, and p

$$d \ln \theta - d \ln T = -\kappa d \ln p \tag{2.48}$$

that we use to evaluate diabatic processes.

Diabatic processes are often responsible for fog formation, but are secondary to adiabatic processes for cloud formation (Chap. 3). Radiation, molecular conduction and consumption of heat and release of latent heat during phase transition processes can contribute notably to diabatic heating (Chap. 4). Frictional dissipation of kinetic energy – another diabatic process – is not a significant source for atmospheric heating, but an important sink of kinetic energy (Chap. 6).

The vertical temperature gradients typically observed in the troposphere are lower than the dry adiabatic temperature gradient, because diabatic processes mean $\partial\theta/\partial z \neq 0$. The change in the potential energy measures the heat exchange between the air parcel and its environment. The profiles of T and θ are related by

$$\frac{\partial T}{\partial z} = \frac{\partial \theta}{\partial z} - \frac{g}{c_p}. \tag{2.49}$$

Example. In a desert, an air parcel heats by conduction when moving from an irrigated cool area to a hot dry area. Assume that potential temperature and temperature increase by 4 and 2 %, respectively. Calculate the fractional change in surface pressure between the irrigated and non-irrigated position of and the heat absorbed by the air parcel.

Solution. Logarithmizing $\frac{\theta}{T} = (\frac{p_0}{p})^\kappa$ yields $d \ln \theta - d \ln T = -\kappa d \ln p$. Integration provides $\int_1^2 d \ln \theta - \int_1^2 d \ln T = -\kappa \int_1^2 d \ln p$ and $\ln(\frac{\theta_2}{\theta_1}) - \ln(\frac{T_2}{T_1}) = -\kappa \ln(\frac{p_2}{p_1})$. An increase by 4 and 2 % means the new values are a fraction 0.04 and 0.02 higher than the old values that correspond to 100 % or 1 unit. Substitution of the new potential temperature and temperature by 1.04 and 1.02, respectively, leads to $\ln 1.04 - \ln 1.02 = -\kappa \ln(\frac{p_2}{p_1})$. The anti-logarithm yields a fraction of $\frac{p_2}{p_1} = 0.93$, i.e. a fractional pressure change of about 7 %. Since $ds = \frac{\delta q}{T} = c_p d \ln \theta$, $\frac{1}{T} = \frac{1}{\theta}(\frac{p_0}{p})^\kappa$, $\delta q = \frac{1}{\theta}(\frac{p_0}{p})^\kappa c_p d \ln \theta$. Integration yields for the heat absorbed by the air parcel $\delta q = (\frac{p_2}{p_1})^\kappa c_p \int_1^2 \frac{d \ln \theta}{\theta} = 0.93^{0.286} \cdot 1{,}004\,\mathrm{J\,kg^{-1}\,K^{-1}} \ln 1.04 \approx 38\,\mathrm{W\,m^{-2}}$.

2.6 Second Law of Thermodynamics

The first law of thermodynamic postulates the conservation of energy, but not the efficiency of the energy transfer. According to the first law of thermodynamics, work can be transformed into heat, heat into work, work can be performed at the cost of

internal energy, etc. If no limiting law would exist, the first law of thermodynamics would allow phenomena that never happen in reality.[28]

The **second law of thermodynamics** is an axiom[29] that tells us how heat is transformed into work.[30] The second law of thermodynamics postulates the impossibility to construct a periodically working engine that does nothing else than cooling a heat reservoir and transferring the heat change into work. During real processes the entropy of a closed system increases. From a molecular point of view, the second law of thermodynamics is a matter of high probability, but not of absolute certainty.

2.6.1 Carnot Cycle

To illustrate the second law of thermodynamics, we apply Carnot's[31] theoretical experiment, a special cycle process that runs only on isotherms and adiabats, to the atmosphere.

The **Carnot cycle** (Fig. 2.12) can be elucidated with respect to meteorology by specifying two temperatures T_w and T_c of isothermal steps and the potential temperatures $\theta_1 = T_w(\frac{1{,}000}{p_1})^{\frac{R_d}{c_p}} = T_c(\frac{1{,}000}{p_4})^{\frac{R_d}{c_p}}$ and $\theta_2 = T_c(\frac{1{,}000}{p_3})^{\frac{R_d}{c_p}} = T_w(\frac{1{,}000}{p_2})^{\frac{R_d}{c_p}}$ of the adiabatic steps with $T_w > T_c$ and $\theta_2 > \theta_1$. Here T_w and T_c stand for the warm and cold temperature, respectively.

- $1 \rightarrow 2$*: Reversible isothermal expansion*
  During isothermal expansion, heat is transferred to the air parcel, otherwise it would cool. The air parcel provides work pdV. Its internal energy, U, remains unchanged as it depends on temperature, T_w that is constant, i.e. $\Delta T = 0$. Thus $\Delta U = C_v \Delta T = 0$. Integration from V_1 to V_2 yields for the work

[28] The first law of thermodynamics would permit that the space shuttle rises by cooling of its heat shield.

[29] Axioms cannot be proven.

[30] Many expressions of the second law of thermodynamics exist:

- **The Clausius statement**: There is no *self-acting* cyclic process or device that only removes heat from one reservoir and discharges an equal amount of heat to a reservoir at higher temperature.
- **The Kelvin-Planck statement**: There is no cyclic process or device that only removes heat from a single reservoir and performs an equal amount of work.
- **Planck statement**: Processes wherein friction occurs are irreversible.
- A perpetuum mobile of second kind is impossible.
- No cycle that operates between any two temperatures can have a higher efficiency than a **Carnot cycle** operating between the same two temperatures.
- Each thermodynamic system has a state variable, the entropy $S = \delta Q / T$ that can be calculated for reversible processes.

[31] Nicolas Léonard Sadi Carnot, French scientist, physicist and military engineer, 1796–1832.

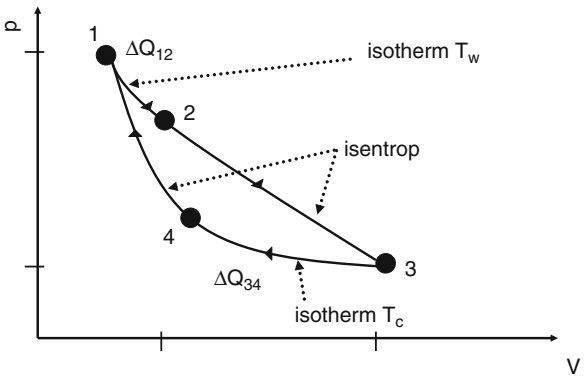

Fig. 2.12 Schematic view of Carnot-process in a p-V-diagram as used in physics. Unlike in meteorology here the lower part of the diagram corresponds to lower pressure and temperatures than the upper part, i.e. the lower part is higher up in the troposphere, while the upper part is closer to the surface. The process begins and ends at p_2, V_1

$$w_{12} = \int_{V_1}^{V_2} p dV = R_d T_w \int_{V_1}^{V_2} \frac{dV}{V} = R_d T_w \ln(\frac{V_2}{V_1}).$$

With the equation of state $\frac{1}{V_1} = \frac{R_d T_w}{p_1}$ and $\frac{1}{V_2} = \frac{R_d T_w}{p_2}$. In evaluating $\frac{1}{V_2}$ we use θ_2 and $p_2 = p_3(\frac{T_w}{T_c})^{\frac{c_p}{R_d}}$ and obtain $\frac{1}{V_2} = \frac{R_d T_w}{p_3}(\frac{T_w}{T_c})^{\frac{c_p}{R_d}}$. Thus,

$$w_{12} = R_d T_w \ln(\frac{p_1}{p_3}(\frac{T_c}{T_w})^{\frac{c_p}{R_d}})$$

$$q_{12} = c_p T_w(\frac{\theta_2}{\theta_1}) = w_{12}.$$

Since $V_2 > V_1$, Δq_{12}, $w_{12} > 0$. Thus, the air parcel absorbs heat from the environment at temperature T_w to do the work.

- $2 \rightarrow 3$*: Reversible adiabatic expansion*
  The air parcel is isolated, $\Delta q_{23} = 0$. It performs work on the environment during its expansion at the cost of its internal energy wherefore temperature drops. The first law of thermodynamics now reads

$$\Delta u_{23} = -c_v(T_w - T_c)$$
$$w_{23} = -\Delta u_{23} = c_v(T_w - T_c).$$

- $3 \rightarrow 4$ *Reversible isothermal compression*
  During isothermal compression, heat is extracted from the air parcel, otherwise it would warm. Work is provided to the air parcel, i.e. pdV is negative. Analogously to process $1 \rightarrow 2$ we obtain

$$\Delta u_{34} = 0$$
$$w_{34} = -R_d T_c \ln(\frac{V_3}{V_4}) = -R_d T_c \ln(\frac{p_1}{p_3}(\frac{T_c}{T_w})^{\frac{c_p}{R_d}})$$

$$q_{34} = -c_p T_c \left(\frac{\theta_2}{\theta_1}\right)$$

$$q_{34} = W_{34}.$$

Thus, work and heat exchange can be expressed in terms of the minimum and maximum temperatures and minimum and maximum pressure of the cycle. Since $V_4 < V_3$, $q_{34}, w_{34} < 0$, i.e. the air parcel releases heat and the environment performs work on the air parcel. Poisson's law ensures that the final pressure is p_3 once T_c is reached.

- $4 \rightarrow 1$ *Reversible adiabatic compression*
  Analogous to process $2 \rightarrow 3$ we obtain

$$q_{41} = 0$$

$$\Delta u_{41} = c_v(T_c - T_w) > 0$$

$$w_{41} = -\Delta u_{41} = -c_v(T_w - T_c) < 0.$$

The total work done and heat added are $w = w_{12} + w_{23} + w_{34} + w_{41}$ and $q = q_{12} + q_{23} + q_{34} + q_{41}$, respectively. Since $q_{23} = q_{41} = 0$ and $w_{12} = -w_{34}$, the adiabatic legs contribute neither heat nor work to the cyclic process. We obtain $q = q_{12} + q_{34} = w_{12} + w_{34}$ or for the work done $w = R_d(T_w - T_c)\ln\left(\frac{p_1}{p_3}\left(\frac{T_c}{T_w}\right)^{\frac{c_p}{R_d}}\right)$ and for the total heat absorbed during the Carnot cycle $q = c_p(T_w - T_c)\ln\left(\frac{\theta_2}{\theta_1}\right)$. Since w is the area enclosed by the cycle, $w > 0$ and $q > 0$. Since $w = q_{12} + q_{34}$ and $q_{34} < 0$ only a fraction of the heat absorbed by the parcel at the higher temperature is transformed into work. The other fraction is lost at the cooler temperature. Thus, we can define the **efficiency** of the Carnot cycle, $\eta = \frac{work\ output}{heat\ input} = \frac{net\ work}{total\ heat\ added}$ as the ratio between the work done and the heat absorbed by the parcel at T_w

$$\eta = \frac{\Delta q_{12} + \Delta q_{34}}{\Delta q_{12}} = 1 + \frac{\Delta q_{34}}{\Delta q_{12}} = 1 - \frac{T_c}{T_w}. \tag{2.50}$$

The Carnot cycle has the maximum possible efficiency of all processes between T_w and T_c.

Example. Assume a dry air parcel that undergoes a complete Carnot cycle between 1,013.25 and 850 hPa where the temperatures are 10 and 5 °C, respectively. Calculate the mechanical work performed and heat absorbed by an air parcel of unit mass. Determine the efficiency of the process.

Solution. $w_{12} = q_{12} \approx 19{,}341\,\mathrm{J\,kg^{-1}}$, $w_{23} \approx 3{,}585\,\mathrm{J\,kg^{-1}}$, $w_{34} \approx -19{,}000\,\mathrm{J\,kg^{-1}}$, $w_{41} \approx -3{,}585\,\mathrm{J\,kg^{-1}}$. Thus, $\Delta w = \Delta q \approx 341\,\mathrm{J\,kg^{-1}}$, $\eta = 0.018$.

2.6.1.1 Lessons Learned from the Carnot Cycle

1. An increase of energy due to addition of heat and an increase in temperature are independent of each other. Under isothermal conditions ($dT = 0$) $\delta q > 0$ and the additional heat serves for expansion. Under adiabatic conditions, ($\delta q = 0$) $dT > 0$ or $dT < 0$ and temperature changes due to compression or expansion.
2. According to the first law of thermodynamics $\oint du = \oint \delta q - \oint \delta w$ with $\oint \delta q = \oint \delta w$ as $\oint du = 0$ because u is a state variable. The system provides work as $\oint \delta w \neq 0$ and w is not a state variable. Similarly $\oint \delta q \neq 0$ because q is not a state variable. The total work provided and net heat input are given by $\Delta q_{12} + \Delta q_{34}$.
3. The efficiency of the ideal cycle process is defined by the work provided divided by the heat put into the system. It is limited even for reversible processes, always lower than 1, and depends only on the temperatures ratio.
4. From Eq. (2.50) we can derive for an ideal process that $\oint \delta q = \Delta q_{12} + \Delta q_{34} \neq 0$, but

$$\oint \frac{\delta q}{T} = \frac{\Delta q_{12}}{T_w} + \frac{\Delta q_{34}}{T_c} = 0 \tag{2.51}$$

   i.e. dividing the heat by temperature leads to a total differential, $\frac{\delta q}{T} = dS$. It being integrated is a state variable called the entropy, S. Equation (2.51) is **Carnot's theorem** that for any reversible cycle between two heat reservoirs of temperatures T_w and T_c we have $\oint \frac{\delta q}{T} = 0$ irrespective of the details of the cycle.
5. The Carnot cycle determines an ideal process performed with an ideal gas without loss of energy. No realization of a Carnot engine exists because there are always losses resulting in a lower efficiency. In the atmosphere, such losses are friction or conduction. More energy, Δq_{12}, has to be put into the process to gain the same work, $w = \Delta q_{12} + \Delta q_{34}$. The process is not reversible, i.e. its evolution cannot be turned around. The efficiency of such an **irreversible process**[32] is less than that of a reversible[33] one

$$1 + \frac{\Delta q_{34}}{\Delta q_{12}}|_{irr} < 1 - \frac{T_c}{T_w} \tag{2.52}$$

   or

$$\oint \frac{\delta q}{T}|_{irr} = (\frac{\Delta q_{12}}{T_w} + \frac{\Delta q_{34}}{T_c})_{irr} < 0. \tag{2.53}$$

[32] Irreversible processes lead to a permanent change in the environment in some way that even when the system returns to its exactly initial state. For instance, when a balloon bursts, its gases mix with the ambient air. The system is destroyed. The sudden expansion causes a sound wave carrying energy that finally dissipates by being converted to heat.

[33] Reversible processes have the best energy transfer for which they serve often as idealized reference processes in meteorology.

Irreversibility reduces the net heat absorbed during the cycle. A total differential exists only for reversible processes $ds \geq \frac{\delta q}{T}$. This identity is called the **Clausius**[34] **identity**. For an irreversible process, $\delta q/T$ is not a total differential

$$\int_A^B \frac{\delta q}{T}|_{irr} < \int_A^B \frac{\delta q}{T}|_{rev} = s_B - s_A. \tag{2.54}$$

For a closed system with $\delta q = 0$ we obtain $\Delta s \geq 0$, i.e. all real changes in the state variables increase the entropy of a closed system.

6. For many atmospheric applications the efficiency of a process can be estimated by the Carnot cycle. The Carnot cycle, for instance, explains why the winter circulation is stronger than the summer circulation. At the equator, the mean temperature and the amount of heat absorbed remain nearly the same throughout the year. In mid-latitudes, the mean temperature is higher in summer than winter. Consequently, in winter, the efficiency of the Carnot cycle is higher and more heat can be transformed into kinetic energy than in summer.

   Other examples are the energy of a hurricane that can be estimated from the difference between the temperatures at the ocean surface and tropopause (Chap. 6), baroclinic instability associated with low pressure systems, or the energy circulation between the equator and the poles for a non-rotating planet.

2.6.2 Thermodynamic Potentials

The previous description of the laws of thermodynamics dealt with two thermal (S, T) and two mechanical (V, p) variables. We now can combine the first and second law of thermodynamics and obtain for the simple system of a non-moving ideal gas the **Tds-equation**

$$Tds = du(T) + pdV \tag{2.55}$$

Using the first law of thermodynamics and the mathematical definition of the total differential yield

$$T = \frac{\partial u}{\partial s}|_v \tag{2.56}$$

and

$$-p = \frac{\partial u}{\partial v}|_s. \tag{2.57}$$

[34] Rudolf Julius Emmanuel Clausius, German physicist, 1822–1888.

The subscripts indicate the quantity hold constant during differentiation. Obviously, four possibilities exist to choose the thermally and mechanically independent variables, namely, (s, v), (s, p), (T, v) and (T, p) leading to the

- Internal energy, $u(s, v)$, with $du = Tds - pdv$ or $U = TS - pV$
- Enthalpy, $h(s, p)$, with $dh = Tds + vdp$ or $H = U + pV$. Enthalpy results when mechanic energy, pv, is added to internal energy, u. This concept permits characterizing an air parcel not only by its temperature-dependent thermal energy, but also by its mechanical energy, pv.
- **Free energy** or **Helmholtz**[35] **function**, $f(T, v) = u - Ts$, with $df = -sdT - pdv$ or $F = U - TS$. The Helmholtz function reflects the energy available for conversion into mechanical work under isothermal, isochoric conditions.
- **Free enthalpy** or **Gibbs function**, $g(T, p) = u - Ts + pv$, with $dg = -sdT + pdv$ or $G = H - TS$. The Gibbs function reflects the energy available for conversion into mechanical work under isothermal-isobaric processes.

by Legendre[36]-Transformation.[37] The four energies, U, H, F, and G are called the **thermodynamic potentials**.[38] Under irreversible conditions, the first two relations above convert to inequalities. The state variables H and G are auxiliary functions. We use the free enthalpy later in this chapter to derive the **Clausius-Clapeyron**[40] **equation** and to understand phase transitions and water-vapor saturation pressure. We use the free energy and free enthalpy for various considerations in atmospheric chemistry (Chap. 5).

Example. The thermodynamic potentials can be written as a function of differential relationships, e.g. $du = (\frac{\partial u}{\partial s})_v ds + (\frac{\partial u}{\partial v})_s dv$ with $(\frac{\partial}{\partial v}(\frac{\partial u}{\partial s})_v)_s = (\frac{\partial}{\partial s}(\frac{\partial u}{\partial v})_s)_v$. We obtain from comparison $T = (\frac{\partial u}{\partial s})_v$, and $-p = (\frac{\partial u}{\partial v})_s$. Build the various thermodynamic relationships.

(continued)

[35] Hermann von Helmholtz, German physiologist and physicist, 1821–1894.

[36] Adrien-Marie Legendre, French mathematician, 1752–1833.

[37] When in an equation like $du = Tds - pdv$ one of the independent variables is to be replaced by a dependent one (e.g. s or T), the product of the independent variables (here Ts) has to be subtracted from the dependent variable (here u). Doing so provides a new quantity that only depends on the two independent variables T and v.

[38] The relationship between the thermodynamic potentials and the state variables can be easily kept in mind by the **Guggenheim**[39] **scheme** where the four energies are framed by their natural state variables:

S	U	V
H		F
p	G	T

[39] Edward Armand Guggenheim, English thermodynamicist and chemist, 1901–1970. He is famous for his 1933 publication of the *Modern Thermodynamics by the Methods of Willard Gibbs*.

[40] Benoît Paul Émile Clapeyron, French engineer and physicist, one of the founders of thermodynamics, 1799–1864.

(continued)

Solution. $(\frac{\partial T}{\partial v})_s = (-\frac{\partial p}{\partial s})_v$,
$(\frac{\partial s}{\partial v})_T = (\frac{\partial p}{\partial T})_v$,
$(\frac{\partial T}{\partial p})_s = (\frac{\partial v}{\partial s})_p$,
$(\frac{\partial s}{\partial p})_T = (-\frac{\partial v}{\partial T})_p$.

These relationships are known as the **Maxwell relations**. For further consequences, see textbooks on thermodynamics.

2.6.3 Consequences of the Laws of Thermodynamics

By applying the laws of thermodynamics, we can discuss the following atmospheric conditions:

2.6.3.1 Conservation of Energy in the Atmosphere

Dividing Eq. (2.22) by δt and assuming $\delta t \longrightarrow 0$ leads to the **thermodynamic energy equation**

$$Q \equiv \frac{DS}{Dt} = c_p \frac{DT}{Dt} - \frac{1}{\rho}\frac{Dp}{Dt}. \tag{2.58}$$

Herein, Q is the diabatic heating rate per unit mass. The main physical processes that change Q are the release and consumption of heat during phase transition processes (Sect. 2.7) as well as radiative cooling and heating associated with emission and absorption of electromagnetic waves (Chap. 4). At the surface, conduction may occur.

For a variety of applications, it is more comfortable to use the potential temperature rather than temperature. Under diabatic heating, the thermodynamic energy equation using potential temperature reads

$$\frac{D\theta}{Dt} = \frac{Q}{c_p}\left(\frac{p}{p_0}\right)^{-\kappa}. \tag{2.59}$$

2.6.3.2 Behavior of Entropy

Entropy cannot decrease in closed systems, while it can decrease in open systems when entropy is exported.

2.6.3.3 Cyclic Transformation

A **cyclic** process leads to $\oint \delta W = \oint \delta Q$, i.e. in dry air, an air parcel can rise and descend to the same level without impact on the environment.

2.6.3.4 Isothermal Transformation

During an isothermal process temperature remains constant, $dT = 0$. Consequently, the amount of heat exchanged is $Q = \int_1^2 \delta W = \int_1^2 p dV = mRT \int_1^2 \frac{dV}{V} = mRT \ln(\frac{V_2}{V_1})$.

2.6.3.5 Isobaric Transformation

For an isobaric process ($dp = 0$), work $\delta W = pdV$ ($W = p(V_2 - V_1)$) is performed or heat $\delta Q = C_p dT$ ($Q = C_p(T_2 - T_1)$) is provided changing the inner energy of the air parcel by $\Delta U = C_p(T_2 - T_1) - p(V_2 - V_1)$.

2.6.3.6 Isochoric Transformation

For an isochoric process ($dV = 0$), the first law of thermodynamics reduces to $\delta Q = dU = C_v dT$ or $\Delta U = C_v(T_2 - T_1)$.

2.6.3.7 Adiabatic Transformations: Poisson's Relations

During adiabatic processes the system and its environment do not exchange heat ($\delta Q = 0$). The first law of thermodynamics now reads after some algebra $\frac{dT}{T} = (1 - \frac{1}{\gamma})\frac{dp}{p}$ with $\frac{1}{\gamma} = \frac{c_v}{c_p}$. Integration yields $\ln T = \ln p^{\frac{\gamma-1}{\gamma}} + \ln(constant)$, which can be transformed to $T p^{\frac{1-\gamma}{\gamma}} = constant$. Using the equation of state (2.1) yields $TV^{\gamma-1} = constant$ or $pV^{\gamma} = constant$. These three equations express the **Poisson's relations** for adiabatic processes. Since for dry air $\gamma = 1.4$, the term $TV^{\gamma-1}$ says that as an air parcel rises and expands, its temperature decreases. As $\delta Q = 0$, this increase of volume is due to the expansion work of the parcel carried out on its environment.

Weather forecasters use thermodynamic charts that base on these relations to evaluate quickly atmospheric processes (Fig. 2.16).

2.7 Moist Air

Despite the low and strongly varying fraction (0–4 %, cf. Table 1.1) of water vapor, it is weather and climate[41] relevant. As part of the water-, energy-, and trace gas cycles, water vapor is involved in cloud and precipitation formation (Chap. 3), affects radiation (Chap. 4) and many gas-phase chemical processes (Chap. 5).

Various measures exist to quantify atmospheric humidity. These measures apply exclusively to water vapor, and not to the liquid (drops) or ice phase (crystals) in the air.

2.7.1 Vapor Pressure

Traditionally the letter e denotes water-vapor pressure.[42] In the atmosphere, e ranges from 0 to 40 hPa. We can approximate atmospheric water vapor as an ideal gas

$$e = \rho_v R_v T. \tag{2.60}$$

2.7.2 Absolute Humidity

The **absolute humidity**[43]

$$a := \rho_v = \frac{e}{R_v T} \tag{2.61}$$

is the density of the water vapor ($\mathrm{kg\,m^{-3}}$) or the water-vapor content. The absolute humidity of an air parcel changes whenever the air parcel expanses or contracts, i.e. despite no water vapor is removed from/added to the air parcel absolute humidity decreases/increases when the parcel expanses/contracts.

Example. Show that absolute humidity increases for a contracting air parcel.

Solution. $a = \rho_v = \frac{1}{V}$. Thus, a contraction yields $V - \Delta V$ and $a\prime = \frac{1}{V-\Delta V} > a$. q.e.d.

[41] According to the World Meteorological Organization (WMO), climate is the average weather over 30 years. See also Chap. 7.

[42] Although in the SI-system, its unit is Pa, meteorologists traditionally use hPa.

[43] Under tropospheric conditions, absolute humidity (in $\mathrm{g\,m^{-3}}$) is approximately 0.8 times the water-vapor pressure in hPa.

2.7.3 Specific Humidity

Specific humidity or **specific mixing ratio**[44] is defined by the ratio of the water-vapor mass m_v to the mass of moist air m_m within the same volume or by the ratio of the density of water vapor ρ_v to that of moist air ρ_m

$$q := \frac{\rho_v}{\rho_m} = \frac{\rho_v}{\rho_d + \rho_v} = \frac{m_v}{m_m} \tag{2.62}$$

where ρ_d is the density of dry air. The unit of the specific mixing ratio is $\mathrm{kg\,kg^{-1}}$ in the SI-system, but cloud physicists often use $\mathrm{g\,kg^{-1}}$.

According to Dalton's law (2.5), the equation of state (2.1) for moist air reads $p = \rho_d R_d T + \rho_v R_v T$ where p is pressure, and R_d and R_v are the individual gas constants for dry air and water vapor, respectively. Rearranging the equation of state for the density of dry air and water-vapor density and inserting yield for the specific mixing ratio[45]

$$q = \frac{\frac{e}{R_v T}}{\frac{p-e}{R_d T} + \frac{e}{R_v T}} = \frac{R_d}{R_v} \frac{e}{p - (1 - \frac{R_d}{R_v})e} = 0.622 \frac{e}{p - 0.378e}. \tag{2.63}$$

Specific humidity is independent of temperature. The main advantage of specific humidity is that it is conserved, i.e. it does not change when the air parcel expands or contracts.

Example. Assume a mole fraction of water vapor of 2.5 mol% and a partial pressure of water vapor that corresponds to a water-vapor density of $0.01\,\mathrm{kg\,m^{-3}}$. Calculate the molar mass M, density ρ, and specific humidity q of the moist air.

Solution. With the molar masses of water and dry air of 18.015 and $28.953\,\mathrm{g\,mol^{-1}}$. $M_m = \alpha M_v + (1-\alpha) M_d = 0.025 \cdot 18.015\,\mathrm{kg\,kmol^{-1}} + 0.975 \cdot 28.953\,\mathrm{kg\,kmol^{-1}} = 28.68\,\mathrm{kg\,kmol^{-1}}$

$$\rho_m = \frac{\rho_{air} M_m}{\alpha M_d} = \frac{0.01\,\mathrm{kg\,m^{-3}} 28.68\,\mathrm{kg\,kmol^{-1}}}{0.025 \cdot 18.015\,\mathrm{kg\,kmol^{-1}}} = 0.637\,\mathrm{kg\,m^{-3}}.$$

$$q = \frac{\rho_v}{\rho_m} = 0.0157\,\mathrm{kg\,kg^{-1}}.$$

[44] At 1,000 hPa, the specific humidity (in $\mathrm{g\,kg^{-1}}$) is about 0.6 times the water-vapor pressure in hPa.

[45] Specific humidity is often approximated by $q \approx 0.622 \frac{e}{p}$ as $p \gg 0.378e$ in the troposphere.

2.7.4 Mixing Ratio

Another possibility to express humidity is the **mixing ratio** that relates the density of water vapor ρ_v in air to that of dry air ρ_d

$$r := \frac{\rho_v}{\rho_d} = \frac{\frac{e}{R_v T}}{\frac{p-e}{R_d T}} = \frac{R_d}{R_v}\frac{e}{p-e} = 0.622\frac{e}{p-e}. \tag{2.64}$$

Where we used the equation of state (2.1). Like the specific humidity, the mixing ratio[46] is a conservative quantity independent of temperature.

Example. Revisit the previous example and determine the water-vapor mixing ratio r of the moist air. Discuss your result.

Solution. $r = \frac{m_v}{m_d} = \frac{M_v \alpha}{M_d(1-\alpha)} = \frac{18.015\,\mathrm{kg\,H_2O\,kmol^{-1}}0.025}{28.953\,\mathrm{kg\,dry\,air\,kmol^{-1}}(1-0.025)} = 0.016\,\mathrm{kg\,kg^{-1}}$. The difference results from the neglecting of moisture in the denominator.

Example. Show that in general, $q = \frac{r}{1+r}$. Note that $\rho_d = \frac{p-e}{R_d T}$.

Solution. $q := \frac{\rho_v}{\rho_d+\rho_v}$ with $\rho = \frac{m}{V}$ yields $q = \frac{\frac{m_v}{V}}{\frac{m_d}{V}+\frac{m_v}{V}} = \frac{m_v}{m_d+m_v}$ with $r_v = \frac{m_v}{m_d}$ we obtain $q = \frac{r_v}{1+r_v}$. q.e.d.

2.7.5 Number Density

Another (seldom-used) measure to express water vapor in air is the number of molecules per unit volume, n_i / V called the **number density**. This measure is often applied with respect to the cloud and ice condensation nuclei (Chap. 3) or in air chemistry for gases or aerosols (Chap. 5). When one follows the motion of an air parcel, the number density can change by phase transition, chemical reactions or through changes of the volume. Thus, for most applications the mass and volume mixing ratios are more appropriate when dealing with chemistry transport, because only phase transition, chemical production and loss, but not an altering volume influence these quantities.

[46] The mixing ratio is often approximated as $r \approx 0.622\frac{e}{p}$ as $p \gg e$ in the troposphere.

2.7.6 Virtual Temperature

Moist air has a lower molecular weight than dry air for which the individual gas constant of moist air exceeds that of dry air (Eqs. 2.2 and 2.6). Since the individual gas constant of moist air depends on the moisture content, R_m has to be recalculated whenever moisture changes (Eqs. 2.6 and 2.5). To avoid this computational burden, we define a **virtual temperature** T_v that a dry air parcel would have to have to have the same density as the moist air parcel at the same pressure. The virtual temperature permits us to use the gas constant for dry air in the equation of state.

$$\frac{p}{R_m T} = \rho_m = \rho_d + \rho_v = \frac{p-e}{TR_d} + \frac{e}{TR_v} =: \frac{p}{R_d T_v}. \tag{2.65}$$

Comparison and rearranging provides

$$\frac{p}{R_d} \frac{1}{\frac{p-e}{R_d T} + \frac{e}{R_v T}} = T \frac{p}{p - e + \frac{R_d}{R_v} e} = T \frac{p}{p - (1 - \frac{R_d}{R_v})e} \tag{2.66}$$

Rearranging the equation for the specific mixing ratio q (Eq. 2.63) results in $p - (1 - \frac{R_d}{R_v})e = \frac{R_d}{R_v}\frac{e}{q}$. Introducing this into the above equation yields the virtual temperature

$$T_v := T \frac{(1 - \frac{R_d}{R_v})e + \frac{R_d}{R_v}\frac{e}{q}}{\frac{R_d}{R_v}\frac{e}{q}} = T(1 + \frac{(1 - \frac{R_d}{R_v})}{\frac{R_d}{R_v}} q) = T(1 + 0.61q). \tag{2.67}$$

Herein, $T \cdot 0.61q$ is the **virtual temperature addition**. Typical values for the virtual temperature addition range between 0 and 5 K. Since at same temperature and pressure, moist air is less dense than dry air, the virtual temperature is always greater than the actual temperature.

The equation of state (2.1) determined with the specific humidity or mixing ratio reads

$$p = \rho_m R_d T(1 + 0.61q) = \rho_m R_d T_v \tag{2.68}$$

and

$$p = \rho_d R_d T(1 + 1.61r) = \rho_d R_d T_v \tag{2.69}$$

respectively. The virtual temperature is a combined temperature-moisture measure that includes air humidity in the equation of state without the necessity of recalculating the individual gas constant.

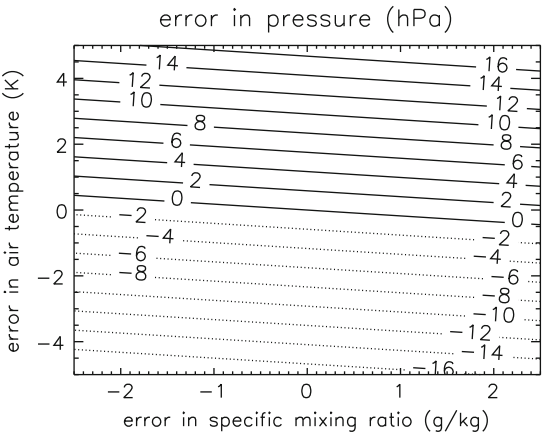

Fig. 2.13 Impacts of temperature and specific mixing ratio errors on simulated surface pressure. The reference (assumed correct) conditions are an atmospheric density, pressure, temperature and specific mixing ratio of 1.19 kg m^{-3}, 1,003.4 hPa, 20 °C, and 3.5 g kg^{-1}, respectively

At same temperature, moist air is less dense than dry air because some of the dry air (molecular weight 28 g mol^{-1}) has been replaced by water vapor (molecular weight 18 g mol^{-1}).[47]

Figure 2.13 exemplarily shows the impact of small changes in specific humidity and temperature on pressure. Small changes (in the order of measurement errors) in moisture marginally affect pressure, while those in temperature can have notable impact.

Example. Determine the virtual temperature T_v at normal pressure for $T_1 = 298.15\,\mathrm{K}$ and $T_2 = 273.15\,\mathrm{K}$ and calculate the deviation in density when using temperature instead of virtual temperature. Assume specific mixing ratios of $19.67 \cdot 10^{-3}$ and $3.76 \cdot 10^{-3}$ kg kg^{-1}, respectively. Discuss the effect of neglecting the moisture effect.

Solution. Equation (2.67) provides $T_{v,1} = 301.73\,\mathrm{K}$ and $T_{v,2} = 273.78\,\mathrm{K}$. Rearranging the equation of state (2.1) provides 1.184 and 1.293 kg m^{-3} when using temperature, and 1.170 and 1.290 kg m^{-3} when using virtual temperature. Here, the neglecting of moisture yields errors of 1 and 0.2 %, respectively.

Example. Derive the virtual temperature equation as a function of the mixing ratio, r.

(continued)

[47] This fact explains why more homeruns occur during humid and warm weather conditions. The ball experiences less resistance than under cold, dry conditions.

(continued)

Solution. Using the equation of state $p = R_d \rho_d T + R_v \rho_v T = \rho_d R_d T(1 + \frac{R_v \rho_v}{R_d \rho_d}) = \rho_d R_d T(1 + 1.61 r_v)$ with $r = \frac{\rho_v}{\rho_d}$.

2.8 Phase Transitions

So far, we applied the fundamental equations derived in the previous sections, only to closed, homogeneous systems (e.g. an air parcel), i.e. one phase. In such systems, we had not to specify how the thermodynamic functions depend on the composition of the system. Clouds, however, are heterogeneous systems that involve at least two, sometimes three phases (Fig. 2.2). Thus, we have to consider the internal equilibrium conditions between phases. Despite a cloud as a whole is a closed system, the phases can be regarded as open subsystems that exchange mass (e.g. evaporation of cloud water, deposition of water vapor onto ice crystals). The cloud dry air is a closed system, and the water substances in the cloud that can exist in three phases (water vapor, water droplets, ice crystals), are three open systems (Fig. 2.2). The chemical potential $\mu = \mu(T, p)$ considers the mass exchanges (evaporation, condensation, deposition, sublimation, freezing, melting) between the subsystems.

2.8.1 Thermodynamic Properties of Water

Water vapor like dry air can be approximated as an ideal gas[48] that obeys the equation of state (2.1) when it exists only by itself. When water vapor and water/ice coexist, the equations applicable to ideal gases are invalid because the mixture is not an ideal gas. One phase has the independent variables T, p, and the other T', p'. The equilibrium requires that $T = T'$ and $p = p'$. Since the mass of the two subsystems does not remain constant, we also have to consider $\mu = \mu'$, which expresses the equilibrium for the mass exchange. This equation reduces the number of independent variables by one more, because $\mu = \mu(p, T) = \mu\prime(p', T')$. Since $\mu(p, T) = \mu'(p, T)$, $p = f(T)$. Consequently, when we fix the temperature at which the phases are in equilibrium, we obtain a fixed pressure value. This relation leads to curves (called saturation curves) along which the two phases coexist in equilibrium. Consequently, in a one-component system with two phases, one independent variable exists.

[48] Note that this approximation is not as good as for dry air because at conditions close to saturation, attractive forces between molecules become significant (Chap. 3).

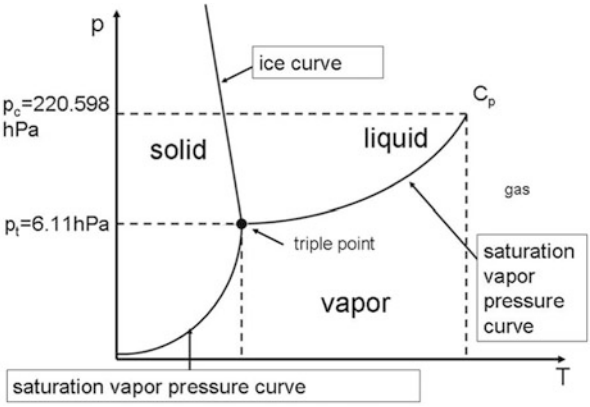

Fig. 2.14 Schematic view of phase diagram of water

At $T > 0\,°C$, and values of e higher than those of the saturation curve only water vapor exists (Fig. 2.14). Below the saturation curve, only water vapor exists independent of air temperature. At $T < 0\,°C$ and $e > 0.6078\,hPa$, only ice should exist. However, in the atmosphere, super-cooled water and ice can co-exist between $-35\,°C$ or so and $0\,°C$. Below $-40\,°C$, super-cooled water freezes instantaneously (Chap. 3).

Analogously, for a one-component system with three phases, the number of independent variables reduces from six to zero, meaning that all values are fixed. This point, at which all three water phases are in equilibrium, is the **triple point** given by 6.1078 hPa, 0.0099 °C.[49]

In summary, the greater the number of phases the fewer the degrees of freedom.[50]

2.8.2 *Latent Heat*

The binding forces within the continuum water hinder the water molecules to establish equilibrium in the entire space taken by the gas. At the surface, water molecules of the liquid go into the gas phase while other water molecules of the gas phase go into the liquid phase. In equilibrium, no net transport occurs. When more molecules leave the liquid than enter the gas phase, a net evaporation results; the opposite case leads to net condensation (Fig. 2.15). When at fixed temperature and pressure, two phases are in equilibrium, isobaric transformations are also isothermal transformation. Thus, the amount of heat exchanged depends on the mass changes, and the work done due to the volume change. Despite the

[49] On the Celsius scale, the zero-point is defined so it corresponds to the freezing point of air-saturated water at 1,013.25 hPa.

[50] According to Gibbs, the number of independent variables, N for a heterogeneous system with C different, non-reactive components in P phases is $N = C + 2 - P$.

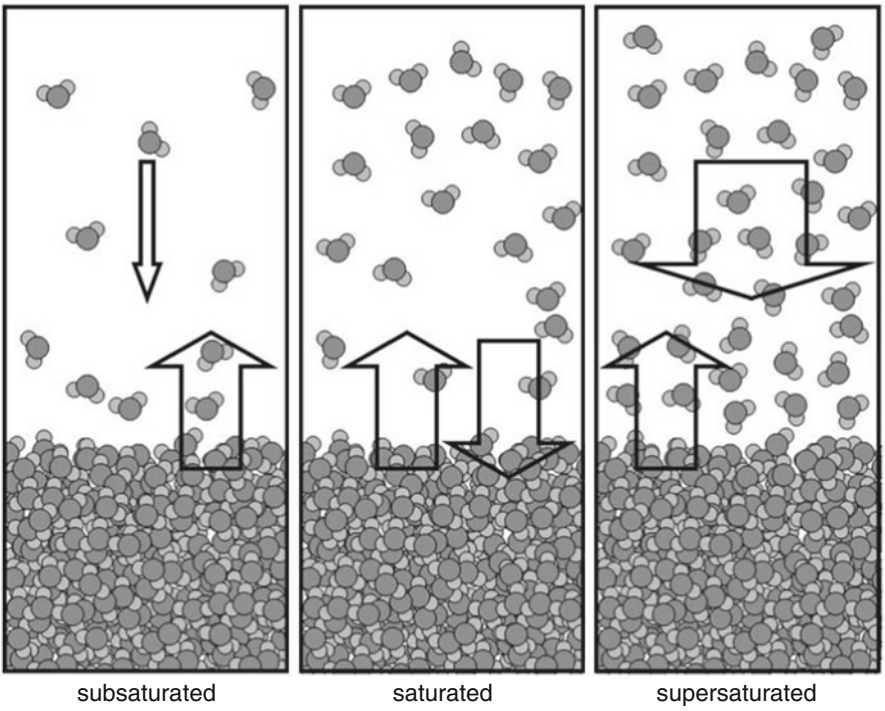

Fig. 2.15 Schematic view of the molecular basis of evaporation, saturation and condensation. The rate at which the molecules leave the continuum water to enter or leave the gas phase is indicated by the upward and downward arrows. Equilibrium ($e = e_s$, $dp = 0$, $dT = 0$) exists when the fluxes are equal. Otherwise evaporation ($e < e_s$, $dp = 0$, $dT < 0$; *left panel*) or condensation ($e > e_s$, $dp = 0$, $dT > 0$; *right panel*) occur

mass changes, the temperature of the system remains the same. By definition the latent heat absorbed/released by the heterogeneous system during an isobaric phase transition is $L = \delta Q_p$. Consequently, the latent heat release or heat consumed during a phase transition is the change in enthalpy

$$L_v = H_v - H_w = U_v - U_w + p_{wv}(V_v - V_w)$$
$$L_f = H_w - H_i = U_w - U_i + p_{wi}(V_w - V_i)$$
$$L_s = H_v - H_i = U_v - U_i + p_{vi}(V_v - V_i)$$

where L_v, L_f, and L_s are the latent heat of vaporization, fusion and sublimation, the subscripts w, v, and i refer to water, water vapor, and ice, respectively, and p stands for the equilibrium pressure between the two phases. At the triple point, $p_{wv} = p_{wi} = p_{vi} = e_{sw,o} = 6.1078\,\text{hPa}$ and the specific latent heats satisfy $l_s = l_f + l_v$.

At 0 °C, the latent heat of deposition, condensation and freezing[51] is $2.833 \cdot 10^6$, $2.5 \cdot 10^6$, and $0.333 \cdot 10^6$ J kg^{-1}, respectively.

According to the first law of thermodynamics, an isobaric phase transition is given by $dU = L - pdV = L - R_v T$. With $dV = V_v - V_{w,i} \approx V_v$ for vaporization and sublimation, and $dV \approx 0$ for fusion, we obtain $dU = L$ for fusion and $dU = L - mR_v T$ for vaporization or sublimation.

To remove a molecule from the crystal structure more energy is required than to take it out of the bounds in the water continuum. The molecules gain potential energy when they get into the less ordered state (e.g. from the solid to the liquid or gaseous state, or from the liquid to the gaseous state). This potential energy is the latent heat of vaporization, fusion or sublimation depending on the phase transition considered. Thus, in the atmosphere, latent heat is available in form of water vapor; it transfers into **sensible heat** or work when condensation or freezing occur.

2.8.3 Clausius-Clapeyron Equation

At point X, the total volume and internal energy of a heterogeneous system in equilibrium consisting of water vapor and water are $V = m_w\alpha_w + m_v\alpha_v$ and $U = m_w u_w + m_v u_v$ where α and u are the specific volume and internal energies of the two phases. When we move the system from X to X', the volume changes by dV in response to the mass exchange dm between the two subsystems. At point X', the volume is $V + dV = (m_w - dm)\alpha_w + (m_v + dm)\alpha_v$ or $dV = (\alpha_v - \alpha_w)dm$. Analogously, we obtain for $dU = (u_v - u_w)dm$. By considering that during the phase transition $u_v - u_w + e_{sw}(\alpha_v - \alpha_w) = l_v$ we obtain $\frac{dU}{dV} = \frac{l_v}{\alpha_v - \alpha_w} - e_{sw}$. The combined first and second law of thermodynamics $TdS = dU + pdV$ and integration for dS using the Maxwell relations provide $T\frac{\partial p}{\partial T}\,|_V = \frac{\partial U}{\partial V}\,|_T + p$. Differentiation of enthalpy $H = U + pV$ yields $\frac{\partial U}{\partial V}\,|_T = T\frac{\partial p}{\partial T}\,|_V - p$. According to Joule's second law[52] $\frac{\partial U}{\partial V}\,|_T = 0$ for an ideal gas. As pointed out above, water and water vapor in equilibrium are not an ideal gas, and U and e_{sw} depend on temperature only. Since the transformation is isothermal, we obtain $\frac{\partial U}{\partial V}\,|_T = \frac{dU}{dV}$ or $\frac{\partial e_{sw}}{\partial T}\,|_V = \frac{de_{sw}}{dT}$ and $\frac{dU}{dV} = T\frac{de_{sw}}{dT} - e_{sw}$. After some algebra, we obtain the **Clausius-Clapeyron-equation**

$$\frac{de_{sw}}{dT} = \frac{l_v}{T\Delta v} \tag{2.70}$$

[51] For the heat consumed during sublimation, vaporization and fusion the sign changes. The latent heats like the specific heats insignificantly depend on temperature $L_v = 2.501 \cdot 10^6 (\frac{T_0}{T})^b$ with $b = 0.167 + 3.67 \cdot 10^{-4} T$ for 233 K $< T <$ 313 K; $L_m = 0.3337 \cdot 10^6 + 2{,}030.6\,T - 10.47\,T^2$ for -50 °C $< T <$ 0 °C. Typically, atmospheric scientists neglect this temperature dependency.

[52] James Prescott Joule, English physicist and brewer, 1818–1889; Joule formulated several physical laws. His second law states that the internal energy of an ideal gas is independent of its volume and pressure, and depends only on its temperature.

that describes the water-vapor pressure curve for equilibrium between water vapor and water at various temperatures. Here, Δv is the difference in the specific volumes of the liquid and gaseous phase, which slightly depends on temperature.

We can solve the Clausius-Clapeyron equation analytically under the assumption $l_v = constant$, and $v_w \ll v_v$ so that $\Delta v \approx v_v$. Inserting the equation of state for water vapor ($\frac{1}{\rho_v} = v_v = \frac{R_v T}{e_{sw}}$) in the Clausius-Clapeyron equation provides $\frac{de_{sw}}{dT} = \frac{l_v}{T}\frac{e_{sw}}{R_v T}$ or

$$\frac{de_{sw}}{e_{sw}} = \frac{l_v}{R_v}\frac{dT}{T^2}. \tag{2.71}$$

Integration provides $\ln \frac{e_{sw}}{e_{sw,o}} = -\frac{l_v}{R_v}(\frac{1}{T} - \frac{1}{T_o}) = \frac{l_v}{R_v T_o}(\frac{T-T_o}{T})$ and

$$e_{sw} = e_{sw,o} \exp(\frac{l_v}{R_v T_o}\frac{T - T_o}{T}) \tag{2.72}$$

with $l_v = 2.5 \cdot 10^6\,\mathrm{J\,kg^{-1}}$, $R_v = 461.5\,\mathrm{J\,kg^{-1}\,K^{-1}}$, $e_{sw,o} = 6.1078\,\mathrm{hPa}$, and $T_o = 273.15\,\mathrm{K}$, and $l_v/(R_v T_o) = 19.81$. The equation serves to calculate the saturated water-vapor pressure. Curves of saturation pressure with respect to water are also shown on thermodynamic diagrams (Fig. 2.16).

Analogous considerations can be made for the interfaces ice-water, and ice-vapor. Figure 2.14 illustrates that the water-vapor pressure over water exceeds that over ice. The difference in vapor pressures over ice and water explains why clouds glaciate (Chap. 3), ice lenses grow in soils, and why snow metamorphism[53] occurs.

The saturation water-vapor pressure expresses how many water vapor could exist, not how many actually exists. The water-vapor pressure of an air parcel cannot exceed the **saturation water-vapor pressure** $e_s = e_s(T)$. The temperature at which the actual vapor pressure equals the saturation over water $e := e_{sw}(T) = e_{sw}(T_d)$ is the **dew-point temperature** or shortly **dew point**, T_d. The dew-point temperature indicates the moisture content. When combined with air temperature, it indicates relative humidity. This moisture measure has no temperature relation although it is expressed as a temperature.

Analogously, the temperature at which the actual vapor pressure equals the vapor pressure at saturation over ice, $e := e_{si}(T)$ defines the **ripe point temperature** or **riming point**. At temperatures below freezing we call the dew point the **frost point** or **frost-point temperature**, i.e. $e := e_{sw}(T_d)$ with $T_d < 0\,^\circ\mathrm{C}$.

We can define for $e = e_s(T)$ the **absolute humidity at saturation**, as $a_s = \frac{e_s}{R_v T}$. The saturated mixing ratio r_s is reached when the actual water-vapor pressure e

[53]The transformation of ice crystals to rounded grains of about 2 mm in diameter is referred to as snow metamorphism. It partly is due to water-vapor transfer from sharply curved edges to smoother surfaces of the ice crystals because of the dependency of water vapor pressure on curvature. Also, temperature gradients within the snow may result in water-vapor transfer and re-deposition within the snowpack.

equals the saturation water-vapor pressure e_s. Using the equation of state (2.1), $\rho_v = \frac{e}{R_v T}$ and $e = e_s(T)$ yield the **specific humidity at saturation** as $q_s = q(e_s(T))$.

2.8.3.1 Empirical Formulae

Various empirical formulae exist to determine the saturation water-vapor pressure, and their results are listed in lookup tables (e.g. WMO). Often the **Magnus-formula**[54] is applied

$$e_{sw} = 6.1078 \exp\left(\frac{17.1\delta}{235 + \delta}\right) \tag{2.73}$$

with the temperature δ in °C and e_{sw} in hPa.

Another often-used relation is that by Murray[55]

$$e_{sw,i} = 6.1078 \exp\left(\frac{a(T - 273.16\,\mathrm{K})}{T - b}\right) \tag{2.74}$$

with $a = 17.2693882$ and $b = 35.86\,\mathrm{K}$ over water (subscript w), and $a = 21.8745584$ and $b = 7.66\,\mathrm{K}$ over ice (subscript i), and $e_{sw,i}$ in hPa. Here, temperature, T, has to be inserted in K. Except for small discrepancies, the constants also result from the analytical integration.

2.8.3.2 Relative Humidity

We now can introduce a further measure for the atmospheric water vapor. The **relative humidity** relates the actual water vapor pressure to the saturation pressure at the same air temperature or the ratio of specific humidity to specific humidity at saturation or the ratio of water vapor mixing ratio to water-vapor mixing ratio at saturation

$$rh = \frac{e}{e_s} = \frac{q}{q_s} = \frac{r}{r_s}. \tag{2.75}$$

In contrast to water-vapor pressure, absolute humidity, specific humidity and the mixing ratio that are absolute measures of the atmospheric water vapor, relative humidity is a relative measure. Relative humidity indicates the degree of saturation and is often expressed in percent ($RH = 100 \cdot rh$). In the troposphere, relative humidity ranges between slightly above 0 to slightly above 1.

---

[54] Heinrich Gustave Magnus, German physicist and chemist, 1802–1870.

[55] Sir John Murray, British oceanographer, 1841–1914.

Relative humidity depends on the atmospheric water-vapor amount, and on the temperature-dependent saturation water-vapor pressure. Consequently, relative humidity is not conserved. Nevertheless, meteorologists use relative humidity because many devices (e.g. hair hygrometer[56]) measure this quantity (Appendix B).

Example. In Arches National Park, an air temperature of 45 °C with a relative humidity of 10 % was observed. In Denali National Park, an air temperature of −5 °C and a relative humidity of 100 % were found. Where does the air contain more water vapor and why?

Solution. The Magnus-formula, $e_{sw} = 6.1078 \exp(\frac{17.1\delta}{235+\delta})$ yields 95 and 4.22 hPa for Arches and Denali, respectively. The water-vapor content is given by $\rho_v = \frac{RH \cdot e_{sw}}{R_v T}$. Inserting the values provides a water-vapor content of 0.0065 and 0.0034 kg m^{-3} at Arches and Denali National Park, respectively. Thus, the unit volume of air with a relative humidity of 100 % contains less water vapor (Fig. 2.14).

2.9 Vertical Temperature Gradients and Mixing in a Moist Atmosphere

Air becomes saturated by any one of the three processes

- Adding water vapor to the air,[57]
- Decreasing air temperature to the dew/frost point, and
- Mixing cold air with warm, moist air.

As phase transition depends on moisture and temperature, we discuss the change of these quantities with height.

2.9.1 Dew-Point Temperature Gradient

According to the hydrostatic equation (2.7) the change of pressure with height reads $\frac{dp}{dz} = -\frac{p}{R_d T} g$ for a dry atmosphere. The gas constant and specific heat at constant pressure of moist air differ slightly from that of dry air. Since the mass and specific humidity are conservative quantities $\frac{dq}{dz} = 0$ or $\frac{dm}{dz} = 0$. According to the

[56] Many organic materials show expansion and shrinking that are functions of humidity.

[57] Warm water from a bath adds moisture to the bathroom and brings it to condensation at the mirrors and surfaces of the room, and fog develops.

Clausius-Clapeyron equation $\frac{1}{e_s}\frac{de_s}{dT} = \frac{L_v}{R_v T^2}$, and applying the mathematical identity $\frac{de_s}{dz} = \frac{de_s}{dT}\frac{dT}{dz}$ as well as introducing the dry adiabatic lapse rate yield

$$\frac{1}{e_s}\frac{de_s}{dz} = \frac{L_v}{R_v T^2}\Gamma_d. \tag{2.76}$$

Since $q \approx 0.622(e/p)$ and $dq = 0$, the relative changes for an adiabatically ascending air parcel are the same for e and p, i.e.

$$\frac{1}{e}\frac{de}{dz} = \frac{1}{p}\frac{dp}{dz}. \tag{2.77}$$

The change of dew-point temperature with height results from the definition of the dew point, i.e. $e := e_s$

$$\frac{dT_d}{dz} = \frac{de}{dz}\left(\frac{de}{dT_d}\right)^{-1} = \frac{1}{e}\frac{de}{dz}\left(\frac{1}{e_s(T_d)}\frac{de_s(T_d)}{dT_d}\right)^{-1} = \frac{0.172\,\mathrm{K}}{100\,\mathrm{m}}. \tag{2.78}$$

The terms on the r.h.s. give the relative change of e that only depends on the temperature of the environment. The term in brackets is only a function of dew-point temperature. Since temperature decreases more quickly with height than the dew-point temperature, relative humidity increases, and saturation with respect to water vapor/ice is reached and condensation/deposition occurs.

The height, z_{lcl}, at which saturation is reached, is called the level of condensation or **lifting condensation level** (LCL). It is identical to cloud base. When the near-surface values of T_0 and $T_{d,0}$ are known from psychrometer measurements (Appendix B), we can determine the lifting condensation level in a thermodynamic chart as the intersection of the dry adiabate and the mixing ratio curve that correspond to the parcel temperature and dew-point temperature (Fig. 2.16). For synoptic purposes, it is important to know that the LCL determined by the near-surface values only establishes when the near-surface parcels are those that condense after ascending.

Example. Near-surface air temperature T_s and dew point $T_{d,s}$ are at 38 and 22 °C, respectively. Determine cloud-base height z, and the temperature T_{cb} and dew point $T_{d,cb}$ at cloud base. What happens when further lifting occurs?

Solution. At cloud base, $T_{d,cb} = T_{cb}$. Furthermore, $T_{cb} = T_s - \frac{0.98\,^\circ\mathrm{C}}{100\,\mathrm{m}}z$ and $T_{d,cb} = T_{d,s} - \frac{0.172\,^\circ\mathrm{C}}{100\,\mathrm{m}}z$. Thus, $T_s - T_{d,s} = z(\frac{0.98\,^\circ\mathrm{C}}{100\,\mathrm{m}} - \frac{0.172\,^\circ\mathrm{C}}{100\,\mathrm{m}})$, and $z = \frac{T_s - T_{d,s}}{\frac{0.98\,^\circ\mathrm{C}}{100\,\mathrm{m}} - \frac{0.172\,^\circ\mathrm{C}}{100\,\mathrm{m}}} \approx 1{,}980\,\mathrm{m}$, $T_{d,cb} = T_{cb} = T_s - \frac{0.98\,^\circ\mathrm{C}}{100\,\mathrm{m}}1{,}980\,\mathrm{m} = 38\,^\circ\mathrm{C} - \frac{0.98\,^\circ\mathrm{C}}{100\,\mathrm{m}}1{,}980\,\mathrm{m} \approx 18.6\,^\circ\mathrm{C}$. Any further lifting results in condensation or deposition of water vapor and temperature decreases slower than the dry adiabatic lapse rate due to the release of latent heat.

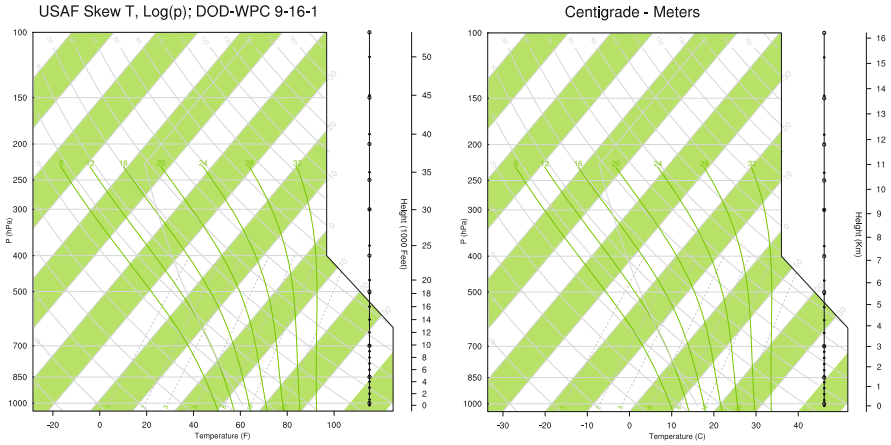

Fig. 2.16 Examples of thermodynamic diagram charts (*left*) as used by the US Air Force, and (*right*) in metric units as used by various weather services

2.9.2 Saturation Adiabatic Temperature Gradient

When an air parcel reaches the LCL, further ascend follows under saturated conditions, and condensation and/or deposition occurs. Due to the release of latent heat, temperature decreases less rapidly with height than during a dry-adiabatic ascend. The derivation of the Clausius-Clapeyron equation introduced this heat as enthalpy of vaporization (Sect. 2.8.3).

When we assume the condensate as part of the thermodynamic system of the rising air parcel and that it remains in the air parcel, the latent heat released represents the conservation of energy within the air parcel. No transfer of heat between the air parcel and its environment occurs. In this sense, the process is still dry adiabatic despite $\delta q \neq 0$ as δq has no external source. In a **saturated adiabatic process** (**moist adiabatic process**) the only source of diabatic heating/cooling is the phase transition process. A moist adiabatic process is reversible when the condensate remains in the air parcel. Cooling is less than the dry adiabatic lapse rate because of the release of latent heat during condensation.

Meteorologists often assume that all condensate falls out immediately. This assumption makes the process irreversible. The air parcel is not a closed system anymore as fallout is an exchange of mass with the environment. Such a process is called **pseudo-adiabatic**.[58]

[58]Many early Global Circulation and numerical weather prediction models used the pseudo-adiabatic assumption, i.e. that once condensed the water falls out immediately. This assumption led to incorrect moisture and temperature profiles as condensate might have undergone further phase-transition processes (e.g. freezing, evaporating below cloud base) thereby consuming heat or releasing latent heat after leaving the cloud.

Based on these considerations we now can write the laws of the previous sections for an atmosphere with different phases of water (Table 2.4).[59] The first law of thermodynamics given with inclusion of phase transition changes reads $ds = c_p dT - (1/\rho)dp + L_v dr_s$. This means the heat of condensation must be multiplied by the change in the saturated mixing ratio $r_s = 0.622 e_s(T)/(p - e_s(T))$ that results from condensation/deposition or evaporation/sublimation.

Similar to the dry adiabatic lapse rate, we can derive the saturated or moist lapse rate $dT/dz = -\Gamma_s$. By using the same concept as for potential temperature, we can define the **equivalent potential temperature**,[60] θ_e that is invariant to saturated ascents and descents of the air parcel, i.e. a conservative quantity. The positive sign for the enthalpy $L_v dr_s$ (first row, right column) indicates that in the case of adiabatic ($Tds = 0$) and isobar ($dp = 0$) processes, r_s decreases and temperature increases with height, i.e. condensation occurs. The equivalent potential temperature introduced in row four of Table 2.4 is the sum of the enthalpy of the air parcel plus its latent heat at the zero level divided by the specific heat at constant pressure, c_p. At a level z, $c_p\theta_e$ is equal to the sum of the enthalpy, potential energy relative to the reference level, and the latent heat (fifth row in Table 2.4). In a more exact derivation, we obtain

$$\theta_e = T\left(\frac{p_0}{p}\right)^{\kappa} \exp\left(\frac{L_v r_s}{c_p T}\right). \tag{2.79}$$

The equivalent potential temperature is the temperature that an air parcel achieves when it ascends dry adiabatically to the LCL, then further ascends according to the saturated moist adiabat until all water is condensed and finally descends dry adiabatically to 1,000 hPa.

Since $T\left(\frac{p_0}{p}\right)^{\kappa} = \theta \approx T + (g/c_p)(z - z_0)$ and $\frac{L_v r_s}{c_p T} \ll 1$ the following approximation is valid[61] $\theta_e \approx (T + (g/c_p)(z - z_0))(1 + \frac{L_v r_s}{c_p T}) \approx T + (g/c_p)(z - z_0) + \frac{L_v}{c_p} r_s$. A more general definition can be obtained by using r instead of r_s. It is also valid for non-saturated air parcels and reads

- Equivalent temperature $c_p T_e := c_p T + L_v r$
- Equivalent potential temperature $c_p\theta_e := c_p T + g(z - z_0) + L_v r$,

[59] The equations of the moist atmosphere listed in this table can also be written for dq_s instead of dr_s because $r \approx 0.622 e/p \approx q$.

[60] Various formulas have been derived for equivalent potential temperature. A comparison and evaluation can be found in Davies-Jones (2009). The accuracy of the formulas can be examined by finding the imitation first law of thermodynamics. The accuracy of the various formulas ranges between 0.015 and 0.4 K for typical atmospheric conditions. The errors result from the temperature dependency of c_p and L that are typically neglected in meteorology.

[61] $e^x \approx 1 + x$ when x is very small.

Table 2.4 Overview of basic laws for the dry and saturated atmosphere

	Dry	Water-vapor saturated
First law of Thermodynamics	$Tds = c_p dT - (\frac{1}{\rho})dp$	$Tds = c_p dT - (\frac{1}{\rho})dp + L_v dr_s$
With $dp = -\rho g dz$	$Tds = c_p dT + g dz$	$Tds = c_p dT + g dz + L_v dr_s$
$Tds = 0$; integration	$c_p(T - T_0) + g(z - z_0) = 0$	$c_p(T - T_0) + g(z - z_0)$ $+L_v(r_s - r_{s,0}) = 0$
Definition	$c_p\theta := c_p T_0$	$c_p\theta_e := c_p T_0 + L_v r_s$
1st consequence	$\theta = T + \frac{g}{c_p}(z - z_0)$	$\theta_e = T + \frac{g}{c_p}(z - z_0) + \frac{L_v}{c_p} r_s$
2nd consequence	$\frac{d\theta}{dz} = 0$	$\frac{d\theta_e}{dz} = 0$
Individual vertical	$\frac{dT}{dz} = -\Gamma_d = -\frac{g}{c_p}$	$\frac{dT}{dz} = -\Gamma_s$
Temperature change		$= -\frac{g}{c_p} - \frac{L_v}{c_p}\frac{dr_s}{dz}$

i.e. in general, we only sum up the existing energy terms. Note that the process described for the equivalent potential temperature yields slightly different values than simply adding the energy terms.

The individual vertical change in temperature of a saturated adiabatically rising air parcel is given in the seventh line of Table 2.4. Since $r_s(T, p) \approx 0.622 e_s(T)/p$ and

$$\frac{dr_s}{dz} = 0.622\left(\frac{1}{p}\frac{de_s}{dz} - \frac{e_s}{p^2}\frac{dp}{dz}\right) = \frac{r_s}{e_s}\frac{de_s}{dT}\frac{dT}{dz} + \frac{r_s}{R_d}\frac{g}{T} \tag{2.80}$$

we obtain

$$\frac{dT}{dz} = -\frac{g}{c_p} - \frac{L_v}{c_p}\frac{r_s}{e_s}\frac{de_s}{dT}\frac{dT}{dz} - \frac{L_v}{c_p}\frac{r_s g}{R_d T} \tag{2.81}$$

and

$$\frac{dT}{dz} = -\Gamma_s = -\frac{g}{c_p}\frac{1 + \frac{L_v r_s}{R_d T}}{1 + \frac{L_v r_s}{c_p e_s}\frac{de_s}{dT}} = -\frac{g}{c_p}\alpha_s \tag{2.82}$$

i.e. the saturated adiabatic lapse rate, Γ_s, is a factor α_s smaller than the dry adiabatic lapse rate, Γ_d, i.e. $\Gamma_s = \alpha_s \Gamma_d$. The saturated adiabatic lapse rate grows with decreasing temperature and increasing pressure (Table 2.5).

The decrease of Γ_s with increasing temperature means an increase of the heating by condensation, i.e. when related to a fixed Δz (e.g. 100 m) more water vapor will condense if temperature increases. The reason is the non-linearity of the saturation-vapor curve where for a higher temperature, the same increment ΔT is related to a greater increment in Δe_s and, consequently, a greater amount of condensed water and released latent heat because of $\Delta r_s \approx 0.622 \Delta e_s / p$. The decrease of Γ_s with decreasing pressure means an increase in the heating by condensation, because air that is relative moist warms more strongly under low than high pressure.

Table 2.5 Saturated adiabatic lapse rate, Γ_s, in K $10^{-2}\,m^{-1}$ as a function of pressure, p, and temperature, T

	T (°C)					
p (hPa)	−20	−10	0	10	20	30
1,000	0.86	0.77	0.65	0.53	0.43	0.36
800	0.84	0.73	0.60	0.49	0.39	0.33
600	0.80	0.68	0.55	0.44	0.35	0.30
400	0.74	0.60	0.47	0.37	–	–
200	0.60	0.46	–	–	–	–

In summary, during an adiabatic ascend of a moist air parcel, in which no liquid water exists and no condensation occurs[62]

- The specific moisture q and the mixing ratio r remain constant
- Temperature decreases about $0.98\,K10^{-2}\,m^{-1}$
- The dew point decreases by about $0.172\,K10^{-2}\,m^{-1}$

2.9.3 Vertical Mixing

Upwards moving parcels cool and may experience potential subsequent condensation leading to cloud formation. Vertical mixing, forced ascends at a mountainous barrier, frontal lifting and convergence of the horizontal wind field (e.g. low pressure systems, squall lines, thunderstorms, local convection) are mechanisms to lift air so that condensation/deposition occurs. Vertical mixing occurs because of turbulent and/or convective processes. Herein strong vertical variations of temperature and pressure exist.

We can simplify the treatment of vertical mixing by consideration of two isolated air parcels with mass m_1 and m_2 at pressure p_1 and p_2 with $p_1 > p_2$ and temperatures T_1 and T_2. These temperatures are taken at the two pressure levels where they mix isobarically. We can consider displacement to level p as an adiabatic ascent/descent. The mixture redistributes in the layer $\Delta p = p_1 - p_2$. The specific humidity q_1 and q_2 are conserved. Thus, the new temperatures are $T_1' = T_1(p/p_1)^\kappa$ and $T_2' = T_2(p/p_2)^\kappa$. Since at level p, the air parcels mix isobarically, we obtain

[62] As a rule of thumb pressure and water-vapor pressure relatively decrease about 1.2 % per 100 m; saturation water vapor pressure relatively decreases by about 7 % per 100 m; relative humidity relatively increases by about 6 % per 100 m, e.g. for a relative humidity of 50 % this means an absolute increase dRH/dz of 3 % per 100 m.

$$T \approx \frac{m_1 T_1' + m_2 T_2'}{m}$$
$$q \approx \frac{m_1 q_1' + m_2 q_2'}{m}$$
$$\theta \approx \frac{m_1 \theta_1' + m_2 \theta_2'}{m}$$

where θ_1 and θ_2 are the initial potential temperatures that remain constant during an adiabatic process. The resulting redistribution of the mixture in layer Δp conserves potential temperature. Consequently, for the well mixed layer θ is constant with height. Generalizing for n air parcels and using a general expression for the weighted average yields

$$\overline{x} = \frac{\int_0^m x\,dm}{m}. \tag{2.83}$$

By using the hydrostatic equation (2.7) we obtain

$$\overline{x} = \frac{\int_0^z x\,dz}{\int_0^z \rho dz} = -\frac{\int_{p_1}^{p_2} x\,dp}{p_1 - p_2} \tag{2.84}$$

where x stands for θ, T, q, or r, respectively.

Example. Mix 1 kg of air at a relative humidity of 95 % and $T = 10\,°\text{C}$ with 1 kg of air at a relative humidity of 52 % and $T = -20\,°\text{C}$. What are the resulting relative humidity and temperature of the mixture? Comment your result.

Solution. According to Dalton's law (2.5), the water-vapor pressure of the mixture is given by $e_{mix} = e_{95} + e_{52}$. The definition of relative humidity $RH = \frac{e}{e_{sw}} 100\,\%$, requires to calculate the saturation water vapor pressure, e.g. by the Magnus formula $e_{sw} = 6.1078 \exp(\frac{17.1\delta}{235+\delta})$. Thus, $e_{95} = 0.95 \cdot 12.27\,\text{hPa} = 11.657\,\text{hPa}$, $e_{52} = 0.52 \cdot 1.24\,\text{hPa} = 0.645\,\text{hPa}$, and $e_{mix} = 11.657\,\text{hPa} + 0.645\,\text{hPa} = 12.302\,\text{hPa}$. The temperature of the mixture is equal to their mass-weighted average, $T_{mix} = \frac{1\,\text{kg}10\,°\text{C}+1\,\text{kg}(-20)\,°\text{C}}{2\,\text{kg}} = -5\,°\text{C}$. The respective water vapor pressure at saturation for T_{mix} is $e_{sw}(T_{mix}) = 4.22\,\text{hPa}$ leading to a relative humidity of 292 %. Such huge relative humidity values do not occur in the atmosphere, i.e. water vapor condenses.

2.10 Stratification and Stability

In synoptic, we have to analyze the vertical structure of the atmosphere. This section introduces thermodynamic diagrams that base on the relations we derived before, as a tool for weather forecasting, and discusses different conditions of the atmosphere and their consequences.

2.10.1 Thermodynamic Diagrams

Thermodynamic diagrams are transformations of the Clapeyron specific volume pressure diagram (Sect. 2.8.3; Fig. 2.16). In general, thermodynamic diagrams encompass isotherms (lines of constant temperature), isobars (lines of constant pressure), and isentrops (lines of equal potential temperature). For short-term weather forecasts (e.g. height of cloud base and top, icing potential, thunderstorms) vertical profiles of temperature and humidity observed by a radiosonde or tethered balloon are plotted on these charts to assess the vertical structure of the atmosphere. The most common thermodynamic diagrams are the $T - \phi$**gram**, **Stüve diagram**, and **emagram**. They are all map projections on one another. Note that the emagram uses T and $-\ln p$ as coordinates.

The Stüve diagram and $T - \phi$ gram make use of potential temperature. By rearranging Eq. (2.41) for temperature we can design the Stüve diagram, a rectangular diagram with increasing values of T on the x-axis and downwards increasing values of $(p/p_0)^\kappa$ on the y-axis. The Stüve diagram is a **pseudo-adiabatic** thermodynamic chart ($T(p^\kappa)$ with $\kappa = \frac{R_d}{c_p}$). In the Stüve diagram, isotherms, isobars and dry adiabats are straight and oriented in the vertical, horizontal, and a 45° inclination to the left, respectively. Moist adiabats are curved. Holding θ constant and plotting $T(p)$ yields the **dry adiabat**. Dry adiabats serve to determine temperature changes of by vertically moving air parcels. The value θ of an adiabatically ascending/descending air parcel corresponds to the temperature at the point where the adiabat crosses the 1,000 hPa level.

The $T - \phi$gram (temperature-entropy) bases on $T(c_p \ln \theta)$ or $T(\ln \theta)$.

On a $p - V$-diagram, isotherms and adiabats are equilateral hyperbolas (Fig. 2.17). Since $\gamma = 1.4$ adiabats are steeper than isotherms. On a $p - V$-diagram, the straight lines on the $p-$ and $V-$axis represent isobaric and isochoric transformations.

In $p - T-$diagrams, isochors are given by $V = mRT/p = constant$ or $T/p = constant$; adiabats are hyperbolas (Fig. 2.17). In $TV-$diagrams, adiabats are hyperbolas and isobars are straight lines (Fig. 2.17).

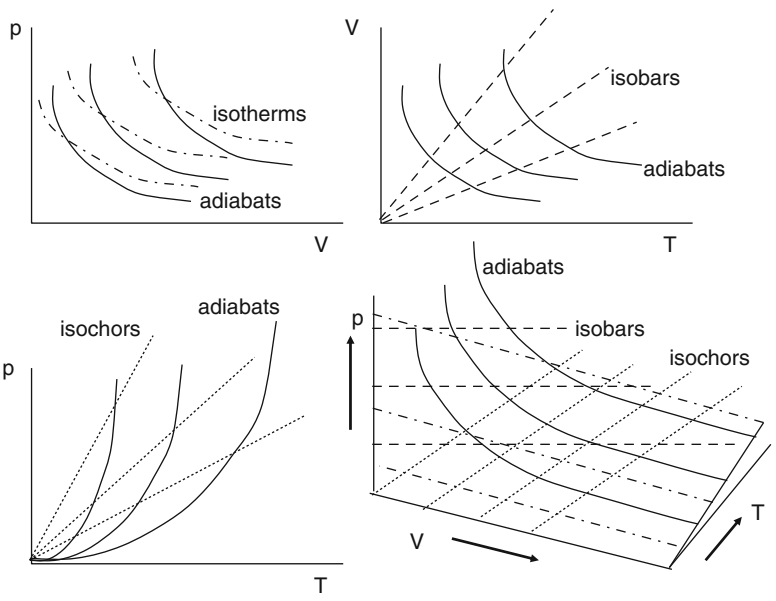

Fig. 2.17 Schematic view of various relationships between adiabats, isotherms, isobars and isochors in the partial and complete state spaces

2.10.2 Stability Analysis

The temperature change of a rising air parcel is either governed by the dry-adiabatic or moist adiabatic lapse rate, while in its environment, the temperature change is governed by the environmental or **ambient lapse rate** that varies strongly. The relative density of the air parcel depends on the environmental lapse rate and whether the air is saturated or not. The latter determines the adiabatic lapse rate we have to apply. Thus, the buoyancy of a rising air parcel depends on its cooling rate relative to the environment. These factors allow four kinds of stratification that determine the ability of the layer to support vertical transfer of momentum, moisture, heat, and chemical constituents:

- **Absolutely unstable:** $\gamma > \Gamma_d > \Gamma_s$ Whenever the environmental lapse rate exceeds that of the dry adiabatic lapse rate, air is absolutely unstable (Fig. 2.18). An air parcel once lifted continues to rise whether or not the air is saturated. The air parcel becomes progressively warmer than the ambient air and continues to rise at increasing speed. The increasing temperature difference between the air parcel and the environmental air increases the buoyancy of the parcel, and the parcel gathers momentum as it rises. An example of an absolutely unstable

atmosphere are the April showers[63] that occur in European mid-latitudes when polar air masses come in from North or Northwest and the land is already strongly heated by the Sun.

- **Absolutely stable:** $\gamma < \Gamma_s < \Gamma_d$ Whenever the environmental lapse rate is less than the dry adiabatic lapse rate, air is absolutely stable (Fig. 2.18). The air resists lifting whether or not the air is saturated. As an air parcel rises, its temperature drops more quickly than that of its environment. The air parcel becomes relatively heavier than the environment, i.e. has negative buoyancy. Thus, it sinks back to its initial level, when the lifting mechanism stops. An inversion is an example for absolutely stable conditions (Fig. 2.11).
- **Conditionally unstable:** $\Gamma_s < \gamma < \Gamma_d$ In a conditionally unstable atmosphere, initially the lapse rate is less than the dry adiabatic lapse rate. After passing cloud base, the air parcel cools according to the saturated adiabatic rate and becomes warmer than the ambient air for which it now rises on its own. When in a conditionally unstable atmosphere, an air parcel is forced to ascend above a critical height called the **level of free convection** (LFC) that typically coincides with the cloud base, the air parcel becomes buoyant as it becomes warmer than the environment. Typically, clouds quickly grow in vertical extension and provide precipitation once conditionally unstable air rises above the LFC.
- **Neutral:** $\gamma = \Gamma_s$ **or** $\gamma = \Gamma_d$ Under neutral conditions, an air parcel is as warm and dense as its environment after any displacement (Fig. 2.18).

Neither Γ_s nor Γ_d have a direct relation to the temperature of the surrounding because a displaced air parcel is thermally isolated under adiabatic conditions.[64] When the lifting process is strong enough to reach the level of saturation, stability changes depend on the way saturation is reached, i.e. among other things, on the vertical moisture and temperature profiles.

2.10.2.1 Factors Influencing Stability

When a layer is not motionless (e.g. due to frontal lifting), the stability of the parcel may be affected. Then we have to express the stability criteria for the layer by the equivalent potential temperature.

- $\frac{d\theta_e}{dz} < 0$ the saturated region is unstable with respect to the saturated parcel process (**convective instability**).
- $\frac{d\theta_e}{dz} = 0$ the saturated region is neutral with respect to the saturated parcel process (**convective neutrality**).

[63] The vertical development of clouds is related to the degree of instability. Less developed cumulus clouds indicate weak, strong developed cumulonimbus clouds strong instability (Chap. 3 for a cloud classification).

[64] Think, for instance, of a balloon ascending into the sky.

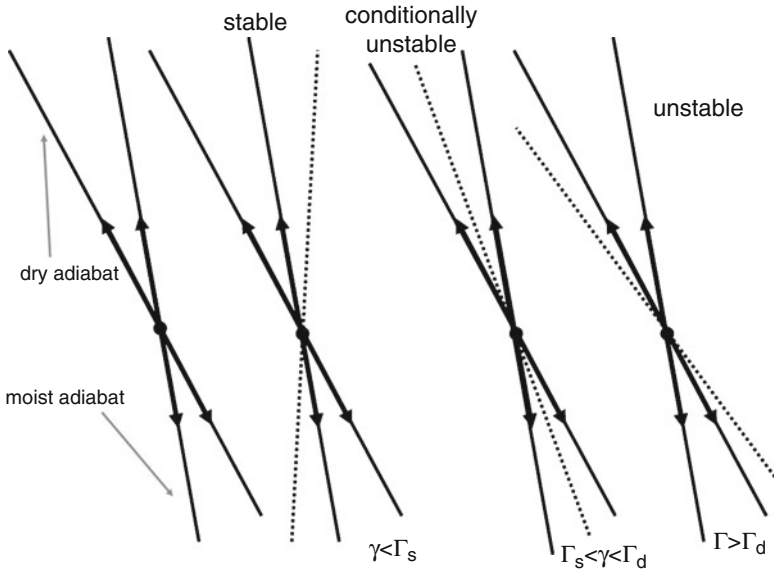

Fig. 2.18 Schematic view of atmospheric stability conditions

- $\frac{d\theta_e}{dz} > 0$ the saturated region is stable with respect to the saturated parcel process (**convective stability**).

These conditions refer to the stratification of an initially unsaturated layer that then is lifted as a whole.

Environmental lapse rates vary strongly in space and time. Any factors that increase the environmental lapse rate render the air to more unstable, while any factors reducing the environmental lapse rate increase the stability of the air. Winds from different directions at different levels can influence the temperature profile by advection of air with different temperature or air masses with different environmental lapse rates.

Instability is enhanced by

- **Heating at the surface.** During the day, solar radiation heats the surface. The near-surface air heats more quickly than the air aloft. Thus, the lower troposphere usually has a steeper environmental lapse rate than the mid- and upper troposphere. This effect is greatest on sunny, clear days over non-vegetated areas in regions of abundant solar radiation and low evaporation (e.g. deserts). The resulting differences in the density and/or temperature field cause buoyancy, i.e. the tendency for a lighter fluid to flow upward through a denser one. By itself, buoyancy can initiate updrafts. Even in deserts where water-vapor content is low, strong heating can result in local convection that is intense enough to cause thunderstorms.

The **lake-snow effect** of the Great Lakes region is an example for destabilizing cold polar air moving over relatively warm water (5 °C). The moisture and heat added to the air from the lakes lead to instability, cloud formation, and snow downwind of the lakes.

- **Lifting.** There are three major mechanisms to lift air: **orographic lifting**, **convergence of the horizontal wind field**, and frontal lifting.

  Orographic lifting refers to air flowing towards a mountain barrier that is deflected over the barrier. The upward lifting of air leads to adiabatic cooling denoted **orographic effect**. As the LCL is reached, clouds form (Fig. 6.48), and eventually precipitation may occur on the upwind side of the barrier. Cloud-top height solely depends on air-mass characteristics, and is independent of mountain height. The cloud top is the level where a change back to stability occurs because the air parcel cools at a higher rate than the environmental air.

  Horizontal movement of air to a common place is denoted **horizontal convergence**. It is compensated by rising of air with adiabatic cooling that can lead to cloud and precipitation formation. The **Inner Tropical Convergence Zone** (ITCZ), where the trade winds converge and huge thunderstorm clouds form (Figs. 4.26 and 4.28) is an example of horizontal moisture convergence (Chaps. 6 and 7).

  Temperature varies slightly, gradually in space.[65] However, at transition zones between two air masses of different density, temperature (and/or moisture) differs strongly over a short distance. These transition zones called **fronts** (Chap. 6) extend in horizontal and vertical direction. At the cold front, cold air advances towards warmer air (Fig. 6.51). The denser cold air displaces the lighter, warm air. At the warm front, warm air is forced to rise above the cold air similar to the orographic effect (Fig. 6.52). At these fronts, the lifting may lead to clouds and precipitation (Chap. 3).
- **Radiative cooling at cloud tops.** The high albedo of cloud tops cools the surrounding atmosphere (Chap. 4), which may trigger a feedback to increase cloud-top heights.

Atmospheric stability is enhanced by:

- **Cooling from below.** After sunset, radiative cooling of the ground (Chap. 4) may result in cooler air close to the surface than aloft. A surface temperature inversion may lead to accumulation of pollutants underneath, and cause severe smog (Chap. 5). Very buoyant plumes may break through the inversion (Fig. 2.11). Inversions are removed by strong horizontal winds.
- **Subsidence.** Long-lasting temperature inversions may occur under high-pressure situations. The air descending in the center of the high-pressure system produces a warming by adiabatic compression. Thus, in the mid-troposphere air becomes warmer than close the surface. These inversions are called subsidence inversions.

[65] When temperature is about 20 °C at a place in flat, homogeneous terrain, chances are high that temperature is not lower/higher 10 km away.

Another example of subsidence is the **Chinook** or **Föhn process**. During ascend of air at a mountain barrier the water load precipitates on the upwind side. The air descends dry adiabatically on the downwind side and warms by compression. This process creates the rain-shadow effect, an area of climatologically low precipitation (Chap. 7).

- **Advection of cold air.** Inversions may form during the passage of a cold front or from advection of maritime air by a relatively cooler onshore breeze (Chaps. 6 and 7).

Example. Suppose an unsaturated air parcel with a temperature of 9.8 °C at sea level rises dry adiabatically to the LCL of 1 km. The parcel continues to rise at a saturated adiabatic lapse rate of 0.5 °C 10^{-2} m and deposits its moisture on the windward side of a 4 km high mountain range. After passing the mountain top, it descends to the valley bottom at 100 m above sea level. Calculate the temperature of the air parcel on the lee side, and for sea level. What would the temperature be at sea level in the lee side, in a model that represents the mountain range by the average terrain height in the grid-cell as 3 km?

Solution. Cloud-base temperature is given by $T_{LCL} = T - \Gamma_d \Delta z = 9.8\,°\text{C} - \frac{0.98\,°\text{C}}{100\,\text{m}} 1{,}000\,\text{m} = 0\,°\text{C}$. Atop the mountain temperature is given by $T_{mt} = T_{LCL} - \Gamma_s \Delta z_{cloud} = 0\,°\text{C} - \frac{0.5\,°\text{C}}{100\,\text{m}} 3{,}000\,\text{m} = -15\,°\text{C}$. On the downwind side, surface temperature is given by $T_{lee} = T_{mt} + \Gamma_d \Delta z_{mt} = -15\,°\text{C} + \frac{0.98\,°\text{C}}{100\,\text{m}} 3{,}900\,\text{m} \approx 23.2\,°\text{C}$, $T_{lee,sealevel} \approx 24.2\,°\text{C}$. The air is 15.4 °C warmer in the lee than upwind side of the mountain. In the model, $T_{mt} \approx -10\,°\text{C}$, $T_{lee,sealevel} \approx 19.4\,°\text{C}$. The model would have a cold bias.

2.10.3 Equation of Motion for an Air Parcel

For an environment in hydrostatic equilibrium, the hydrostatic equation (2.7) applies. For an air parcel that moves up or down, this equation is not applicable as the parcel is accelerated (d^2z/dt^2). According to Newton's law, we obtain for a unit volume of air

$$\rho' \frac{d^2 z}{dt^2} = -\rho' g - \frac{dp'}{dz} \tag{2.85}$$

or

$$\frac{d^2 z}{dt^2} = -g - \alpha' \frac{dp'}{dz}. \tag{2.86}$$

At a given level, the pressure of the parcel and its environment are equal meaning $p = \rho R_d T = \rho' R_d T' = p'$, and

$$\frac{d^2 z}{dt^2} = g(\frac{T' - T}{T}) = g(\frac{\rho - \rho'}{\rho'}). \tag{2.87}$$

The r.h.s. gives the force per unit mass acting on the air parcel by the pressure gradient and gravity, and is the **buoyancy** B of the parcel. Now assume a small displacement δz from the original position. A Taylor series provides

$$T = T_0 + \frac{dT}{dz} z + 0.5 \frac{d^2 T}{dz^2} z^2 + \cdots . \tag{2.88}$$

We can express T' analogously. Comparison yields $-dT/dz = \gamma$ and $-dT'/dz = \gamma'$, and

$$\frac{d^2(\delta z)}{dt^2} = -\frac{g}{T}(\gamma - \gamma')\delta z \tag{2.89}$$

or

$$\frac{d^2(\delta z)}{dt^2} + N^2(\delta z) = 0 \tag{2.90}$$

where

$$N^2 = \frac{g}{T}(\gamma - \gamma') = \frac{g}{T}(\frac{dT}{dz} + \frac{g}{c_p}). \tag{2.91}$$

Here, N is the **Brunt-Väisälä frequency** or **buoyancy frequency** and T is the temperature of the environment. The Brunt[66]-Väisälä[67] frequency is a measure of atmospheric stratification. In a statically stable region ($\gamma > \gamma'$ and $N^2 > 0$), the above equation describes a harmonic motion with sinusoidal solutions. The parcel oscillates up and down at an angular frequency N around its equilibrium altitude. In the lower atmosphere, the corresponding period $2\pi/N$ is a few minutes.

In a statically unstable region ($\gamma < \gamma'$, and $N^2 < 0$), N is imaginary, and the solutions are exponential. Only one of these solutions makes sense in the atmosphere. It describes the displaced air parcel continuing to move at increasing speed.

The Brunt-Väisälä frequency can also be expressed as a function of potential temperature by taking the logarithms of Eq. (2.41), differentiating and use of the equation of state (2.1) as

[66] Sir David Brunt, English meteorologist, 1886–1965.

[67] Vilho Väisälä, Finnish meteorologist, 1899–1969.

$$N^2 = \frac{g}{\theta}\frac{d\theta}{dz}. \tag{2.92}$$

A region is statically stable (unstable) when its potential temperature increases (decreases) with height.

We can make the same derivations for moist air using the virtual temperature. Doing so includes the effect of moist air being lighter than dry air in the buoyancy term.

2.10.4 Stability and Buoyancy

2.10.4.1 Convective Inhibition

The vertically integrated negative buoyancy that a parcel must overcome by heating or mechanical means to experience free convection, is a function of the vertical velocity squared. The vertical acceleration of an air parcel (of unit mass) that is lifted vertically and pseudo-adiabatically and that is always adjusted to the pressure of its hydrostatically balanced environment, can be expressed by

$$\frac{dw}{dt} = \frac{g}{T_v}(T_{v,p} - T_v). \tag{2.93}$$

Here, w and g are the vertical velocity of the air parcel and the acceleration due to gravity, and $T_{v,p}$ and T_v are the virtual temperatures of the air parcel and environment, respectively. Multiplying by the differential of height dz and some algebra yield

$$dz\frac{dw}{dt} = \frac{dz}{dt}dw = wdw = \frac{d}{dt}\frac{w^2}{2} = \frac{g}{T_v}(T_{v,p} - T_v)dz. \tag{2.94}$$

Using the rearranged hydrostatic equation (2.7) expressed for moist air $dz = -\frac{1}{\rho g}dp = -\frac{R_d T_v}{g}\frac{dp}{p}$ provides

$$\frac{d}{dt}(\frac{w^2}{2}) = -R_d(T_{v,p} - T_v)d(\ln p). \tag{2.95}$$

Integration from the originating pressure level, p_{OL}, to the pressure level of free convection, p_{LFC}, where the two temperature curves intersect, gives the kinetic energy change per unit mass for the moving air parcel

$$w_{LFC}^2 - w_{OL}^2 = -2R_d \int_{p_{OL}}^{p_{LFC}} (T_{v,p} - T_v)d(\ln p). \tag{2.96}$$

When in the region between p_{OL} and p_{LFC}, the temperature of the air parcel exceeds that of the environment $T_{v,p} \leq T_v$, the energy amounts

$$CIN = R_d \int_{p_{LFC}}^{p_{OL}} (T_{v,p} - T_v) d(\ln p) \leq 0. \tag{2.97}$$

This *negative energy* region in the thermodynamic chart, called the **convective inhibition** (CIN), represents a stability barrier that an air parcel has to overcome to reach the LFC. A certain amount of energy per unit mass is required to lift the air parcel vertically and pseudo-adiabatically from its originating level to its LFC, which can be expressed by

$$w_{LFC}^2 = w_{OL}^2 + 2CIN \geq 0. \tag{2.98}$$

To guarantee the occurrence of free convection $w_{OL}^2 \geq 2CIN$ must be fulfilled, i.e. a minimum of $w_{OL} = +\sqrt{-2CIN}$ is required. A 5 % increase in vertical velocity from 0.1 to 0.105 m s^{-1}, for instance, enhances the negative buoyancy that a parcel can overcome by 12.5 % and increases the potential for convection. For weather forecasting, an area with high CIN in the thermodynamic chart is considered stable and means low likelihood for thunderstorm development.

For synoptic purposes, it is important to know that CIN increases by low altitude dry air advection, and cooling of near-surface air which can lead to small capping inversions aloft. Incoming fronts and shortwaves (Chap. 6) influence the strengthening or weakening of CIN.

Example. Determine what decrease in vertical velocity at the original level has to occur to increase CIN by 5 %.

Solution. The vertical velocity has to decrease by $\Delta w_{OL} = \sqrt{-2\Delta CIN} = \sqrt{2 \cdot 0.05} = 3.16\,\%$.

2.10.4.2 Convective Available Potential Energy

At the LFC and above, $T_{v,p} > T_v$ until the two temperature curves intersect again at the cloud top (subscript CT) so that $R_d \int_{p_{LFC}}^{p_{CT}} (T_{v,p} - T_v) d(\ln p) > 0$. This *positive energy* region in the thermodynamic chart called the Convective Available Potential Energy (CAPE) represents the amount of buoyant energy available to accelerate an air parcel vertically.

By using the hydrostatic equation (2.7) and Poisson equation (Eq. 2.41), we can express the buoyancy and stability conditions as a function of height

$$CAPE = g \int_{LFC}^{z_{CT}} \frac{\theta(z) - \overline{\theta}(z)}{\overline{\theta}(z)} dz. \tag{2.99}$$

Here, θ is the potential temperature of the air parcel that was lifted from $z = 0$ to the cloud top z_{CT} without mixing with the environment. The air parcel ascends dry-adiabatically (θ remains constant) until saturation is reached. Then it raises according to the saturated adiabat, i.e. θ_e remains constant. The overbar denotes the mean potential temperature of the environment. At cloud top, $\theta = \overline{\theta}$.

Neglecting the virtual temperature addition in calculating CAPE may result in notable errors for small CAPE values. In synoptic, it is important to know that the amount and shape of the positive area determines the speed of updrafts. Large CAPE is required to produce large hail as hail production needs strong updrafts (Chap. 3). High CAPE can result in explosive thunderstorm development. Such rapid development typically occurs when the CAPE stored by a capping inversion is released suddenly. Heating or mechanical lifting can break the capping inversion. The amount of CAPE within the lowest 1–3 km is important for **tornadogenesis** (formation of tornadoes). Tornados typically occur in high CAPE environments. The depth and width of the CAPE layer at mid-levels is important for supercell formation. Large CAPE promotes lightning activity. Days with severe weather typically exhibit $CAPE > 5{,}000\,\mathrm{J\,kg^{-1}}$.

2.11 Genesis, Identification, and Modification of Air Masses

Air-mass formation is a consequence of the temporal and spatial differences in incoming solar radiation (Chap. 4) and different heat capacities of the various surfaces on Earth.

The characteristics of atmospheric state variables depend on the continuous exchange of energy and water vapor near the surface. When the energy input exceeds the energy losses, air temperature increases and vice versa. When **evapotranspiration**[68] exceeds the water-vapor transport away from an area, atmospheric humidity increases in the area until saturation is reached and clouds form. Since cooling and warming, as well as the land and water masses are not distributed equally around the globe, water supply to the atmosphere varies too. Consequently, an air mass over the tropical Atlantic Ocean, for instance, has different thermal and moisture states than an air mass over Alaska, or Central Africa.

The formation of an air mass requires several days, i.e. the air mass must rest over the same area called the **source region** for a substantial length of time. Air-mass source regions only occur in high or low latitudes (Fig. 2.19). Here, the atmospheric conditions vary less than in mid-latitudes (Chap. 7). Consequently, the probability is high for an air mass to rest long enough over large enough an area to be modified from the underlying surface.

[68] Evapotranspiration is an artificial word used in meteorology and hydrology to describe the combined effects of evaporation of water and sublimation of ice/snow from various surface and the transpiration of water by plants.

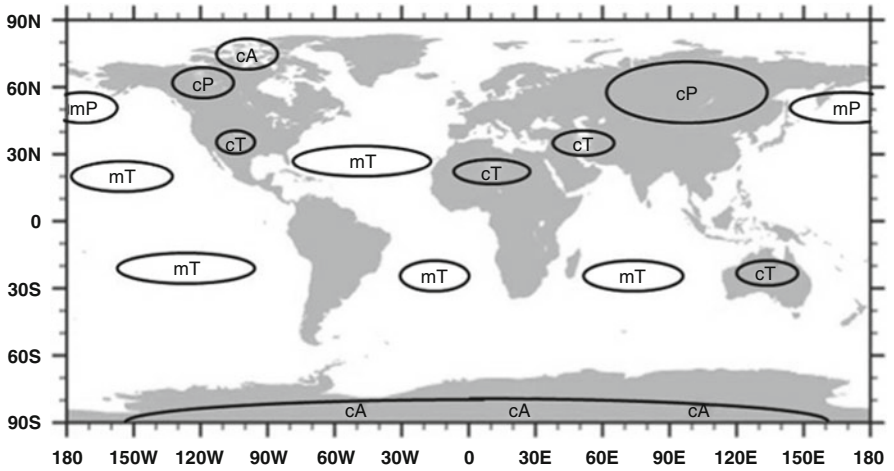

Fig. 2.19 Schematic view of air-mass source regions

Despite air masses have fairly homogeneous temperature and moisture characteristics they are not uniform from the surface to the tropopause. There are vertical temperature and moisture gradients that affect stability. Stability is an important ramification with regard to the likelihood of precipitation. Consequently, some air masses have a higher probability to provide precipitation than others do.

We classify air masses by a two-letter shorthand scheme according to the thermal and humidity properties of their source regions. The letters **c** or **m** stand for the moisture conditions representing **continental** (dry) or **maritime** (humid). The letters **T**, **P**, and **A** denote the thermal condition indicating **tropical** (warm), **polar** (cold) and **arctic** (extremely cold) air, respectively. Combining these letters of thermal and moisture conditions results in six possible air masses, namely, continental tropical, cT, maritime tropical, mT, continental polar, cP, maritime polar, mP, continental arctic, cA, and maritime arctic. The latter, however, does not occur, as no large open ocean exists in the Arctic.

2.11.1 Continental Polar and Continental Arctic Air

Continental Polar (cP) air masses build over large landmasses in high latitudes (e.g. northern Canada, Siberia, Russia). In winter, short days, low solar angles, and extended snow coverage characterize these regions. Due to the high albedo of snow, huge amounts of solar radiation (Chap. 4) are reflected back to space. These circumstances lead to loss of radiant energy, cooling of the air, highly stable stratification, and sometimes the formation of inversions. In addition, the

air is extremely dry. Due to the combination of dry air and stable conditions, few clouds form over the source region, if at all. The low water-vapor content marginally absorbs incoming solar radiation leading to bright and sunny conditions over the source region during daylight hours. The extreme stability inhibits vertical mixing for which air pollutants can accumulate. The low temperatures lead to huge consumption of coal, wood, and oil for heating. Thus, cP air masses often have poor air quality in conurbations.

In summer, these source regions are warmer and more humid than in winter. The white nights, and the snow-free surface lead to unstable conditions and frequently convective clouds develop. Since the air mass builds over a continent, it does not possess enough moisture for significant precipitation.

Continental arctic air masses are colder than continental polar air masses. They form over the high Arctic or Antarctica. The most important difference between continental polar and continental arctic air masses is that they are separated by the Arctic front (Sect. 6.10).

2.11.2 Maritime Polar Air

Maritime Polar (mP) air masses form over high latitude oceans (e.g. southern and north-west Atlantic, North Pacific). They represent modified cP air masses with an ocean trajectory. Consequently, they are cool, moist, and unstable with a steeping lapse rate.

2.11.3 Continental Tropical Air

The major deserts on Earth (e.g. Australia, Sahara) and the excessively heated northern mid-latitude continents in summer (e.g. the southwestern United States, northern Mexico) have scarce vegetation, low moisture supply to the atmosphere, strong solar radiation input (in summer), and dry, warm soils. Thus, their surfaces heat the overlying atmosphere by fluxes of sensible heat leading to very hot, dry, and unstable air masses with a steeping environmental lapse rate in summer and to cool, dry, stable air masses in winter.

2.11.4 Maritime Tropical Air

Over the large subtropical oceans (e.g. Azores, Bermuda, Mauritius, Fiji), very warm, moist and unstable air masses with a steeping environmental lapse rate

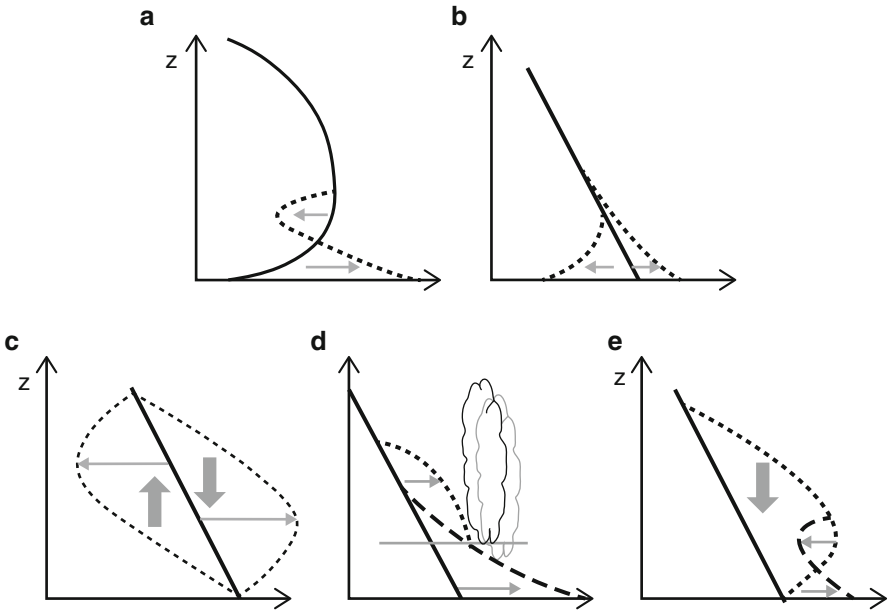

Fig. 2.20 Schematic view of air-mass transformation by (**a**) turbulent mixing, (**b**) diabatic heat conduction to and from the surface, (**c**) release of latent heat, (**d**) stretching and shrinking, and turbulent mixing plus stretching and sinking (for further discussion see Chap. 6)

develop over warm ocean currents (e.g. Gulf of Mexico, South China Sea), while relatively cooler and more stable air masses build over the cold ocean currents (e.g. Canaries, Benguela, Peru Current).

2.11.5 Air Mass Modifications

The concept of air masses is useful to define the frontal boundaries of air masses and their origin, as air masses do not stay permanently in their source regions. Moreover, it permits forecasting weather from the knowledge that certain air masses bring certain weather, and how air masses transform.

The dynamic processes occurring during transport change the air-mass characteristics (Fig. 2.20). Shrinking and stretching (Chap. 6) of the air mass alters stability. The movement of air masses changes the thermal and moisture conditions of the region that the air mass moves into (Fig. 2.21), and the air mass becomes more moderate.

A cP-air mass moving equator-wards to temperate latitudes brings cold weather. Due to the gradual modification of the air mass, the areas located more closely to the source region experience a stronger drop in temperature than those located

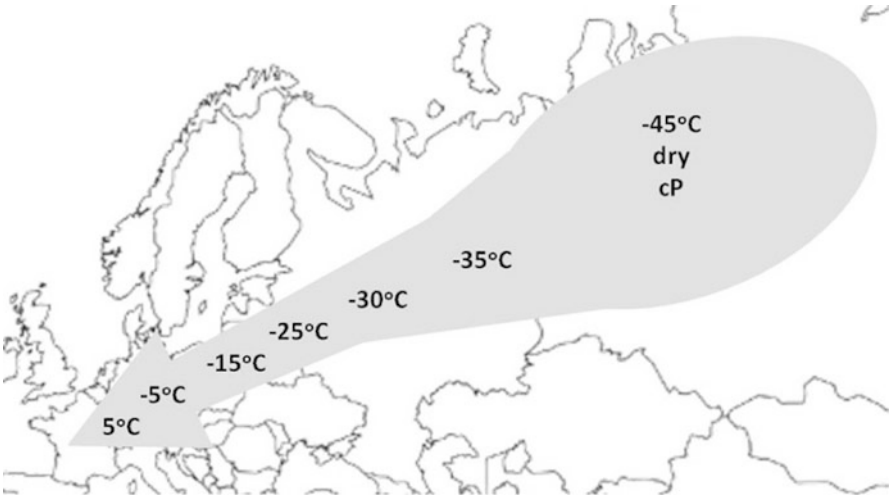

Fig. 2.21 Schematic view of gradual temperature changes of an air mass moving from Siberia into West Europe. Note that moisture, composition, and stability change concurrently as well

farther away. When moving equator-wards over the ocean, the air mass becomes increasingly unstable as the environmental lapse rate steepens. Thus, the probability of thunderstorms increases.

By moving equator-wards, a mP-air mass becomes increasingly unstable with its environmental lapse rate steeping. Sometimes thunderstorms form. Two types of mP-air masses are of main interest for North America. The first is a maritime polar air mass that formed originally as a continental polar air mass over the central Asia before moving over the North Pacific where it rested awhile. Here, the warm Japan Current heats and moistens the air mass converting it into a mP-air mass. Such air masses influence the northern West Coast all year and the California Coast in winter. The second type of mP-air mass is associated with the circulation around a mid-latitude cyclone at the East Coast after the cyclone passed the area.

By moving pole-wards over the ocean, continental tropical air masses acquire moisture and the prevailing instability favors thunderstorm formation. In middle Europe, advection of air masses from the Sahara and uptake of water over the Mediterranean Sea yield to serve precipitation.

By moving pole-wards, mT-air masses become increasingly stable and are associated with advection of fog. Maritime tropical air masses influence the southeastern United States, especially during summer when they form over the Atlantic or in the Gulf of Mexico. When these air masses migrate into North America, the combination of high moisture content and increased instability leads to thunderstorms with heavy, short-lived precipitation over relatively small areas. In East Arizona and eastern California, mT air masses advected from the eastern tropical Pacific can cause what is (incorrectly) called the **Arizona monsoon** (Chap. 7).

Problems

Knowledge and Comprehension

1. When is a gas said to be an ideal gas?
2. Argue why an ideal gas is not as good an approximation for moist air as it is for dry air.
3. Why can we consider the concept of an air parcel?
4. Does temperature depend on the mass and kind of atmospheric molecules or particles?
5. Why is moist air lighter than dry air?
6. Where would the 1 hPa level be located approximately in the standard atmosphere (Table 2.2) and at what temperature?
7. How is the absolute zero point of temperature defined?
8. How can the internal energy of an air parcel change?
9. How is work provided to an air parcel?
10. Why does air warm whenever it sinks?
11. Discuss what happens to temperature-profile measurements in the first decameters above ground when a radiosonde that was prepared in a heated hangar is directly released outside at an air temperature of $-40\,^{\circ}\mathrm{C}$.
12. When an air parcel is only subject to adiabatic transformation as it ascends through the troposphere what happens to its potential temperature?
13. Why is the potential temperature a useful parameter in meteorology?
14. Give the definitions of a dry adiabat and an isotherm.
15. What measure describes the difference between two adiabats?
16. Explain the difference between diabatic and adiabatic processes and name four diabatic processes.
17. Discuss how entropy can maximize in the atmosphere. What does this imply for the equilibrium temperature of isolated layers when no condensation or evaporation occurs?
18. What does a large wind-energy farm mean for the atmosphere with respect to the first law of thermodynamics?
19. The core of a tropical cyclone is warmer than its environment (Chap. 6). What does this mean for the intensity of the tropical cyclone with increasing height above the ocean as measured by the depression of isobaric surfaces?
20. Why does the virtual temperature of moist air always exceed the actual temperature?
21. Argue why relative humidity does not denote to the amount of the air that is water vapor by the example of $RH = 100\,\%$. What would it mean if $100\,\%$ relative humidity would denote to the amount of the air that is water vapor?
22. We learned that both q and r are conservative quantities. Give reasons why a and e are not conservative.
23. How is the latent heat of melting defined?

24. What does the non-linear relationship between saturation-water pressure and temperature mean for global warming?
25. What causes unstable air to stop rising?
26. How does potential temperature change with height in an unstable, neutral, and stable atmosphere?
27. What weather conditions would lead you to believe that air is unstable?
28. Name four ways instability can increase.
29. Why is there usually no or few precipitation in high pressure areas?
30. Why are the mid-latitudes not suitable as air mass source regions?
31. In a 850 hPa chart, temperature is 15 °C above Seattle on July 9 at 1500 UTC. Do you think you can use this chart to predict maximum temperature, T_{max}? Give reasons for your answer.
32. Use the NOAA isentropic backwards trajectory program. Calculate the backward trajectories for a region of your choice for 5 days. Take the satellite images and weather maps of these days and discuss the reliability of the calculated trajectories.

Analysis and Application

2.1. Determine the molecular weight and individual gas constants for moist air with 1 and 4 % water vapor content. What does this mean for moist air?

2.2. The atmosphere of Mars consists of about $3 \cdot 10^{-2}$ % H_2O, $2.8 \cdot 10^{-4}$ % Ne, 95.4 % CO_2, 2.7 % N_2, $1.3 \cdot 10^{-1}$ % O_2, $7 \cdot 10^{-2}$ % CO, and 1.6 % Ar. Mean surface pressure and temperature are about 6 hPa and 223 K, respectively. Determine the density, molecular weight and individual gas constant.

2.3. Argue why continuum mechanics can be applied for an air parcel of 1 mm^3.

2.4. For a well-mixed troposphere that obeys the barometric law show how the concentration of an inert trace gas changes with height.

2.5. Derive the specific gas constant of dry air and calculate the gas constant of water vapor.

2.6. Determine how many molecules are in an air parcel of 1 m^3.

2.7. Determine the kinetic energy of an ozone molecule that moves at 5 m s^{-1}.

2.8. Determine the density of air for a pressure of 1,013.25 hPa and air temperature of $T = 20$ °C by use of the Dalton's law and the individual gas constant of water vapor for an air mass containing 1 and 4 % water vapor.

2.9. Determine the mole volume of the atmosphere at normal pressure at the freezing point.

2.10. Use the equation of state (2.1) for an ideal gas and show the validity of **Boyle-Mariotte's law**.

2.11. Show from the equation of state (2.1) the validity of Gay-Lussac's law for an ideal gas.

2.12. Use Gay-Lussac's second law and Boyle's law to show that $\frac{pV}{T}$ remains constant and to derive the equation of state (2.1). Use the equation of state to show that at same temperature and pressure the density of moist air is less than that of dry air.

2.13. Use the values of Table 1.1 to determine the partial pressure of 0.0062 kg CO_2 at 21° in 1 m^3 of air.

2.14. You drop a radiosonde balloon into the sky at 123 m above sea level. The maximum volume the balloon can be stretched to is given as $V = 0.02\,m^3$ and its mass is 0.01 kg. Assume an air pressure of 540 hPa and an air temperature of −17.5 °C at an altitude of 5 km. Will the balloon burst before it reaches 5 km? Calculate the pressure that the balloon can have at maximal expansion.

2.15. Calculate the percentage of sea-level pressure that pressure has at an altitude of 0, 5.6, 16.2, 31.2, 48, 65.1, 79.2, and 100 km altitude in an isothermal and in a homogeneous atmosphere. Made reasonable assumptions and discuss your results. How do they compare with the US standard atmosphere (Table 2.2)?

2.16. In the Arctic, a dry cabin was empty for a while. Its temperature inside is −40 °C. After burning some wood, temperature reaches 20 °C. Calculate the increase in pressure due to the heating. Discuss your results.

2.17. Show for an air parcel in a hydrostatic atmosphere that the quantity $h + \Phi = constant$ when the considered gas neither gains nor losses heat ($\delta q = 0$). What does this mean for the change in temperature?

2.18. Calculate the pressure in 2,500 m height in the case that at the ground, air pressure is 1,013.25 hPa, and the column between these heights has (a) a constant air temperature of $0°C$, (b) a constant density of 1.29 kg m^{-3}, and (c) an environmental lapse rate of 0.65 K 10^{-2} m^{-1}. How do we call these atmospheres? Discuss the pressure behaviors you obtain.

2.19. Calculate the geopotential height of 755 hPa pressure-surface assuming a sea-level pressure of 1,024 hPa, and a scale height of the atmosphere of 8.23 km.

2.20. Mt. Everest is about 8.848 km above sea level. Calculate the surface air pressure atop of Mt. Everest for (a) an isotherm, (b) a homogeneous, and (c) an atmosphere with an environmental lapse rate of 0.8 K10^{-2} m^{-1} that has a temperature of 15 °C and a sea-level pressure of 1,013.25 hPa. Calculate the lapse rates for these atmospheres and for the US standard atmosphere (Table 2.2). Compare your results and discuss them.

2.21. Derive the height dependency of an atmospheric non-reactive trace gas for an isotherm atmosphere in the absence of sinks and sources. By which factor does the concentration of the gas decrease with increasing height?

2.22. Show that the equations derived for the homogeneous and isothermal atmosphere are special cases of Eq. (2.21) that describes the polytrop atmosphere.

2.23. Determine the scale heights for the ozone, oxygen atom and nitrogen assuming an isothermal atmosphere.

2.24. Calculate the thickness of the layers for the values given in Table 2.1.

2.25. Combine the hydrostatic equation (2.7) with ideal gas law to derive an expression for the pressure variation in an isothermal layer of the atmosphere.

2.26. A model using entropy as a forecast variable predicts a decrease of 6 % in pressure, and of 4 % in air temperature. By how much did the entropy change? Make reasonable assumptions.

2.27. A parcel of dry air located at 700 hPa receives 10^7 J of heat by solar radiation, for which the volume increases by 22 m^3. Assume the center of the air parcel's mass remains in place. Determine the change in the internal energy of the air parcel. Calculate the increase in temperature of the air parcel under the assumption that the air molecules do not exert forces on each other for an air parcel mass of 7,000 kg.

2.28. The specific entropy of an air parcel that descends from 900 to 950 hPa decreases by 30 J kg^{-1} K^{-1}. Its initial temperature is 273 K. Determine the internal energy and potential temperature.

2.29. An air parcel has a temperature of 230 K at 400 hPa. Determine its potential temperature at this level and after displacement in 600 hPa. Discuss your results.

2.30. Express the first law of thermodynamics as a function of the specific heat capacity at (a) constant volume, and (b) at constant pressure. How would the first law of thermodynamics look like for an adiabatic process?

2.31. Calculate the potential temperature at 1,013.25, 500, 100, and 10 hPa assuming that the air temperatures at these pressure levels are 15, −10, −55, and −30 °C, respectively. Explain your results.

2.32. Calculate the potential temperature, θ, at 10 km height under the assumption that air temperature is 10 °C at the surface, and temperature decreases with height at the environmental lapse rate. Alternatively assume an average temperature to determine the potential temperature at 10 km. Comment on the differences.

2.33. Derive the dry adiabatic lapse rate from the first law of thermodynamics and the hydrostatic equation (2.7).

2.34. A hailstone has collected 10^{-4} kg of cloud water at 0 °C. Determine the work, the heat required for freezing at 700 hPa. By how much would the internal energy change? For simplicity ignore temperature dependency of thermodynamical quantities. Discuss how the change in internal energy and hence temperature would affect the freezing processes.

2.35. Show that an isolated ideal gas can spontaneously expand, but not spontaneously contract.

2.36. Show that static stability with respect to dry air will be positive in an atmosphere where the potential temperature increases with height.

2.37. Derive the dry adiabatic lapse rate from $d(c_p T + \Phi) = 0$.

2.38. For an air and dew-point temperature of -10 and $-25\,^{\circ}\mathrm{C}$, respectively, determine the partial pressure of water, the saturation water vapor pressure, and the relative humidity.

2.39. An air parcel has a temperature, pressure, and water-vapor pressure of $30\,^{\circ}\mathrm{C}$, 1,013.25, and 38 hPa, respectively. Determine its specific mixing ratio, mixing ratio, density, absolute and relative humidity.

2.40. According to Poisson's law the adiabatic reduction in pressure implies a reduction in temperature and saturation water-vapor pressure. Discuss how the denominator and numerator decrease, and what it means for the saturated mixing ratio. Use algebra to show how you came to your conclusions.

2.41. Show that $rh \approx \frac{q}{q_s} \approx \frac{r}{r_s} \approx \frac{e}{e_s}$.

2.42. Determine the virtual temperature at a location whose air temperature is $-25\,^{\circ}\mathrm{C}$ and saturation vapor pressure is 0.42 hPa, air pressure is 1,015 hPa, and relative humidity is 50 %. By how much does the use of virtual temperature vs. air temperature affect the calculated air density? What do you conclude from your results?

2.43. Determine the temperature that an air parcel rising dry-adiabatically to 750 or 500 hPa will have if it has a temperature $T_o = 283\,\mathrm{K}$ at $p_o = 1{,}000\,\mathrm{hPa}$. Comment on the decrease with height, z.

2.44. The initial state of an air parcel is $p = 997\,\mathrm{hPa}$, $T = 26.5\,^{\circ}\mathrm{C}$, $q = 15.4\,\mathrm{g\,kg^{-1}}$. Determine the mixing ratio r, relative humidity RH, virtual temperature T_v, the potential temperature, and virtual potential temperature.

2.45. Determine the density of air masses having a relative humidity of 0, 50, and 100 % at an air pressure of 1,013.25 hPa at $9.85\,^{\circ}\mathrm{C}$. Comment on the weight of these air masses.

2.46. Calculate the initial water-vapor pressures for an air of $-10\,^{\circ}\mathrm{C}$ with an relative humidity of 60 and 90 %, respectively, at sea level. How high has the air parcel to rise to form upslope fog?

2.47. Determine the dew-point temperature for a mixing ratio of $15\,\mathrm{g\,kg^{-1}}$ at 1,020 hPa and $25\,^{\circ}\mathrm{C}$.

2.48. Derive the equation of state (2.1) for the moist atmosphere for both the mixing ratio and the specific mixing ratio and comment on the differences. Assume the moist atmosphere as an ideal gas.

2.49. Calculate the mixing ratio for air with specific humidity of $10\,\mathrm{g\,kg^{-1}}$ and determine the difference in percent.

2.50. At 1,000 hPa, air is at saturation and has a temperature of 10 °C. Due to radiation loss the air cools and fog forms. During the fog formation $12 \cdot 10^3\,\mathrm{J\,kg^{-1}}$ of heat is lost to the environment. Determine the final temperature and the decrease in water-vapor pressure. Comment on the thermodynamic behavior of the process, on the saturation status, the heat, your assumptions, and how you could make your results more accurate. What kind of process is this?

2.51. Calculate the relative humidity of an air parcel that has a mixing ratio of $0.00138\,\mathrm{kg\,kg^{-1}}$ and water-vapor pressure at saturation of ≈ 42.3 hPa.

2.52. Determine the virtual temperature at normal pressure and saturation for an air temperature of 25 and 0 °C and give the virtual temperature addition.

2.53. Show that the equation of state (2.1) expressed with the virtual temperature in dependence of the mixing ratio is given by $p = \rho_a R_d T(1 + 1.61r)$, while that expressed with the virtual temperature in dependence of specific humidity is given by $p = \rho_m R_d(1 + 0.61q)T$. Hint: It will not be possible to do this calculations if you assume $q \approx 0.611\frac{e}{p} \approx r$.

2.54. In the Arctic, the mean virtual temperature of the 1,000 to 500 hPa layer is −40 °C. Determine the thickness of the layer between these levels.

2.55. In numerical weather prediction models, the mean terrain height within a grid cell represents the elevation of the area covered by the grid cell. Assume that in nature, a mountain range is 2.5 km high, while in the model it is projected to be 1.75 km. An air parcel with an initial air and dew point temperature of 11 and 6 °C at 10 m flows over the mountain range into a valley at 100 m. The wet adiabatic lapse rate is $0.55\,\mathrm{K10^{-2}\,m^{-1}}$. Calculate the lee side temperature, dew-point temperature, relative humidity, and heat released for both nature and model. Discuss the differences and consequences.

2.56. A power plant releases hot dry air with a temperature of 20 °C. To what height does the plume ascend when the ambient air temperature varies with height according to (a) $T(z) = (-10 - 6z)$ °C and (b) $T(z) = (-10 + z)$ °C where z is in km? Comment on your results.

2.57. Potential temperature increases with height. Show that the atmosphere has a static stability with respect to dry air.

2.58. Formulate the equations given in Table 2.4 as functions of the specific mixing ratio.

2.59. Determine the temperature at the mean tropopause height in mid-latitudes for an atmosphere with a surface temperature of 10 °C and environmental lapse rate of $0.65\,\mathrm{K10^{-2}\,m^{-1}}$.

2.60. An air parcel undergoes a complete Carnot cycle. For each step calculate the mechanical work w (per unit mass) performed by the air parcel and the heat q added to the air parcel. Starting point is $p_1 = 600$ hPa, $T_1 = 262$ K. Adiabatic

compression goes to $T_2 = 25\,°C$. Isothermal expansion will be to $P_3 = 990\,hPa$. Also determine the total work performed and heat added for the complete cycle and the efficiency of this cycle. Discuss your results.

2.61. At the beginning of your hike in the mountains you set your altimeter to 400 m. After 5 h the altimeter indicates 2,400 m. During the hike your measurements indicated an air temperature of -1.5, 6 and $-14\,°C$ at 400, 900 and 2,400 m, respectively, with a linear behavior between these levels. Correct your altimeter measurement and determine at what elevation you are really.

2.62. At a point x, y in the 500 and 850 hPa maps, geopotential heights amount 53,955 and $12{,}029\,m^2\,s^{-2}$, respectively. Virtual temperature amounts $10\,°C$ at 850 hPa. By using the relative topography as a temperature map determine the virtual temperature at 500 hPa.

2.63. How much does air density ($kg\,m^{-3}$) vary between a Yukon high pressure cell during winter ($p = 1{,}060\,hPa$, $T = -40\,°C$) and a thermal low pressure cell in Arizona during summer ($p = 1{,}000\,hPa$, $T = 40\,°C$)? Explain your results.

2.64. Determine the thickness of the 1,000 to 500 hPa layer for an average temperature equal to 0 °C. What type of precipitation may occur? Hint: Calculate the average air temperature, $\overline{T}$, in a layer of air from 1,000 to 500 hPa with a thickness of 5,400 m.

2.65. A dry adiabatic pressure decrease goes along with a decrease in temperature, which in accord with the Poisson equation reduces the saturation water-vapor pressure. Examine for an adiabatic process whether the net result means a decrease or increase in the saturation water-vapor mixing ratio and discuss your results.

2.66. Derive the equivalent potential temperature.

2.67. The following radiosonde chart was obtained at Lindenberg, Germany on May 17, 1993 at 1200 UTC.

Pressure (hPa)	Temperature (°C)	Dew point temperature (°C)
1,019	20.6	3.1
994	21	6
982	17	2
952	15	2
907	11	0
845	5	−1
808	2	−3
770	3	−9
742	2	−25
716	0	−22
625	−6	−40
573	−10	−35

(continued)

Pressure (hPa)	Temperature (°C)	Dew point temperature (°C)
419	−30	−46
387	−35	−47
280	−53	−64
228	−60	−72
186	−59	−74
169	−56	−73
160	−58	−77
127	−54	−82
113	−54	−86
100	−56	−87

Give the pressure at the tropopause, the pressure ranges for which the air is stable for dry air and for saturated air, and calculate the mixing ratio at 500 hPa and 1,000 hPa. If there were a lot of radiative cooling, how much would the temperature at 1,000 hPa have to fall for clouds to form? At what height would clouds form? Estimate the cloud top height.

2.68. Suppose a jet exhaust has (a) a temperature of 262 °C and a dew-point temperature of 162 °C, the same dewpoint temperature, but (b) an exhaust temperature of 562 °C, and (c) the same exhaust temperature, but a dew-point temperature of 446 °C. At flight level, the ambient pressure, temperature and dew-point temperature are at 310 hPa, −46, and −43 °C, respectively. Determine whether a visible contrail will form. Assume that the air and exhaust mix 1:1. Discuss your results.

2.69. Assume an outside and inside temperature of −15 and 21 °C, respectively, and an inside water-vapor pressure of 1.915 hPa. Assume that good water-vapor exchange between inside and outside and that no sources and sinks of water vapor exist. Compare the relative humidity inside and outside.

2.70. Determine the dew-point temperature corresponding to a mixing ratio of $4\,\mathrm{g\,kg^{-1}}$ at 995 hPa and 17 °C.

2.71. Derive the equation of vapor pressure over ice. What values have the constants?

2.72. Analogous to the derivation of the dry adiabatic lapse rate, derive the saturated lapse rate.

2.73. Derive the Brunt-Väisälä frequency for moist air. Hint: use virtual temperature.

References

Material, concepts, ideas and problems of the following books and articles inspired this chapter. These sources are recommended for further reading.

Andrews DG (2000) Introduction to atmospheric physics. Cambridge University Press, New York, 237pp

Angevine WM, Ecklund WL (1994) Errors in radio acoustic sounding of temperature. J Atmos Ocean Technol 11:837–842

Bergmann-Schäffer (1997) Lehrbuch der Experimental Physik Erde und Planeten. In: Raith W (ed) de Gruyter, Berlin, 727pp

Broeckner WS (1997) Mountain glaciers: recorders of atmospheric water vapor content. Glob Biogeochem Cycles 11:589–597

Cerbe G, Hoffmann H-J (1994) Einführung in die Thermodynamik. Carl Hanser Verlag, München, 468pp

Cotton WR, Anthes RA (1989) Storm and cloud dynamics. Academic, San Diego/New York/Berkley/Boston/London/Sydney/Tokyo/Toronto, 883pp

Davies-Jones R (2009) On formulas for equivalent potential temperature. Mon Wea Rev 137: 3137–3148

de Groot SR (1951) Thermodynamics of irreversible processes. Interscience Publishers Inc., New York, 244pp

Finkelstein RJ (1969) Thermodynamics and statistical physics. W.H. Freeman, San Francisco

Foken T (2014) Micrometeorology (trans: Nappo CJ). Springer, Heidelberg, 350pp

Haltiner GJ, Martin FL (1957) Dynamical and physical meteorology. McGraw-Hill, New York/Toronto/London, 470pp

Hobbs PV (2000a) Introduction to atmospheric chemistry. Cambridge University Press, Cambridge, 262pp

Hobbs PV (2000b) Basic physical chemistry for atmospheric sciences. Cambridge University Press, Cambridge, 209pp

Jacobson MZ (2005) Fundamentals of atmospheric modeling. Cambridge University Press, New York, 813pp

Kraus H (2000) Die Atmosphäre der Erde. Eine Einführung in die Meteorologie. Vieweg, Braunschweig/Wiesbaden, 470pp

Laube M, Höller H (1988) Cloud physics. In: Landolt-Börnstein, Gruppe V: Geophysik und Weltraumforschung 4b, pp 1–100

Lin Y-L (2007) Mesoscale dynamics. Cambridge University Press, Cambridge, 630pp

McKnight (1996) Physical geography, 5th edn. Prentice Hall, Upper Saddle River, 624pp

Mölders N (2011/2012) Land-use and land-cover changes – impact on climate and air quality. Atmospheric and oceanographic sciences library 44. Springer. doi:10.1007/978-94-007-1527-1 3

Mölders N, Kramm G (2007) Influence of wildfire induced land-cover changes on clouds and precipitation in Interior Alaska – a case study. Atmos Res 84:142–168

Möller F (1973) Einführung in die Meteorologie – Physik der Atmosphäre – Band 1. BI Hochschultaschenbücher, Mannheim, 222pp

Peixto JP, Oort AH (1992) Physics of climate. Springer, New York, 520pp

Petty GW (2008) A first course in atmospheric thermodynamics. Sundog Publishing, Madison/Wisconsin, 336pp

Pichler H (1984) Dynamik der Atmosphäre. BI Wissenschaftsverlag, Mannheim/Wien/Zürich, 456pp

Pielke RA (1984) Mesoscale meteorological modeling. Academic, London, 612pp

Prigogine I (1961) Introduction to thermodynamics of irreversible processes. Interscience, New York/London

Pruppacher HR, Klett JD (1978) Microphysics of clouds and precipitation. D. Reidel, Dordrecht/Boston/London, 714pp
Riegel CA (1999) Fundamentals of atmospheric dynamics and thermodynamics. In: Bridger AFC (ed). World Scientific, Singapore, 496pp
Tsonis AA (2002) An introduction to atmospheric thermodynamics. Cambridge University Press, New York, 171pp
Wallace JM, Hobbs PV (1977) Atmospheric science – an introductory survey. Academic, San Diego/New York/Boston/London/Sydney/Tokyo/Toronto, 467pp
Wallace JM, Hobbs PV (2006) Atmospheric Science – an introductory survey. Academic, San Diego/New York/Boston/London/Sydney/Tokyo/Toronto, 483pp
Wayne RP (1985) Chemistry of atmospheres – an introduction to the chemistry of the atmospheres of Earth, the planets, and their satellites. Clarendon Press, Oxford, 361pp

Chapter 3
Clouds and Precipitation

Abstract This chapter introduces the theoretical basis of the seven microphysical processes and the terms of their sub-processes. It discusses the concepts of conservation of total water mass, as well as bulk-parameterizations and spectral cloud models. The various cloud types and cloud morphology as a result of their microphysical properties and formation processes are presented as well. Furthermore, links to applications in remote sensing, and links to the role of clouds in atmospheric chemistry are given.

Keywords Cloud morphology • Cloud microphysics • Nucleation • Diffusion • Sedimentation • Collection • Breakup • Melting • Ice enhancement • Conservation of water • Cloud modeling • Precipitation

Earth when seen from space water in all phases seems to dominate (Fig. 4.26). Essential aspects of clouds are the release of latent heat and the consumption of heat connected with phase transition processes (Chap. 2), the interrelation between cloud microphysics and dynamics (Chap. 6), the interaction between clouds and radiation (Chap. 4), and the removal of pollutants from the atmosphere by hydrometeors (Chap. 5). We introduced the aspects of the vertical profiles of temperature and dewpoint temperature for cloud base and cloud top height (Chap. 2). For convection, stability plays an important role. The concepts of forced convection, convective inhibition (CIN), and convective available potential energy (CAPE) have already been introduced in Chap. 2 as well. Within the framework of the discussion of the moist atmosphere, we learned that vertical mixing, forced ascends at a mountainous barrier, frontal lifting, and convergence of the horizontal wind field (e.g. low pressure systems, squall lines, thunderstorms, local convection) are mechanisms to lift air to become saturated. This chapter focuses on the microphysical, modeling, and phenomenological aspects of clouds. Details on the role of large scale and mesoscale phenomena for cloud formation are discussed in Chaps. 6 and 7, respectively.

N. Mölders and G. Kramm, *Lectures in Meteorology*, Springer Atmospheric Sciences,
DOI 10.1007/978-3-319-02144-7_3,

Besides the availability of sufficient amounts of water vapor, vertical motions are required to generate clouds and precipitation. Clouds themselves can affect vertical motions in several ways. In cloudy regions, the various paths of cloud microphysics may alter the vertical wind components due to their thermodynamic forcing associated with the phase transition processes. For example, the freezing of cloud droplets and the growth of ice crystals by water-vapor deposition and riming contribute to latent heat release, enhance buoyancy and cloud growth, affect precipitation formation and alter the dynamics of cloud fields. Cooling by melting and/or evaporation may initiate downdrafts. Beyond that, rain-shafts may influence vertical motions as the additional condensate from sedimentation may turn a thermally induced upward motion into a downward motion. The latent heating associated with cloud and precipitation formation processes often has a paramount role as an energy source in mesoscale weather systems (Chap. 6), even though its importance may vary compared to other forcing mechanism. The way in which cloud and precipitating systems distribute this heat affects the regional water cycle (Chap. 7).

Clouds affect the energy budget and hence regional climate. Clouds and the distribution and intensity of precipitation influence the recycling of water via evapotranspiration within a region and how the available radiation energy at the surface is partitioned between **sensible** and **latent heat** characterized by the **Bowen-ratio** (Chap. 4). Over land, precipitation as a source for water availability is essential for habitability. The vegetation-soil and the natural water systems may release water vapor into the atmosphere by evapo(transpi)ration, where clouds form when the air becomes supersaturated. Over oceans, precipitation affects salinity, ocean-water density and the related ocean mixing processes, circulation and deep convection.

Clouds affect the trace-gas cycle by vertical redistributing species, chemical transformations in the aqueous and ice phase, altering the photolysis rates, and the gas phase chemistry below, within and above clouds, and by removing trace species and particles (Chap. 5). The distribution of a species between the gas and aqueous phases and the relative importance of gas and aqueous phase chemistry in clouds strongly depend on the degree of solubility characterized by the Henry's law constant and the liquid water content (LWC) (Chap. 5). At temperatures between the freezing point and $-35\,^{\circ}\mathrm{C}$ or so a fraction of the condensed water is ice, i.e. super-cooled water and ice coexist. Ice particles reduce the liquid water content by water-vapor deposition and riming. The latter occurs when the terminal velocities of the ice crystals are larger than for cloud droplets. Since raindrops and ice-crystals differ in shape, size, and density, their terminal velocities and scavenging rates differ. Raindrops evaporate and ice crystals sublimate in unsaturated layers, and alter the chemical composition of these layers.

The following sections describe cloud microphysical and precipitation formation processes, the chemical and dynamic processes leading to cloud formation, and discuss the resulting cloud morphology.

3.1 Nucleation

Nucleation is the process when water-vapor molecules accumulate to build an initial drop or ice crystal. In the air, water molecules collide randomly and build embryo droplets. We call this process **homogeneous nucleation** in the case of pure water, and **heterogeneous nucleation** when a droplet or ice crystal form on a **cloud condensation nuclei** (CCN) or **ice nuclei** (IN), respectively. Homogeneous nucleation rarely occurs in the atmosphere because it requires extremely high super-saturation values non-existent in the atmosphere. Nevertheless, discussing homogeneous nucleation provides valuable insight on nucleation.

3.1.1 Homogeneous Nucleation

In Sect. 2.8.3, we considered saturation over an infinite plane surface. To discus nucleation of cloud droplets, we have to include the effects of surface tension and curvature.

Assume that at time $t = 0$ a mass m_0 of water vapor at partial pressure e and temperature T exists in the absence of any droplets. Then, the total Gibbs free energy is $G_0 = G_v(T, e)m_0$ (subscript v for vapor, 0 for the initial state). When an embryo droplet of pure water starts to form at fixed temperature and pressure with radius r, its surface area, volume and mass are $A = 4\pi r^2$, $V = \frac{4}{3}\pi r^3$, and $m_w = \frac{4}{3}\pi r^3 \rho_w$. Here, ρ_w is the density of water (subscript w) and the mass of the surrounding water vapor is m_v. The total Gibbs free energy of the system droplet-environment is the sum of the Gibbs free energies of the droplet and water vapor plus a contribution due to the work required to form the unit surface at the vapor-liquid boundary $G = G_v(T, e)m_v + G_w(T, e)m_w + \sigma A$. This work is the energy per unit area called the **surface tension** σ. When the initial droplet is in equilibrium with its environment, the specific Gibbs free energies are equal.

Conservation of mass and energy requires $m_v = m_0 - m_w$ and $G - G_0 = (G_w - G_v)m_w + \sigma A$. The difference in the chemical potentials μ_v and μ_w of water vapor and water are related to the phase transition, and are the Gibb's free energy of an individual water-vapor molecule and water molecule (Chap. 2). The net Gibbs free energy required for nucleation is

$$\Delta G = G - G_0 = 4\pi r^2 \sigma - \frac{4}{3}\pi r^3 n_w(\mu_v - \mu_w) \tag{3.1}$$

where n_w is the number of molecules per unit volume of the droplet. The first term on the r.h.s. of Eq. (3.1) is the work needed to build a surface around the droplet, i.e. the vapor-liquid interface. The second term on the r.h.s. is the exchange of energy by the water molecules that go into the liquid phase.

When the work ($\Delta G > 0$), which exceeds the change in Gibb's free energy, is required to establish the surface, an accidentally formed droplet evaporates immediately. When the work is less than the change of Gibb's free energy ($\Delta G < 0$), the droplet survives.

The surface tension of water, however, decreases with decreasing temperature. It amounts $7.28 \cdot 10^{-4}\,\mathrm{N\,m^{-1}}$ at 25 °C.[1] Furthermore, surface tension increases inverse proportional to the radius. The pressure difference sustained across the interface water droplet – air can be determined with the Young-Laplace equation $\Delta p = 2\sigma\left(\frac{1}{r_1} + \frac{1}{r_2}\right)$. This means that smaller droplets have higher surface tension than larger droplets.

According to the laws of thermodynamics (Chap. 2), the chemical potentials differ

$$\mu_v - \mu_w = kT \ln\left(\frac{e}{e_s}\right) \tag{3.2}$$

where k, e, and e_s are the Boltzmann-constant, water-vapor pressure and water-vapor pressure at saturation above a plane surface. Thus,

$$\Delta G = 4\pi r^2\sigma - \frac{4}{3}\pi r^3 n_w kT \ln\left(\frac{e}{e_s(T)}\right) = 4\pi r^2\sigma - \frac{4}{3}\pi r^3 \rho_w R_v T \ln\left(\frac{e}{e_s(T)}\right). \tag{3.3}$$

Here R_v is the individual gas constant of water vapor. For the term on the r.h.s., we make use of the equation of state (2.1) at the interface water-gas. Some algebra yields the critical radius

$$r_c = \frac{2\sigma}{n_w kT \ln\left(\frac{e}{e_s}\right)} = \frac{2\sigma}{\rho_w R_v T} \ln\left(\frac{e_s(T)}{e}\right) \tag{3.4}$$

that satisfies $\frac{\partial G}{\partial r} = 0$, i.e. the Gibb's free energy and work required for the change in the droplet's surface are in equilibrium. Equation (3.4) is the **Kelvin equation**.[2] The critical radius depends on temperature directly (denominator), but also indirectly because the surface tension and saturation-vapor pressure depend on temperature. An important thermodynamic result is that at constant pressure and temperature, a system evolves in such a way that its Gibbs free energy decreases. Thus, a system is in equilibrium when its Gibbs free energy is at minimum.[3] When the Gibbs free

[1] Hot water is better for cleaning as the reduced surface tension allows the water to more easily into pores.

[2] This name is in recognition of Lord William Kelvin, formerly Sir William Thomson, a British physicist, 1824–1907. He was the first derived this equation.

[3] The Gibbs free energy is called the thermodynamic potential at constant pressure (and temperature) to indicate its analogy with the potential energy of a mechanical system that also has a minimum value under equilibrium conditions. For equilibrium transformations (e.g. phase transition) at constant temperature and pressure $ds = dh/T$.

energy has a maximum, the system is in an unstable equilibrium. When a droplet is at equilibrium with its environment at radius r, further water-vapor uptake increases the radius slightly and the droplet keeps growing by condensation. When a small loss of water by evaporation occurs for a droplet at the equilibrium radius, the droplet shrinks and disappears eventually.

The Kelvin equation rearranged for water-vapor pressure yields

$$e = e_s \exp\left(\frac{2\sigma}{n_w k\, T\, r_c}\right) = e_s \exp\left(\frac{2\sigma}{\rho_w R_v T\, r_c}\right). \tag{3.5}$$

According to Eq. (3.4) the critical radius depends on relative humidity for which $r_c \longrightarrow \infty$ if $e/e_s \longrightarrow 1$, i.e. $RH \longrightarrow 100\,\%$. This case corresponds to a plane surface as considered in Sect. 2.8.3. Consequently, air must be supersaturated for the radius to become finite. The greater the super-saturation is, the smaller the droplet can be for a random initial nucleation of molecules. Thus, the nucleation rate of droplets with critical radius, r_c, depends strongly on the degree of super-saturation $s = (\frac{e}{e_s} - 1)$ given as values between 0 and 1 or alternatively in percent by $S = (\frac{e}{e_s} - 1)100\,\%$. The curve derived from the Kelvin equation provides a relationship between the radius and saturation, i.e. that for $r \longrightarrow \infty$ $S \longrightarrow 0$. We can calculate the degree of super-saturation by the laws of statistic quantum mechanics applied to an ideal gas of randomly moving molecules. According to this simple theory, it is impossible for a droplet of pure water to form in the atmosphere. At sufficiently high super-saturation, clusters of water-vapor molecules may form and water embryos may build, i.e. homogeneous nucleation may occur despite of the aforementioned facts. Worth mentioning homogeneous nucleation rates occur at 300–400 % super-saturation. The mean atmospheric super-saturation amounts 0.1 % and super-saturation seldom exceeds 1 %, i.e. homogeneous nucleation plays no role in natural clouds.

Example. Assume a super-saturation of 0.00001 %, and a surface tension of $1{,}436\,\mathrm{N\,m^{-1}}$. Neglect the temperature dependency of surface tension. How large a drop can survive at 8 and −18 °C? Discuss your results.

Solution. The definition of relative humidity and the Kelvin's equation yield $rh = \frac{e}{e_s} = \exp(\frac{2\sigma}{n_w k\, T\, r_c}) = 1.00001$, $r_c = \frac{2\sigma}{\rho_w R_v T} \ln(\frac{e_s(T)}{e})$. $r_c(8\,^\circ\mathrm{C}) = \frac{2 \cdot 1436}{1000 \cdot 461 \cdot 281{,}15} \ln(1.00001) = 2.2 \cdot 10^{-10}\,\mathrm{m} = 0.00022\,\mu\mathrm{m}$, $r_c(-18\,^\circ\mathrm{C}) = 2.4 \cdot 10^{-10}\,\mathrm{m} = 0.00024\,\mu\mathrm{m}$. The molecular diameter of water is about $2.75\,\text{Å} = 2.75 \cdot 10^{-10}\,\mathrm{m}$. This means no homogeneous nucleation would occur at typical cloud-temperature ranges, and only slight super-saturation.

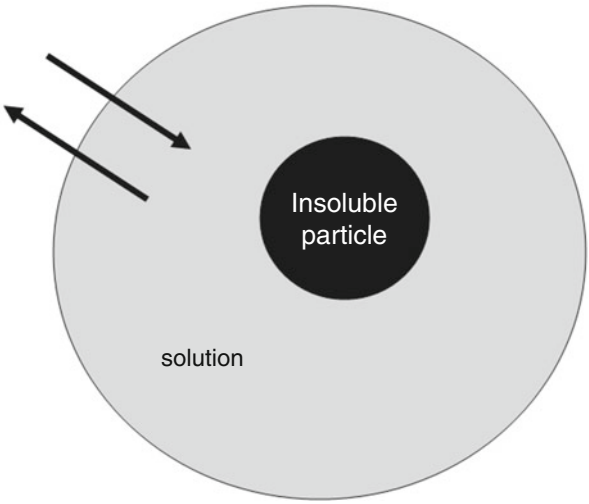

Fig. 3.1 Simplified model of a drop

3.1.2 Heterogeneous Nucleation

Cloud droplets form by heterogeneous nucleation on small aerosols, the cloud condensation nuclei. When the surface tension between the surface of a particle and water is small enough, a small film of water builds around the particle, and the particle serves as CCN (Fig. 3.1). CCNs may be of natural and/or anthropogenic origin (Chap. 1). Usually, sufficient amounts of wetable aerosols exist so that cloud droplets may form under slightly super-saturated atmospheric conditions. The number of active CCNs grows with super-saturation $N_{CCN} = C\, S^K$ where K and C are nearly constant. Typical values for K and C are 0.7 and 10^8 m^{-3} for maritime and 0.5 and $6 \cdot 10^8$ m^{-3} for continental air.

The efficiency of the nucleation process increases for soluble CCNs because according to **Raoult's law**[4] the saturation-vapor pressure over a solute is lower than over pure water. The solute reduces the critical radius and nucleation can more easily occur at environmental water-vapor pressure. The fractional reduction in water-vapor pressure due to the solute amounts

$$\frac{e'}{e} = f \ . \tag{3.6}$$

Here e' is the saturation-vapor pressure over the solution droplet that contains a **mole fraction**, f, of pure water, and e is the saturation-vapor pressure over a pure water droplet at same size and temperature. The mole fraction of pure water is the number of molecules in solution divided by the total number of molecules in solution.

[4]Francois Marie Raoult, French chemist, 1830–1901.

In a droplet of radius, r, dissolved salt of molecular weight, M_s, and mass, m_s, dissociates into i **ions** where i is the **van't Hoff**[5] **factor**. The effective number of moles of salt in the droplet is $i m_s/M_s$. For a density, ρ_w, and molecular weight of water, M_w, the number of moles in the droplet is $(\frac{4}{3}\pi r^3\rho_w - m_s)/M_w$ leading to a mole fraction of water of

$$f = \frac{(\frac{4}{3}\pi r^3\rho_w - m_s)/M_w}{(\frac{4}{3}\pi r^3\rho_w - m_s)/M_w + i m_s/M_s} = \left(1 + \frac{i m_s M_w}{M_s(\frac{4}{3}\pi r^3\rho_w - m_s)}\right)^{-1} . \quad (3.7)$$

Rearranging the Kelvin equation (Eq. (3.4)) provides the vapor pressure over a pure water droplet as $e = e_s \exp(\frac{2\sigma}{n_w k r T})$. Combining Eqs. (3.4) and (3.7) yields the saturation-vapor pressure over a solution droplet of radius, r as

$$e' = e_s \exp\left(\frac{2\sigma'}{n' k r T}\right)\left(1 + \frac{i m_s M_w}{M_s(\frac{4}{3}\pi r^3\rho_w - m_s)}\right)^{-1} . \quad (3.8)$$

Here the prime denotes the values appropriate for the solute. In the following, we drop the primes for convenience. The curve due to solubility effects depends on the mass of the salt, M_s. The critical radius and critical super-saturation decrease with increasing mass of salt.

Considering the effects of curvature and solubility yields for a droplet with dissolved nuclei

$$\rho_v(r) = \rho_{v,s}(T(r))(1 + \frac{a}{r} - \frac{b}{r^3}) . \quad (3.9)$$

The term $\frac{a}{r}$ describes the curvature effects on the droplet's equilibrium-vapor pressure. The value

$$a = \frac{2\sigma}{n_w k T} = \frac{2\sigma}{\rho_w R_v T} \quad (3.10)$$

depends on the surface tension, σ, at the droplet-air interface. The density of liquid water, ρ_w, is usually taken as constant ($1{,}000\,\mathrm{kg\,m^{-3}}$) despite of its slight temperature dependency.[6]

The factor $\frac{b}{r^3}$ describes the effects of dissolved salts on the droplet's equilibrium-vapor pressure with

$$b = \frac{3 i m_s M_w}{4\pi\rho_w M_s} . \quad (3.11)$$

[5] Jacobus Hendricus van't Hoff, Dutch physio-chemist, 1852–1911.

[6] This value is only exact at 0 °C.

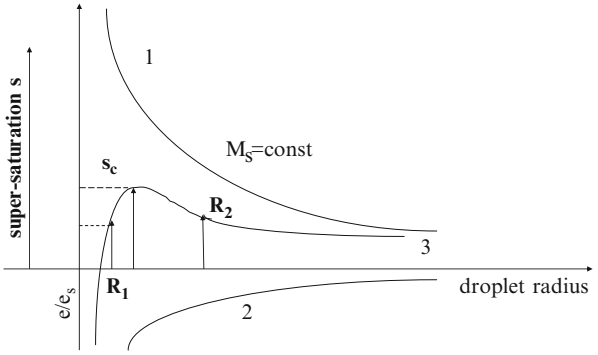

Fig. 3.2 Schematic view of the Köhler-curve (*curve 3*). *Curve 1* describes the curvature effects (Kelvin equation) and *curve 2* the solution effects (Raoult's law)

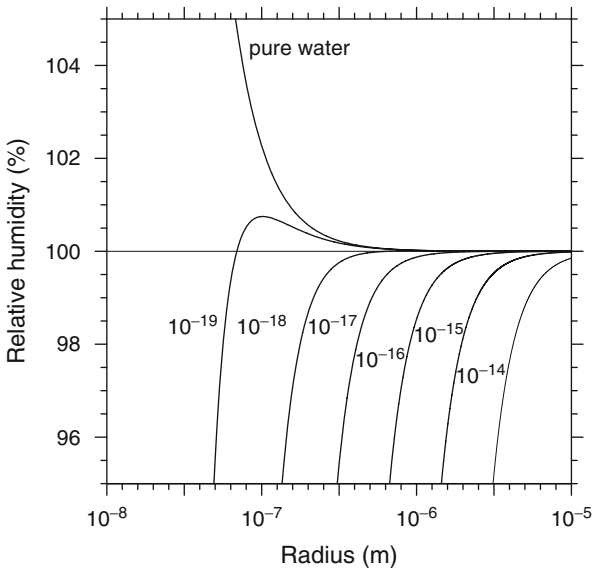

Fig. 3.3 Equilibrium super-saturation over droplets containing various amounts of dissolved salt

Assuming constant temperature and adding the values that make up the curves of the droplet curvature and solubility, provides the **Köhler-curve** (Fig. 3.2). The Köhler-curve represents the thermodynamic equilibrium of a droplet that neither grows nor evaporates. The regions above (below) the curve represent super-saturated (sub-saturated) conditions.

In general, a water-soluble CCN becomes activated in ambient air with super-saturation, s, when $s > s_c$. Here s_c is the peak value of super-saturation derived from the Köhler-curve for that kind of CCN. Figure 3.3 illustrates the effect of salt on saturation. Typically a droplet of radius $r = 0.01\,\mu\text{m}$ requires a relative humidity of 112 %, while a droplet of radius $r = 0.1\,\mu\text{m}$ only needs a relative humidity of 101 %.

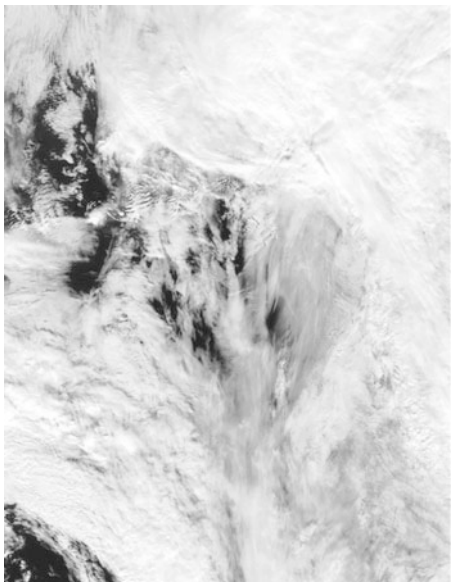

Fig. 3.4 Examples of ship tracks within the Gulf of Alaska on October 7, 2009 01:11 pm Alaska Standard Time as seen by the Terra satellite. Black and white version of the color original (From University of Alaska Fairbanks, Geographic Information Network of Alaska, http://www.gina.alaska.edu (2009))

3.1.2.1 Consequences

Droplets can nucleate when relative humidity is high enough. For non-soluble CCNs, the laws for homogeneous nucleation apply, i.e. the survival of a droplet is more probable for great than small non-soluble CCNs. Cloud droplet formation is more likely for great than small aerosol particles, for which the first cloud droplets form above the greatest and most soluble CCNs. The magnitude and composition of the CCNs and aerosol spectrum appreciably influence the size distribution of cloud droplets. An increased cloud-droplet formation is often observed in the leeside region of towns with industries producing large wetable and/or soluble aerosols, or downwind of ash spitting volcanoes. In the marine atmospheric boundary layer (ABL), additional aerosols emitted from ships may affect stratus clouds (Fig. 3.4).

Example. In a rain drop of 1 mm radius with a surface tension of $1.436 \cdot 10^{-3}\,\mathrm{N\,m^{-1}}$, $10^{-6}\,\mathrm{kg}$ H_2SO_4 (sulfuric acid) is dissolved at 5 °C. For simplicity assume $1{,}000\,\mathrm{kg\,m^{-3}}$ for the density of water, and $3.43 \cdot 10^{28}$ molecules $\mathrm{m^{-3}}$ per unit volume. The van't Hoff factor of H_2SO_4 is 3. Calculate the saturation relative humidity RH for these conditions.

Solution. Rearranging Kelvin's equation yields $\frac{2\sigma}{r\,n_w k T} = \ln(\frac{e}{e_s})$. The masses of H_2SO_4 and water amount to $98.079 \cdot 10^{-3}\,\mathrm{kg\,mol^{-1}}$ and $18.02 \cdot 10^{-3}\,\mathrm{kg\,mol^{-1}}$. $e = e_s \frac{\exp(\frac{2\sigma}{n_w k\,T\,r})}{(1+\frac{i\,m_S\,M_w}{M_S(\frac{4}{3}\pi r^3 \rho_w - m_S)})}$

(continued)

(continued)

After inserting the values we obtain $e = e_s \frac{1.00}{(1+\frac{3\cdot10^{-12}\,\mathrm{kg}\,18.02\cdot10^{-3}\,\mathrm{kg\,mol^{-1}}}{98.079\cdot10^{-3}\,\mathrm{kg\,mol^{-1}}(\frac{4}{3}3.14\cdot(10^{-3}\,\mathrm{m})^3\,1{,}000\,\mathrm{kg\,m^{-3}}-10^{-6}\,\mathrm{kg})})} = e_s \frac{1.00}{1.173003} \approx e_s 0.853$

Thus, $RH = \frac{e}{e_s} 100\,\% = 85.3\,\%$.

3.1.3 Ice Nucleation

Super-cooled droplets are unstable. To freeze, they must collect enough water molecules to form an ice embryo. Analogous considerations as presented in Sect. 3.1.1 yield that the embryo ice crystal must exceed a critical size to survive and grow. However, the hexagonal ice-crystal structure (non-spherical shape of ice embryos) makes these considerations more complex. When the critical size is exceeded, further growth decreases the total energy of the system, while any increase in size smaller than the critical size increases the total energy, for which such embryos tend to break up. A pure ice crystal can only form by homogeneous nucleation, i.e. an ice embryo of critical size builds accidentally by aggregation of a sufficient number of water molecules. Since heat is released during the freezing process, such chance aggregation typically never occurs at temperatures above $-35\,^\circ$C. Thus, this process only occurs in high-level clouds for droplets with radii of $20-60\,\mu$m. At temperatures less than $-35\,^\circ$C, the radii can amount a few micrometer.

When a droplet contains a **freezing nucleus**, the droplet freezes by heterogeneous nucleation. Freezing nuclei have a hexagonal-like structure on which the ice grows when the freezing nucleus collects water molecules. Heterogeneous nucleation occurs at higher temperatures than homogeneous nucleation, as no heat release is involved for reaching the initial size of the freezing nucleus.

Ice crystals can also form directly from the water-vapor phase upon **deposition nuclei** in cold air that is super-saturated with respect to water. At super-saturation with respect to water, some particles can serve either as a freezing nucleus or as a deposition nucleus. In the first case, condensation with subsequent freezing occurs, while in the latter no liquid phase is involved at least on the macroscopic scale.

Cloud droplets also can freeze when they collide with a **contact nucleus**, a process called **contact nucleation**. Laboratory experiments showed that a droplet can freeze at higher temperature due to contact nucleation than it would freeze if a nucleus were embedded in the droplet.

Freezing nuclei, deposition nuclei, and contact nuclei are all ice nuclei (IN). The threshold temperature at which a particle can act as an IN depends on the mechanism by which the IN nucleates ice and the history of the IN. Particles with a hexagonal-like structure tend to be good INs. About 87 % of the snow crystals have clay minerals as IN. Organic IN stem from sea-water plankton or decayed plant leaves and can be active even at $-4\,^\circ$C. Most IN are non-soluble in water.

Due to the saturation and temperature dependency of INs and the various re-suspension dependent sources, IN-concentrations can vary by several orders of magnitude within several hours. The number of active IN per liter of air is often estimated by the Fletcher formula[7]

$$N = \exp(a(T_{active} - T)) \tag{3.12}$$

where T_{active} stands for the temperature at which the IN becomes active and T is air temperature. The empirical value, a, ranges between 0.3 and 0.8.

3.2 Diffusion

Water-vapor diffusion can be directed towards the particle (condensation or deposition) or from a particle into its environment (evaporation or sublimation). The facts that (1) the binding forces of ice are stronger than those of water, (2) the saturation pressure of water exceeds that of ice, (3) the saturation pressure over a concave surface exceeds that over a convex surface, and (4) the saturation pressure is higher for pure water than for a solute have consequences for mixed phase clouds (Sect. 3.1.2).

3.2.1 Condensation and Evaporation

When a cloud droplet forms, it can grow further by water-vapor diffusion denoted condensation. The reverse process is evaporation. We can quantify these diffusion processes by assuming that the flux of water-vapor molecules in air is proportional to the gradient of the water-vapor molecules (Fig. 3.5). The diffusion equation (**Fick's first law of diffusion**) reads

$$\frac{\partial \rho_v}{\partial t} = \nabla \cdot (D_v \nabla \rho_v) = D_v \nabla^2 \rho_v \tag{3.13}$$

where $D_v \nabla^2 \rho_v$ is the water-vapor flux by molecular diffusion, D_v is the diffusion coefficient for water vapor in air, here assumed as constant, and ρ_v is water-vapor density. For a symmetric distribution of water vapor around a droplet (of pure water) of radius, r, and a stationary diffusion, water-vapor density depends on the distance, R, from the center of the droplet

[7]The Fletcher (1962) formula results in too low IN concentrations at small ranges of super-cooling temperatures. Meyers et al. (1992) and Cotton et al. (1982) suggested a modified formulation that is sensitive to the saturation conditions to correct the overestimation of ice nuclei in very cold clouds.

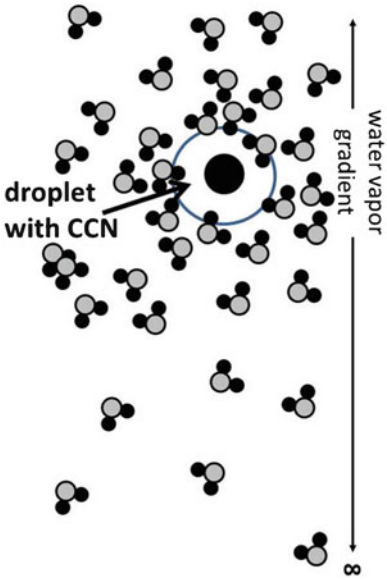

Fig. 3.5 Schematic view of diffusion

$$\nabla^2 \rho_v(R) = \frac{1}{R^2} \frac{\partial}{\partial R} \left(R^2 \frac{\partial \rho_v}{\partial R} \right) = 0 \, . \tag{3.14}$$

At the droplet surface, water-vapor density is $\rho_v(r)$. As distance R approximates infinity, water-vapor density approximates that of the environmental air. The solution that fulfils these boundary conditions is

$$\rho_v(R) = \rho_v(\infty) - \frac{r}{R}(\rho_v(\infty) - \rho_v(r)) \, . \tag{3.15}$$

The rate of change in mass, m, is

$$\frac{dm}{dt} = 4\pi r^2 D_v \frac{d\rho_v}{dR}|_r \tag{3.16}$$

where $D_v \frac{d\rho_v}{dR}|_r$ is the water-vapor flux in radial direction for a spherical surface of radius, r. Inserting this into Eq. (3.15) yields

$$\frac{dm}{dt} = 4\pi r D_v(\rho_v(\infty) - \rho_v(r)) \, . \tag{3.17}$$

Since mass is related to r^3 by the volume of the droplet this equation contains two unknowns, m and r. The conditions of the environment ($R = \infty$) are known.

To solve the equation we introduce the heat-balance equation as condensation is associated with the release of latent heat, L_v, at a rate $\frac{dm}{dt} L_v$ (Chap. 2). Under the

assumption that the heat is transported away from the droplet immediately after its release, we obtain

$$L_v \frac{dm}{dt} = 4\pi\kappa_a r(T(r) - T(\infty)) \tag{3.18}$$

where κ_a is the thermal conductivity of air,[8] and T is temperature. Applying the equation of state (2.1) for water vapor at saturation and assuming that the water-vapor pressure density at the droplet surface is given by the saturation water-vapor pressure density, $\rho_{v,s}$, yield $\rho_v(r) = \rho_{v,s}(T(r))$. We can solve these equations numerically for $\frac{dm}{dt}$, $T(r)$, and $\rho_v(R)$. We can solve them analytically for the special case of a growing or evaporating droplet in a saturated environment ($e(\infty) = e_s(T(\infty))$) by use of the Clausius-Clapeyron equation. The equation of state for an ideal gas (2.1) under saturated conditions over a pure plane of water combined with the Clausius-Clapeyron equation (2.71) provide

$$\frac{d\rho_{v,s}}{\rho_{v,s}} = \frac{L_v}{R_v}\frac{dT}{T^2} - \frac{dT}{T} \; . \tag{3.19}$$

After some algebra, the mass change reads

$$\frac{dm}{dt} = \frac{4\pi r s}{F_K + F_D} \tag{3.20}$$

with the heat conductivity,

$$F_K = \frac{L_v^2}{\kappa_a R_v T^2(\infty)} \tag{3.21}$$

and water vapor diffusivity,

$$F_D = \frac{R_v T(\infty)}{D_v e_s(\infty)} \; . \tag{3.22}$$

Here s and R_v are the super-saturation, and individual gas constant of water vapor, respectively. The above results mean that diffusion growth depends on the temperature and humidity of the droplet's environment and the droplet's radius.

Since in nature, cloud droplets form on CCN, we have to include the solubility and curvature effects in the calculation of the mass change

$$\frac{dm}{dt} = \frac{4\pi r}{F_K + F_D}\left(s - \frac{a}{r} + \frac{b}{r^3}\right) \; . \tag{3.23}$$

[8] The slight temperature dependency of thermal conductivity is neglected here.

This equation provides the condensation rate for saturated air. Under unsaturated conditions, the solution must be gained iteratively.

When the drops become large enough, they start to settle. In this case, diffusion and ambient temperature changes have to be considered by a ventilation factor that is simply multiplied on the r.h.s. of Eq. (3.23).

Drops of all size can grow/shrink by water-vapor diffusion. Raindrops falling through the cloud base start to evaporate. Evaporation of raindrops, among other things, depends on the cinematic viscosity, relative humidity, thermal conductivity and diffusivity for water vapor. Whether a raindrop that left the cloud, reaches the ground depends on the relative humidity profile below cloud base, cloud-base height, and the raindrop size.

At the edges of clouds condensation (evaporation) may occur due to entrainment (detrainment) of relatively cooler (warmer) air parcels. Mixing processes and turbulence are discussed in Chap. 6. The release of latent heat during condensation contributes to increase buoyancy (Chap. 2), and may enhance the updraft. The consumption of heat during evaporation leads to evaporative cooling and may initiate and/or enhance downdrafts. This interaction is known as cloud-microphysics-dynamics interaction

Example. Show that diffusion is too slow to produce raindrops. Exemplarily assume a final radius of 0.1 mm for the raindrops, an environmental temperature of 244 K, an actual vapor pressure of 0.516 hPa, a saturation-vapor pressure of 0.509 hPa, an initial drop radius of 0.01 mm, and a thermal conductivity of the air and diffusion coefficient of $0.025\,\mathrm{K\,m^{-1}}$ and $2.1 \cdot 10^{-6}\,\mathrm{kg\,s^{-1}}$, respectively.

Solution. Inserting provides $S = \frac{e}{e_s} - 1 = \frac{0.516}{0.509} - 1 = 0.0146 = 1.46\,\%$ and $F_k = 9{,}108{,}763.6\,\mathrm{m}$ and $F_D = 105{,}233{,}417.5\,\mathrm{m}$. For a radius $r = 10^{-5}\,\mathrm{m}$, diffusion changes the mass by $1.6 \cdot 10^{-15}\,\mathrm{kg\,s^{-1}}$. Growth from $r = 0.01\,\mathrm{mm}$ to $r = 0.1\,\mathrm{mm}$ requires a mass change of $m(0.1\,\mathrm{mm}) - m(0.01\,\mathrm{mm}) = \frac{4}{3}\pi\rho_w(r_{0.1}^3 - r_{0.01}^3) = \frac{4}{3}\pi 1{,}000\,\mathrm{kg\,m^{-3}} 9.999 \cdot 10^{-13}\,\mathrm{m^3} = 4 \cdot 10^{-9}\,\mathrm{kg}$. At the above diffusion rate, the droplet needs ≈30 days to grow from 0.01 to 0.1 mm.

3.2.2 Deposition and Sublimation

The growth behavior of ice crystals is known from in situ and laboratory experiments. Basic crystals show hexagonal shape. Diffusion growth of an ice crystal depends on the temperature and humidity of its environment and the ice-crystal shape (Fig. 3.6). Shape is described by an axis rectangular to the hexagonal surface. When this axis is long (short) as compared to the hexagonal surface, the crystals

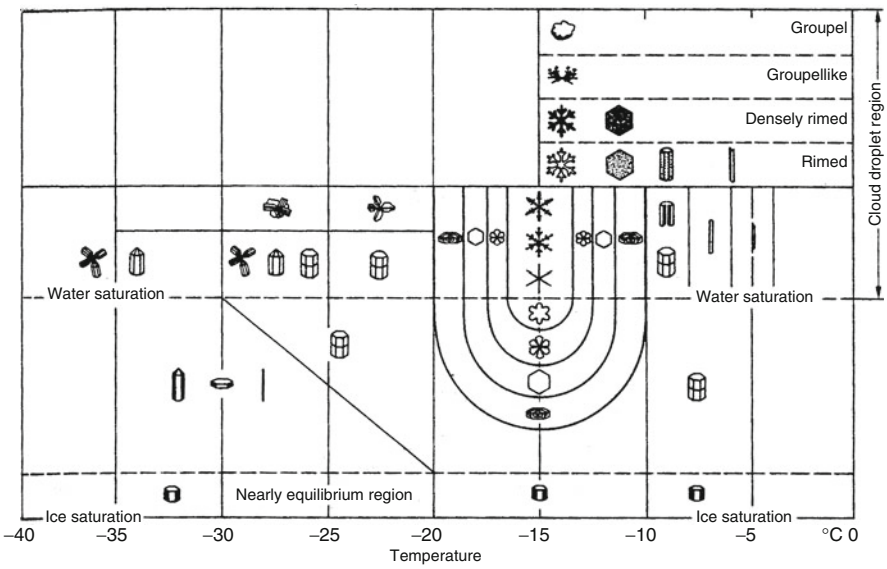

Fig. 3.6 Schematic view of relation of ice crystal shape to temperature and saturation (From Laube and Höller (1988))

are denoted prisms (plates). The **habitus** varies from prism-like to plate-like as the ambient temperature changes. Increasing super-saturation grows the surface to volume ratio of the ice crystal. The larger surface provides more space for the excess water vapor to deposit. Complex ice crystals (dendrites) form between −16 and −12 °C. On the six major axes, additional axes are visible. These ice crystals exist in the temperature range where the difference between the saturation-vapor pressure with respect to ice and water is the greatest. As super-saturation with respect to ice decreases, the less delicate ice crystals grow at the cost of the more delicate ones due to the differences in saturation pressure over convex and concave surfaces.

We can describe the water-vapor diffusion onto ice crystals by similar considerations as for condensation. Main differences are (1) ice crystals are non-spherical, the saturation-vapor pressure over ice is lower than over water, and (3) the differences in saturation-vapor pressure with respect to ice over concave and convex planes. The mass change for a spherical ice crystal reads

$$\frac{dm}{dt} = 4\pi r D_v(\rho_v(\infty) - \rho_{vi}) \tag{3.24}$$

where ρ_{vi} is the water-vapor density at the interface crystal-environment. For an arbitrary ice crystal, we yield

$$\frac{dm}{dt} = 4\pi C D_v(\rho_v(\infty) - \rho_{vi}) \tag{3.25}$$

where the empirical value C considers the ice-crystal shape.

Analogous consideration as for condensation/evaporation allow inclusion of ventilation, heat conductivity, water vapor diffusivity and saturation with respect to ice

$$\frac{dm}{dt} = \frac{4\pi C s_i}{F_{K,i} + F_{D,i}} \,. \tag{3.26}$$

Here $F_{K,i}$ and $F_{D,i}$ are the same as for condensation except that the latent heat of deposition and the water-vapor pressure at saturation with respect to ice are taken. As for evaporation, the above equation has to be solved numerically for sublimation.

In air sub-saturated with respect to water, but supersaturated with respect to ice, the **Bergeron**[9]**-Findeisen**-Wegner[10]**process** becomes effective. Cloud water evaporates and the released water vapor deposits on ice crystals. This process is an important path for glacification of clouds.

The rate at which an ice particle gains heat by deposition is given by

$$\frac{dQ_d}{dt} = 4\pi r D_v(\rho_v(\infty) - \rho_v(r))v_{fs}L_s \tag{3.27}$$

where v_{fs} and L_s are the ventilation factor and latent heat of sublimation.

Like for condensation/evaporation, depostion/sublimation interact with the cloud dynamics via release of latent heat/consumption of heat by increasing/decreasing buoyancy (Chaps. 2 and 6).

Example. Assume an air volume with a mass of 1,000 kg at −15 °C and a relative humidity of 100 % with respect to water at 1,000.18 hPa. Initially no ice or cloud droplets are present. Suddenly small ice crystals form by nucleation on INs. How much water vapor (kg) can deposit?

Solution. At −15 °C, $e_{sw} \approx 0.81$ hPa and $e_{si} \approx 0.63$ hPa. The water-vapor reduction is $e_{sw} - e_{si} = (0.81 - 0.63)$ hPa $= 0.18$ hPa. Further, $r = 0.622\frac{e}{p-e} = 0.622\frac{0.18\,\text{hPa}}{(1{,}000.18-0.18)\,\text{hPa}} \approx 0.0001\,\text{kg kg}^{-1}$. Since the considered air mass of these characteristics is 1,000 kg, a total ice crystal mass of about 0.1 kg can be deposited.

3.3 Sedimentation

Gravity acts on all frozen and liquid particles (Chap. 2), for which they start to settle. Typically, cloud droplets, and small ice crystals with radii $\leq 10\,\mu$m (Fig. 3.9) are considered airborne. Drops or crystals with radii up to 100 μm have notable

[9] Tor Bergeron, Swedish meteorologist, 1891–1977.

[10] Alfred Lothar Wegner, German geophysicist and meteorologist, 1897–1954.

Table 3.1 Examples for the relationship between the size of hydrometeors and their terminal velocity

Radius (μm)	Rate of fall ($m\,s^{-1}$)	Type of hydrometeor
2,500	8.9	Large raindrop
500	4	Small raindrop
250	2.8	Large drizzle
100	1.5	Drizzle
50	0.3	Large cloud drop
25	0.076	Normal cloud droplet
5	0.003	Small cloud droplet
0.5	0.00004	Large condensation nucleus
5,000	1.7	Snow flake
5,000	2.5	Graupel

fall speeds (Table 3.1). Typically, a diameter of 0.1 mm serves as the threshold for distinguishing between cloud droplets and raindrops. The smallest precipitating drops ($0.1 \leq r \leq 0.25$ mm) are **drizzle**. Drops with radii greater than 0.25 mm are called raindrops. Rain, snow, graupel and hail are all **hydrometeors**.

During sedimentation, hydrometeors experience the friction force due to the downward increasing air density. The ventilation effect is negligibly small for droplets smaller than 0.1 mm. The final velocity of any droplet/crystal becomes a non-accelerated **terminal velocity**, v_T that grows with increasing radius. For drops with $r < 500\,\mu$m the terminal velocity nearly linearly increases with the radius; for larger drops, the rate is less and becomes nearly constant for radii of 3 mm. This asymptotic behavior results from the deformation of the drops that becomes notable for large drops (Fig. 3.11). Table 3.1 lists typical values of terminal velocities for various precipitation particles. In the case of ice columns, densely rimed ice particles, dendrites, graupel, or snow flakes, the fallspeed depends on their shape and/or their length vs. width (Fig. 3.7).

In cloud models, often the **mass-weighted mean terminal velocity** for hydrometeors serves to describe the mean sedimentation behavior of hydrometeors

$$v_T = \frac{\int_0^\infty v_k(D_k) N_k(D_k) D_k^3 dD_k}{\int_0^\infty N_k(D_k) D_k^3 d\ D_k} \tag{3.28}$$

where the subscript k denotes the type of precipitating particle, $v_k(D_k)$ is the fall velocity of the particle with diameter D_k, and $N_k(D_k)$ is the number of particles with diameter D_k.

Since only few CCN act as IN, the size distributions of ice crystals are spread over few large particles developing quickly fall-speeds of tens of $cm\,s^{-1}$. This effect can be seen in form of **virga** underneath cirrus clouds and is an example for how the microphysical processes determine the appearance of clouds.

Note that large amounts of falling hydrometeors may drag adjacent air with them thereby introducing downward motion to the air through which they fall. Below the cloud, together with evaporative and sublimative cooling this process may enhance downdrafts. Ice crystals and snow aggregates may survive up to 1 km or so below the freezing line. Here cooling by melting also may initiate and/or support downdrafts.

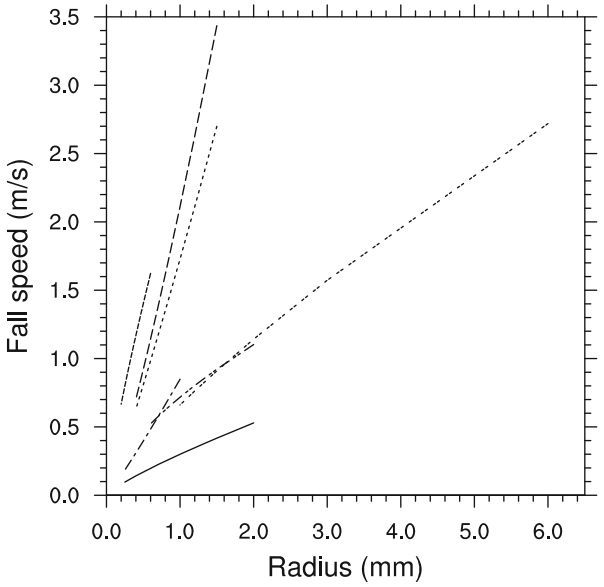

Fig. 3.7 Fallspeeds of various ice crystals as a function of shape and size. *Solid line* – aggregates of unrimed side planes, *long dashed line* – conical graupel, *dotted line* – hexagonal graupel, *long dash dot line* – graupel-like snow of lump type, *long dash dot dot line* – densely rimed dendrites, *short dashed line* – unrimed side planes, *double dot line* – aggregates of densely rimed dendrites or dendrites

3.4 Collection

Once cloud particles of different size exist, they can collide with each other and form larger particles. Several termini distinguish the various **collection** processes.

3.4.1 Accretion and Coalescence

Cloud droplets grow by collection, i.e. collision with smaller droplets and subsequent **coalescence** (*latin coalescere* to flow together). The process of collision plus coalescence of two or more droplets is called **accretion**.

The **collision efficiency** mainly depends on the relative airflow around the falling droplet. A collection efficiency of one means that the large drop collects every droplet in its path called the **collection kernel** (Fig. 3.8). Aerodynamic effects can redirect small droplets out or into the collection kernel. Redirection out of (into) the collection kernel reduces (increases) the collision efficiency to values smaller (greater) than one.

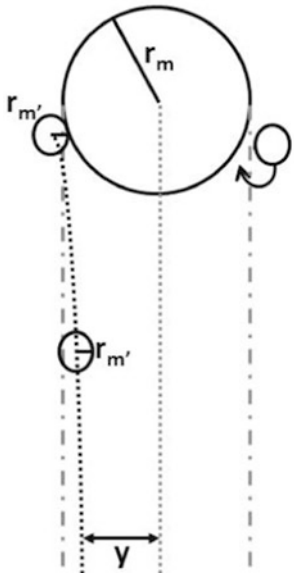

Fig. 3.8 Schematic view of collection of small drops of radius $r_{m'}$ by a large drop of radius r_m. y indicates the range in which collection occurs. The *dash-dotted line* serves just as an aid to the reader for eyeballing the path of the large drop. The *left dotted line* gives the path of the small droplet. The *center dotted line* marks the path of the center of the large drop. The *curved arrow* indicates aerodynamic effects can sweep droplets outside of the large drop's path into its path

The **coalescence efficiency** expresses that a collision of two droplets can fail to result in coalescence. Usually the coalescence efficiency is high for electrically charged droplets. Since the present knowledge on coalescence efficiency is low, it is usually set equal to one in models.

The **collection efficiency** with which droplets collide and coalesce, is the product of the collision efficiency and coalescence efficiency. It gives the fraction of droplets that are in the collection kernel and become part of the collecting drop

$$E = \frac{y^2}{(r_m + r_{m'})^2} \ . \tag{3.29}$$

Since the collection efficiency depends on the radii of the drops and on hydrodynamic forces, its calculation is mathematically difficult. This is especially true for droplets of similar size, because they affect each other's motion strongly. When large drops collect small drops, collection efficiency reaches unity.

For simplicity we describe the collection process by means of a droplet of mass m falling through a cloud with droplets of mass m'. Let us assume that the droplets of mass m' and of radii $r_{m'}$ are equally distributed and have a liquid water content $w_l = \rho q_{m'}$ where ρ and $q_{m'}$ are air density and the specific cloud-water mixing ratio, respectively. For a continuously growing falling droplet, the rate of mass increase by collection is

$$\frac{dm}{dt} = A|v_m - v_{m'}|w_l E \ . \tag{3.30}$$

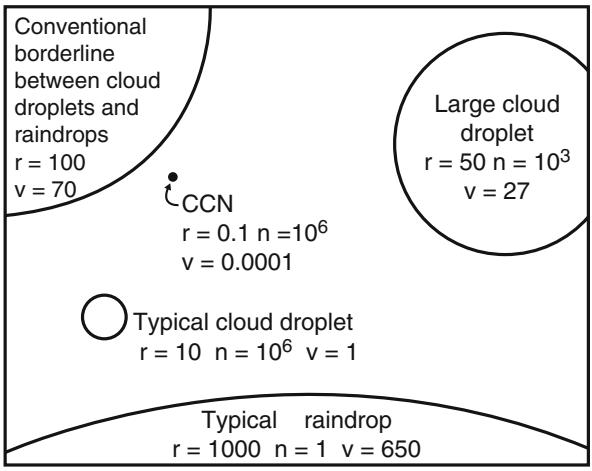

Fig. 3.9 Relative comparison of sizes of cloud and precipitating particles (From Marshall et al. (1958))

Here, v_m and $v_{m'}$ are the terminal velocity of the droplets in calm air, and A is the effective area wherein droplets are collected. For simplicity, we assume the droplets as spheres so that $A = \pi(r_m + r_{m'})^2$. These areas base on the sum of the droplets' radii as each droplet within the distance $r_m + r_{m'}$ from the center of the droplet with the greater radius can be collected. Since collection only depends on the relative motion of the droplets to each other, we take the absolute value. When large droplets collect small droplets, taking the absolute values becomes redundant as large droplets fall quicker than small droplets.

Replacing $m = \frac{4}{3}\pi r_m^3 \rho_w$ (with ρ_w being the density of water) in the above equation provides the change in the drop's radius. For $v_m \gg v_{m'}$ and $E = 1$ we obtain

$$\frac{dr_m}{dt} = \left(\frac{v_m w_l E 3}{4\pi\rho_w}\right)^{\frac{1}{3}} . \tag{3.31}$$

Since fall speed and collection efficiency increase with increasing radius, dr_m/dt increases with increasing r_m as well. The growth of a droplet by collision and subsequent coalescence accelerates. Updrafts may affect the collection.

Typical concentrations of cloud droplets are about $10^8\ \mathrm{m}^{-3}$, i.e. the particles are about 1 mm apart. Clouds consist of water droplets with radii of about 10 μm or so (Fig. 3.9). Because of the non-monotone droplet distribution, we have to integrate over the entire distribution

$$\frac{dm}{dt} = \int_0^\infty A_m |v_m - v_{m'}| m' N(m') E(m, m') dm' \tag{3.32}$$

where $N(m')$ is the number of droplets with mass m' to $m' + dm'$ in a unit volume of air.

In clouds, droplet growth by coalescence is stochastic (non-continuous). During a time Δt, some droplets experience more, other less collisions. Consequently, the growth rates differ resulting in a non-monotone drop-size distribution. We can consider the stochastic nature by a time-dependent size distribution where $N(m,t)dm$ is the number of droplets per unit air volume with masses between m and $m+dm$ at time t. The rate at which the droplets of mass m' are in the collection kernel of the droplet with mass m is defined by

$$K(m,m') = A_m|v_m - v_{m'}|E(m,m') \; . \tag{3.33}$$

The droplet number decreases by coalescence according to

$$\frac{PN(m,t)}{\Delta t} = K(m,m')N(m',t)N(m,t)dm' \tag{3.34}$$

Where P is the probability that a droplet of mass m collides and coalesces with a droplet of mass m' during Δt. We have to choose the time interval small enough to ensure that only one collision occurs per time interval. Similar considerations for the generation of smaller droplets and integration provide the stochastic collection equation. As time progresses, a bimodal distribution of droplet develops with the greater portion of water accumulated at large radii (raindrops) and a smaller amount in small radii (cloud droplets).

3.4.2 Aggregation and Riming

Aggregation is the process of ice crystals collecting ice crystals. Like coalescence, aggregation reduces the particle number, but not the total particle mass, i.e. it changes the particle-size distribution. We can modify the equations used to describe the collection of droplets by droplets for ice crystals collecting ice crystals. On average, the collection efficiency is much lower than unity for aggregation. Aggregation is strongest at temperatures above $-5\,°C$ where the ice-crystal surface is the stickiest. A secondary maximum exists at temperatures around $-15\,°C$ where many ice crystals are dendrites that easily tangle each other (Fig. 3.6). Below $-20\,°C$, aggregation hardly occurs.

Riming is the collection of liquid particles by solid particles, a process that involves phase transition. Collection of cloud drops (raindrops) by ice crystals yields graupel (hail; (Fig. 3.10)). Since the fall speeds of solid and liquid particles differ (Table 3.1) and falling crystals tumble, the collection efficiency is usually lower than unity. The collection efficiency, among other things, depends on ice-crystal shape. The riming efficiency is highest for column-type ice crystals.

The density of ice particles or snowflakes is smaller than the density of pure ice ($916\,kg\,m^{-3}$) and depends on the (1) moisture available during the growth process, (2) size of the collected drops, and (3) time needed for the freezing of the collected

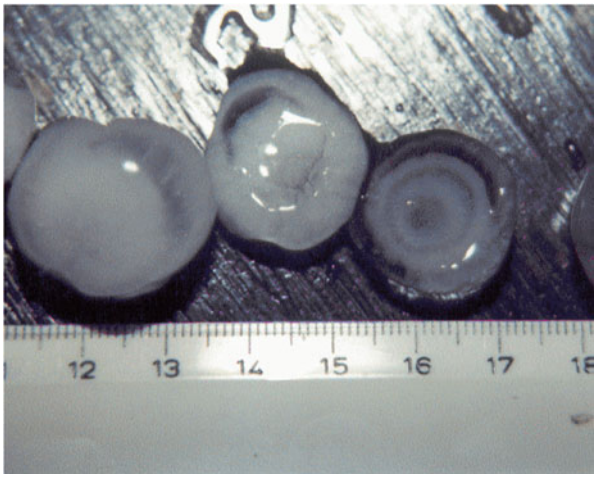

Fig. 3.10 Hailstone from a thunderstorm at Leipzig, Germany. The ruler has metric units (Photo by Mölders (1998))

cloud droplet or raindrop. Laboratory experiments suggested density values of 20–450 kg m^{-3} for graupel and rimed columns, 250–700 kg m^{-3} for conical graupel, and 50–890 kg m^{-3} for snowflakes.

Hail may form in intense thunderstorms, where graupel and super-cooled raindrops can coexist in strong updrafts. When the updrafts compensate the fall speed of the raindrops, the raindrops remain at about the same level for long time. Graupel falling through the trapped raindrops collects them and the super-cooled water freezes onto the graupel forming ice pellets. The growth rate depends on drop temperature and the potential water sphere around the ice, the transport of heat from the growing hail towards the atmosphere, and hydro-dynamical effects. Upon reaching cloud base, updrafts may take some of these frozen particles up again. Thus, the frozen particles may undergo the growth cycle several times under continuous growth of the hailstone. The stronger the updrafts, the more times hail can repeat this cycle and the larger it can grow. Hailstones can become several centimeter in size (Fig. 3.10). The time between leaving the cloud and reaching the ground is too short to melt the entire hailstone in the relatively warm air below the thunderstorm cloud.

We can use the rate $\frac{dQ_f}{dt}$ at which heat is gained during riming, to determine the mass change due to collection of liquid water

$$\frac{dQ_f}{dt} = \frac{dm}{dt} L_f - c_w(T(r) - T_w) \tag{3.35}$$

where L_f and c_w are the heat of fusion released as the droplets hit the ice, and the specific heat of water, respectively. The second term is the heat per unit mass gained as the water droplet of temperature T_w achieves thermodynamic equilibrium with the ice. In an unsaturated surrounding, T_w can be several degrees colder than the ambient air. In saturated air, T_w can be approximated by the wet-bulb temperature of the air ($T_w = T_\infty$).

The rate of conductive heat loss reads

$$\frac{dQ_c}{dt} = 4\pi r \kappa_a (T(r) - T(\infty)) v_{fc} \tag{3.36}$$

where v_{fc} is a ventilation factor for conduction. In equilibrium, we obtain $\frac{dQ_c}{dt} = \frac{dQ_f}{dt} + \frac{dQ_d}{dt}$ where $\frac{dQ_d}{dt}$ is the heat gained by water vapor deposition (Eq. (3.27)). We can solve this equation for the equilibrium temperature. As long as this temperature is below freezing, the ice particle remains dry, and we speak of **dry growth**. Otherwise, we have **wet growth** that leads to the spongy look of some hail.

3.5 Breakup

When a drop reaches a critical size, it becomes unstable. The concave depression at the base of the falling drop almost explosively deepens and develops quickly a bag-like form that is supported by an annular ring made up by the bulk of water (Fig. 3.11). The bag-like drop bursts into a large number of relatively small drops of

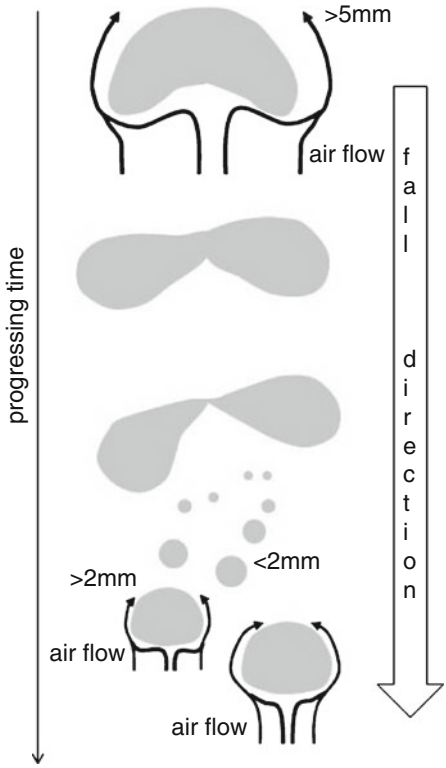

Fig. 3.11 Sequence of breakup of a drop. The *black arrows* indicate the air flow. The *big arrow* indicates the direction of gravity

different sizes. The ring breaks into a small number of relatively large drops. This process is known as **breakup**.

A thoroughly theoretical description of the growth of the large amplitude drop distortion is still subject to research. We can obtain a simple estimate of the maximum stable drop radius r_{max} by assuming that the incipient instability occurs when the drag stress $C_D \rho_a v_T^2/2$ exceeds the surface tension of the drop $2\sigma/r$

$$r_{max} = \frac{4\sigma}{C_D \rho_a v_T^2} \ . \tag{3.37}$$

Here C_D, ρ_a and v_T are the drag coefficient, air density and fall speed, respectively. The value of C_D ranges between 0.46 for a sphere and 1.17 for a disk.

Laboratory experiments showed that the probability a droplet of mass m breaks up is nearly zero for droplet radii less than 3.5 mm. The probability for breakup increases exponentially with the droplet radius for $r > 3.5$ mm according to

$$P(m) = 2.94 \cdot 10^{-7} \exp(3.4\, r) \tag{3.38}$$

where r is in mm and P in s^{-1}. The number of resulting droplets with mass between m and $m + dm$ can be estimated as

$$N(m', m) = 0.1\, r_{m'}^3 \exp(-15.6\, r_m) \ . \tag{3.39}$$

Here the radii are given in cm. We can use this empirical formula to assess the effect of a bursting raindrop on the drop-size distribution

$$\frac{\partial N(m,t)}{\partial t} = -N(m,t) P(m) + \int_0^\infty N(m',t) N(m',m) P(m') dm' \ . \tag{3.40}$$

Break-up conserves the total water amount, but redistributes the water towards smaller dropsizes.

Example. Determine the maximum stable radius for a drop with a surface tension of $0.00728\,\mathrm{N\,m^{-1}}$, drag coefficient of 1.17 and terminal velocity of $5\,\mathrm{m\,s^{-1}}$ in an environment with an air density of $0.5\,\mathrm{kg\,m^{-3}}$.

Solution. $r_{max} = \frac{4 \cdot 0.00728\,\mathrm{N\,m^{-1}}}{1.17 \cdot 0.5\,\mathrm{kg\,m^{-3}}\, 10^2\,\mathrm{m^2\,s^{-2}}} = 0.009956\,\mathrm{m} \approx 1\,\mathrm{mm}$.

3.6 Melting

Besides from accretion, raindrops can form by melting of frozen particles that fall into air warmer than the freezing point.[11] The **melting** process depends on air temperature, ice-crystal type, hydro-dynamical and shedding effects, saturation, evaporative cooling and cooling by melting. The latter two processes slow down the melting.

By assuming a heat balance for the melting particle, we can determine the change rate of the ice-particle mass due to melting

$$-L_f \frac{dm}{dt} = 4\pi r \kappa_a (T(\infty) - T_0) v_{fc} + \frac{dm_{col}}{dt} c_w (T_w - T_0) + \frac{dQ_d}{dt} \,. \tag{3.41}$$

Here $\frac{dm_{col}}{dt}$ is the mass change by collection that can be calculated by Eq. (3.32). The first term on the r.h.s. is the diffusion of heat towards the particle from the surrounding. The second term is the heat transfer rate to the ice from the drops of temperature T_w that the melting particle collects. The last term is the gain or loss of heat by vapor diffusion. When both the drop and air temperature are above the freezing point T_0, both the first and second term contribute to the melting process.

3.7 Ice Enhancement

In clouds, ice-crystal concentrations often exceed the number of ice crystals expected from the number of IN typically activated at these temperatures. The process that increases the number of ice crystals is denoted **ice enhancement**. Its mechanisms are still subject to research, but several hypotheses exist:

- Fragmentation of ice crystals. Crystals break due to collision and/or thermal shocks.
- Ice splitter production or **Hallett-Mossop-mechanism**. Laboratory experiments showed that the collision of super-cooled droplets with diameter $>23\,\mu\text{m}$ on ice surfaces at velocities $\geq 1.4\,\text{m}\,\text{s}^{-1}$ at temperatures between -8 and $-3\,^\circ\text{C}$ produces small ice splitter.
- Contact nucleation. Some aerosols can yield increased nucleation at higher temperatures than they do under other nucleation conditions, when they get into contact with super-cooled water droplets.
- Condensation and deposition nucleation. The ice nucleation activity of atmospheric aerosols can increase by condensation or deposition nucleation, when the super-saturation of the ambient air exceeds 1 % with respect to water. The region of high super-saturation within a cloud is an ideal environment for the sudden existence of a high number of ice crystals.

[11] Aggregates can survive fall distances of up to 1 km before melting is completed.

Since for the last two mechanisms no ice crystals have to pre-exist, these mechanisms permit sudden existence of high ice concentrations at relatively high temperatures.

3.8 Conservation of Water

The seven cloud microphysical processes must be considered when modeling cloud processes. In cloud models, the mixing ratios (or specific mixing ratios) of water vapor, r_v (q_v), cloud-water, r_c (q_c), and ice, r_i (q_i), can be determined diagnostically by distributing the excess water-vapor amount between the liquid and solid phase at temperatures below freezing and to the liquid phase only at temperatures above the freezing point. In saturated air masses warmer than 0 °C, only cloud-water forms. In saturated air masses with temperatures between −35 and 0 °C, both ice and cloud water can coexist. In this temperature range in and below clouds, water can exist in all three phases. Cloud models must consider the various forms of solid and liquid cloud particles and hydrometeors, their interaction and exchange of mass and heat during phase transition, and that at the same time, the total mass of water remains constant

$$q_{total} = \sum_{i=1}^{n} q_i \tag{3.42}$$

or

$$r_{total} = \sum_{i=1}^{n} r_i \tag{3.43}$$

where n is the number of cloud and precipitation hydrometeor categories. Once we specified n and the categories for a model, we can formulate the sink and source terms

$$\frac{Dq_k}{Dt} = S_k \tag{3.44}$$

by means of the seven basic microphysical processes discussed in Sects. 3.1–3.7. Here $k = 1, \ldots, n$. Cloud microphysical models base on this concept and often use various simplified formulations of the seven microphysical processes discussed above. The complexity of cloud microphysical models depends on the classes or size of the **bins** chosen, and on which processes are considered. They become even more complex with inclusion of solution processes (Chap. 5).

Cloud microphysical models using classes are referred to as using **bulk microphysical parameterizations**; those that consider the droplet-size distribution by fine resolved bins are called **spectral cloud models**. Note that when these models

are used as modules within mesoscale, climate or Earth system models convective clouds are at sub-grid scale, i.e. too small to be resolved. In these cases, an additional parameterization for convective processes is needed. Such so-called cumulus parameterizations base on the concepts like CAPE, stability analysis, buoyancy, etc. (Chap. 2).

In a simple form, bulk-parameterizations just account for the phases leading to three classes, water vapor, liquid water and ice that may be further subdivided into cloud-water, rainwater, cloud-ice, graupel, snow, and hail, etc. Usually, sedimentating and non-sedimentating classes for liquid and solid water are distinguished. In its simplest form, this distinction leads to five classes, water vapor, cloud-water, rainwater, cloud-ice and snow. Six-water class bulk parameterizations also consider graupel.

In spectral cloud models, the droplet spectrum is divided into bins of equal size. Thus, each bin holds the drops that have radii larger than the lower and smaller than the upper bound of the bin. The total water is conserved, but the number of drops may change due to microphysical processes.

In all bulk and spectral formulations, we have to decide which collections are to be considered, and we have to define to which class the result of the collection is attributed. This means the cloud modeler makes assumptions on the heterogeneous ice forming processes, the form and density of the ice as well as on the terminal velocities of the hydrometeors. Due to secondary effects related to latent heat release and consumption of heat, and cloud-microphysics-dynamic interaction as well as radiative effects, model results may differ not only with respect to simulated clouds and precipitation, but also for temperature, wind and other quantities when changing the cloud-microphysical parameterization. The choices for the interactions within the cloud affect assumptions on particles size/shape with consequences for terminal velocity (Fig. 3.7; Table 3.1), etc. Figure 3.12 schematically illustrates the variety of possible interaction of cloud and precipitation particles.

Various different concepts exit to parameterize cloud microphysics and its interaction with aerosols and radiation. Consequently, results from different bulk-cloud microphysical schemes even with same classes may differ tremendously. Inter-comparison of results from various cloud microphysical parameterizations showed that the different formulations of microphysical processes that compete with each other for the available cloud-water (e.g. formulation of coalescence, accretion versus riming) cause primarily the differences in the results. Small differences in the predicted rates of transition processes and terminal velocities accumulate with time, leading finally to notable differences in predicted cloud fields and precipitation pattern. Differences in terminal velocities, rainwater and ice, melting and evaporation, for instance, affect the onset of precipitation at the ground, the rain intensities and distribution with consequences for evapotranspiration, soil wetness and runoff. Differences in the assumptions on the partitioning between the cold and the warm path of precipitation formation affect the release of latent heat and the consumption of heat and cause differences in the temperature fields with consequences for vertical motions, and other cloud-microphysical processes. The combined differences may

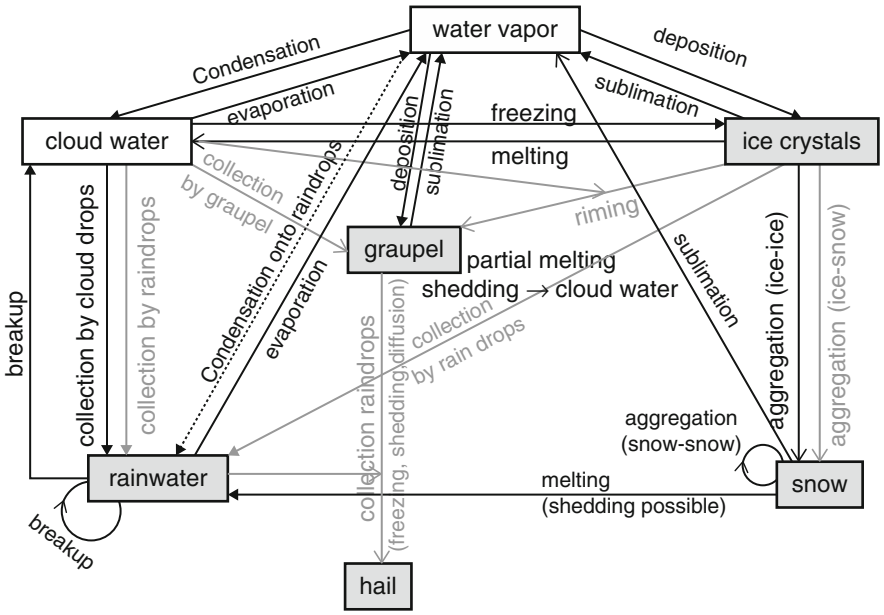

Fig. 3.12 Schematic view of some interaction of cloud and precipitation particles in a bulk-microphysical parameterization. *Gray boxes* indicate particles subject to sedimentation. *Arrows* indicate process direction. *Black* means two particles of different categories are involved leading to loss in one of them and gain in the other. *Gray* indicates that two different categories lead to loss in these categories and are a source for a non-involved category. In nature, all thermodynamically and dynamically potential processes occur concurrently, and shifts from one category to the next are continuous

become so strong that simulated clouds and precipitation may appear to be of more stratiform or convective character in the one or the other scheme (Fig. 3.13).

3.9 Cloud Morphology and Precipitation

The various microphysical processes discussed occur at different locations in the atmosphere and under different ambient conditions. Thus, the ambient conditions determine the appearance of the clouds. From their appearance, we may deduct what happens where in a cloud. The anvil of a thunderstorm cloud (cumulonimbus) is an example of strong glacification at subzero temperature. The anvils sharp shape visualizes the inversion of temperature and spread of the air along the tropopause. The vigils of cirrus clouds indicate strong sedimentation, which gives them the crochet hook-like appearance. Figure 3.14 exemplary elucidates for a convective cloud where which microphysical processes occur most frequently.

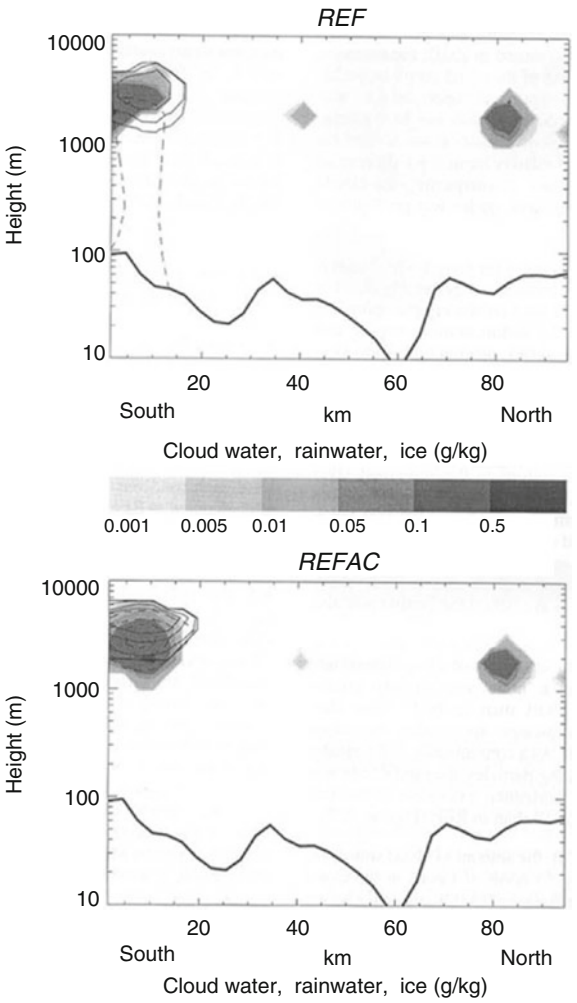

Fig. 3.13 Comparison of the results as obtained by two different five-water-class cloud microphysical schemes. *Solid lines*, *dashed lines* and *gray shades* represent ice, rainwater, and cloud-water mixing ratios, respectively. Contour intervals for ice are 0.001, 0.01, 0.1, and 0.5 g kg^{-1}, and for rainwater 0.1, 0.5, and 1 g kg^{-1} (From Mölders (1999a,b))

3.9.1 Cloud Types and Classification

Traditionally, clouds are classified by their appearance as seen by an observer on the ground: the height of their cloud base (Fig. 3.15), and their physical properties (Table 3.2). The cloud-classification indicates indirectly via the typical height the cloud phase/composition and some cloud characteristics.

The prefix *cirr-*, as in **cirrus** (*latin* curl of hair), indicates clouds located at high levels above 7 km (in mid-latitudes). Due to the low temperatures at such height, these clouds primarily, consist of ice crystals. High-level clouds are usually thin and appear to be white (e.g. Figs. 3.16, 3.17, and 4.18), but a magnificent array of colors is possible when the Sun is low in the sky. The disc of the Sun can be seen as such.

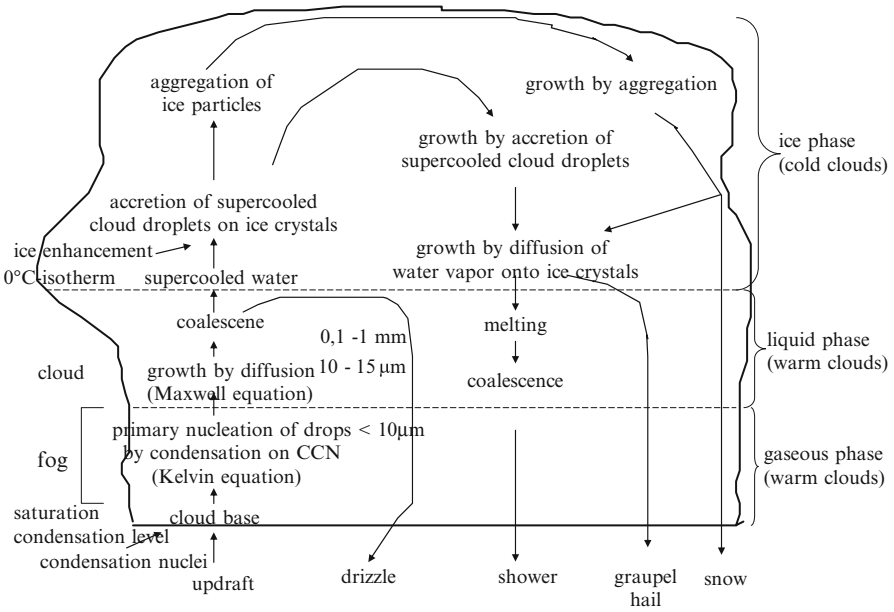

Fig. 3.14 Schematic view of microphysical processes in a cumulus-type cloud

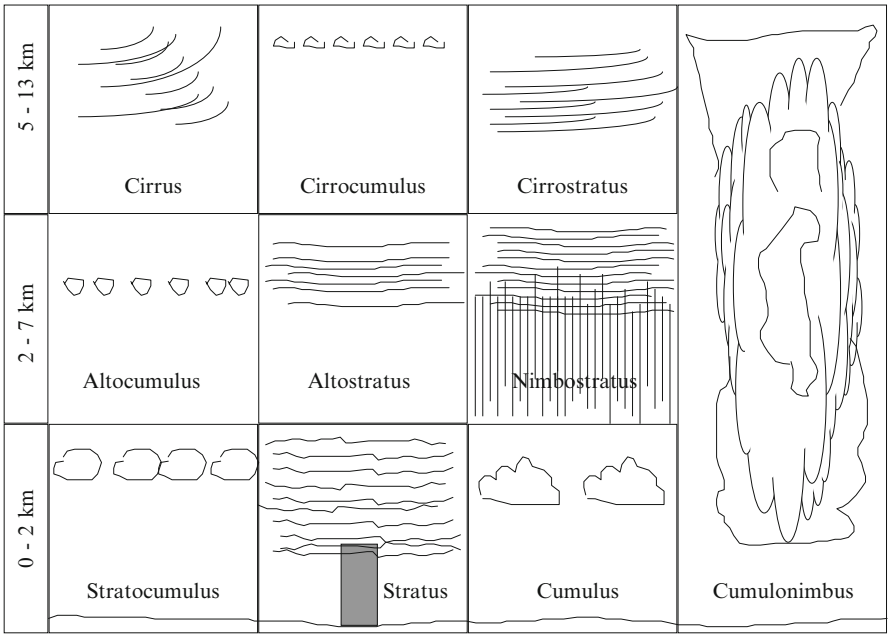

Fig. 3.15 Schematic view of cloud classification according to the location of their cloud base in the troposphere

Table 3.2 Characteristic properties of various clouds and fog. The parameter T_c, T_p, w, CR_r, CR_γ, LWC, and Δz stand for the lifetime of the cloud, residence time of an air parcel in the cloud, the typical mean vertical velocity, long-wave radiative cooling, wet-adiabatic cooling, liquid/ice water content, and the vertical cloud extension. Question marks stand for unknown

Cloud type	T_c (h)	T_p (s)	w ($m\,s^{-1}$)	CR_r ($K\,h^{-1}$)	CR_γ ($K\,h^{-1}$)	LWC ($g\,m^{-3}$)	Δz (m)	Remarks
Fog	2–6	10^4	0.01	1–4	0.2	0.05–0.2	100	Turbulence determines transport and physical processes
Stratus/ Strato-cumulus	6–12	10^5	0.1	2	2	0.05–0.25	1,000	Turbulence determines energetic, transport and physical processes
Cumulus	0.17–0.5	0.17	3	4	50	0.3–1	1,500	Turbulence determines energetic, transport and physical processes, wet-adiabatic cooling dominates
Cumulus congestus	0.34–0.75	500	10	4	??	0.5–2.5	5,000	Turbulence high, residence times often longer than expected by T_p; wet-adiabatic cooling dominates
Cumulonimbus	>0.75 h	400	30	4	??	1.5–4.5	12,000	Turbulence high, residence times often longer than expected by T_p; wet-adiabatic cooling dominates
Altocumulus lenticularis	>10	1,200	15	2	18	0.2	18,000	Wet-adiabatic cooling dominates; near-surface turbulence can be significant

Fig. 3.16 Cirrocumulus (Photo by Kramm (2013))

Fig. 3.17 Cirrostratus with sun dog (Photo by Kramm (2003))

The prefix *alto-* denotes clouds with cloud bases in the mid-troposphere between 2 and 7 km. Here the temperatures allow super-cooled drops to exist. Therefore, mid-level clouds mainly consist of droplets, but ice crystals are possible at temperatures below the freezing point. The position of the Sun is visible through all types of mid-level clouds (Figs. 3.18 and 3.19).

Cumulus (*Latin* heap; Fig. 3.20) has its cloud base in the atmospheric boundary layer, usually below 2 km height. Low-level clouds mostly consist of water droplets. At temperatures below the freezing point, these clouds may also contain ice crystals and snow. Typically cumulus looks like cauliflower. As the updrafts in a cumulus slow down and break down, the cloud top may start glacifying, and eventually the cloud dissipates. The onset of glacifying leads to a fringes-like appearance of the cloud tops.

Stratus (*Latin* layer) refers to layered clouds (Fig. 3.4). The pre-fixes cirro, alto and strato refer to the appearance of clouds like **cirrocumulus** (Fig. 3.16), **cirrostratus** (Fig. 3.17), **altocumulus** (Fig. 3.18), **altostratus** (Fig. 3.19), and **stratocumulus** (Fig. 3.21).

Fig. 3.18 Altocumulus over boreal forest (Photo by Kramm (2013))

Fig. 3.19 Altostratus over boreal forest (Photo by Kramm (2013))

The cloud classes can be further specified by vertical cloud extension (e.g. **humilis** (*Latin*, flat), **medicoris** (middle, mean), **congestus** (tower-like)), form (e.g. **mammatus** (breast-like), **lenticularis** (lense-like)), appearance (e.g. **unicus** (alone, single), **duplicatus** (twice)), optical impression (e.g. **translucidus** (transparent)) or whether clouds precipitate (*Latin* **nimbus** rain) (Fig. 3.22). Despite the cloud base of cumulonimbi are usually located in the lower troposphere cumulonimbi do not classify as low-level clouds, because they extend through the entire troposphere. Some cumulonimbus clouds may sprout a funnel cloud (Fig. 6.20).

3.9.1.1 Other Cloud Types

Other cloud types include contrails, billow clouds, mammatus, orographic and pileus clouds. Billow clouds may result from Kelvin-Helmholtz instability and

Fig. 3.20 Cumulus clouds over Fairbanks (Photo by Mölders (2002))

Fig. 3.21 Stratocumulus clouds over the University of Alaska Fairbanks' experimental farmland (Photo by Mölders (2013))

Fig. 3.22 Nimbostratus during a parade (Photo by Kramm (2013))

Fig. 3.23 Fog over the Tanana Valley as seen from the University of Alaska Fairbanks campus. In the back, the Alaska Range is seen (Photo by Mölders (2014))

visualize a row of horizontal eddies (Fig. 6.50). This instability is associated with airflow having marked vertical shear and weak thermal stratification. See Chap. 6 for an explanation of their formation mechanism.

3.9.1.2 Fog

Fog is a cloud of which the cloud base lays on the ground. Fog can consist of cloud droplets and/or ice crystals. In mountainous terrain, stratus over the valley may be fog at the mountain slopes (Fig. 3.23). Fog can form through radiative cooling (Chap. 4), advection of cold air over warm surfaces, or moist air over cold surfaces (Chaps. 2, 6, and 7). According to the World Meteorological Organization (WMO), fog is not a separate cloud class.

3.9.2 Precipitation

3.9.2.1 Convective Precipitation

Convective precipitation varies strongly in space and yields high precipitation rates. It is associated with high atmospheric instability and convective clouds (e.g. cumulus congestus, cumulonimbus). Typical synoptic situations for convective precipitation are thunderstorms or cold fronts (Chap. 6). The time to form convective precipitation is about 1 h. In convective clouds, vertical motions are about $1 < w < 10\,\mathrm{m\,s^{-1}}$, which exceeds the typical terminal velocities of ice crystals and snow. Because of the short time, precipitation particles cannot form high above cloud base. Growth of precipitation particles already starts in the updrafts. The updrafts lift the

particles as long as the updrafts are strong enough to compensate the fall velocity of the particle. The only microphysical process quick enough to permit growth of precipitation particles within less than one hour is riming.

3.9.2.2 Stratiform Precipitation

Stratiform precipitation results when the vertical velocities are small as compared to the fall velocities of the ice crystals (subscript i) and snow (subscript s) $v_{T_k}(k = i, s)$

$$\mid w \mid < v_{T_k} \ . \tag{3.45}$$

The fall velocity amounts to about $1-3\,\mathrm{m\,s^{-1}}$ (Table 3.1), while the large-scale vertical velocity, w, amounts several centimeter per second.

In the upper part of the cloud, ice particles play an important role in precipitation formation. Here temperatures may be below freezing and ice crystals grow at the expense of cloud droplets. The vertical velocity is smaller than the fall speeds of ice crystals v_{T_k}, but large enough to transport further water vapor upwards. Because of the long distance and the low terminal velocity of ice crystals, enough time exists for growth by diffusion. Once the particles are large enough (in about 2.5 km height above ground) aggregation and riming occur. Irregular-formed snow crystals develop. Be aware that aggregation does not increase the amount of precipitation, but concentrates the water substances on large particles that after melting become quickly falling raindrops.

Stratiform precipitation is relative homogeneous in space and time. Precipitation rates are low, but accumulated precipitation may be high. Stratiform precipitation occurs at warm fronts and is associated with nimbostratus or decaying thunderstorms (Chap. 6).

3.9.2.3 Freezing Rain

Freezing rain forms as falling snow encounters a layer of warm air thick enough for the snow to melt completely (Fig. 3.24). When the resulting raindrops pass through a thin layer of air being at temperatures below the freezing point that is located just above the surface, the drops become super-cooled, but do not freeze. As soon as these drops hit surfaces (e.g. the ground, power lines, tree branches), they immediately freeze, forming a thin film of ice. We denote this phenomenon **freezing rain**. When the super-cooled drops partly refreeze before reaching the ground, we refer to the precipitation as **sleet** (Fig. 3.24).

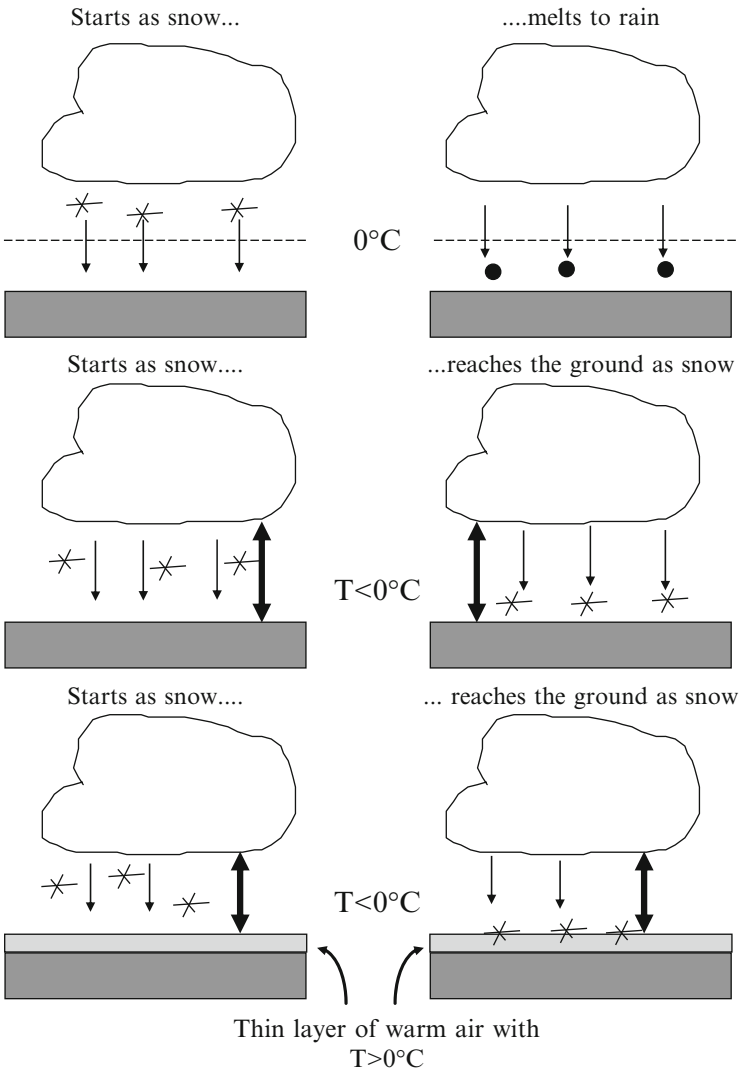

Fig. 3.24 Schematic view of the evolution of various kinds of precipitation

3.9.2.4 Blue Sky Precipitation

In polar regions, often small ice-crystals exit airborne typically with slight downward sedimentation despite the sky is blue and the Sun, other stars and/or the Moon are clearly visible. The light from street lights or other light sources is reflected at the ice crystals (Chap. 4). Vertical light columns become visible (Fig. 3.25).

Fig. 3.25 Light reflection columns over Fairbanks (Photo by Mölders (2004))

Problems

Knowledge and Comprehension

1. Why do continental air masses usually contain more aerosols than maritime air masses, and what does this mean for cloud-droplet formation and cloud-droplet size distribution?
2. Why does the number of CCN grow with saturation?
3. Explain why ship emissions may modify maritime stratus clouds along their path and lead to visible signatures in satellite imagery.
4. What do the different saturation-vapor pressures over ice and water mean for clouds?
5. What does the difference in the latent heat of vaporization, melting, and sublimation mean for cloud physical processes and energy conservation in models?
6. Describe the change of the spectrum of cloud particles with time.
7. What does the Findeisen-Bergeron-Wegner process mean?
8. Explain the difference between condensation and nucleation.
9. How do cloud droplets become raindrops?
10. What happens when a cold, dry air mass flows over warm water? What happens when a warm, moist air mass flows over cold water?
11. Why does it rain?
12. What does the size of a drop mean for its probability to evaporate/grow?
13. What can a cut through a hailstone tell you about its growth and its fate in the cloud?
14. What are the seven microphysical processes? Give at least one example for each of them.
15. Make a sketch like in Fig. 3.14, but for nimbostratus.
16. Why does a drop in the atmosphere look like a boomerang and not like a drop falling from an outlet?

Analysis, Application and Evaluation

3.1. Get a cloud watcher chart (various charts are available on the internet). For the next six weeks take notes (if possible) every three hours during the day of what types you see. Assess the percentage fraction with which they cover the sky. How do the clouds change over the time of 10 min or so? Can you see a pattern regarding which cloud types occur concurrently? Can you recognize some systematic in their sequence of appearance? Relate the cloud types to the microphysical and thermodynamic processes (Chap. 2).

3.2. The gravitational force a droplet experiences is proportional to mass $m = \rho\frac{4}{3}\pi r^3$ where ρ is density and r is the radius. The drag force that a falling droplet experiences depends on the velocity and droplet size according to $F = kv^2 4\pi r^2$ where k is a constant. Determine the terminal velocity of the droplet and discuss your result.

3.3. A radar provides a reflectivity of 30 dB. Estimate the precipitation rate assuming large-scale precipitation, stratiform-type precipitation, aggregates of snowflakes, and snowflakes.

3.4. Assume a stratus clouds of 1,000 m vertical extent and a typical lifetime of 6 h. In stratus clouds, the average vertical velocity is of the order of $0.1\,\mathrm{m\,s^{-1}}$. Determine the time scale for a parcel from its entering cloud base and leaving cloud top. Compare your result to the lifetime of the stratus and give an interpretation.

3.5. A developing cumulus cloud in a tropical thunderstorm grows upward at a rate of $15\,\mathrm{m\,s^{-1}}$. When the cloud starts forming with a base at 2 km, how long does it take from the onset of cloud formation for the cloud top to reach the tropopause at 15 km height?

3.6. Locatelli and Hobbs (1974) measured the diameter, D (in mm) and speed (in $\mathrm{m\,s^{-1}}$) of falling densely rimed assemblages of dendrites. They found a relationship of $v = aD^b$ with $a = 0.79$ and $b = 0.27$. What are the units of these empirical constants a and b? Give the value of these empirical constants in the SI system.

3.7. An isolated raindrop having a temperature of 10 °C evaporates in an air having a temperature of 15 °C. Determine the mixing ratio of the environmental air. Ignore the curvature effect.

3.8. Stratiform rain falls at a rate of 2mm/h from a cloud base at 2 km height into the unsaturated air below. Due to evaporation only 1.5 mm/h reach the ground. Assume the loss as mass of water evaporated per unit time and unit mass of air and calculate the average cooling rate due to evaporation occurring below cloud base.

3.9. Show that many small hailstones of 0.01 m in diameter cause less damage than a hailstone of 0.06 m in diameter. Comment also on the increase in damage when the hailstone is 0.01 m instead of 0.006 m and compare this increase to the increase obtained for the size increment from 0.01 to 0.06 m. Hint: Damage depends on energy.

3.10. The precipitation rate in the eye-wall of a tropical cyclone is $100\,\mathrm{mm\,h^{-1}}$. At cloud base, water vapor mixing ratio, air pressure and temperature are $20\,\mathrm{g\,kg^{-1}}$, 900 hPa and 28 °C, respectively. Calculate the vertical updraft velocity under the assumption that entrainment is negligible and that all condensed water reaches the Earth's surface.

3.11. Calculate the precipitation rate in millimeter of liquid water per second due to $2 \cdot 10^{-5}$ kg of snow crystals that exist in a concentration of $30{,}000\,\mathrm{m^{-3}}$ and fall at $1.3\,\mathrm{m\,s^{-1}}$ on an unit area.

3.12. Potential instability is an important type of instability for generating severe weather. It arises when dry air overlies a warm, humid layer. In Tornado Alley, the following synoptic situation occurs in the morning. The atmospheric boundary layer (ABL) has a height of 2 km. 2m air temperature and dewpoint temperature are 22 °C. The top of the ABL is much drier and has a temperature of 10 °C. Calculate the stability and lapse rate of this air column. Then assume that the entire layer is forced upward by 2 km and the top of the layer remains unsaturated during ascent. Determine the new stability and lapse rate of this air column, assuming a saturated adiabatic lapse rate of $0.5\,\mathrm{K10^{-2}\,m^{-1}}$. What would happen if this layer would further ascend? Discuss the further ascend in sense of what we learned about cloud formation. What would stop the ascend? Hint: Have a look at Chaps. 1 and 2. Based on your results make a forecast for the weather of that day.

References

Material, concepts, ideas and problems of the following books and articles inspired this chapter. These sources are recommended for further reading.

Andrews DG (2000) Introduction to atmospheric physics. Cambridge University Press, New York, 237pp

Beheng K (1992) Wolkenmikrophysik. Karlsruhe, unpublished manuscript

Braham RR (1968) Meteorological basis for precipitation development. Bull Am Meteorol Soc 49:343–353

Cotton WR, Anthes RA (1989) Storm and cloud dynamics. Academic, San Diego/ New York/Berkley/Boston/London/Sydney/Tokyo/Toronto, 883pp

Cotton WR, Pielke RA (1995) Human impacts on weather and climate. Cambridge University Press, Cambridge/New York, 288pp

Cotton WR, Stephens MA, Nehrkorn T, Tripoli GJ (1982) The Colorado State University three-dimensional cloud/ mesoscale model. Part II: An ice phase parameterization. J Rech Atmos 16:295–320

Dingman SL (1994) Physical hydrology. Macmillan Publishing, New York/Oxford/ Singapore/Sydney, 557pp

Fletcher NH (1962) The physics of rain clouds. Cambridge University Press, Cambridge

Hobbs PV (2000a) Introduction to atmospheric chemistry. Cambridge University Press, Cambridge, 262pp

Hobbs PV (2000b) Basic physical chemistry for atmospheric sciences. Cambridge University Press, Cambridge, 209pp

Houze RA (1993) Cloud dynamics. Academic, San Diego/New York/Berkley/Boston/London/Sydney/Tokyo/Toronto, 573pp
Keidel CC, Windolf R (1982) Wolkenbilder-Wettervorhersage. BLV Verlag, München, 119pp
Kertz W (1969) Einführung in die Geophysik. Band 1. Erdkörper. BI Wissenschaftsverlag, Mannheim/Leipzig/Wien/Zürich, 232pp
Kraus H (2000) Die Atmosphäre der Erde. Eine Einführung in die Meteorologie. Vieweg, Braunschweig/Wiesbaden, 470pp
Laube M, Höller H (1988) Cloud physics. In: Landolt-Börnstein, Gruppe V: Geophysik und Weltraumforschung 4b. Springer, Berlin/Heidelberg, pp 1–100
LeMone MA (1993) The stories clouds tell. American Meteorological Society, Boston, 32pp
Li D, Shine KP (1995) A 4-dimensional ozone climatology for UGAMP models. U.K. Universities – Global Atmospheric Modelling Programme internal report no. 35
Lin Y-L (2007) Mesoscale dynamics. Cambridge University Press, Cambridge, 630pp
Locatelli JD, Hobbs P (1974) Fall speeds and masses of solid precipitation particles. J Geophys Res 79:2185–2197
Marshall JS, Hitschfeld W, Gunn KLS (1958) Advances in radar weather. Adv Geophys 2:1–56
McKnight TL (1996) Physical geography, 5th edn. Prentice Hall, Upper Saddle River, 624pp
Meyers MP, DeMott PJ, Cotton WR (1992) New primary ice-nucleation parameterizations in an explicit cloud model. J Appl Meteorol 31:708–721
Mölders N (1999a) On the effects of different flooding stages of the Odra and different landuse types on the local distributions of evapotranspiration, cloudiness and rainfall in the Brandenburg-Polish border area. Contrib Atmos Phys 72:1–24
Mölders N (1999b) Einfache und akkumulierte Landnutzungsänderungen und ihre Auswirkungen auf Evapotranspiration, Wolken- und Niederschlagsbildung. Wiss. Mitt. Leipzig, 15, Habilitation thesis, 206pp
Mölders N (2011/2012) Land-use and land-cover changes – impact on climate and air quality. Atmospheric and oceanographic sciences library, vol 44. Springer, Dordrecht/Heidelberg/London/New York. doi:10.1007/978-94-007-1527-1 3
Mölders N, Kramm G (2007) Influence of wildfire induced land-cover changes on clouds and precipitation in Interior Alaska – a case study. Atmos Res 84:142–168
Mölders N, Olson MA (2004) Impact of urban effects on precipitation in high-latitudes. J Hydrometeorol 5:409–429
Mölders N, Hass H, Jakobs HJ, Laube M, Ebel A (1994) Some effects of different cloud parameterizations in a mesoscale model and a chemistry transport model. J Appl Meteorol 33:527–545
Mölders N, Laube M, Kramm G (1995) On the parameterization of ice microphysics in a mesoscale-α-weather forecast model. Atmos Res 38:207–235
Mölders N, Kramm G, Laube M, Raabe A (1997) On the influence of bulk parameterization schemes of cloud relevant microphysics on the predicted water cycle relevant quantities – a case study. Meteorol Z 6:21–32
Möller F (1973) Einführung in die Meteorologie – Physik der Atmosphäre – Band 1. BI Hochschultaschenbücher, Mannheim, 222pp
Mossop SC (1978) The influence of the drop size distribution on the production of secondary ice particles during graupel growth. Q J R Meteorol Soc 104:45–57
Peixto JP, Oort AH (1992) Physics of climate. Springer, New York, 520pp
Petty GW (2008) A first course in atmospheric thermodynamics. Sundog Publishing, Madison, 336pp
Pichler H (1984) Dynamik der Atmosphäre. BI Wissenschaftsverlag, Mannheim/Wien/Zürich, 456pp
Pielke RA (1984) Mesoscale meteorological modeling. Academic, London, 612pp
Prigogine I (1961) Introduction to thermodynamics of irreversible processes. Interscience Publishers, New York/London
Pruppacher HR, Klett JD (1978) Microphysics of clouds and precipitation. D. Reidel, Dordrecht/Boston/London, 714pp

Riegel CA (1999) In: Bridger AFC (ed) Fundamentals of atmospheric dynamics and thermodynamics. World Scientific, Singapore, 496pp
Sorbjan Z (1996) Hands-on meteorology: stories, theories, and simple experiments – project atmosphere. American Meteorological Society, Boston
Srivastava RC (1967) A study of effects of precipitation on cumulus dynamics. J Atmos Sci 24:36–45
Staley DO (1957) Some comments on physical processes at and near the tropopause. Meteorol Atmos Phys 10:1–19
Tsonis AA (2002) An introduction to atmospheric thermodynamics. Cambridge University Press, New York, 171pp
Twomey S, Wojciechowski TA (1969) Observations of the geographical variation of cloud nuclei. J Atmos Sci 26:648–651
Wallace JM, Hobbs PV (1977) Atmospheric science – an introductory survey. Academic, San Diego/New York/Boston/London/Sydney/Tokyo/Toronto, 467pp
Wallace JM, Hobbs PV (2006) Atmospheric Science – an introductory survey. Academic, San Diego/New York/Boston/London/Sydney/Tokyo/Toronto, 483pp
Wayne RP (1985) Chemistry of atmospheres – an introduction to the chemistry of the atmospheres of earth, the planets, and their satellites. Clarendon Press, Oxford, 361pp
Zikmunda J, Vali B (1972) Fall patterns and fall velocities of rimed ice crystals. J Atmos Sci 29:1334–1347

Chapter 4
Atmospheric Radiation

Abstract This chapter covers the nomenclature and basic quantities used in meteorology to describe the atmospheric radiation processes. The principle of black-body radiation, shortwave and long-wave radiation are applied to the atmosphere. The basics of the interaction radiation-atmosphere and the radiative transfer are presented. The radiative transfer equation including the solution for a plane-parallel non-scattering atmosphere are discussed. Finally the concepts are applied to the global radiation and surface energy budgets and discussed in view of climate. The chapter also covers remote sensing applications from satellites and the greenhouse effect.

Keywords Wavelength and frequency domain • Black and graybody radiation • Short- and long-wave radiation • Radiative transfer • Global radiation budget • Interaction radiation-atmosphere-surface • Application in remote sensing • Atmospheric greenhouse effect

Virtually all the energy available on Earth originates from the Sun. Upward conduction of heat from the interior of the Earth (due to radiation decay) is negligible. About one two-billionth of the energy emitted by the Sun is transferred to the Earth as electromagnetic radiation. Clouds, atmospheric gases and aerosols absorb and scatter parts of incoming radiation. The reminder reaches the surface where a small part is reflected and a large part is absorbed by the ocean, biosphere, lithosphere, and cryosphere. According to the first law of thermodynamics, the absorbed heat can be transferred to internal energy to do work against the environment (e.g. atmospheric energetic, evaporation of water, growth of plants). Radiative fluxes and radiation balance generate all weather processes in the atmosphere. According to the second law of thermodynamics the Earth cannot warm by cooling the space (Chap. 2).

To maintain the long-term quasi-equilibrium state of the Earth-atmosphere system, the absorbed energy must be balanced by an equal amount of radiant

N. Mölders and G. Kramm, *Lectures in Meteorology*, Springer Atmospheric Sciences,
DOI 10.1007/978-3-319-02144-7_4,

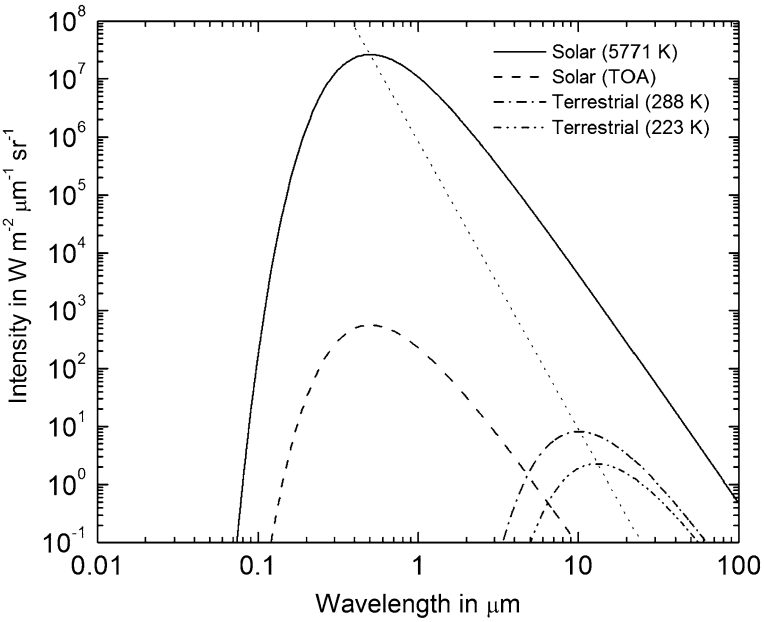

Fig. 4.1 Planck functions of solar (5771 K) and terrestrial radiation (288 and 223 K). The *dotted curve* illustrates the intensity at the top of the atmosphere (TOA) inferred from the former for the mean distance between the Sun and the Earth. The *dotted line* represents Wien's displacement relationship $\lambda_{max} T = const$

energy (emitted by the surface and atmosphere) going into the outer space. Thus, all exchange of energy between the Earth and space is through radiation.

According to Prevost, all bodies having temperatures greater than 0 K emit radiant energy over a wide range of wavelengths. Due to the great difference in solar and terrestrial temperatures incoming **solar radiation** emits at maximum in the **visible** ($\approx$0.5 μm), while outgoing **terrestrial radiation** emits at maximum in the **infrared** (IR) ($\approx$10 μm) range when considered in the wavelength domain (Fig. 4.1). The solar energy of interest for atmospheric energetics is ranging between 0.1 μm in the **ultra violet** (UV) to 4 μm at the end of the **near infrared**. In our climate system, the range from UV to near IR is the most significant portion of the spectrum. The outgoing terrestrial radiation ranges mainly from 4 to 50 μm called the thermal IR range, i.e. terrestrial radiation is also called the **thermal radiation**. For the reasons outlined above we break the radiant energy into the **shortwave** (solar) radiation with wavelength $\lambda < 4\,\mu m$ and **long-wave** (terrestrial) radiation with wavelength $\lambda \geq 4\,\mu m$ (Fig. 4.1).

Solar radiation can be dealt with as parallel unidirectional radiation because the Sun is a very distant point-like source (Fig. 4.2). Emission from such sources is often denoted **parallel-beam-radiation**. On the contrary, terrestrial radiation comes from all directions because each molecule is involved in diffuse **thermal radiation**.

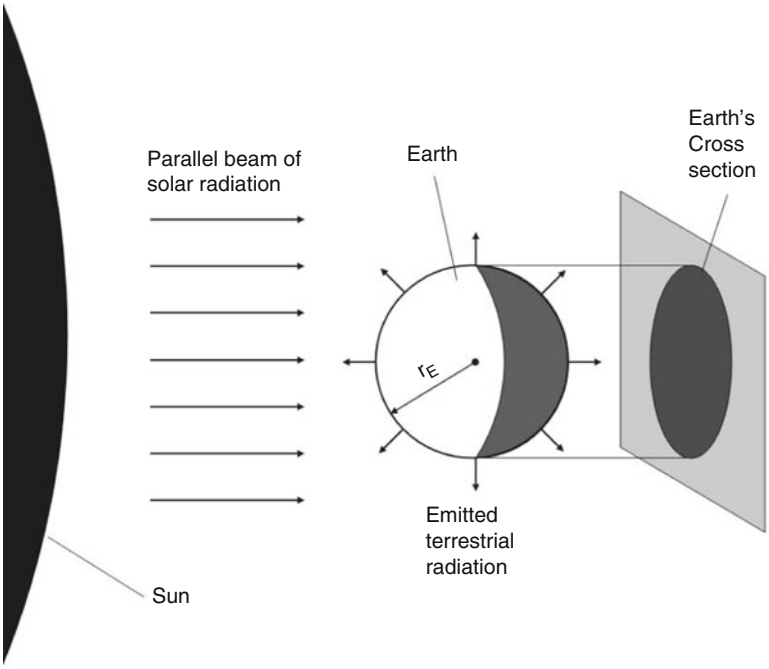

Fig. 4.2 Schematic view of solar (*left*) and terrestrial radiation (*right*)

Emission and absorption play an equal role for terrestrial radiation, while absorption is dominant in solar radiation. Note that the physical and mathematical treatment of solar and terrestrial radiation also differs.

Dealing with radiation requires geometrical and mathematical details. We tried to keep them at a minimum to not distract the attention from the basic physics of radiation needed in meteorology. The focus is on understanding and application, and the introduced formulas are restricted to the basics.

4.1 Nomenclature and Basic Quantities

As pointed out in Chap. 2, energy can be transferred by **conduction**, **convection**, and **radiation**. Conduction is the movement of heat through a substance without movement of its molecules into the direction of the heat transfer.[1] Conduction is most effective in solid materials, but also in a very thin layer of air near the surface of the Earth.

[1]Think of a fork put at one end in a grill fire. It will get hot on the other one.

Table 4.1 Wavelengths, approximate frequencies, and waves within the solar electromagnetic spectrum

Region	Spectral range (μm)	Frequency range (Hz)
Gamma rays	$<3{\cdot}10^{-4}$	$>10^{18}$
X rays	$10^{-4} - 10^{-2}$	$3 \cdot 10^{18} - 3 \cdot 10^{16}$
Ultraviolet (UV)		$3 \cdot 10^{16} - 7.9 \cdot 10^{14}$
Far UV	0.01–0.20	
UV-C	0.20–0.28	
UV-B	0.28–0.32	
UV-A	0.32–0.38	
Visible		$7.9 \cdot 10^{14} - 4 \cdot 10^{14}$
Violet	0.38–0.45	
Blue	0.45–0.495	
Green	0.495–0.57	
Yellow	0.57–0.59	
Orange	0.59–0.62	
Red	0.62–0.75	
Infrared (IR)		$4 \cdot 10^{14} - 3 \cdot 10^{11}$
Near IR	0.75–4	
Thermal IR	4–50	
Far IR	$50 - 10^3$	
Micro and radio waves	$>10^3$	$<3{\cdot}10^{11}$

Convection transfers heat by mixing of a fluid or gas. It is associated with displacement of the medium (e.g. a raising air pacel[2]). In the atmosphere, convection results from the heating of the Earth's surface (Chap. 2) and a very thin layer of air (about 1 mm) in contact to the surface during daytime. Above this thin layer, air heated from below expands and rises upwards due to the inherent buoyancy of warm air. Unlike boiling water in a pot, the atmosphere experiences convection even without buoyancy by forced convection (Chap. 3). This vertical mixing can happen by wind shear (Chap. 6).

Radiation is the only energy transfer mechanism that can propagate in vacuum, i.e. a transfer medium is not required. All forms of electromagnetic radiation travel through space nearly at the **speed of light in vacuum**. At that speed, energy emitted by the Sun reaches the Earth after 8 min. The spectrum of the electromagnetic energy comprises all wavelengths. For the sake of simplicity, we classify them into individual bands (Table 4.1).

Electromagnetic radiation consists of alternating electric and magnetic fields where the electric field vector is perpendicular to the magnetic field vector and the direction of propagation is perpendicular to both (Fig. 4.3).

[2]For example boiling water in a pot.

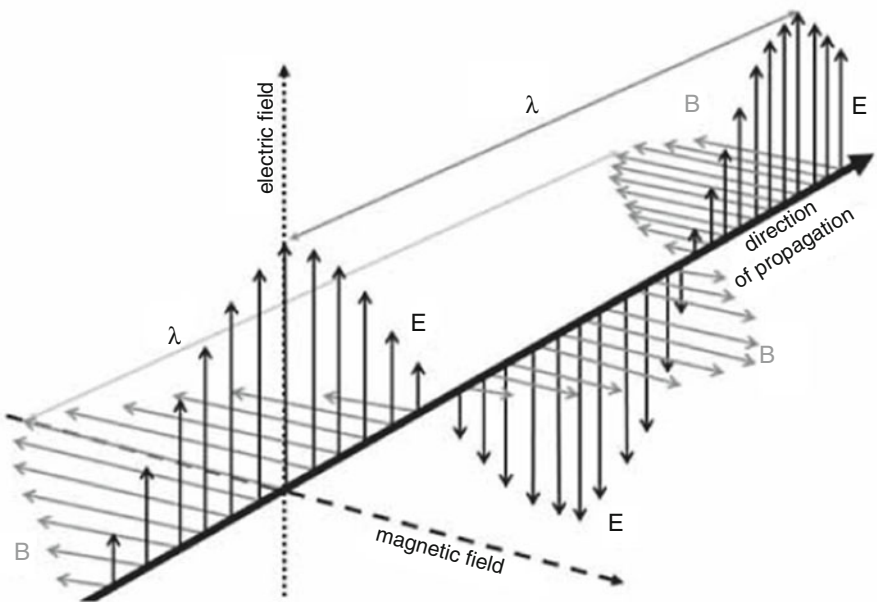

Fig. 4.3 Schematic view of electromagnetic waves

Radiation is specified by its **frequency**, ν, which is the rate of the oscillations of the magnetic or electric field when observed at a point. The unit of frequency is called **Hertz**, (Hz). Note that a subscript ν characterizes a quantity considered in the frequency domain. Alternatively, radiation is described by the **wavelength**, λ, that gives the distance between crests of the magnetic and electric field (Fig. 4.3). Any quantity considered in the wavelength domain is characterized by the subscript λ. Frequency and wavelength are related to each other by

$$\nu = \frac{c}{\lambda} \tag{4.1}$$

where $c = 2.9979 \cdot 10^8\,\mathrm{m\,s^{-1}}$ is the speed of light in vacuum. In the atmosphere, light travels slightly slower than in vacuum because of the interaction with matter. In spectroscopy, also the reciprocal of the wavelength, the **wave number**, κ, is applied to characterize radiation. This wave number, however, differs from that customarily used in physics by the factor of 2π. The direction of propagation is perpendicular to the vector of the electric and magnetic field (Fig. 4.3).

The index of **refraction**, n, of a substance is the ratio of the speed of light in vacuum to the speed of the light traveling through a substance. At sea level, the index of refraction of air is about 1.0003. Vertical gradients of atmospheric density and humidity cause strong vertical gradients of n and can cause bending of electromagnetic rays and slight mislocation of satellite scan spots.

Table 4.2 Radiation symbols and units

Quantity	Commonly used symbol	SI unit
Frequency	ν	Hz
Wavelength	λ	m
Wavenumber	κ	m^{-1}
Radiant energy	Q	J
Radiant flux	Φ	W
Radiant flux density	M, E, F	$\mathrm{W\,m}^{-2}$
Radiant exitance	M	$\mathrm{W\,m}^{-2}$
Radiative flux	R	$\mathrm{W\,m}^{-2}$
Irradiance	E, F, R	$\mathrm{W\,m}^{-2}$
Radiance	I, L	$\mathrm{W\,m}^{-2}\,\mathrm{sr}^{-1}$
Emittance	ϵ	−.−
Absorptance	a, α	−.−
Refectance	ρ	−.−
Transmittance	T	−.−
Albedo	α	−.−
Absorption coefficient	σ_a	m^{-1}
Scattering coefficient	σ_s	m^{-1}
Extinction coefficient	σ_e	m^{-1}
Vertical optical depth	δ	−.−
Scattering angle	ψ_s	rad

A fundamental characteristic of electromagnetic radiation is that it can transport energy for which many quantities are based on energy (Table 4.2). The unit of **radiant energy** is Joule (J). The **radiant flux** often denoted as **power** is the radiant energy per unit time. It refers to the rate at which energy is released, transferred or received, and is given in Watts (W) or Joules per second ($\mathrm{J\,s}^{-1}$).

The radiant flux passing through an unit area is called the **radiant flux density** ($\mathrm{W\,m}^{-2}$). Note that especially in micrometeorology, hydrometeorology, agricultural and forest meteorology it has become the customs to speak (incorrectly) just of fluxes.

Irradiance is the radiant flux density incident on an area. **Radiant exitance** is the radiant flux density emerging from an area.

Quantum theory predicts that energy transmitted by electromagnetic radiation occurs in discrete units denoted **photons**. Each photon has the energy $W = h\nu$ where ν is the frequency of radiation (number of waves passing a point per unit time) and $h = 6.6261 \cdot 10^{-34}\,\mathrm{J\,s}$ is the **Planck**[3] **constant**. According to quantum mechanics, an isolated molecule can emit and absorb energy in discrete amounts that are allowed by changes in its energy level. Thus, molecules only

[3]Max Karl Ernst Planck, German physicist, 1858–1947.

Table 4.3 Absorption bands of some atmospheric gases

Gas	Wavelength (μm)
H_2O	0.72, 0.81, 0.93, 1.13, 1.37, 1.85, 2.66, 3.2, 6.3, >13
CO_2	1.46, 1.60, 2.04, 2.75, 4.27, 4.80, 5.20, 9.3, 13.3, >15
O_3	0.242–0.31 (Hartley bands), 0.31–0.40 (Huggins bands) 0.69–0.76 (Chappuis bands)
O_2	0.10–0.175 (Schumann-Runge continuum), 0.175–0.20 (Schumann-Runge bands), 0.20–0.242 (Herzberg continuum)

interact with radiation of certain discrete wavelength (Table 4.3). Therefore, the absorption and emission properties of an isolated molecule can be described by a line spectrum,[4] which is separated by gases where absorption and emission of radiation is impossible. Usually vibrational changes occur for wavelengths in the IR. Rotational transitions need the lowest amount of energy and are usually associated with microwave radiation. Some molecules (e.g. CO_2, H_2O, O_3) have structures that allow absorption and emission of a photon when they simultaneously undergo rotation-vibration transitions. These molecules have closely spaced absorption lines in the IR called the **line clusters**. Other molecules (e.g. O_2, N_2) cannot interact with radiation this way for which they do not have many absorption lines in the IR. In addition, a molecule may absorb radiation that is sufficient to break it down in its atomic components (**photo-dissociation**) or to ionize it (**photo-ionization**). An example for photo-dissociation is

$$O_2 + h\nu \longrightarrow O + O \text{ with } \lambda < 0.242\,\mu\text{m}$$

where $h\nu$ is the energy of the photon and λ the wavelength of radiation. Further examples are discussed in Chap. 5.

Photo-dissociation may involve a continuum of wavelength if the wavelength is short enough that a photon will increase the chemical energy of the molecule to allow photo-dissociation. Any excess energy goes into the kinetic energy of the atmosphere thereby raising the temperature of the gas. Most photo-dissociation occurs in the UV and visible range (Chap. 5). Photo-ionization requires sufficiently short wavelengths that provide energy to strip one or more of the outer electrons from the orbits around the atomic nucleus. It typically occurs at wavelengths smaller than 0.1 μm and can involve a continuum of wavelengths. To describe electromagnetic radiation completely we need information on the amount of energy transferred (quantity) and the type of energy (quality). Quantity is associated with

[4] $NaCl$, for instance, when put into a flame emits yellow light.

the height of the wave or its amplitude (Fig. 4.3). If everything is equal, the amount of energy carried will be directly proportional to the amplitude of the wave.[5] The quality is related to the distance between two wave crests.

4.1.1 Solid Angle

It is convenient to express the direction of radiation by the **solid angle**, Ω, defined by

$$\Omega = \frac{\sigma}{r^2} \tag{4.2}$$

where σ is the area, and r is the distance (radius). The solid angle is expressed in terms of steradian (sr). In the case of a sphere whose surface is $\sigma = 4\pi r^2$, the solid angle reads

$$\Omega = \frac{\sigma}{r^2} = 4\pi \text{ sr}. \tag{4.3}$$

As illustrated in Fig. 4.4, the differential area on the surface of a hemisphere can be related to the **azimuthal angle**, ϕ, and the **zenith angle** (or zenith distance), θ, i.e.

$$d\Omega = \frac{d\sigma}{r^2} = \frac{r\ d\theta\ r\sin\theta\ d\phi}{r^2} = \sin\theta\ d\theta\ d\phi = -d\mu\ d\phi \tag{4.4}$$

where $\mu = \cos\theta$.

The radiant flux density per solid angle is called the **radiance**. It represents the radiation incident on or leaving an area perpendicular to the beam. Other directions can be addressed by the angle θ which the direction considered makes with the outward normal to $d\sigma$ so that $\cos\theta\ d\sigma$ is the effective area at which the energy is being intercepted (Fig. 4.5).

4.1.2 Monochromatic and Integrated Intensities

The analysis of a radiation field often requires us to consider the differential amount of radiant energy, dE_ν, in a specific frequency interval, $(\nu, \nu + d\nu)$, which is transported across an area element, $d\sigma$, in directions confined to a differential

[5] X-rays, for example, have an extremely short wavelengths (Table 4.1) and can be used to detect broken bones as the waves can travel through tissue. Compared to X-rays, ordinary light has longer wavelengths and is absorbed by the skin.

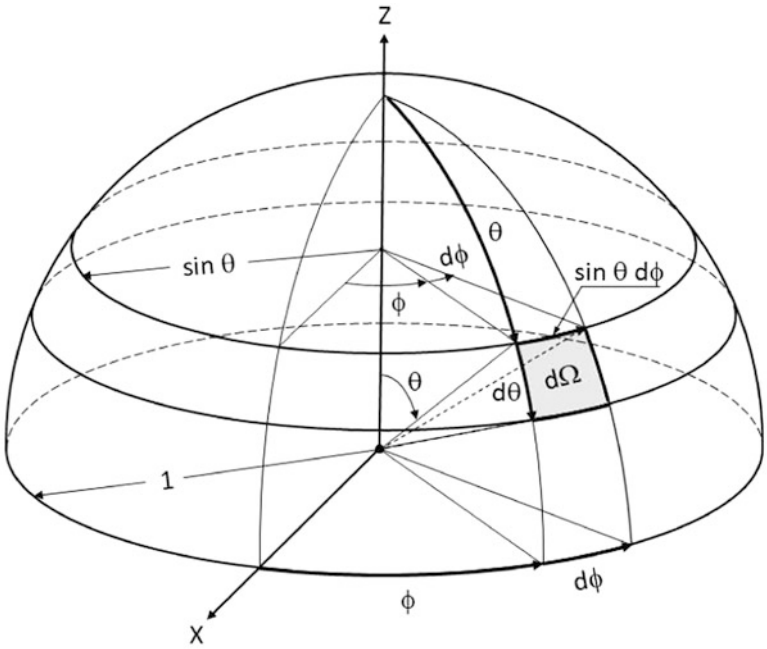

Fig. 4.4 Mathematical representation of solid angle

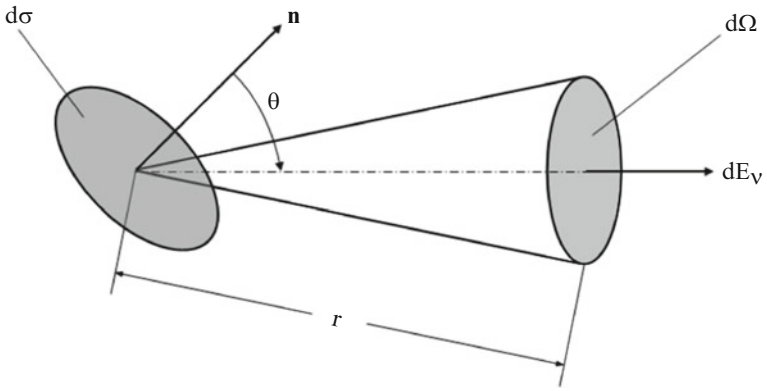

Fig. 4.5 Radiant energy, dE_ν, which is transported across an area element, $d\sigma$, in the direction confined to an element of the *solid angle*, $d\Omega$, where r is the distance (radius), and θ is the angle which the direction makes with the outward normal, **n**, to $d\sigma$

solid angle, $d\Omega$ (Fig. 4.5), during the time interval, $(t, t + dt)$. This energy is expressed by

$$d E_\nu = I_\nu \cos\theta \, d\sigma \, d\nu \, d\Omega \, dt \tag{4.5}$$

where I_ν is the **specific intensity** also called the **monochromatic intensity** or the spectral radiance. This equation can be used to define I_ν by

$$I_\nu = \frac{d\,E_\nu}{\cos\theta\; d\sigma\; d\nu\; d\Omega\; dt.} \tag{4.6}$$

It is expressed in units of $\mathrm{J\,m^{-2}\,sr^{-1}}$ or $\mathrm{W\,s\,m^{-2}\,sr^{-1}}$. Commonly, the intensity is said to be confined in a pencil of radiation.

Integrating I_ν over the entire spectrum provides the **integrated intensity** also called the radiance, i.e.

$$I = \int_0^\infty I_\nu\; d\nu. \tag{4.7}$$

The integrated intensity is expressed in units of $\mathrm{J\,m^{-2}\,s^{-1}\,sr^{-1}}$ or $\mathrm{W\,m^{-2}\,sr^{-1}}$. To use the frequency instead of the wavelength has the advantage that the frequency does not change if radiation is propagating through matter.

4.1.3 Monochromatic and Integrated Flux Densities

The **monochromatic flux density** of radiant energy is defined by

$$F_\nu = \int_\Omega I_\nu\;\cos\theta\; d\Omega \tag{4.8}$$

where Ω is the entire hemispheric solid angle. As the differential solid angle is given by $d\Omega = \sin\theta\; d\theta\; d\phi$, and the integration over the entire hemispheric solid angle is related to the integration over the zenith angle, $0 \leq \theta \leq \pi/2$, and the azimuthal angle, $0 \leq \phi \leq 2\,\pi$ (Fig. 4.4), we obtain

$$F_\nu = \int_0^{2\,\pi}\int_0^{\pi/2} I_\nu\,(\theta,\;\phi)\;\cos\theta\;\sin\theta\; d\theta\; d\phi \tag{4.9}$$

or

$$F_\nu = \int_0^{2\,\pi} d\phi \int_0^{\pi/2} I_\nu\,(\theta,\;\phi)\;\cos\theta\;\sin\theta\; d\theta. \tag{4.10}$$

It is expressed in units of $\mathrm{J\,m^{-2}}$ or $\mathrm{W\,s\,m^{-2}}$. The monochromatic flux density of radiant energy is also called the **monochromatic irradiance** or, when it is emitted, the **monochromatic exitance**. Since the radiation field is a vector field, this integration corresponds to an integration over a vector field.

In the case of isotropic radiance, i.e. I_ν is independent of θ and ϕ, we have

$$F_\nu = I_\nu \int_0^{2\,\pi} d\phi \int_0^{\pi/2} \cos\theta \ \sin\theta \ d\theta. \tag{4.11}$$

As $1/2 \ \sin(2\,\theta) = \sin\theta \ \cos \ \theta$, Eq. (4.11) may also be written as

$$F_\nu = \frac{I_\nu}{2} \int_0^{2\,\pi} d\phi \int_0^{\pi/2} \sin(2\,\theta) \ d\theta. \tag{4.12}$$

Defining $x = 2\,\theta$ yields

$$F_\nu = \frac{I_\nu}{4} \int_0^{2\,\pi} d\phi \int_0^{\pi} \sin(x) \ dx = \frac{I_\nu}{2} \int_0^{2\,\pi} d\phi = \pi \ I_\nu. \tag{4.13}$$

Blackbody radiance is considered as an example of isotropic radiance.

Integrating F_ν over all frequencies provides the **integrated flux density** of radiant energy, i.e.

$$F = \int_0^{\infty} F_\nu \ d\nu. \tag{4.14}$$

It is also called the irradiance and is expressed in units of $\mathrm{J\,m^{-2}\,s^{-1}}$ or $\mathrm{W\,m^{-2}}$. The **total flux** is given by

$$\Phi = \int_\sigma F \ d\sigma. \tag{4.15}$$

It is also called the **radiant power**, and is expressed in units of $\mathrm{J\,s^{-1}}$ or W.

4.1.4 Relationship Between the Wavelength Domain and the Frequency Domain

The differential amount of the flux density can be expressed either by

$$dF = F_\lambda \, d\lambda \quad \Rightarrow \quad F_\lambda = \frac{dF}{d\lambda} \tag{4.16}$$

or by

$$dF = F_\nu \, d\nu \quad \Rightarrow \quad F_\nu = \frac{dF}{d\nu} \tag{4.17}$$

where, again, ν is the frequency. By considering the chain rule of differentiation, we may write

$$\frac{dF}{d\lambda} = \frac{dF}{d\nu} \, \frac{d\nu}{d\lambda} \tag{4.18}$$

or with respect to Eqs. (4.16) and (4.17)

$$F_\lambda = F_\nu \, \frac{d\nu}{d\lambda}. \tag{4.19}$$

Since wavelength and frequency are related to each other by Eq. (4.1), we obtain

$$\frac{d\nu}{d\lambda} = -\frac{c}{\lambda^2}. \tag{4.20}$$

Introducing this expression into Eq. (4.19) yields

$$F_\lambda = -\frac{c}{\lambda^2} \, F_\nu \tag{4.21}$$

In a similar way, we obtain for the monochromatic intensities

$$I_\lambda = -\frac{c}{\lambda^2} \, I_\nu \, . \tag{4.22}$$

4.1.5 Solar Constant and Insolation

The solar irradiance reaching the TOA is given by (Fig. 4.6)

$$F = \left(\frac{r_S}{d}\right)^2 \, F_S \tag{4.23}$$

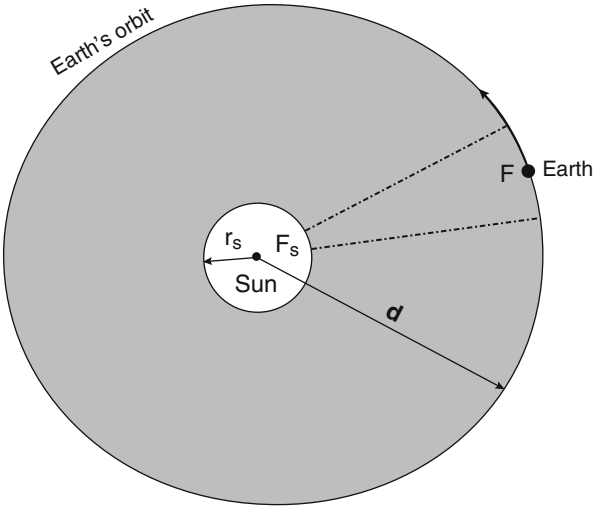

Fig. 4.6 Sketch for deriving Eq. (4.23). The symbols are explained in the text

where $r_S = 6.96 \cdot 10^8$ m is the visible radius of the Sun, d is the actual distance between the Sun's center and the orbit of the Earth[6] ranging from $d = 1.471 \cdot 10^{11}$ m at the **Perihelion** (around January 4) to $d = 1.521 \cdot 10^{11}$ m at the **Aphelion** (around July 5; Fig. 4.7), and $F_S = 6.288 \cdot 10^7\,\mathrm{W\,m^{-2}}$ denotes the solar exitance. Formula (4.23) is called the **inverse square law**. The inverse square law is based on the fact that the radiant power ($= 4\pi {r_S}^2 F_S$) of the Sun is kept constant when the solar radiation is propagating through the space because of energy conservation principles in the absence of an intervening medium. It describes the influence of the distance being traveled on the intensity of emitted radiation from a radiation source like the Sun. For the mean distance of $d_0 = 1.496 \cdot 10^{11}$ m (Fig. 4.7) that is close to the so-called **Astronomic Unit** (= AU) F becomes the solar constant. Thus, we may write

$$F = \left(\frac{d_0}{d}\right)^2 S \tag{4.24}$$

where $(d_0/d)^2$ is the **orbital effect**. Since $(d_0/d)^2$ does not vary more than 3.5 % (Fig. 4.7), this orbital effect is often ignored.

To determine the actual distance we may consider Keplerian elements, i.e.,

$$d = \frac{p}{1 + e\,\cos\,\upsilon} \tag{4.25}$$

[6]Correctly spoken, the orbit of the barycenter of the Earth-Moon system.

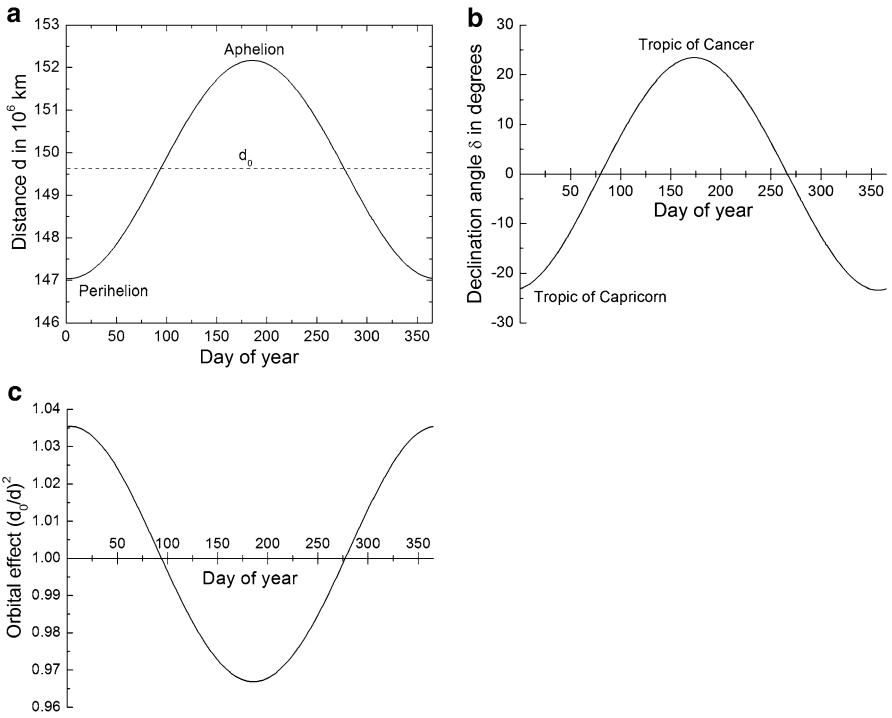

Fig. 4.7 Variation of (**a**) distance, (**b**) declination, and (**c**) orbital effect in dependence of the day of year

where $p = a\ \left(1 - e^2\right)$ is the parameter of the elliptic orbit (i.e. the radius for $\upsilon\ = \pi/2$), $a\ = 1.49598{\cdot}10^{11}$ m is the semi-major axis (still called the Astronomical Unit, AU, even though its definition has changed in 1976 by relating it to the Gaussian gravitational constant), $e\ = 0.0167$ is the eccentricity, and υ is the true anomaly, i.e., the positional angle of the Earth on its orbit counted counterclockwise from the Perihelion (Fig. 4.8). For determining the true anomaly and, hence, the actual distance of the Earth the transcendental equation for the eccentric anomaly called the Kepler equation,

$$f\ (E) = E - e\ \sin\ E - M = 0 \tag{4.26}$$

has to be solved iteratively, for instance, by a Newton-Raphson method

$$E^{(n+1)} = E^{(n)} - \frac{f\left(E^{(n)}\right)}{f'\left(E^{(n)}\right)}\ , \quad n = 0,\ 1,\ 2,\ \ldots \tag{4.27}$$

where $f'\left(E^{(n)}\right) = 1 - e\ \cos\ E^{(n)}$, $M\ = 2\ \pi\ \ (t - T)\,/U\ = L - \varpi$ is the mean anomaly, $U\ = 2.978 \cdot 10^4\,\mathrm{m\,s^{-1}}$ is the mean orbital speed of the Earth, $t - T$ is

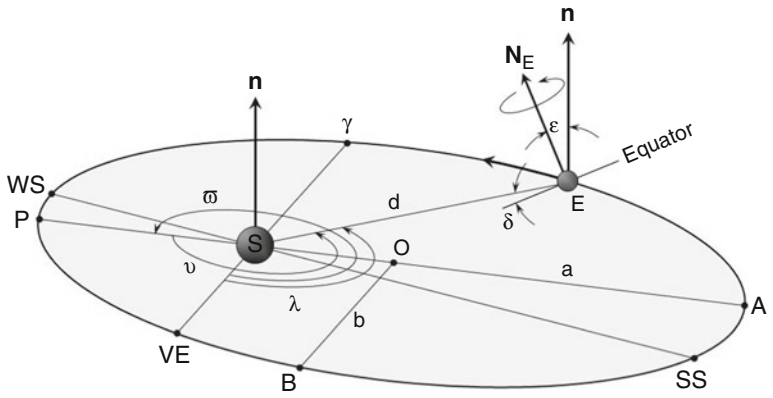

Fig. 4.8 Elements of the Earth-Sun geometry: S denotes the position of the Sun, E the position of the Earth (strictly spoken of the Earth-Moon barycenter), P the Perihelion, A the Aphelion, WS the Winter Solstice, SS the Summer Solstice, VE the Vernal Equinox, γ the vernal point, O the center of the ellipse, $\overline{OA}$ (or $\overline{OP} = a$) the semimajor axis, $\overline{OB} = b$ the semiminor axis, and $\overline{SE} = d$ the actual distance between the Sun's center and the Earth's orbit. Furthermore, **n** is normal (perpendicular) to the ecliptic plane, $\mathbf{N}_E$ is parallel to the Earth's axis, δ is the declination of the Sun, and ε is the oblique angle. Moreover, ϖ denotes the longitude of the Perihelion relative to the Vernal Equinox, υ the true anomaly of the Earth at a given time, and λ the true longitude of the Earth

the time since Perihelion, L is the mean longitude, and ϖ is the longitude of the Perihelion counted counterclockwise from the moving vernal equinox (Fig. 4.8). Values of the Keplerian elements and their rates, with respect to the mean ecliptic and equinox of J2000, valid for the time-interval 1800 AD–2050 Values for AD can be found online or in Standish and Williams (1992; their Table 8.10.2). The procedure may be stopped if after k iteration steps the condition $\left|E^{(k)} - E^{(k-1)}\right| < 10^{-6}$ deg is fulfilled. Our calculated values for distance, declination, and orbital effect in dependence of the day of year are illustrated in Fig. 4.7.

Frequently, a value for the solar constant close to 1,367 W m^{-2} is recommended, but the value obtained from recent satellite observations using SORCE/TIM (Total Irradiance Monitoring; launched in 2003) is close to 1,361 W m^{-2} (Fig. 4.9). The basis for this modified value is a more reliable, improved absolute calibration.

Example. Determine the solar constant for Mars assuming a mean distance Mars-sun of $2.279 \cdot 10^{11}$ m (Williams 2007).

Solution. Inserting the mean distance of Mars into Eq. (4.23) yields $(\frac{6.96 \cdot 10^8 \text{ m}}{2.279 \cdot 10^{11} \text{ m}})^2 \, 6.29 \cdot 10^7 \text{ W m}^{-2} = 586.7 \text{ W m}^{-2}$ for the solar constant of Mars.

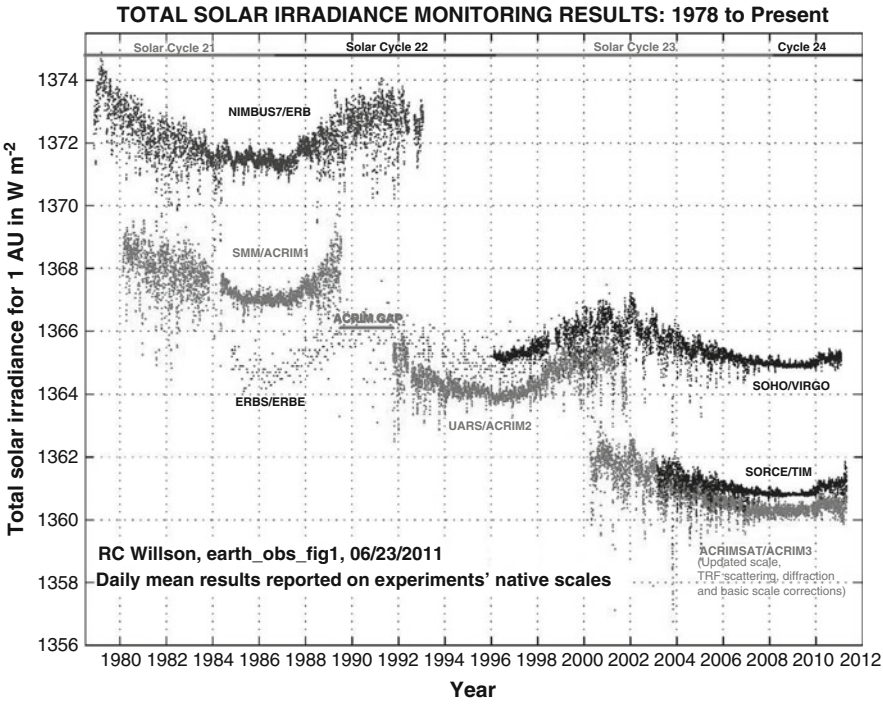

Fig. 4.9 Satellite observations of total solar irradiance. The plot comprises of the observations of seven independent experiments: (a) Nimbus 7/Earth Radiation Budget Experiment (ERBE; 1978–1993), (b) Solar Maximum Mission/Active Cavity Radiometer Irradiance Monitor 1 (1980–1989), (c) Earth Radiation Budget Satellite/Earth Radiation Budget Experiment (1984–1999), (d) Upper Atmosphere Research Satellite/Active cavity Radiometer Irradiance Monitor 2 (1991–2001), (e) Solar and Heliospheric Observer/Variability of solar Irradiance and Gravity Oscillations (launched in 1996), (f) ACRIM Satellite/Active cavity Radiometer Irradiance Monitor 3 (launched in 2000), and (g) Solar Radiation and Climate Experiment/Total Irradiance Monitor (launched in 2003)

Figure 4.8 illustrates the Sun-Earth geometry. The oblique angle of the Earth's axis of $\varepsilon = 23.45°$ is the reason for the seasons, but not the varying distance d between the Sun's center and the Earth-Moon barycenter during the Earth's revolution around the Sun. This revolution is responsible for the variation of the solar irradiance at the TOA from $F = 1{,}407\,\mathrm{W\,m^{-2}}$ at Perihelion to $F = 1{,}316\,\mathrm{W\,m^{-2}}$ at Aphelion. This means that during the various seasons caused by the oblique angle of the Earth's axis the Earth's revolution is responsible for the changes of the solar irradiance at the TOA, and for the different heating of the Earth's surface on its bright side.

The local zenith angle of the Sun's center can be determined using the rules of spherical trigonometry. Thus, we obtain

$$\cos\Theta_0 = \sin\varphi\sin\delta + \cos\varphi\cos\delta\cos\ h \tag{4.28}$$

where φ is the latitude, δ is the solar declination angle, and h is the hour angle from the local meridian. The solar declination angle can be determined using $\sin\delta = \sin\varepsilon \ \sin\lambda$, where λ is the true longitude of the Earth counted counterclockwise from the Vernal Equinox (Fig. 4.8). The latitude is related to the zenith angle by $\varphi = \pi/2 - \theta$ so that formula (4.28) may be written as $\cos\Theta_0 = \cos\theta \sin\delta + \sin\theta \cos\delta \cos h$. Note that θ is ranging from zero to π, δ from 23.45°S (Tropic of Capricorn) to 23.45°N (Tropic of Cancer), and h from $-H$ to H, where H represents the half-day, i.e. from sunrise to solar noon or solar noon to sunset. It can be deduced from Eq. (4.28) by setting $\Theta_0 = \pi/2$ (invalid at the poles) leading to $\cos H = -\tan\varphi \tan\delta$.

Based on this information we can calculate the solar insolation that is defined as the flux of solar radiation per unit of horizontal area for a given location. The daily solar insolation is given by

$$f_{S\downarrow} = \int_{t_r}^{t_s} F \cos\Theta_0 \, dt = \int_{t_r}^{t_s} \left(\frac{d_0}{d}\right)^2 S \cos\Theta_0 \, dt. \tag{4.29}$$

Here, t is time, where t_r and t_s correspond to sunrise and sunset, respectively. The variation of the actual distance, d, between the Sun and the Earth in 1 day can be neglected. Thus,

$$\begin{aligned} f_{S\downarrow} &= \left(\frac{d_0}{d}\right)^2 S \int_{t_r}^{t_s} \cos\Theta_0 \, dt \\ &= \left(\frac{d_0}{d}\right)^2 S \int_{t_r}^{t_s} (\cos\theta \sin\delta + \sin\theta \cos\delta \cos h) \, dt. \end{aligned} \tag{4.30}$$

Defining the angular velocity of the Earth by $\omega = dh/dt = 2\pi$ rad/day (to avoid any confusion with the solid angle, Ω, in this chapter) leads to

$$f_{S\downarrow} = \left(\frac{d_0}{d}\right)^2 \frac{S}{\omega} \int_{-H}^{H} (\cos\theta \sin\delta + \sin\theta \cos\delta \cos h) \, dh \tag{4.31}$$

and, finally, to

$$f_{S\downarrow} = \left(\frac{d_0}{d}\right)^2 \frac{S}{\pi} (H \cos\theta \sin\delta + \sin\theta \cos\delta \sin H). \tag{4.32}$$

According to Eq. (4.32), the daily solar insolation is a function of latitude and time of the year (Fig. 4.10). We may deduce from this figure for the current values of $(d_0/d)^2$ and δ that (a) the time-latitude maximum of insolation occurs at the

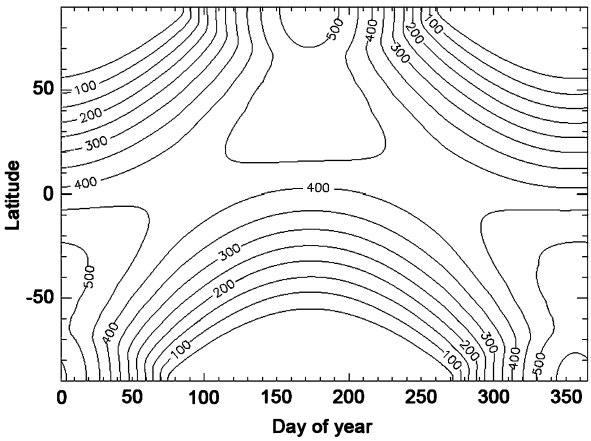

Fig. 4.10 Daily mean solar insolation at the top of the atmosphere as a function of latitude and day of year

summer solstice at the pole because of the long solar day of 24 h, where a secondary maximum on this date occurs near the latitude of 35° in the summer hemisphere, and (b) for each latitude, the southern hemisphere summer (winter) insolation is greater (less) than that of the corresponding northern hemisphere latitude in its summer (winter). Its distribution depends on the latitude, but is independent of longitude. As illustrated in that figure, there is a slight asymmetry between the northern and the southern hemisphere. This is due to the variation in the Sun-Earth distance when the Earth revolves around the Sun. However, when Eq. (4.29) is integrated over all days of a year, the annual insolations are equal at corresponding latitudes of each hemisphere.

The values of $(a/d)^2$ and δ depend on the eccentricity, e, the oblique angle, ϵ, and the longitude of the Perihelion relative to the vernal equinox, ω (Fig. 4.8). Thus, on long-term scales we have to pay attention to the Milankovitch cycles (Chap. 7) that are related to the change of the eccentricity (400 and 100 kyr) and the oblique angle (axial tilting: 41 kyr) and the axial precession (23 kyr) due to the perturbations that other principal planets of our solar system exert on the Earth's orbit.

4.2 Blackbody Radiation

4.2.1 Planck's Law

In 1860, Kirchhoff[7] proposed his famous theorem that for any body at a given temperature the ratio of emittance, E_ν, i.e. the intensity of the emitted radiation

[7]Gustav Robert Kirchoff, German physicist, 1824–1887.

at a given frequency ν, and absorptance, a_ν, of the radiation of the same frequency is the same generally expressed by

$$\frac{E_\nu}{a_\nu} = J(\nu, T). \tag{4.33}$$

Kirchhoff called a body perfectly black when $a_\nu = 1$ ($r_\nu = 0$) so that $J(\nu, T)$ is the emissive power of such a blackbody. Obviously, E_ν has the same physical units like $J(\nu, T)$, i.e. the units of an intensity. An example of a perfect blackbody is the **Hohlraumstrahlung** that describes the radiation in a cavity bounded by any emitting and absorbing substances of uniform temperature which are opaque. The state of the thermal radiation, which takes place in this cavity is entirely independent of the nature and properties of these substances and only depends on the absolute temperature, T, and the frequency (or the wavelength λ or the angular frequency $\omega = 2\ \pi\ \nu$). For this special case the radiation is homogeneous, isotropic and unpolarized

$$J(\nu, T) = \frac{c}{8\ \pi}\ U(\nu, T). \tag{4.34}$$

Here, $U(\nu, T)$ is called the monochromatic (or spectral) energy density of the radiation in the cavity. As already pointed out by Wien[8] during his Nobel Lecture given in 1911, Kirchhoff's theorem has become one of the most general of radiation theory and expresses the existence of thermal equilibrium for radiation. Expressions for the monochromatic energy density called the blackbody radiation laws[9] were derived by (a) Rayleigh[10] in 1900 and 1905 and corrected by Jeans in 1905, the so-called Rayleigh-Jeans law, (b) Wien and Paschen[11] in 1896, (c) Thiesen in 1900, (d) Rayleigh in 1900, and (e) Planck in 1900.

Planck's function for the spectral energy density is, by far, the most important one. It reads

$$U(\nu, T) = \frac{8\ \pi\ h}{c^3} \frac{\nu^3}{\exp(\frac{h\ \nu}{k\ T}) - 1} \tag{4.35}$$

where T is the absolute temperature, and $k = 1.3806 \cdot 10^{-23}\,\mathrm{J\,K^{-1}}$ is the **Boltzmann**[12] constant. The radiation that ranges from ν to $\nu + d\nu$ contributes to

[8] Wilhelm Karl Werner Wien, German physicist 1864–1928.

[9] The reader is referred to the paper of Kramm and Herbert (2006) in which these radiation laws are derived using principles of dimensional analysis and discussed.

[10] Lord Rayleigh (John William Strutt), English mathematician and physicist, 1842–1919.

[11] Louis Carl Heinrich Friedrich Paschen, German physicist, 1865–1947.

[12] Ludwig Eduard Boltzmann, Austrian physicist, 1844–1906.

the field of energy within a volume dV, on average, an amount of energy that is proportional to $d\nu$ and dV expressed by

$$dE_\nu = U\,(\nu,\ T)\ d\nu\ dV. \tag{4.36}$$

Inserting formula (4.35) into this equation yields

$$dE_\nu = \frac{8\,\pi\,h}{c^3}\ \frac{\nu^3}{\exp\left(\frac{h\,\nu}{k\,T}\right)-1}\ d\nu\ dV. \tag{4.37}$$

According to Eq. (4.5), the monochromatic intensity, now denoted as $B\,(\nu,\ T)$, is generally related to the differential amount of radiant energy, dE_ν, that crosses an area element, $d\sigma$, in directions confined to a differential solid angle, $d\Omega$, being oriented at an angle θ to the normal of $d\sigma$,

$$dE_\nu = B\,(\nu,\ T)\ \cos\theta\ d\sigma\ d\Omega\ d\nu\ dt \tag{4.38}$$

in the time interval between t and $t\ +\ dt$ and the frequency interval between ν and $\nu\ +\ d\nu$. Thus, we obtain

$$\begin{aligned} dE_\nu &= \frac{8\,\pi\,h}{c^3}\ \frac{\nu^3}{\exp\left(\frac{h\,\nu}{k\,T}\right)\ -\ 1}\ d\nu\ dV = B\,(\nu,\ T)\ \cos\theta\ dA\ d\Omega\ dt\ d\nu \\ &= \frac{4\,\pi}{c}\ B\,(\nu,\ T)\ \underbrace{\cos\theta\ dA\ \frac{d\Omega}{4\,\pi}\ c\ dt}_{=\,dV}\ d\nu = \frac{4\,\pi}{c}\ B\,(\nu,\ T)\ d\nu\ dV \end{aligned} \tag{4.39}$$

and, hence

$$B\,(\nu,\ T) = \frac{2\,h}{c^2}\ \frac{\nu^3}{\exp\left(\frac{h\,\nu}{k\,T}\right)\ -\ 1}. \tag{4.40}$$

This blackbody radiation law customarily called the **Planck function** may be interpreted as the monochromatic intensity (also called the spectral radiance) emitted by a blackbody. It comprises two asymptotic solutions namely the **Rayleigh-Jeans law**,

$$B\,(\nu,\ T) = \frac{2\,\nu^2}{c^2}\ k\ T \tag{4.41}$$

for $h\ \nu \ll k\ T$ and the **exponential law of Wien and Paschen**,

$$B\,(\nu,\ T) = \frac{2\,h}{c^2}\ \nu^3\ \exp\left(-\frac{h\,\nu}{k\,T}\right) \tag{4.42}$$

for $h\ \nu \gg k\ T$, and, hence, $\exp\left(h\ \nu/(k\ T)\right) \gg 1$. This means that the Rayleigh-Jeans law is only valid for the so-called red range. For $\nu \to \infty$ the monochromatic

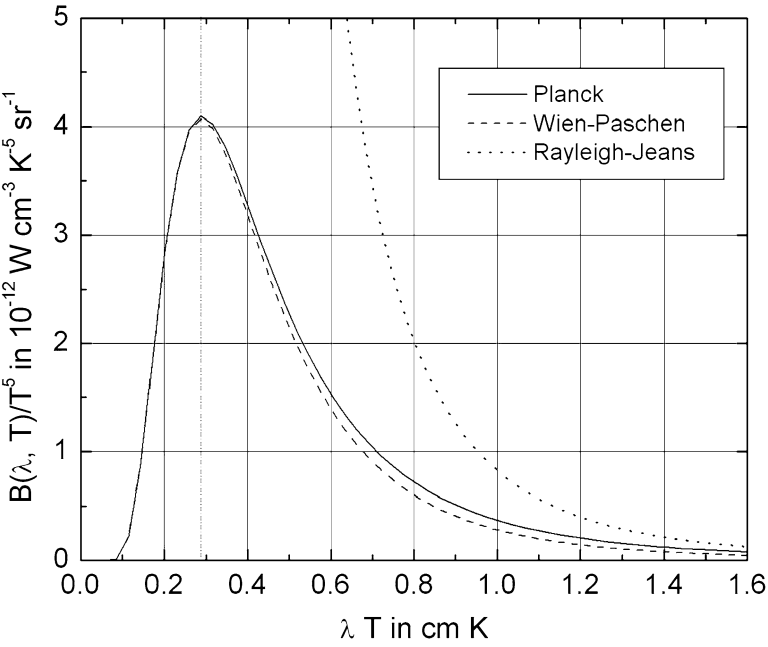

Fig. 4.11 Planck's function as expressed by Eq. (4.44). The *curve* represents $B\,(\lambda,\ T)\,/\,T^5$ versus $\lambda\ T$ so that it becomes independent of T. Note that the constant, $C\ =\ 0.2897\,\text{cm K}$, occurring in Wien's displacement relationship $C\ =\ \lambda_{max}\ T$ can be inferred from this figure. Also shown are the "asymptotic" laws of Rayleigh and Jeans as well as Wien and Paschen, respectively

intensity, $B\,(\nu,\ T)$, given by Eq. (4.41) would tend to infinity. Ehrenfest[13] coined it the **Rayleigh-Jeans catastrophe in the ultraviolet**. On the other hand, the Wien-Paschen law (4.42) is invalid in the red range (Fig. 4.11).

The frequency domain is given by $[0,\ \infty]$. In accord with Eq. (4.22), we may write

$$B\,(\lambda,\ T)\ =\ -\ \frac{c}{\lambda^2}\ B\,(\nu\,(\lambda)\,,\ T)\,. \tag{4.43}$$

We obtain for the Planck function in the wavelength domain $[\infty,\ 0]$

$$B\,(\lambda,\ T)\ =\ -\ \frac{2\,h\,c^{\,2}}{\lambda^5\ \left\{\exp\left(\frac{h\,c}{\lambda\,k\,T}\right)\ -\ 1\right\}}. \tag{4.44}$$

The relationship (4.43) can be applied to derive the Rayleigh-Jeans law and the Wien-Paschen law in the wavelength domain. The Planck function and these two "asymptotic" laws are illustrated in Fig. 4.11. When Planck's radiation law is plotted

[13] Paul Ehrenfest, Austrian and Dutch physicist, 1880–1953.

as a function of wavelength for any given temperature a spectrum results with a sharp short wavelength cutoff, a steep raise to the maximum and a gentle drop off toward longer wavelength (Figs. 4.1 and 4.11).

If the monochromatic radiance, I_ν, of radiation emitted by a blackbody is known, we can find the respective temperature by

$$T_B = \frac{h\ \nu}{k\ \ln\left(1 + \frac{2\ h\ \nu^3}{c^2\ I_\nu}\right)}. \tag{4.45}$$

The quantity T_B is called the **brightness temperature**. It is used in many remote sensing applications as is discussed later in this chapter.

4.2.2 Wien's Displacement Relationship

Even though **Wien's displacement relationship** was known before Planck published his famous radiation law, the former can simply be derived by determining the maximum of the latter using both the first derivative test and the second derivative test. The first derivative of Eq. (4.40) reads

$$\frac{\partial}{\partial \nu}\ B\ (\nu,\ T) = \frac{2\ h\ \nu^2}{c^2\ \left\{\exp\left(\frac{h\ \nu}{k\ T}\right) - 1\right\}^2}\ \left\{3\ \left\{\exp\left(\frac{h\ \nu}{k\ T}\right) - 1\right\}\right.$$
$$\left. - \frac{h\ \nu}{k\ T}\ \exp\left(\frac{h\ \nu}{k\ T}\right)\right\}. \tag{4.46}$$

This derivative is only equal to zero when the numerator of the term on the right-hand side of Eq. (4.46) is equal to zero (the corresponding denominator is larger than zero for $0 < \nu < \infty$), i.e.

$$3\ \{\exp\left(x_\nu\right)\ -\ 1\}\ =\ x_\nu\ \exp\left(x_\nu\right) \tag{4.47}$$

with $x_\nu = h\ \nu / (k\ T)$. This transcendental function can only be solved numerically. We obtain $x_\nu \cong 2.8214$, and in a further step

$$\frac{\nu_{ext}}{T} = x_\nu\ \frac{k}{h} = const. \tag{4.48}$$

where ν_{ext} is the frequency at which the extreme (either a minimum or a maximum) of the in the frequency domain occurs. It can simply be proved that for this extreme the second derivative fulfills the condition $\partial^2 B\ (\nu,\ T)/\partial \nu^2 < 0$ so that the extreme corresponds to the maximum, ν_{max}. When we use Eq. (4.1) we obtain

$$\lambda_{\max}^{(\nu)}\ T = \frac{c}{x_\nu}\ \frac{h}{k} \cong 5.098 \cdot 10^{-3}\ \text{m K} = const. \tag{4.49}$$

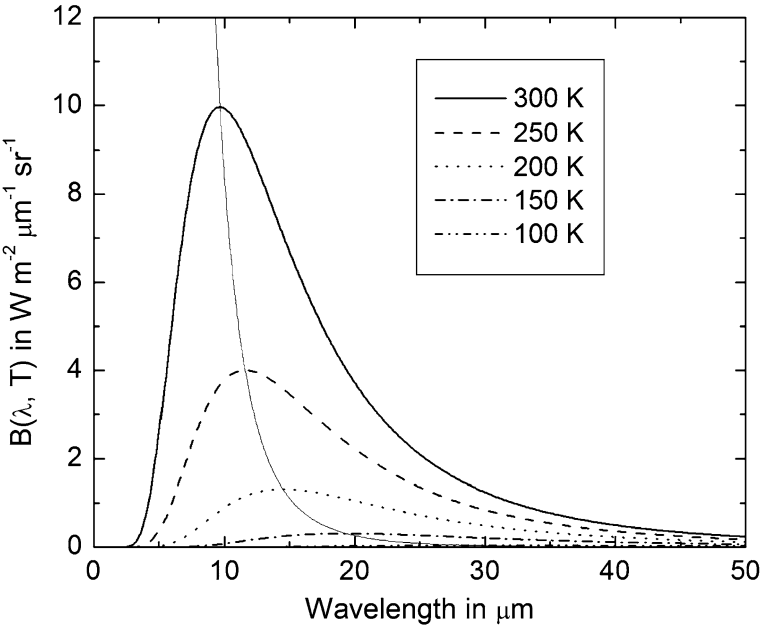

Fig. 4.12 The Planck function illustrated for different temperatures in the wavelength domain

We should call this formula Wien's displacement relationship, rather than Wien's displacement law because the latter is customarily used for $U\ (\nu,\ T) \propto \nu^3 f\left(\frac{\nu}{T}\right)$. For the wave number domain, we obtain the same result.

When we consider the Planck function (4.44) in the wavelength domain, we find in a similar manner

$$\lambda_{\max}^{(\lambda)}\ T = \frac{c}{x_\lambda}\ \frac{h}{k} \cong 2.897 \cdot 10^{-3}\ \text{m K} = const. \tag{4.50}$$

with $x_\lambda \cong 4.9651$. This relationship means that hotter obstacles radiate energy at shorter wavelength than cooler ones (Figs. 4.12 and 4.13). Shorter wavelengths correspond to higher energies. Hot objects possess more thermal energy. They radiate a high fraction of energy at short, energetic wavelengths.[14] Inserting Wien's displacement relationship into the Planck function (4.44) yields

$$B\ (\lambda_{max},\ T) = const.T^5. \tag{4.51}$$

High temperatures of blackbodies (e.g. temperature of the Sun) are determined by measuring the wavelength of maximum emission in the spectrum and using Wien's displacement relationship.

[14]Think of a stove that is black as it is cold and turns to red as it gets hot.

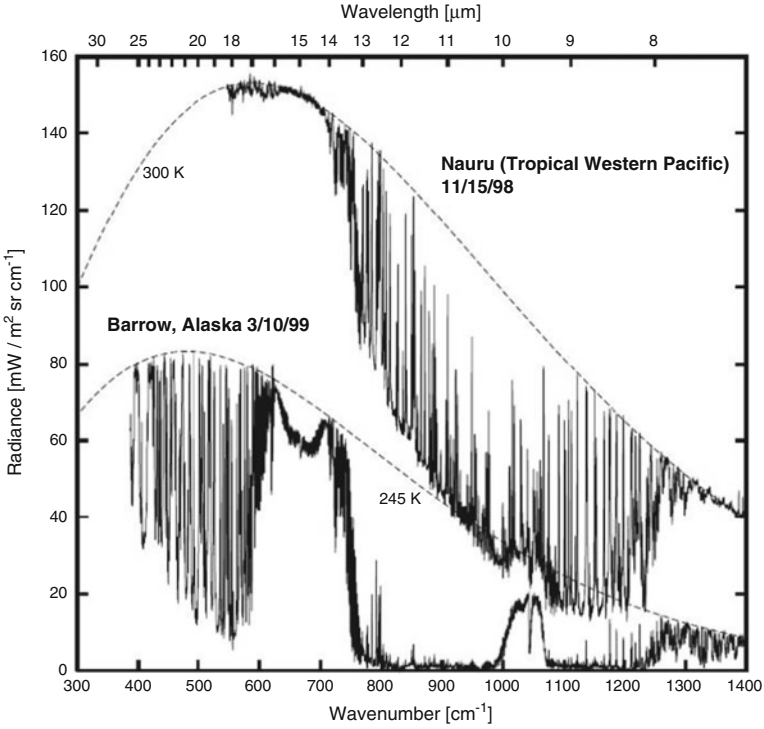

Fig. 4.13 The Planck function illustrated for different temperatures in the wave number domain. The latter, adopted from Petty (2004), shows two examples of measured emission spectra together with the Planck functions corresponding to the approximate surface temperatures *dashed lines* (Data courtesy of R. Knuteson, Space Science and Engineering Center, University of Wisconsin-Madison (2012))

As expressed by Eqs. (4.49) and (4.50), Wien's displacement relationship, derived for the frequency domain on the one hand and the wavelength domain on the other hand notably differ from each other being expressed by

$$\lambda_{\max}^{(\nu)} = \frac{x_\lambda}{x_\nu}\,\lambda_{\max}^{(\lambda)} \cong 1.76\,\lambda_{\max}^{(\lambda)}. \tag{4.52}$$

Example. The peak wavelengths with respect to the wavelength domain of the energy emitted by two different stars are about 0.70 and 1.43 μm, respectively. What are the temperatures of their surfaces?

Solution. Inserting the values in Eq. (4.50) yields to $T(0.70\,\mu\text{m}) \approx 4{,}139\,\text{K}$ and $T(1.43\,\mu\text{m}) \approx 2{,}026\,\text{K}$, respectively.

4.2.3 The Power Law of Stefan and Boltzmann

Integrating equation (4.40) over all frequencies yields for the integrated intensity (see also Eq. (4.7))

$$B\,(T) = \int_0^\infty B\,(\nu,\ T)\,d\nu = \frac{2\,h}{c^2}\int_0^\infty \frac{\nu^3}{\exp\left(\frac{h\,\nu}{k\,T}\right)\ -\ 1}\,d\nu. \tag{4.53}$$

Defining $X = h\,\nu/\,(k\ T)$ leads to

$$B\,(T) = \frac{2\,k^4}{c^2\,h^3}\,T^4\int_0^\infty \frac{X^3}{\exp\,(X)\ -\ 1}\,dX \tag{4.54}$$

where the integral amounts to

$$\int_0^\infty \frac{X^3}{\exp\,(X)\ -\ 1}\ dX = \frac{\pi^4}{15}. \tag{4.55}$$

Thus, Eqs. (4.54) and (4.55) provide for the integrated intensity

$$B\,(T) = \beta\ T^4 \tag{4.56}$$

with

$$\beta = \frac{2\,\pi^4\,k^4}{15\,c^2\,h^3}. \tag{4.57}$$

Since blackbody radiance may be considered as an example of isotropic radiance, we obtain for the radiative flux density (see also Eq. (4.14))

$$F\,(T) = \pi\ B\,(T) = \pi\ \beta\ T^4 \tag{4.58}$$

or

$$F\,(T) = \sigma\ T^4 \tag{4.59}$$

where $\sigma\ =\ \pi\ \beta\ =\ 5.67\cdot 10^{-8}$ J m^{-2} s^{-1} K^{-4} is the **Stefan**[15] constant.[16] According to Stefan's empirical findings and Boltzmann's thermodynamic derivation, formula (4.59) is customarily called the power law of Stefan and Boltzmann.

[15] Josef Stefan, Austrian physicist, 1835–1893.

[16] The value of this constant is easy to remember: know that it begins with 5, count to 8, and keep in mind that there are digits after the 5, a minus before the 8, and a 10 in between.

Here, we have performed the integration in the frequency domain. When we do this in the wavelength domain or the wave number domain, we obtain identical results. This can be explained as follows: When we consider the transformation from the frequency domain to any ϑ domain, where ϑ stands for the wavelength, λ, or the wave number, κ, we have to recognize that $B(\vartheta,\ T)\ d\vartheta = B(\nu(\vartheta),\ T)\ d\nu$ (see also Eqs. (4.19) and (4.43)). This relationship was already used in deriving Eq. (4.44). On the other hand, according to the theorem for the substitution of variables in an integral, we have

$$\int_{\nu_1}^{\nu_2} B(\nu,\ T)\ d\nu = \int_{\vartheta_1}^{\vartheta_2} B(\nu(\vartheta),\ T)\ \frac{d\nu(\vartheta)}{d\vartheta} d\vartheta \tag{4.60}$$

where $\nu(\vartheta)$ is the transformation from ν to ϑ, $\nu_1 = \nu(\vartheta_1)$, and $\nu_2 = \nu(\vartheta_2)$. The results of these integrals are identical because any variable substitution does not affect the solution of an integral. Thus, the solution is independent of the domain.

Consequently, the temperature of a blackbody determines the energy radiated[17] (Figs. 4.12 and 4.13). Furthermore, the **intensity of energy** emitted by a blackbody increases by the fourth power of its absolute temperature. Due to this relationship, a doubling of temperature yields to a 16-fold growth of the emitted intensity.

Solving Eq. (4.59) for a mean temperature of the Earth's surface of 288 K leads to a terrestrial exitance of 390 W m^{-2}. For a mean temperature of the Sun's surface of 5,771 K we obtain a solar exitance of $6.29 \cdot 10^7$ W m^{-2}. This means that the solar exitance is more than 160,000 times larger than the terrestrial exitance. However, the determination of the Stefan constant requires the integration of the intensity over the adjacent hemisphere. As mentioned before, this integration corresponds to an integration over a vector field. Consequently, Eq. (4.59) should only be applied to actual surface temperatures, but not to mean surface temperatures.

Now we are able to explain the shape of the solar spectrum at the TOA as illustrated in Fig. 4.1. We can write Eq. (4.23) as

$$\begin{aligned} F &= \pi \left(\frac{r_S}{d}\right)^2 \frac{F_S}{\pi} = \pi \left(\frac{r_S}{d}\right)^2 \int_0^\infty B(\nu,\ T_S)\ d\nu \\ &= \pi \int_0^\infty \left(\frac{r_S}{d}\right)^2 B(\nu,\ T_S)\ d\nu \end{aligned} \tag{4.61}$$

where $B(\nu, T_S)$ represents Planck's radiation formula, and T_S is the Sun's surface temperature. Thus, to determine the monochromatic intensity of solar radiation

[17] Hotter bodies emit more energy than cooler ones.

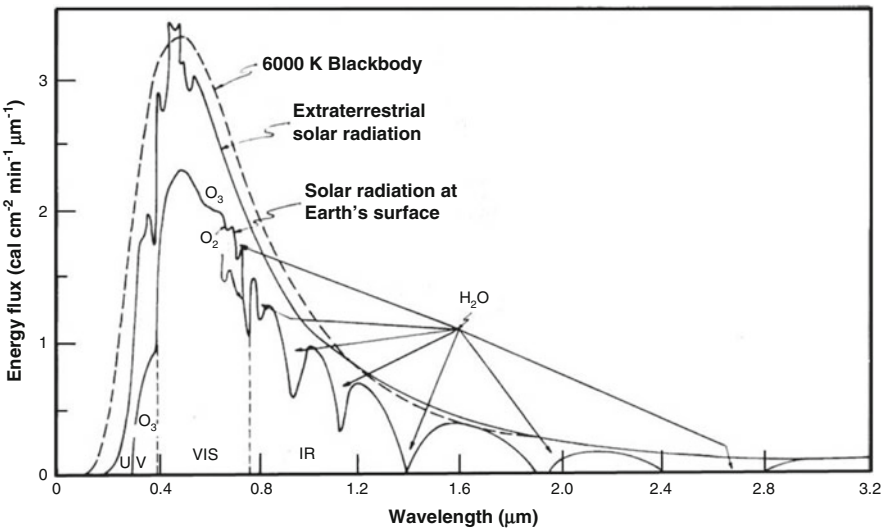

Fig. 4.14 Spectral distribution of solar radiation at the top of the atmosphere, and a typical distribution of that which reaches the Earth's surface, compared with the radiation emitted by a blackbody at a temperature of 6,000 K (From Coulson 1975)

with respect to the TOA, Planck's radiation formula has to be scaled by $(r_S/d)^2$. Sometimes $\pi(r_S/d)^2$ is also considered for the purpose of scaling to obtain the monochromatic irradiance (Fig. 4.14). Figure 4.28 is taken in the peak of the blackbody curve for terrestrial radiation. High and mid-level clouds show up clearly, as they are colder than the Earth's surface.

Example. The mean distance Earth-Sun is $1.496 \cdot 10^{11}$ m. The average irradiance of solar radiation reaching the Earth stems from the outermost visible layer of the Sun, which has a mean radius of $6.96 \cdot 10^8$ m. Determine the temperature of this layer using the blackbody assumption.

Solution. The irradiance at the top of the layer is given by $F_S = 1.361 \cdot 10^3 (\frac{1.496 \cdot 10^{11}}{6.96 \cdot 10^8})^2 \,\mathrm{W\,m^{-2}} \approx 6.29 \cdot 10^7 \,\mathrm{W\,m^{-2}}$. Rearranging Eq. (4.59) yields $T = (\frac{F_S}{\sigma})^{\frac{1}{4}} = (\frac{6.29 \cdot 10^7}{5.67 \cdot 10^{-8}})^{\frac{1}{4}} \approx 5{,}771$ K.

Example. The Sun emits $3.83 \cdot 10^{26}$ W and has a radius of $6.96 \cdot 10^8$ m. Determine the irradiance at its surface.

Solution. $F_S = \frac{\Phi}{4\pi r_{sun}^2} = \frac{3.83 \cdot 10^{26} \,\mathrm{W}}{4\,\pi (6.96 \cdot 10^8 \,\mathrm{m})^2} \approx 6.29 \cdot 10^7 \,\mathrm{W\,m^{-2}}$

Table 4.4 Energy emitted in the shortwave (3–4 μm) and long-wave (10–12 μm) range of the spectrum for various surface types

	Energy emitted		
Surface type	Visible	Shortwave	Long-wave
Snow	None	Low	Low
Ice	None	Low	Low
Lake	None	Medium	Medium
Land	None	High	Medium
Water cloud	None	Medium	Medium
Ice cloud	None	Low	Low
Dust	None	Medium	Medium

4.2.4 *Kirchhoff's Law*

Equation (4.33) expresses the theorem as published by Kirchhoff in 1860. We already introduced the spectral absorptance, which is a relative non-dimensional quantity. Rearranging Eq. (4.33) yields

$$\frac{E_\nu}{J(\nu, T)} = a_\nu. \tag{4.62}$$

The quantity $\epsilon_\nu = \frac{E_\nu}{J(\nu,T)}$ is the relative spectral emittance or spectral emissivity. **Kirchhoff's law** states that the spectral emittance ϵ_ν of a body is equal to its spectral absorptance a_ν, i.e. for a given temperature and frequency we have

$$\epsilon_\nu = a_\nu. \tag{4.63}$$

This means that bodies absorbing at one wavelength also emit at this wavelength.

Example. Based on recent satellite observations, the solar constant is $S = 1{,}361\,\mathrm{W\,m^2}$. Assume a totally snow-covered Earth with an absorptance of 0.1 in the solar range and absorptance of 0.8 in the infrared, where most of the emission takes place. Ignore the atmosphere and determine the temperature of the radiative equilibrium at the subsolar point.

Solution. $F(absorbed) = F(emitted)$. Thus, $0.1 \cdot 1{,}361\,\mathrm{W\,m^{-2}} = 0.8\sigma T^4$. Rearranging leads to $T = (\frac{0.1 \cdot 1{,}361}{0.8 \cdot 5.67 \cdot 10^{-8}})^{\frac{1}{4}}\,\mathrm{K} = 234\,\mathrm{K}$.

Despite real blackbodies do not exist this assumption is a useful model to understand the maximum emittance of radiation. Earth and Sun are close to blackbodies. The Earth surface, clouds and many other obstacles emit some percentage of the maximum amount of radiation possible at a given temperature. They are **gray bodies** (Table 4.4).

Blackbody radiation represents the upper limit of the amount of radiation that an object may emit at a given temperature. At any wavelength (or frequency), the **relative spectral emittance**

$$\epsilon_\lambda = \frac{F_\lambda^*}{F_\lambda} \tag{4.64}$$

is a measure of how strongly the object radiates at these wavelength (or frequency) and is a useful tool to define the relative spectral emittance of a gray body, where the star characterizes either the monochromatic irradiance or the total irradiance of the gray body. We define the mean emittance (or, alternatively, the mean absorptance) by

$$\epsilon = \frac{\int_0^\infty \epsilon_\lambda \, F_\lambda \, d\lambda}{\int_0^\infty F_\lambda \, d\lambda} = \frac{1}{F} \int_0^\infty \epsilon_\lambda \, F_\lambda \, d\lambda. \tag{4.65}$$

In case of the atmosphere, the integral of the r.h.s. of this equation is related to certain bands (or even lines)

$$\int_0^\infty \epsilon_\lambda \, I_{\lambda,E} \, d\lambda = \sum_i \int_{\Delta_i \lambda} \epsilon_\lambda \, I_{\lambda,E} \, d\lambda. \tag{4.66}$$

The relative emittance is the percentage of energy radiated by a substance relative to that of a blackbody. It ranges from just above 0 to close to 1. Table 4.5 exemplarily lists typical values for various surface types.

Inserting the relative emittance leads to the gray-body form of Eq. (4.59)

$$F^* = \epsilon \sigma T^4. \tag{4.67}$$

In most cases, temperature differences govern the variations in emittance. The atmosphere is an exception from this rule. Here, emission depends among other things, on water-vapor content, and wavelength. The atmosphere emits less radiation at any temperature than would a blackbody. Table 4.4 relatively compares the energy emitted in the shortwave and long-wave range of the spectrum.

In general, the radiative equilibrium temperature of a substance that is a relatively weak absorber at visible and near infrared wavelength, but strong absorber in the infrared region is lower than that of a gray body exposed to the same incident radiation. Note that this is quite different for gases that absorb weak in the visible and near infrared, but strong in the infrared.

Table 4.5 Typical values of the relative emittance of long-wave radiation

Surface type	ϵ
Fresh snow	0.99
Old snow	0.82
Dry sand	0.95
Wet sand	0.98
Dry peat	0.97
Wet peat	0.98
Soils	0.90–0.98
Asphalt	0.96
Concrete	0.71–0.90
Tar and gravel	0.92
Limestone gravel	0.92
Light sandstone rock	0.98
Desert	0.84–0.91
Grass lawn	0.97
Grass	0.90–0.95
Deciduous forest	0.97–0.98
Coniferous forest	0.97–0.98
Urban area	0.85–0.95
Pure water	0.993
Water with a thin film of petroleum oil	0.972

Example. Compare the energy radiated by a blackbody at 288 K to that of a gray-body having an emittance of 0.9.

Solution. The blackbody emits about 390 W m^{-2}, while the assumed gray-body radiates about 351 W m^{-2}.

4.3 Shortwave Radiation

Solar radiation is the most intense in the visible portion of the spectrum. Most of the radiation has wavelengths shorter than 4 μm (Table 4.1). The spectrum of shortwave radiation is concentrated at wavelength shorter than 4 μm with a peak at 0.5 μm. Tails of the shortwave spectrum reach into the UV ($\lambda < 0.3\,\mu m$) and into the near-infrared region ($\lambda > 0.7\,\mu m$) (Figs. 4.1 and 4.14).

4.3.1 Scattering

Scattering is a fundamental physical process that takes place within the atmosphere. It is associated with light and its interaction with matter. Atmospheric scattering

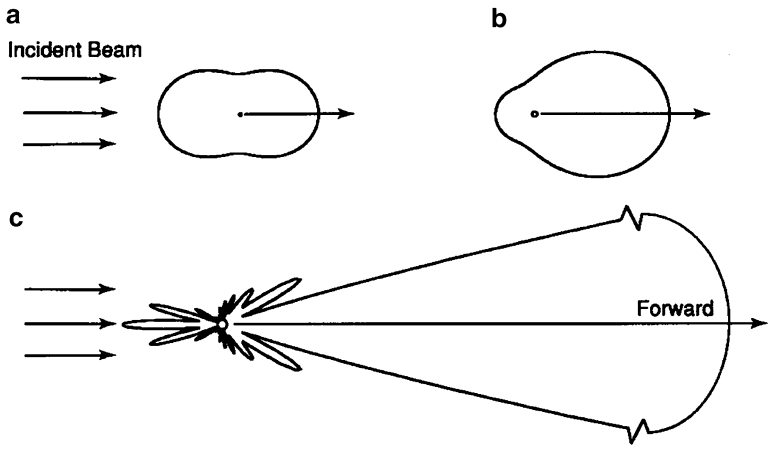

Fig. 4.15 Schematic view of angular patterns of scattered intensity from particles of three different sizes (**a**) small, (**b**) large, and (**c**) huge particles (From Liou 1980)

occurs at all wavelengths throughout the entire electromagnetic spectrum. It is a process, by which a particle in the path of an electromagnetic wave continuously detracts energy from the incident wave and redirects that energy in all directions (Fig. 4.15). We distinguish between **single scattering** and **multiple scattering**. When a particle at a given position removes the incident light by scattering just once in all directions, we call it single scattering. A portion of this scattered light, of course, may reach another particle, where it is scattered again in all directions (secondary scattering). Likewise, a tertiary scattering involving a third particle may occur. Scattering more than once is called multiple scattering. Light is said to be reflected when the angle, at which light initially strikes a surface, equals to the angle at which light bounces off the same surface. While in the terrestrial spectral range, absorption and emission play the dominant role, scattering prevails in the solar spectrum at cloud-free conditions.

Scattering is also a selective process by which light is scattered by

- Air molecules ($\sim 10^{-4}\,\mu\text{m} = 1\,\text{Å}$),
- Aerosol particles ($\sim 1\,\mu\text{m}$),
- Hydrometeors (Chap. 3)
  - Water droplets ($\sim 10\,\mu\text{m}$),
  - Ice crystals ($\sim 100\,\mu\text{m}$),
  - Large raindrops and hail particles ($\sim 10^4\,\mu\text{m} = 1\,\text{cm}$).

Scattering of light by particles depends on particle shape, particle size, particle index of refraction, viewing geometry, and the wavelength of radiation (Fig. 4.15).

In 1908, Mie[18] applied Maxwell's[19] equations of electromagnetic radiation for a plane electromagnetic wave incident on a sphere. Far away from the sphere (distance, $d \gg r$, radius of the sphere), the scattered radiation is a function of viewing angle, index of refraction and the size parameter that can be given by

$$\chi = \frac{particle\ circumference}{wavelength\ of\ the\ incident\ light} = \frac{2\pi r}{\lambda}. \tag{4.68}$$

Atmospheric molecules and particles are separated widely enough so that each particle scatters light in exactly the same way as if all other particles would not exist. It is referred to as **independent scattering**. The assumption of independent scattering greatly simplifies the problem of light scattering by a collection of particles because it allows the use of energy quantity instead of electrical field in the analysis of the propagation of electromagnetic waves in planetary atmospheres.[20] In atmospheric scattering, it is generally assumed that light scattered by molecules and particulates has the same frequency (or wavelength) as the incident light. This assumption is not entirely correct in case of **Raman**[21] scattering (inelastic scattering of photons by an atom or a molecule, where the scattered photon has a frequency different from that of the incident photon) that can produced, for instance, by high-energy laser light. Raman spectroscopy can be used, for instance, in remote sensing of water vapor.

By using the size parameter χ scattering can be divided into the three regimes within the solar spectral range

- Geometric optics for $\chi \geq 50$,
- Mie-scattering for $0.1 < \chi < 50$, $(k\rho)_{aerosol} \propto \frac{1}{\lambda^{1.3}}$, and
- Rayleigh-scattering for $\chi \leq 0.1$, $(k\rho)_{molecule} \propto \frac{1}{\lambda^4}$.

In case of $\chi < 10^{-3}$, scattering can mainly be ignored (Fig. 4.16).

Scattering is often accompanied by absorption. Grass, for instance, looks green because it scattered green light, while it absorbs red and blue light. Red and blue light is, therefore, no longer present. Both scattering and absorption remove energy from a beam of light traversing the medium, i.e. the beam of light is attenuated. **Attenuation** is also called **extinction**.

4.3.1.1 Geometric Optics

Geometric optics can explain a wide variety of optical phenomena (Fig. 4.18). For χ greater or equal to 50, the sphere is large as compared to the wavelength. Under

[18] Gustav Adolf Ludwig Mie, German physicist, 1868–1957.

[19] James Clerk Maxwell, British physicist, 1831–1879.

[20] The reader is referred to Liou's textbook.

[21] Chandrasekhara Venkata Raman, Indian physicists, 1888–1970.

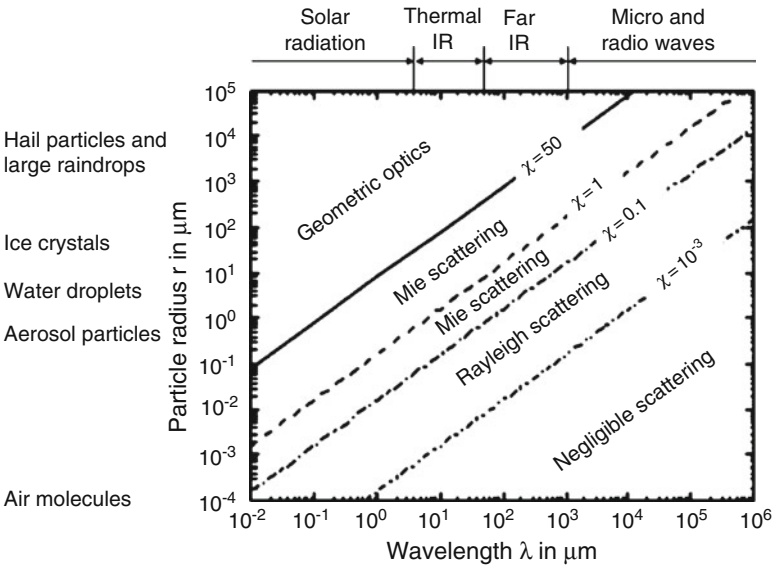

Fig. 4.16 Scattering regimes (With respect to Wallace and Hobbs 1977)

these conditions the laws of geometrical optics can be applied where rays, which are refracted or reflected at a surface, can be traced (Fig. 4.17). The interaction of solar radiation with virtually all types of hydrometeors and of infrared radiation with hydrometeors in general falls into this category.

A rainbow results from reflection of light in raindrops. Sometimes a primary and a secondary rainbow are visible. A secondary rainbow develops when light entering a raindrop undergoes two internal reflections instead of just one. The colors of the primary rainbow go from red on the outside to violet on the inside. The opposite is true for the secondary rainbow (Fig. 4.17). Since the intensity of light is reduced even further by the second reflection, the secondary rainbow appears to be less bright than the primary one.

When light from the Sun or moon is refracted by some defined ice crystals of thin, high-level clouds (e.g. cirrus, cirrostratus) 22° and 46° **halos**, so-called **sundogs**, numerous arcs, and bright spots can occur. Most halos appear as bright white rings. Sometimes the dispersion of light as it passes through the ice crystals found in cirrus can cause a halo to have color (Fig. 4.18). A 22°-halo is the most common type of halo (Fig. 4.18). It is a ring of light that occurs 22° from the Sun or the moon and is formed by hexagonal ice crystals with diameters less than 20.5 µm.

In the solar range of the spectrum, the reflection at an optically thick surface or at the Earth's surface is called the **albedo**, α. It is the ratio of outgoing reflected radiation to the incoming radiation. The albedo depends on the viewing angle with respect to the Sun. Surface reflection varies with the kind of surface and its properties (Table 4.6). The size of the surface roughness compared to that of the

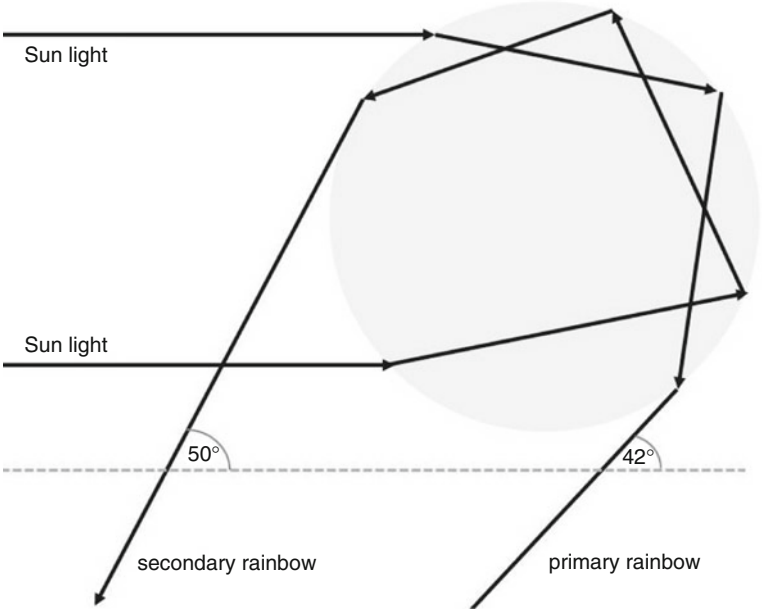

Fig. 4.17 Schematic view of geometry of the rays that contribute to a secondary rainbow. The primary rainbow has always and angle of 40–42° from the path of the Sun rays

Fig. 4.18 Halo formed in cirrostratus as seen from the University of Alaska Fairbanks campus above the Alaska Range (Photo courtesy to Hartmann 2002)

Table 4.6 Solar albedo of various surfaces

Surface type	α	Remarks
Bare soil	0.1–0.25	Depends on soil type and soil moisture
Desert	0.25–0.4	Depends on soil type and soil moisture
Tundra	0.18–0.25	
Glaciers	0.25–0.35	
Grass	0.15–0.25	Depends on vegetation status, length, health
Agriculture	0.15–0.2	Depends on vegetation type and cycle
Ochards	0.15–0.20	
Forest (pine, fir, oak)	0.1–0.18	
Forest (coniferous)	0.1–0.15	
Red pine forest	0.1	
Deciduous forest	0.15	Bare of leaves
Deciduous forest	0.15–0.2	
Deciduous forest	0.2	Bare with snow on the ground
Rain forest	0.15	
Fresh snow	0.75–0.95	
Old (dirty) snow	0.25–0.75	Depends on age, area
Ocean	<0.1	Values of 0.1–0.7 are possible in the Sun-glint area or for low sun
Average planetray albedo	0.3	
Urban areas	0.1–0.27	With an average of 0.15

wavelength determines the type of reflector. Calm water reflects the incident visible radiation in nearly one direction (like a mirror). Such type of surface is called a **specular reflector**. Fresh snow reflects light in nearly all directions. Such a surface is an **ideal diffuse reflector**. The wavelength determines what kind of reflector the surface is. A surface may be more like a diffuse reflector at one wavelength, but more like a specular reflector at another wavelength, i.e. albedo depends on wavelength[22] Table 4.6 lists typical values of albedo for various types of surfaces. Table 4.7 gives some subjective comparisons of reflected energy in shortwave (3–4 μm) and visible (0.4–0.7 μm) part of the spectrum.

4.3.1.2 Mie Scattering

At size parameters in the range $0.1 < \chi < 50$, the particle and wavelength are of similar size. Radiation strongly interacts with the particle, i.e. the full Mie-equation has to be applied. A full discussion of Mie scattering (also called **Lorenz-Mie scattering**) is beyond the scope of this book and the interested reader is encouraged to take a look at respective textbooks on radiations.[23] Mie scattering is sensitive to

[22] A paved parking lot, for instance, is a specular reflector in the radio part of the spectrum, but a diffuse reflector in visible part.

[23] See reference list for suggestions.

Table 4.7 Solar albedo of various surfaces

Surface type	Energy reflected Visible	Shortwave	Long-wave
Snow	High	Low	None
Ice	Medium	Low	None
Lake	Low	Low	None
Land	Low	Medium	None
Water cloud	High	High	None
Ice cloud	Low	Medium	None
Dust	Medium	Medium	None

the shape of the particle. Prominent applications of Mie scattering are the detection of raindrops by radar, using visible radiation to detect haze, smoke, dust and aerosols, or infrared radiation to sense cloud droplets (Appendix B).

4.3.1.3 Rayleigh Scattering

For $\chi \leq 0.1$, the particles are small in comparison with the wavelength of radiation and we speak of **Rayleigh scattering**. Rayleigh scattering is insensitive to the shape of the particle. In the Rayleigh regime, the scattering coefficient is proportional to the radius of the particle, r.

Air molecules act as Rayleigh-scatters for visible and ultraviolet radiation. Shorter wavelengths of the incoming visible light (violet and blue; Table 4.1) about $0.48\,\mu m$ are scattered more strongly than the longer (red) wavelengths by small molecules of oxygen and nitrogen that are much smaller than the wavelength of the light because of the λ^4-dependency. Since the violet and blue light is scattered over and over by the molecules all throughout the atmosphere, blue light comes from all directions yielding in the blue appearance of the sky. Sky polarization that is important for many atmospheric remote sensing applications can also be explained by Rayleigh scattering.

4.3.2 Diffraction

In general, **diffraction** denotes to the slight bending of light as it passes around the edge of an obstacle. The strength of diffraction depends on the relative size of the wavelength of light compared to that of the opening. When the opening is much larger than the wavelength, diffraction is almost unnoticeable. When the opening is close in size or equal to the size of the wavelength, a considerable diffraction exists.

In the atmosphere, diffraction occurs at the tiny water droplets in clouds. When the distance between the drops is similar to the wavelength of visible light, the light shining through the space between two cloud droplets is diffracted and dispersed. Thus, diffraction can produce fringes of light, dark, or colored bands.

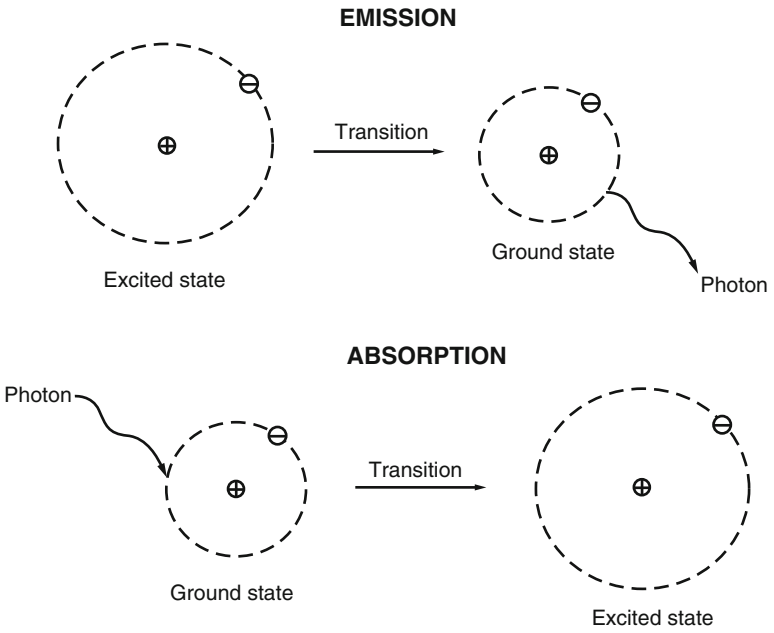

Fig. 4.19 Schematic view of emission and absorption for a hydrogen atom that is composed of one proton and one electron. The radius of the orbit r is $n^2 \cdot 0.53$ A where n is the quantum number (From Liou 1980)

Examples for diffraction of light are coronas surrounding the Sun or moon and the silver-line sometimes found around the edges of clouds. When the cloud-droplet spectrum is nearly mono-disperse, i.e. the droplets are very uniform in size, the diffracted light can cause the corona to be separated into its component colors, with blue light to the inside of the red light. These colors may repeat themselves, leading to a series of colored rings around the Sun or moon.

4.3.3 Absorption

Absorption is the interaction between radiation and matter (Fig. 4.19). It means a loss of incident radiation. In contrast to scattering, absorption does not just redirect the radiation. When absorption occurs, electromagnetic radiation energy is transformed into

- Kinetic energy of the molecule (heat), or
- Vibrational energy of the molecules (exciting).

Absorption can occur due to atmospheric gases, aerosols, cloud- and precipitation particles. In the atmosphere, molecules absorb radiation in selective wavelength bands creating a complicated pattern of atmospheric absorption bands (Fig. 4.14). The latter can be used to determine the concentration of the respective absorbing molecules from satellite. In the solar spectrum, H_2O, CO_2, O_3, O_2, N_2, NO_2, N_2O, and CH_4 are the main absorbers of solar energy. In the ultra-violet part of the spectrum, the main absorbers are O_2, and O_3. We call areas of weak absorption a **window**. One of the greatest windows resides in the visible portion of the spectrum.

Absorption of shortwave radiation by the atmosphere and the Earth's surface "heats" the Earth-atmosphere system (correctly spoken contributes to the increase of internal energy). To determine the heating rate we consider a slab of atmosphere of thickness dz between the heights z and $z + dz$. At these heights, the monochromatic irradiation at wavelength, λ, is given by $F(z)$ and $F(z+dz)$, respectively, where (downward directed) net monochromatic irradiance at these height z reads

$$F_\lambda(z) = F_\lambda \downarrow (z) - F_\lambda \uparrow (z) \tag{4.69}$$

and

$$F_\lambda(z + dz) = F_\lambda \downarrow (z + dz) - F_\lambda \uparrow (z + dz). \tag{4.70}$$

The decrease of this net flux density due to absorption by the layer of air of the thickness dz is given by

$$dF_\lambda(z) = F_\lambda(z) - F_\lambda(z + dz) \tag{4.71}$$

where the term on the l.h.s. of this equation is negative due to absorption. Thus, we can determine the heating rate for this infinitesimal layer dz by

$$\rho_a c_p \frac{\partial T}{\partial t} = -\frac{\partial F_\lambda(z)}{\partial z}. \tag{4.72}$$

Here, ρ_a is the density of the air in the layer, c_p is the heat capacity at constant pressure, and $\frac{\partial T}{\partial t}$ is the temperature increase with respect to time due to the absorption of solar radiation. Note that $\frac{\partial F(z)}{\partial z}$ is the vertical contribution of the divergence of the solar irradiance.

Let Δz be the thickness of a given layer of air. If there are no losses at the sides of the solar beam and atmospheric backscattering can be ignored, we may use the definition of the monochromatic transmittance, $T_\lambda = 1 - a_\lambda$, where a_λ is the corresponding monochromatic absorptance (Sect. 4.5.2), to estimate the absorption of monochromatic radiation in this layer by

$$\Delta F_\lambda(z) = -a_\lambda F_\lambda \downarrow (z + \Delta z). \tag{4.73}$$

In accord with Eqs. (4.72) and (4.73), the change of the temperature ΔT with respect to time due to absorption can be estimated by

$$\Delta T = \frac{a_\lambda}{\rho_a c_p} F_\lambda \downarrow (z + \Delta z) \frac{\Delta t}{\Delta z}. \tag{4.74}$$

Obviously, the absorption of solar radiation contributes to a change of the temperature distribution and the related pressure and wind fields (Chap. 6).

4.4 Long-wave Radiation

In accord with the Stefan-Boltzmann's law, and Wien's displacement law all components of the climate system emit radiant energy in the long-wave spectrum. All real bodies emit and absorb less radiant energy than a blackbody at the same temperature and wavelength, for which their emittance is less than 1 and varies with the wavelength in accord with Kirchhoff's law. In solids and liquids, emittance only slightly varies with the wavelength, while it strongly varies in gases. Atomic gases absorb (emit) radiant energy in distinct wavelength intervals that are called the spectral absorption lines. Molecular gases show absorption bands. Various types of surfaces have slightly different emissivities. Absorption and emission depend on the gases' atomic or molecular structure and the wavelength. Thus, each chemical element or combination of elements has its characteristic absorption and emission spectrum. Emission lines can result from transitions to the ground state or between excited states (Fig. 4.19). According to Kirchhoff's law if radiation penetrating a gas can excite atoms (molecules), its energy will not be absorbed or emitted.

4.4.1 Rotational and Vibrational Bands and Spectral Lines

As pointed out in Chap. 2, molecules have several degrees of freedom. Diatomic molecules, for instance, can rotate about a common axis yielding rotational energy or its atoms can vibrate towards and away from each other. Quantum mechanics postulates certain preferred models of behavior for each gas being the specific emission characteristics for that gas. Diatomic molecules can either have vibrational or rotational transitions, if vibration or rotation lead to an oscillating electric dipole moment. N_2 and O_2 have no electric dipoles (because of their symmetric charge distribution) and therefore no vibrational or rotational spectrum. However, they have absorption and emission spectra in the UV and VIS as mentioned before.

In the terrestrial range, the main gases active are CO, CH_4, N_2O, O_3, CO_2, and H_2O (Table 4.8). The modes listed in this table are related to symmetric stretching (ν_1), bending (ν_2), and asymmetric stretching (ν_3) illustrated in Fig. 4.20. (Note that the vibration mode ν_4 of CH_4 is not sketched.) Linear molecules like N_2O and

Table 4.8 The most important vibrational and rotational transitions for H_20, CO_2, O_3, CH_4, N_2O, and CO. Here, the modes ν_1, ν_2, and ν_3 are related to symmetric stretching, bending, and asymmetric stretching, respectively. The symbols P, Q, and R denote various branches

Gas	Center $\tilde{\nu}(\text{cm}^{-1})$ [$\lambda(\mu\text{m})$]	Transition	Band interval $\tilde{\nu}(\text{cm}^{-1})$
H_2O	–	Pure rotational	0–1,000
	1,594.8 [6.3]	ν_2; P, R	640–2,800
	Continuum	Far wings of the strong lines; Water vapor dimers $(H_2O)_2$	200–1,200
CO_2	667 [15]	ν_2; P, R, Q	540–800
	961 [10.4]	Overtone and	850–1,250
	1,063.8 [9.4]	combination	
	2,349 [4.3]	ν_3; P, R	2,100–2,400
		Overtone and combination	
O_3	705 [14.2]	ν_2; P, R	600–800
	1,043 [9.59]	ν_3; P, R	600–800
	1,110 [9.01]	ν_1; P, R	950–1,200
CH_4	1,306.2 [7.6]	ν_4	950–1,650
N_2O	588.8 [17.0]	ν_2	520–660
	1,285.6 [7.9]	ν_1; P, R	1,200–1,350
	2,223.5 [4.5]	ν_3	2,120–2,270
CO	2,150 [4.67]	Pure rotational	2,102–2,181

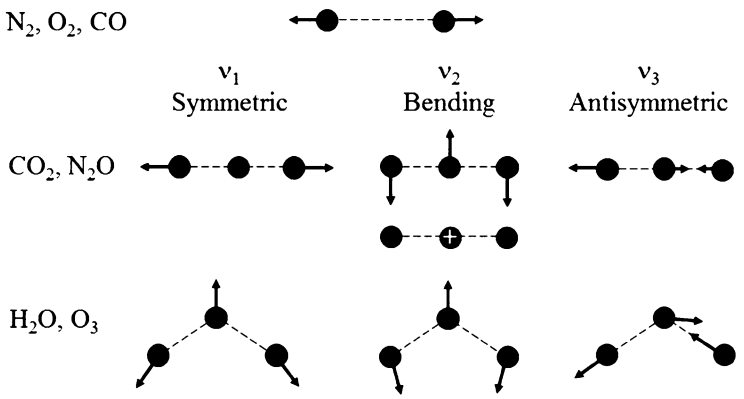

Fig. 4.20 Sketch of the vibrational modes of diatomic and triatomic atmospheric molecules (Adopted from Liou 2002)

CO_2 have two bending modes denoted as ν_{2a} and ν_{2b} which have the same energy (degenerated modes). The combination of rotational and vibrational states of water vapor yields to very complex and irregular absorption spectra. Vibrational bands exist at higher energy than rotational bands. The energies of vibrational quanta are two orders of magnitude greater than those of rotational quanta. As listed in Table 4.8, the pure H_2O rotational band ranges from 0 to 1,000 cm^{-1}. This band

is important in the generation of tropospheric cooling. The ν_2 fundamental band centered at 1,594.8 cm^{-1} (6.3 μm) is the most important vibrational-rotational one of water vapor. The other two fundamental bands, ν_1 and ν_3, are found to be close to one another and are centered at 3,703.7 cm^{-1} (2.7 μm). The continuum absorption by H_2O in the range of the **atmospheric window**, 800–1,200 cm^{-1} (8–12 μm), remains unexplained. It has been suggested that the continuum results from the accumulated absorption of the distant wings of the water vapor lines, principally in the far-infrared part of the spectrum. There is some evidence that contributions to continuous absorption may be caused by water vapor dimers, $(H_2O)_2$. The bending mode of CO_2 is degenerated and consists of ν_{2a} and ν_{2b} vibrations at the same frequency. This ν_2 fundamental band is centered at 667 cm^{-1} (15 μm), where the band interval is ranging from 540 to 800 cm^{-1}. There are also some overtone and combination bands ranging from 850 to 1,250 cm^{-1}. The ν_3 fundamental band is centered at 2,349 cm^{-1} (4.3 μm), where the band interval is ranging from 2,100 to 2,400 cm^{-1}. The ν_1 and ν_3 fundamental vibration modes of ozone are centered at 1,110 and 1,043 cm^{-1}, respectively. They constitute the well-known 9.6 μm O_3 band. The ν_2 fundamental band is centered at 705 cm^{-1} (14.2 μm). Thus, it is well masked by the strong CO_2 15 μm band and appears less important in atmospheric radiative transfer. Methane (CH_4) has no permanent electrical dipole moment and, hence, no pure rotational spectrum. Its most important fundamental band ν_4 is centered at 1,306.2 cm^{-1} (7.6 μm). Similar to CO_2, in case of nitrous oxide (N_2O) numerous bands are produced by the fundamental, overtone, and combination frequencies. The ν_1 to ν_3 fundamental bands of N_2O are centered at 588.8 cm^{-1} (17.0 μm), 1,285.6 cm^{-1} (7.9 μm), and 2,223.5 cm^{-1} (4.5 μm), where the corresponding band intervals are ranging from 520 to 660 cm^{-1}, 1,200 to 1,350 cm^{-1}, and 2,120 to 2,270 cm^{-1}, respectively. Carbon monoxide (CO) has a pure rotational band centered at 2,150 cm^{-1} (4.67 μm). Its band interval is ranging from 2,102 to 2,181 cm^{-1}. This range is also covered by the N_2O ν_3 fundamental band.

Monochromatic emission has never been observed. The spectral lines of the emission (absorption) spectrum of an isolated molecule have a very small, but finite width on the frequency scale. There are various effects that lead to the so-called line broadening. These effects are related to (1) the damping of oscillator vibrations resulting from the loss of energy in emission, where the broadening of lines in this case is considered to be normal, (2) the perturbation due to the reciprocal collision between the absorbing molecules and between the absorbing and non-absorbing molecules, and (3) the Doppler[24] effect resulting from the difference in thermal motions of atoms and molecules. The broadening of lines resulting from the loss of energy in emission also called natural broadening is practically negligible in comparison with that caused by collisions and the Doppler effect. In the lower atmosphere (below 20 km) collision broadening prevails caused by the pressure effect. It is, therefore, referred to as pressure broadening. The shape of the spectral

[24]Christian Andreas Doppler, Austrian physicist, 1803–1853.

lines due to collision is given by the Lorentz[25] profile. In the upper atmosphere there is a combination of both pressure broadening and Doppler broadening. In the range between 20 and 50 km or so above ground effective line shapes are related to this combination. The convolution of the Lorentz and Doppler line shapes can be performed by adding the Doppler shift component to the pressure-broadening lines at the respective wavenumbers. The resulting line shape is called the Voigt[26] profile.

4.5 Radiative Transfer

The radiative transfer coins in large part the stratification and thermal structure of the atmosphere. The radiation balance and radiative flux densities vary in time and space (e.g. Fig. 4.10). The total input of solar energy depends on the direction of the rays and length of daylight. This input is greater at the equator where the Sun is nearly overhead than at the poles where the Sun is low above the horizon. The Sun is higher in the sky in summer than winter. The dependence of the optical properties of the atmosphere on the distribution of its constituents, cloudiness, and water vapor, as well as on geographical latitude makes radiative transfer horizontally non-uniform and complex. The heating of the Earth due to the Sun varies with geographical latitude, elevation, and season (Fig. 4.10). These differences in radiation drive the general circulation and local circulation systems (Chap. 7).

In radiative calculation, we usually assume that the radiative properties are a function of height using the height, z, or pressure, p, as coordinates. Radiance is an appropriate variable because the radiance would not change if there were no material in the volume considered. By excluding polarization, four processes can modify the beam of radiation as it travels a distance, ds, through the volume (Fig. 4.21)

- Radiation from the beam can be absorbed (A),
- Radiation can be scattered out of the volume into other directions (B),
- Radiation can be emitted (C),
- Radiation from other directions can be scattered into the beam (D).

These radiation processes have to be considered in the radiative transfer equation. For calculations of spectral radiation transport, the spectral dependency of the extinction coefficient, k, has to be considered for each absorber, where ρ is the density of water vapor, carbon-dioxide, methane, etc. to determine the respective optical path length.

The change of the monochromatic radiance along the path, $\frac{dI_\lambda}{ds}$, can be expressed by

$$\frac{dI_\lambda}{ds} = A + B + C + D \tag{4.75}$$

[25] Hendrik Lorentz, Nobel Price Laureate in 1902 with Pieter Zeeman, Dutch physicist, 1853–1928.
[26] Woldemar Voigt, German physicist, 1850–1919.

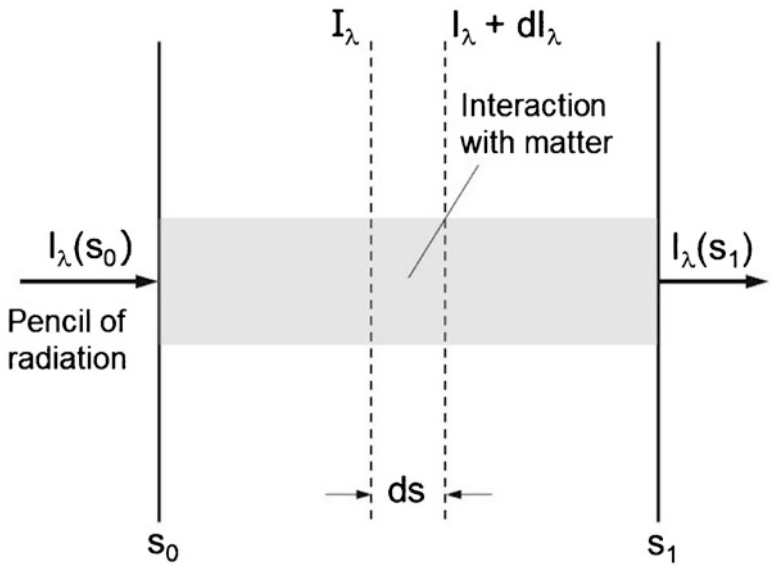

Fig. 4.21 Depletion of the radiant intensity in traversing an extinction medium (Adopted from Liou 2002)

where the letters A to D denote the aforementioned processes. The terms A and B remove radiation from the beam and are called depletion terms. The terms C and D add radiation to the beam and are denoted source terms. The next subsection discusses the general form of the radiative transfer equation (RTE) and its solution.

4.5.1 The Radiative Transfer Equation

The general form of the radiative transfer equation (RTE) reads

$$d I_\lambda = - \rho \, \beta_\lambda \, I_\lambda \, ds \; + \; \rho . \, j_\lambda \, ds \tag{4.76}$$

Here, ρ is the density of air, β_λ is the mass extinction cross section for radiation of the wavelength λ, I_λ is the monochromatic intensity of radiation, j_λ is the source function coefficient for the same wavelength, and ds is the infinitesimal thickness of the layer crossing by the pencil of radiation (Fig. 4.21). Equation (4.76) describes two concurrent processes, namely attenuation of radiation by absorption (A) and single scattering (B) on the one hand and emission of radiation (C) by the constituents of the atmosphere plus multiple scattering of radiation from all other directions into this pencil of radiation (D) on the other hand.

The ratio $J_\lambda = j_\lambda/\beta_\lambda$ is called the **monochromatic source function**. Inserting this source function into Eq. (4.76) yields

$$\frac{1}{\rho\,\beta_\lambda}\,\frac{d\,I_\lambda}{ds} \;=\; -\,I_\lambda \;+\; J_\lambda. \tag{4.77}$$

Introducing the monochromatic optical depth defined by

$$\tau_\lambda\,(s_1,\;s) = \int_s^{s_1} \rho\;\beta_\lambda\;ds \tag{4.78}$$

or

$$d\,\tau_\lambda\,(s_1,\;s) = -\,\rho\;\beta_\lambda\;ds \tag{4.79}$$

and multiplying all terms of Eq. (4.77) by $\exp\,(-\,\tau_\lambda(s_1,\;s))$ provide

$$\exp\,(-\,\tau_\lambda\,(s_1,\;s))\;\frac{d\,I_\lambda}{d\,\tau_\lambda\,(s_1,\;s)} = I_\lambda\;\exp\,(-\,\tau_\lambda\,(s_1,\;s))\;-\;J_\lambda\;\exp\,(-\,\tau_\lambda\,(s_1,\;s))\,. \tag{4.80}$$

Since

$$\frac{d}{d\,\tau_\lambda\,(s_1,\;s)}\;\{I_\lambda\;\exp\,(-\,\tau_\lambda\,(s_1,\;s))\} = \exp\,(-\,\tau_\lambda\,(s_1,\;s))\;\frac{d\,I_\lambda}{d\,\tau_\lambda\,(s_1,\;s)} - I_\lambda\;\exp\,(-\,\tau_\lambda\,(s_1,\;s)) \tag{4.81}$$

we obtain

$$\frac{d}{d\,\tau_\lambda\,(s_1,\;s)}\;\{I_\lambda\;\exp\,(-\,\tau_\lambda\,(s_1,\;s))\} = -\,J_\lambda\;\exp\,(-\,\tau_\lambda\,(s_1,\;s))\,. \tag{4.82}$$

Integration over the layer $s_0 \le s \le s_1$ yields

$$I_\lambda\,(s_1) = I_\lambda\,(s_0)\exp\,(-\tau_\lambda\,(s_1, s_0)) - \int_{s_0}^{s_1} J_\lambda \exp\,(-\tau_\lambda\,(s_1, s))\,d\,\tau_\lambda\,(s_1, s)\,. \tag{4.83}$$

There are two special cases of this solution: (a) the **Beer-Bouguer-Lambert law**, and (b) the solution of the **Schuster-Schwarzschild equation**.

When we presuppose that only extinction due to absorption and/or single scattering exists we obtain the Beer-Bouguer-Lambert law,

$$I_\lambda\,(s_1) = I_\lambda\,(s_0)\;\exp\,(-\,\tau_\lambda\,(s_1,\;s_0))\,. \tag{4.84}$$

Equation (4.84) serves to define the monochromatic transmittance by

$$T_\lambda(s_1, s_0) = \frac{I_\lambda\,(s_1)}{I_\lambda\,(s_0)} = \exp\,(-\,\tau_\lambda\,(s_1,\ s_0)). \tag{4.85}$$

It decreases exponentially with increasing optical depth in an absorbing column of air. The monochromatic absorptance a_λ stands for the fraction of incident radiation absorbed from the beam. Since in the absence of scattering and emission

$$T_\lambda + a_\lambda = 1 \tag{4.86}$$

we obtain for the monochromatic absorptance

$$a_\lambda = 1 - T_\lambda = 1 - \exp\,(-\,\tau_\lambda) \tag{4.87}$$

i.e. monochromatic absorptance exponentially may tend unity with increasing path length through an absorbing column of air.

An atmospheric layer is referred to as **optically thick** when the total optical path through that layer is greater than 1 and **optically thin** otherwise. In an optically thick layer, a photon has a great probability to be scattered or absorbed, while it has a great probability to pass an optically thin layer without being absorbed or scattered. In absence of emission, the spectral radiance decreases exponentially by a factor of e over a given unit optical path.

The solution of the Schuster-Schwarzschild equation can be derived by assuming a non-scattering medium and local thermodynamic equilibrium (LTE) so that the source function in Eq. (4.77) may be replaced by the Planck function given by Eq. (4.44), where now β_λ becomes the mass absorption coefficient. Inserting the Planck function (4.44) into Eq. (4.83) yields

$$\begin{aligned} I_\lambda\,(s_1) = {} & I_\lambda\,(s_0)\ \exp\,(-\,\tau_\lambda\,(s_1,\ s_0)) \\ & - \int_{s_0}^{s_1} B_\lambda\,(T\,(s))\ \exp\,(-\,\tau_\lambda\,(s_1,\ s))\ d\,\tau_\lambda\,(s_1,\ s)\,. \end{aligned} \tag{4.88}$$

This equation seems to be well appropriate when the infrared radiation emitted by both the Earth and the constituents of the atmosphere is considered. Obviously, the first term of the right-hand side of Eq. (4.88) describes the absorption of infrared radiation along the path $[s_0,\ s_1]$ and the second term the emission of infrared radiation along the path $[s_0,\ s_1]$ performed simultaneously.

4.5.2 Interaction Radiation-Atmosphere

In the absence of scattering and emission, we found that $T_\lambda + a_\lambda = 1$ (Eq. (4.86)). In the atmosphere, however, radiation is not only absorbed, but also dispersed by scattering. Some of the scattered radiation is directed backward. A portion of

solar radiation, for instance, is backscattered to space. The remainder is scattered forward as the light visible from the portion of the sky away from the solar disk. In either case, the energy that is scattered is not absorbed by the atmosphere and does not contribute to its internal energy. The remaining non-scattered, non-absorbed radiation passes through the atmosphere without modification and reaches the surface as direct radiation. At the surface, some of the radiant energy is absorbed, while another part is reflected to the atmosphere. This part does not contribute to the heating of the planet. Absorption and transmission of solar radiation affect the distribution of temperature throughout the atmosphere.

We already found that the monochromatic transmittance fulfills the condition: $0 \leq T_\lambda \leq 1$ (Eq. (4.85)). This means when $I_{\lambda,a}$ and $I_{\lambda,r}$ are the portions of the monochromatic intensity that are absorbed (subscript a) and reflected (or back-scattered; subscript r) on the path through the layer $[s_0, s_1]$ of the atmosphere, we can define the monochromatic absorptance and the monochromatic reflectance by

$$a_\lambda = \frac{I_{\lambda,a}}{I_\lambda(s_0)} \tag{4.89}$$

and

$$\rho_\lambda = \frac{I_{\lambda,r}}{I_\lambda(s_0)}. \tag{4.90}$$

Since

$$I_\lambda(s_0) = I_\lambda(s_1) + I_{\lambda,a} + I_{\lambda,r} \tag{4.91}$$

we may write

$$T_\lambda + a_\lambda + \rho_\lambda = 1 \tag{4.92}$$

where T_λ, a_λ, and ρ_λ are transmittance, absorptance, and reflectance, respectively. This partitioning can differ from wavelength to wavelength. The various colors of nature are a consequence of this fact.

The reflectance can be decomposed into that, which by scattering (multiple reflections) is transmitted into forward direction, and that, through scattering propagating at an angle that differs from that of the incoming radiation.

Scattering plays only a minor role in the infrared range so that $T_\lambda + a_\lambda = 1$ (Eq. (4.86)) is acceptable. In accord with Kirchhoff's law, we can replace the monochromatic absorptance by the monochromatic emittance. However, we have to incorporate scattering of infrared radiation in case of ice clouds.

We can describe the radiative properties of a medium in integral manner by the coefficients α, ϵ, T, and ρ that range between 0 and 1. Equation (4.65) already defined the mean value of the emittance. We can define the mean transmittance and mean reflectance in a similar manner. Scattering cannot be quantified by an integral key quantity.

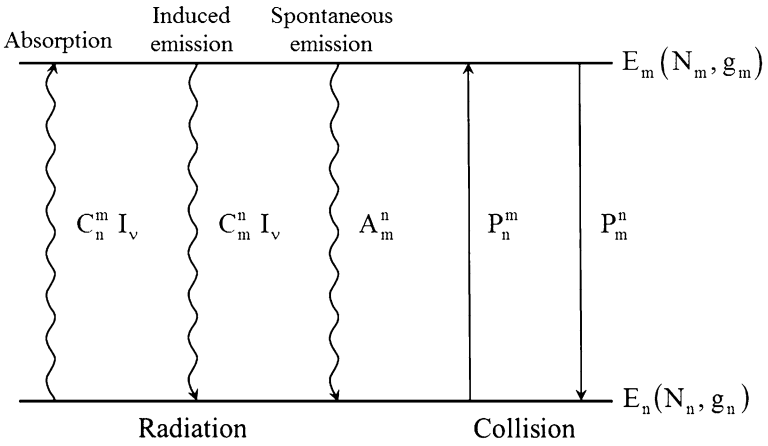

Fig. 4.22 Sketch of radiative and collisional transitions connecting two energy states E_n and E_m

4.5.3 The Breakdown of Thermodynamic Equilibrium

The use of Planck's radiation law in the RTE (Eq. (4.88)) is not a matter of course, but it may be justified in accord with Einstein's[27] paper on the quantum theory of radiation published in 1917. Its use, of course, requires the existence of thermal equilibrium. Such a thermal equilibrium does not generally exist in the atmosphere. Thus, the LTE mentioned before is assumed. Based on Milne's[28] work on the effect of collisions between molecules and atoms, ions, electrons, etc. on monochromatic radiative equilibrium, we discuss under which conditions the assumption of an LTE is reasonable.

In his paper, Einstein presented a very instructive and simplified derivation of Planck's radiation law in which he introduced the important concept concerning the probability of the emission and absorption of radiation by molecules. He not only presupposed absorption of radiative intensity, I_ν, of an isotropic radiation field by a Planck resonator leading to a higher energy state, E_m, that differs from its former lower energy state, E_n, just by a photon, $E_m - E_n = h\,\nu$ (where ν is the frequency of the radiation emitted when the oscillator goes from E_m to E_n and it is also the frequency of radiation absorbed by an oscillator when it raised from E_n to E_m), but also so-called induced emission stimulated by the radiation field and spontaneous emission because a Planck resonator emits in accord with Hertz energy independent of whether it is excited by an external field or not. Both forms of emission lead to the transition of the molecule from a higher to a lower energy state (Fig. 4.22). The emitted radiation is also considered as isotropic radiation.

[27] Albert Einstein, German-American physicist, 1879–1955.

[28] Edward Arthur Milne, British astrophysicist, 1896–1950.

Absorption and both types of emission are related to certain probabilities that an oscillator changes its energy state from E_n to E_m or vice versa in the same unit of time, dt, expressed by $dW_{se} = A_m^n\ dt$ (spontaneous emission), $dW_a = C_n^m\ I_\nu\ dt$ (absorption), and $dW_{ie} = C_m^n\ I_\nu\ dt$ (induced emission), where A_m^n, C_n^m, and C_m^n are the probability coefficients, today called the Einstein coefficients. Thus, the probability for the transition of a molecule from E_m to E_n is given by $dW_e = dW_{se} + dW_{ie} = \left(A_m^n + C_m^n\ I_\nu\right) dt$. Note that Einstein and others considered the density of monochromatic radiation, $\rho_\nu = 4\ \pi\ I_\nu/c$, but not the monochromatic intensity. This means that the coefficients C_n^m and C_m^n are related to the true Einstein coefficients B_n^m and B_m^n by $C_m^n = (4\ \pi/c)\ B_m^n$ and $C_n^m = (4\ \pi/c)\ B_n^m$, respectively. The Einstein coefficients are considered as atomic constants that are independent of the temperature.

When we assume that the radiation field is in equilibrium with the oscillators, the number of molecules, $N_m^n = N_m\ dW_e$, going from the upper energy level, E_m, to the lower energy level, E_n, during the time interval dt will be balanced by the number of molecules, $N_n^m = N_n\ dW_a$, raising from level E_n to level E_m during the same time interval, i.e., $N_m\ dW_e = N_n\ dW_a$, where N_j, $j = m,\ n$, is the number of oscillators that occupies the energy level E_j. Thus, we have

$$N_m^n = N_m\ \left(A_m^n + C_m^n I_\nu\right) \tag{4.93}$$

$$N_n^m\ =\ N_n\ C_n^m\ I_\nu \tag{4.94}$$

and

$$N_n\ C_n^m\ I_\nu\ =\ N_m\ \left(A_m^n\ +\ C_m^n\ I_\nu\right). \tag{4.95}$$

If molecules of this kind form a gas at the temperature T, the relative occurrence of these energy states $W_j = W\left(E_j\right)$, $j = m,\ n$, is given by the formula

$$\frac{N_j}{N} = W_j = W\left(E_j\right) = \chi\ g_j\ \exp\left(-\frac{E_j}{k\ T}\right) \tag{4.96}$$

that corresponds the canonical distribution of states in statistical mechanics. Here, N is the total number of oscillators given by

$$N = \sum_{j=0}^{\infty} N_n = \sum_{j=0}^{\infty} N\ W_j = N\ \underbrace{\sum_{n=0}^{\infty} \chi\ g_j\ \exp\left(-\frac{E_j}{k\ T}\right)}_{=1} \tag{4.97}$$

and χ is a constant given by

$$\chi = \frac{1}{\sum\limits_{n=0}^{\infty} g_j\ \exp\left(-\frac{E_j}{k\ T}\right)}. \tag{4.98}$$

Furthermore, g_j is a temperature-independent quantity which is characteristic for the molecule and its j^{th} quantum. It can be called a statistical "weight" of this state. Because of Eq. (4.98), it is related to N_j by

$$\frac{N_j}{N} = \frac{g_j \ \exp\left(-\frac{E_j}{k\,T}\right)}{\sum\limits_{j=0}^{\infty} g_j \ \exp\left(-\frac{E_j}{k\,T}\right)}. \tag{4.99}$$

Einstein pointed out that the exchange of energy between radiation and molecules according to the statistical laws described here by Eqs. (4.93)–(4.95) is necessary and sufficient not to perturb the canonical distribution of molecules as expressed by Eq. (4.96). This equation can be derived either from Boltzmann's principle or by purely thermodynamic means. It may be considered as the greatest generalization of Maxwell's velocity distribution law. Thus, we obtain

$$g_n \ \exp\left(-\frac{E_n}{k\,T}\right) \ C_n^m \ I_\nu = g_m \ \exp\left(-\frac{E_m}{k\,T}\right) \ \left(A_m^n + C_m^n \ I_\nu\right). \tag{4.100}$$

Furthermore, if I_ν together with T will increase to infinity, one obtains

$$g_n \ C_n^m = g_m \ C_m^n \tag{4.101}$$

and, hence,

$$I_\nu = \frac{A_m^n}{C_m^n} \ \frac{1}{\exp\left(\frac{E_m - E_n}{k\,T}\right) - 1} = \frac{\sigma}{\exp\left(\frac{h\,\nu}{k\,T}\right) - 1} \tag{4.102}$$

where, by comparing with Eq. (4.40), $\sigma = A_m^n / C_m^n = 2\ h\ \nu^3 / c^2$. Equation (4.102) reflects Planck's blackbody radiation law, i.e., $B_\nu\,(T) = I_\nu$. In accord with Wien's displacement law $\rho_\nu = \nu^3\ f\,(\nu/T)$, Einstein already pointed out that $A_m^n / C_m^n = \alpha\ \nu^3$, where $\alpha = 2\ h/c^2$, must be an universal constant. Ten years later, Dirac[29] derived correct expressions for the Einstein coefficients on the basis of his quantum theory of the emission and absorption of radiation. Fowler and Milne pointed out that modern formulations of the principle of detailed balancing really all derive their inspiration from Einstein's classical paper written in 1917. Tolman[30] called it the principle of microscopic reversibility. He stated that Einstein used this principle of microscopic reversibility without, however, making any explicit statement of it. This is, indeed, true because Einstein used the relationship (4.101) but not $C_n^m = C_m^n$ that can be derived on the basis of this principle of microscopic reversibility.

[29] Paul Adrien Maurice Dirac, British physicist, 1902–1984.

[30] Richard Chace Tolman, American physical chemist, 1881–1948.

Milne eventually argued that molecules can also be excited by collision with any atom, ion, or electron present in the assembly denoted as collision of the first kind (or inelastic collision), where the energy of excitation, $h\ \nu$, is derived from the kinetic energy of the colliding particles, and de-excited by collision of the second kind (or super-elastic collision). The colliding particles rebound with additional kinetic energy $h\ \nu$. The collision of first kind plays an important role in the Franck-Hertz experiment. The collision of second kind is related to Klein and Rosseland. These authors also coined the notions collision of first kind and collision of second kind. Milne, therefore, not only considered radiative transition, but also collisional transition

In case of thermodynamic equilibrium at temperature T, Eq. (4.96) leads to

$$\frac{N_m}{N_n} = \frac{g_m}{g_n}\ \exp\left(-\frac{E_m - E_n}{k\ T}\right) = \frac{g_m}{g_n}\ \exp\left(-\frac{h\ \nu}{k\ T}\right). \tag{4.103}$$

Let P_n^m represent the probability of the transition by collision per unit of time from the lower level of energy, E_n, to the upper level of energy, E_m, and P_m^n represent that from E_m to E_n. The number of molecules per unit time, N_m^n, going from E_m to E_n is then given by $N_m^n = P_m^n\ N_m$, and that, raising from E_n to E_m is given by $N_n^m = P_n^m\ N_n$. According to the principle of detailed balancing, if the assembly were in thermodynamic equilibrium we have super-elastic collisions exactly balancing inelastic collisions [41], i.e. $N_n^m = N_m^n$. Thus, in thermodynamic equilibrium at temperature T we have

$$\frac{P_n^m}{P_m^n} = \frac{N_m}{N_n} = \frac{g_m}{g_n}\ \exp\left(-\frac{h\ \nu}{k\ T}\right) \tag{4.104}$$

where the ratio P_n^m/P_m^n is independent of the density. According to Milne, this equation must subsist in virtue of the velocity distribution of the particles present. Although it has been proved in the first instance only for thermodynamic equilibrium, it must also hold whenever the velocity-distribution may be described by a parameter-temperature T.

Milne considered the transfer of radiant energy through the system, a thin slab of the area and the thickness. The number of quanta of monochromatic radiation at frequency entering the slab in directions inclined within the solid angle $d\Omega$ normal to the slab is given by

$$\frac{I_\nu\ \Delta\nu\ d\Omega\ dA}{h\ \nu}. \tag{4.105}$$

Furthermore, the number of quanta leaving the slab in the same direction is given by

$$\frac{(I_\nu + d\,I_\nu)\ \Delta\nu\ d\Omega\ dA}{h\ \nu}. \tag{4.106}$$

He pointed out that "the excess of the latter over the former, in the steady state, must be equal to the excess of emissions of ν-quanta from the matter inside the slab in

directions included in $d\Omega$ over the number of similar absorptions." The number of such emissions is given by

$$N_m \, ds \, dA \, \left(A_m^n + C_m^n \, I_\nu\right) \frac{d\Omega}{4\,\pi} \tag{4.107}$$

and the number of such absorptions is given by

$$N_n \, ds \, dA \, C_n^m \, I_\nu \, \frac{d\Omega}{4\,\pi}. \tag{4.108}$$

Combining the expressions (4.105)–(4.108) leads to

$$\begin{aligned} \frac{d\,I_\nu \, \Delta\nu}{h \, \nu \, ds} &= \frac{1}{4\,\pi} \, \left(N_m \, \left(A_m^n + C_m^n \, I_\nu\right) - N_n \, C_n^m \, I_\nu\right) \\ &= \frac{C_n^m}{4\,\pi} \, \left(\frac{g_n}{g_m} \, N_m \, (\sigma + I_\nu) - N_n \, I_\nu\right) \end{aligned} \tag{4.109}$$

where we used $\sigma = A_m^n / C_m^n$ and Eq. (4.101).

Let $\alpha\,(\nu)$ be the atomic absorption coefficient for an atom in the state n, then we have approximately

$$\int\limits_{\Delta\nu} \alpha\,(\nu) \; d\nu = \frac{C_n^m \, h \, \nu}{4\,\pi}. \tag{4.110}$$

This integral characterizes the narrow range of frequencies within which the atom can absorb. If we assume for simplification a uniform absorption within the interval, we will obtain

$$\alpha_\nu \, \Delta\nu = \frac{C_n^m \, h \, \nu}{4\,\pi} \tag{4.111}$$

where α_ν is the mean atomic absorption coefficient in the frequency interval $[\nu - 1/2 \, \Delta\nu, \; \nu + 1/2 \, \Delta\nu]$. Inserting this formula into Eq. (4.109) yields

$$\frac{1}{\alpha_\nu} \, \frac{d\,I_\nu}{ds} = - \, N_n \, I_\nu + \frac{g_n}{g_m} \, N_m \, (\sigma + I_\nu)\,. \tag{4.112}$$

When we assume a strict thermodynamic equilibrium, we obtain with

$$\rho_a \, \beta_\nu = \alpha_\nu \, \left(N_n - N_m \frac{g_n}{g_m}\right) \tag{4.113}$$

$$\rho_a \, \beta_\nu \, B_\nu\,(T) = \alpha_\nu \, N_m \frac{g_n}{g_m} \, \sigma \tag{4.114}$$

and, hence,

$$B_\nu(T) = \frac{N_m \frac{g_n}{g_m}}{N_n - N_m \frac{g_n}{g_m}} \sigma = \frac{\sigma}{\frac{g_m}{g_n}\frac{N_n}{N_m} - 1} = \frac{\sigma}{\exp\left(\frac{h\nu}{kT}\right) - 1} \tag{4.115}$$

(where the relationship (4.104) for thermodynamic equilibrium at temperature T has been used) the following expression:

$$\frac{1}{\rho_a \beta_\nu} \frac{dI_\nu}{ds} = -I_\nu + B_\nu(T). \tag{4.116}$$

Here, ρ_a is the air density, and β_ν is the absorption coefficient. Equation (4.116) is called the radiative transfer equation for a non-scattering medium under the condition of the LTE at temperature T.

By including collisional transition, Milne obtained

$$\frac{N_m \frac{g_n}{g_m}}{N_n - N_m \frac{g_n}{g_m}} = \frac{\frac{1}{4\pi} \int\limits_\Omega I_\nu \, d\Omega + \varepsilon}{\sigma + \varepsilon \left(\exp\left(\frac{h\nu}{kT}\right) - 1\right)} \tag{4.117}$$

where the ratio of the probabilities of raising from the lower level E_n to the upper level E_m by radiative and collisional transition is given by

$$\varepsilon = \frac{c}{4\pi} \frac{P_n^m}{B_n^m} = \frac{P_n^m}{C_n^m}. \tag{4.118}$$

Equation (4.117) is considered to estimate the breakdown of the LTE. Combining Eqs. (4.112) and (4.117) yields then

$$\frac{1}{\alpha_\nu} \frac{dI_\nu}{ds} = \left(N_n - N_m \frac{g_n}{g_m}\right) \left\{ -I_\nu + \frac{\frac{1}{4\pi} \int\limits_\Omega I_\nu \, d\Omega + \varepsilon}{1 + \frac{\varepsilon}{\sigma} \left(\exp\left(\frac{h\nu}{kT}\right) - 1\right)} \right\}. \tag{4.119}$$

Using Eq. (4.113) and, in addition,

$$\eta = \frac{\varepsilon}{B_\nu(T)} = \frac{\varepsilon}{\sigma} \left(\exp\left(\frac{h\nu}{kT}\right) - 1\right) \tag{4.120}$$

leads to

$$\begin{aligned} \frac{1}{\rho_a \beta_\nu} \frac{dI_\nu}{ds} &= -I_\nu + \frac{\frac{1}{4\pi} \int\limits_\Omega I_\nu \, d\Omega + \eta B_\nu(T)}{1 + \eta} \\ &= -I_\nu + \frac{\eta}{1+\eta} B_\nu(T) + \frac{1}{4\pi (1+\eta)} \int\limits_\Omega I_\nu \, d\Omega \end{aligned} \tag{4.121}$$

where in this equation, T is the parameter-temperature fixing the velocity distribution. In accord with Milne, this is the form taken by the RTE when the existence of a stationary state is taken into account.

For ε, we have seen that approximately $\varepsilon \propto \rho_a \exp(-h\nu/(kT))$. Hence, as already argued by Milne, except for very low temperatures, η is approximately independent of temperature and proportional to the total density. When Eq. (4.121) is applied to the Earth's atmosphere, we have to recognize that η is close to zero at the TOA and increases towards the Earth's surface. For $\eta \to 0$, Eq. (4.121) tends to the form

$$\frac{1}{\rho_a \beta_\nu} \frac{dI_\nu}{ds} = -I_\nu + \frac{1}{4\pi} \int_\Omega I_\nu \, d\Omega \tag{4.122}$$

called the RTE for monochromatic radiative equilibrium. This means that the absorbed radiation is re-emitted uniformly in direction. For $\eta \to \infty$, we obtain

$$\frac{1}{\rho_a \beta_\nu} \frac{dI_\nu}{ds} = -I_\nu + B_\nu(T). \tag{4.123}$$

This equation is identical with Eq. (4.116), the RTE for local thermodynamic equilibrium at temperature T. As the collisional transition depends on pressure, there is a level within the atmosphere (60 km or so above the Earth's surface) below which the LTE condition is appropriate, and, hence, Planck's radiation law is an acceptable approximation to describe the transition between neighboring energy levels. For higher levels the use of Planck's radiation law is not recommended because the LTE condition is not fulfilled.

4.5.4 Solution for a Plane-parallel Non-scattering Atmosphere

Let us consider a plane-parallel atmosphere, where the vertical coordinate, z, is parallel to the gradient of the density. Variation of the intensity and the atmospheric quantities like temperature, pressure, and mass fractions are only permitted in the vertical direction. Then the RTE reads

$$\frac{\cos\theta}{\rho \beta_\lambda} \frac{dI_\lambda(z, \theta, \phi)}{dz} = -I_\lambda(z, \theta, \phi) + J_\lambda(z, \theta, \phi). \tag{4.124}$$

Here, θ is the zenith angle and ϕ is the azimuthal angle. Defining the corresponding monochromatic optical depth by

$$\tau_\lambda(z) = \int_z^\infty \rho(z') \beta_\lambda \, dz' \tag{4.125}$$

and, hence, the differential monochromatic optical depth by

$$d\tau_\lambda(z) = -\rho(z)\,\beta_\lambda\,dz \tag{4.126}$$

yields

$$\mu\,\frac{dI_\lambda(\tau_\lambda,\,\mu,\,\phi)}{d\tau_\lambda} = I_\lambda(\tau_\lambda,\,\mu,\,\phi) - J_\lambda(\tau_\lambda,\,\mu,\,\phi) \tag{4.127}$$

where $\mu = \cos\theta$.

A formal solution of Eq. (4.127) can be obtained by considering the upward ($1 \geq \mu > 0$) and downward ($-1 \leq \mu < 0$) directed monochromatic intensities separately. For $1 \geq \mu > 0$, we obtain

$$I_\lambda^{\uparrow}(\tau_\lambda,\,\mu,\,\phi) = I_\lambda^{\uparrow}\left(\tau_\lambda^*,\,\mu,\,\phi\right)\exp\left(-\frac{\tau_\lambda^* - \tau_\lambda}{\mu}\right) + \int_{\tau_\lambda}^{\tau_\lambda^*}\frac{J_\lambda\left(\tau_\lambda',\,\mu,\,\phi\right)}{\mu}\exp\left(-\frac{\tau_\lambda' - \tau_\lambda}{\mu}\right)d\tau_\lambda'. \tag{4.128}$$

The solution for the downward directed intensities ($-1 \leq \mu < 0$) reads

$$I_\lambda^{\downarrow}(\tau_\lambda,\,-\mu,\,\phi) = I_\lambda^{\downarrow}(0,\,-\mu,\,\phi)\exp\left(-\frac{\tau_\lambda}{\mu}\right) + \int_0^{\tau_\lambda}\frac{J_\lambda\left(\tau_\lambda',\,-\mu,\,\phi\right)}{\mu}\exp\left(-\frac{\tau_\lambda - \tau_\lambda'}{\mu}\right)d\tau_\lambda'. \tag{4.129}$$

Now, let us consider the transfer of infrared radiation from the Earth's surface to the TOA and vice versa. If we assume that the monochromatic intensity at the Earth's surface, $I_\lambda^{\uparrow}\left(\tau_\lambda^*,\,\mu,\,\phi\right)$, can be expressed by

$$I_\lambda^{\uparrow}\left(\tau_\lambda^*,\,\mu,\,\phi\right) = B_\lambda\left(T\left(\tau_\lambda^*\right),\,\mu,\,\phi\right) \tag{4.130}$$

and that the monochromatic intensity at the TOA, $I_\lambda^{\downarrow}(0,\,-\mu,\,\phi)$, is equal to zero, we will obtain

$$I_\lambda^{\uparrow}(\tau_\lambda,\,\mu,\,\phi) = B_\lambda\left(T\left(\tau_\lambda^*\right),\,\mu,\,\phi\right)\exp\left(-\frac{\tau_\lambda^* - \tau_\lambda}{\mu}\right) + \int_{\tau_\lambda}^{\tau_\lambda^*}\frac{J_\lambda\left(\tau_\lambda',\,\mu,\,\phi\right)}{\mu}\exp\left(-\frac{\tau_\lambda' - \tau_\lambda}{\mu}\right)d\tau_\lambda' \tag{4.131}$$

and

$$I_\lambda^{\downarrow}(\tau_\lambda, -\mu, \phi) = \int_0^{\tau_\lambda} \frac{J_\lambda\left(\tau_\lambda', -\mu, \phi\right)}{\mu} \exp\left(-\frac{\tau_\lambda - \tau_\lambda'}{\mu}\right) d\tau_\lambda'. \tag{4.132}$$

Let us define the monochromatic transmittance by

$$T_\lambda\left(\frac{\tau_\lambda}{\mu}\right) = \exp\left(-\frac{\tau_\lambda}{\mu}\right). \tag{4.133}$$

The derivative of the monochromatic transmittance with respect to the monochromatic optical depth reads

$$\frac{d}{d\tau_\lambda} T_\lambda\left(\frac{\tau_\lambda}{\mu}\right) = -\frac{1}{\mu} \exp\left(-\frac{\tau_\lambda}{\mu}\right). \tag{4.134}$$

Thus, we obtain

$$\begin{aligned} I_\lambda^{\uparrow}(\tau_\lambda, \mu, \phi) = {} & B_\lambda\left(T\left(\tau_\lambda^*\right), \mu, \phi\right) T_\lambda\left(\frac{\tau_\lambda^* - \tau_\lambda}{\mu}\right) \\ & - \int_{\tau_\lambda}^{\tau_\lambda^*} J_\lambda\left(\tau_\lambda', \mu, \phi\right) \frac{d}{d\tau_\lambda'} T_\lambda\left(\frac{\tau_\lambda' - \tau_\lambda}{\mu}\right) d\tau_\lambda' \end{aligned} \tag{4.135}$$

and

$$I_\lambda^{\downarrow}(\tau_\lambda, -\mu, \phi) = \int_0^{\tau_\lambda} J_\lambda\left(\tau_\lambda', -\mu, \phi\right) \frac{d}{d\tau_\lambda'} T_\lambda\left(\frac{\tau_\lambda - \tau_\lambda'}{\mu}\right) d\tau_\lambda'. \tag{4.136}$$

The corresponding monochromatic flux densities read

$$F_\lambda^{\uparrow\downarrow} = \int_0^{2\pi} d\phi \int_0^1 I_\lambda^{\uparrow\downarrow}(\tau_\lambda, \mu, \phi)\, \mu\, d\mu = 2\pi \int_0^1 I_\lambda^{\uparrow\downarrow}(\tau_\lambda, \mu, \phi)\, \mu\, d\mu. \tag{4.137}$$

When we define the slab (diffuse) transmittance by

$$T_\lambda^f(\tau_\lambda) = 2 \int_0^1 T_\lambda\left(\frac{\tau_\lambda}{\mu}\right) \mu\, d\mu \tag{4.138}$$

we can write

$$F_\lambda^{\uparrow}(\tau_\lambda) = \pi\ B_\lambda\left(T\left(\tau_\lambda^*\right)\right)\ T_\lambda^f\left(\tau_\lambda^* - \tau_\lambda\right) - \pi \int_{\tau_\lambda}^{\tau_\lambda^*} J_\lambda\left(\tau_\lambda^{'}\right)\ \frac{d}{d\,\tau_\lambda^{'}} T_\lambda^f\left(\tau_\lambda^{'} - \tau_\lambda\right)\ d\,\tau_\lambda^{'} \tag{4.139}$$

and

$$F_\lambda^{\downarrow}(\tau_\lambda)\ =\ \pi \int_0^{\tau_\lambda} J_\lambda\left(\tau_\lambda^{'}\right)\ \frac{d}{d\,\tau_\lambda^{'}} T_\lambda^f\left(\tau_\lambda\ -\ \tau_\lambda^{'}\right) d\,\tau_\lambda^{'}. \tag{4.140}$$

Finally, we obtain the total upward and downward directed flux densities by integrating over the IR spectrum formally expressed by

$$F^{\uparrow\downarrow}\ =\ \int_0^{\infty} F_\lambda^{\uparrow\downarrow}\, d\lambda. \tag{4.141}$$

The infrared cooling is then given by

$$c_p\ \rho\left(\frac{\partial T}{\partial t}\right)_{IR}\ =\ -\ \frac{\partial F\,(z)}{\partial z} \tag{4.142}$$

where the IR flux density at a given height is defined by

$$F\,(z)\ =\ F^{\uparrow}(z)\ -\ F^{\downarrow}(z)\,. \tag{4.143}$$

For the Earth's surface, i.e. $\tau_\lambda\ =\ \tau_\lambda^*$, we obtain

$$F^{\uparrow}\left(\tau_\lambda^*\right)\ =\ \pi\ B\left(T\left(\tau_\lambda^*\right)\right)\ =\ \pi\ B\,(T_s) \tag{4.144}$$

and

$$F^{\downarrow}\left(\tau_\lambda^*\right)\ =\ \pi \int_0^{\infty} d\lambda \int_0^{\tau_\lambda^*} J_\lambda\left(\tau_\lambda^{'}\right)\ \frac{d}{d\,\tau_\lambda^{'}} T_\lambda^f\left(\tau_\lambda^*\ -\ \tau_\lambda^{'}\right) d\,\tau_\lambda^{'}. \tag{4.145}$$

Here, T_s is the surface temperature. Note that the source function may be substituted by Planck's function if the LTE condition is fulfilled.

4.6 Global Radiation Budget

Generally, **net radiation** is the difference between the absorbed radiation and the emitted radiation. The absorbed solar radiation is given by the incoming solar radiation minus its reflected portion, where the latter is expressed as a percentage of the former using the albedo. The net radiation at a given location or globally averaged for a period shorter than 1 year can be positive or negative.[31]

It is assumed that the global annual net radiation at the TOA is equal to zero because the solar radiation absorbed by the entire Earth-atmosphere system is usually balanced by the infrared radiation emitted to space (Fig. 4.23) expressed by

$$(1 - \alpha_E)\,\frac{S}{4} - R_{L,TOA} = 0. \tag{4.146}$$

The quantity $R_{L,TOA}$ comprises the infrared radiation emitted by atmospheric constituents, $R_{L,a}\uparrow$, and by the Earth's surface (strictly spoken by the layers of water, soil, ice, and vegetation adjacent to the Earth's surface), $T_a\ R_L\uparrow$, on global average, to space, i.e.

$$R_{L,TOA} = R_{L,a}\uparrow + T_a\ R_L\uparrow \tag{4.147}$$

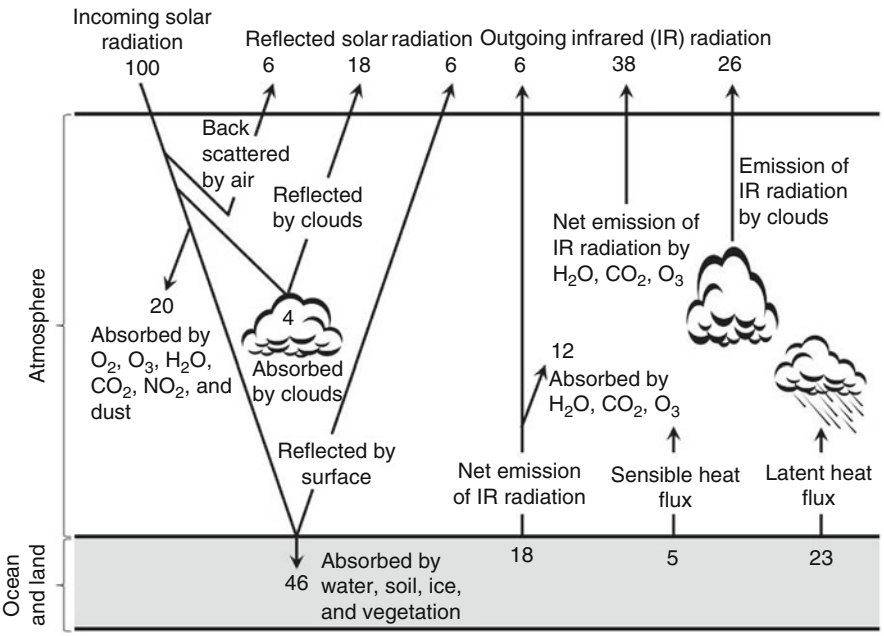

Fig. 4.23 Sketch of the global energy balance

[31] The reader is referred, for instance, to the textbook of Kidder and Vonder Haar (1995).

where T_a is the transmittance of the atmosphere in the infrared range. The quantity α_E is called the **planetary albedo**.

At the Earth's surface, the global annual net radiation is negative because a huge portion of the solar radiation absorbed by the Earth's surface is converted into heat and eventually transferred to the atmosphere in form of the flux densities of sensible (H) and latent heat (E), respectively. According to Fig. 4.23, the sum of these flux densities is notably larger than the net radiation in the infrared range approximated by $\Delta R_L = R_L \uparrow - \epsilon_E \; R_L \downarrow$, where $R_L \downarrow$ is the down-welling infrared radiation, and ϵ_E may be interpreted as a **planetary emittance**.

4.6.1 Global Shortwave Radiation Budget

The global shortwave radiation cascade describes the relative amounts of shortwave radiation partitioned to various processes as its travels through the atmosphere. Assuming a total of 100 units[32] available at the TOA (i.e. the incoming solar radiation), where these 100 units amount to $S/4 = 340\,\mathrm{W\,m^{-2}}$, about 20 units are absorbed by dust and gases like O_2, O_3, H_2O, CO_2, and NO_2, i.e. these units of solar radiation are converted into heat energy and long-wave radiation. Herein, absorption makes up about 2 and 18 units in the stratosphere and troposphere, respectively. In the stratosphere, absorption results mainly from ozone (Chaps. 1 and 5). In the troposphere, also clouds are notable absorbers (4 units). About 22 units of the incoming solar radiation are absorbed at the Earth's surface as direct insolation, and about 24 units of the incoming solar radiation are forward scattered in the atmosphere by constituents and clouds and subsequently absorbed at the surface as diffused insolation. This means that the layers of water, soil, snow, ice, and vegetation adjacent to the Earth's surface absorb about 46 units of the incoming solar radiation. Consequently, the entire Earth-atmosphere system absorbs 70 units.

About six units of the incoming solar radiation are lost to space due to backscattering by air. Clouds reflect about 18 units, and the Earth's surface reflects 6 units of the incoming solar radiation to space. These 30 units of solar radiation do not contribute to the energetics of the Earth-atmosphere system. The average **Earth albedo** of $\alpha_E = 0.3$ (i.e. the aforementioned 30 units) characterizes the combined effect of all of these radiative losses in the solar range. Similar to this planetary albedo, we may define a **planetary absorptance** of the entire atmosphere in the solar range denoted as A_a. Thus, the solar radiation absorbed at the Earth's surface is given by

$$R_S \downarrow = (1 - \alpha_E - A_a)\,\frac{S}{4} = (100 - 30 - 24)\ \text{units} = 46\ \text{units}. \tag{4.148}$$

[32]Be aware of the fact that the following values of the units slightly vary from author to author. These values just intend to assess the processes relative to each other.

4.6.2 Global Long-wave Radiation Budget

The partitioning of energy leaving the Earth's surface requires the global long-wave or infrared radiation budget. Three different processes play a role in this partitioning of energy.

About 5 units leave the surface as sensible heat, i.e. they are transferred to the atmosphere by conduction and convection characterized by the sensible heat flux density, H. The evaporation of water, sublimation and melting of snow and/or ice at the Earth's surface provide about 23 units of energy to the atmosphere as latent heat characterized by the latent heat flux density, E. About 18 units are transferred to the atmosphere by the net radiation in the infrared range, ΔR_L, where about 12 units are absorbed by gases like H_2O, CO_2, and O_3 and clouds and converted into heat or energy and finally into the emission of infrared radiation in all directions. The remaining part of six units is directly emitted to space. Thus, the global energy budget at the Earth's surface can by quantified by

$$(1 - \alpha_E - A_a)\frac{S}{4} - H - E - \Delta R_L = (46 - 5 - 23 - 18)\,units = 0. \quad (4.149)$$

Combining Eqs. (4.146) and (4.149) yields

$$R_{L,TOA} = A_a\frac{S}{4} + H + E + \Delta R_L = (24 + 5 + 23 + 18)\,units = 70\,units. \quad (4.150)$$

This means that the solar energy directly transferred to the atmosphere by absorption and – via the Earth's surface – indirectly transferred to the atmosphere by the flux densities of sensible and latent heat and the net radiation in the infrared range is emitted to space. Note that none of the globally averaged energy flux densities depends on globally averaged temperatures for the Earth's surface and the entire atmosphere.

4.6.3 Energy Budget at the Land Surface

Planet Earth has a variety of different surface types. They behave differently because of their various hydrological and radiative properties. The albedo and emittance depend on soil, vegetation type and coverage and snow/ice age and coverage (Tables 4.5 and 4.6). The following subsection exemplarily discusses the energy and water budget equations for an area partly covered by vegetation and a closed snow-cover.

4.6.3.1 Soil-Vegetation System

To determine the exchange of energy and matter between the vegetation, soil and atmosphere we have to consider that the foliage affects soil temperature by shading

parts of the ground. Even when vegetation seems to cover the entire surface, parts of bare soil may exist. The shaded fraction, called a **shielding factor**, σ_f, is associated with the degree to which foliage prevents shortwave radiation from reaching the ground (Fig. 5.6; Chap. 5).

The temperature and moisture at the surfaces of foliage and soil differ because of their different radiative and hydrological behavior.[33]

The energy- and water-budget equations of a surface covered by both vegetation and bare ground are coupled. The energy and water budgets read

$$R_{sf}\downarrow - R_{sf}\uparrow + R_{lf}\downarrow - R_{lf}\uparrow + R_{sg}\uparrow - R_{sg}\downarrow - H_f - L_v E_f = 0\,, \quad (4.151)$$

$$R_{sg}\downarrow - R_{sg}\uparrow + R_{lg}\downarrow - R_{lg}\uparrow - H_g - L_v E_g + G_g = 0\,, \quad (4.152)$$

$$S_F + W_S - E_g = 0\,, \quad (4.153)$$

where $R_{sf}\downarrow$, $R_{sf}\uparrow$, $R_{lf}\downarrow$, $R_{lf}\uparrow$, $R_{sg}\downarrow$, $R_{sg}\uparrow$, $R_{lg}\downarrow$, and $R_{lg}\uparrow$, are the downward ($\downarrow$) and upward ($\uparrow$) directed flux densities of shortwave (subscript s) and long-wave (subscript l) radiation. The subscripts f and g represent the surfaces of foliage and soil. The upward directed long-wave radiation denotes the loss from the surface. The quantities $R_{sf}\uparrow = \alpha_f R_{sf}\downarrow$ and $R_{sg}\uparrow = \alpha_g R_{sf}\downarrow$ are the diffuse shortwave radiation, i.e. the scattered insolation at the surface. The diffuse shortwave radiation depends on surface albedo. The incoming downward shortwave radiation is the same over the ground as over the foliage.

The global radiation, $R_{sf}\downarrow$, and the long-wave radiation of the atmosphere, $R_{lf}\downarrow$, can be delivered by respective radiation sensors at the measuring site. In modeling, they stem from simple parameterization schemes, or sophisticated radiative transfer models.

Furthermore, G_g and W_S are the soil heat and water flux densities at the surface, and L_v is the latent heat of vaporization. Infiltration S_F is a function of soil hydraulic conductivity and precipitation.

The governing flux equations for sensible heat, H, and water vapor, E, at the surfaces of foliage (subscript f) and soil (subscript g) read

$$H_f = -\sigma_f c_p \rho_a \left(\frac{1}{r_{mt,f}}(\theta_\delta - T_f) - \frac{1}{r_{mt,fg}}(T_f - T_g)\right)\,, \quad (4.154)$$

$$E_f = -\sigma_f \rho_a \left(\frac{1}{r_{mt,f}}(q_\delta - q_f) - \frac{1}{r_{mt,fg}}(q_f - q_g)\right)\,, \quad (4.155)$$

$$H_g = -c_p \rho_a \left(\frac{1-\sigma_f}{r_{mt,f}}(\theta_\delta - T_g) - \frac{\sigma_f}{r_{mt,fg}}(T_f - T_g)\right)\,, \quad (4.156)$$

$$E_g = -\rho_a \left(\frac{1-\sigma_f}{r_{mt,f}}(q_\delta - q_g) - \frac{\sigma_f}{r_{mt,fg}}(q_f - q_g)\right) \quad (4.157)$$

[33] Remind yourself of the difference in walking over grass and dark, dry bare soil or the difference in walking over black dry and black wet sand at a beach on a hot summer day.

where θ_δ, and q_δ are the values of potential temperature and specific humidity at the height δ close above the foliage. The surface temperature and specific humidity of foliage and soil are denoted T_f, q_f, T_g, and q_g, respectively. Furthermore, $r_{mt,f}$, $r_{mt,g}$, and $r_{mt,fg}$ are the resistances of the molecular-turbulent layer close to the surfaces of foliage and soil as well as the molecular-turbulent environment between the foliage and soil surface (subscript fg) against the transfer of heat and matter.

Moreover, ρ_a and c_p are the density and specific heat at constant pressure of air. The quantities θ_δ, q_δ, and q_f can be derived by using **Kirchhoff's law** of electrostatics. The eddy flux densities of sensible heat, H_t, and water vapor, E_t,

$$H_t = -\frac{\rho_a c_p}{r_t}(\theta_R - \theta_\delta) \,, \tag{4.158}$$

$$E_t = -\frac{\rho_a}{r_t}(q_R - q_\delta) \tag{4.159}$$

across the turbulent region of the atmospheric surface layer between δ and the reference height z_R, at which the meteorological measurements were performed, are considered. In numerical modeling, the reference height is usually the first half level of the first model layer above ground.

4.6.3.2 Snow

The energy and water budgets of a closed snow cover read

$$R_{ss}\downarrow - R_{ss}\uparrow + R_{ls}\downarrow - R_{ls}\uparrow - H_s - L_s E_s + G_s + P_H = 0 \,, \tag{4.160}$$

$$P + S - E_s = 0 \tag{4.161}$$

where $R_{ss}\downarrow$, and $R_{ls}\downarrow$ are the downward directed flux densities of shortwave and long-wave radiation. Furthermore, $R_{ss}\uparrow = \alpha_s R_{ss}\downarrow$, and $R_{ls}\uparrow = \epsilon_s \sigma T_s^4 + (1 - \epsilon_s) R_{ls}\downarrow$ are the upward directed flux densities of short- and long-wave radiation. The emittance ϵ_s and albedo α_s of snow usually are a function of time since last snowfall. Moreover, S and P (in $\mathrm{kg\,m^{-2}\,s^{-1}}$) stand for solid and liquid precipitation, E_s is sublimation and L_s is the latent heat of sublimation. The input of heat into the snow-pack by rain, P_H, depends on the difference between the temperature of the rain, and the snow surface, T_s. It is

$$P_H = c_w P(T_R - T_s) + L_f P \tag{4.162}$$

for snow temperatures below the freezing point, and

$$P_H = c_w P(T_R - T_s) \tag{4.163}$$

for snow temperatures above the freezing point. Here, c_w and L_f are the specific heat capacity of water and latent heat of fusion. The flux densities of sensible heat and water vapor over the snow coverage

$$H_s = -\frac{c_p \rho_a}{r_{mt,s} + r_t}(\theta_R - T_s) \tag{4.164}$$

and

$$E_s = -\frac{\rho_a}{r_{mt,s} + r_t}(q_R - q_s) \tag{4.165}$$

are functions of the potential temperature, θ_R, and the difference between the water-vapor mixing ratio at reference height, q_R, and at the surface of the snow-pack, q_s, respectively. Here, ρ_a, r_t, and $r_{mt,s}$, are the density of air, turbulent resistance of air and molecular turbulent resistance. The snow heat flux density reads

$$G_s = -\lambda_s \frac{\partial T_s}{\partial z_s} - L_v \rho_w k_v \frac{\partial q_s}{\partial z_s} \tag{4.166}$$

where q_s, and T_s are the mixing ratio at saturation with respect to ice and snow temperature. Moreover, ρ_w, k_v, L_v, and λ_s are the density of water, molecular diffusion coefficient of water vapor within air-filled pores of the snow-pack, the latent heat of condensation, and the thermal conductivity of snow, which depends on snow density, ρ_s.

The energy and water budgets of the underlying soil read

$$R_{sg}\downarrow - R_{sg}\uparrow + G_g - G_{s,g} = 0\,, \tag{4.167}$$

$$S_F + W_S = 0. \tag{4.168}$$

Here, $R_{sg}\downarrow = R_{ss}\downarrow exp(-k_{ext}h_s)$, and $R_{sg}\uparrow = \alpha_g R_{sg}\downarrow$ denote to the downward and upward directed flux densities of shortwave radiation through the snow-pack to and from the ground. Both quantities depend on the extinction coefficient of snow, k_{ext}, which is a function of grain diameter and density. The soil albedo α_g depends on soil moisture and soil type. The quantities W_S, G_g, and $G_{s,g}$ denote to the moisture and soil heat flux densities as well as the snow heat flux density. Ponding of water on the soil starts when precipitation or melt-water exceed the hydraulic conductivity of the soil at saturation or the ground is frozen.

Example. Use the Gibbs formula to derive a differential form of the energy equation and discuss it with respect to the climate system. Assume a static atmosphere to estimate the heating rate.

(continued)

(continued)

Solution. From thermodynamics we obtain $\rho c_p \frac{dT}{dt} = \rho T \frac{ds}{dt} + \frac{dp}{dt}$. The first term on the r.h.s. is the entropy flux density due to heat. If the atmospheric heating only results from transformation of radiative energy in heat we obtain $\rho Q = -\nabla \cdot T = -\frac{\partial E(z)}{\partial z}$, i.e. the convergence of the energy flux vector leads to heating. This is the fundamental energy budget equation of the climate system. For a static atmosphere $\frac{dp}{dt} = 0$, the resulting heating rate $\frac{dT}{dt} = \frac{\partial T}{\partial t}$ can be determine by $\rho c_p \frac{\partial T}{\partial t} = -\frac{\partial E_z(z)}{\partial z}$. Using the hydrostatic equation and rearranging yield $\frac{\partial T}{\partial t} = -\frac{g}{c_p} \frac{\partial E_p(p)}{\partial p}$. Vertical averaged temperature changes yield $\frac{\partial \overline{T}}{\partial t} = -\frac{g}{c_p} \frac{E_p(p_s) - E_p(0)}{p_s}$. The worldwide average is $E_p(p_s) - E_p(0) \approx 100\,\mathrm{W\,m^{-2}}$. With $p_s \approx 1{,}000\,\mathrm{hPa}$ we obtain for the average heating rate $\frac{\partial \overline{T}}{\partial t} \approx -10^{-5}\,\mathrm{K\,s^{-1}}$. Radiative heating is basically expressed in form of a virtual radiative heating. It is negative, i.e. a cooling of $1\,\mathrm{K\,d^{-1}}$. This means the atmosphere is a deficit enterprise because solar radiation is absorbed (acts as a heating), but terrestrial radiation is emitted (acts as cooling). The terrestrial emission is greater than the solar absorption. If the deficit would be given to space, the atmosphere would be cooler than it actually is. However, the deficit is given to the surface. The Earth in turn gives the excess radiation back by latent and sensible heat. Thus, the terrestrial atmosphere is in a radiation-convective equilibrium.

4.7 Remote Sensing from Satellites

Since the 1960s, various radiometers were developed and put on board of satellites to sense the atmosphere remotely. **Polar-orbiting satellites** pass the Earth in about 850 km height about 14 times a day. For each area, they provide data twice at day and night as the Earth spins below them. **Geostationary satellites** are located at a height of about 36,000 km above the equator. This position allows them to observe the same part of the Earth the entire time.

The geostationary satellites in orbit and their longitudinal positions are shown in Fig. 4.24. Images from these satellites show the Earth as a disk like in Figs. 4.26 and 4.28. Often a section of the full image for a region can be downloaded (e.g. Fig. 4.27). At the edges of the disk, the resolution gets coarser due to the Earth's curvature. Thus, information is less for high latitudes and areas at the edge of the **field of view** (FOV) of the satellite (Fig. 4.25) than at the **sub-satellite point**. Figure 4.24 also shows various polar orbiting satellites as well as the A-train. The A-train is a satellite constellation that permits observation with various instruments over the same region with a short temporal (a few minutes) lack. The collective

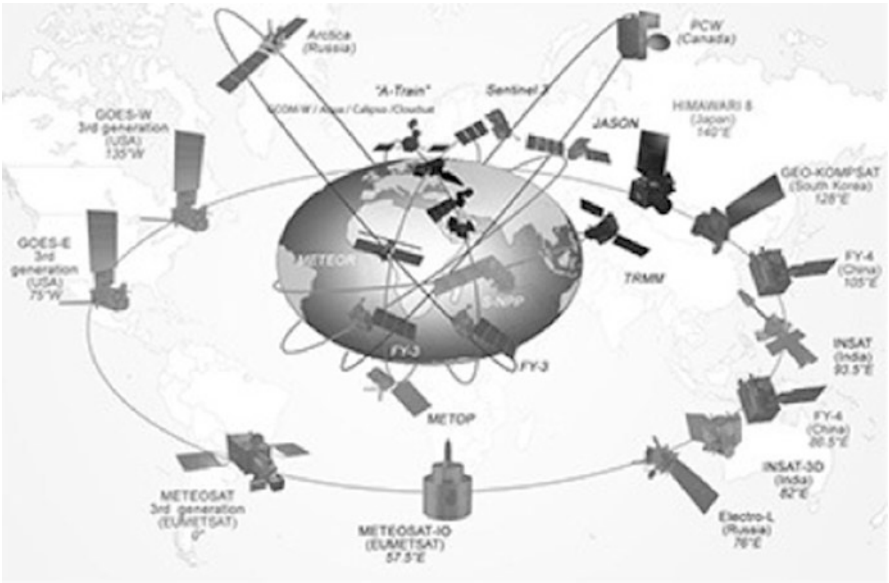

Fig. 4.24 Positions of geostationary satellites and exemplary orbits of a polar orbiting satellites (Black and white after the color version from http://www.wmo.int/pages/prog/sat/images/cgms_satellites_1000.jpg (2014))

observations permit to construct high-definition 3D images of the surface and Earth's atmosphere. The satellites' orbit is configured in such a way that the satellites cross the equator each day around 0130 pm solar time one after the other. Therefore, the name A-train like afternoon. The A-train consists of GCOM-W1, Aqua, CloudSat, CALIPSO and Aura. Prior to 2009, PARASOL also belonged to the A-train, but it was put on a lower orbit that year.

Depending on the wavelengths of the radiometer on board of a satellite, eddies and waves become visible by clouds and/or water-vapor distribution. Radiometers that operate in the window regions serve to observe surface characteristics. To detect radiation being emitted from close to ground, instruments sensitive to wavelengths that are close to a window region are applied as these wavelengths are still able to pass through most of the atmosphere.

The various phases of water are excellent tracers to observe the motions in some parts of the atmosphere (Figs. 4.26–4.28).

4.7.1 Microwave Spectrum

The microwave spectrum has three parts suitable for atmospheric applications

- <22 GHz where absorption dominates,

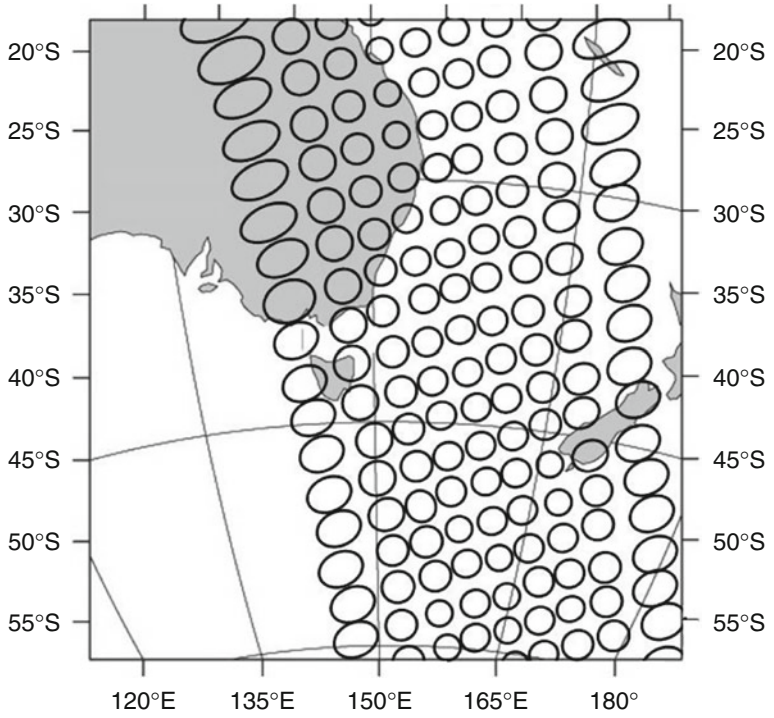

Fig. 4.25 Schematic view of MSU scan pattern to illustrate the increase in pixel size towards the edges of the satellite path of a polar orbiting satellite. Note that for geostationary satellites pixels become coarse towards the edges of the image too

- $\approx$60 GHz scattering is dominant for ice, and
- 22–60 GHz scattering and absorption are important.

In the microwave region ($\chi \approx 0.01$), absorption by cloud droplets is very small and scattering is negligible. In a cloud, absorption by Rayleigh-size cloud droplets is proportional to the liquid water content. The latter is of use for microwave measurements of the vertically integrated liquid water content by remote sensing techniques, because it means that cloud droplets do not scatter, but absorb microwave radiation.

Raindrops strongly interact with microwave radiation. Therefore, raining clouds are not transparent, while non-raining clouds typically have a transmittance of greater than 90 % in the microwave region. Detection of precipitating clouds by remote sensing techniques bases on these facts.

Since ice clouds have fewer particles per unit volume, and absorb less radiation than water-clouds, ice clouds also have a higher transmittance. Consequently, it is much more difficult to detect ice clouds by remote sensing techniques than water or mixed phase clouds.

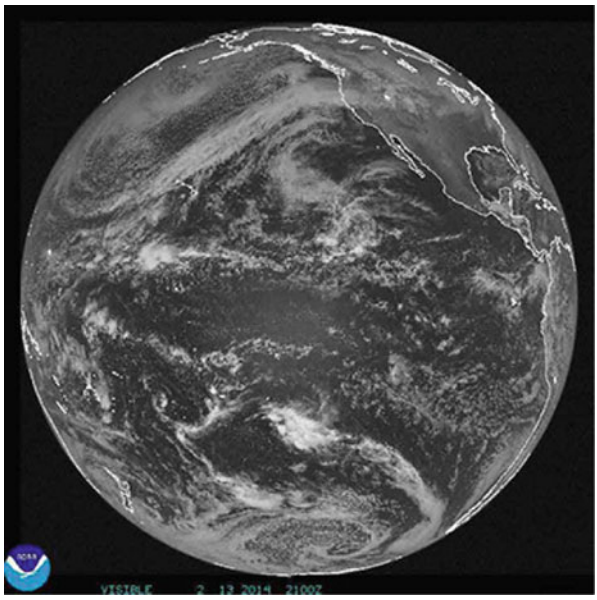

Fig. 4.26 Visible image of the Earth as taken from a geostationary satellite on February 13, 2014 2100 UTC (From NOAA http://www.goes.noaa.gov/FULLDISK/GWVS.JPG (2014))

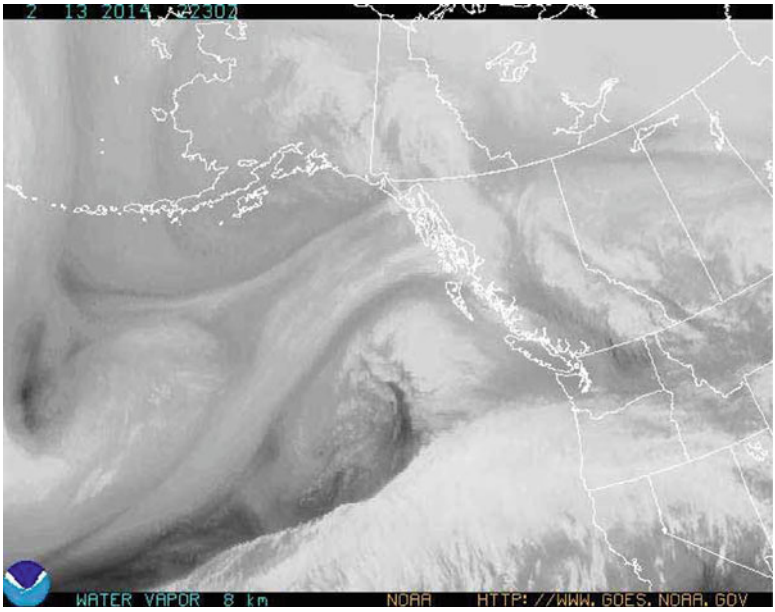

Fig. 4.27 Water vapor image of Alaska, western Canada and the Pacific Northwest as taken from a geostationary satellite on February 13, 2014 2230 UTC (From NOAA http://www.goes.noaa.gov/GIFS/ALWV.JPG (2014))

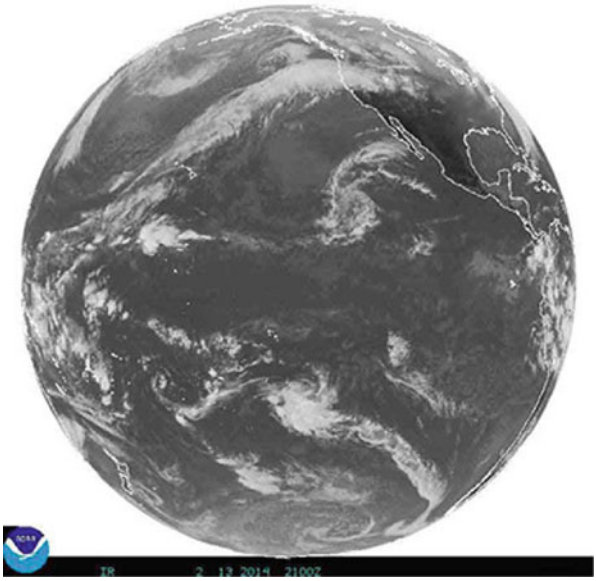

Fig. 4.28 Infrared image of the Earth as taken from a geostationary satellite on February 13, 2014 2100 UTC (From NOAA http://www.goes.noaa.gov/FULLDISK/GWIR.JPG (2014))

The main disadvantage of passive microwave techniques for rain detection is the poor spatial and temporal resolution that bases on the scattering and absorption properties of rain for three reasons.

1. Ice does not absorb microwave radiation, but scatters it.
2. Liquid drops absorb and scatter, but absorption dominates.
3. Scattering and absorption increase with frequency and rain rate, and the scattering increases more rapidly with frequency than with the amount of liquid.

4.7.2 Visible Spectrum

In the visible range of the spectrum ($\lambda \approx 0.5\,\mu\text{m}$), cloud droplets act as geometrical scatters. The scattering efficiency is about two corresponding to a scattering coefficient of about $0.1\,\text{m}^{-1}$. Since the mean free path of a photon is inverse to the volume scattering coefficient (i.e. $\approx 10\,\text{m}$ in this case), a cloud extending a few tens of meters scatters the entire visible radiation incident on it. Due to the size distribution of cloud drops and the large size parameter, all visible wavelengths are scattered nearly equally well for which clouds appear to be white (Fig. 4.26).

In the visible spectral range, we see the system as if we were at that height (Fig. 4.26). Warm and hot areas are black. Clouds appear white with the highest clouds being the coldest. Usually, along the equator high-reaching cloud clusters exist. They mark the **inner tropical convergence zone** (ITCZ). North and south of the ITCZ lower, warmer clouds occur, which are mainly cumulus or stratocumulus.

These clouds indicate the area of the sub-tropical highs and the trade-wind zone (Chaps. 2 and 7). In the mid-latitudes, large eddies can be found, which are extra-tropical cyclones.

As cloud-liquid water is a bad absorber, it only slightly absorbs visible radiation.

4.7.3 Near-Infrared Spectrum

In the near-infrared region of the spectrum, absorption by water vapor and liquid water increases. In the water-vapor channel (Fig. 4.27), we see the water-vapor distribution in the mid- and upper troposphere at 6.7 μm. The less water vapor is in the atmosphere the deeper we can see into it.

4.7.4 Infrared Spectrum

In the infrared region between 8.5–12.5 μm, cloud droplets act as Mie-scatters. The scattering efficiency ranges between 1 and 3, while the absorption efficiency is about 1. Consequently, clouds absorb nearly all of the infrared radiation falling onto them. This means that they behave nearly as blackbodies. Thus, cold targets appear black, while warm targets appear white in the infrared region. Since such images are strange to us, infrared images are usually inverted to again get the cold white and the warm dark as shown in Fig. 4.28. Since dry air or water vapor do not absorb or emit at those wavelengths, the IR-sensors can see the clouds through the atmosphere, or the surface in cloud-free areas.

4.8 The Atmospheric Effect

The common idea of interpreting emission temperatures is that where the atmospheric gases have a non-absorbing window, the satellite views the ground or a layer close to it (e.g. a snow surface, canopy surface). At wavelengths of absorption by atmospheric trace gases, the emission comes from higher levels in the atmosphere, i.e. colder regions. It is said that radiation by the Earth's surface is "trapped" in the spectral regions of absorption bands. Finally, it is re-radiated to space at lower temperatures than those of the Earth's surface. Averaged over all wavelengths the emitters seem to be about 33 K cooler than the globally averaged Earth's surface. Throughout most of the wavelengths emitted by the cooler Earth, compared to the Sun, the atmosphere is opaque. It lets shorter wavelength radiation in, but does not let the longer wavelength radiation out. The effect is often denoted as **greenhouse**

effect.[34] Since species absorb at the same wavelength than it emits, radiation is pushed back and forth between the infrared-active molecules. The radiation escapes to space when it reaches a height where the absorption becomes weak. Since the upper atmosphere has fewer particles, this region suffers a net loss of energy (Chaps. 1 and 2).

Several atmospheric species can affect radiation. Each of them is likely to exist with a varying mixing ratio, horizontal and vertical distribution. Each of these species absorbs and emits radiation with an intensity and spectral feature (e.g. vibrational, rotational, isotropic) of its own. Many of the atmospheric constituents given in Table 1.1 have absorption/emission bands in the infrared range.

Meanwhile, this common idea has strongly been criticized because averaged temperatures of the Earth's surface and the entire atmosphere are not related to the globally averaged energy flux budgets at the Earth's surface and at the TOA (Sect. 4.6). As illustrated in Fig. 4.23, the solar irradiance absorbed in the entire Earth-atmosphere system is balanced by the infrared radiation emitted to space.

Problems

Knowledge and Comprehension

1. Why appears a secondary rainbow less bright than the primary one?
2. Does Rayleigh-scattering change with height? Give reasons for your answer.
3. How can radiative cooling and condensation at the cloud top interact? Comment on cloud depletion and enhancement.
4. How much greater (approximately) is the latent heat loss by the Earth's surface compared with sensible heat loss on the global average?
5. What happens to the photons when you switch off the light?
6. How can energy be transferred?
7. What does the inverse square law mean?
8. Why are shortwave and long-wave radiation treated differently?
9. What impacts can radiation have on a molecule?
10. What is the relation between altitude and optical depth?
11. When radiation reaches the top of the atmosphere, where is it absorbed, and at what height is the absorption rate the greatest?
12. When does scattering matter?
13. Explain why the sky is blue.
14. Compare the atmospheres of Earth, Mars, and Venus and explain how the greenhouse effect works.

[34] Greenhouses are more effective because they inhibit convection than they are because they trap radiation. Thus, the comparison to a greenhouse is somehow awkward.

Application, Analysis, and Evaluation

4.1. On July 4 2019 (January 3 2019), the distance Earth-Sun[35] amounts $1.521 \cdot 10^8$ km ($1.471 \cdot 10^8$ km). Calculate the total irradiance at the top of the atmosphere on these days, and give the absolute and relative variance in irradiance.

4.2. The Earth's average surface temperature is 288 K because the atmosphere effectively absorbs terrestrial radiation, warms and radiates energy. Determine how much radiation will be emitted if the Earth's blackbody temperature is 255 K. The average surface temperature of the Sun can be assumed to be equal to 6,000 K. How much radiation is emitted from the Sun's surface? How many times warmer is the Sun than Earth? What is this number raised to the fourth power? Is the ratio of solar/Earth emitted radiation equal to the result? Given that the peak wavelength of the energy emitted by the Sun is about 0.5 μm what would the surface temperature of the Sun be in this case? What does this temperature change mean for the wavelength? The surface of Venus has a temperature of 475 °C. Determine its peak wavelength of emitted radiation. Compare your results for Venus with those of the Earth and Sun.

4.3. Calculate how long it takes energy emitted from the Sun to reach Mars. Assume a distance of $\approx 2.28 \cdot 10^8$ km.

4.4. Apply the basic physics of energy transfer to develop a zero-dimensional energy-balance model of the temperature of the Earth-atmosphere system. Show how the radiating temperature of the system depends on solar constant and the reflectance of the system. The Earth area is assumed to be $5.10 \cdot 10^{14}$ m^2. Assume that the Sun's energy that arrives at the outer edge of the atmosphere has an average rate of $S = 1.74 \cdot 10^{17}$ W. How is this related to the solar constant? Determine the planetary temperatures for typical values of albedo of a forest ($\alpha = 0.1$), a desert ($\alpha = 0.35$), and the average planetary albedo ($\alpha = 0.3$). Comment on your results.

4.5. The solar constant of Earth is 1,361 W m^{-2}, while that of Mars is only 445 W m^{-2}. Mars is farther away from the Sun. Mercury is $5.8 \cdot 10^7$ km from the Sun. Determine its solar constant (in W m^{-2}). Comment on the relation of the distance and solar constant.

4.6. At a place, observed intensity of radiation is 400 W m^{-2}. Determine the surface temperature for a blackbody and gray-body with an emittance of 0.9. Compare the temperatures and comment on the relation to emittance and intensity of radiation. What would be the intensity of a gray-body of same temperature than the blackbody?

4.7. Assumed that if the Earth had no atmosphere, its long-wave radiation emission would be lost quickly to space resulting the Earth to be approximately 33 K cooler,

[35] Aristarchus was the first to determine this distance in 250 BC.

on average. Determine the rate of radiation emitted, E, and the wavelength of maximum radiation emitted (λ_{max}) for an Earth at 255 K. Where is the wavelength located in the spectrum?

4.8. A climate model suggests that polar regions will warm by 10 °C during winter because of a doubling of greenhouse gases. Barrow, Alaska has an average winter temperature of −27 °C. By how much would its emitted radiation increase (in percent) under this scenario?

4.9. An laser beam passes vertically through a layer having a gas concentration of $0.013\,m^2\,kg^{-1}$ with an absorption coefficient of $0.95\,kg\,m^{-2}$. For simplicity assume the same absorption for all wavelengths. What percentage of the beam is absorbed? What concentration would the gas have to have to absorb 20 or 80 % of the incident laser beam? How would the results change if the absorption coefficient would be 20 or 80 % higher or lower? Discuss your results.

4.10. The planetary albedo of Earth is about 0.3, but the albedo would be less if there were no clouds, ice, and oceans covered more of the surface. An aqua planet would have an albedo of about 0.07, except for the sunglint. How would the equilibrium of temperature change from its present 255 K value if the estimated planetary albedo were cut in half, doubled and for the aqua planet? What would the new equilibrium temperature be in these cases? What do you conclude from your results?

4.11. A (near) polar orbiting environmental satellite (POES) and a geostationary satellite are at about 700 and 35,790 km altitude, respectively. Determine the long-wave radiation flux density from the Earth experienced at the satellites' orbits. Assume a uniform effective emitting temperature of 255 and 285 K. Discuss your findings.

4.12. Determine the temperature of the Sun assuming that the Sun is a blackbody and that its most intense radiation has a wavelength of approximately 0.475 μm. Often a value of 0.5 μm is used. Discuss the differences. Determine the peak wavelength of the moon equator under the assumption of a mean temperature of 220 K.

4.13. Determine the maximum spectral density of radiation of a blackbody irradiating at 6,000, 285, and 170 K. Calculate the wavelengths at which these bodies irradiate and comment on the shift in the spectrum.

4.14. An instrument on board of a satellite has sensors in the visible, near-infrared, mid-infrared, and infrared range with peak sensitivity to $\lambda = 0.5\,\mu m$, $\lambda = 0.75\,\mu m$, $\lambda = 3\,\mu m$, and $\lambda = 15\,\mu m$ wavelengths. Examine the relation between the energy emitted per photon, the frequency, and the wave-number for these sensors. What do you conclude from your results?

4.15. Assume that due to glaciations the average albedo of the Earth were 0.6. The irradiance of solar radiation incident on the Earth amounts to $1{,}361\,W\,m^{-2}$. Assume the mean radius of the Earth is equal to 6,371 km. Determine the equivalent

blackbody temperature of these conditions. Redo the exercise, but now assume an aqua planet with an albedo of about 0.07. Compare and discuss your results.

4.16. Assume that there is a layer of pollutants of 1 km thickness that absorbs 30 % of the downward directed irradiation of $280\,\mathrm{W\,m^{-2}}$. Take air density to be equal to $1.29\,\mathrm{kg\,m^{-3}}$. Determine the change in temperature due to absorption in $\mathrm{K\,h^{-1}}$.

4.17. Use the simple energy budget $\sigma T^4 = \frac{S(1-\alpha)}{4}$ where $S = 1{,}361\,\mathrm{W\,m^{-2}}$ is its solar constant, and α is its albedo. Derive the quantity $\frac{\partial T}{\partial \alpha}$ and determine the change of albedo required to obtain a 2.5 K temperature increase on that planet.

4.18. On a meteor, a gray flat surface with an absorptance of 0.92 is exposed to direct, overhead solar radiation. Due to its position to the Sun its solar constant is $1{,}380\,\mathrm{W\,m^{-2}}$. Determine the radiative equilibrium temperature at the surface. Determine the net irradiance immediately above the surface assuming the actual temperature of the surface were 200 K. Comment on the net radiation. How far would the meteorit be from the Sun? Discuss your results.

References

Material, concepts, ideas and problems of the following books and articles inspired this chapter. These sources are recommended for further reading.

Andrews DG (2000) Introduction to atmospheric physics. Cambridge University Press, New York, 237pp

Bohren CF, Clothiaux EE (2006) Fundamentals of atmospheric radiation. Wiley-VCH, Berlin, 490pp

Bruno TJ, Svoronos P (2004) Handbook of basic tables for chemical analysis, 2nd edn. CRC Press, Boca Raton, 223pp

Chandrasekhar S (1960) Radiative transfer. Dover, New York, 393pp

Coulson (1975) Solar and terrestrial radiation: methods and measurements. Academic, New York/San Francisco, 322pp

Dingman SL (1994) Physical hydrology. Macmillan, New York/Oxford/Singapore/Sydney, 557pp

Dirac PAM (1927) The quantum theory of the emission and absorption of radiation. Proc R Soc A114:243–267

Döring F (1973) Atomphysik und Quantenmechanik: I. Grundlagen. de Gruyter, Berlin/New York, 389pp

Einstein A (1917) Zur Quantentheorie der Strahlung. Physikalische Zeitschrift XVIII:121–128

Einstein A, Ehrenfest P (1923) Zur Quantentheorie des Strahlungsgleichgewichts. Zeitschrift für Physik A Hadrons and Nuclei 19:301–306

Finkelstein RJ (1969) Thermodynamics and statistical physics. W.H. Freeman, San Francisco, 113pp

Foken T (2014) Micrometeorology (Translated by Nappo, C.J.). Springer, Heidelberg, 350pp

Fowler RH, Milne EA (1925) A note on the principle of detailed balancing. Proc Natl Acad Sci 11:400–402

Franck J, Hertz G (1914) Über Zusammenstöße zwischen Elektronen und Molekülen des Quecksilberdampfes und die Ionisierungsspannung desselben. Verh Dtsch Phys Ges 16:457–467

Goody RM, Yung YL (1989) Atmospheric radiation: theoretical basis. Oxford University Press, New York/Oxford, 501pp

Haltiner GJ, Martin FL (1957) Dynamical and physical meteorology. McGraw-Hill, New York/Toronto/London, 470pp
Iqbal M (1983) An introduction to solar radiation. Academic Press, New York, 101pp
Jacobson MZ (1999) Fundamentals of atmospheric modeling. Cambridge University Press, New York, 656pp
Jacobson MZ (2005) Fundamentals of atmospheric modeling. Cambridge University Press, New York, 813pp
Kasten F, Raschke E (1974) Reflection and transmission terminology by analogy with scattering. Appl Opt 13:450–464
Kidder SQ, Vonder Haar TH (1995) Satellite meteorology. Academic, San Diego, 466pp
Klein O, Rosseland S (1921) Über Zusammenstöße zwischen Atomen und freien Elektronen. Zeitschr Phys A Hadrons and Nuclei 4:46–51
Kondratyev KYA (1969) Radiation in the atmosphere. Academic, New York/London, 912pp
Kramm G, Dlugi R (2011) Scrutinizing the atmospheric greenhouse effect and its climatic impact. Nat Sci 3:971–998
Kramm G, Herbert F (2006) Heuristic derivation of blackbody radiation laws using principles of dimensional analysis. J Calcutta Math Soc 2:1–20
Kramm G, Meixner FX (2000) On the dispersion of trace species in the atmospheric boundary layer: a re-formulation of the governing equations for the turbulent flow of the compressible atmosphere. Tellus A 52:500–522
Kramm G, Mölders N (2009) Planck's blackbody radiation law: presentation in different domains and determination of the related dimensional constants. J Calcutta Math Soc 5:37–61
Kramm G, Beier N, Foken T, Müller H, Schröder P, Seiler W (1996) A SVAT scheme for NO, NO_2, and O_3 – model description and test results. Meteorol Atmos Phys 61:89–106
Landau LD, Lifshitz EM (1980) Statistical physics. Course of theoretical physics, vol 5. Pergamon Press, Oxford/New York/Toronto/Sydney/Paris/Frankfurt, 484pp
Liou K-N (1980) An introduction to atmospheric radiation. Academic, San Diego/ New York/Boston/London/Sydney/Tokyo/Toronto, 432pp
Liou K-N (2002) An introduction to atmospheric radiation, 2nd edn. Academic, San Diego, 583pp
Lutgen FK, Tarbuck EJ (2001) The atmosphere – an introduction to meteorology. Pearson, Boston, 506pp
Milne EA (1928) The effect of collisions on monochromatic radiative equilibrium. MNRAS 88:493–502
Modest MF (2003) Radiative heat transfer. Academic, Amsterdam/Boston/London/ New York/Oxford/Paris/San Diego/San Francisco/Singapore/Sydney/Tokyo, 822pp
Mölders N (1987) Wolkenerkennung in AVHRR Daten mit besonderer Berücksichtigung der Gebiete über der Arktis. M.S. Thesis, Institut für Geophysik und Meteorologie, Universität zu Köln, 81pp
Mölders N, Laube M, Raschke E (1995) Evaluation of model generated cloud cover by means of satellite data. Atmos Res 39:91–111
Mölders N, Haferkorn U, Döring J, Kramm G (2003a) Long-term investigations on the water budget quantities predicted by the hydro-thermodynamic soil vegetation scheme (HTSVS) – part I: description of the model and impact of long-wave radiation, roots, snow, and soil frost. Meteorol Atmos Phys 84:115–135
Mölders N, Haferkorn U, Döring J, Kramm G (2003b) Long-term investigations on the water budget quantities predicted by the hydro-thermodynamic soil vegetation scheme (HTSVS) – part II: evaluation, sensitivity, and uncertainty. Meteorol Atmos Phys 84:137–156
Mölders N, Luijting H, Sassen K (2008) Use of atmospheric radiation measurement program data from Barrow, Alaska, for evaluation and development of snow albedo parameterizations. Meteorol Atmos Phys 99:199–219
Mölders N (2011/2012) Land-use and land-cover changes – Impact on climate and air quality. Atmospheric and oceanographic sciences library, vol 44. Springer, Dordrecht, 189pp. doi:10.1007/978-94-007-1527-1 3

Möller F (1973) Einführung in die Meteorologie – Physik der Atmosphäre – Band 1. BI Hochschultaschenbücher, Mannheim, 222pp
Moore WJ (1986) Physikalische Chemie (Hummel DO (ed)). Walter de Gruyter, Berlin/New York, 1236pp
Pais A (1995) Introducing atoms and their nuclei. In: Brown LM, Pais A, Pippard B (eds) Twentieth century physics – vol I. Institute of Physics Publishing, Bristol/Philadelphia/American Institute of Physics Press, New York, pp 43–141
Peixto JP, Oort AH (1992) Physics of climate. Springer, New York, 520pp
Petty GW (2004) A first course in atmospheric radiation. Sundog Publishing, Madison, 458pp
Pielke RA (1984) Mesoscale meteorological modeling. Academic, London, 612pp
Salby ML (1996) Atmospheric physics. Academic, San Diego/New York/Boston/London/Sydney/Tokyo/Toronto, 627pp
Semat H, Albright JR (1972) Introduction to atomic and nuclear physics. Holt, Rinehart, Winston, New York, 670pp
Standish EM, Williams EM (1992) Orbital ephemerides of the Sun, Moon, and planets. Updated version (unpublished) of Standish EM, Newhall XX, Williams JG, Yeomans DK (eds) Orbital ephemerides of the sun, moon and planets. Explanatory Supplement to the Astronomical Almanac. University Books, Mill Valley, pp 279–374
Tolman RC (1925) The principle of microscopic reversibility. Proc Natl Acad Sci 11:436–439
Vardavas IM, Taylor FW (2007) Radiation and climate. Oxford University Press, Oxford, 512pp
Wallace JM, Hobbs PV (1977) Atmospheric science – an introductory survey. Academic, San Diego/New York/Boston/London/Sydney/Tokyo/Toronto, 467pp
Wallace JM, Hobbs PV (2006) Atmospheric science – an introductory survey. Academic, San Diego/New York/Boston/London/Sydney/Tokyo/Toronto, 483pp
Wayne RP (1985) Chemistry of atmospheres – an introduction to the chemistry of the atmospheres of Earth, the planets, and their satellites. Clarendon Press, Oxford, 361pp
Wendisch M, Yang P (2012) Theory of atmospheric radiative transfer. Wiley VCH, Weilheim, 311pp
Williams DR (2007) Mars fact sheet. National Space Science Data Center. NASA. http://nssdc.gsfc.nasa.gov/planetary/factsheet/marsfact.htmlRetrieved2007

Chapter 5
Atmospheric Chemistry

Abstract Since the industrial revolution, the anthropogenic emissions of various trace species changed the composition of the atmosphere appreciably. This chapter presents the basics of atmospheric chemistry of the polluted and unpolluted atmosphere including some basic modeling concepts. The sources, transformation in the gas phase and aqueous phase, gas-to-particle conversion, aerosol physics and chemistry, transport, and removal of atmospheric trace gases as well as their relation to atmospheric physics and biogeochemical cycles are discussed and the relations of air chemistry to thermodynamics, radiation and cloud physics are elucidated.

Keywords Gas and aqueous phase chemistry • Aerosol physics and chemistry • Gas-to-particle formation • Removal of gases and aerosols • Biogeochemical cycles

5.1 Basic Concepts

5.1.1 Half-Life

In atmospheric chemistry, it is important to have a measure of the characteristic time that chemicals spend in the atmosphere. Let $[A]$ be the concentration of chemical A at time t. Then the depletion rate reads

$$-\frac{d[A]}{dt} = k[A] \tag{5.1}$$

where k is the rate coefficient for the reaction. Integration from the initial concentration $[A]_0$ to the final concentration $[A]_t$ and applying logarithm laws yield

$$\ln(\frac{[A]_t}{[A]_0}) = -k\,t \tag{5.2}$$

N. Mölders and G. Kramm, *Lectures in Meteorology*, Springer Atmospheric Sciences,
DOI 10.1007/978-3-319-02144-7_5,

or converting to base 10 logarithm

$$\log_{10}[A]_t = -\frac{k\,t}{2.303} + \log_{10}[A]_0 \; . \tag{5.3}$$

We define the **half-life time**[1] $t_{1/2}$ as the time that the concentration needs to decrease to half of its initial value $[A]_0$

$$t_{1/2} = \frac{0.693}{k} \; . \tag{5.4}$$

According to this definition, the half-life time is independent of the initial concentration.

5.1.2 Residence Time and Renewal Rate

Natural (e.g. wildfires, vegetation, volcanoes, soil) and anthropogenic sources (e.g. combustion, industry) continuously emit species and particles into the atmosphere. Secondary pollutants form by chemical reactions of the primary pollutants. The overall chemical composition of the atmosphere nearly remains the same over short time scales because sources and sinks balance so that most chemicals are roughly in **steady-state** conditions. The **residence time** or **life-time** τ is defined by the ratio of the amount of species or particles in the atmosphere M to the **efflux** F (rate of removal plus destruction) that both may depend on time t

$$\tau = \frac{M(t)}{F(t)} \; . \tag{5.5}$$

The **renewal rate** is the time needed to completely displace the original chemical from the atmosphere, i.e. residence time and renewal rate are identical.

The chemical reactions and physical removal processes determine the residence time. Very stable gases (e.g. N_2) have residence times of 1–100 million years, which allows inter-hemispheric mixing. On the contrary, highly reactive (short-lived) gases have residence times of less than an hour (Table 1.1) and spatial scales of about hundreds of meters. Thus, high concentration gradients exist on the microscale (Chap. 6). Moderately long-lived species show a spatial variability from hundreds of meters to about 1,000 km. This means the relatively faster reacting moderately long-lived species can show large concentration gradients at the local (e.g. urban) scale. Species with residence times of a day or so can experience mixing in the atmospheric boundary layer (ABL), and may be even mixed into the free troposphere where temperatures are lower (Chap. 2) and wind speeds are higher

[1] Radio-carbon dating bases on this principle.

(Chaps. 6 and 7) so they become subject to long-range transport, i.e. have regional or mesoscale-α spatial distributions. Residence times of the order of months permit intra-hemispheric mixing.

5.1.3 Chemical Families

It is convenient to identify closely related species, called the **chemical families**. Examples are the **odd oxygen** family consisting of O, O^{1D}, and O_3. Here the word odd refers to the number of electrons available for bounding with other chemicals. This availability makes the atom/molecule reactive. Other examples are **odd hydrogen** (HO_x with $x = 0, 1, 2$, i.e. atoms (H), hydroxyl radicals (OH), and hydroperoxyl radicals (HO_2)), **odd chlorine** (ClO_x with $x = 0, 1, 2$, i.e. inorganic chlorine compounds including chlorine atoms (Cl), chlorine monoxide (ClO), hydrogen chloride (HCl), chlorine nitrate ($ClNO_3$), hypochlorous acid ($HOCl$), and chlorine monoxide dimer (Cl_2O_2)), and **odd nitrogen** or **active nitrogen** (NO_x, i.e. nitric oxide (NO), and nitrogen dioxide (NO_2)).

NO_y is a collective name for all oxidized nitrogen species in the air that are sinks and sources of NO_x (e.g. NO_3, N_2O_5, nitric acid (HNO_3), peroxy-acetyl-nitrate PAN), and organic nitrates). The odd hydrogen, chlorine, and nitrogen participate in ozone (O_3) destruction.

5.2 Gas-Phase Atmospheric Chemistry

Primary pollutants (e.g. carbon monoxide (CO), carbon dioxide (CO_2), sulfur dioxide (SO_2), nitrogen oxides (NO, NO_2), volatile organic compounds (VOC), particulate matter (PM)) are directly emitted in the atmosphere (Chap. 1). In urban atmospheres, high concentrations of primary pollutants can be found. Concurrent processes of transport and transformation of trace species lead to high concentrations of **secondary pollutants** like **photochemical oxidants** in rural areas.

5.2.1 Chemical Equilibrium

A chemical system is in equilibrium when the rate at which the chemical reactants combine equals the rate at which the product decomposes. Analogous to the equilibrium between water and water vapor at saturation, at every temperature partial pressures of gases exist for which the forward and reverse reaction have the same rate. In general,

$$aA + bB + \cdots \rightleftharpoons cC + dD + \cdots . \tag{5.6}$$

Here a, b, c, d are the **stoichiometric coefficients** in the balanced chemical reaction equation and A, B and C, D are the chemical reactants and products, respectively. For an ideal gas or ideal solute the **equilibrium constant** for forward reaction or reverse reaction is given by

$$k_c = \frac{[C]^c[D]^d \cdots}{[A]^a[B]^b \cdots} . \tag{5.7}$$

Here the bracket [ ] indicates concentration. Concentrations may be given in molarity (M; for gases: moles liter^{-1} of air; for solutes: moles liter^{-1} of solute). When a reaction only involves gases, atmospheric chemists often use the partial pressures of the reactants and products instead of molarity. Molarity and partial pressure are related via the equation of state $pV = nR^*T = n_0kT$ where $R^* = 8.3143\,\mathrm{J\,K^{-1}\,mol^{-1}}$, n, n_0, and $k = \frac{R^*}{N_A} = 1.381 \cdot 10^{-23}\,\mathrm{J\,K^{-1}}$ molecule^{-1} are the universal gas constant, number of moles of gas, number of molecules per cubic-meter, and the Boltzmann constant. Recall, at constant temperature and pressure, the volume taken by a gas is proportional to the numbers of moles in the gas (Chap. 2).

Example. On a summer day in Berlin, Germany, temperature, pressure, and ozone were recorded as 27 °C, 1,030 hPa, and 150 ppm or ppmv (part per million by volume of air). Determine how many ozone molecules were in 1 m^3 of air.

Solution. Rearranging $p = n_{air}kT$ yields $n_{air} = \frac{1{,}030 \cdot 10^2}{1.381 \cdot 10^{-23} \cdot 300.15}$ molecules m^{-3} $= 2.48 \cdot 10^{25}$ molecules m^{-3}. At same T and p, the volumes V occupied by gases are proportional to the number of molecules in the gases (Chap. 2) $\frac{V_{ozone}}{V_{air}} = \frac{n_{ozone}}{n_{air}}$. As $V_{ozone} = 150 \cdot 10^{-6}$ m^3, $V_{air} = 1$ m^3, and n_{air} are the number of molecules per meter cube of air, the number of ozone molecules in 1 m^3 amounts $n_{ozone} = 150 \cdot 10^{-6} \cdot 2.48 \cdot 10^{25} \approx 3.73 \cdot 10^{21}$.

In atmospheric chemistry, the equation of state is often given as $p_AV_A = nR_c^*T$ where $R_c^* = 0.0821\,\mathrm{liter\,atm\,K^{-1}\,mol^{-1}}$ is the universal gas constant in chemical units, and n is the number of moles of gas A at pressure p_A in volume V_A. As n/V_A is the number of moles of gas per liter (molarity)

$$[A] = \frac{n}{V_A} = \frac{p_A}{R_c^*T} \tag{5.8}$$

the equilibrium constant k_c depends on temperature

$$k_c = \frac{[p_C/(R_c^*T)]^c[p_D/(R_c^*T)]^d \cdots}{[p_A/(R_c^*T)]^a[p_B/(R_c^*T)]^b \cdots} = \frac{p_C^c\,p_D^d \cdots}{p_A^a\,p_B^b \cdots}(R_c^*T)^{\Delta m} = k_p(R_c^*T)^{\Delta m} \tag{5.9}$$

where $\Delta m = (a + b + \cdots) - (c + d + \cdots)$. Here, $k_p = \frac{p_C^c p_D^d \cdots}{p_A^a p_B^b \cdots}$ is the equilibrium constant of gaseous reactions and the coefficients are set equal to zero in the expression of Δm. Of course, the units[2] of k_c (M^{-1}) and k_p (atm^{-1} or Pa) differ. Using k_c requires concentrations in molarity, using k_p requires partial pressures in atm. For example, the units of $k_c = \frac{[N_2O_5]}{[NO_2][NO_3]}$ and $k_p = \frac{p_{N_2O_5}}{p_{NO_2} p_{NO_3}}$ are $\frac{M}{M \cdot M} = M^{-1}$ and $\frac{atm}{atm \cdot atm} = atm^{-1}$, respectively.

Example. Determine the equilibriums constant and Δm for the reaction

$$2NO + O_2 \rightleftharpoons 2NO_2$$

at $-10\,°C$ with $[NO_2] = 0.053$ ppm and $[NO] = 0.5$ ppm.

Solution.

$$\Delta m = (2 + 1) - 2 = 1$$

$$k_c = \frac{[NO_2]^2}{[NO]^2[O_2]}$$

with molarity $= \frac{\text{ppm}}{M \cdot 10^3}$ $k_c = \frac{(0.053 \cdot 22.99 \cdot 14 \cdot 10^3 \cdot 2 \cdot 16 \cdot 10^3)^2}{(0.5 \cdot 22.99 \cdot 14 \cdot 10^3 \cdot 16 \cdot 10^3)^2 (0.21 \cdot 10^6 \cdot 2 \cdot 16 \cdot 10^3)} = 6.688 \cdot 10^{-12}$. Thus, $k_p = \frac{k_c}{(R_c^* T)^{\Delta m}} = \frac{6.688 \cdot 10^{-12}}{263.15 \cdot 0.0821} = 1.433 \cdot 10^{-14}$.

First, second, and third order reaction rate coefficients depend on temperature and can be determined with the **Arrhenius**[3] **equation** by integrating

$$\frac{d \ln k_c}{dT} = \frac{\Delta \overline{H}^\circ}{R_c^* T^2} \tag{5.10}$$

where $\Delta \overline{H}^\circ$ ($kJ\,mol^{-1}$) is the molar standard enthalpy (or heat) of reaction and is the activation energy for the reaction. It is the smallest amount of energy needed to form an activated complex or transition state before forming the products. Integration yields the equilibrium constant

$$k_c = A \exp\left(\frac{-\Delta \overline{H}^\circ}{R_c^* T}\right) . \tag{5.11}$$

[2] It is common practice in air chemistry to not write the units down in equilibrium constants.

[3] Svante August Arrhenius, Swedish physicist, chemist, one of the founders of physical chemistry, 1859–1927.

Here $\exp(\frac{-\Delta\overline{H}^\circ}{R_c^* T})$ is the fraction of reactant molecules that have the critical energy $\Delta\overline{H}^\circ$ needed for the reaction to occur. The **collisional prefactor** A and $\Delta\overline{H}^\circ$ are usually nearly constant over typical atmospheric temperature ranges for any chemical reaction. The collisional prefactor gives the frequency of collisions with appropriate orientation to produce a reaction. It depends on the charge, relative size, kinetic energy and molecular weight of the reactants. $\Delta\overline{H}^\circ$ depends on the forward chemical reactions. The superscript zero indicates that the reactants/products are at the **standard state** of 1 atm and 25 °C.

5.2.2 Reaction Quotient

Typically, chemical reactions are not in equilibrium. We can define a ratio of concentrations called the reaction quotient

$$Q = \frac{[C]^c[D]^d \cdots}{[A]^a[B]^b \cdots} \,. \tag{5.12}$$

For a reaction in equilibrium $Q = k_c$, and for a forward (reverse) reaction $Q < k_c$ ($Q > k_c$) until $Q = k_c$.

5.2.3 Kinetic Treatment of Combination and Dissociation Reactions

Many atmospheric reactions are of type

$$A + B + M \longrightarrow AB + M \tag{5.13}$$

where M is a third molecule (e.g. N_2, O_2, Ar). The elementary processes of this reaction are

$$A + B \rightleftharpoons_{k_{-1}}^{k_1} AB^* \,, \tag{5.14}$$

$$AB^* + M \longrightarrow^{k_2} AB + M \tag{5.15}$$

where AB^* is an interim energetic state of the molecule. Collision with M removes the excess energy and generates a stable state of AB. The step from the reaction equations to the production (destruction) rates means a positive (negative) sign for the reaction rate coefficient times the required concentrations needed to produce (deplete) the molecule for which the production (depletion) rate is to be determined.

In a reaction chain, we have to consider all sources and sinks of the concentration, for which the production (depletion) rate is to be determined. The rate of formation reads

$$\frac{d[AB]}{dt} = k_2[AB^*][M] \; . \tag{5.16}$$

Using the steady-state approximation yields the concentration

$$[AB^*]|_{steady-state} = \frac{k_1[A][B]}{k_{-1} + k_2[M]} \; . \tag{5.17}$$

Inserting the steady-state concentration provides

$$\frac{d[AB]}{dt} = \frac{k_1 k_2}{k_{-1} + k_2[M]}[M][A][B] \tag{5.18}$$

with an overall rate of

$$\frac{d[AB]}{dt} = k[A][B] \; . \tag{5.19}$$

Here k depends on $[M]$ as shown above. The number of excited molecules $[AB^*]$ falling back to A and B depends on the availability of a third molecule, M.

5.2.3.1 High Pressure Condition

In the troposphere, always enough molecules exist for collision (high pressure). The high-pressure limit is independent of $[M]$ and can be determined as

$$k_\infty = \lim_{[M]\to\infty} k = k_1 \; . \tag{5.20}$$

5.2.3.2 Low Pressure Condition

In the thermosphere, collision becomes less frequent (cf. Chaps. 1 and 2) due to the low density (low pressure). The low-pressure limit reads

$$k_0 = \lim_{[M]\to 0} k = \frac{k_1 k_2}{k_{-1}}[M] \tag{5.21}$$

and the overall rate is of **third order**. The product of a third order reaction rate constant and the concentration of the third molecule are often expressed by a **second order reaction rate** constant.

Example. Compare the reaction rate coefficients for

$$NO + O_3 \rightarrow^{k_1} NO_2 + O_2$$

$$OH + O_3 \rightarrow^{k_2} HO_2 + O_2$$

with each other for a −10 °C winter and a 25 °C summer day. What do your findings mean for air quality forecast models?

Solution. From Table 5.1 $k_1 = 1.8 \cdot 10^{-12} \exp(\frac{-1{,}370}{T}) = 9.869 \cdot 10^{-15}\,\mathrm{cm^3\,molecules^{-1}\,s^{-1}}$ and $k_2 = 1.9 \cdot 10^{-12} \exp(\frac{-1{,}000}{T}) = 4.245 \cdot 10^{-14}\,\mathrm{cm^6\,molecule^{-1}\,s^{-1}}$. The reaction with radicals is much faster than the other reaction for which the radicals' lifetime is short. On the summer day, the reaction rate coefficients are $1.8184 \cdot 10^{-14}\,\mathrm{cm^3\,molecules^{-1}s^{-1}}$ and $6.639 \cdot 10^{-14}\,\mathrm{cm^6\,molecule^{-1}\,s^{-1}}$, respectively. This means reaction rates increase non-linearly with increasing temperatures for the two reactions. Thus, errors in simulated temperature may lead to errors in simulated concentrations.

5.2.4 Photochemistry

Photochemistry denotes the reaction of species with reactants that stem from **photolysis**. A molecule A can be involved in photolysis when it is hit by a photon of electromagnetic radiation and absorbs sufficient energy to dissociate. We express the initial step of a photochemical reaction as

$$A + h\nu \longrightarrow^{j} A^* \,. \tag{5.22}$$

Here A^* is an excited state of A and $h\nu$ is the energy of a photon. The excited molecule may undergo dissociation, direct reaction, fluorescence or collisional deactivation (see following equations):

$$A^* \longrightarrow^{k_1} B_1 + B_2 + B_3 \ldots\,, \tag{5.23}$$

$$A^* + B \longrightarrow^{k_2} C_1 + C_2 + C_3 \ldots\,, \tag{5.24}$$

$$A^* \longrightarrow^{k_3} A + h\nu\,, \tag{5.25}$$

$$A^* + M \longrightarrow^{k_4} A + M\,. \tag{5.26}$$

Dissociation and direct reaction result in a chemical change, while fluorescence and deactivation by collision return the molecule to its original state.

Table 5.1 Gas-phase kinetic reaction and reaction rates (Data from Jacobson (2005))

Kinetic reaction	Rate coefficient ($cm^3\ s^{-1}$) or ($cm^6\ s^{-1}$)
$O + O_2 + M \rightarrow O_3 + M$	$6.0 \cdot 10^{-34}(300/T)^{2.3}$
$O + O_3 \rightarrow 2O_2$	$8 \cdot 10^{-12} \exp(2{,}060/T)$
$O^{1D} + O_3 \rightarrow 2O_2$	$1.2 \cdot 10^{-10}$
$O^{1D} + O_3 \rightarrow O_2 + 2O$	$1.2 \cdot 10^{-10}$
$O^{1D} + O_2 \rightarrow O_2 + O$	$3.2 \cdot 10^{-11} \exp(67/T)$
$O^{1D} + N_2 \rightarrow N_2 + O$	$1.8 \cdot 10^{-11} \exp(107/T)$
$O^{1D} + N_2 + M \rightarrow N_2O + M$	$3.5 \cdot 10^{-37}(300/T)^{0.6}$
$O^{1D} + N_2O \rightarrow N_2 + O_2$	$4.4 \cdot 10^{-11}$
$O^{1D} + N_2O \rightarrow 2NO$	$7.2 \cdot 10^{-11}$
$O^{1D} + H_2 \rightarrow OH + H$	$1.1 \cdot 10^{-10}$
$O^{1D} + H_2O \rightarrow 2OH$	$2.2 \cdot 10^{-10}$
$H + O_2 + M \rightarrow HO_2 + M$	$5.4 \cdot 10^{-32}(300/T)^{1.8}$
$H + O_3 \rightarrow O_2 + OH$	$1.4 \cdot 10^{-10} \exp(-470/T)$
$H + HO_2 \rightarrow H_2 + O_2$	$5.6 \cdot 10^{-12}$
$H + HO_2 \rightarrow 2OH$	$7.2 \cdot 10^{-11}$
$H + HO_2 \rightarrow H_2O + O$	$2.4 \cdot 10^{-12}$
$OH + O \rightarrow H + O_2$	$2.3 \cdot 10^{-11} \exp(110/T)$
$OH + O_3 \rightarrow HO_2 + O_2$	$1.9 \cdot 10^{-12} \exp(-1{,}000/T)$
$OH + H_2 \rightarrow H_2O + H$	$7.7 \cdot 10^{-12} \exp(-2{,}100/T)$
$OH + OH \rightarrow H_2O + O$	$4.2 \cdot 10^{-12} \exp(-240/T)$
$OH + OH + M \rightarrow H_2O_2 + M$	$6.9 \cdot 10^{-31} \exp(300/T)^{0.8}$
$OH + HO_2 \rightarrow H_2O + O_2$	$4.8 \cdot 10^{-11} \exp(250/T)$
$OH + H_2O_2 \rightarrow HO_2 + H_2O$	$2.9 \cdot 10^{-12} \exp(160/T)$
$OH + NO + M \rightarrow HONO$	$7.4 \cdot 10^{-31} \exp(300/T)^{2.4}$
$OH + NO_2 \rightarrow HNO_3$	$2.6 \cdot 10^{-30} \exp(300/T)^{2.9}$
$OH + NO_3 \rightarrow HO_2 + NO_2$	$2 \cdot 10^{-11}$
$OH + HONO \rightarrow H_2O + NO_2$	$1.8 \cdot 10^{-11} \exp(-390/T)$
$HO_2 + O \rightarrow OH + O_2$	$2.7 \cdot 10^{-11} \exp(224/T)$
$HO_2 + O_3 \rightarrow OH + 2O_2$	$1.4 \cdot 10^{-14} \exp(-600/T)$
$HO_2 + NO \rightarrow OH + NO_2$	$3.7 \cdot 10^{-12} \exp(240/T)$
$HO_2 + NO_2 + M \rightarrow HO_2NO_2$	$1.8 \cdot 10^{-31} \exp(300/T)^{3.2}$
$HO_2 + NO_3 \rightarrow HNO_3 + O_2$	$4 \cdot 10^{-12}$
$H_2O_2 + O \rightarrow OH + HO_2$	$1.4 \cdot 10^{-12} \exp(-2{,}000/T)$
$NO + O \rightarrow NO_2$	$10^{-31} \exp(300/T)^{1.6}$
$NO + O_3 \rightarrow NO_2 + O_2$	$1.8 \cdot 10^{-12} \exp(-1{,}370/T)$
$NO_2 + O \rightarrow NO + O_2$	$6.5 \cdot 10^{-12} \exp(120/T)$
$NO_2 + O + M \rightarrow NO_3$	$9 \cdot 10^{-32} \exp(300/T)^2$
$NO_2 + O_3 \rightarrow NO_3 + O_2$	$1.2 \cdot 10^{-13} \exp(-2{,}450/T)$
$NO_3 + O \rightarrow NO_2 + O_2$	$1.7 \cdot 10^{-11}$
$NO_3 + NO \rightarrow 2NO_2$	$1.8 \cdot 10^{-11} \exp(110/T)$
$NO_3 + NO_2 + M \rightarrow N_2O_5 + M$	$2.7 \cdot 10^{-30}(300/T)^{3.4}$

(continued)

Table 5.1 (continued)

Kinetic reaction	Rate coefficient ($cm^3\ s^{-1}$) or ($cm^6\ s^{-1}$)
$N_2O_5 + M \rightarrow NO_3 + NO_2 + M$	$10^{-3}(300/T)^{3.5}\exp(-11{,}000/T)$
$N_2O_5 + H_2O \rightarrow 2HNO_3 + NO_2 + M$	$2 \cdot 10^{-21}$
$HO_2NO_2 + M \rightarrow HO_2 + NO_2 + M$	$5 \cdot 10^{-6}\exp(-10{,}000/T)$
$CH_4 + O^{1D} \rightarrow CH_3O2 + OH$	$1.4 \cdot 10^{-10}$
$CH_4 + O^{1D} \rightarrow HCHO + H_2$	$1.5 \cdot 10^{-11}$
$CH_3O + O_2 \rightarrow HCHO + HO_2$	$7.2 \cdot 10^{-14}\exp(-1{,}080/T)$
$CH_3O + NO \rightarrow HCHO + HO_2 + NO$	$4 \cdot 10^{-12}\exp(300/T)^{0.7}$
$CH_3O + NO + M \rightarrow CH_3ONO + M$	$1.6 \cdot 10^{-29}(300/T)^{3.5}$
$CH_3O + NO_2 + M \rightarrow CH_3ONO_2 + M$	$2.8 \cdot 10^{-29}(300/T)^{4.5}$
$SO_2 + OH \rightarrow HSO_3$	$4.0 \cdot 10^{-31}(300/T)^{3.3}$
$HSO_3 + O_2 \rightarrow SO_3 + HO_2$	$1.3 \cdot 10^{-12}\exp(-330/T)$
$SO_3 + H_2O \rightarrow H_2SO_4$	$6 \cdot 10^{-15}$
$SO + O_2 \rightarrow SO_2 + O$	$1.6 \cdot 10^{-13}\exp(-2{,}280/T)$
$S + O_2 \rightarrow SO + O$	$2.1 \cdot 10^{-12}$
$Cl + O_3 \rightarrow ClO + O_2$	$2.9 \cdot 10^{-11}\exp(-260/T)$
$ClO + O_3 \rightarrow ClOO + O_2$	$1.5 \cdot 10^{-17}$
$ClO + O \rightarrow Cl + O_2$	$3.8 \cdot 10^{-11}\exp(70/T)$
$ClO + OH \rightarrow Cl + HO_2$	$9.9 \cdot 10^{-12}\exp(120/T)$
$ClO + OH \rightarrow HCl + O_2$	$1.1 \cdot 10^{-12}\exp(120/T)$
$Cl + H_2 \rightarrow HCl + H_2$	$3.7 \cdot 10^{-11}\exp(-2{,}300/T)$
$HCl + OH \rightarrow Cl + H_2O$	$2.4 \cdot 10^{-12}\exp(-330/T)$

The ratio of the number of molecules A^* undergoing a process to the number of photons absorbed is the **quantum yield** Φ_i. The quantum yield measures the probability of an absorbed photon to have one of the four fates. When a concentration can undergo several fates, the quantum yield indicates the partitioning among the potential processes and determines the rate of change in the resulting products. Consequently, the sum of all possible paths for A^* equals 1

$$\sum_{i=1}^{4} \Phi_i = 1 \ . \tag{5.27}$$

When every A^* immediately undergoes one of the four paths, the **total rate of depletion** of A^* equals the **total rate of production**, i.e. the **absorption rate**. The rate of change of A due to absorption of light reads

$$\frac{d[A]}{dt} = -j[A] \ . \tag{5.28}$$

Here j (unit s^{-1}) is the **first order photolysis rate** or **specific absorption rate**. The rate of change of A^* due to dissociation reads

$$\frac{d[A^*]}{dt} = -k_1 \Phi_1 [A] \tag{5.29}$$

where Φ_1 is the quantum yield from the dissociation process and k_1 (unit s^{-1}) is the **specific dissociation rate**. The rate of change is usually independent of $[A^*]$. A positive (negative) sign in the rate coefficient means production (depletion). We can write the rate of change of $[A^*]$ by reaction with B as

$$\frac{d[A^*]}{dt} = -\Phi_2 k_2 [A][B] \tag{5.30}$$

and the formation rate of $C_1, C_2, \ldots$. by direct chemical reactions as

$$\frac{d[C_n]}{dt} = \Phi_2 k_2 [A][B] \; . \tag{5.31}$$

Here C_n stands for the products obtained by the process and Φ_2 is the quantum yield from these chemical reactions. Analogously, we determine the rates of change by fluorescence or collision deactivation.

5.2.4.1 Photolysis Rates

The probability of absorbing enough energy to undergo photolysis depends on the radiant flux from all directions incident on an air parcel, the **actinic flux** F. The units of the actinic flux and actinic flux within a wavelength interval are $m^{-2}\,s^{-1}$ and $m^{-2}\,s^{-1}\,\mu m^{-1}$, respectively. The magnitude of the first order photolysis rate coefficient j for A depends on the actinic flux and the probability that the molecule A absorbs a photon and dissociates. Integration over the wavelength range and consideration of the dependencies on wavelength, λ, and temperature, T yields the photolysis rate coefficient

$$j = \int_{\lambda_1}^{\lambda_2} \sigma(\lambda, T) \Phi(\lambda, T) F(\lambda) d\lambda \; . \tag{5.32}$$

Summation over wavelength intervals $\Delta\lambda_i$ of 10–20 nm width also provides the photolysis rate coefficient

$$j = \sum_i \overline{\sigma}(\lambda_i, T) \Phi(\lambda_i, T) \overline{F}(\lambda_i) \Delta\lambda_i \; . \tag{5.33}$$

Here the overbars denote the average over the wavelength interval $\Delta\lambda_i$ centered around λ_i and Φ is the quantum yield at given temperature for that wavelength interval. The **absorption cross-section** σ measures the probability of absorption. The absorption cross-section and quantum yield are fundamental characteristics of the respective molecule and stem from laboratory experiments.

Due to the vertical distribution of atmospheric species and their different absorption of electromagnetic energy (i.e. sensitivity to wavelength, see Chap. 4), photolysis rates vary with height for the various dissociating species. For instance, under clear sky conditions, the photolysis rates for N_2O_5 to NO_2 and NO_3 at wavelengths smaller than 0.385 µm are about $4.73 \cdot 10^{-5}\,s^{-1}$ and $5.04 \cdot 10^{-5}\,s^{-1}$ at 25 km height and the ground, respectively. Looking at the photolysis of Cl_2 to $2Cl$ at wavelengths lower than 0.45 µm, we have an example where photolysis rates are higher at 25 km ($3.51 \cdot 10^{-3}$) than close to the ground ($2.37 \cdot 10^{-3}$). In addition to the aforementioned sensitivities, photolysis rates may also increase locally around clouds due to the high albedo of clouds, and over snow covered surfaces, white roofs, or near white walls.

Obviously, photolysis rates have to be calculated depending on the vertical profiles, cloud fraction, and surface albedo. Most air quality models calculate the photolysis rate for clear sky conditions and then apply corrections for cloud fraction or cloudiness. In air-quality models, photolysis rates are often calculated up front with climatological profiles and used as lookup tables, rather than being calculated inline with the actual profiles simulated by the air quality model itself. The latter method, however, is state-of-the-art, but computationally expensive.

Example. Assume an actinic flux of $1.88 \cdot 10^{23}\,m^{-2}\,s^{-1}\,\mu m^{-1}$ in the wavelength range of 0.595–0.600 µm. The experiment for the photolysis of NO_3 to NO and O_2 showed an absorption cross-section, and quantum yield of $4.82 \cdot 10^{-23}\,m^2$ and 0.87 at 25 °C and 1,000 hPa. Calculate the photolysis rate coefficient.

Solution. $j = \sum_i \overline{\sigma}(\lambda_i, T)\overline{\phi}(\lambda_i, T)\overline{F}(\lambda_i)\Delta\lambda_i = 4.82 \cdot 10^{-23}\,m^2\,0.87 \cdot 1.88 \cdot 10^{23}\,m^{-2}\,s^{-1}\,\mu m^{-1}\,0.005\,\mu m = 2.49 \cdot 10^{-2}\,s^{-1}$.

5.2.5 Tropospheric Homogeneous Gas-Phase Reactions

Since photolysis requires the energy of daylight, different chemical reaction processes occur at night than at day and concentrations of chemically reactive trace gases have a diurnal cycle. We speak of **daytime** and **nighttime chemistry**. In Polar Regions, these differences lead to tremendous differences in winter and summer air pollution.

Photochemical reactions initiate most of the **homogeneous gas-phase reactions**. Homogeneous gas-phase reaction refers to reaction sequences between atmospheric constituents that are all in the gas-phase. Some of them convert trace gases to water-soluble trace gases that are the link to **aqueous chemistry** and wet removal.

5.2.5.1 Tropospheric Background Chemistry

The atmosphere is mainly composed of N_2, O_2, Ar and CO_2 (Chap. 1). In addition, there are noble (non-reactive) and trace gases (reactive) and water vapor (Table 1.1). Typical concentrations of CO, SO_2, NH_3, NO, NO_2, O_3 and HNO_3 are 0.05–0.2, 10^{-5}–10^{-4}, 10^{-4}–10^{-3}, 10^{-6}–10^{-2}, 10^{-6}–10^{-2}, 10^{-2}–10^{-1}, and 10^{-5}–10^{-3} ppm, respectively. Typical background concentrations of CH_4, H_2 and N_2O are 1.65, 0.58 and 0.33 ppm.

Since some of the trace gases (e.g. NO, NO_2, NO_3, N_2O_5, HNO_2, HNO_3) are chemically reactive, chemical reaction occur even in the non-polluted atmosphere. The reaction that triggers the **background chemistry** is

$$O_3 + h\nu \longrightarrow O_2 + O^{1D} \tag{5.34}$$

at $\lambda < 0.315\,\mu$m. Reaction with water vapor yields

$$O^{1D} + H_2O \longrightarrow OH + OH\ . \tag{5.35}$$

Methane (CH_4), a greenhouse gas (Chap. 4), is the key hydrocarbon in background chemistry. It reacts with the hydroxyl radical (OH)

$$CH_4 + OH \rightarrow CH_3 + H_2O\ . \tag{5.36}$$

Hydroxyl radicals also react with CO

$$CO + OH \rightarrow CO_2 + H\ . \tag{5.37}$$

The methyl radical CH_3 and hydrogen atom H both immediately react with O_2 to produce methylperoxyl CH_3O_2 and hydroperoxyl HO_2 radicals

$$CH_3 + O_2 + M \rightarrow CH_3O_2 + M \tag{5.38}$$

$$H + O_2 + M \rightarrow HO_2 + M\ . \tag{5.39}$$

Thus, the net effects of the $CO - OH$ and $CH_4 - OH$ reaction chains are

$$CO + OH + O_2 \rightarrow HO_2 + CO_2 \tag{5.40}$$

$$CH_4 + OH + O_2 \rightarrow CH_3O_2 + H_2O\ . \tag{5.41}$$

Peroxy radicals participate in reaction chains that convert NO to NO_2 and produce OH and peroxy radicals like

$$CH_3O_2 + NO \rightarrow NO_2 + CH_3O \tag{5.42}$$

$$CH_3 + 2O_2 \rightarrow HCHO + HO_2O \tag{5.43}$$

$$HO_2 + NO \rightarrow NO_2 + OH\ . \tag{5.44}$$

Formation of nitric acid HNO_3 and hydrogen peroxide H_2O_2 terminate the major reaction chain

$$OH + NO_2 \rightarrow HNO_3 \tag{5.45}$$

$$HO_2 + HO_2 \rightarrow H_2O_2 + O_2\ . \tag{5.46}$$

A small fraction of the hydrogen peroxide photolyzes and produces OH-radicals. The CH_3O_2 radical can react with NO or HO_2.

$$CH_3O_2 + HO_2 \rightarrow CH_3OOH + O_2 \tag{5.47}$$

with a ratio of 1:1 at 300 K. The fate of CH_3OOH is still unknown. Investigation of the reaction chains shows that CO_2 – also a greenhouse gas (Chap. 4) – is the ultimate product of the methane-oxidation chain with CO being a long-lived intermediate state.

Formaldehyde H_2CO formed by reaction of O_2 with CH_3O may react with hydroxyl radicals to produce CO and HO_2 radicals or photolyze. Thus, formaldehyde is a temporary reservoir of OH.

5.2.5.2 Polluted Troposphere

Reactive nitrogen compounds like NO, NO_2, NO_3, N_2O_5, HNO_2 and HNO_3 are key players in tropospheric chemistry. With respect to urban pollution, we distinguish photosmog and London-type smog. Smog is an artificial word combined from smoke and fog. It originally referred to smoky fog conditions in London early in the twentieth century. London type smog forms when large amounts of coal are burned in a city under very humid and stagnant conditions. London-type smog contains, among other things, high concentrations of soot particles, and sulfur dioxide.

Photosmog refers to the product of photochemical reactions of nitrogen oxides and volatile organic compounds (VOC), i.e. it can be related to emissions by traffic and industrial facilities in the urban atmosphere and its conurbations, biomass burning, and wildfire emissions. It produces high ground-level ozone concentrations, and airborne particles.

Urban photosmog preferably occurs in cities with sunny, warm, but dry climates (Chap. 7). When the topographic conditions support the formations of inversions

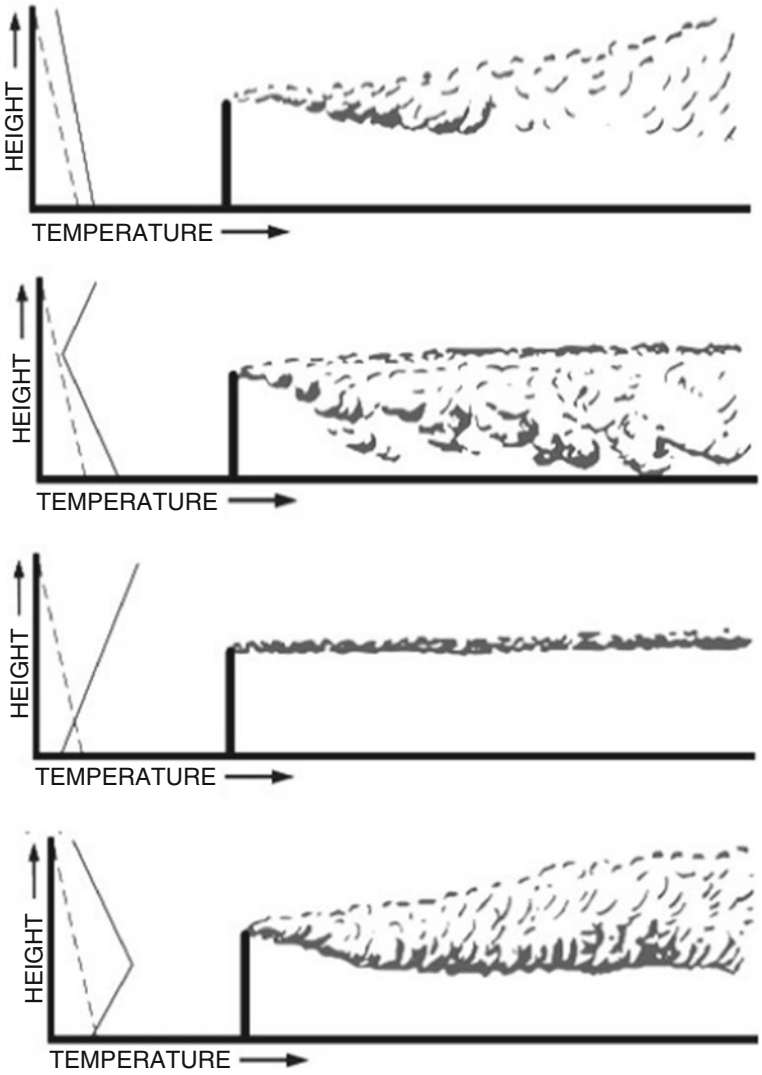

Fig. 5.1 Schematic view of interaction of atmospheric stability and dispersion of pollutants (With permission from Cummis (2013))

photosmog can lead to health problems. The photosmog reduces visibility and can often be seen as a brown cloud from higher levels. Whether or not the primary emissions accumulate under an inversion depends on the plumes buoyancy (Chap. 2; Fig. 2.11). Figure 5.1 exemplarily shows how atmospheric stability may affect air pollution. Under normal conditions, temperature decreases with height, and emitted pollutants undergo mixing (Fig. 5.1 top). An elevated inversion may trap the pollutants and the plume spreads along the inversion when its buoyancy is too low to

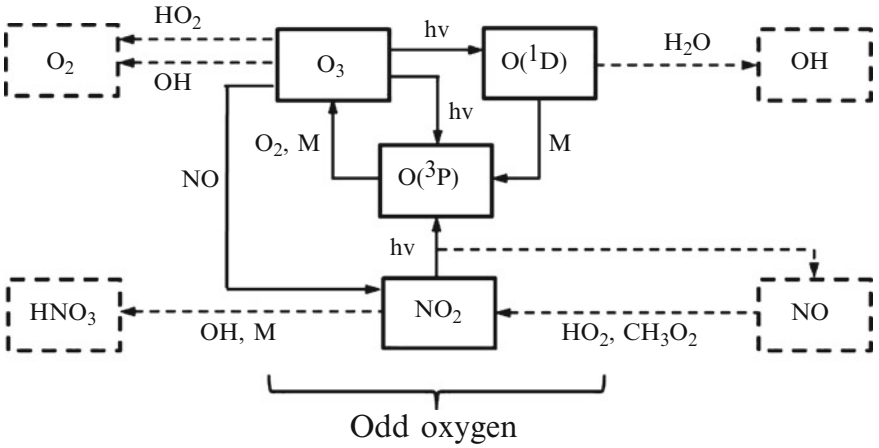

Fig. 5.2 Schematic view of major chemical reactions affecting odd oxygen (O_3, O^{3P}, O^{1D}, NO_2) in the troposphere. The letter M stands for air molecules (e.g. N_2, O_2, Ar, H_2O) serving as a third body in the reactions

break through the inversion (Fig. 5.1 third from the top). In the case of emissions into a surface inversion, vertical mixing is suppressed and the plume remains very sharp (Fig. 5.1 second from the top). When a facility emits into layers above a surface inversions the pollutants undergo vertical mixing and when hitting the inversion top spread along the its top (Fig. 5.1 bottom).

Ozone, and Hydroxyl and Nitrate Radicals

Tropospheric ozone (O_3) makes up only 10 % of the total atmospheric ozone. However, it initiates most of the primary oxidation chains in the polluted troposphere as it produces hydroxyl (OH) and nitrate (NO_3) radicals (Figs. 5.2 and 5.3). UV-radiation (at $\lambda < 0.315\,\mu m$) decomposes ozone into an energetically exited oxygen atom, O^{1D}, and molecular oxygen, O_2 (Eq. (5.34)). Most O^{1D} dissipates the excess energy as heat (but not energetically relevant; Chap. 4) and recombines with O_2 to ozone

$$O + O_2 + M \longrightarrow O_3 + M \ . \tag{5.48}$$

A cycle of no net chemical effects, like described by Eqs. (5.34) and (5.48), is called a **null cycle**. About 1 % of the O^{1D} reacts with water vapor- also a greenhouse gas – to produce OH (Eq. (5.35)). The net effect of Eqs. (5.34) and (5.35) is

$$O_3 + H_2O + h\nu \longrightarrow O_2 + 2OH \ . \tag{5.49}$$

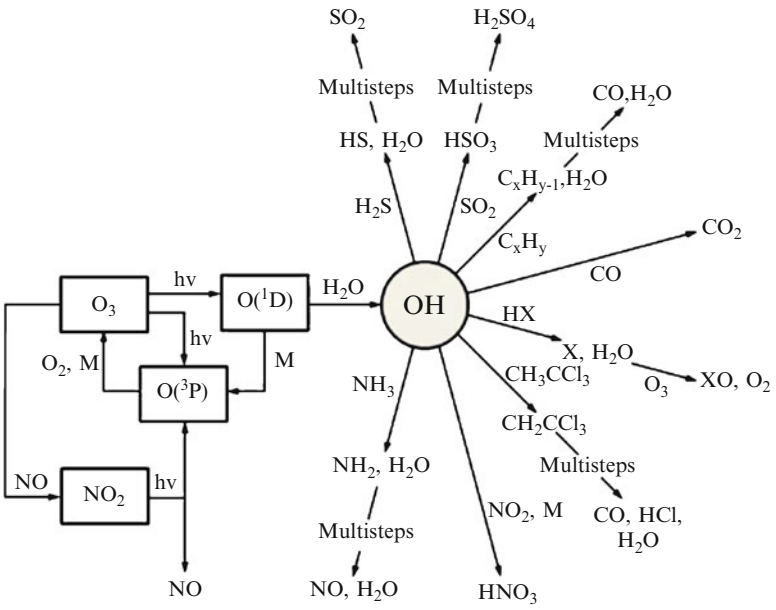

Fig. 5.3 Schematic view of the role of the *OH* radical in the oxidation of tropospheric trace gases

Since the highly reactive *OH* results primarily from photochemistry, it exists in measurable amounts only at day with mean concentrations of about $7.7 \cdot 10^{12}$ molecules m^{-3}. Daytime summer (winter) concentrations range between $5(1) \cdot 10^{12}$ and $10(5) \cdot 10^{12}$ molecules m^{-3}.

At night, *OH* concentrations are less than $2 \cdot 10^{11}$ molecules m^{-3} and the nitrate radical (NO_3) is the major reactive oxidant. NO_3 is less reactive than *OH*, but nighttime NO_3 concentrations often exceed daytime *OH* concentrations. NO_3 results from

$$NO_2 + O_3 \longrightarrow NO_3 + O_2 \,. \tag{5.50}$$

During day, NO_3 plays a minor role as it quickly photolyzes ($\tau \approx 5\,\mathrm{s}$ at noon) according to

$$NO_3 + h\nu \longrightarrow NO + O_2 \tag{5.51}$$

at $\lambda < 0.700\,\mu\mathrm{m}$ and

$$NO_3 + h\nu \longrightarrow NO_2 + O \tag{5.52}$$

$\lambda < 0.580\,\mu\mathrm{m}$.

$NO - NO_2 - O_3$

The triad $NO - NO_2 - O_3$ is the simplest mechanism of ozone formation in the absence of other reactive species. In the **photosmog** of polluted cities, such as Los Angeles, sunlight at $\lambda < 0.380\,\mu m$ dissociates tropospheric NO_2 (Fig. 5.2)

$$NO_2 + h\nu \rightarrow NO + O\ . \tag{5.53}$$

Once ozone is produced (Eq. (5.48)), it reacts with NO to re-build NO_2

$$O_3 + NO \rightarrow NO_2 + O_2 \tag{5.54}$$

The net reaction is $O_3 + h\nu \rightarrow O + O_2$. In equilibrium, we obtain for Eqs. (5.53), (5.48) and (5.54)

$$NO_2 + O_2 \rightleftharpoons NO + O_3\ . \tag{5.55}$$

The reactions given by Eqs. (5.53), (5.48), and (5.54) are in equilibrium in the absence of other chemical reactions, transport processes, sources and sinks. High (low) concentrations of NO drive the reactions backwards (forward).

Predicting the atmospheric distribution of species requires determining the production and destruction rates. We can treat the concentration of O_2 as constant ($\frac{d[O_2]}{dt} = 0$) because $[O_2] \gg [NO_2], [NO], [O], [O_3]$. Doing so reduces the system to four species, NO_2, NO, O, and O_3. The rate of change in the concentrations reads

$$\frac{d[NO_2]}{dt} = -j_1[NO_2] + k_3[O_3][NO] \tag{5.56}$$

$$\frac{d[O]}{dt} = j_1[NO_2] - k_2[O][O_2][M] \tag{5.57}$$

$$\frac{d[NO]}{dt} = -k_3[O_3][NO] + j_1[NO_2] \tag{5.58}$$

$$\frac{d[O_3]}{dt} = -k_3[O_3][NO] + k_2[O][O_2][M]\ . \tag{5.59}$$

Here j_1 is the dissociation rate coefficient and k_2 to k_4 are the reaction rate coefficients. These rates apply to a homogeneous mixture. In emission plumes, segregation and heterogeneity due to turbulence, entrainment, and detrainment alter the reaction rates (Chaps. 3 and 6).

Steady-State Approximation for the Triad $NO - NO_2 - O_3$

Evaluation of Eqs. (5.56) to (5.59) yields that the oxygen atom disappears virtually as fast as it forms. In dealing with such highly reactive constituents, often a **pseudo-steady state approximation** is made. It assumes the rate of production to be equal

to the rate of destruction $j_1[NO_2] = k_2[O][O_2][M]$. The pseudo-steady state approximation does not mean that the concentration (here $[O]$) remains constant; rather it varies with the dependent concentrations (here $[NO_2]$) in such a way that the production rate balances the loss rate at any time. The steady-state concentration of ozone is called the **photo-stationary state relation**.

For the **pseudo reaction** $NO_2 + O_2 \rightarrow NO + O_3$ an analytical solution exists

$$T_c = \frac{1}{\Delta^{1/2}} \ln \frac{X(t = t_c)}{X(t = 0)} \tag{5.60}$$

with

$$X(t = t_c) = \frac{2\alpha[O_3](t = t_c) + \beta - \Delta^{1/2}}{2\alpha[O_3](t = t_c) + \beta + \Delta^{1/2}} \tag{5.61}$$

$$[O_3](t = t_c) = \frac{1}{2\alpha}(\Delta^{1/2} \frac{1 + X(t = 0)\exp(t_c\Delta^{1/2})}{1 - X(t = 0)\exp(t_c\Delta^{1/2})} - \beta) \tag{5.62}$$

and $\alpha = -k_1$, $\beta = k_1([O_3](t = 0) - [NO](t = 0)) - k_3$ and $\Delta = 4k_2k_3([NO](t = 0) + [NO_2](t = 0) + (k_3 + k_1([O_3](t = 0) - [NO](t = 0))))^2$. Here t_c is the response time to achieve nearly chemical equilibrium between NO, NO_2 and O_3. These equations serve to assess the effects of chemical reactions of these components when applying dynamic chambers (Appendix B).

Example. Derive the steady state oxygen and ozone concentrations.

Solution. Steady-state means $\frac{d[O]}{dt} = 0$, $\frac{d[O_3]}{dt} = 0$. Rearranging provides

$$[O] = \frac{j_1[NO_2]}{k_2[O_2][M]}$$

$$[O_3] = \frac{j_1[NO_2]}{k_3[NO]}$$

The latter is the **Leighton-relationship**.

Presence of Non-methane Carbons, HO_2- and OH-Radicals

Non-methane carbons (e.g. HO_2-radicals, OH-radicals) initiate complex reaction chains (Fig. 5.2) that lead to much higher ozone concentrations than possible in the equilibrium of the triad $NO - NO_2 - O_3$. OH radicals quickly oxidize various other atmospheric constituents (e.g. NO_2 to HNO_3, H_2S to SO_2, SO_2 to H_2SO_4, CH_2O

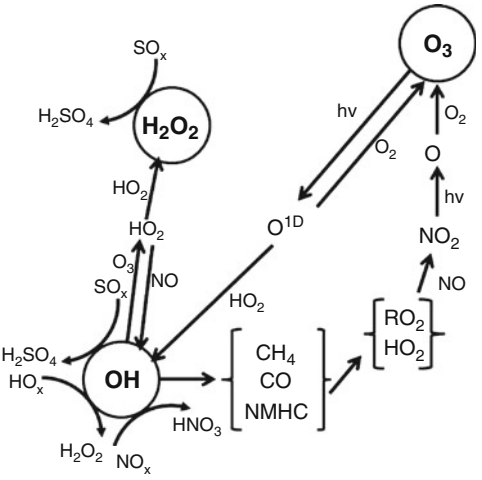

Fig. 5.4 Schematic view of the roles of H_2O_2, O_3, and OH in atmospheric reactions

to CO, and CO to CO_2) (Fig. 5.3). OH-radicals may also produce HO_2 and H_2O_2 (Fig. 5.4). These species are short-lived oxidizing radicals in the atmosphere (cf. Table 1.1).

Possible reactions that finally destroy ozone and shift the equilibrium of $NO - NO_2 - O_3$ are

$$O_3 + OH \longrightarrow O_2 + HO_2 \tag{5.63}$$

$$HO_2 + O_3 \longrightarrow 2O_2 + OH\ . \tag{5.64}$$

The latter reaction is of greater importance than the former as OH reacts to form the hydroperoxy radical HO_2. The hydroperoxy radical primarily reacts with CO and CH_4 and provides links to aqueous chemistry (Sect. 5.3).

The reaction of OH and CO may finally lead to hydrogen peroxide (H_2O_2) by

$$OH + CO \longrightarrow CO_2 + H \tag{5.65}$$

$$H + O_2 + M \longrightarrow HO_2 + M \tag{5.66}$$

$$HO_2 + HO_2 \longrightarrow H_2O_2 + O_2\ . \tag{5.67}$$

Hydrogen peroxide can dissolve in water and oxidizes the absorbed SO_2 to H_2SO_4 (Sect. 5.3).

Presence of Methane and OH-Radicals

Methane (CH_4) oxidizes through a number of steps started by the reaction with hydroxyl radicals

$$CH_4 + OH \rightarrow CH_3 + H_2O\ . \tag{5.68}$$

The net reaction is

$$CH_4 + 2O_2 + 2NO \rightarrow HCHO + H_2O + 2NO_2 \,. \tag{5.69}$$

Another reaction path involving CH_4 represents the main atmospheric source of formaldehyde ($HCHO$), an eye-irritant,

$$CH_4 + 4O_2 \rightarrow HCHO + H_2O + 2O_3 \,. \tag{5.70}$$

The reaction of CH_4 with OH results in methyl-peroxyl (CH_3O_2) by

$$OH + CH_4 \longrightarrow CH_3 + H_2O \tag{5.71}$$

$$CH_3 + O_2 + M \longrightarrow CH_3O_2 + M \tag{5.72}$$

$$CH_3O_2 + HO_2 \longrightarrow CH_3OOH + O_2 \,. \tag{5.73}$$

CH_3OOH can dissolve in cloud droplets and/or raindrops. Since usually the concentration of dissolved CH_3OOH is small, it is not a major oxidant in the aqueous phase (Sect. 5.3).

Other reaction chains are

$$CH_3 + O_2 \longrightarrow CH_3O_2 \tag{5.74}$$

$$CH_3O_2 + NO \longrightarrow HCHO + HNO_2 \tag{5.75}$$

$$HO_2 + NO \longrightarrow NO_2 + OH \,. \tag{5.76}$$

Since NO_2 can be photolyzed (Eq. (5.53)), it can contribute to tropospheric ozone formation. The released NO_2 can react with NO to produce OH and then formaldehyde $HCHO$, which is photochemically very reactive

$$HCHO + h\nu \longrightarrow H + HCO \,. \tag{5.77}$$

The resulting products can react with oxygen

$$H + O_2 + M \longrightarrow HO_2 + M \tag{5.78}$$

$$HCO + O_2 + M \longrightarrow CO + HO_2 + M \,. \tag{5.79}$$

The latter reaction reproduces the HO_2 radical. Obviously, in tropospheric chemistry, NO_x provides the path for methane oxidation by oxidizing NO to NO_2 and by producing formaldehyde.

Role of $OH - NO_2$ and $OH - SO_2$

A small quantity of OH oxidizes NO_2 and SO_2 in homogeneous reactions to build weak acids

$$NO_2 + OH \rightarrow HNO_3 \tag{5.80}$$

$$SO_2 + OH \rightarrow HSO_3\ . \tag{5.81}$$

The reaction with NO_2 is very fast as compared to that with SO_2. Other sinks of SO_2 than the above reaction are absorption by vegetation and at ocean surfaces and uptake by cloud and rain drops (Sect. 5.3).

5.2.6 Stratospheric Chemistry

The little vertical mixing at the tropopause yields a strong gradient between the ozone poor, relatively water-vapor rich troposphere and ozone rich and relatively water-vapor poor stratosphere. Thunderstorms breaking through the tropopause, and tropopause folding (Chaps. 3 and 6) permit the exchange of tropospheric and stratospheric air.

Only several kilometers above the tropopause, ozone concentrations are about an order of magnitude higher than in the troposphere. The stratospheric ozone results from photolysis and forms a shield that protects life from the most tissue damaging radiation by reducing the intensity of UV radiation between 0.23 and 0.32 μm. As mentioned in Chaps. 1 and 4, absorption of radiation by ozone yields to the stratospheric temperature profile. Ozone production is highest in the stratosphere over the Tropics as it depends on photochemistry. Ozone-concentration maxima result from transport away from the equator, flux divergence, and the balance between production and loss (Chap. 6). Thus, the thickness of the ozone layer highly varies (Chap. 1; Fig. 1.4). The largest column densities of ozone occur in northern hemispheric polar region, and southern hemispheric mid-latitude spring.

5.2.6.1 Chapman Cycle

In 1930, Chapman[4] explained the presence of the stratospheric ozone layer. He applied the following set of oxygen-only reactions that start with photolysis of molecular oxygen at wavelengths $\lambda < 0.240\,\mu m$

$$O_2 + h\nu \longrightarrow^{j_1} 2O \tag{5.82}$$

$$O + O_2 + M \longrightarrow^{k_1} O_3 + M\ . \tag{5.83}$$

[4]Sydney Chapman, British geophysicist and mathematician, 1888–1970.

The molecule M (N_2 or O_2) takes up the energy released in the reaction, and accelerates, i.e. it takes up kinetic energy. Photolysis at wavelengths $0.2 < \lambda < 0.3\,\mu\text{m}$ yields

$$O_3 + h\nu \longrightarrow^{j_2} O + O_2 \,. \tag{5.84}$$

Absorption of energy by vibrationally and rotationally excited ozone from O_3 photolysis in the Huggins band (0.305–0.325 μm) has a quantum yield of O^{1D} of about 0.2–0.3 for wavelengths between 312 and 320 nm at 298 K.[5]

Ozone reacts with O to form O_2

$$O + O_3 \longrightarrow^{k_2} 2O_2 \,. \tag{5.85}$$

The net production and depletion amount

$$3O_2 \longrightarrow 2O_3 \tag{5.86}$$

or

$$2O_3 \longrightarrow 3O_2 \,. \tag{5.87}$$

The balance between these reactions maintains a steady-state concentration of ozone at approximately $7 \cdot 10^{18}$ molecules m^{-3} with a peak at about 30 km height. Thus, we get for the change of ozone

$$\frac{d[O_3]}{dt} = k_1[O][O_2][M] - j_2[O_3] - k_2[O][O_3] \tag{5.88}$$

and oxygen

$$\frac{d[O]}{dt} = 2j_1[O_2] + j_2[O_3] - k_1[O][O_2][M] - k_2[O][O_3] \,. \tag{5.89}$$

The total number of oxygen atoms is conserved. Adding the temporal change of ozone and oxygen provides the change of odd oxygen, $O_x = O + O_3$,

$$\frac{d[O_x]}{dt} = \frac{dO}{dt} + \frac{dO_3}{dt} = 2j_1[O_2] - 2k_2[O][O_3] \,. \tag{5.90}$$

Obviously, Eqs. (5.88)–(5.90) are coupled. Under steady-state conditions, $\frac{d[O_x]}{dt} = 0$, $\frac{d[O]}{dt} = 0$, and $\frac{d[O_3]}{dt} = 0$. Expressing them in terms of each other yields

$$k_1[O][O_2][M] = j_2[O_3] + k_2[O][O_3] \tag{5.91}$$

[5]Research suggests that photolysis of vibrationally excited oxygen can provide an extra source of ozone.

and

$$j_1[O_2] = k_2[O][O_3] \; . \tag{5.92}$$

In the stratosphere, on average, $j_2 \gg k_2[O]$. Thus, we can approximate Eq. (5.91) by $k_1[O][O_2][M] \approx j_2[O_3]$ and express the equilibrium ratio of odd-oxygen constituents as a function of j_2, k_1, and the number density of O_2 and air, indicated by the molecule M, by

$$\frac{[O]}{[O_3]} = \frac{j_2}{k_1[O_2][M]} \; . \tag{5.93}$$

The rapid reactions (Eqs. (5.82 and 5.83)) govern the above ratio that is very small in the lower and middle stratosphere. Consequently, atomic oxygen is much less abundant than is ozone at these levels. Inserting this ratio into Eq. (5.92) yields the equilibrium number density of ozone as a function of the number density of molecular oxygen, air, and the rate coefficients

$$[O_3] = [O_2]\sqrt{(\frac{j_1 k_1[M]}{j_2 k_2})} \; . \tag{5.94}$$

Equations (5.82)–(5.94) are known as the **Chapman-theory**. The Chapman theory predicts too high ozone maxima as compared to observations. Shortcomings of the Chapman theory are the neglecting of further ozone-depletion processes, especially, catalytic reactions, transport of ozone and other species. Furthermore, the time-scale for odd oxygen production is a few minutes, while that for destruction is several weeks. O and O_3 adjust quickly, while O_x changes very slowly.

5.2.6.2 Catalytic Destruction of Stratospheric Ozone

Catalytic cycles with a catalyst X can deplete stratospheric ozone

$$X + O_3 \longrightarrow^{k_3} XO + O_2 \tag{5.95}$$

$$XO + O \longrightarrow^{k_4} X + O_2 \; . \tag{5.96}$$

Providing a net reaction of

$$O + O_3 \longrightarrow 2O_2 \; . \tag{5.97}$$

Gases acting as catalysts in the stratosphere are OH, NO, and chlorine (Cl). Some catalysts can temporally exist in inactive reservoir species like dinitrogen pentoxide (N_2O_5), hydrochloric acid (HCl) or chlorine nitrate ($ClONO_2$). In the lower stratosphere, mixed hydrogen-halogen, halogen or NO reactions are most common.

In the middle stratosphere, catalytic reactions with Cl play a key role, while in the upper stratosphere catalytic reactions with H and OH dominate.

Chlorofluorocarbons

The ozone "hole" over Antarctica results from a combination of dynamical processes (strong vortex; Chap. 6) and chemical destruction of ozone by chlorofluorocarbons CFC, also called the **freons**. CFC absorbs in the infrared, for which it is also a greenhouse gas (Chap. 4). CFC are produced as aerosol propellants, solvents, and refrigerants and are nearly inert in the troposphere. The most common CFC are $CFC-11$ ($CFCl_3$) and $CFC-12$ (CF_2Cl_2). Once CFCs reach the stratosphere, it can be photolyzed between $0.19\,\mu\text{m} < \lambda < 0.22\,\mu\text{m}$

$$CFCl_3 + h\nu \longrightarrow CFCl_2 + Cl \tag{5.98}$$

$$CF_2Cl_2 + h\nu \longrightarrow CF_2Cl + Cl \tag{5.99}$$

The produced Cl acts as a catalyst destroying ozone

$$Cl + O_3 \rightarrow ClO + O_2 \tag{5.100}$$

$$O_3 + h\nu \rightarrow O + O_2 \tag{5.101}$$

$$ClO + O \rightarrow Cl + O_2 \tag{5.102}$$

The net reaction is

$$O_3 + h\nu \rightarrow 3O_2\,. \tag{5.103}$$

Probably Cl is removed from the atmosphere as HCl.

Nitrogen Monoxide

Photolysis of NO_2 that originates from the troposphere, produces stratospheric NO

$$N_2O + h\nu \rightarrow N_2 + O^{1D} \tag{5.104}$$

$$N_2O + O^{1D} \rightarrow 2NO \tag{5.105}$$

NO catalytically destructs ozone as follows

$$NO + O_3 \rightarrow NO_2 + O_2 \tag{5.106}$$

$$O_3 + h\nu \rightarrow O + O_2 \tag{5.107}$$

$$NO_2 + O \rightarrow NO + O_2 \tag{5.108}$$

leading to the same net reactions as discussed for CFC.

Polar Stratospheric Clouds (PSC) provide surfaces for heterogeneous chemical reactions and HNO_3 formation. These HNO_3 particles sediment out. The presence of ice particles greatly enhances the reaction.

Example. Assume that in the stratosphere, NO reacts with ozone to build NO_2 at $k_1 = 3.5 \cdot 10^{-15}\,\mathrm{cm^3\ molecules^1\ s^{-1}}$ which then further reacts with O to reproduce NO with a rate of $k_2 = 9.3 \cdot 10^{-12}\,\mathrm{cm^3\ molecules^1\ s^{-1}}$. Concurrently, O and O_3 react to $2O_2$ at $k_3 = 6.8 \cdot 10^{-16}\,\mathrm{cm^3\ molecules^1\ s^{-1}}$. Write down the reaction chain, net reaction, and the concentration NO_2 can have to destroy O_3 faster than the reaction cycle.

Solution.

$$NO + O_3 \longrightarrow^{k_1} NO_2 + O_2$$

$$NO_2 + O \longrightarrow^{k_2} O_2 + NO$$

$$O + O_3 \longrightarrow^{k_2} 2O_2\ .$$

The net reaction of the first two reactions is

$$O + O_3 \longrightarrow 2O_2\ .$$

The net reaction cannot be faster than the rate at which atomic oxygen is destroyed. Thus, k_2 determines the rate

$$-\frac{d[O]}{dt} = k_2[NO_2][O]$$

In the last reaction, O is destroyed at

$$-\frac{d[O]}{dt} = k_3[O_3][O]\ .$$

To destroy O and hence O_3 faster by the last reaction $k_2[NO_2][O] < k_3[O_3][O]$. Thus, $[NO_2] < \frac{k_3[O_3]}{k_2} = 7.3 \cdot 10^{-5}[O_3]$.

Hydrogen Atom, Hydroxyl and Hydroperoxyl

Reaction with water vapor and methane produce hydrogen-containing species (hydrogen atoms (H), hydroxyl (OH), hydroperoxyl (HO_2)). Water vapor naturally occurs in low concentrations in the stratosphere. The mean residence time of

tropospheric methane (CH_4) is long enough that it can migrate into the stratosphere. Methane and water vapor react with an excited oxygen atom stemming from ozone photolysis

$$O^{1D} + H_2O \longrightarrow 2OH \tag{5.109}$$

$$O^{1D} + CH_4 \longrightarrow CH_3 + OH\ . \tag{5.110}$$

Hydrogen containing species cause about 10 % of the stratospheric ozone destruction without being destroyed

$$O + HO_2 \longrightarrow OH + O_2 \tag{5.111}$$

$$OH + O_3 \longrightarrow HO_2 + O_2\ . \tag{5.112}$$

The net reaction is $O + O_3 \longrightarrow 2O_2$.

5.3 Heterogeneous Chemistry

5.3.1 Dissolution of Gases

In aqueous chemistry, we consider open and closed systems. A drop is an open system when we consider equilibrium and/or uptake from or release to the gas phase. The gas phase partial pressure is assumed to be constant as the ambient air volume is large compared to the drop. When we consider a decrease/increase of the partial pressure in the ambient air, as the drop takes up/releases the gas, we have a closed system, i.e. the total quantity of the species would be fixed.

Gases in the immediate vicinity of a droplet or water surface absorb and dissolve in the liquid (Fig. 3.1). The liquid in which the gas dissolves is called the **solvent** and makes up the bulk of the **solution**. A **solute** (units moles) is a gas, liquid or solid that dissolves in a solution. Two common writings for the absorption of species in water exist

$$A(g) \rightleftharpoons A(aq) \tag{5.113}$$

or

$$A(g) + H_2O \rightleftharpoons A \cdot H_2O \tag{5.114}$$

where $A(aq)$ or $A \cdot H_2O$ are the dissolved state. Any dissolvable gas $[A]_{total}$ is distributed between the gasphase and aqueous phase

$$[A]_{total} = \frac{p_a}{RT} + [A(aq)]\, LWC \tag{5.115}$$

where LWC is the liquid water content.

Solubility is the maximum amount of gas that can dissolve under the given temperature condition and amount of solvent. Under these conditions, the solution $[A \cdot H_2O]$ is saturated. We can determine the solubility by **Henry's law**[6]

$$[A \cdot H_2O] = k_H p_A \tag{5.116}$$

where k_H and p_A are the temperature-dependent **Henry's law coefficient** or **Henry's law constant** and the partial pressure (in atm) of the gas. The unit of Henry's law coefficient is mole liter^{-1} atm^{-1} = molarity = M. Since techniques to measure Henry's law coefficients and thermodynamic data improve in accuracy over time, we recommend checking sources like http://www.henrys-law.org/ for the most recent values.

We can define a dimensionless Henry's law coefficient when the gaseous and aqueous concentration are given on a molar basis

$$\hat{k}_H = \frac{[A \cdot H_2O]}{[A(g)]} \frac{k_H p_g}{p_g/(R_c^* T)} = k_H R_c^* T \tag{5.117}$$

where $R_c^* = 0.082 \cdot 10^5\,\mathrm{Pa\,M^{-1}\,K^{-1}}$ is the universal gas constant in chemical units. Water completely absorbs gases having high Henry's law coefficients ($k_H > 10^3$).

Example. Give the fraction of total H_2O_2 when H_2O_2 dissolves in water. Discuss the behavior.

Solution.

$$[H_2O_2]_{total} = \frac{p_{H_2O_2}}{R\,T} + [H_2O_2(aq)]\,LWC$$

$$[H_2O_2(aq)] = k_{H_2O_2} p_{H_2O_2}$$

$$\frac{k_{H_2O_2}}{LWC} \frac{1}{R\,T} + k_{H_2O_2} LWC\ .$$

The aqueous-phase fraction decreases with increasing liquid water content as there is more water available to accommodate the H_2O_2.

According to **van't Hoff**[7]**'s equation** the temperature of an equilibrium constant reads

$$\frac{d \ln k_H}{dT} = \frac{\Delta H}{R_c^* T^2} \tag{5.118}$$

[6] William Henry, British physicist and chemist, 1774–1836.

[7] Jacobus Henricus van't Hoff, Dutch physical chemist and first winner of the Nobel Prize for Chemistry (1901), 1852–1911.

where ΔH is the molar enthalpy (or heat) of reaction at constant pressure and temperature (Chap. 2), i.e. the negative of the heat involved for the reaction. We can assume the enthalpy as being independent of temperature for small temperature ranges. This approximation for the Henry's law coefficient reads

$$k_H(T_2) = k_H(T_1) \exp\left(\frac{\Delta\overline{H_0}}{R_c^*}(\frac{1}{T_1} - \frac{1}{T_2})\right) \tag{5.119}$$

where T_1 and T_2 are temperature (in K). According to Eq. (5.119), the Henry's law coefficient decreases with increasing temperature, i.e. solubility is greater at lower temperatures.[8]

The subscript 0 in ΔH_0 indicates the standard state (25 °C, 1 atm). Values of the molar enthalpy of atmospheric species are listed in data bases like http://www.nist.gov/srd/index.cfm that are regularly updated. In general, we can determine the molar enthalpy for a given forward reaction by

$$[g\Delta H_0(G) + h\Delta H_0(H) + \cdots] - [a\Delta H_0(A) + b\Delta H_0(B) + \cdots]\,. \tag{5.120}$$

Positive (negative) molar enthalpy values indicate that heat is absorbed (released) when a molecule forms from its constituents at standard state. When due to a change in temperature and/or composition of the gas the solubility changes, dissolved gas can move from the solution to the gas phase.

5.3.2 Ionization

Dissociation breaks dissolved molecules into simpler components, **ions**. Ions may combine with other components and precipitate out of the solution as solids. An acid HA reacts with water according to

$$HA(aq) + H_2O(l) \rightleftharpoons H_3O^+(aq) + A^-(aq) = [H^+] + A^-(aq)\,. \tag{5.121}$$

Note that $[H_3O^+(aq)]$ is an equivalent expression for $[H^+]$. The strength of HA can be measured by the equilibrium constant for the forward reaction

$$k_a = \frac{[H_3O^+(aq)][A^-(aq)]}{[HA(aq)]} \tag{5.122}$$

[8] This relationship is the reason why shells of mussels or water snails are more structured in tropical than Arctic waters. It also explains why there is less CO_2 in the ocean during warm climate periods than ice ages.

with k_a being the **ionization constant** or **acid dissociation constant** of HA. The conjugate base of A^- of HA undergoes the forward reaction

$$A^-(aq) + H_2O(l) \rightleftharpoons HA(aq) + OH^-(aq) \tag{5.123}$$

with the equilibrium constant

$$k_b = \frac{[HA(aq)][OH^-(aq)]}{[A^-(aq)]} \,. \tag{5.124}$$

Leading to

$$\begin{aligned} k_w = k_a k_b &= \frac{[H_3O^+(aq)][A^-(aq)]}{[HA(aq)]} \frac{[HA(aq)][OH^-(aq)]}{[A^-(aq)]} \\ &= [H_3O^+(aq)][OH^-(aq)] = [H^+][OH^-] \,. \end{aligned} \tag{5.125}$$

For water, ionization yields

$$H_2O \rightleftharpoons^{k'_w} H^+ + OH^- \,. \tag{5.126}$$

At equilibrium

$$k'_w = \frac{[H^+][OH]}{[H_2O]} \tag{5.127}$$

where $k'_w = 1.82 \cdot 10^{-16}\,\mathrm{M}$ at 25 °C. Incorporation of the molar concentration of pure water into k'_w provides

$$k_w = [H^+][OH^-] \tag{5.128}$$

i.e. for pure water $[H^+] = [OH^-]$.

Example. Determine the reaction-coefficient rates and the concentration of NH_4^+ when NH_3 absorbs in water according to

$$NH_3(g) + H_2O \rightleftharpoons^{k_1} NH_3 \cdot H_2O$$

$$NH_3 \cdot H_2O \rightleftharpoons^{k_2} NH_4^+ + OH^-$$

as a function of the involved concentrations.

(continued)

(continued)

Solution. Henry's law provides

$$k_1 = \frac{[NH_3 \cdot H_2O]}{p_{NH_3}}$$

$$k_2 = \frac{[NH_4^+][OH^-]}{[NH_3 \cdot H_2O]}$$

Rearranging k_2 for $[NH_4^+]$, replacing $[NH_3 \cdot H_2O]$ from k_1, and considering that at equilibrium $k_w = [H^+][OH^-]$ provides

$$[NH_4^+] = \frac{k_2[NH_3 \cdot H_2O]}{[OH^-]} = \frac{k_2 k_1 p_{NH_3}[H^+]}{k_w}.$$

5.3.2.1 pH-Scale

At equilibrium, $k_w = [H^+][OH^-] = 10^{-14}\,\mathrm{M}^2$ for pure water at standard state, i.e. $[H^+] = \sqrt{10^{-14}\,\mathrm{M}^2} = 10^{-7}\,\mathrm{M}$. A solution, for which this relation is valid, is called **neutral**. When $[H^+(aq)] > [OH^-(aq)]$, the solution is **acidic** and when $[H^+(aq)] < [OH^-(aq)]$ it is **basic**. Defining

$$pH = -\log[H^+] = -\log[H_3O^+(aq)] \tag{5.129}$$

provides a measure ranging from 1 to 14 to characterize the severity of a solution (e.g. **acid rain**). Thus, pure water has a pH-value of 7.

On this logarithmic pH-scale, the magnitude of acidity increases with decreasing pH-value ($acidity = 1 \cdot 10^{-pH}$). Thus, the acidity of a rain sample with $pH = 4$, for example, is 10^{-4} units, the acidity for $pH = 5$ is 10^{-5} units, etc. A change of hydrogen ion concentration by an order of 10 alters the pH-value by one unit.

Seawater typically has pH between 8 and 8.3. In absence of decay vegetation, soil water pH is 4 or less. The pH of normal rainwater ($pH = 5.6$ at 298 K) is less than that of pure water ($pH = 7$ at 298 K) due to the natural presence of weak carbonic acid. During freezing, some species leave the drop as the amount of water decreases and the concentration in the solute increases. Drop growth by collection or change in size by diffusion (Chap. 3) alters the equilibrium between the gas phase and solution. Typically large drops are less acidic than small drops.

Example. An exhaust plume has a liquid water content of $0.4\,\mathrm{g\,m^{-3}}$ in which $46\,\mu\mathrm{g\,m^{-3}}$ sulfuric acid are dissolved. Calculate the pH-value of the water droplets in the plume. Ignore any interaction with the ambient air.

Solution. Ionization of H_2SO_4 yields

$$H_2SO_4(l) + 2H_2O(aq) \rightleftharpoons SO_4^{=}(aq) + 2H_3O^+(aq)$$

For every mole of $H_2SO_4(l)$ two moles of $H_3O^+(aq)$ form. Thus,

$$pH = -\log[H^+] = -\log[H_3O^+(aq)]^2 = -\log[H_2SO_4(l)]$$

The molecular weight of H_2SO_4 is $96\,\mathrm{g\,mol^{-1}}$. The concentration in the plume droplets is

$$[H_2SO_4(l)] = \frac{46 \cdot 10^{-6}\,\mathrm{g\,m^{-3}}}{96\,\mathrm{g\,mol^{-1}} \cdot 0.4\,\mathrm{g\,m^{-3}}} = 1.198 \cdot 10^{-3}\,\mathrm{mol\,kg^{-1}}.$$

With 1 kg of water being 1 L

$$pH = -\log(1.198 \cdot 10^{-4}) = 2.9\,.$$

5.3.3 Acid-Base Equilibrium

Henry's law equilibrium depends on aqueous sinks such as ionization or complexation. In nature, drops are usually far away from equilibrium because the mass transfer into the drop may be too slow. Atmospheric gases that build strong electrolytes when in solution (e.g. hydrogen iodide, methane sulfuric acid, nitric acid) also affect the pH-value. Due to their huge Henry's law coefficients, these gases can dissolve in even very small droplets or even the water of hydrated aerosols and lead to very high concentrations of the solution. Since the determination of thermodynamic data for temperature dependence of aqueous equilibrium constants at standard state (25 °C, 1 atm) is ongoing, we recommend to use databases like http://www.nist.gov/srd/index.cfm to use the most recent equilibrium constant, and thermodynamic data for ΔH_0.

The Henry's law coefficient accounts only for the physical solubility of a gas. When gas dissolves and participates in aqueous reactions, solubility becomes greater than that derived from Henry's law (Eq. (5.119)). The acid-base equilibrium namely pulls further material into solution. The **effective Henry constant** reads

$$k_{eff}(A) = k_H(A)\left(1 + \frac{k_1}{[B(aq)]^b} + \frac{k_2}{[C(aq)]^c} + \cdots\right) . \tag{5.130}$$

Hydrolysis refers to a reaction between ionic species in the aqueous solution and liquid water. Its equilibrium constant is the hydrolysis constant. It is advantageous to describe the chemical reactions occurring in an aqueous system by defining a chemical basis made of independent components. Elements (Na, K, Ca, Mg, S, O, H, C, Cl, ...) can form an appropriate basis, but are not always an easy basis to use. We need to choose the best components. They must also be independent, i.e. the **stoichiometry** of one reaction cannot be expressed as the linear combination of two or more other reactions.[9] This so-called **Tableau Method** transforms the chemical problem into a mathematical set of equations that we can solve numerically or by simple approximations. Respecting the notion of basis, i.e. independent components, we can alter easily the basis, and change components by algebra. In dilutes, the number of moles of water is large compared to the number of moles of solutes. It is best to always choose H_2O as a component. Since H_2O entails solving a trivial equation, we typically omit it from the notation. The proton H^+ has to be selected systematically as a component. The proton conservation equation serves to express all chemical species as a linear combination of the components' species, the stoichiometry of the chemical reactions. Each chemical species has a unique decomposition on the components' basis. All aqueous solutions are electro-neutral, i.e. they have no net electrical charge despite consisting of charged species (ions). The **electro-neutrality** equation expresses the balance of positive and negative charges

$$\sum_{i=1}^{n} z_i m_i = 0 \tag{5.131}$$

where z_i is the charge of the ith ion and m_i is its concentration. We need to select the neutral species.

Example. Carbon dioxide dissolves in drops according to $[CO_2(aq)] = k_{eff}(CO_2)p_{CO_2}$ where $[CO_2(aq)]$ and 395 ppm are the total concentration of CO_2 in the droplet and the CO_2 concentration in air. Calculate the equilibrium partial pressure p_{CO_2} in air, and determine the effective Henry's law coefficient under consideration of the subsequent hydrolysis of carbonic acid to calculate the $CO_2(aq)$ concentration in water. Assume air pressure is 1,000 hPa.

(continued)

[9] A rule of thumb (necessary, but not sufficient condition) is that the number of components must equal the number of species minus the number of independent reactions.

(continued)

Solution. According to the literature, at standard state, the Henry constant of CO_2 and dissociation constants are $\approx 3.4{\cdot}10^{-2}\,\mathrm{M\,atm^{-1}}$, $\approx 4.238{\cdot}10^{-7}\,\mathrm{M^{-1}}$, and $\approx 4.687 \cdot 10^{-11}\,\mathrm{M^{-1}}$, respectively. For simplicity, let us name the latter two k_1 and k_2, respectively. Carbonic acid ($H_2CO_3(aq)$) forms according to

$$CO_2(g) + H_2O(aq) \rightleftharpoons CO_2 \cdot H_2O(aq) \rightleftharpoons H_2CO_3(aq)$$
$$H_2CO_3(aq) + H_2O(aq) \rightleftharpoons HCO_3^-(aq) + H_3O^+(aq)$$
$$HCO_3^-(aq) + H_2O(aq) \rightleftharpoons CO_3^{2-}(aq) + H_3O^+(aq)$$

$[H_3O^+(aq)] = [H^+] = 10^{-7}\,M$. According to Henry's law

$$k_H(CO_2) = \frac{[H_2CO_3(aq)]}{p_{CO_2}} = \frac{[CO_2 \cdot H_2O]}{p_{CO_2}}$$

When the last two reactions are in equilibrium, the successive acid dissociation constants are

$$k_1 = \frac{[H_3O^+(aq)][HCO_3^-(aq)]}{[H_2CO_3(aq)]}$$
$$k_2 = \frac{[H_3O^+(aq)][CO_3^{2-}(aq)]}{[HCO_3^-(aq)]}\,.$$

The concentrations are

$$[H_2CO_3(aq)] = k_H(CO_2)\,p_{CO_2}$$
$$[HCO_3^-(aq)] = \frac{k_1[H_2CO_3(aq)]}{[H_3O^+(aq)]} = \frac{k_1 k_H(CO_2)\,p_{CO_2}}{[H_3O^+(aq)]}$$
$$[CO_3^{2-}(aq)] = \frac{k_2[HCO_3^-(aq)]}{[H_3O^+(aq)]} = \frac{k_1 k_2 k_H(CO_2)\,p_{CO_2}}{[H_3O^+(aq)]^2}\,.$$

The total concentration of dissolved CO_2 is

$$[CO_2(aq)] = [H_2CO_3(aq)] + [HCO_3^-(aq)] + [CO_3^{2-}(aq)]$$
$$[CO_2(aq)] = k_H(CO_2)\,p_{CO_2}\left(1 + \frac{k_1}{[H_3O^+(aq)]} + \frac{k_1 k_2}{[H_3O^+(aq)]^2}\right)$$

The effective Henry's law constant is

(continued)

(continued)

$$k_{eff}(CO_2) = k_H(CO_2)\left(1 + \frac{k_1}{[H_3O^+(aq)]} + \frac{k_1 k_2}{[H_3O^+(aq)]^2}\right) =$$

$$k_H(CO_2)\left(1 + \frac{4.238 \cdot 10^{-7}}{[H_3O^+(aq)]} + \frac{1.9864 \cdot 10^{-17}}{[H_3O^+(aq)]^2}\right) > k_H(CO_2)$$

$$= 3.4 \cdot 10^{-7}\,\mathrm{M\,Pa^{-1}}$$

as all terms are positive. With $p_{CO_2} = 395\,\mathrm{ppm}\,10^5\,\mathrm{Pa} = 3.95 \cdot 10^7\,\mathrm{Pa}$, we obtain $[CO_2(aq)] = 3.4 \cdot 10^{-7}\,\mathrm{M\,Pa^{-1}}\,3.95 \cdot 10^7\,\mathrm{Pa} = 1{,}343\,\mathrm{M}$.

5.3.4 Aqueous Phase Reactions

Sulfate, nitrate, ammonium, and cloud chemical composition vary in time and space. In the northeastern US, eastern Canada, eastern Europe and Scandinavia, sulfate dominates the environment because of coal-usage with high sulfur amounts.[10] In the western US, nitrate prevails. Observations reveal drop-size dependent compositions of droplets. Some species are enriched in small, others in large droplets. This finding may be explained by differential uptake and inertial CCNs (Fig. 3.1).

Many aqueous reactions start with the diffusion of $SO_2(g)$ to a water surface, for instance, a drop, and its dissolution therein. At the gas-drop interface, the reversible reaction is

$$SO_2(g) \rightleftharpoons SO_2(aq) \tag{5.132}$$

which produces sulfur dioxide ($SO_2(aq)$). In the solution, conversion to sulfate ions (SO_4^{2-}) through various heterogeneous reactions occurs, for instance

$$SO_2 + H_2O \rightarrow H^+ + HSO_3^- \tag{5.133}$$

$$2HSO_3^- + O_2 + M \rightarrow 2H^+ + 2SO_4^{2-} + M\ . \tag{5.134}$$

Sulfuric acid (H_2SO_4) and bisulfite (HSO_3) are removed from the atmosphere as dissolved constituents in raindrops. The highly reactive trace species contained in liquid hydrometeors by gas dissolution and scavenging can lead to rapid chemical aqueous phase reactions.

[10]Note that after the unification of the German states, air chemistry changed from a London-type smog to Los Angles type smog in East Germany when the traffic amount increased, filters were installed, plants were shut down, and the usage of sulfur-rich coal was reduced.

A huge amount of sulfur gases (e.g. CS_2, H_2S, COS, DMS) can oxidize to SO_4^{2-} (sulfate). Heterogeneous reactions of SO_2 in drops prevail the sulfate formation

$$SO_2 + OH + M \longrightarrow HSO_3 + M \tag{5.135}$$

$$HSO_3 + O_3 \longrightarrow HO_2 + SO_3 \tag{5.136}$$

$$SO_3 + H_2O \longrightarrow H_2SO_4\ . \tag{5.137}$$

Here, we exemplary discuss the conversion of dissolved sulfur dioxide ($S(IV)$) to sulfate ($S(VI)$). In a drop, the sulfur dioxide ($SO_2(aq)$) builds sulfurous acid ($SO_2{\cdot}H_2O(aq)$ also known as $H_2SO_3(aq)$), bisulfite ions ($HSO_3^-(aq)$), and sulfite ions ($SO_3^{2-}(aq)$).

$$SO_2(g) + H_2O(aq) \rightleftharpoons^{k_H} SO_2 \cdot H_2O(aq) \tag{5.138}$$

$$SO_2 \cdot H_2O(aq) + H_2O \rightleftharpoons^{k_1} HSO_3^-(aq) + H_3O^+(aq) \tag{5.139}$$

$$HSO_3^-(aq) + H_2O(aq) \rightleftharpoons^{k_2} SO_3^{2-}(aq) + H_3O^+(aq)\ . \tag{5.140}$$

All these species belong to the $S(IV)$ family as sulfur is in state 4. Thus, the $[SO_3^{2-}]$ and $SO_2(aq)$ are also known as $[S(IV)]$ concentrations. They can be expressed as a function of the partial pressure of SO_2. After some algebra, the concentration of the total dissolved $SO_2(aq)$ reads

$$[SO_2(aq)] = [S(IV)] = [SO_2 \cdot H_2O(aq)] + [HSO_3^-(aq)] + [SO_3^{2-}(aq)]\ . \tag{5.141}$$

The Henry coefficient is given by $k_H(SO_2) = \frac{[SO_2 \cdot H_2O]}{p_{SO_2}}$. We can express the reaction coefficients as a function of the concentrations and the partial pressure, i.e. concentration in air as $k_1 = \frac{[H_3O^+(aq)][HSO_3^-(aq)]}{[SO_2 \cdot H_2O]}$ and $k_2 = \frac{[H_3O^+(aq)][SO_3^{2-}(aq)]}{[HSO_3^-]}$. Rearranging provides that $[SO_2 \cdot H_2O] = k_H(SO_2)p_{SO_2}$ and $[HSO_3^-] = \frac{k_1[SO_2 \cdot H_2O]}{[H_3O^+(aq)]} = \frac{k_1 k_H p_{SO_2}}{[H_3O^+(aq)]}$. Since $[H_3O^+] = [H^+]$, we obtain

$$[HSO_3^-] = \frac{k_1 k_H p_{SO_2}}{[H^+]} \tag{5.142}$$

and

$$[SO_3^{2-}] = \frac{k_2[HSO_3^-]}{[H^+]} = \frac{k_2 k_1 K_H p_{SO_2}}{[H^+]^2}\ . \tag{5.143}$$

Conversion from $S(IV)$ to $S(VI)$ (sulfuric acid $H_2SO_4(aq)$, bisulfate ion HSO_4^-, sulfate ion SO_4^{2-}) yields to acid rain. In the $S(VI)$ family, sulfur is in state 6.

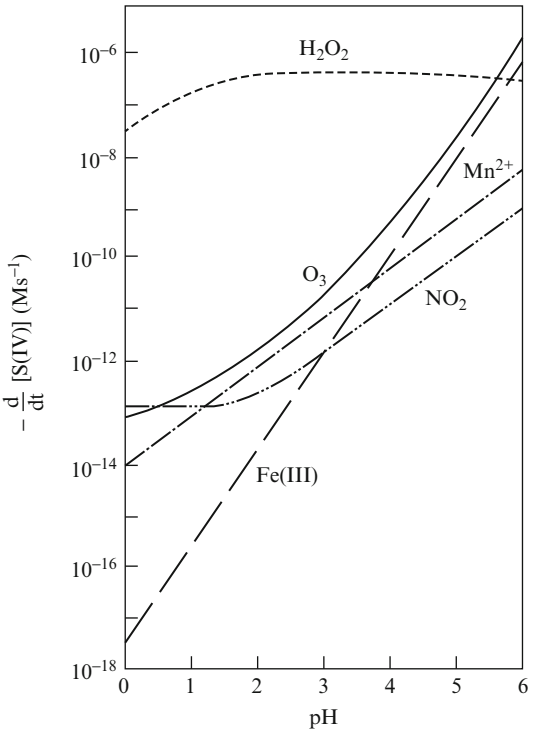

Fig. 5.5 Comparison of the most important aqueous phase pathways in the oxidation of $S(IV)$ to $S(VI)$. The environmental conditions assumed are $[O_3(g)] = 50\,\text{ppb}$, $[SO_2(g)] = 5\,\text{ppb}$, $[H_2O_2(g)] = 1\,\text{ppb}$, $[NO(g)] = 1\,\text{ppb}$, $[Fe(III)] = 0.3\,\mu\text{M}$, and $[Mn(II)] = 0.03\,\mu\text{M}$ (From Seinfeld and Pandis (1998))

Over a broad range of pH-values the most important oxidation path in drops is that involving H_2O_2, followed by O_3, some metal-catalytic reactions, and NO_2. Catalytic reactions with OH, Cl_2^-, and Br_2^+ are also possible (Fig. 5.5). H_2O_2, HO_2, OH, and O_3 are available from the gas phase. H_2O_2, HO_2, and OH are also generated photochemically in the solution. For large drops, the reaction rates can be so large that the mass transport into the drop limits the reactions. The reactions may be mass-transport limited in drops with high pH-values (e.g. radiation fog $pH \approx 7$).

5.3.4.1 Oxidation by Hydrogen Peroxide

Hydrogen peroxide is highly soluble and reacts with $HSO_3^-(aq)$ as follows

$$HSO_3^-(aq) + H_2O_2(aq) \rightleftharpoons SO_2OOH^-(aq) + H_2O(aq) \tag{5.144}$$

$$SO_2OOH^-(aq) + H_3O^+(aq) \rightleftharpoons H_2SO_4(aq) + H_2O(aq)\,. \tag{5.145}$$

The empirical oxidation rate reads

$$-\frac{d[S(IV)]}{dt} = \frac{k[H_3O^+(aq)][H_2O_2(aq)][HSO_3^-(aq)]}{1 + K[H_3O^+(aq)]} \tag{5.146}$$

where $k = (7.5 \pm 1.6) \cdot 10^{-7}\,\mathrm{M^{-1}\,s^{-1}}$ and $K = 13\,\mathrm{M^{-1}}$ at 298 K. The oxidation rate is essentially independent of the pH-value (Fig. 5.5) because the pH-dependency of the $S(IV)$-solubility and the reaction rate coefficient offset each other. Due to the rapid reaction $H_2O_2(g)$ and $SO_2(g)$ seldom coexist in liquid water.

5.3.4.2 Oxidation by Ozone

Another oxidant for $S(IV)$ is O_3. As pH-values exceed 5.5, O_3 becomes more important than H_2O_2 (Fig. 5.5) despite it is less soluble in water. The aqueous phase reaction reads

$$SO_2 \cdot H_2O(aq) + HSO_3^-(aq) + SO_3^{2-}(aq) + O_3(aq) \longrightarrow SO_4^{2-}(aq) + O_2(aq) \tag{5.147}$$

or equivalently

$$S(IV) + O_3(aq) \longrightarrow S(VI) + O_2(aq)\ . \tag{5.148}$$

Laboratory experiments suggest the change in $S(IV)$ as

$$-\frac{d[S(IV)]}{dt} = (k_0[SO_2 \cdot H_2O(aq)] + k_1[HSO_3^-(aq)] + k_2[SO_3^{2-}])[O_3(aq)] \tag{5.149}$$

with $k_0 = (2.4 \pm 1.1) \cdot 10^4\,\mathrm{M^{-1}\,s^{-1}}$, $k_1 = (3.7 \pm 0.7) \cdot 10^5\,\mathrm{M^{-1}\,s^{-1}}$, and $k_2 = (1.5 \pm 0.6) \cdot 10^9\,\mathrm{M^{-1}\,s^{-1}}$ at 298 K. The effective oxidation rate grows rapidly with increasing pH-value from about $10^5\,\mathrm{M^{-1}\,s^{-1}}$ at $pH = 2$ to about to $3 \cdot 10^7\,\mathrm{M^{-1}\,s^{-1}}$ at $pH = 6$ (Fig. 5.5).

5.3.4.3 Catalytic Processes

Oxygen dissolves easily, but it oxidizes slowly in water. Catalytic processes involving iron (Fe^{3+} or equivalently $Fe(III)$) and manganese (Mn^{2+} or equivalently $Mn(II)$) that naturally always exist as traces in drops increase the reaction rate significantly

$$2HSO_3^-(aq) + O_2(aq) + 2H_2O(aq) \longrightarrow^{Fe^{3+},Mn^{2+}} 2(SO_4^{2-}(aq) + H_3O^+(aq))\ . \tag{5.150}$$

The catalytic reaction rate depends on the pH-value of the drop (Fig. 5.5). When both iron and manganese exist simultaneously, the reaction rate exceeds that of the sum of the single catalytic rates three to ten times. The catalyzed reaction of O_2 may exceed the oxidation of O_3. At high pH-values, it often is not much less than that of H_2O_2.

5.3.4.4 Oxidation by Nitrogen Dioxide

Oxidation of dissolved SO_2 by nitrogen dioxide provides another path to generate $S(VI)$

$$2NO_2(aq)+HSO_3^-(aq)+4H_2O(aq) \longrightarrow 3H_3O^+(aq)+2NO_2^-(aq)+SO_4^{2-}(aq)\ . \tag{5.151}$$

Due to the solubility of NO_2, the rate of the latter reaction remains low (Fig. 5.5).

5.3.4.5 Oxidation by Ammonia

Ammonia (NH_3) is a net source of alkalinity in the atmosphere. The equilibrium between the gas and aqueous phase reads

$$NH_3 + H_2O \rightleftharpoons NH_4^+ + OH^- \tag{5.152}$$

NH_3 may react with sulfuric and nitric acids leading to aerosols that can be deposited (dry) by fallout or dissolved and rained out

$$2NH_3 + H_2SO_4 \rightarrow (NH_4)_2SO_4\ . \tag{5.153}$$

5.3.4.6 General Remarks

The partitioning of trace species between the gas and aqueous phases depends on the liquid water content (LWC), drop size, and the degree of solubility characterized by Henry's law constant. The relative importance of gas and aqueous phase chemistry also depends on the partitioning of excess water vapor between ice and supercooled water in clouds at temperatures between $-35\,°C$ or so and the freezing point (Chap. 3). Freezing reduces the LWC thereby modifying the equilibrium between gaseous and aqueous phases. Some of the dissolved constituents go back to the gas phase. Ice chemistry is a hot research topic and differs from aqueous phase chemistry.

Typically air contains SO_2, HNO_3, NH_3, O_3, and H_2O_2 concurrently, and the aqueous and gas phase are in equilibrium with each other for all species. As the aqueous phase reactions occur the ion concentrations adjust to fulfil electroneutrality

$$[H^+]+[NH_4^+] = [OH^-]+[HSO_3^-]+2[SO_3^{2-}]+2[SO_4^{2-}]+[HSO_4^-]+[NO_3^-]\ . \tag{5.154}$$

Except for $[SO_4^{2-}]$ we can express the ion concentrations in terms of $[H^+]$, their Henry's law and dissociation constants, and partial pressure. However, when using

the definition for $[S(IV)]$, we can express $[HSO_4^-]$, and $[SO_4^{2-}]$ in terms of $[H^+]$ and the dissociation constants for the reaction

$$H_2SO_4(aq) \rightleftharpoons H^+ + HSO_4^- \tag{5.155}$$

$$HSO_4^- \rightleftharpoons H^+ + SO_4^{2-} \, . \tag{5.156}$$

The concentrations change can be expressed in terms of $\frac{d[SO_4^{2-}]}{dt}$.

When H_2O_2 is the main oxidant in the sulfate production, the pH-values, and LWC are of minor importance. The oxidation path via O_3 gains importance in rainwater below cloud base and in the upper part of high reaching, not totally glaciated clouds. But even then, oxidation via H_2O_2 dominates in most cases.

The water temperature influences the oxidation rate due to the temperature dependency of the Henry constant. Here, two effects work in opposite directions. The reaction constant decreases and solubility increases with decreasing temperature, but the latter effect is more efficient than the former.

5.4 Aerosol Formation, Growth, and Chemistry

The term aerosol refers to solid and liquid particles suspended in the atmosphere. The interest in aerosols grew in recent decades due to their impacts on climate, and the relations found between ambient particulate matter (PM) concentrations and adverse health effects. The concerns about healths and climate has led to numerous emissions regulations worldwide. We already discussed the central role of aerosols in cloud formation (Chap. 3), and their role in radiation transfer (Chap. 4). We address the role of aerosols for our climate in Chap. 7. Thus, here we restrict us to the chemical aspects not yet discussed in Chap. 3.

Aerosols have natural and anthropogenic sources, and differ in concentration and composition in space and time (Chap. 1). Besides the natural sources discussed there, another source for particles is evaporation of drops. Nitric acid formed from N_2O_5 in cloud drops, for instance, makes their evaporation a source for nitrate particles. Evaporation (sublimation) of raindrops (ice crystals) alters the chemical environment of unsaturated layers. Total evaporation (sublimation) produces particles that settle (Sect. 5.5.2).

Many aerosols serve as cloud condensation nuclei (CCN). Their physical function as CCN was already discussed in Chap. 3. When the particle is soluble, its constituents can participate in aqueous phase chemistry as discussed earlier in this chapter. Particle growth influences subsequent CCN activity, visibility and climate. Aerosols strongly affect the light scattering cross-section.

5.4.1 Aerosol Modes

We distinguish various aerosol size ranges: **nucleation mode** ($<0.01\,\mu m$) **Aitken mode** ($0.01-0.1\,\mu m$), **accumulation mode** ($0.1-2.5\,\mu m$), **coarse mode** ($>2.5\,\mu m$),[11] and **ultra-fine mode**. The lifetime in the Aitken mode, accumulation mode, coarse mode, and ultrafine mode are hours to days, weeks, hours to days, and minutes to hours, respectively. The chemical size distribution resembles the mass, not the number of aerosols. Sulfate and organics dominate in the accumulation mode, but huge amounts of sea-salt may exist as well. Many of the organics are unidentified. Sea-salt aerosol stems from bubble bursting when the surface film of air bubbles bursts causing many droplets that may evaporate quickly. Seasalt aerosol can also be produced by jet drops that cause few, but large drops. The coarse mode encompasses mechanically formed aerosols, nitrate, and occasionally sulfate.

5.4.1.1 Gas-to-Particle Conversion and Aerosol Growth

Aerosol that is emitted is called primary particulate matter. Primary aerosols produced by combustion span all three size ranges. Secondary PM forms already in plumes, but also elsewhere in the atmosphere, from gas-to-particle conversion. Any PM from gas-to-particle conversion is called secondary PM.

Gas-to-particle conversion refers to particle formation by physio-chemical processes, condensation of precursor gases or condensation on other particles thereby increasing the mass of these particles. Physiochemical processes involve changes in the physical properties and chemical structure of species. Actually, more particles result from gas-to-particle conversion than from direct emissions.

When the surface area of an existing particle is high and the super-saturation of gases is low, condensation on particles prevails. Newly condensed particle are in the **Aitken nucleus** size range, i.e. nucleation mode. Sulfur, nitrogen, organic and carbonaceous materials are the major chemical species involved in gas-to-particle conversion. In the nucleation mode, most particles consist of sulfuric compounds, and stem from the oxidation of sulfur containing precursor gases (e.g. SO_2, H_2S, CS_2, COS, CH_3SCH_3, and CH_3SSCH_3) to sulfate (SO_4^{2-}), and subsequent condensation into particle form. This process is called **homogenous** gas-to-particle conversion.

Water vapor and sulfuric acid can form new particles by binary nucleation. Sulfuric acid can lead to growth of preexisting aerosols via condensation. Since sulfuric acid is the strongest acid in the atmosphere, it can displace other acids, but cannot be from aerosols except by evaporation of all their liquids. Like in cloud droplets, in aerosols, SO_2 dissociates to form bisulfite and sulfite, and various aqueous phase reactions occur.

[11] Some authors make the cut at $1\,\mu m$.

Sulfate aerosols are probably the most abundant particles in the atmosphere when regarding the number of particles. Much of the sulfate aerosol from gas-to-particle conversion finally ends up in the 0.1−1.0 μm size range. Sulfur dioxide, for instance, can yield the formation of various sulfates in the presence of ammonia (NH_3) and water vapor via gas-to-particle conversion. Recall that sources for SO_2 in the atmosphere are volcanic emissions, and emissions from fires, traffic, power-production and combustion for heating (Chap. 1). Important anthropogenic sources for ammonia are domestic animals and fertilizer.

In the well-mixed atmosphere, particles of diameters less than 1 μm permanently collide with atoms, molecules and particles by **Brownian motion**. Very fine particles also collide frequently with each other with potential subsequent coagulation. Coagulation like coalescence or aggregation in cloud microphysics (Chap. 3) increases the particles in size, but decreases the number of particles simultaneously.

When every collision results in adherence, the number concentration of particles per unit volume, N, of a **mono-dispersed**[12] particle distribution decreases according to

$$-\frac{dN}{dt} = \frac{4}{3}\frac{kT}{\mu}\left(1 + \frac{2AL}{D}\right)N^2 \tag{5.157}$$

where k, T, μ, L and D are the Boltzmann's constant, temperature (in K), dynamic viscosity of air, mean free path of the gas molecules, and particle diameter, respectively. We can calculate the **Stokes-Cunningham correction factor** as

$$A \approx 1.257 + 0.4\exp\left(\frac{-0.55D}{L}\right) . \tag{5.158}$$

In the accumulation mode (0.1−2.5 μm in diameter), **heterogeneous condensation** of gases onto existing particles and/or **coagulation** of smaller particles occur. Nitrate (NO_3^-) containing particles typically exceed 1 μm in diameter, i.e. they are an example for **heterogeneous** gas-to-particle conversion. Ammonium (NH_4^+) particles, for instance, form by the reaction of ammonia in the gasphase with sulfur, nitrogen, and other acidic species forming ammonium nitrate and ammonium-sulfate particles. Ammonium nitrate, for instance, forms from the NO_x-reaction by-product nitric acid and ammonia.

Wind tunnel experiments indicate that in the accumulation mode, diffusion is slow, for which particle coagulation is slower than in the nucleation mode. However, the particles are still small enough that removal by inertial impaction and gravitational settling remains low. Thus, their residence time is large, for which this size of aerosols seem to accumulate in the atmosphere.

The nucleation and accumulation modes together constitute the **fine-particle mode**. The terms nucleation mode and accumulation mode denote the mechanical and chemical processes, respectively that produce aerosol particles in these size ranges.

[12] A spectrum consisting of particles of same size is called mono-dispersed.

The coarse-particle mode (diameter $>2.5\,\mu m$) consists of airborne mineral dust, large salt particles from sea spray, volcanic ash, ash from biomass burning, and mechanically produced anthropogenic particles (e.g. from agriculture, open-pit mining). Due to their large size, coarse particles quickly settle for which their atmospheric lifetime is only a few hours.

5.4.1.2 Secondary Organic Aerosol Formation

Organics in aerosols can stem directly from soil humics, plants, and sea-surface organic compounds. Secondary organic aerosol (SOA) refers to organics that form in the atmosphere when VOC are oxidized by reactions with OH, O_3, NO_3 radicals, or Cl to less volatile organic compounds. SOA makes up a large percentage of the atmospheric aerosol mass.

These less volatile products can go into aerosols. Large organics with $C > 6$ can form aerosols. The actual water-vapor pressure determines the partitioning between the gas and aerosol phase. High (low) equilibrium pressure favors the gas (aerosol) phase. The organic compounds can react in the aqueous phase forming higher oxidized or oligomeric products. This means that SOA can notably influence atmospheric chemistry. Thus, and due to its radiative properties, carbon components of aerosols are a hot research topic.

We distinguish elemental and organic carbon. Elemental carbon components form during combustion of diesel, gasoline, wood, coal, and biomass. They consists almost totally of carbon and can be measured reasonably well with combustion analyzers. Elemental carbon is of interest because of its low spectral dependence of absorption properties, and its more than an order of magnitude varying optical absorption properties. Elemental carbon is often referred to as “black” soot.

Organic carbon aerosols span a wide range of composition from sugars, alcohols, aromatics, ketoacids, hydracids, to di/tri acids. They stem from burning of forests or grasslands. The pyrolysis of cellulose forms anhydrous sugars directly. Organic carbon is chemically and optically, in terms of light absorption and scattering properties, more complex than elemental carbon. Organic carbon is often referred to as “brown”.

5.4.2 Aerosols and Meteorological Conditions

Energy and heat production, chemical reactions and secondary pollutant formation as well as gas-to-particle conversion depend on meteorological conditions (temperature, insolation, humidity, wind). Thus, aerosol concentrations and compositions strongly differ even at the same location depending on the weather conditions.

Hygroscopic aerosols shrink/grow with decreasing/increasing relative humidity. This process shows hysteresis. A major aspect related to aerosol chemistry was that at the deliquescence point, solid particle become liquid droplets. This process

marks the onset of particle growth (Chap. 3). The deliquescence point differs among species. A liquid solution does not produce a solid particle before it is about 20–30 % below the deliquescence point (effluorescence).

For ammonium nitrate formation not only the NO_x reaction by-product nitric acid and ammonia have to be available, but also ambient temperatures must be low and relative humidity must be high. This means that the local change rate $\partial[C]/\partial X$ in the concentration $[C]$ with changes in the meteorological quantity X can differ in winter from those in summer or, in a warmer than colder climate. In summary, PM is a complex mixture of components nitrate, sulfate, organic carbon, elemental carbon (EC), other primary particulate matter, ammonium and water that show strong seasonal variations due to differences in sources, temperature and humidity.

5.5 Atmospheric Removal Processes

Dry and **wet removal** are important sinks for trace gases and particles and represent burden on ecosystems. Air pollutants are removed from the atmosphere by either dry deposition, sedimentation, wet deposition, or occult deposition. The contributions of these removal processes to the total deposition vary strongly by species in space and time due to the high variance in emissions. In Mid-Europe, for instance, wet and dry deposition of sulfate and nitrate are of same order of magnitude. In the US, sulfate dominates for the East Coast, and nitrate prevails for the West Coast.

5.5.1 Dry Deposition

Dry deposition denotes the removal of gaseous species from the atmosphere onto a surface (e.g. soil, vegetation, artificial surface). The vertical downward flux, F, of a specie of concentration, $C(x, y, z, t)$, is related to the **deposition velocity** by

$$v_d = \frac{F}{C(x, y, z, t)} \,. \tag{5.159}$$

This empirical factor depends on the height above the surface, particular specie being deposited, micrometeorological conditions in the atmospheric surface layer (e.g. wind, atmospheric stability), and the surface characteristics (e.g. stomatal resistance, hydrologic conditions, surface roughness). In the case of vegetation, vegetative controls (sensitivity to photosynthetic active radiation, specific humidity deficit between leaf and ambient air, leaf temperature, soil moisture deficit, volumetric CO_2 concentration) play a role via the stomatal resistance of the plants for uptake of air.

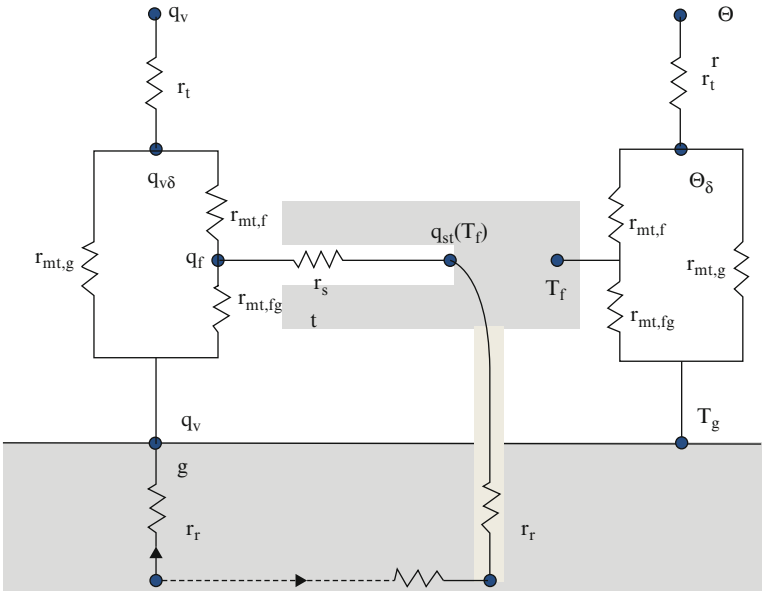

Fig. 5.6 Schematic view of a resistance network for a surface area partly covered by vegetation. Here σ is the fractional vegetation cover. The subscripts f and s denote the foliage and soil surface, respectively. Furthermore, T and q are temperature and specific humidity. See text for further details, r_t is the resistance against the transfer of heat and matter, $r_{mt,f}$, $r_{mt,g}$, and $r_{mt,fg}$ are the resistances of the molecular-turbulent layer close to the surfaces of foliage and soil as well as the molecular-turbulent environment between the foliage and soil surface (subscript fg) against the transfer of heat and matter and r_{st} is the stomatal resistance (From Mölders (2011/2012))

The dry deposition process can be viewed conceptually by using a **resistance network** (Fig. 5.6) in analogy to **Ohm's law**[13] of electrostatic. The dry deposition velocity expressed in the resistance network analogy reads

$$v_d = \frac{1}{r_a + r_s + r_t} \,. \tag{5.160}$$

The aerodynamic resistance, r_a describes the turbulent diffusion of constituents from the free atmosphere to the surface of the laminar surface layer. The surface layer resistance, r_s depends on molecular transfer rather than turbulence. The transfer resistance, r_t describes the physico-chemical interaction between the constituent and the surface.

The **constant flux approximation** (Sect. 6.8.6.1), on which the resistance approach is based, is acceptable for chemically conservative species or for very thin layers (e.g. the sublayer close to the surface). Therefore, the characteristic

[13] Georg Simon Ohm, German physicist, 1798–1854.

response times of diffusive transfer and chemical processes differ considerably. Using the constant flux approach for a layer of several meters may provide erroneous results when sources (emissions, reactions) and sinks (reactions) lead to variations in concentrations and fluxes within that layer.

Sometimes the ground emits trace species (e.g. NO, NO_2, CH_4, CO_2). In determining dry deposition, exhalation of such trace species from the soil can be considered by so-called Kramm's μ-factors that are empirical functions of time

$$\mu(t) < 1 \text{ deposition}$$
$$\mu(t) = 1 \text{ compensation}$$
$$\mu(t) > 1 \text{ emission.}$$

Example. At a site, the following concentrations and fluxes were measured for NO, NO_2, and O_3.

Height (m)	NO (ppb)	NO_2 (ppb)	O_3 (ppb)	F_{NO} (ppb m s^{-1})	F_{NO_2} (ppb m s^1)	F_{O_3} (ppb m s^{-1})
0.1	3.5	8	6	0.012	−0.02	−0.004
3.0	3.3	8.5	8	0.01	−0.015	−0.004
18.0	2.5	8.6	10	0.021	−0.021	−0.004

Determine the deposition velocities at these heights. What would a constant flux approach mean for a layer of 18 m thickness?

Solution. The dry deposition velocities at these heights are:

Height (m)	v_{NO} (10^{-3} m s^{-1})	v_{NO_2} (10^{-3} m s^{-1})	v_{O_3} (10^{-3} m s^{-1})
0.1	3.4	−2.5	−0.7
3.0	3.0	−1.8	−0.5
18.0	0.8	−2.4	−0.4

The negative signs mean that the fluxes are upward, i.e. O_3 and NO_2 have sources (e.g. emissions, chemical reactions). Using the constant flux approximation for a layer of 18 m would underestimate the deposition fluxes.

5.5.2 Sedimentation of Aerosols

Sedimentation removes about 10–20 % of the aerosol mass from the atmosphere. **Dry removal** of aerosols encompasses sedimentation, coagulation, and **impaction**. The ratio of the aerosol flux onto the surface to the mass concentration of aerosols near the surface provides the deposition velocity of aerosols. In contrast to dry

deposition of gases, no transfer resistance exists for particles. The particles have an appreciable **settling velocity**, v_s. The deposition velocity of aerosols reads

$$v_d = \frac{1}{r_a + r_s + r_a r_s v_s} + v_s \tag{5.161}$$

where the terminal settling velocity of a particle v_s is given by **Stokes equation**

$$v_s = \frac{D^2 g}{18\mu}(\rho_p - \rho) \; . \tag{5.162}$$

Herein, D, ρ_p, μ, ρ, and g are the particle diameter and density, the viscosity and density of air, and the acceleration of gravity, respectively. Since $\rho_p \gg \rho$ we can approximate the terminal settling velocity as

$$v_s \approx \frac{D^2 g \rho_p}{18\mu} \; . \tag{5.163}$$

Gravitational settling and the terminal settling velocity of a particle depend on its mass. Thus, the sedimentation velocities differ for poly-disperse particle spectra,[14] for which particles settling at different speeds may collide. Typical settling velocities of 10 μm (1 μm) size particles are 10 m h^{-1} (0.1 m h^{-1}).

Small particles can stick onto obstacles when they come close enough to them by winds relative to the surface. To contact the surface the particles must be transported across a thin stagnant layer, the **viscous sublayer** (Chap. 6). This transport can be by sedimentation, vertical motions, diffusion, Brownian motion or **phoretic diffusion** (ordered fluxes of molecules superimposed on disordered molecular motion).

In the atmosphere, **diffusiophoresis** (flux of water vapor molecules during condensation or evaporation), and **thermophoresis** (heat fluxes during condensation or evaporation) occur. When, for instance, dew forms on a leaf, diffusiophoresis drives the aerosol into direction of the water-vapor flux. The related release of latent heat increases air temperature around the leaf. This thermophoresis shifts the particle down the temperature gradient, away from the leaf. The opposite occurs for evaporation of dew or intercepted water.

5.5.2.1 Deposition of HNO_3

Meteorological, hydrological and chemical conditions can strongly affect particle deposition. This sensitivity is here exemplary discussed for the $HNO_3 - NH_3 - NH_4NO_3$-sulfate system. Three categories of behavior of the observed HNO_3-fluxes can be distinguished.

[14] Poly-disperse means particles have different sizes.

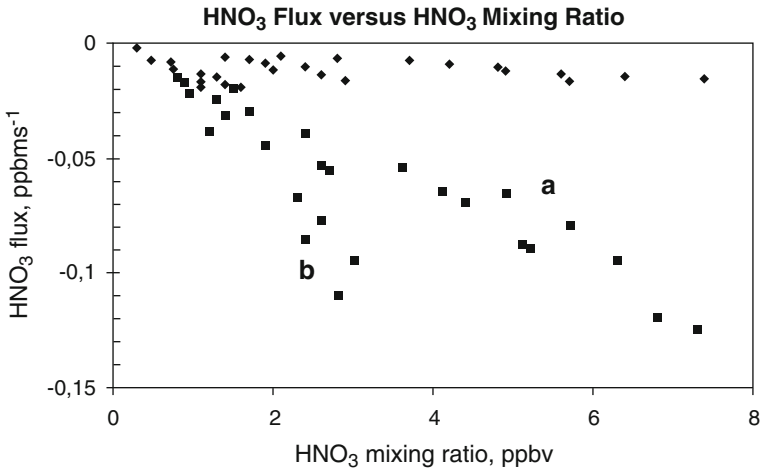

Fig. 5.7 Fluxes of HNO_3 as a function of HNO_3-mixing ratio as observed during the German reunification experiment SANA. *Diamonds* stand for $[HNO_3]/[NH_3] > 3$, relative humidity lower than 65 % and air temperatures greater than 18 °C, *squares* represent $[HNO_3]/[NH_3] \leq 1$ and (**a**) relative humidity lower than 80 %, air temperatures between 14 and 18 °C, and (**b**) relative humidity greater equal 80 %, and air temperatures lower than 15 °C (From Tetzlaff et al. (2002))

- For high nitric to ammonia ratios ($HNO_3/NH_3 > 3$) in combination with low relative humidity and air temperatures higher than 15 °C the system $HNO_3 - NH_3 - NH_4NO_3$-sulfate shifts towards the gas phase. Ammonium nitrate (NH_4NO_3) dissociates when present. HNO_3 also exists in the gas phase and deposits in gaseous form, while NO_3^- and NH_4^+ are in the particle phase and settle as particles. Under these conditions, ammonium nitrate has typical radii of less than 1 μm. At a soil-grass surface, for instance, deposition velocities of HNO_3 are lower than 0.06 m s^{-1} (Fig. 5.7).
- Under cooler and wetter conditions like those of the first category, the thermodynamic conditions favor the formation of ammonium nitrate on sulfate- and/or carbon-dioxide-containing particles. Thus, there are sinks for HNO_3 and NH_3 in the presence of great amounts of the particles (35−85 μ g m^{-3}). At a soil-grass surface, HNO_3 deposition velocities are about 0.02−0.03 m s^{-1} (Fig. 5.7).
- When dew exists, two concurrent sinks occur, transfer to the particle phase and the wet grass and/or soil. Thus, in the presence of many particles, the HNO_3 fluxes are greatest with increasing mixing ratio of HNO_3. When only a few particles exist, only the wet surface serves as a sink with a resistance close to zero, and a HNO_3 deposition velocity of about 0.018 − 0.03 m s^{-1}, at that exemplary soil-grass surface (Fig. 5.7). The transfer processes in the viscous sublayer control the fluxes. When a great number of particles exists, the HNO_3 deposition velocity reaches up to 0.035–0.04 m s^{-1} at the soil-grass surface (Fig. 5.7).

5.5.3 Wet Deposition

The wet removal of trace specie depends on their solubility and on their chemical reactions in water. Scavenging is irreversible for particles, and highly soluble gases. We can describe the local removal rate of such gases or particles by wet deposition as a first order process. The rate of **wet removal** linearly depends on the airborne concentration of the pollutants $C(x, y, z, t)$ or number of particles $n(D, x, y, z, t)$ of different diameters D and is independent of the amount of pollutants scavenged already.

Wet deposition onto a surface is the sum of wet removal from the column aloft assuming that the scavenged gases and particles are in the precipitation given by

$$W_g = \int_0^\infty \Lambda(z,t) C(x,y,z,t) dz \tag{5.164}$$

and

$$W_p = \int_0^\infty \Lambda(D,z,t) n(D,x,y,z,t) dz \tag{5.165}$$

where, $\Lambda(z,t)$ and $\Lambda(D,z,t)$ are the height- and time-dependent gaseous and particulate **washout coefficients**, respectively. We can define a **wet deposition velocity**

$$v_w = \frac{W_g}{C(x,y,z,t)} \tag{5.166}$$

When the pollutants are distributed uniformly in the vertical, the wet deposition velocity is

$$v_w = \int_0^H \Lambda(z,t) dz = \overline{\Lambda} H \ . \tag{5.167}$$

The **washout ratio**, w_r, is defined as the ratio of the concentration of the respective specie in the surface level precipitation to the concentration of the respective specie in surface level air,

$$w_r = \frac{C(aq)}{C(x,y,z,t)} \tag{5.168}$$

where $C(aq)$ is the concentration in the aqueous phase. We can define the removal of particles analogously.

In general, the wet deposition flux is given by $W = C(aq)P$ where P is the precipitation intensity in $\mathrm{mm\,h^{-1}}$. Washout and wet deposition velocity are related as

$$v_w = \frac{W}{C(x,y,0,t)} = \frac{C(aq)P}{C(x,y,0,t)} = w_r P \ . \tag{5.169}$$

Wet deposition of pollutants varies with size and specie. Due to their different shapes, sizes, densities, and terminal velocities (Table 3.1) raindrops and ice crystals have different scavenging rates. Typically, small droplets contain more sulfate and large drops contain more nitrate. Strong gradients in ammonium concentration with height can be found because of the different distribution of sources.

Example. Determine the wet deposition velocity for $H = 2\,\mathrm{km}$, and $\Lambda = 10^{-4}\,\mathrm{s^{-1}}$.

Solution. Under these assumptions $v_w = \int_0^{2{,}000} 10^{-4}\mathrm{s^{-1}} dz = 10^{-4}\mathrm{s^{-1}} 2{,}000\,\mathrm{m} = 0.2\,\mathrm{m\,s^{-1}}$.

Example. Determine the wet deposition velocity when the washout ratio is 10^5 and precipitation intensity is $3.6\,\mathrm{mm\,h^{-1}}$.

Solution. Under these assumptions $v_w = w_r P_0 = 10^5 \cdot 3.6\,\mathrm{mm\,h^{-1}} = 10^5 \cdot 3.6 \cdot 10^{-3}\,\mathrm{m}\,(3{,}600\,\mathrm{s})^{-1} = 0.1\,\mathrm{m\,s^{-1}}$.

5.5.4 *Occult Deposition*

Surfaces and vegetation may scavenge droplets from clouds hitting them. As the drops hold dissolved trace gases, particles, and their reaction products, these materials are deposited when the drops hit a surface. Since, on average, the acidity of small cloud droplets is much higher than for raindrops, occult deposition may harm vegetation more strongly than acid rain.

Before the German unification, for instance, burning of sulfur-rich coal gained from open-pit mining in East-Germany could have led to occult deposition in the Czech Republic and the mountainous southeastern East-Germany under north-westerly winds. Thus occult acid deposition was blamed for the forest dying in that area.

5.6 Biogeochemical and Biophysical Cycles

Modern environmental questions, such as global change, or eutrophication in marine and freshwater environments, require knowledge of the interaction of trace-gas, energy and water cycles at various scales. The water, energy and most element cycles interact strongly with each other (Chaps. 3, 4, and 7). Thus, most biogeochemical and biogeophysical questions require combining information from several different cycles. Addressing questions related to acid rain, for instance, requires understanding the controls on the interrelation between the water-, energy- and trace-gas cycle.

Understanding cycles requires the knowledge on the distribution of the respective material (e.g. water, nitrogen compounds), the cycling (e.g. the sources and sinks), and the factors controlling the cycles and distributions (e.g. temperature, water, liquid water content). Knowledge of these three aspects allows for answering questions on future changes and gaining predictive understanding of the **Earth system**.

5.6.1 Hydrological Cycle

The **hydrological cycle** describes the largest chemical flux on earth. The hydrological cycle is composed of sub-cycles at various scales (Fig. 5.8). Water in all phases transports heat around the globe and contributes to climate (Chap. 7).

The availability of water is the single most important pre-requisite for life and land-plant productivity. Under an increasing population,[15] changing climate and land-use, the availability of water (ground water, plant available water for food production) is of central interest. In a region, precipitation depends on the large-scale transport of precipitation into the region (e.g. by frontal passages) and the regional/local recycling of water (Fig. 5.8). Land-use changes and modified radiative forcing may affect the amount and time of water availability. Changes in evapotranspiration may appreciably affect cloud and precipitation formation, and the local recycling of precipitation.

5.6.2 Fundamentals of Biogeochemical Cycles

We can divide the global biogeophysical cycle (Chap. 7) into the hydrological cycle, gaseous cycles (e.g. nitrogen cycle, oxygen cycle, carbon cycle, sulfur cycle), **biogeochemical cycle**, sedimentary cycle (geological time scales) and the energy

[15] In the time from 1930 to 2000, human population tripled.

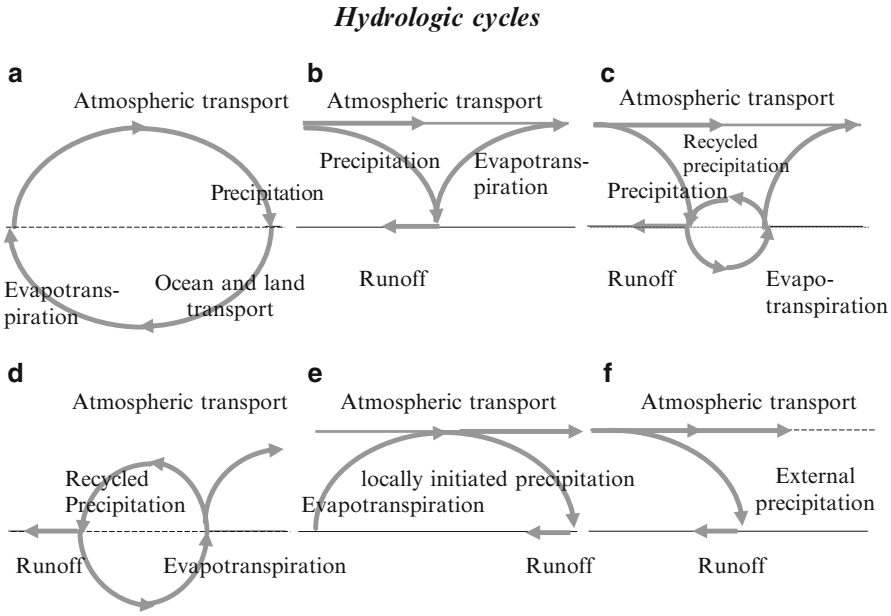

Fig. 5.8 Schematic view of the water cycle at the (**a**) global, (**b**) local, (**c**) regional scale, and of the (**d**) internal, (**e**) locally initiated, and (**f**) external components of the regional water cycle (From Mölders (1999))

cycle. We discussed the energy cycle already in Chap. 4 and the atmospheric part of the hydrological cycle in Chaps. 2–4. Here we restrict us to the biogeochemical cycle.

Biogeochemical cycle refers to a cyclic system that transfers chemical elements between **biotic** (living) and **abiotic** (non-living) parts of an ecosystem. Bacteria decay and decompose organic matter, thereby producing a variety of chemicals (e.g. carbon, oxygen, nitrogen, sulfur).

5.6.2.1 Gaseous Cycles

Gaseous cycles involve gases like oxygen, nitrogen, and processes like carbon formation, or nitrification.

Carbon Cycle

Inorganic-C exists in rocks. Organic-C occurs in gaseous form as carbon dioxide (CO_2), methane (CH_4), and carbon monoxide (CO). Naturally atmospheric CO_2 stems from volcanic activity. The atmospheric CO_2-concentration is limited to

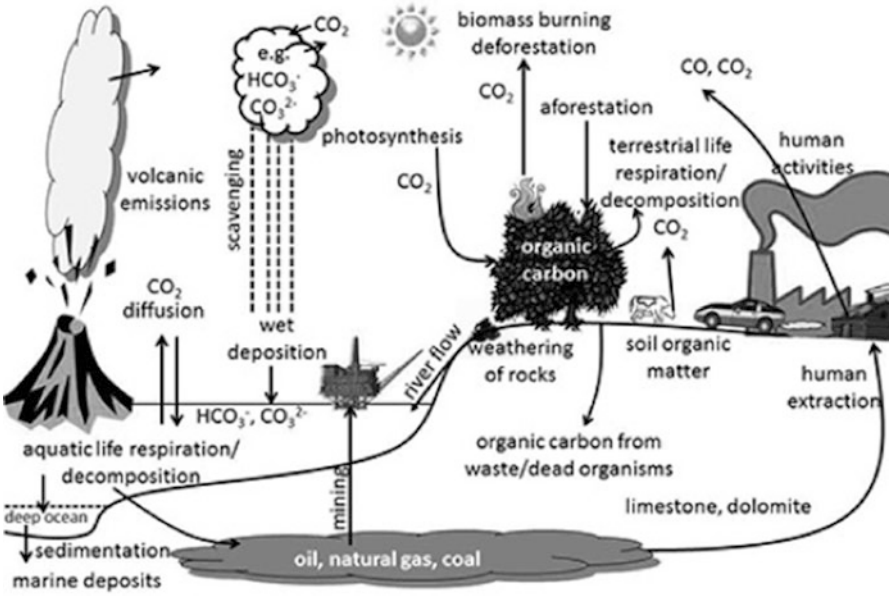

Fig. 5.9 Schematic view of various paths, processes, and storage reservoirs of the global carbon cycle

a range of about 200−6,000 ppm due to weathering of rocks and formation of carbonate minerals (Fig. 5.9). Photosynthesis consumes atmospheric CO_2 and implements it into plants. By respiration it returns to the atmosphere (Fig. 5.9).

Carbon monoxide oxidizes as follows

$$CO + OH \rightarrow CO_2 + H \tag{5.170}$$

$$H + O_2 + M \rightarrow HO_2 + M \tag{5.171}$$

$$HO_2 + NO \rightarrow OH + NO_2 \tag{5.172}$$

$$NO_2 + h\nu \rightarrow NO + O \tag{5.173}$$

$$O + O_2 + M \rightarrow O_3 + M \tag{5.174}$$

With a net reaction of

$$CO + 2O_2 \rightarrow CO_2 + O_3 \tag{5.175}$$

Changes in atmospheric CO_2 may shift the equilibrium of the carbon cycle. Mankind alters the carbon cycle by combustion of fossil fuels (e.g. coal, oil, gas, peat). Naturally and anthropogenically initiated biomass burning release CO_2 to the atmosphere as well (Fig. 5.9). Decomposition releases CO_2 in the atmosphere.

The atmospheric main constituents only exist in physically soluble form in the ocean. Water solubility of CO_2 is much higher than that of N or O, and oceans are a sink for CO_2 (Fig. 5.9). They exchange CO_2 and other gases with the atmosphere in ways that modify ocean circulation and climate. Generally, water solubility of a gas decreases with temperature and salinity, while it increases with increasing pressure. The capacity to solve and take up CO_2 is greater for cold than warm water (Eq. (5.119)). In climatic equilibrium, diffusion into and out off the ocean balance.

The oceans absorb heat at the surface, store it for varying durations, and release it in different places. The ocean circulation redistributes heat and fresh water around the globe (Chap. 7). The thermohaline circulation, which is driven by differences in water density due to temperature and/or salinity effects, allows that ocean surface water moves into the deep abyss where it is isolated from atmospheric influences. Consequently, heat and dissolved CO_2 can be stored for long time (>1,000 year). As climate warms (or cools), the oceans can release (take up) CO_2. Being a greenhouse gas (GHG), an increase (decrease) of atmospheric CO_2 may feedback to further warming (cooling) again altering the equilibrium of aquatic and atmospheric CO_2-concentrations.

In the ocean, the presence of CO_2 can lead to different equilibria of carbonate- and hydro-carbonate. These species are also more soluble in cold than warm water. The uptake of atmospheric CO_2 by the ocean can be described as

$$CO_2(g) \rightleftharpoons CO_2(aq) \tag{5.176}$$

$$CO_2(aq) + H_2O \rightleftharpoons HCO_3^- + H^+ \tag{5.177}$$

$$HCO_3^- \rightleftharpoons H^+ + CO_3^= \tag{5.178}$$

$$CaCO_3(aq) \rightleftharpoons Ca^{++}(aq) + CO_3^= \; . \tag{5.179}$$

Climate changes affect marine biota and ecosystems with potentially important feedbacks on climate. Plants, for instance, depend on temperature and precipitation (Chap. 7). Their growth can be affected by the atmospheric CO_2-concentration that the plants again modify to certain degree.

On average, oceans take up about $1.6 \cdot 10^{12}\,\mathrm{kg\,C\,year^{-1}}$. Photosynthesis and respiration consume and produce $100 \cdot 10^{12}\,\mathrm{kg\,C\,year^{-1}}$. About $5 \cdot 10^{12}\,\mathrm{kg\,C\,year^{-1}}$ enter the atmosphere from burning of fossil fuels. Biomass burning releases about $1.8 \cdot 10^{12}\,\mathrm{kg\,C\,year^{-1}}$ into the atmosphere. The atmosphere CO_2 increases by $3 \cdot 10^{12}\,\mathrm{kg\,C\,year^{-1}}$. Budgeting the input, output and internal changes leads to a still unexplained deficit of C of about $2.2 \cdot 10^{12}\,\mathrm{kg\,C\,year^{-1}}$.

Oxygen Cycle

The oxygen cycle is closely linked to the water and carbon cycle (Sect. 5.3). We discussed the stratospheric part of the oxygen-cycle already in Sect. 5.2.6.

Virtually all atmospheric oxygen results from photosynthesis. Plants take up carbon dioxide for photosynthesis. In this process, oxygen serves to split water chemically. The net reaction reads

$$CO_2 + 2H_2O \rightarrow CH_2O + H_2O + O \tag{5.180}$$

Respiration removes oxygen from the atmosphere that is oxidized to CO_2 by living beings.

Nitrogen Cycle

Roots take up nitrates from the soil. This N_2 to organic-N transfer is called the **N-fixation**. Animal wastes and dead remains bring nitrates back into the soils where bacteria and fungi mineralize the organic-N to NH_4^+. Bacteria produce NO and N_2O on the pathway NH_4^+ to NO_3^- (**nitrification**). Uptake by plants leads to the conversion of NO_3^- and NH_4^+ to organic-N during photosynthesis. These bacteria use nitrogen as an energy source for other chemical reactions similar to the respiration in other organisms (5.10).

Bacteria form NO_3^- to N_2 thereby producing N_2O. This **denitrification** reduces nitrates in the soil to molecular nitrogen NO. Both NO and NO_2 are released to the atmosphere.

Lightning flashes affect the atmospheric part of the nitrogen cycle by causing the combination of atmospheric nitrogen and oxygen to form oxides of nitrogen (Fig. 5.10).

Fluxes with respect to the atmosphere approximately amount to a loss of N_2 and NO_x from the atmosphere of about $240 \cdot 10^9\,\mathrm{kg\,year^{-1}}$ (N-fixation), and $60 \cdot 10^9\,\mathrm{kg\,year^{-1}}$ leading to typical residence times of 16.25 million years and 3.6 days, respectively.

Sulfur Cycle

The sulfur cycle involves atmospheric and geological paths (Fig. 5.11). Most of the sulfur in the abiotic environment occurs in rocks. Only a small amount of sulfur exists in the atmosphere as sulfur dioxide (SO_2), produced by combustion of fossil fuels or volcanoes (Chap. 1). Sulfate forms in cloud- and raindrops or waters by heterogeneous chemistry (Sect. 5.3) and by weathering and oxidation of rocks.

5.6.3 Interaction Between Energy, Water and Trace-Gas Cycles

Atmospheric chemical reactions are not energetically relevant. Nevertheless, pollutants may affect temperature due to reflection at surfaces and absorption of radiation

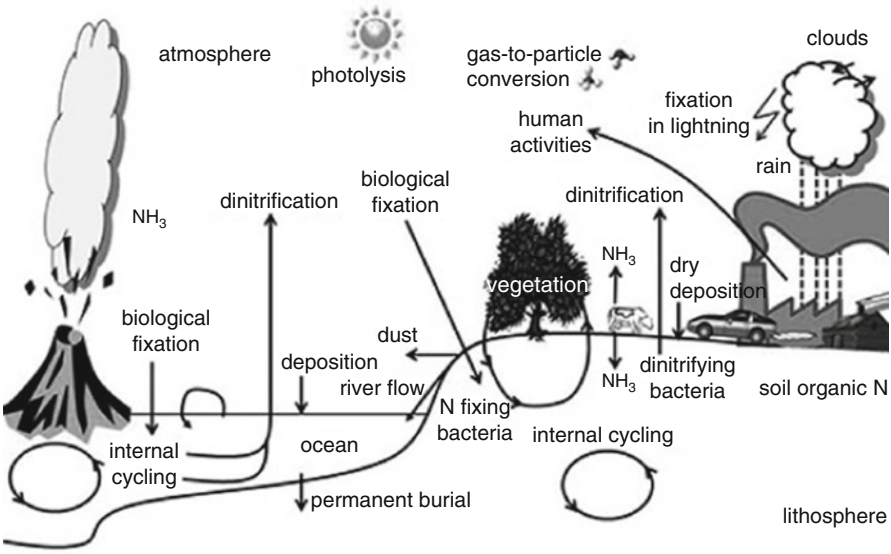

Fig. 5.10 Schematic view of various paths, storage reservoirs, and processes of the global nitrogen cycle

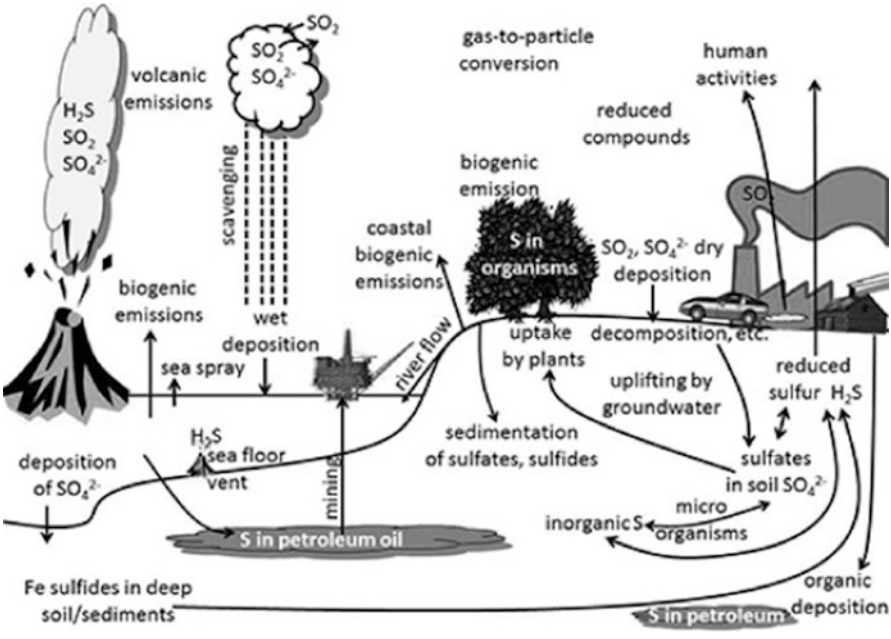

Fig. 5.11 Schematic view of various paths, processes, and storage reservoirs of the global sulfur cycle

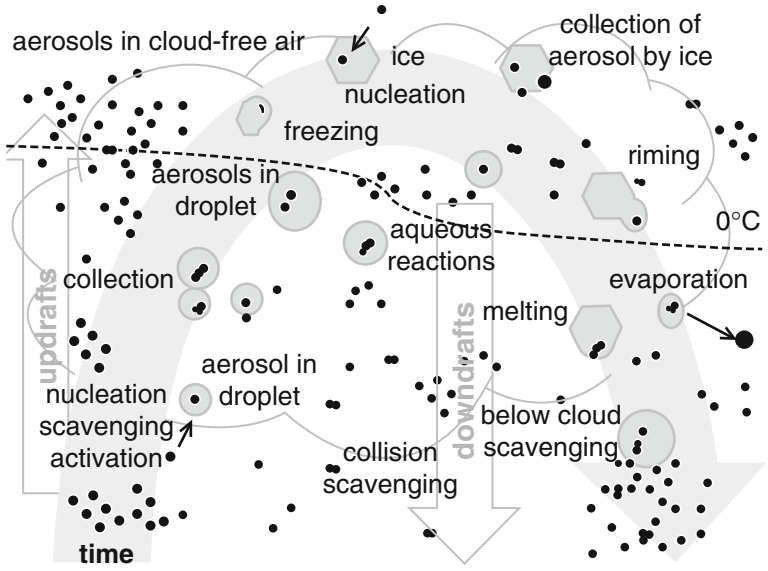

Fig. 5.12 Schematic view of major processes affecting the chemical composition of cloud droplets, ice, and rain drops in a cumulus cloud

(Chap. 4) with impacts on the wind field (Chap. 6). The influence of pollutants on radiation and temperature is greatest at low angle of the sun, when light has a long path through the atmosphere.

Scattering at the molecules or absorption at certain wavelengths reduce visibility. In a humid atmosphere with high SO_2-concentrations, SO_2-molecules may lead to particle formation that provides condensation nuclei for formation of fog or cloud droplets (Fig. 5.12) that also reduce visibility.

Trace gases are usually emitted into the atmospheric boundary layer (ABL) or along the flight tracks of aircrafts. Once being released they undergo turbulent mixing. During the day, they may show a well-mixed distribution within the ABL except in the immediate vicinity of sources. As the height of the ABL is higher at day, the concentration of air pollutants in the ABL is less than at night.

Clouds contribute to chemical transformation, redistribution, and removal of trace gases. Clouds vertically redistribute all kind of trace gases by entrainment or detrainment, up- and downdrafts, scavenging and cloud microphysics. Clouds affect the gas distribution differently for various classes of chemical compounds:

- Insoluble non-reactive passive tracers are only vertically redistributed by entrainment or detrainment or by being collected.
- Soluble gases without chemical production or destruction (e.g. NH_4, HNO_3) can dissolve in droplets.

- Soluble reactive gases dissolved in droplets react with other constituents in the aqueous phase (e.g. SO_2, $SO_4^=$, H_2O_2).
- The high cloud albedo alters the photolysis rates for photochemically active gases and hence, gasphase chemistry below, within and above the cloud.

Clouds transport pollutants from the ABL into the free atmosphere (Chap. 6). Here the low concentrations and temperatures increase the lifetimes. Due to the high wind speeds (Chap. 7) and increased lifetime in the upper troposphere the pollutants can be transported over long distance far away from their source following the synoptic scale pattern (Table 1.1). In the mid and upper troposphere of mid-latitudes, zonal wind, for instance, is on average $10-30\,\mathrm{m\,s^{-1}}$ (Chap. 7). At these levels, long-lived species can be distributed around the globe within 1–2 months (Table 1.1). Since the meridional wind component is much smaller (Chap. 7), inter-hemispheric exchange of pollutants takes longer than longitudinal transport (Chaps. 6 and 7). Inter-hemispheric exchange is most likely for less reactive and less soluble trace species.

In summary, air pollutants affect the atmospheric properties by

- Lowering saturation vapor pressure (Chap. 3),
- Reducing visibility (Chap. 4),
- Absorbing solar radiation (Chap. 4),
- Changing the atmospheric composition by chemical reactions, and
- Particle formation.

5.6.3.1 Interaction of Cycles: Example Acid Rain

In the troposphere, NO_x leads to

$$NO + O_3 \longrightarrow NO_2 \tag{5.181}$$

$$NO_2 + OH \longrightarrow HNO_3\,. \tag{5.182}$$

In the gas phase. In the presence of droplets, HNO_3 (nitric acid) dissolves and dissociates to H^+ and NO_3^-.

Another important atmospheric process in the presence of droplets is sulfuric acid (H_2SO_4) formation. H_2SO_4 dissolves establishing an equilibrium between the amount in the gas and aqueous phase where it dissociates to $2H^+$ and SO_4^{2-} (Eq. (5.153)).

Thus, acid rain cleans the atmosphere, neutralizes H^+ by weathering reactions in soils and plants (i.e. H^+ exchange of other positively charged elements), and acidifies waters and soils. As pH of rain drops, rain can harm aquatic life and the biosphere. The buffering capacity of soils namely may be limited. By measuring the buffering capacity of soils, we can identify regions of sensitivity to acid rain.

Problems

Knowledge and Comprehension

1. When is the influence of pollutants on radiation and temperature most effective?
2. What does the dependency of some reaction cycles on radiation mean for Polar Regions?
3. What does stability mean for the distribution of pollutants?
4. Discuss the main differences in air chemistry at high latitudes compared to mid-latitudes.
5. What is the main difference between dissociation and direct reaction of an excited molecule and fluorescence and deactivation by collision?
6. Discuss how gasphase chemistry taking place during night differs from that during daylight. What does this mean for Polar Regions?
7. Comment on the general practice in chemistry transport modeling to calculate dry deposition fluxes by use of the concentrations in at the first model layer above the surface (usually at 20–30 m) and a fixed, vegetation-type dependent dry deposition velocity, i.e. the constant flux-approach.
8. What is the difference in the removal process of trace gases and aerosol particles?
9. Define wet deposition.
10. Explain how diffusiophoresis and thermophoresis affect aerosol deposition.
11. How does lightning affect the atmospheric nitrogen oxide concentration?
12. In cloud physics, the terms homogeneous and heterogeneous processes occurred with respect to nucleation. Define homogeneous and heterogeneous process and point out the differences with respect to the substances involved. Define homogeneous and heterogeneous reaction as it is used in air chemistry.
13. Why is the change in the concentration of O_2 in the reactions of the $NO-NO_2-O_3$-system negligible?
14. Explain why small droplets usually are more acidic than large drops.
15. What are the main constituents that make up acid rain?
16. What are the linkages between biosphere and atmospheric composition?
17. How do anerobic bacteria affect the atmosphere?

Analysis and Application

5.1. On a winter day, observed 2 m temperature and relative humidity, pressure, and N_2O_5 concentration were $-10\,°C$, 80 %, 1,010 hPa, and 220 ppt, respectively. Assume the total number of molecules in 1 m^3 of air is $2.7 \cdot 10^{25}$ at these atmospheric conditions, and give the concentration in $\mu g\, m^{-3}$. Hint: Review Chap. 2.

5.2. In an air quality model, all HNO_3 over the continents has an average deposition velocity of $7.5\,\mathrm{cm\,s^{-1}}$ in the first 5 km above the model ground level. When no sources are considered how long would it take for all HNO_3 to be deposited? Discuss your result in the perspective that we learned about the mean residence time. What are potential sources and sinks for this specie?

5.3. Assume temperature and NO and NO_2 concentrations of 20 °C, 0.6 ppb and 12 ppb, respectively, and that no other reactions than those of the triade $NO-NO_2-O_3$ occur. Calculate the concentration of ozone for a reaction rate coefficient of $51.67\exp(-\frac{1.45}{T})\,\mathrm{ppm^{-1}\,s^{-1}}$ (T in K) and a photolysis rate of $3.06\,\mathrm{min^{-1}}$.

5.4. In a stable in Farchant, Bavaria, ammonia (NH_3) makes up a partial fraction of $2\cdot10^{-8}$ % of the air, which has a mass of about 10^3 kg. About $7\cdot10^{-5}\,\mathrm{kg\,day^{-1}}$ of NH_3 escape through badly closing doors and windows to the outside. Determine the residence time of NH_3 in the stable in hours.

5.5. Assume the total sulfur dioxide and nitrogen oxide emissions amount to $19.9\cdot10^6$ t and $21.3\cdot10^6$ t, respectively. Transport accounts for 3.3 % of the total sulfur dioxide and 44.5 % of the total nitrogen oxide. Determine the ratio of the total amount of nitrogen oxide generated by transport to the total amount of sulfur dioxide produced by transport.

5.6. All other factors being equal, by how much will the concentration of air pollution change for a wind-speed decrease from 10 to $5\,\mathrm{m\,s^{-1}}$? Give the reason for your answer.

5.7. In winter, a SO_2 concentration of 360 ppb, temperature of 0 °C, and an air pressure of 1,013.25 hPa were recorded at an urban site. Determine the amount of SO_2 molecules in $1\,\mathrm{m^3}$ of air.

5.8. Between 0.395 and 0.400 µm, the absorption cross-section, and quantum yield were to $6.2\cdot10^{-23}\,\mathrm{m^2}$, and 0.75, respectively. In two different model layers, the simulated actinic fluxes of the reaction of $NO_2+h\nu\longrightarrow NO+O$ were $4.6\cdot10^{19}$ and $1.30\cdot10^{18}\,\mathrm{m^{-2}\,s^{-1}}$. Calculate the photolysis rate coefficient at these model layers. Discuss your results under the aspect why the photolysis rate would be different at different heights. What are your conclusions with respect to the use of climatological actinic fluxes for use in air quality modeling?

5.9. Calculate the photo-stationary-state mixing ratio of O_3, $p = 750$ hPa, $T = -15$ °C, $j = 0.01\,\mathrm{s^{-1}}$ for NO and NO_2 mixing ratios of 4.6 and 9 ppt, respectively. Assume a reaction rate of $k = 1.75\cdot10^{-14}\,\mathrm{cm^3\,molecule^{-1}\,s^{-1}}$. Convert the ozone-mixing ratio to number concentration. Where and/or under which conditions could this situation occur? For which other region of the troposphere are these ozone values typical?

5.10. Give the net reaction rate for a reaction chain including the triad plus Eq. (5.63) and $HO_2 + HO_2 \rightarrow H_2O_2 + O_2$. Outline the concentration change with time for the triad plus the reactions given in Eqs. (5.63) and (5.64). Give the net reaction rate and compare it to the results you obtained before.

5.11. In the troposphere, nitric oxides, NO, reacts with hydroperoxyl, HO_2, to form NO_2 and the hydroxyl radical, OH. In addition, the paths of the triad $NO - NO_2 - O_3$ occur. Assume that no other relevant paths exist and write down the balanced chemical mechanism. Formulate the temporal change of concentrations for each of the involved trace gases, and express the ozone concentration for steady-state conditions.

5.12. The 1,000 MW engine of a ship burns 1,000 t of fuel with a 4 % sulfur content in an hour. How much SO_2 does it emit?

5.13. We introduced the triad $NO - NO_2 - O_3$ as a simplified chemical mechanism for ozone formation. Assume that NO_2 is produced as quickly as it is depleted, and express the ratio of NO_2 and NO in equilibrium as a function of ozone.

5.14. In an urban atmosphere, the following reactions occur

$$
\begin{aligned}
&OH + CH_4 \longrightarrow^{k_1} H_2O + CH_3\\
&OH + CO \longrightarrow^{k_2} H + CO_2\\
&OH + CH_3CHO \longrightarrow^{k_3} H_2O + CH_3CO\\
&CH_3 + O_2 \longrightarrow^{k_4} CH_3O_2\\
&CH_3O_2 + NO \longrightarrow^{k_5} CH_3O + NO_2\\
&CH_3O + O_2 \longrightarrow^{k_6} HCHO + HO_2\\
&HO_2 + NO \longrightarrow^{k_7} NO_2 + OH
\end{aligned}
$$

Determine the net balanced reaction. Provide the temporal change of CH_4, CO_2, NO, and NO_2. How many NO_2 molecules result from two CH_4 molecules? Methane is a good example for VOCs. Discuss how the reactions above would shift the ozone formation assuming that the reactions of the triad NO-NO_2-O_3 occur concurrently to those given above. How would the temporal change of NO and NO_2 now look like? What do you conclude?

5.15. Assume the following reactions affecting ozone chemistry in the stratosphere. Determine the steady-state concentrations of O^{1D}, HO, and HO_2. Calculate the HO_2 concentration assuming $4 \cdot 10^{12}$ molecules m^{-3}. What else can you say about these conditions?

$$
\begin{aligned}
&O_3 + h\nu \longrightarrow^{j_1} O_2 + O^{1D} \text{ with } j_1 = 10^{-4}\,\mathrm{s}^{-1},\\
&O^{1D} + M \longrightarrow^{k_1} O + M \text{ with } k_1 = 10^{-17}\,\mathrm{m}^3\,\mathrm{s}^{-1},\\
&O^{1D} + H_2O \longrightarrow^{k_2} HO + HO \text{ with } k_2 = 2 \cdot 10^{-12}\,\mathrm{m}^3\,\mathrm{s}^{-1},\\
&O + O_2 + M \longrightarrow^{k_3} O_3 + M \text{ with } k_3 = 6 \cdot 10^{-46}\,\mathrm{m}^6\,\mathrm{s}^{-1},\\
&HO + O_3 \longrightarrow^{k_4} HO_2 + O_2 \text{ with } k_4 = 2 \cdot 10^{-20}\,\mathrm{m}^3\,\mathrm{s}^{-1},\\
&HO_2 + O_3 \longrightarrow^{k_5} HO + O_2 + O_2 \text{ with } k_5 = 3 \cdot 10^{-22}\,\mathrm{m}^3\,\mathrm{s}^{-1},\\
&HO + HO_2 \longrightarrow^{k_6} H_2O + O_2 \text{ with } k_6 = 3 \cdot 10^{-17}\,\mathrm{m}^3\,\mathrm{s}^{-1}.
\end{aligned}
$$

5.16. Show that for HNO_3 dissociating in droplets the aqueous-phase fraction decreases with increasing liquid water content as there is more water available to accommodate the species. Hint: determine the concentrations of $[HNO_3(aq)]$, and $[NO_3^-]$.

5.17. In parts of the western US, rain has a pH-value of about 5.6, while in the Northeast, the average pH is 4. Calculate how much more acidic is normal rainwater than pure water and in the different regions.

5.18. In meteorology, precipitation less than $0.1\,\mathrm{mm\,day^{-1}}$ is typically neglected (cf. Chap. 3). Take this threshold value, and assume this amount of rain falls onto $1\,\mathrm{m^2}$, and has a pH value of 5 at 25 °C. How many H^+ and OH^- ions are received in that rain-fall event?

5.19. Fog formed at Mauno Loa where a CO_2 concentration of 395.1 ppm was observed. Assume equilibrium between the CO_2 in the gasphase and aqueous phase and $K = 4.16 \cdot 10^{-7}$ for the ion product and calculated the pH of the fog under neglection of the self-ionization in the fog droplets.

5.20. Determine the *S(VI)* concentration for a rain with a pH of 6 when the ambient partial pressures of SO_2, NH_3, O_3, H_2O_2, and HNO_3 are 2.99 ppb, 1.76, 5.5, 0.62 ppb, and $9 \cdot 10^{-6}$ ppt for a total $S(IV)$, NH_3, O_3, H_2O_2, and HNO_3 concentration of 4.6, 4.6, 4.6, 0.8, and 0.8 ppb, respectively. Assume an open system, and a liquid water content of $10^{-6}\,\mathrm{M\,atm^{-1}}$. How would your results change for a closed system?

References

Material, concepts, ideas and problems of the following books and articles inspired this chapter. These sources are recommended for further reading.

Andrews DG(2000) Introduction to atmospheric physics. Cambridge University Press, New York, 237pp

Brimblecombe P (1986) Air composition and chemistry. Cambridge University Press, London/New York/New Rochelle/Melbourne/Sydney, 247pp

Bruno TJ, Svoronos P (2004) Handbook of basic tables for chemical analysis, 2nd edn. CRC, Boca Raton

Dlugi R, Berger M, Zelger M, Hofzumahaus A, Siese M, Holland F, Wisthaler A, Grabmer W, Hansel A, Koppmann R, Kramm G, Möllmann-Coers M, Knaps A (2010) Turbulent exchange and segregation of HO_x radicals and volatile organic compounds above a deciduous forest. Atmos Chem Phys 10:6215–6235

Eltahir EAB, Bras RL (1996) Precipitation recycling. Rev Geophys 34:367–378

Fletcher NH (1962) The physics of rain clouds. Cambridge University Press, Cambridge/New York, 386pp

Foken T (2014) Micrometeorology (trans: Nappo CJ). Springer, Heidelberg, 350pp

Goody RM, Yung YL (1989) Atmospheric radiation: theoretical basis. Oxford University Press, New York/Oxford, 503pp

Haltiner GJ, Martin FL (1957) Dynamical and physical meteorology. McGraw-Hill, New York/Toronto/London, 470pp
Hobbs PV (2000a) Introduction to atmospheric chemistry. Cambridge University Press, Cambridge, 262pp
Hobbs PV (2000b) Basic physical chemistry for atmospheric sciences. Cambridge University Press, Cambridge, 209pp
Iqbal M (1983) An introduction to solar radiation. Academic Press, Toronto, 408pp
Jacobson MZ (1999) Fundamentals of atmospheric modeling. Cambridge University Press, New York, 656pp
Jacobson MZ (2005) Fundamentals of atmospheric modeling. Cambridge University Press, New York, 813pp
Kertz W (1969) Einführung in die Geophysik. Band 1. Erdkörper. BI Wissenschaftsverlag, Mannheim/Leipzig/Wien/Zürich, 232pp
Kramm G (1995) Zum Austausch von Ozon und reaktiven Stickstoffverbindungen zwischen Atmosphäre und Biosphäre. Maraun-Verlag, Frankfurt, 268pp
Kramm G, Dlugi R (1994) Modelling of vertical fluxes of nitric acid, ammonia, and ammonium nitrate in the atmospheric surface layer. J Atmos Chem 18:319–357
Kramm G, Meixner FX (2000) On the dispersion of trace species in the atmospheric boundary layer: a reformulation of the governing equations for the turbulent flow of the compressible atmosphere. Tellus A 52:500–522
Kramm G, Dlugi R, Mölders N, Müller H (1994) Numerical investigations of the dry deposition of reactive trace gases. In: Baldasano JM et al (eds) Computer simulation, air pollution II, vol 1. Computational Mechanics, Southhampton/Boston, pp 285–307
Kramm G, Dlugi R, Dollard GJ, Foken T, Mölders N, Müller H, Seiler W, Sievering H (1995) On the dry deposition of ozone and reactive nitrogen compounds. Atmos Environ 29:3209–3231
Kramm G, Beier N, Foken T, Müller H, Schröder P, Seiler W (1996) A SVAT scheme for NO, NO_2, and O_3 - model description and test results. Meteorol Atmos Phys 61:89–106
Kramm G, Dlugi R, Mölders N (2004) On the vertically averaged balance equation of atmospheric trace constituents. Meteorol Atmos Phys 86:121–141
Lichtfouse E, Schwarzbauer J, Robert D (2012) Environmental chemistry for a sustainable world. Springer, Heidelberg, 541pp
Logan JA, Prather MJ, Wofsy SC, McElroy MB (1981) Tropospheric chemistry – a global perspective. J Geophys Res 86:7210–7254
Lutgen FK, Tarbuck EJ (2001) The atmosphere – an introduction to meteorology. Pearson, Boston, 506pp
Mölders N (1999) Einfache und akkumulierte Landnutzungsänderungen und ihre Auswirkungen auf Evapotranspiration, Wolken- und Niederschlagsbildung. Wiss. Mitt. Leipzig, 15, Habilitation thesis, 206pp
Mölders N (2005) Feedbacks at the hydro-meteorological interface. In: Bronstert A, Carrera J, Kabat P, Lütkemeier S (eds) Coupled models for the hydrological cycle – integrating atmosphere, biosphere, and pedosphere. Springer, Berlin/Heidelberg, pp 192–208
Mölders N (2011/2012) Land-use and land-cover changes – impact on climate and air quality. Atmospheric and oceanographic sciences library, vol 44. Springer, Dordrecht. doi:10.1007/978-94-007-1527-1 3
Mölders N, Olson MA (2004) Impact of urban effects on precipitation in high-latitudes. J Hydrometeorol 5:409–429
Mölders N, Hass H, Jakobs HJ, Laube M, Ebel A (1994) Some effects of different cloud parameterizations in a mesoscale model and a chemistry transport model. J Appl Meteor 33:527–545
National Academy of Sciences (1984) Global tropospheric chemistry. National Academic, Washington, DC, 194pp
Pais A (1995) Introducing atoms and their nuclei. In: Brown LM, Pais A, Pippard B (eds) Twentieth century physics, vol I. Institute of Physics, Bristol/Philadelphia/American Institute of Physics, New York, pp 43–141

Pruppacher HR, Klett JD (1978) Microphysics of clouds and precipitation. D. Reidel, Dordrecht/Boston/London, 714pp
Salby ML (1996) Fundamentals of atmospheric physics. Academic, San Diego/New York/Boston/London/Sydney/Tokyo/Toronto, 627pp
Seinfeld JH (1986) Atmospheric chemistry and physics of air pollution. Wiley, New York/Chichester/Brisbane/Toronto/Singapore, 738pp
Seinfeld JH, Pandis SN (1998) Atmospheric chemistry and physics: from air pollution to climate change. Wiley-Interscience, New York, 1326pp
Sportisse B (2010) Fundamentals in air pollution. Springer, Heidelberg, 299pp
Tetzlaff G, Dlugi R, Friedrich K, Gross G, Hinneburg D, Pahl U, Zelger M, Mölders N (2002) On modeling dry deposition of long-lived and chemically reactive species over heterogeneous terrain. J Atm Chem 42:123–155
Thompson AM (1992) The oxidizing capacity of the Earth's atmosphere: probable past and future changes. Science 256:1157–1165
Twomey S, Wojciechowski TA (1969) Observations of the geographical variation of cloud nuclei. J Atmos Sci 26:648–651
Visconti G (2001) Fundamentals of physics and chemistry of the atmosphere. Springer, Heidelberg, 593pp
Wallace JM, Hobbs PV (2006) Atmospheric science – an introductory survey. Academic, San Diego/New York/Boston/London/Sydney/Tokyo/Toronto, 483pp
Wayne RP (1985) Chemistry of atmospheres – an introduction to the chemistry of the atmospheres of Earth, the planets, and their satellites. Clarendon, Oxford, 361pp

Chapter 6
Dynamics and Synoptic

Abstract In the chapter Dynamics, and Synoptic, the basic laws for describing the kinematic and dynamic behavior of tropospheric flows are presented and discussed. The conservation equations for momentum (Newton's 2nd law), total mass (equation of continuity), dry air, water substances, trace constituents, and energy (1st principle of thermodynamics) are presented and explained, where inertial frames and moving frames rotating with the Earth are considered. This presentation includes different kinds of coordinate systems. Simplifications like the hydrostatic and geostrophic approximations are related to scaling considerations (scale analysis). Balanced curved flows, streamlines and trajectories are explained as well. Circulation and vorticity principles are discussed to analyze rotational flows. This part includes, for instance, the balance equation for vorticity and the distinction between absolute and relative vorticity. Wave analysis is explained by examples like gravity waves and Rossby waves. Principles of Ekman's physics of the atmospheric boundary layer (ABL) are presented to point out the effects of turbulent motion. The chapter also encompasses how principles of dynamics and kinetic as well as numerical weather prediction model results are used in weather forecasting.

Keywords Coordinate systems • Coordinate transformations • Macroscopic equations • Scale analysis • Primitive equations • Kinematic • Frontal theories • Weather forecasting • Concepts of numerical modeling

Dynamic meteorology deals with the atmospheric motions and their time evolution using analytical approaches that base on the principle of fluid dynamics. The kinematic branch of dynamics looks at the flow properties in terms of translation, advection, and deformation. **Synoptic** (*Greek* synopsis = showing together) meteorology encompasses the description, analysis, and forecasting of weather. Since numerical weather prediction (NWP) models became involved in weather forecasting, the distinction between dynamics and synoptic became artificial. Thus, we discuss them together in this chapter. In doing so, we consider the atmosphere as a fluid wherein various types of flows occur on length scales of several centimeters

N. Mölders and G. Kramm, *Lectures in Meteorology*, Springer Atmospheric Sciences,
DOI 10.1007/978-3-319-02144-7_6,

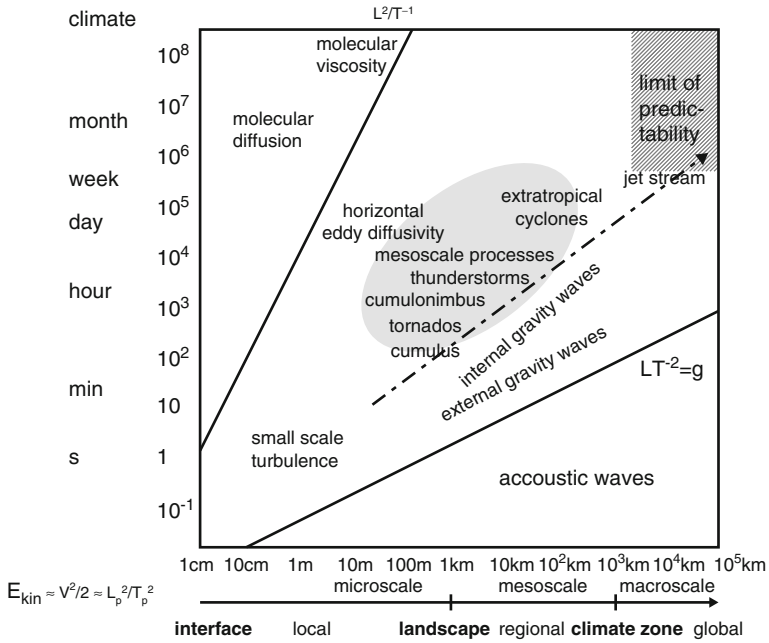

Fig. 6.1 Schematic view of temporal and spatial scales in the atmosphere

to the global scale and on time scales of less than a second to decades. The temporal and spatial scales relate to each other, as velocity is a distance per time (Fig. 6.1). Consequently, kinetic energy provides a relation between the temporal and spatial scale of length squared and time squared.

In this chapter, we derive the macroscopic equations of motions and use scale analysis to introduce simplifications to describe atmospheric motions.[1] We can apply the macroscopic consideration and basics of continuum mechanics (continuum hydrodynamics) because in the troposphere, an air parcel consists of so many molecules that meteorological quantities are defined in a statistical sense as the average over many molecules (Chap. 2).

The different weather conditions can be explained by changes of air masses (Chap. 2), the fronts that separate them, and the frontal disturbances that develop over or move into a region. Within this sense, this chapter provides an overview on atmospheric waves, extends the knowledge on air-mass development presented in Chap. 2, and on how we can apply radiosonde and remote sensing data (Chaps. 2 and 4), synoptic weather maps, as well as NWP for weather forecasting.

[1]This chapter pre-assumes basic knowledge of calculus. A short review of the fundamental concepts relevant for understanding of this chapter is given in Appendix A.

6.1 Natural Coordinates

Natural coordinates are useful for describing and understanding the kinematic and dynamic behavior of flows. Let us consider the motion of an air parcel along a trajectory (Fig. 6.2). The velocity of this air parcel reads

$$\mathbf{v}(t) = \frac{d\mathbf{r}}{dt} = \frac{d\mathbf{r}}{ds}\frac{ds}{dt} = V\,\mathbf{t} \tag{6.1}$$

where s is the arc length, $V = ds/dt$, $\mathbf{t}$ is the unit tangent given by

$$\mathbf{t} = \frac{d\mathbf{r}}{ds} \tag{6.2}$$

and $\mathbf{r}$ is the position vector. From this equation we can infer that $(ds)^2 = d\mathbf{r} \cdot d\mathbf{r}$. The acceleration of this air parcel reads

$$\mathbf{a}(t) = \frac{d\mathbf{v}(t)}{dt} = \frac{d}{dt}(V\,\mathbf{t}) = \frac{dV}{dt}\,\mathbf{t} + V\frac{d\mathbf{t}}{dt} = \frac{dV}{dt}\,\mathbf{t} + V^2\frac{d\mathbf{t}}{ds}. \tag{6.3}$$

The derivative $d\mathbf{t}/ds$ that occurs in this equation is given by

$$\frac{d\mathbf{t}}{ds} = K_t\,\mathbf{n}_t \tag{6.4}$$

where K_t is the curvature of the trajectory at a given point. The curvature is defined as the magnitude of $d\mathbf{t}/ds$. The radius of curvature R_t is related to it by $R_t = {K_t}^{-1}$. As illustrated in Fig. 6.3, the quantity R_t can be positive or negative. For the purpose of completeness, the torsion T_t is defined as the magnitude of $d\mathbf{b}_t/ds$, i.e.

$$\frac{d\mathbf{b}_t}{ds} = -\,T_t\,\mathbf{n}_t. \tag{6.5}$$

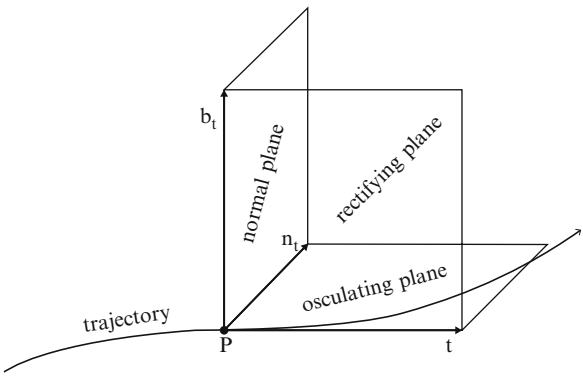

Fig. 6.2 Unit tangent, $\mathbf{t}$, principal normal, $\mathbf{n}_t$, and binormal, $\mathbf{b}_t$, to the trajectory at a certain point P

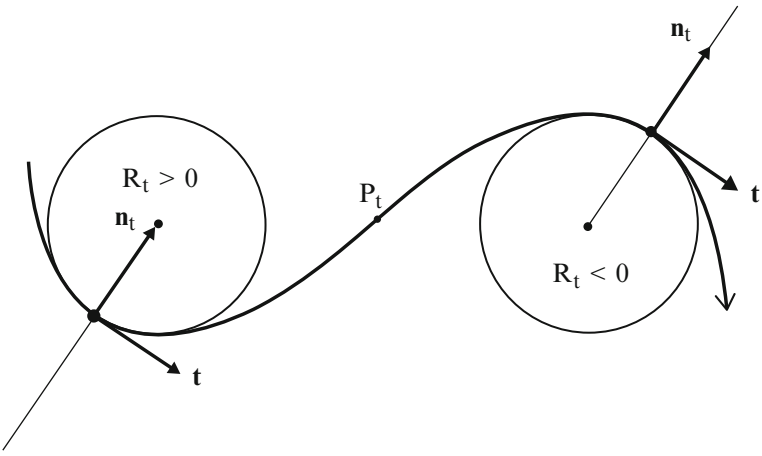

Fig. 6.3 Vector basis of a plane trajectory. Here, $\mathbf{t}$ is the unit tangent, $\mathbf{n}_t$ is the principal normal, R_t is the radius of curvature, and P_t is the turning point

Here, $\mathbf{n}_t$ is the principal normal to the unit tangent of the trajectory (subscript t), and $\mathbf{b}_t$ is the corresponding binormal which is perpendicular to the osculating plane spanned by $\mathbf{t}$ and $\mathbf{n}_t$ (Fig. 6.2). In case of a pure horizontal flow field, the binormal serves as the unit vector in the vertical direction (Fig. 6.3). The plane spanned by $\mathbf{n}_t$ and $\mathbf{b}_t$ is the normal plane, and the plane spanned by $\mathbf{t}$ and $\mathbf{b}_t$ is the rectifying plane. Obviously, $\mathbf{t}$, $\mathbf{n}_t$ and $\mathbf{b}_t$ span a right-handed rectangular coordinate frame (trihedron) at any given point of a curve in space like a trajectory (Fig. 6.2). Such a frame of natural coordinates serves to describe the motion of an air parcel along its trajectory. It is called an intrinsic system because it is closely related to the motion itself. As the unit tangent $\mathbf{t}$ is time-dependent, the other two basis vectors also depend on time.

The moving trihedron spanned by $\mathbf{t}$, $\mathbf{n}_t$ and $\mathbf{b}_t$ is an orthonormal frame, i.e. the orthonormal conditions $\mathbf{t}\cdot\mathbf{t} = \mathbf{n}_t\cdot\mathbf{n}_t = \mathbf{b}_t\cdot\mathbf{b}_t = 1$ and $\mathbf{t}\cdot\mathbf{n}_t = \mathbf{t}\cdot\mathbf{b}_t = \mathbf{n}_t\cdot\mathbf{b}_t = 0$ are fulfilled. Thus,

$$\left.\begin{aligned}\mathbf{t} &= \mathbf{n}_t \times \mathbf{b}_t\\ \mathbf{n}_t &= \mathbf{b}_t \times \mathbf{t}\\ \mathbf{b}_t &= \mathbf{t} \times \mathbf{n}_t\end{aligned}\right\} \tag{6.6}$$

and, for the derivative of $\mathbf{n}_t$ with respect to s we obtain

$$\frac{d\,\mathbf{n}_t}{ds} = \frac{d}{ds}\,(\mathbf{b}_t \times \mathbf{t}) = \frac{d\,\mathbf{b}_t}{ds} \times \mathbf{t} + \mathbf{b}_t \times \frac{d\,\mathbf{t}}{ds} = T_t\,\mathbf{b} - K_t\,\mathbf{t}. \tag{6.7}$$

Equations (6.4), (6.5), and (6.7) are the central equations in the theory of space curves. They are customarily called the **Serret-Frenet formulae**.

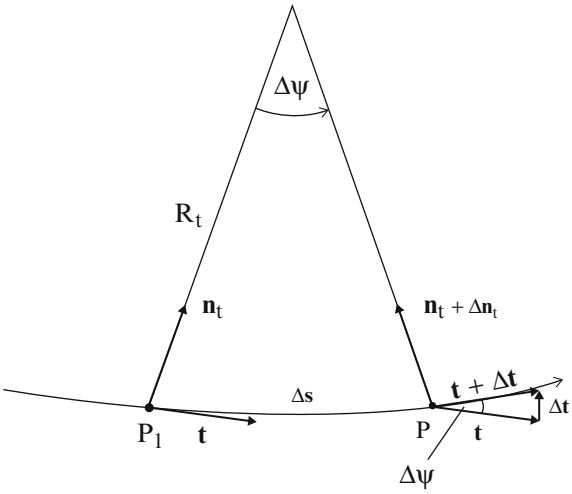

Fig. 6.4 Variation of the unit tangent, **t**, and the principal normal, $\mathbf{n}_t$, in the case of a plane trajectory

As illustrated in Fig. 6.4, we can determine the curvature by

$$K_t = \frac{1}{R_t} = \lim_{P_1 \to P} \frac{\Delta\psi}{\Delta s} = \frac{d\psi}{ds}. \tag{6.8}$$

Since we can write the derivative of the unit tangent with respect to the arc length as

$$\frac{d\mathbf{t}}{ds} = \frac{d\mathbf{t}}{d\psi}\frac{d\psi}{ds} \tag{6.9}$$

and $d\mathbf{t} = d\psi\,\mathbf{n}_t$ (Fig. 6.4), we directly obtain Eq. (6.4), and, hence, $K_t = d\psi/ds$.

Combining Eqs. (6.3) and (6.4) yields

$$\mathbf{a}(t) = \frac{dV}{dt}\mathbf{t} + \frac{V^2}{R_t}\mathbf{n}_t. \tag{6.10}$$

Equation (6.10) illustrates that in addition to the acceleration, dV/dt, along the tangent to the trajectory of the air parcel called the tangential acceleration, there exists also an acceleration, V^2/R_t, in the direction of the principal normal called the centripetal acceleration.

It is convenient to express the divergence and the relative vorticity of the horizontal flow with respect to natural coordinates. The divergence reads

$$\nabla\cdot\mathbf{v} = \left(\mathbf{t}\frac{\partial}{\partial s} + \mathbf{n}_t\frac{\partial}{\partial n_t} + \mathbf{b}_t\frac{\partial}{\partial b_t}\right)\cdot(V\,\mathbf{t}) = \frac{\partial V}{\partial s} + \frac{V}{R_{n_t}} + \frac{V}{R_{b_t}} \tag{6.11}$$

where the curvatures of the normals, $\partial \mathbf{t}/\partial n_t = K_{n_t}\mathbf{n}_t = \mathbf{n}_t/R_{n_t}$ and $\partial \mathbf{t}/\partial b_t = K_{b_t}\mathbf{b}_t = \mathbf{b}_t/R_{b_t}$, have been used. For a pure horizontal flow,

$$\nabla_H \cdot \mathbf{v}_H = \frac{\partial V}{\partial s} + \frac{V}{R_{n_t}}. \tag{6.12}$$

This divergence term consists of two parts, namely the divergence due to directional change and the velocity divergence. The curl of the velocity field is

$$\nabla \times \mathbf{v} = \left(\mathbf{t}\frac{\partial}{\partial s} + \mathbf{n}_t\frac{\partial}{\partial n_t} + \mathbf{b}_t\frac{\partial}{\partial b_t}\right) \times (V\mathbf{t}) = V\,K_t\,\mathbf{b}_t - \mathbf{b}_t\frac{\partial V}{\partial n_t} + \mathbf{n}_t\frac{\partial V}{\partial b_t}. \tag{6.13}$$

When we scalarly multiply this equation by $\mathbf{b}_t$ used in this case to characterize the vertical direction we obtain for the relative vorticity

$$\xi = \mathbf{b}_t \cdot (\nabla \times \mathbf{v}) = V\,K_t - \frac{\partial V}{\partial n_t} = \frac{V}{R_t} - \frac{\partial V}{\partial n_t}. \tag{6.14}$$

Obviously, ξ consists of two parts caused by the curvature of the trajectories and the velocity shear.

6.1.1 Trajectories Versus Streamlines

A trajectory is the actual path of an air parcel, i.e. it characterizes the direction of the velocity that such an air particle is taking successively during a time interval. When the velocity field $\mathbf{v}(\mathbf{r},\ t)$ is always known during that time interval, the trajectory can be calculated by integrating $d\mathbf{r} = \mathbf{v}\,dt$ leading to $\mathbf{r} = \mathbf{r}(a_1,\ a_2,\ a_3,\ t) = \mathbf{r}(\mathbf{a},\ t)$, where a_1, a_2, and a_3 are the **Lagrangian coordinates** of a vector $\mathbf{a}$ to identify the position of an air particle at a given time t_0. This vector is related to the position vector by $\mathbf{r}(t_0) = \mathbf{a}$. In the Lagrangian sense, the position vector, $\mathbf{r}$, is not an independent variable, in complete contrast to the **Eulerian consideration**. A streamline represents a "snapshot" of the directions of the velocity field $\mathbf{v}(\mathbf{r},\ t)$ at various locations at a given time t_0. As at each location, a streamline is parallel to the flow field, we may write $d\mathbf{r}_s \times \mathbf{v} = \mathbf{0}$.

As shown in Fig. 6.5, a trajectory is the envelope of the corresponding streamlines. Thus, at a given point $P(t)$, the unit tangent $\mathbf{t}$ represents both the direction of this trajectory and the direction of the streamline touching the trajectory at this point. Even though the unit tangent is the same, the principal normal $\mathbf{n}_t$ and the binormal $\mathbf{b}_t$ of the trajectory generally differ from the principal normal $\mathbf{n}_s$ and the binormal $\mathbf{b}_s$ of the streamline, i.e. $\mathbf{n}_t \neq \mathbf{n}_s$ and $\mathbf{b}_t \neq \mathbf{b}_s$, but we still have

$$\mathbf{t} = \mathbf{n}_t \times \mathbf{b}_t = \mathbf{n}_s \times \mathbf{b}_s. \tag{6.15}$$

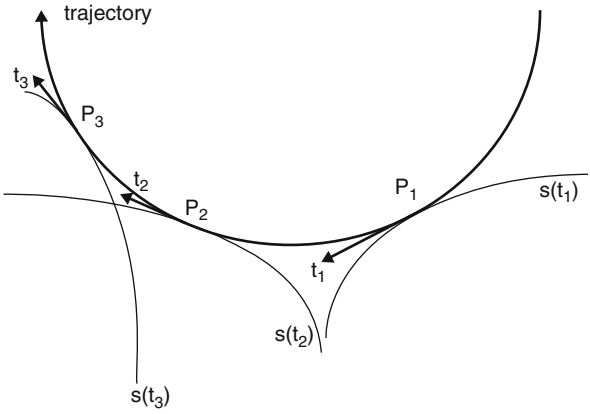

Fig. 6.5 Chronologically ordered streamlines enveloped by a trajectory, where P_1 to P_3 denote various points on the trajectory. The letter S denotes the streamlines going through these points

When we express the substantial derivative of the unit tangent in the Eulerian form, we obtain

$$\frac{d\mathbf{t}}{dt} = \frac{\partial \mathbf{t}}{\partial t} + V\,\frac{\partial \mathbf{t}}{\partial s} = \frac{\partial \mathbf{t}}{\partial t} + V\,K_s\,\mathbf{n}_s. \tag{6.16}$$

Here, the partial derivative of the unit tangent with respect to the arc length was replaced by $\partial \mathbf{t}/\partial s = K_s\,\mathbf{n}_s$, where $K_s = {R_s}^{-1}$ is the curvature of the streamline and R_s is the corresponding radius of the curvature. On the other hand, we have

$$\frac{d\mathbf{t}}{dt} = \frac{d\mathbf{t}}{ds}\,\frac{ds}{dt} = V\,K_t\,\mathbf{n}_t. \tag{6.17}$$

Combining Eqs. (6.16) and (6.17) yields

$$\frac{\partial \mathbf{t}}{\partial t} = V\,\left(K_t\,\mathbf{n}_t - K_s\,\mathbf{n}_s\right). \tag{6.18}$$

We can infer from Eq. (6.15) that in a pure horizontal (two-dimensional) case, we have $\mathbf{n}_t = \mathbf{n}_s$ because $\mathbf{b}_t = \mathbf{b}_s$. In such a case, Eq. (6.18) reads

$$\frac{\partial \mathbf{t}}{\partial t} = V\,\left(K_t - K_s\right)\,\mathbf{n}_t. \tag{6.19}$$

With respect to the unit vectors **i** (west-east direction) and **j** (south-north direction) of a **Cartesian frame** the unit tangent of a plane trajectory can be expressed by

$$\mathbf{t} = \mathbf{i}\,\cos\,\vartheta + \mathbf{j}\,\sin\,\vartheta \tag{6.20}$$

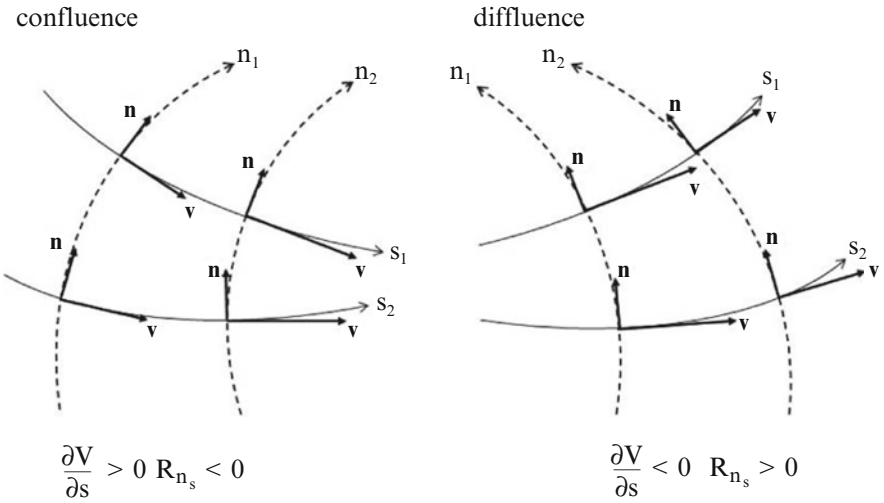

Fig. 6.6 Schematic view of confluence and diffluence of a two-dimensional flow field

where ϑ is the angle between **i** and **t**. It is also the angle between **j** and $\mathbf{n}_t$. This angle usually depends on time. Thus, the local rate of change of the unit tangent reads

$$\frac{\partial \mathbf{t}}{\partial t} = -\frac{\partial \vartheta}{\partial t}\,\mathbf{i}\,\sin\vartheta + \frac{\partial \vartheta}{\partial t}\,\mathbf{j}\,\cos\vartheta = \frac{\partial \vartheta}{\partial t}\,\mathbf{n}_t. \tag{6.21}$$

Combining Eqs. (6.19) and (6.21) yields

$$\frac{\partial \vartheta}{\partial t} = V\,(K_t - K_s)\,. \tag{6.22}$$

This relation is called **Blaton's equation**. Under steady-state conditions, $(\partial/\partial t = 0)$, the l.h.s. of Eqs. (6.19) and (6.22) vanish. Hence, the curvatures of the trajectories and the streamlines are identical, i.e. the trajectories and streamlines coincide.

In case of a pure horizontal flow, the divergence and relative vorticity of streamlines can be derived like that of trajectories. We obtain

$$\nabla_H \cdot \mathbf{v}_H = \frac{\partial V}{\partial s} + V\,\frac{\partial \psi}{\partial n_s} \tag{6.23}$$

and

$$\xi = \mathbf{b}_s \cdot \nabla \times \mathbf{v} = V\,K_s - \frac{\partial V}{\partial n_s}. \tag{6.24}$$

The first term on the r.h.s. of Eq. (6.23) is the velocity **divergence**, and the second term is the direction divergence. The latter is also called the **diffluence** (Fig. 6.6) and represents streamlines that flow apart. In the case of opposite signs, these terms

are called the velocity **convergence** and the **confluence**. A confluence represents streamlines that flow together (Fig. 6.6). Under normal atmospheric conditions, velocity divergence and direction divergence have opposite signs. These two terms tend to compensate each other. The relative vorticity in Eq. (6.24) consists of two terms, namely the curvature vorticity, $V\,K_s$, and the shear vorticity, $-\frac{\partial V}{\partial n_s}$.

6.2 Kinematics of the Large-scale Flow

Flow can sharpen or reduce differences between air masses of different characteristics (Fig. 6.7). The flow can experience shear $-\frac{\partial V}{\partial n_s}$, curvature $V\frac{\partial \psi}{\partial s}$, diffluence $V\frac{\partial \psi}{\partial n_s}$, stretching $\frac{\partial V}{\partial s}$, vorticity $V\frac{\partial \psi}{\partial s}-\frac{\partial V}{\partial n_s}$, divergence $V\frac{\partial \psi}{\partial n_s}+\frac{\partial V}{\partial s}$ and deformation. Divergence is the sum of diffluence and stretching, i.e. the time rate of change of an area. Vorticity is the sum of shear and curvature. We define the rotation of velocity (i.e. spin of flow) as the vorticity of the velocity field.

An example of vorticity can be seen in every eddy, whether it is a low-pressure system, a tropical cyclone, a mountain-valley circulation, a land-sea-breeze or just a dust devil (Chap. 7). An astronaut on the moon sees a rotational motion due to the Earth's rotation and the various points on Earth have different rotation velocities depending on their distance to the axis of rotation.[2] We distinguish the **absolute vorticity** or **Rossby**[3]**Ertel**[4] **vorticity** in the inertial system[5] and the **relative velocity** that is the velocity in the coordinate system related to the Earth. When $\boldsymbol{\Omega} = 7.29 \cdot 10^{-5}\,\mathrm{s}^{-1}$ is the angular velocity of the Earth,[6] $\mathbf{r}$ is the vector of the distance from the Earth's center to a location. A point without motion relative to the Earth moves with the Earth's velocity $\mathbf{v}_E = \boldsymbol{\Omega} \times \mathbf{r}$. A point moving relative to the Earth has an absolute velocity $\mathbf{v}_A = \mathbf{v} + \boldsymbol{\Omega} \times \mathbf{r}$, i.e. the relative velocity plus the velocity of the Earth. The vorticity of the Earth is given by $\nabla \times \mathbf{v}_E = \nabla \times (\boldsymbol{\Omega} \times \mathbf{r}) = 2\,\boldsymbol{\Omega}$.[7]

---

[2] Due to the rotation of the Earth a classroom with its center at the pole turns around once a day. At the equator, a classroom makes a free trip at its distance from the Earth's center around the rotation axis.

[3] Carl-Gustaf Arvid Rossby, Swedish-U.S. meteorologist, 1898–1957. He was the first to explain the large-scale motions of the atmosphere in terms of fluid mechanics.

[4] Hans Ertel, German natural scientist and pioneer in geophysics, meteorology and hydrodynamics, 1904–1971.

[5] The inertial system is a coordinate system realized by coordinates that are fixed in space.

[6] $\Omega = \frac{2\pi}{\mathit{sideriand ay}} = \frac{2\pi}{86{,}164\,\mathrm{s}} = 7.292 \cdot 10^{-5}\,\mathrm{s}^{-1}$. Note that a sidereal (or star) day has 23 h, 56 min and 4.09 s. The rotational velocity of the Earth with respect to a fixed point in the space is slightly shorter than a day (24 h).

[7] The triple vector product of three vectors, $\mathbf{a}$, $\mathbf{b}$, and $\mathbf{c}$ is given by $\mathbf{a} \times (\mathbf{b} \times \mathbf{c}) = (\mathbf{a} \cdot \mathbf{c})\,\mathbf{b} - (\mathbf{a} \cdot \mathbf{b})\,\mathbf{c}$. Furthermore, $\boldsymbol{\Omega}$ is spatially constant, $\nabla \cdot \mathbf{r} = 3$ and $\nabla \mathbf{r} = \mathbf{E}$, where $\mathbf{E}$ is the identity tensor.

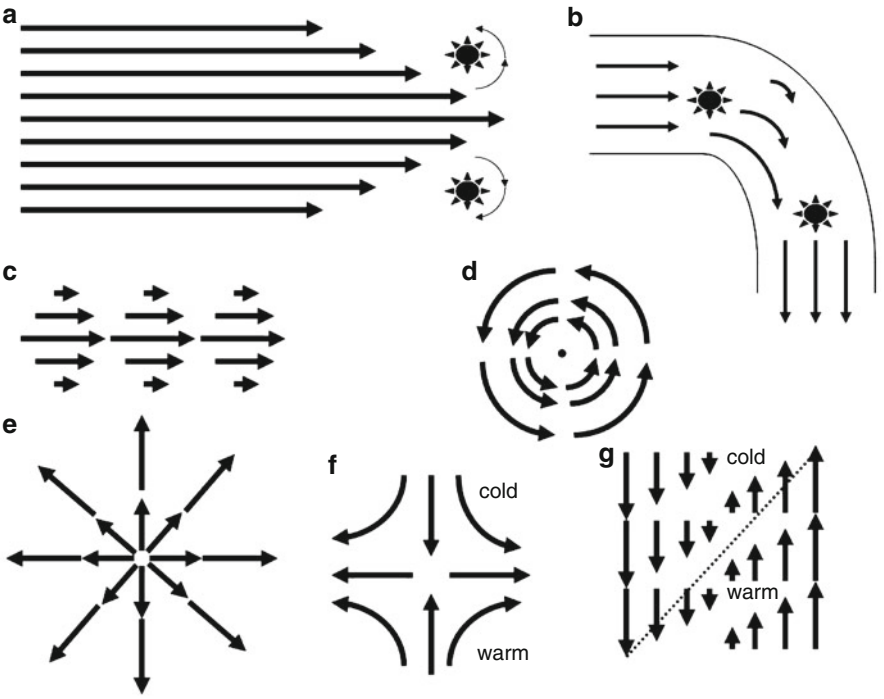

Fig. 6.7 Schematic view of a flow (**a**) with and (**b**) without relative vorticity. (**c**) Sheared flow without curvature, diffluence, stretching or divergence. Shear and vorticity are cyclonic for the upper part and anticyclonic for the lower part when on the Northern Hemisphere (e.g. jet stream). (**d**) Rotation with cyclic shear, vorticity and curvature, but without diffluence, stretching or divergence (e.g. cyclones). (**e**) Radial flow with velocity directly proportional to the radius, with diffluence, stretching, divergence, but no curvature, shear or vorticity (e.g. near-surface wind field in a high-pressure system). (**f**) Hyperbolic flow with diffluence, stretching, shear and curvature. The flow is non-divergent and non-rotational because terms cancel out. (**g**) Shear flow. Parts (**f**) and (**g**) schematically illustrate how flow may sharpen temperature gradients

$$\nabla \times \mathbf{v}_A = \nabla \times \mathbf{v} + \nabla \times (\boldsymbol{\Omega} \times \mathbf{r}) = \overbrace{\nabla \times \mathbf{v}}^{\textit{relative vorticity}} + \underbrace{2\,\boldsymbol{\Omega}}_{\textit{vorticity of the Earth}} . \qquad (6.25)$$

Example. Determine how much your classroom rotates during this class (5,400 s). The period of the rotation of the Earth is 86,163 s.

Solution. The class room turns $\frac{5{,}400\,\mathrm{s}}{86{,}163\,\mathrm{s}} 360° = 22.56°$.

The scalar product of the last equation with the unit vector in z-direction, **k**, provides the vertical component of the absolute and relative vorticity caused by the Earth's rotation. Generally, we only consider the vertical components of the absolute vorticity, ξ_A, and the relative vorticity, ξ, respectively. Thus, with respect to a Cartesian coordinate frame, we obtain (Sect. 6.3.2)

$$\xi_A = \mathbf{k} \cdot (\nabla \times \mathbf{v}_A) = \frac{\partial v}{\partial x} - \frac{\partial u}{\partial y} + 2\,\Omega \sin\varphi = \xi + f$$

with $\xi = \mathbf{k} \cdot (\nabla \times \mathbf{v}) = \frac{\partial v}{\partial x} - \frac{\partial u}{\partial y}$, $\mathbf{k} \cdot \boldsymbol{\Omega} = \Omega \sin\varphi$, and

$$f = 2\,\Omega \sin\varphi. \tag{6.26}$$

Being the vertical component of the Earth's vorticity called the **Coriolis parameter** f, where $\Omega = |\boldsymbol{\Omega}|$ and φ is the latitude. We associate the rotation of the Earth with a positive f on the Northern ($\varphi \geq 0$) and a negative f on the Southern Hemisphere ($\varphi < 0$) because $\sin(-\epsilon) = -sin(\epsilon)$, where $\epsilon \geq 0$ is an arbitrary angle.

Example. Estimate the Coriolis parameter for Fairbanks ($\varphi \approx 64°$N), Philadelphia ($\varphi \approx 40°$N), New Orleans ($\varphi \approx 30°$N), and Sydney ($\varphi \approx 33.5°$S).

Solution. The Southern Hemisphere is addressed by a negative value of φ. The Coriolis parameters of these cities are $1.31 \cdot 10^{-4}\,\mathrm{s}^{-1}$, $0.937 \cdot 10^{-4}\,\mathrm{s}^{-1}$, $0.729 \cdot 10^{-4}\,\mathrm{s}^{-1}$, and $-0.804 \cdot 10^{-4}\,\mathrm{s}^{-1}$, respectively.

We call the sense of rotation in the $x - y$-plane[8] **cyclonic** when its direction is the same as the Earth's rotation. Cyclonic means a positive relative vorticity and a counter-clockwise motion on the Northern Hemisphere, a negative relative vorticity and a clockwise motion on the Southern Hemisphere. The opposite rotation is denoted **anticyclonic** and means a negative (positive) relative vorticity on the Northern (Southern) Hemisphere. In accord with these definitions, on both hemispheres, air moves cyclonically (anticyclonically) around low-pressure (high-pressure) systems. Therefore, the lows and highs are called cyclones and anticyclones, respectively.

[8]In meteorology, the x-direction of the coordinate system is defined positive from west to east, the y-direction points from the south to the north and the z-direction is directed upwards positive. Winds from west/south have a positive sign while winds coming from east/north have a negative sign.

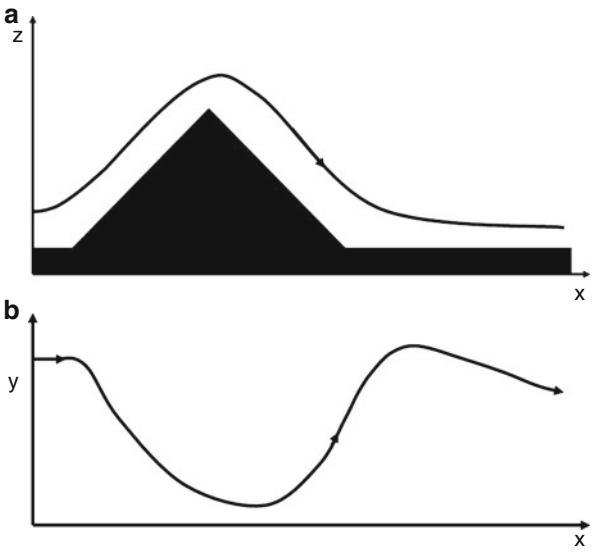

Fig. 6.8 Schematic view of a westerly flow passing a mountain range (**a**) in the $x-z$-plane and (**b**) shown in the $x-y$-plane

In synoptic, the relative vorticity, ξ serves to investigate systems rotating in the $x-y$-plane like, for instance, cyclones wherein ξ is positive. In natural coordinates, the relative vorticity reads $\xi = -\frac{\partial v}{\partial n} + \frac{v}{R_t}$. The net vertical vorticity component is the result of the rate of change in wind speed normal to the direction of the flow ($-\frac{\partial v}{\partial n}$; **shear vorticity**) and the turning of the wind along a streamline ($\frac{v}{R_T}$; **curvature velocity**). Consequently, a straight flow has vorticity when the speed changes normal to the flow axis.[9] A straight homogeneous flow has no relative vorticity. A curved flow may have zero vorticity when the shear vorticity is equal and opposed to the curvature vorticity, i.e. shear and curvature vorticity cancel each other out. An example is a frictionless fluid with no relative vorticity upstream that flows around a bend in a canal (Fig. 6.8). The flow is faster at the inner than outer wall.

Potential vorticity is the ratio of absolute vorticity to the effective depth of a vortex. Combination of the first law of thermodynamics (Chap. 2) and momentum conservation shows that potential vorticity can only change by diabatic processes. Thus, in an adiabatic frictionless motion, potential vorticity is conserved

$$(\xi + f)\frac{\partial \theta}{\partial p} \equiv constant$$

where θ is the potential temperature. Potential vorticity is a useful concept to understand the generation of vorticity in cyclogenesis, tracking intrusions of

[9]This phenomenon often occurs in jet streams.

stratospheric air into the troposphere (Chap. 5) and motion in the vicinity of jet streaks, and orographically induced Rossby waves.

For $\frac{\partial\theta}{\partial p} \equiv constant$, $\xi_A = \xi + f$ is conserved following the motion at any point, $\xi + f = f_0$. Since f increases towards the North (South), $\xi = f_0 - f < 0\ (> 0)$ and decreases (increases), the flow must remain zonal for conservation of potential vorticity. Consequently, for a westerly flow hitting a mountain barrier on the Northern Hemisphere, the motion first turns south while passing the mountains to conserve vorticity, and then turns north as the air descends (Fig. 6.8).

6.3 Navier-Stokes Equation

The local balance equation of momentum also called the **Navier-Stokes equation** is based on Newton's second law. This law states that in an unaccelerated reference frame, the resulting force, $\mathbf{F}$, acting on an air parcel, for instance, equals the change of the momentum, $m\,\mathbf{v}$, of this body with respect to time, t, expressed by

$$\mathbf{F} = \frac{d}{dt}\,(m\,\mathbf{v}) \tag{6.27}$$

where m is the mass of the air parcel, and $\mathbf{v}$ is its velocity. Such an unaccelerated reference frame is called an **inertial frame** of reference (hereafter simply called inertial frame). A Cartesian coordinate frame which may be considered as fixed with respect to the fixed stars is nearly an inertial frame for an earthbound observer. With respect to an inertial frame, the Navier-Stokes equation reads

$$\frac{\partial}{\partial t}\,(\rho\,\mathbf{v}_A) + \nabla\cdot(\rho\,\mathbf{v}_A\,\mathbf{v}_A + p\,\mathbf{E} + \mathbf{J}) = -\rho\,\nabla\phi_a. \tag{6.28}$$

Here, ρ is the density of air, $\mathbf{v}_A$ is the velocity with respect to the inertial frame also denoted the absolute velocity, ∇ is the Nabla operator, $\rho\,\mathbf{v}_A$ is the density of momentum, $\rho\,\mathbf{v}_A\,\mathbf{v}_A$ is the convective flux of momentum, and $p\,\mathbf{E} + \mathbf{J}$ is the corresponding non-convective flux of momentum or total stress tensor, where p is air pressure, $\mathbf{E}$ is the identity tensor, and $\mathbf{J}$ is the friction stress tensor or **Stokes stress tensor**. This friction stress vector reads

$$\mathbf{J} = \rho\,\nu\,\left(\nabla\mathbf{v}_A + (\nabla\mathbf{v}_A)^T\right) + \left(\mu_d - \frac{2}{3}\,\rho\,\nu\right)(\nabla\cdot\mathbf{v}_A)\,\mathbf{E} \tag{6.29}$$

where ν is the kinematic viscosity, μ_d is the bulk viscosity (near zero for most gases), and the superscript T denotes the transpose. Obviously, the elements of this symmetric tensor of second rank only depend on the straining motion because motion due to pure elongation (or compression) and pure rotation do not contribute to the deformation of a volume element. This fact is important when we formulate

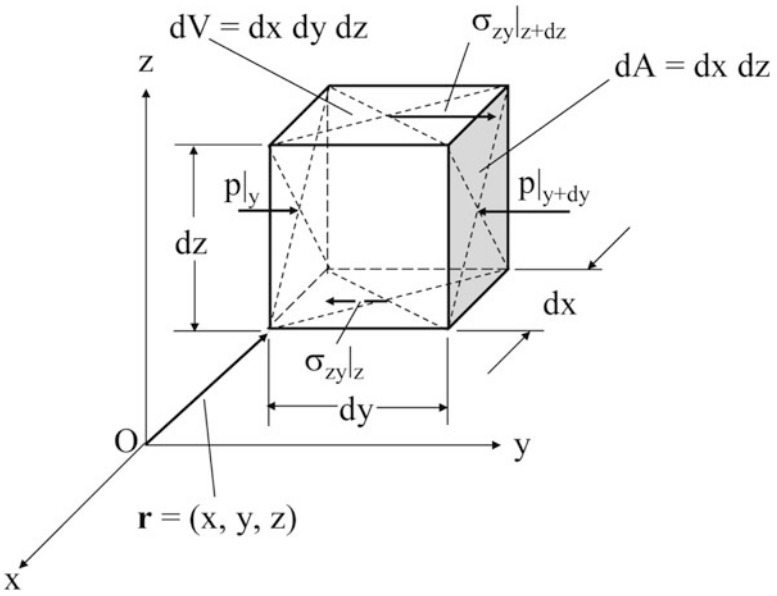

Fig. 6.9 Schematic representation of friction stress

the friction stress tensor for a moving frame of reference. In contrast to the pressure stress tensor, it only tangentially acts on a surface element dA as illustrated in Fig. 6.9 for the y-z-plane with respect to a Cartesian coordinate frame.

Furthermore, $\phi_a = -\gamma\, M_E \left(\frac{1}{r} - \frac{1}{r_p}\right)$ is the gravitational potential or attraction potential (Chap. 2), where $\gamma = 6.674 \cdot 10^{-11}\,\mathrm{m^3\,kg^{-1}\,s^{-2}}$ is the gravitational constant,[10] $M_E = 5.977 \cdot 10^{24}\,\mathrm{kg}$ is the mass of the Earth related to its center, r is the magnitude of the position vector $\mathbf{r}$, and $r_P = 6{,}356.75\,\mathrm{km}$ represents the radius at either of the poles for which the gravitational potential is arbitrarily taken to be zero. We may interpret the term $-\rho\,\nabla\phi_a$ as a source of momentum.

The equation of continuity formulated with respect to the inertial frame

$$\frac{\partial \rho}{\partial t} + \nabla \cdot (\rho\, \mathbf{v}_A) = 0 \tag{6.30}$$

describes the conservation of total mass. By using this equation we can rearrange Eq. (6.28) to

$$\rho\, \frac{d_A \mathbf{v}_A}{dt} + \nabla \cdot (p\, \mathbf{E} + \mathbf{J}) = -\rho\, \nabla \phi_a \tag{6.31}$$

[10] The gravitational constant was first determined by Cavendish in 1798.

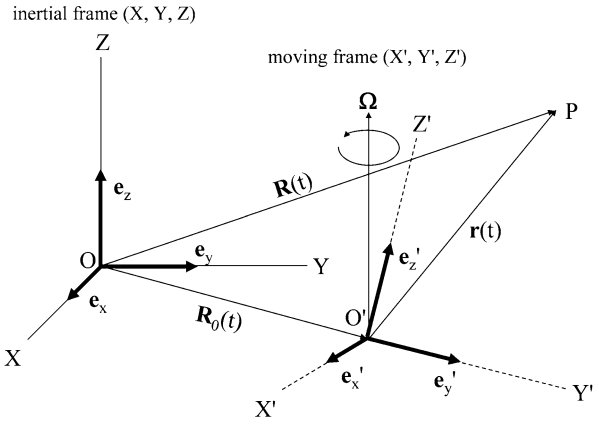

Fig. 6.10 Motion of the point P with respect to both an inertial frame (X, Y, Z) and a moving frame (X', Y', Z') of reference

where

$$\frac{d_A \mathbf{v}_A}{dt} = \frac{\partial \mathbf{v}_A}{\partial t} + \mathbf{v}_A \cdot \nabla \mathbf{v}_A \tag{6.32}$$

is the individual derivative with respect to time.

On the rotating Earth, an air parcel experiences active and **fictitious** forces due to the Earth' rotation. A fictitious force[11] also called pseudo force or d'Alembert force,[12] is an apparent force that acts on all masses in a moving frame of reference, such as a reference frame uniformly rotating with the Earth. Consequently, we have to transform the Navier-Stokes equation derived for an inertial frame with respect to a reference frame uniformly rotating with the Earth. In doing so, the time-dependent motion of an arbitrary point in the inertial frame denoted in Fig. 6.10 by (X, Y, Z) has to be described also in the moving frame of reference denoted in Fig. 6.10 by (X', Y', Z'). Then, we can express the absolute velocity by

$$\mathbf{v}_A = \frac{d_A \mathbf{R}(t)}{dt} = \underbrace{\frac{d_R \mathbf{r}(t)}{dt}}_{\mathbf{v}} + \underbrace{\frac{d_A \mathbf{R}_0(t)}{dt} + \boldsymbol{\Omega} \times \mathbf{r}(t)}_{\mathbf{v}_L} = \mathbf{v} + \mathbf{v}_L \tag{6.33}$$

where the subscripts A and R refer to the inertial frame and moving frame of reference, respectively. Here, $\mathbf{v}$ is the velocity with respect to the moving frame of reference also called the relative velocity. Furthermore, $d_A \mathbf{R}_0(t)/dt$ is the translatory velocity with which the origin O' and each other fixed point $P(\mathbf{r})$ of the moving frame is shifted parallel to itself. $\boldsymbol{\Omega} \times \mathbf{r}(t)$ is the tangential velocity, and

[11] There are four fictitious forces, rectilinear acceleration, centrifugal force, Coriolis force, and the Euler force.

[12] Jean le Rond d'Alembert, French mathematician, mechanician, physicist and philosopher, 1717–1783.

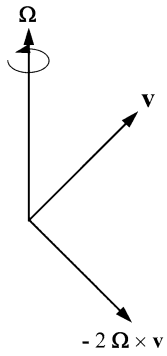

Fig. 6.11 Relationship between the (relative) velocity $\mathbf{v}$, angular velocity $\boldsymbol{\Omega}$ of the Earth and the Coriolis acceleration $-2\,\boldsymbol{\Omega} \times \mathbf{v}$

$\mathbf{v}_L = d_A\,\mathbf{R}_0(t)/dt + \boldsymbol{\Omega} \times \mathbf{r}\,(t)$ is the leading velocity. The absolute velocity equals the sum of the relative velocity and leading velocity.

For convenience, we consider $\mathbf{R}_0$ as independent of time. Thus, the leading velocity is $\mathbf{v}_L = \boldsymbol{\Omega} \times \mathbf{r}\,(t)$. The absolute velocity reads

$$\mathbf{v}_A = \left(\frac{d_R}{dt} + \boldsymbol{\Omega}\times\right)\mathbf{r}\,(t) \tag{6.34}$$

where the derivative with respect to time in the inertial frame may be expressed by

$$\frac{d_A}{dt} = \left(\frac{d_R}{dt} + \boldsymbol{\Omega}\times\right). \tag{6.35}$$

When we apply this operator to the absolute velocity we obtain

$$\frac{d_A\mathbf{v}_A}{dt} = \left(\frac{d_R}{dt} + \boldsymbol{\Omega}\times\right)(\mathbf{v} + \boldsymbol{\Omega} \times \mathbf{r}\,(t)) = \frac{d_R\mathbf{v}}{dt} + \underbrace{2\,\boldsymbol{\Omega} \times \mathbf{v}}_{\mathbf{C}_a} + \underbrace{\boldsymbol{\Omega} \times (\boldsymbol{\Omega} \times \mathbf{r}\,(t))}_{\mathbf{Z}_a}. \tag{6.36}$$

Here, $\mathbf{C}_a = 2\,\boldsymbol{\Omega} \times \mathbf{v}$ is the Coriolis acceleration, and $\mathbf{Z}_a = \boldsymbol{\Omega} \times (\boldsymbol{\Omega} \times \mathbf{r}\,(t))$ is the centripetal acceleration. Both forms of acceleration are fictitious accelerations and the related forces are fictitious forces. As shown, they arise when the balance equation of momentum is formulated in any coordinate frame that is rotating with respect to an inertial frame, i.e. it appears to an observer in the rotating frame like that of the rotating Earth as an additional acceleration.

The Coriolis acceleration is always perpendicular to $\boldsymbol{\Omega}$ and to $\mathbf{v}$, i.e. it does no work (Chap. 2). For an observer aligned with $\boldsymbol{\Omega}$, the Coriolis force, $-2\,\rho\boldsymbol{\Omega} \times \mathbf{v}$, appears as a force tending to deflect moving fluid elements to their right (Fig. 6.11), where its vector is always parallel with the plane of equator. Obviously, the Coriolis acceleration vanishes when $\mathbf{v} = 0$, or $\boldsymbol{\Omega}$ and $\mathbf{v}$ are collinear.

With respect to Fig. 6.12 we can express the angular velocity $\boldsymbol{\Omega}$ of the Earth in Cartesian coordinates by

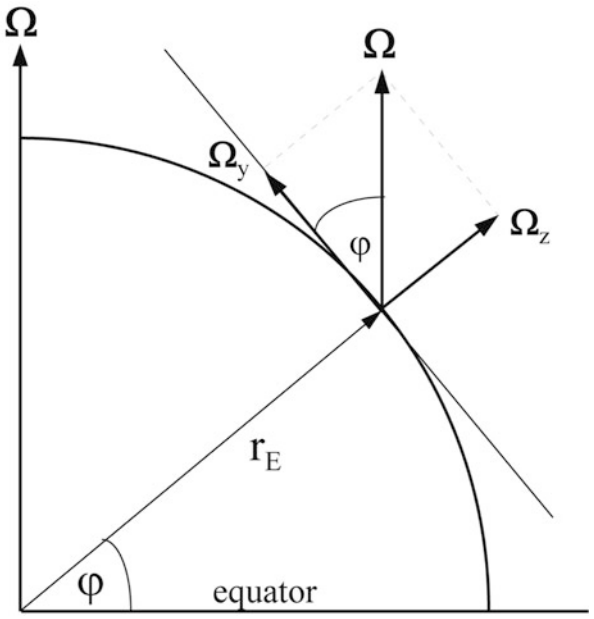

Fig. 6.12 Schematic representation for calculating the components of the angular velocity $\boldsymbol{\Omega}$ of the Earth in the Cartesian coordinate frame

$$\boldsymbol{\Omega} = \Omega_y + \Omega_z = \Omega \cos\varphi\, \mathbf{j} + \Omega \sin\varphi\, \mathbf{k} \tag{6.37}$$

where $\Omega = |\boldsymbol{\Omega}|$, φ is the latitude, and $\mathbf{j}$ and $\mathbf{k}$ are the unit vectors in y and z direction, respectively. When we also express the Coriolis acceleration in the Cartesian coordinate frame we obtain

$$\left.\begin{aligned} 2\,\boldsymbol{\Omega} \times \mathbf{v} &= 2\,(\Omega \cos\varphi\, \mathbf{j} + \Omega \sin\varphi\, \mathbf{k}) \times (u\,\mathbf{i} + v\,\mathbf{j} + w\,\mathbf{k}) \\ &= 2\,\Omega\,(w\cos\varphi - v\sin\varphi)\,\mathbf{i} + 2\,u\,\Omega \sin\varphi\,\mathbf{j} - 2\,u\,\Omega\cos\varphi\,\mathbf{k} \end{aligned}\right\} \tag{6.38}$$

where $\mathbf{i}$ is the unit vector in x-direction, and u, v, and w are the coordinates of the velocity vector $\mathbf{v}$ in x, y, and z direction, respectively. This equation may also be formulated in the sense of a determinant

$$2\,\boldsymbol{\Omega} \times \mathbf{v} = 2\,\Omega \begin{vmatrix} \mathbf{i} & \mathbf{j} & \mathbf{k} \\ 0 & \cos\varphi & \sin\varphi \\ u & v & w \end{vmatrix}. \tag{6.39}$$

Typically, the terms $2\,\Omega \sin\varphi$ and $2\,\Omega \cos\varphi$ are defined by f and f^*, respectively. By using these definitions we can write the Coriolis acceleration as

$$2\,\boldsymbol{\Omega} \times \mathbf{v} = \left(f^* w - f\, v\right)\mathbf{i} + f\, u\,\mathbf{j} - f^*\, u\,\mathbf{k}. \tag{6.40}$$

Since in most cases $|f^* w| \ll |f v| |f^* w| \ll |f v|$, the term $f^* w$ may usually be negligible. Furthermore, $|f^* u|$ is negligible compared to other terms occurring in the vertical component of the balance equation of momentum. In case of the Southern Hemisphere, the latitude has to be taken as negative.

In describing or measuring the wind velocity, usually given locations at the Earth's surface serve as reference frame. Since the Earth rotates, wind measured or simulated at a site is a relative motion on the rotating surface. Consequently, an air parcel moving along a straight line with respect to the inertial system appears to follow a curved path on the Earth's rotating surface.[13] The deflection results from the apparent acceleration named **Coriolis acceleration**. In describing the motion of wind relative to the Earth's surface, we have to include the Coriolis force or **Coriolis effect** to account for the motion we observe. This means

- The Coriolis force is a fictitious force that arises when the balance equation of momentum is transferred from an inertial frame of reference to a reference frame rotating with the Earth. It accounts for motions relative to the surface and applies to all motions.
- The Coriolis force is largest for the velocity normal to the Earth's axis.
- The Coriolis force will vanish if $\mathbf{v} = 0$, or $\boldsymbol{\Omega}$ and $\mathbf{v}$ are collinear.
- The Coriolis force increases with increasing speed of an object.
- The Coriolis force alters the direction of a moving object, but not its speed.

The centripetal acceleration, $\mathbf{Z}_a = \boldsymbol{\Omega} \times (\boldsymbol{\Omega} \times \mathbf{r}\,(t))$, also arises when the balance equation of momentum is formulated in any coordinate system that is rotating with respect to an inertial frame. When the origins of the inertial frame and the rotating coordinate frame are identical and fixed in the center of the Earth, the leading velocity due to the Earth's rotation is $\mathbf{v}_L = \boldsymbol{\Omega} \times \mathbf{r}$. The centripetal acceleration is directed toward the axis of rotation and always parallel with the plane of equator, and its magnitude depends on latitude (Fig. 6.13). Since $\nabla \times (\boldsymbol{\Omega} \times \mathbf{v}_L) = 0$, the centripetal acceleration can also be derived from the scalar potential function

$$\boldsymbol{\Omega} \times \mathbf{v}_L = \nabla \left(\frac{{\mathbf{v}_L}^2}{2} + const. \right) \tag{6.41}$$

where $\phi_c = {\mathbf{v}_L}^2/2 + const.$ is the centrifugal potential that has the opposite sign of the centripetal potential. As long as the Earth rotates and $\mathbf{r}$ is not aligned with $\boldsymbol{\Omega}$ the centripetal (or centrifugal) acceleration is not zero. Combining the gravitational potential, ϕ_a, and the centrifugal potential, ϕ_c, leads to

$$\phi = \phi_a + \phi_c = -\gamma\, M_E \left\{ \frac{1}{r} - \frac{1}{r_P} \right\} + \frac{{\mathbf{v}_L}^2}{2} + const. \tag{6.42}$$

[13] To visualize the curved path on a rotating surface, try to draw a straight line on a piece of paper while a classmate rotates it slightly.

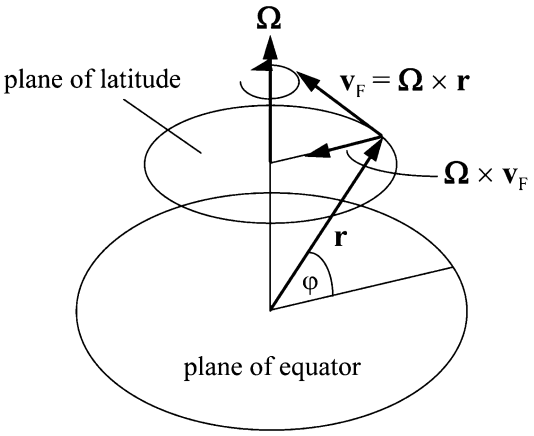

Fig. 6.13 Sketch of the centripetal acceleration. It is directed toward the axis of rotation. On the contrary, the gravitational acceleration would be directed along **r** to the center of the Earth's mass

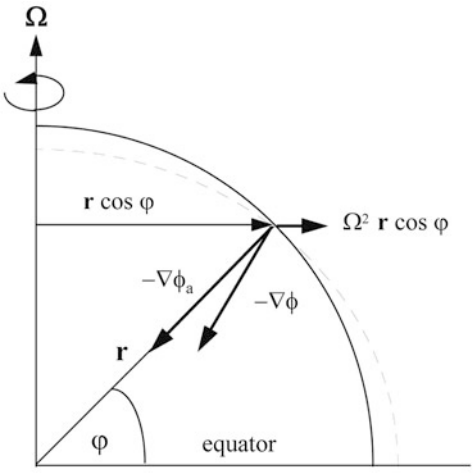

Fig. 6.14 Difference between the acceleration of gravity and that of gravitation

The acceleration of gravity is then given by $\mathbf{g} = \nabla\phi$. The difference between gravity, $\nabla\phi$, and gravitation, $\nabla\phi_a$, schematically illustrated in Fig. 6.14, is relatively small. Nevertheless, this difference has produced an equator-ward displacement of mass, which has resulted in a slight flattening of the Earth at the poles and a slight bulge at the equator. Hence, the Earth is an oblate spheroid rather than a sphere. However, in most meteorological problems, the Earth may be considered as a perfect sphere of radius $r_E = 6{,}371.04\,\text{km}$ with no significant loss of accuracy. As the field of meteorology comprises the lowest layer of the atmosphere of a thickness, Δ, of about 10–15 km (i.e. the troposphere), the approximation $r = r_E + \Delta r = r_E\,(1 + \Delta r/r_E) \cong r_E$ is acceptable because $\Delta r/r_E \cong 0.002 \ll 1$.

Combining Eqs. (6.31), (6.36), and (6.42) yields

$$\rho \frac{d_R \mathbf{v}}{dt} + \nabla \cdot (p\,\mathbf{E} + \mathbf{J}) = -\rho \nabla \phi - 2\rho\, \boldsymbol{\Omega} \times \mathbf{v}. \tag{6.43}$$

This equation is the local balance equation for momentum with respect to the frame of reference uniformly rotating with the Earth. However, we have to show that the friction stress tensor and equation of continuity are not affected by the transformation from the inertial frame to this moving frame of reference. Replacing $\mathbf{v}_A$ in Eq. (6.29) by $\mathbf{v} + \mathbf{v}_L$ leads to

$$\mathbf{J} = \rho\,\nu \left(\nabla (\mathbf{v} + \mathbf{v}_L) + (\nabla (\mathbf{v} + \mathbf{v}_L))^T \right) + \left(\mu_d - \frac{2}{3} \rho\,\nu \right) (\nabla \cdot (\mathbf{v} + \mathbf{v}_L))\, \mathbf{E} \tag{6.44}$$

Considering the identities

$$\nabla \mathbf{v}_L = \nabla (\boldsymbol{\Omega} \times \mathbf{r}) = \underbrace{(\nabla \boldsymbol{\Omega})}_{=0} \times \mathbf{r} - \underbrace{(\nabla \mathbf{r})}_{=\mathbf{E}} \times \boldsymbol{\Omega} = -\mathbf{E} \times \boldsymbol{\Omega} \tag{6.45}$$

$$(\nabla \mathbf{v}_L)^T = (\nabla (\boldsymbol{\Omega} \times \mathbf{r}))^T = -((\nabla \mathbf{r}) \times \boldsymbol{\Omega})^T = \mathbf{E} \times \boldsymbol{\Omega} \tag{6.46}$$

and

$$\nabla \cdot \mathbf{v}_L = \nabla \cdot (\boldsymbol{\Omega} \times \mathbf{r}) = -\nabla \cdot (\mathbf{r} \times \boldsymbol{\Omega}) = -\underbrace{(\nabla \times \mathbf{r})}_{=0} \cdot \boldsymbol{\Omega} = 0 \tag{6.47}$$

leads to the friction stress tensor with respect to the moving frame of reference

$$\mathbf{J} = \rho\,\nu \left(\nabla \mathbf{v} + (\nabla \mathbf{v})^T \right) + \left(\mu_d - \frac{2}{3} \rho\,\nu \right) (\nabla \cdot \mathbf{v})\, \mathbf{E} \tag{6.48}$$

This result that $\mathbf{J}$ is not affected by the leading velocity, of course, is not surprising because motion due to pure elongation (or compression) and pure rotation as represented by the leading velocity do not contribute to the deformation of a volume element.

In the inertial frame, the equation of continuity (Eq. (6.30)) reads

$$\frac{\partial_A \rho}{\partial t} + \nabla \cdot (\rho\, \mathbf{v}_A) = \frac{\partial_A \rho}{\partial t} + \mathbf{v}_A \cdot \nabla \rho + \rho \nabla \cdot \mathbf{v}_A = \frac{d_A \rho}{dt} + \rho \nabla \cdot \mathbf{v}_A = 0. \tag{6.49}$$

For the moving frame of reference we obtain

$$\frac{\partial_R \rho}{\partial t} + \nabla \cdot (\rho\, \mathbf{v}_R) = \frac{\partial_R \rho}{\partial t} + \mathbf{v}_R \cdot \nabla \rho + \rho \nabla \cdot \mathbf{v}_R = \frac{d_R \rho}{dt} + \rho \nabla \cdot \mathbf{v}_A \tag{6.50}$$

because $\nabla \cdot \mathbf{v}_L = 0$. We have learnt that in the case of an arbitrary vector $\mathbf{A}$ the operator

$$\frac{d_A \mathbf{A}}{dt} = \left(\frac{d_R}{dt} + \boldsymbol{\Omega} \times \right) \mathbf{A} = \frac{d_R \mathbf{A}}{dt} + \boldsymbol{\Omega} \times \mathbf{A} \tag{6.51}$$

can be used. This operator cannot be applied to a scalar field quantity, $\Phi(\mathbf{r})$, because a vector product between a vector and a scalar is not defined. Thus, the individual temporal change of $\Phi(\mathbf{r})$ cannot be affected by the fixed rotation of the frame of reference as considered here, i.e.

$$\frac{d_A \Phi\,(\mathbf{r})}{dt} = \frac{d_R \Phi\,(\mathbf{r})}{dt}. \tag{6.52}$$

Introducing this identity into Eq. (6.50) yields finally

$$\frac{\partial_R \rho}{\partial t} + \nabla \cdot (\rho\, \mathbf{v}_R) = \frac{\partial_R \rho}{\partial t} + \mathbf{v}_R \cdot \nabla \rho + \rho\, \nabla \cdot \mathbf{v}_R = \frac{d_A \rho}{dt} + \rho\, \nabla \cdot \mathbf{v}_A = 0 \tag{6.53}$$

i.e. the equation of continuity is invariant when it is transferred from the inertial frame to the reference frame uniformly rotating with the Earth.

By using Newton's second law we can summarize all forces acting at the moving air parcel and obtain the Navier-Stokes equation formulated with respect to the reference frame uniformly rotating with the Earth (Eq. (6.43))

$$\frac{\partial\,(\rho\, \mathbf{v})}{\partial t} + \nabla \cdot (\rho\, \mathbf{v}\, \mathbf{v} + \mathbf{J}) = -\nabla p - \rho\, \mathbf{g} - 2\, \rho\, (\boldsymbol{\Omega} \times \mathbf{v}) \tag{6.54}$$

where the equation of continuity, the acceleration of gravity, $\mathbf{g} = \nabla \phi$, and the identity $\nabla \cdot (p\, \mathbf{E}) = \nabla p$ have been used. Here, we have dropped the subscript R because a distinction between the inertial frame (subscript A) and the moving frame of reference (subscript R) is not further necessary. We can also write the Navier-Stokes equation as

$$\frac{d\, \mathbf{v}}{dt} = \frac{\partial \mathbf{v}}{\partial t} + (\mathbf{v} \cdot \nabla)\mathbf{v} = -\frac{1}{\rho} \nabla p + \frac{1}{\rho} \nabla \cdot \mathbf{J} - \mathbf{g} - 2\, \boldsymbol{\Omega} \times \mathbf{v}. \tag{6.55}$$

For an incompressible fluid, the term $\nabla \cdot \mathbf{J}$ can be expressed by $\nabla \cdot \mathbf{J} = \mu\, \nabla^2 \mathbf{v}$, where $\mu = \rho\, \nu$ is the dynamic viscosity.

On a coordinate system fixed with respect to the Earth, the acceleration or motion of an air parcel of unit mass of 1 kg is the sum of the forces acting onto this parcel[14]

[14] In meteorology, the basic equations are written commonly without explicitly writing the mass. The density of air is close to 1 kg m^{-3} in the lower atmosphere. Using a unit volume of 1 m^3 leads to the unit mass of air being approximately 1 kg.

by assuming a unit mass of 1 kg. In the following, we use this notation, if not mentioned otherwise.

Atmospheric pressure not only varies in the vertical direction, but also in the horizontal direction. Contour lines of equal atmospheric pressure are isobars (Chap. 2). The space between two isobars indicates the change in pressure with distance expressed by the **pressure gradient**. Since any system strives to achieve equilibrium, pressure differences result in an acceleration to overcome the imbalance. This pressure gradient force is directed from high to low pressure and causes wind to blow from high to low pressure. As the pressure gradient steepens, the acceleration and wind strengthens.

Example. At Fairbanks and Anchorage, which are 423 km apart, sea-level pressure is 1,000 and 1,003 hPa, respectively. Estimate the pressure gradient force for an air density of 1.29 kg m^{-3}.

Solution. Putting the y-axis along the distance between the two cities allows writing the pressure gradient force as $F_{pressure} = -\frac{m}{\rho}\frac{\partial p}{\partial y} = \frac{1}{1.29}\frac{300}{423{,}000}$ kg m s^{-2} $\approx 5.49 \cdot 10^{-4}$ kg m s^{-2}.

The frictional drag at the Earth's surface reduces wind speed. Friction depends on the roughness of the surface and viscosity of the fluid. The air above experiences drag, as it is in contact with the slower moving air below. Thus, this layer also slows down affecting levels aloft until the effect becomes negligible at about 1–2 km height. For turbulent friction, the dynamic viscosity can be interpreted as an exchange coefficient. The idea is that in a fluid, internal friction results from exchange of momentum perpendicular to the direction of motion. The tangential pressure (momentum flux) is the momentum transport perpendicular to the direction of motion. Turbulent eddy viscosity can reduce the wind speed by 25 % and more. Friction causes a net inflow (convergence) around a cyclone and a net outflow (divergence) around an anticyclone. In the upper atmosphere, friction can become notable due to the low density; however, at synoptic scale, the vertical scale is much larger than several centimeters. Thus, it is justifiable to neglect molecular friction.

Example. Assume wind speed increases from zero at the surface to 15 and 25 ms^{-1} at 1 and 2 km height, respectively. Determine the friction force for a unit mass of air and density and a viscosity of 10^{-5} kg m^{-1} s^{-1}. Compare your results with typical values of Coriolis force at mid-latitudes ($\approx 10^{-3}$ kg m s^{-2}). What does this mean for friction above the ground? Are your conclusion

(continued)

(continued)

the same when the wind at 1 and 2 cm above ground is 1.5 and 2.5 ms^{-1}, respectively?

Solution. With $\mathbf{F}_{fric} = m\,\frac{\mu}{\rho}\nabla^2\mathbf{v}$ we obtain $\frac{\partial^2 u}{\partial z^2} \approx (\frac{(25-15)\,\mathrm{m\,s^{-1}}}{1{,}000\,\mathrm{m}})^2 - (\frac{(15-0)\,\mathrm{m\,s^{-1}}}{1{,}000\,\mathrm{m}})^2 = -1.25 \cdot 10^{-4}\,\mathrm{m^{-1}\,s^{-1}}$. For unit mass and density $\mathbf{F}_{fric} \approx 1\,\mathrm{kg}|\frac{10^{-5}\,\mathrm{kg\,m^{-1}s^{-1}}}{1\,\mathrm{kg\,m^{-3}}}|(-1.25 \cdot 10^{-4}\,\mathrm{m^{-1}\,s^{-1}}) = -1.25 \cdot 10^{-9}\,\mathrm{kg\,m\,s^{-2}}$. The friction force is six orders of magnitude smaller than the typical Coriolis force at mid-latitudes. Analogously for the low wind speed we obtain $\frac{\partial^2 u}{\partial z^2} \approx 12{,}500\,\mathrm{m^1\,s^{-1}}$ and $\mathbf{F}_{fric} \approx -0.125\,\mathrm{kg\,m\,s^{-2}}$ which is about a factor two larger than the Coriolis force. Thus, molecular friction is important close to the ground.

6.3.1 Euler Equation

A frictionless fluid ($\mathbf{F}_{friction} = \nabla \cdot \mathbf{J} = 0$) is said to be an **ideal fluid**. In case of an ideal fluid, Eq. (6.55) reduces to **Euler's equation of motion**. This non-linear differential equation is a slightly simplified version of the budget equation of **specific momentum** and fundamental for dynamic meteorology.[15] It also allows determining the local change of the wind velocity with respect to time, $\partial\mathbf{v}/\partial t$. Because of the non-linear term $(\mathbf{v} \cdot \nabla)\mathbf{v}$ we can only solve this equation elementarily (i.e. exact) in some special cases.[16] The non-linearity leads to appreciably mathematical and numerical difficulties in dynamic meteorology, NWP and climate modeling.

6.3.2 Vorticity Equation

With the aid of Lamb's transformation

$$(\mathbf{v} \cdot \nabla)\,\mathbf{v} = \nabla\left(\frac{\mathbf{v}^2}{2}\right) - \mathbf{v} \times (\nabla \times \mathbf{v}) \tag{6.56}$$

[15] General circulation models (GCMs) and NWP models usually base on the Euler equation and re-introduce the friction at the atmosphere-surface interface and in the atmospheric boundary layer indirectly by parameterizations.

[16] Examples of analytical solutions can be found in textbooks on atmospheric dynamics or numerical modeling. These solutions are used to test numerical models during their development phase.

we can write the Navier-Stokes equation (6.55) as

$$\frac{\partial \mathbf{v}}{\partial t} + \nabla\left(\frac{\mathbf{v}^2}{2}\right) - \mathbf{v} \times (\nabla \times \mathbf{v} + 2\,\boldsymbol{\Omega}) = -\frac{1}{\rho}\nabla \cdot \mathbf{J} - \frac{1}{\rho}\nabla p - \mathbf{g}. \tag{6.57}$$

The curl of this equation leads to the prognostic equation for the vorticity

$$\left.\begin{aligned} &\frac{\partial}{\partial t}\,(\nabla \times \mathbf{v}) + \nabla \times \nabla\left(\frac{\mathbf{v}^2}{2}\right) - \nabla \times (\mathbf{v} \times (\nabla \times \mathbf{v} + 2\,\boldsymbol{\Omega})) \\ &\quad = -\nabla \times \left(\frac{1}{\rho}\nabla \cdot \mathbf{J}\right) - \nabla \times \left(\frac{1}{\rho}\nabla p\right) - \nabla \times \nabla\phi \end{aligned}\right\} \tag{6.58}$$

where $\mathbf{g} = \nabla\phi$ was used. As the curl of a gradient of a scalar field is zero, we obtain

$$\frac{\partial}{\partial t}\,(\nabla \times \mathbf{v}) + \nabla \times ((\nabla \times \mathbf{v} + 2\,\boldsymbol{\Omega}) \times \mathbf{v}) = -\nabla \times \left(\frac{1}{\rho}\nabla \cdot \mathbf{J}\right) - \nabla \times \left(\frac{1}{\rho}\nabla p\right). \tag{6.59}$$

This prognostic equation for the vorticity serves to describe rotational flows.

Since $\boldsymbol{\Omega}$ is spatially constant, the curl of the absolute velocity, $\mathbf{v}_A = \mathbf{v} + \boldsymbol{\Omega} \times \mathbf{r}$, reads $\nabla \times \mathbf{v}_A = \nabla \times \mathbf{v} + 2\,\boldsymbol{\Omega}$. In typical meteorological applications, we assume that $\partial\boldsymbol{\Omega}/\partial t = 0$. Thus, Eq. (6.59) reads

$$\frac{\partial \mathbf{W}_A}{\partial t} + \nabla \times (\mathbf{W}_A \times \mathbf{v}) = -\nabla \times \left(\frac{1}{\rho}\nabla \cdot \mathbf{J}\right) - \nabla \times \left(\frac{1}{\rho}\nabla p\right) \tag{6.60}$$

where $\mathbf{W}_A = \nabla \times \mathbf{v}_A$. By considering the identity

$$\nabla \times (\mathbf{W}_A \times \mathbf{v}) = (\mathbf{v} \cdot \nabla)\ \mathbf{W}_A - (\mathbf{W}_A \cdot \nabla)\ \mathbf{v} + (\nabla \cdot \mathbf{v})\ \mathbf{W}_A$$

and that the second term of the r.h.s. of Eq. (6.60) can be expressed as

$$\nabla \times \left(\frac{1}{\rho}\nabla p\right) = -\frac{1}{\rho^2}\nabla\rho \times \nabla p \tag{6.61}$$

we obtain for a frictionless flow (i.e. $\nabla \cdot \mathbf{J} = 0$)

$$\frac{\partial \mathbf{W}_A}{\partial t} + (\mathbf{v} \cdot \nabla)\ \mathbf{W}_A - (\mathbf{W}_A \cdot \nabla)\ \mathbf{v} + (\nabla \cdot \mathbf{v})\ \mathbf{W}_A = \frac{1}{\rho^2}\nabla\rho \times \nabla p \tag{6.62}$$

Typically, we are only interested in the horizontal pattern of the flow field. Therefore, this equation for a frictionless flow is scalarly multiplied by the unit vector $\mathbf{k}$ of the z-direction. In doing so, we obtain

$$\left.\begin{aligned} &\frac{\partial}{\partial t}\,(\mathbf{k} \cdot \mathbf{W}_A) + (\mathbf{v} \cdot \nabla)\ (\mathbf{k} \cdot \mathbf{W}_A) - (\mathbf{W}_A \cdot \nabla)\ \mathbf{k} \cdot \mathbf{v} \\ &\quad + (\nabla \cdot \mathbf{v})\ \mathbf{k} \cdot \mathbf{W}_A = \tfrac{1}{\rho^2}\,\mathbf{k} \cdot (\nabla\rho \times \nabla p) \end{aligned}\right\}. \tag{6.63}$$

Considering that $w = \mathbf{k} \cdot \mathbf{v}$, $\mathbf{k} \cdot \boldsymbol{\Omega} = \Omega \sin\varphi$, $f = 2\,\Omega \sin\varphi$ and $f^* = 2\,\Omega \cos\varphi$ and remembering that the relative vorticity, ξ, and the absolute vorticity, ξ_A, are defined by

$$\xi = \mathbf{k} \cdot \nabla \times \mathbf{v} = \frac{\partial v}{\partial x} - \frac{\partial u}{\partial y} \tag{6.64}$$

and

$$\xi_A = \mathbf{k} \cdot \mathbf{W}_A = \xi + f \tag{6.65}$$

yield

$$\frac{\partial \xi_A}{\partial t} + (\mathbf{v} \cdot \nabla)\ \xi_A - (\mathbf{W}_A \cdot \nabla)\ w + \xi_A\ (\nabla \cdot \mathbf{v}) = \frac{1}{\rho^2}\ \mathbf{k} \cdot (\nabla\rho \times \nabla p) \tag{6.66}$$

Because of

$$(\mathbf{W}_A \cdot \nabla)\ w = -\mathbf{k} \cdot \left(\nabla_H w \times \frac{\partial \mathbf{v}_H}{\partial z}\right) + \xi_A \frac{\partial w}{\partial z} + f^* \frac{\partial w}{\partial y} \tag{6.67}$$

we obtain

$$\left.\begin{array}{l} \frac{\partial \xi_A}{\partial t} + (\mathbf{v} \cdot \nabla)\ \xi_A + \mathbf{k} \cdot \left(\nabla_H w \times \frac{\partial \mathbf{v}_H}{\partial z}\right) + \xi_A\,(\nabla_H \cdot \mathbf{v}_H) - f^* \frac{\partial w}{\partial y} \\ = \frac{1}{\rho^2}\,\mathbf{k} \cdot (\nabla\rho \times \nabla p) \end{array}\right\} \tag{6.68}$$

The term $f^* \partial w/\partial y$ is often negligible in comparison with the other terms. In these premises, we finally obtain

$$\left.\begin{array}{l} \frac{\partial \xi_A}{\partial t} + (\mathbf{v}_H \cdot \nabla_H)\,\xi_A + w\,\frac{\partial \xi_A}{\partial z} + \xi_A\,(\nabla_H \cdot \mathbf{v}_H) \\ + \mathbf{k} \cdot \left(\nabla_H w \times \frac{\partial \mathbf{v}_H}{\partial z}\right) = \frac{1}{\rho^2}\,\mathbf{k} \cdot (\nabla_H \rho \times \nabla_H p) \end{array}\right\} \tag{6.69}$$

where $\mathbf{k} \cdot (\nabla\rho \times \nabla p) = \mathbf{k} \cdot (\nabla_H \rho \times \nabla_H p)$ was used. This equation is the prognostic equation for absolute vorticity. The first term on its l.h.s. is the local rate of change of absolute vorticity. The next two terms describe the horizontal and vertical advection[17] of absolute vorticity. The fourth term is the divergence term. Here, we have to distinguish between two cases: First, when $\nabla_H \cdot \mathbf{v}_H > 0$ (i.e. divergence), vorticity decreases, when $\xi_A > 0$, but vorticity increases when $\xi_A < 0$. Second, when $\nabla_H \cdot \mathbf{v}_H < 0$ (i.e. convergence), vorticity increases when $\xi_A > 0$, but vorticity decreases when $\xi_A < 0$. The fifth term is the **twisting term** or **tilting term**. As illustrated in Fig. 6.15, vorticity generates shear eddies. The term of the r.h.s. of this equation represents baroclinicity, also known as baroclinity. It is called the

[17] Advection is the horizontal movement of air.

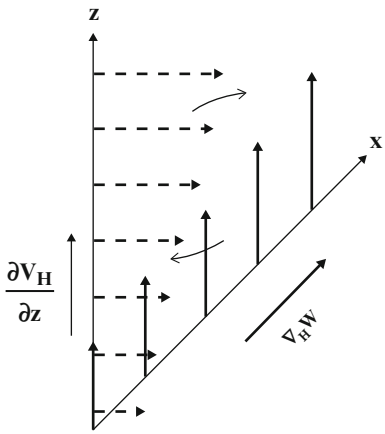

Fig. 6.15 Sketch of the twisting term

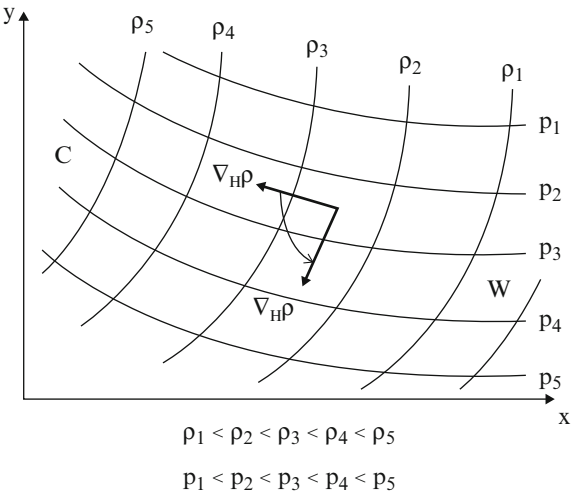

Fig. 6.16 Sketch of the solenoid term

solenoidal term. The effect of this solenoidal term is illustrated in Fig. 6.16. It can be considered as a source of vorticity. Of course, under barotropic conditions, $\rho = \rho(p)$, the solenoid term vanishes.

6.4 Simplifications of the Equation of Motion

In atmospheric numerical modeling or synoptic meteorology, we apply scale analysis to Eq. (6.55) to obtain valuable approximations for easy applications (Table 6.1).

Table 6.1 Types of horizontal winds in the atmosphere classified according to their important forces. The cyclostrophic and geostrophic wind balance models are special cases of the gradient wind model where one of the three forces in the three-way balance becomes negligibly small as compared to the other two

	$\mathbf{F}_{pressure}$	$\mathbf{F}_{coriolis}$	$\mathbf{F}_{friction}$	$\mathbf{F}_{gravity}$	$\mathbf{F}_{centrifugal}$
Geostrophic wind	$\neq 0$	$\neq 0$	0	0	0
Gradient wind	$\neq 0$	$\neq 0$	0	0	$\neq 0$
Cyclostrophic wind	$\neq 0$	0	0	$\neq 0$	$\neq 0$
Wind with friction	$\neq 0$	$\neq 0$	$\neq 0$	0	
Antitriptic wind	$\neq 0$	0	$\neq 0$	0	0

6.4.1 Hydrostatic Approximation

Typical spatial and temporal scales of an extratropical cyclone (synoptic scale) are about 1,000 and 10 km in horizontal, L, and vertical extension, H, and about 3 days, T (Fig. 6.1). Vertical motions, W are of the order of centimeters per second, while horizontal motions, U, V, are in the order of $10\,\mathrm{m\,s^{-1}}$. Estimating the contributions of the various terms for a cyclone to the vertical component of the equation of motion

$$\frac{\partial w}{\partial t} + u\frac{\partial w}{\partial x} + v\frac{\partial w}{\partial y} + w\frac{\partial w}{\partial z} + g + \frac{1}{\rho}\frac{\partial p}{\partial z} = 0$$

yields

$$\frac{\partial w}{\partial t} \approx \frac{W}{T} \approx \frac{10^{-2}\,\mathrm{m\,s^{-1}}}{10^{5}\,\mathrm{s}} \approx 10^{-7}\,\mathrm{m\,s^{-2}}$$

$$u\frac{\partial w}{\partial x} + v\frac{\partial w}{\partial y} \approx \frac{UW}{L} \approx \frac{10^{-1}\,\mathrm{m^2 s^{-2}}}{10^{6}\,\mathrm{m}} \approx 10^{-7}\,\mathrm{m\,s^{-2}}$$

$$w\frac{\partial w}{\partial z} \approx \frac{W^2}{H} \approx \frac{10^{-4}\,\mathrm{m^2\,s^{-2}}}{10^{4}\,\mathrm{m}} \approx 10^{-8}\mathrm{m\,s^{-2}}$$

This means that

$$\frac{dw}{dt} = \frac{\partial w}{\partial t} + u\frac{\partial w}{\partial x} + v\frac{\partial w}{\partial y} + w\frac{\partial w}{\partial z} \approx 10^{-7}\mathrm{m\,s^{-2}}$$

which is much smaller than the term due to the acceleration of gravity ($g \approx 10\,\mathrm{m\,s^{-2}}$). Consequently, in the vertical component of the Navier-Stokes equation, $\frac{1}{\rho}\frac{\partial p}{\partial z}$ is the remaining term that can possibly balance the acceleration of gravity. The resulting equation is the hydrostatic equation (2.7),

$$\frac{\partial p}{\partial z} = -\rho\, g \tag{6.70}$$

introduced in Chap. 2, where $g = |\mathbf{g}|$. Thus, on the synoptic scale we can assume a **hydrostatic balance** and replace the prognostic equation for the vertical motion, w by a diagnostic equation. Atmospheric models that are based on this assumption are called **hydrostatic models**.

6.4.2 Geostrophic Wind Approximation

Let us now estimate the order of magnitude with which the various terms of the horizontal components of the Euler equation

$$\frac{\partial u}{\partial t} + u\frac{\partial u}{\partial x} + v\frac{\partial u}{\partial y} + w\frac{\partial u}{\partial z} - f v + \frac{1}{\rho}\frac{\partial p}{\partial x} = 0$$

and

$$\frac{\partial v}{\partial t} + u\frac{\partial v}{\partial x} + v\frac{\partial v}{\partial y} + w\frac{\partial v}{\partial z} + f u + \frac{1}{\rho}\frac{\partial p}{\partial y} = 0$$

contribute to a synoptic scale system (e.g. an extra-tropical cyclone). We obtain

$$\frac{\partial u}{\partial t} \approx \frac{U}{T} \approx \frac{10^1\,\mathrm{m\,s^{-1}}}{10^5\,\mathrm{s}} \approx 10^{-4}\,\mathrm{m\,s^{-2}}$$

$$u\frac{\partial u}{\partial x} + v\frac{\partial u}{\partial y} \approx \frac{U^2}{L} \approx \frac{10^2\,\mathrm{m^2\,s^{-2}}}{10^6\,\mathrm{m}} \approx 10^{-4}\,\mathrm{m\,s^{-2}}$$

$$w\frac{\partial u}{\partial z} \approx \frac{U\,W}{L} \approx \frac{10^{-1}\,\mathrm{m^2\,s^{-2}}}{10^4\,\mathrm{m}} \approx 10^{-5}\,\mathrm{m\,s^{-2}}$$

Herein, U, V, W, T, and L are the horizontal and vertical wind components, the time, and length, respectively. Analogously, we can estimate the y-component that are of the same order of magnitude

$$\frac{d u}{d t} \approx \frac{d v}{d t} \approx 10^{-4}\,\mathrm{ms^{-2}}$$

We can further estimate for $f\,v = 2\,\Omega\,v\,\sin\varphi$ and $-f\,u = 2\,\Omega\,u\sin\varphi$

$$f V \approx f U \approx 10^{-4}\,\mathrm{s^{-1}} 10\,\mathrm{ms^{-1}} \approx 10^{-3}\,\mathrm{ms^{-2}}$$

The result of this scale analysis indicates that the Coriolis-acceleration term contributes the most to the horizontal components of the equation of motion. It is balanced by the pressure-gradient term expressed by (Fig. 6.17)

$$\nabla_H p = -\rho\, f\, \mathbf{k} \times \mathbf{v}_H \tag{6.71}$$

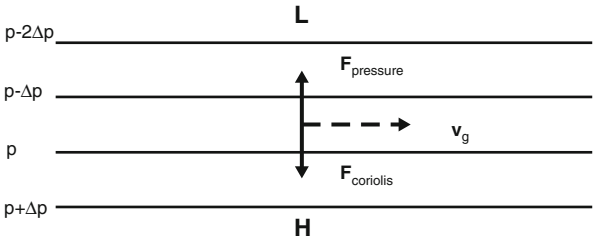

Fig. 6.17 Schematic view of the geostrophic wind vector $\mathbf{v}_g$ (*dashed*) that corresponds to the balance of the pressure gradient force $\mathbf{F}_{pressure}$ and the Coriolis force $\mathbf{F}_{coriolis}$. The letters L and H denote low and high pressure and the contour lines symbolize isobars

or in Cartesian coordinates by

$$f\,v = \frac{1}{\rho}\frac{\partial p}{\partial x} \qquad\qquad -\,f\,u = \frac{1}{\rho}\frac{\partial p}{\partial y} \tag{6.72}$$

This result is the **geostrophic approximation**. Vectorial multiplication of Eq. (6.71) with $\mathbf{k}$ yields

$$\mathbf{k} \times \nabla_H\, p = -\,\rho f\, \mathbf{k} \times (\mathbf{k} \times \mathbf{v}_H) = \rho f\, \mathbf{v}_H \tag{6.73}$$

or

$$\mathbf{v}_g = \frac{1}{\rho\, f}\, \mathbf{k} \times \nabla_H\, p \tag{6.74}$$

This equation defines the **geostrophic wind vector** $\mathbf{v}_g = (u_g, v_g, 0)$. The subscript H is, therefore, replaced by the subscript g. The subscript H in this equation can be omitted because $\mathbf{k} \times \mathbf{k}\,(\partial p/\partial z) = 0$. Since the geostrophic wind vector is perpendicular to the pressure gradient, i.e. the principle normal, $\mathbf{n}$, and the pressure gradient force are collinear, there is no tangential acceleration. Furthermore, the centripetal acceleration is equal to zero. Hence, as illustrated in Fig. 6.17, the geostrophic wind must flow along straight isobars (i.e. the curvature is equal to zero) on a horizontal plane (i.e. $z = const$), where in the Northern Hemisphere the principle normal is directed towards the lower pressure, and in the Southern Hemisphere towards the higher pressure. As the Coriolis parameter depends on the latitude φ, the geostrophic wind would become indeterminable if $\nabla_H\, p \neq 0$ and $\varphi \to 0$ (equator). Generally, Eq. (6.74) should not be applied to tropical regions.

When we consider the geopotential in

$$\Phi = \int_0^z g\; dz' \approx g\, z \tag{6.75}$$

we can express the geostrophic wind vector by

$$\mathbf{v}_g = \frac{1}{f}\,\mathbf{k} \times \nabla_p \Phi \tag{6.76}$$

Obviously, the geostrophic wind must not only flow along straight isobars, but also along straight isohypses, i.e. lines of constant geopotentials, on an isobaric surface. In the Northern Hemisphere, the principle normal is directed towards the lower Φ values, and in the Southern Hemisphere it is directed towards the higher Φ values. Note that the Montgomery potential $M = c_p\,T + \Phi$ can also be used to compute the geostrophic wind vector.

Example. Assume the pressure observed at two cities about 200 km apart from each other at about 63°N differs about 5 hPa. Calculate the geostrophic wind speed for an air density of $1.29\,\mathrm{kg\,m^{-3}}$.

Solution. Rearranging Eq. (6.72) leads to $v = \frac{1}{f\,\rho}\frac{\partial p}{\partial x} = \frac{1}{1.29\,\mathrm{kg\,m^{-3}}\,1.3{\cdot}10^{-4}\,\mathrm{s^{-1}}}\frac{500\,\mathrm{Pa}}{2{\cdot}10^{5}\,\mathrm{m}} \approx 14.91\,\mathrm{m\,s^{-1}}$.

6.4.2.1 The Divergence and the Vorticity of the Geostrophic Wind

The divergence of the geostrophic wind vector reads

$$\nabla \cdot \mathbf{v}_g = \nabla \cdot \left(\frac{1}{\rho\,f}\,\mathbf{k} \times \nabla p\right) = -\mathbf{v}_g \cdot \left(\frac{1}{\rho}\,\nabla\rho + \frac{1}{f}\,\nabla f\right) \tag{6.77}$$

As the Coriolis parameter, $f = 2\,\Omega\,\sin\varphi$, only depends on latitude, Eq. (6.77) reduces to

$$\nabla \cdot \mathbf{v}_g = -\,\mathbf{v}_g \cdot \left(\frac{1}{\rho}\,\nabla\rho + \frac{\beta}{f}\,\mathbf{j}\right) \tag{6.78}$$

where $\beta = \partial f/\partial y$ is the **Rossby parameter**. When we consider air density and the Coriolis parameter f as spatially constant, we obtain $\nabla \cdot \mathbf{v}_g = 0$. Obviously, in such a case, a scalar field $\psi = p/(\rho\,f)$ exists that fulfils the condition $\mathbf{v}_g = \mathbf{k} \times \nabla\psi$ because $\nabla \cdot (\mathbf{k} \times \nabla\psi) = -\,\mathbf{k} \cdot (\nabla \times \nabla\psi) = 0$. This scalar field is the **stream function**. In the case where only the air density is spatially constant, we have

$$\nabla \cdot \mathbf{v}_g = -\,\frac{\beta}{f}\,v_g \tag{6.79}$$

The curl of the geostrophic wind vector reads

$$\nabla \times \mathbf{v}_g = \nabla \times \left(\frac{1}{\rho\, f}\, \mathbf{k} \times \nabla p \right) = \frac{1}{(\rho\ f)^2}\ (\mathbf{k} \times \nabla p) \times (\rho\, \nabla f + f\ \nabla \rho) \quad (6.80)$$

When we consider ρ and f as spatially constant, we obtain $\nabla \times \mathbf{v}_g = 0$. Then, $\mathbf{v}_g$ can be derived from a **velocity potential** χ by $\mathbf{v}_g = \nabla \chi$ so that the condition

$$\mathbf{k} \cdot \left(\nabla \times \mathbf{v}_g \right) = \mathbf{k} \cdot (\nabla \times \nabla \chi) = \frac{\partial^2 \chi}{\partial x\, \partial y} - \frac{\partial^2 \chi}{\partial y\, \partial x} = 0 \quad (6.81)$$

is fulfilled. Therefore, when ρ and f are spatially constant, we can express the geostrophic wind vector by

$$\mathbf{v}_g = \mathbf{k} \times \nabla \psi + \nabla \chi \quad (6.82)$$

or in Cartesian coordinates,

$$u_g = -\frac{\partial \psi}{\partial y} + \frac{\partial \chi}{\partial x} \qquad v_g = \frac{\partial \psi}{\partial x} + \frac{\partial \chi}{\partial y} \quad (6.83)$$

The vorticity of the geostrophic wind also called the **geostrophic vorticity** reads

$$\xi_g = \mathbf{k} \cdot \left(\nabla \times \mathbf{v}_g \right) = \frac{\partial v_g}{\partial x} - \frac{\partial u_g}{\partial y} = \Delta\, \psi \quad (6.84)$$

The divergence of the geostrophic wind reads

$$D_g = \nabla \cdot \mathbf{v}_g = \frac{\partial u_g}{\partial x} + \frac{\partial v_g}{\partial y} = \Delta\, \chi \quad (6.85)$$

Here, $\Delta = \nabla^2$ is, again, the Laplace operator. When only air density is considered as spatially constant, the geostrophic vorticity is

$$\xi_g = \frac{1}{\rho\, f}\, \Delta p + \left(\mathbf{v}_g \right)_\lambda \frac{\beta}{f} \quad (6.86)$$

In this geostrophic wind model, the following synoptic rules apply (Fig. 6.17)

- The pressure gradient force balances the Coriolis force, $F_{pressure} = -F_{coriolis}$.
- Both forces are perpendicular to the streamlines because the wind vector is perpendicular to the pressure gradient force and Coriolis force, i.e. the wind blows parallel to the isobars at each height.
- The geostrophic wind blows with the down-slope side of the isobaric surfaces to their left in the Northern Hemisphere. This is **Buys-Ballot**[18]**'s law** (1857) which

[18]Christophorus Henricus Diedericus Buys Ballot, Dutch chemist and meteorologist, 1817–1890.

says that when you stand with your back to the wind in the Northern Hemisphere the low pressure system is to your left.
- The steeper the slope of the isobaric surface, the stronger the geostrophic wind blows.
- The geostrophic wind is a pure horizontal vector representing a rotating flow that blows in the horizontal plane, i.e. its vertical component is zero.

Example. Revisit the example on the pressure gradient force between Anchorage and Fairbanks, and determine from where the wind blows.

Solution. The wind blows from west.

Example. Show that for a given (constant) Coriolis parameter, f, and a constant air density, ρ, the divergence of the geostrophic wind is zero. Note that these assumptions only apply at very small spatial scales.

Solution. $\nabla \cdot \mathbf{v}_g = \nabla \cdot \left(\frac{1}{\rho f} \mathbf{k} \times \nabla p \right) = - \frac{1}{\rho f} \mathbf{k} \cdot (\nabla \times \nabla p) = 0$

6.4.2.2 The Ageostrophic Wind Component

The velocity vector $\mathbf{v}_g = (u_g, v_g, 0)$ describes the geostrophic flow. When we substitute the pressure gradient in Eq. (6.55) with the aid of the geostrophic wind (Eq. (6.72)) and only consider a horizontal frictionless flow and assume that $f^* u \mathbf{i}$ is negligible, we obtain

$$\frac{d\mathbf{v}_H}{dt} = - f \, \mathbf{k} \times \left(\mathbf{v}_H - \mathbf{v}_g \right) = - f \, \mathbf{k} \times \delta \mathbf{v}_g \tag{6.87}$$

where $\delta \mathbf{v}_g = \mathbf{v}_H - \mathbf{v}_g$ is the **ageostrophic wind component**. The **ageostrophic velocity** is the difference between the real horizontal velocity and the geostrophic velocity, i.e the real wind $\mathbf{v}$ can be expressed as the sum of the geostrophic wind and the ageostrophic wind component, $\mathbf{v}_H = \mathbf{v}_g + \delta \mathbf{v}_g$. To obtain $\delta \mathbf{v}_g$, we have to vectorially multiply the equation by $\mathbf{k}$ and obtain

$$\delta \mathbf{v}_g = \mathbf{v}_H - \mathbf{v}_g = \frac{1}{f} \, \mathbf{k} \times \frac{d\mathbf{v}_H}{dt} \tag{6.88}$$

As illustrated in Fig. 6.18, the ageostrophic wind component is perpendicular to the horizontal acceleration and its magnitude is directly proportional to that of the

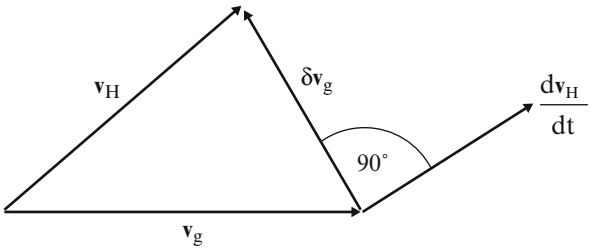

Fig. 6.18 Sketch of the ageostrophic wind component

horizontal acceleration. When $d\mathbf{v}_H/dt$ can be determined with a sufficient degree of accuracy, Eq. (6.88) can serve to calculate $\delta\mathbf{v}_g$. This acceleration, however, is often not well known because it cannot be determined directly from the observation by a meteorological network. Therefore, we are interested in an acceptable approximation for the ageostrophic wind component as described by the **Philipps' series**. The substitution of the horizontal wind vector by the geostrophic wind vector in the derivative with respect to time provides a good approximation called Philipps' 1st approximation given by

$$\mathbf{v}_1 - \mathbf{v}_g = \frac{1}{f}\,\mathbf{k} \times \frac{d\mathbf{v}_g}{dt} \tag{6.89}$$

The comparison of this approximation with Eq. (6.88) provides

$$\delta\mathbf{v}_g \approx \mathbf{v}_1 - \mathbf{v}_g = \frac{1}{f}\,\mathbf{k} \times \frac{d\mathbf{v}_g}{dt} \tag{6.90}$$

This equation usually serves to calculate the ageostrophic wind component with a sufficient degree of accuracy. We obtain a higher degree of accuracy by inserting $\mathbf{v}_H = \mathbf{v}_g + \delta\mathbf{v}_g$ into Eq. (6.88)

$$\delta\mathbf{v}_g = \frac{1}{f}\,\mathbf{k} \times \frac{d}{dt}\left(\mathbf{v}_g + \delta\mathbf{v}_g\right) = \frac{1}{f}\,\mathbf{k} \times \frac{d\mathbf{v}_g}{dt} + \frac{1}{f}\,\mathbf{k} \times \frac{d}{dt}\left(\frac{1}{f}\,\mathbf{k} \times \frac{d\mathbf{v}_H}{dt}\right) \tag{6.91}$$

The next substitution of $\mathbf{v}_H$ by $\mathbf{v}_g + \delta\mathbf{v}_g$ would provide a still better approximation. In deducing still higher derivatives we yield an infinite series given by

$$\delta\mathbf{v}_g = \sum_{n=1}^{\infty} \left\{ (-1)^{n+1}\,\frac{1}{f^{2n-1}}\,\mathbf{k} \times \frac{d^{2n-1}\mathbf{v}_g}{dt^{2n-1}} + (-1)^n\,\frac{1}{f^{2n}}\,\frac{d^{2n}\mathbf{v}_g}{dt^{2n}} \right\} \tag{6.92}$$

that we can use to determine the ageostrophic wind component.

6.4.3 Other Balanced Flows

Let us consider a pure horizontal flow field expressed by

$$\mathbf{v}_H = V\,\mathbf{t} \tag{6.93}$$

where $\mathbf{t}$ is the unit tangent (Sect. 6.1). The horizontal components of the pressure gradient, $\nabla_H p$, and the Coriolis acceleration, $\mathbf{C}_{a,H}$, are given by

$$\nabla_H p = \frac{\partial p}{\partial s}\,\mathbf{t} + \frac{\partial p}{\partial n_t}\,\mathbf{n}_t \tag{6.94}$$

and

$$\mathbf{C}_{a,H} \approx -f\,\mathbf{b}_t \times \mathbf{v}_H = -f\,V\,\mathbf{b}_t \times \mathbf{t} = -f\,V\,\mathbf{n}_t \tag{6.95}$$

respectively. Here, the binormal $\mathbf{b}_t$ is used as the unit vector of the vertical direction. Thus, taking Eqs. (6.10), (6.94), and (6.95) into consideration, the simplified balance equation of momentum for a pure horizontal flow may be written as

$$\left(\frac{d\,\mathbf{v}_H}{dt}\right)_H = \frac{dV}{dt}\,\mathbf{t} + \frac{V^2}{R_t}\,\mathbf{n}_t = -\frac{1}{\rho}\frac{\partial p}{\partial s}\,\mathbf{t} - \frac{1}{\rho}\frac{\partial p}{\partial n_t}\,\mathbf{n}_t - f\,V\,\mathbf{n}_t \tag{6.96}$$

or in coordinates

$$\frac{dV}{dt} = -\frac{1}{\rho}\frac{\partial p}{\partial s} \tag{6.97}$$

and

$$\frac{V^2}{R_t} = -\frac{1}{\rho}\frac{\partial p}{\partial n_t} - f\,V \tag{6.98}$$

Equation (6.98) is called the **gradient wind equation**. It describes the balance of the centrifugal, Coriolis and pressure gradient forces in the direction normal to the flow.

Rearranging Eq. (6.98) leads to

$$V\left(1 + \frac{V}{f\,R_t}\right) = -\frac{1}{\rho\,f}\frac{\partial p}{\partial n_t} \tag{6.99}$$

where the ratio

$$Ro = \frac{V}{|f\,R_t|}$$

defines the non-dimensional **Rossby number** Ro.

As illustrated in Fig. 6.17, Eqs. (6.72) are valid for an infinite extended flow without any curvature in the trajectories. In nature, isobars are curved because troughs and ridges exist (Chap. 2). Thus, the Rossby number may serve to estimate the departure from the geostrophic balance due to the curvature expressed by radius R_t and, to characterize the **quasi-geostrophic approximation**. When $Ro \ll 1$ Eq. (6.99) tends to the geostrophic wind equation (6.74). When $|R_t|$ tends to infinity, the Rossby number, of course, fulfills this condition. For finite values of $|R_t|$, the Coriolis parameter plays the key role for the flow.

A quasi-geostrophic flow may be described by a geostrophic flow. However, this quasi-geostrophic approximation requires that $Ro \ll 1$ and that the timescales are large in comparison with $\frac{1}{f}$ (couple of hours). Thus, except in low latitudes, for large-scale, low frequency applications, we typically use the quasi-geostrophic approximation.

The geostrophic wind approximation generally overestimates the actual wind speed, among other things, because it neglects the centrifugal force and, close to the ground, friction. Friction retards the flow in the ABL and makes the wind **sub-geostrophic**. Consequently, the forces do not balance exactly and air flows across the isobars from the high to the low pressure (i.e. from high to low geopotential height). In an anticyclone, the geostrophic wind approximation always underestimates the actual wind speed and meteorologists speak of **super-geostrophic** wind.

The following subsections present various kinds of balanced flows that can be derived from equation set (6.97) and (6.98) by various further simplifications.

6.4.3.1 Inertial Flow

When the pressure field is horizontally uniform so that $\partial p/\partial s = \partial p/\partial n_t = 0$, equation set (6.97) and (6.98) reduces to

$$\frac{dV}{dt} = 0 \tag{6.100}$$

and

$$\frac{V^2}{R_t} = -f\,V \tag{6.101}$$

According to Eq. (6.100), the magnitude of the velocity vector is a constant with respect to time. Equation (6.101) expresses the balance between the centripetal acceleration and the Coriolis acceleration that characterizes the **inertial flow**. Equations (6.100) and (6.101) provide

$$V = -f\,R_t = const. \tag{6.102}$$

Since the centripetal acceleration is only balanced by the Coriolis acceleration, the inertial flow is necessarily anticyclonic. When the Coriolis parameter only varies slightly, the path of the inertial flow is nearly circular. The period of the oscillation of this kind of inertial flow reads

$$P = -\frac{2\,\pi\,R_t}{V} = \frac{2\,\pi}{f} = \frac{\pi}{\Omega\,\sin\varphi} \tag{6.103}$$

This period is called the one-half pendulum day. For large velocity, the radius of curvature is also large (Eq. (6.102)), so that the inertial motion has relatively great horizontal extent. Since in this case, V is a constant, the radius of curvature has to compensate the variation of the Coriolis parameter. Thus, the magnitude of R_t decreases when the latitude (and, hence, the Coriolis parameter) increases.

6.4.3.2 Cyclostrophic Flow

When no tangential acceleration exists, i.e. $\partial p/\partial s = 0$, and the horizontal scale is small enough, so that the magnitude of Coriolis acceleration is small in comparison with those of the centripetal acceleration and the acceleration due to the pressure gradient, Eqs. (6.97) and (6.98) reduce to

$$\frac{dV}{dt} = 0$$

and

$$\frac{V^2}{R_t} = -\frac{1}{\rho}\frac{\partial p}{\partial n_t}$$

The solution of this equation set is given by

$$V = \pm\sqrt{-\frac{R_t}{\rho}\frac{\partial p}{\partial n_t}} \tag{6.104}$$

This equation describes the cyclostrophic flow. Obviously, $\partial p/\partial n_t$ and R_t must have opposite signs to ensure that

$$-\frac{R_t}{\rho}\frac{\partial p}{\partial n_t} \geq 0$$

Figure 6.19 illustrates the solution. Both cyclonic and anticyclonic flows are possible. Water sprouts and dust devils can show both clockwise and counterclockwise rotation. For tornadoes and funnel clouds (Fig. 6.20), also both rotational directions are possible. However, most tornadoes in the Northern Hemisphere rotate counterclockwise because they develop from rotating supercell thunderstorms that may already be affected by the Coriolis force.

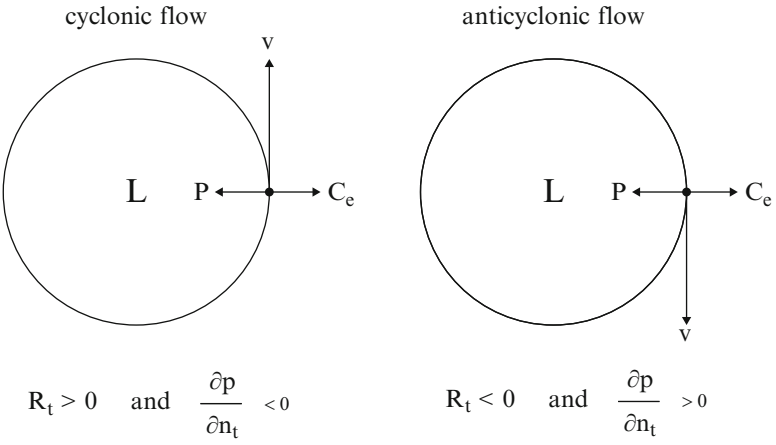

Fig. 6.19 Sketch of a cyclostrophic flow. The quantity **P** designates the pressure gradient force, and $\mathbf{C}_e$ designates the centrifugal force

Fig. 6.20 Funnel cloud over Fairbanks as seen from the University of Alaska Fairbanks campus (Photo taken by Bhatt in 2010, with permission)

The cyclostrophic approximation is reasonable when the Rossby number $Ro = \frac{V}{|f\,R_t|}$ is very large. For instance, for a tornado characterized by $V = 30\,\mathrm{m\,s^{-1}}$, $R_t = 300\,\mathrm{m}$, and $f = 10^{-4}\,\mathrm{s^{-1}}$, the Rossby number is $Ro = 10^3$.

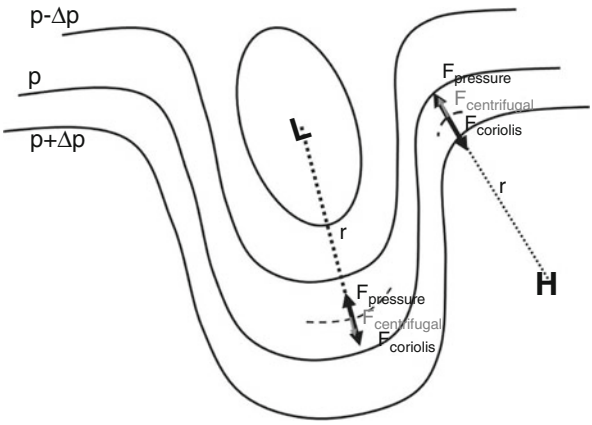

Fig. 6.21 Schematic view of the gradient wind model. The contour lines are isobars. The letters *L* and *H* represent high and low pressure, and *r* is the radius of curvature of the trough or ridge

Example. Calculate the centripetal acceleration in a tornado with a wind speed of $50\,\mathrm{m\,s^{-1}}$ and radius of $R_t = 250\,\mathrm{m}$.

Solution. $C_a = \frac{V^2}{R_t} = \frac{(50\,\mathrm{m\,s^{-1}})^2}{250\,\mathrm{m}} = 10\,\mathrm{m\,s^{-2}}$.

Example. In a tornado of radius $R_t = 300\,\mathrm{m}$, wind speed is $V = 30\,\mathrm{m\,s^{-1}}$. Determine the centrifugal force and the pressure difference between the inside and outside of the funnel for a density of $1\,\mathrm{kg\,m^{-3}}$. Assume unit mass.

Solution. $F_{centrifugal} = m\frac{V^2}{R_t} = 3\,\mathrm{kg\,m\,s^{-2}}$. Rearranging the pressure gradient force $F_{pressure} = -\frac{m}{\rho}\frac{\partial p}{\partial n_t}$ yields for the pressure difference $3\,\mathrm{kg\,m\,s^{-1}}\,300\,\mathrm{m} = 9\,\mathrm{hPa}$.

6.4.4 Gradient Flow

When the centripetal acceleration associated with sharply curved flows (strong troughs, ridges) causes a great departure from the geostrophic approximation, a more exact approximation is the **gradient wind balance** (Table 6.1). It describes the balance between the pressure gradient force, Coriolis force, and centrifugal force (Fig. 6.21) for cyclonically or anticyclonically curved trajectories. The resulting wind is the **gradient wind**. The gradient wind approximation is exact for the

horizontal frictionless flow with circular streamlines around a vortex (e.g. a tropical cyclone in the mid-troposphere).

When no tangential acceleration exists, i.e. $\partial p/\partial s = 0$, equation set (6.97) and (6.98) reduces to

$$\frac{dV}{dt} = 0 \tag{6.105}$$

and

$$\frac{V^2}{R_t} = -\frac{1}{\rho}\frac{\partial p}{\partial n_t} - f\,V \tag{6.106}$$

The solution of this equation set reads

$$V = -\frac{f\,R_t}{2} \pm \sqrt{\left(\frac{f\,R_t}{2}\right)^2 - \frac{R_t}{\rho}\frac{\partial p}{\partial n_t}} \tag{6.107}$$

It is called the gradient wind equation. From a mathematical point of view it is necessary that the condition

$$\left(\frac{f\,R_t}{2}\right)^2 - \frac{R_t}{\rho}\frac{\partial p}{\partial n_t} \geq 0 \tag{6.108}$$

is fulfilled because the solution (6.107) must be real and non-negative because in a natural coordinate frame the wind speed, V, is always positive. If $\partial p/\partial n_t$ and R_t have opposite signs, this condition is generally fulfilled, but the sign of the root has to be chosen with respect to $V \geq 0$. If $\partial p/\partial n_t$ and R_t have the same sign, then the condition

$$\left(\frac{f\,R_t}{2}\right)^2 \geq \frac{R_t}{\rho}\frac{\partial p}{\partial n_t} \tag{6.109}$$

has to be satisfied. When both terms are equal, we have

$$R_t = \frac{4}{f^2\,\rho}\frac{\partial p}{\partial n_t} = -\frac{4}{f}\,V_g \tag{6.110}$$

Based on this relationship between the radius of curvature and the geostrophic wind, we may state that in an anticyclone, the maximum value of the geostrophic wind is $V_g = |f\,R_t|/4$. The force balances for the four permitted solutions are illustrated in Fig. 6.22. In all cases except the anomalous low, the normal pressure gradient force is oppositely directed to the Coriolis force. The anomalous low is antibaric because

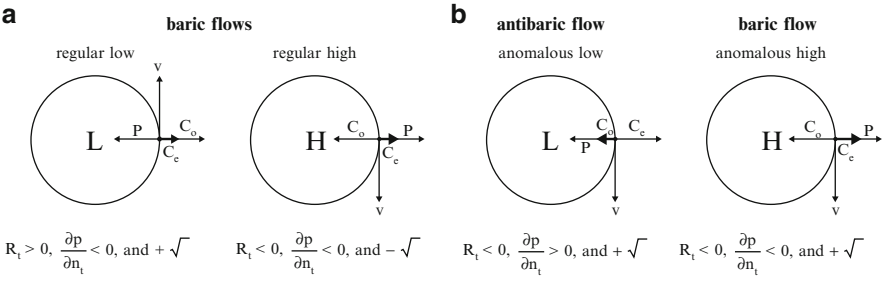

Fig. 6.22 Schematic view of the force balances in the Northern Hemisphere for the four types of gradient flows: regular low, regular high, anomalous low, and anomalous high. **P** is the pressure gradient force, $\mathbf{C}_e$ is the centrifugal force, and $\mathbf{C}_o$ is the Coriolis force. The letters *L* and *H* denote low and high pressure. Contour lines are isobars

the normal pressure gradient force and Coriolis force have the same direction. We can write Eq. (6.98) as

$$\frac{V^2}{R_t} = f\,V_g - f\,V \;= f\,V\left(\frac{V_g}{V} - 1\right) \tag{6.111}$$

Rearranging yields

$$\frac{V_g}{V} = \frac{V}{f\,R_t} + 1 \tag{6.112}$$

For normal cyclonic flow ($f\,R_t > 0$), V_g is larger than V, whereas for anticyclonic flow ($f\,R_t < 0$), V_g is smaller than V. Therefore, the geostrophic wind is an overestimate of the balanced wind in a region of cyclonic curvature and an underestimate in a region of anticyclonic curvature. For mid-latitude synoptic systems, the difference between gradient and geostrophic wind speeds generally does not exceed 10–20 %.

As illustrated in Fig. 6.21, the centrifugal force is directed outward from the center of the trough of radius r and is given by V^2/r. Under cyclonic conditions, the centrifugal force reinforces the Coriolis force so that the forces balance with a velocity smaller than required when the Coriolis force acted alone. A sub-geostrophic flow parallel to the isobars is maintained.

In sharp mid-latitude troughs, the observed wind is often sub-geostrophic by as much as 50 %, despite the streamlines are still parallel to the isobars. Under anticyclonic conditions, the centrifugal force opposes the Coriolis force and requires a super-geostrophic wind velocity to balance the three forces.

When a sharp anticyclonic curvature and strong pressure gradient occur simultaneously, it is impossible to achieve a three-way balance of the forces, i.e. $\mathbf{F}_{pressure} > f\mathbf{v} - \frac{\mathbf{v}^2}{r}$. The combination of a sharp trough and strong pressure gradient is not uncommon, but sharp ridges are rarely observed with tight pressure gradients.

The following synoptic rules can be derived for the gradient wind model

- The steeper the slope of the isobaric surface is, the stronger the geostrophic and gradient winds blow.
- The geostrophic and gradient winds blow with the down-slope side of the isobaric surfaces to their left in the Northern Hemisphere (see Buys-Ballot's law).

6.4.4.1 Tropical Cyclones

Tropical cyclones are an example to apply the gradient wind balance. They appear as a **cut off low** in the tropical easterlies (Chap. 7). At the beginning, there is a tropical perturbation or an area of low pressure. The onset of a tropical storm is defined by closed isobars and strong near-surface winds ($v > 17\,\mathrm{m\,s^{-1}}$). Six parameters are relevant for the genesis of tropical cyclones:

1. **Sea surface temperatures (SST) higher than** 26 °C**, and a sufficiently thick layer of warm surface water**. These quantities correspond to the thermal energy of the ocean, and represent the main energy source of a tropical cyclone (Chap. 2).
2. **Vertical gradient of the equivalent potential temperature**. This gradient is a measure for the convective instability (Chap. 2). The stratification of temperature and humidity must be moderate conditionally unstable. Under these unsaturated, but humid conditions, the environmental lapse rate is lower than the dry adiabatic lapse rate. Thus, an air parcel can ascend to the level of saturation and keeps warmer than the unperturbed surrounding air.
3. **High relative humidity in the mid-troposphere** is required for the storm to persist. A low relative humidity of the environment would inhibit the storm in its development by entrainment or downdrafts (Chap. 3).
4. **Sufficient magnitude of near-surface relative vorticity** which corresponds to a convergence of the near-surface wind field. Tropical cyclones form, when the near-surface vorticity exceeds the mean near-surface vorticity of those latitudes.
5. **Coriolis force**. Tropical cyclones build between 5° and 20° north and south of the equator, respectively.
6. **Vertical shear of the horizontal wind** gives the spin-up relative to the vorticity of the environment.

The first and last three points relate to the thermodynamic and dynamic conditions for the genesis of tropical cyclones. The fact that the atmospheric conditions for the genesis of a tropical cyclone are fulfilled does not mean that a tropical cyclone develops. Perturbations of independent origin trigger the genesis of tropical cyclones. The frequency of the genesis depends on the number of suitable initial perturbations. However, it is still unknown what makes a perturbation suitable or not. Usually the tropical mid-troposphere is relatively dry. When the six conditions above are fulfilled, an additional required and probably sufficient condition for the genesis is the existence of an about 85–150 km horizontally extended area of

very moist air that reaches throughout the entire troposphere. Thunderstorms that develop in such an area do not form dry, cold downdrafts. Dry, cold downdrafts result from partial evaporation of falling hydrometeors due to consumption of heat. These downdrafts would diminish the evaporation of ocean water, and counteract the moistening of the troposphere. In wet air, evaporation is reduced which suppresses the formation of downdrafts that could evolve by evaporative cooling. Moist areas can build:

- By rising of the tropical ABL in a tropical perturbation in the easterly waves,
- Naturally within a tropical cloud cluster,
- Due to SST higher than 26 °C, and
- Due to slight rising in a huge area (atmospheric waves)

The uptake of latent and sensible heat from the ocean is important for the persistence of a tropical cyclone.

Dynamics of Tropical Cyclones

In the atmosphere on the typical scale of a tropical cyclone, buoyancy and Coriolis force act simultaneously. Frictional convergence in the ABL is compensated by vertical motion and divergence at the tropopause. Tropical cyclones have a poleward drift that is independent of the mean winds in the mid-troposphere. In addition to the motion along their tracks, tropical cyclones have two distinct motions, namely the tangential winds around their center called the **primary circulation**, and the radial-vertical motion in the convective towers called the **secondary circulation** (Fig. 6.23). At the side of the cyclone, where the wind vector of the primary circulation and of the system motion point in the same direction, wind speeds are strongest. The vorticity equation describes the change of the radial-vertical circulation required to remain hydrostatic equilibrium. In the mature stage, the secondary circulation balances the gradient-wind and hydrostatic forces of the primary circulation in equilibrium.

Due to the high wind speeds and the relatively small scale, we cannot neglect the centrifugal force as compared to the Coriolis and pressure gradient forces. For a tropical cyclone, the approximation by the gradient wind relationship and conservation of angular momentum, m, apply. A material ring diverging from the center of the cyclone must spin up and get wider to conserve angular momentum for which the eye wall obtains a trumpet-like shape when seen from above. Angular momentum decelerates organized motion in the free atmosphere. The simplified equations for its horizontal motion read

$$\frac{du}{dt} = -\frac{1}{\rho}\frac{\partial p}{\partial r} + fv + \frac{v^2}{r} \tag{6.113}$$

$$\frac{dv}{dt} = -fu - \frac{uv}{r} \tag{6.114}$$

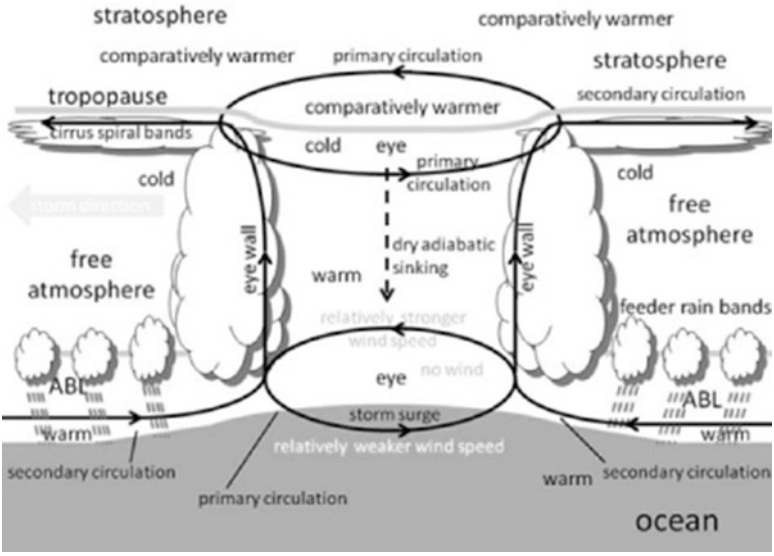

Fig. 6.23 Schematic view of the secondary circulation imposed on the geostrophic motion above the ABL

Here u and v are the radial and tangential components of the horizontal wind vector dr/dt and $rd\varphi/dt$. Furthermore, r is the radial coordinate measured from the eye of the storm, and f ($\approx 5 \cdot 10^{-5}$) is the Coriolis parameter. The centrifugal term, v^2/r, and the term, $-uv/r$, are the apparent forces due to the use of cylinder coordinates.

The angular momentum around the vertical axis of the storm is given by

$$m = rv + \frac{fr^2}{2} \tag{6.115}$$

Due to $du/dt = 0$ and the gradient wind balance[19]

$$0 = -\frac{1}{\rho}\frac{\partial p}{\partial r} + \frac{m^2}{r^3} - \frac{f^2 r}{4} \tag{6.116}$$

[19] Rearranging for v and inserting in $\frac{dv}{dt} = -fu - \frac{uv}{r}$ provides

$$\begin{aligned} &-\tfrac{1}{\rho}\tfrac{\partial p}{\partial r} + \tfrac{fm}{r} - \tfrac{f^2 r}{2} + (\tfrac{m^2}{r^2} - \tfrac{2mf}{2} + \tfrac{f^2 r^2}{4})/r \\ &= -\tfrac{1}{\rho}\tfrac{\partial p}{\partial r} + \tfrac{fm}{r} - 2\tfrac{f^2 r}{4} + \tfrac{m^2}{r^3} - \tfrac{mf}{r} + \tfrac{f^2 r}{4} \\ &= -\tfrac{1}{\rho}\tfrac{\partial p}{\partial r} - \tfrac{f^2 r}{4} + \tfrac{m^2}{r^3} \end{aligned}$$

Above the ABL, friction is negligible, i.e. angular momentum[20] is conserved

$$\frac{dm}{dt} = 0 \tag{6.117}$$

The trumpet-shaped eye wall builds for hydrostatic reasons. The radial pressure gradient decreases with height, for which the balancing of the pressure gradient with the centrifugal and Coriolis forces leads to a widening of the eye. We can calculate the degree to which the surfaces of equal mean angular momentum slope from the hydrostatic and gradient wind balance by

$$\frac{\partial r}{\partial p}|_{\mathbf{m}} = -\frac{\partial \mathbf{m}/\partial p}{\partial \mathbf{m}/\partial r} \tag{6.118}$$

i.e. the slope is the ratio of the vertical to horizontal shear of angular momentum. The vertical gradient of angular momentum is related to the horizontal gradient of density by the thermal wind equation (Eqs. (6.124) and (6.125) for components).

The surfaces of the saturated equivalent potential temperature (Chap. 2) on a surface of equal angular momentum do not change with height. The contour lines of angular momentum coincide with the isotherms of equal equivalent potential temperature. The slope of the eye wall suggests that a certain part of the tropospheric column consists of the relatively warmer and less dense air of the eye and contributes to the inward directed surface pressure gradient.

Tropical cyclones owe their existence from the effective interaction between the cumulus scale and the large-scale wind field. The air motions in the clouds are closely related to the dynamics of the tropical cyclone for convection dynamical and hydrostatic reasons. The horizontal and vertical motions characterize the eddy. The vertical equation of motion reduces to the hydrostatic equation (2.7). The mesoscale motions keep in hydrostatic equilibrium, although the individual cumuli are not in hydrostatic equilibrium (Chaps. 2 and 3). Large-scale temperature fluctuations exist.

$$\frac{v^2}{r} + fv = g\frac{\partial z}{\partial r} \tag{6.119}$$

$$\frac{\partial \Phi}{\partial z} = \frac{R_d T}{H} \tag{6.120}$$

$$\frac{\partial v}{\partial z}\left(\frac{2v}{r} + f\right) = \frac{R_d T}{H}\frac{\partial T}{\partial r} \tag{6.121}$$

[20] $\frac{dm}{dt} = r\frac{dv}{dt} + v\frac{dr}{dt} + \frac{f2r}{2}\frac{dr}{dt}$
$= r\frac{dv}{dt} + (v + fr)\frac{dr}{dt}$
$= r(-fu - \frac{uv}{r}) + (v + fr)\frac{dr}{dt}$
$= -fru - uv + uv + fru = 0$

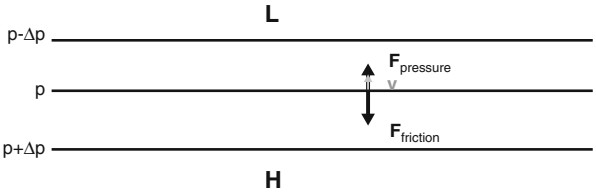

Fig. 6.24 Schematic view of antitriptic wind (dashed vector). The pressure gradient force $F_{pressure}$ and friction force $F_{friction}$ balance. The letters L and H indicate low and high pressure

In the free atmosphere, $\partial v/\partial z < 0$ and $\partial T/\partial r < 0$, for which the temperature is maximal in the center of the storm. In the eye dry adiabatic sinking occurs.

The secondary circulation takes its energy from the water surface and tends to neutral or conditionally unstable conditions (Chap. 2). The convection that sometimes is superimposed to the secondary circulation is seemingly important in the initial stage of the storm, but still subject of research. The wet-adiabatic ascend of air parcels having near-surface properties warms the mid-troposphere in the area of precipitation as compared to the unsaturated environment.

6.4.5 *Antitriptic Wind*

The wind controlled by the pressure gradient force and friction force is the **antitriptic wind**. It blows in direction of the lower pressure, opposite to the direction of the friction (Fig. 6.24). The antitriptic wind approximation is about 15 % accurate. Examples for the application are the near-surface layer, areas close to the equator where the Coriolis effect is negligible, or small-scale systems of time scales much smaller than the Coriolis parameter.

6.4.6 *Thermal Wind*

As shown by scale analysis, on the synoptic scale, virtually all kinetic energy is contained in the horizontal wind components, i.e. vertical accelerations are negligibly small. Most time the pressure gradient force and gravity force balance, and the hydrostatic equation is satisfied not only for the mean atmosphere, but also for large-scale deviations from the mean. Inserting the equation of state (2.3) into the geostrophic wind equation (6.74) yields

$$\mathbf{v}_g = \frac{R\,T}{f}\,\mathbf{k} \times \nabla_H \ln p \tag{6.122}$$

Differentiating this equation with respect to z provides

$$\frac{\partial \mathbf{v}_g}{\partial z} = \frac{R\,T}{f}\,\frac{\partial}{\partial z}\,(\ln\,T)\,\mathbf{k}\times\nabla_H\,(\ln\,p) + \frac{R\,T}{f}\,\mathbf{k}\times\nabla_H\,\left\{-\frac{g}{R\,T}\right\} \tag{6.123}$$

or

$$\frac{\partial \mathbf{v}_g}{\partial z} = \mathbf{v}_g\,\frac{1}{T}\,\frac{\partial T}{\partial z} + \frac{g}{f\,T}\,\mathbf{k}\times\nabla_H\,T \tag{6.124}$$

or expressed in Cartesian coordinates by

$$f\,\frac{\partial u_g}{\partial z} = u_g\,\frac{f}{T}\,\frac{\partial T}{\partial z} - \frac{g}{T}\,\frac{\partial T}{\partial y} \qquad\qquad f\,\frac{\partial v_g}{\partial z} = v_g\,\frac{f}{T}\,\frac{\partial T}{\partial z} + \frac{g}{T}\,\frac{\partial T}{\partial x} \tag{6.125}$$

Equations (6.124) and (6.125) are the **thermal wind shear equations**, commonly called the **thermal wind equations**. In case of an isothermal atmosphere, the derivative $\partial T/\partial z = 0$. Thus, we obtain

$$f\,\frac{\partial u_g}{\partial z} = -\frac{g}{T}\,\frac{\partial T}{\partial y} \qquad\qquad f\,\frac{\partial v_g}{\partial z} = \frac{g}{T}\,\frac{\partial T}{\partial x} \tag{6.126}$$

They relate the horizontal temperature gradients to the vertical gradients of the horizontal wind when both the hydrostatic and geostrophic balances apply.

The change of the geostrophic wind between two heights $z_1 < z_2$ is then given by

$$\Delta\mathbf{v}_g = \mathbf{v}_g\,(z_2) - \mathbf{v}_g\,(z_1) = \int_{z_1}^{z_2} \frac{\partial \mathbf{v}_g}{\partial z}\,dz' \tag{6.127}$$

When we assume that the temperature and the vertical shear of the geostrophic wind vector are constant with height, we obtain

$$\Delta\mathbf{v}_g = \frac{\partial \mathbf{v}_g}{\partial z}\,(z_2 - z_1) = \frac{\partial \mathbf{v}_g}{\partial z}\,\frac{R\,T}{g}\,\ln\frac{p_2}{p_1} \tag{6.128}$$

The **thermal wind** is the rate of change of the geostrophic wind with height. It refers to the vector difference of the geostrophic wind at two different levels. The thermal wind "blows" parallel to the isotherms (perpendicular to the temperature gradient) with the lower thickness to the left (right) on the Northern (Southern) Hemisphere. This means it blows with the cold air on its left (right) side in the Northern (Southern) Hemisphere.

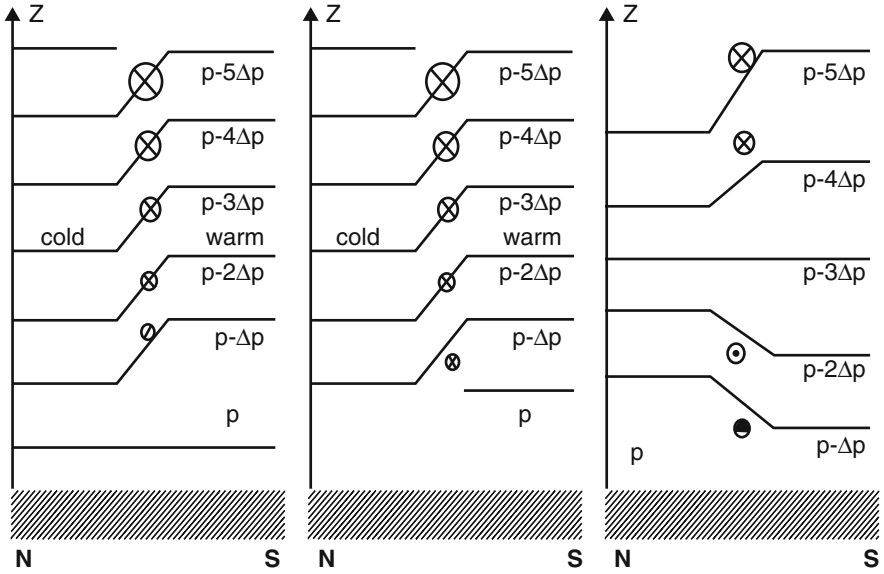

Fig. 6.25 North-south cross-sections showing schematically the pressure decrease with height for various temperature conditions for the Northern Hemisphere. The panels show geopotential height ϕ at different pressure levels in air masses of different temperature decrease with height and their transition zone. In the transition zone between the warm (south) and cold (north) air, the geostrophic wind changes with height. *Circles with crosses and dots* indicate west and east wind, respectively

The thermal wind equation implies that for higher pressure in the warm air pressure at height is greater in the warm air than cold air. Consequently, high reaching highs are always warm and high reaching lows are cold. When pressure levels out at a certain height, pressure is lower below that level in the warm than cold air. Consequently, flat cold highs (e.g. over continents in winter) and flat warm lows (e.g. over continents in summer) exist. The geostrophic wind changes with height in areas with horizontal temperature decrease when the hydrostatic and geostrophic approximation apply.

The thermal wind equation permits us to explain strong wind fields like the jet stream, why the west-wind increases with height and why a jet forms with a maximum wind speed in the tropopause region (Chap. 7). It also explains the westerlies as a flow from the west with warmer air to the south and colder air to the north (Fig. 6.25).

The thermal wind equation links the surface to upper level maps. The thermal wind equation helps in interpreting synoptic maps with respect to **advection** of warm and cold air masses (Fig. 6.26), and to analyze frontal structures.

Warm air advection occurs when the air flowing from the warmer towards the colder region maintains its temperature when moving into the area of colder air (Fig. 6.26). The opposite is true for cold air flowing towards a warm region.

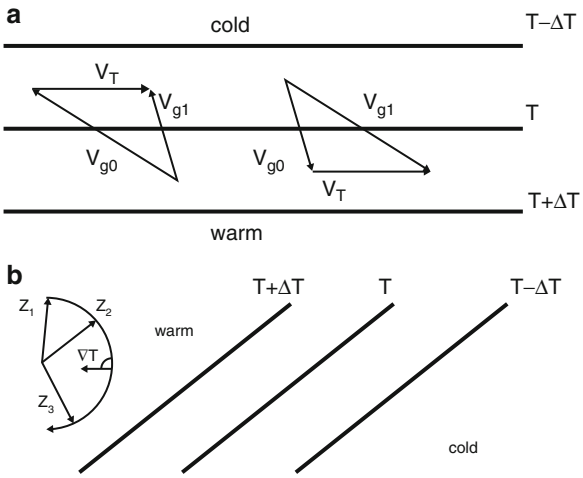

Fig. 6.26 Schematic view of (**a**) thermal wind v_T, geostrophic wind v_g and temperature advection. The subscripts 0 and 1 denote the lower and higher level. (**b**) Hodograph of geostrophic wind at various heights z_n where n increases with height. At all levels, warm air advection occurs. Contours are isotherms

Example. Determine the geostrophic wind at 500 hPa for a mean horizontal temperature gradient of $1\,\mathrm{K}\,10^{-2}$ km in the $850-500$ hPa layer for a Coriolis parameter of $10^{-4}\,\mathrm{s}^{-1}$.

Solution. $v = -\frac{R}{f}\frac{\partial\overline{T}}{\partial y}|_p \ln(\frac{p_0}{p_1}) = -\frac{287\,\mathrm{J\,kg^{-1}}}{10^{-4}\,\mathrm{s^{-1}}}\frac{1\,\mathrm{K}}{100{\cdot}10^3\,\mathrm{m}}\ln(\frac{850}{500}) = 15.23\,\mathrm{m\,s^{-1}}$

Example. In a surface weather map, the geostrophic wind blows from east with $10\,\mathrm{m\,s^{-1}}$ in mid-latitudes. The horizontal south to north temperature gradient amounts 10 K per 1,000 km in the lower troposphere. Determine the vertical wind shear of the geostrophic wind per kilometer and the direction of the thermal wind vector when near-surface air temperature is 15 °C. At what height will the geostrophic wind vanish? What happens aloft?

Solution. In mid-latitudes, the Coriolis parameter is $\approx 10^{-4}\,\mathrm{s}^{-1}$. The thermal wind points from west to east. A south to north temperature gradient means $\frac{\partial T}{\partial y}$. Thus, the geostrophic wind shear with height is $|\frac{\partial \mathbf{v}_g}{\partial z}| = \frac{\mathbf{g}}{fT}|\frac{\partial T}{\partial y}| = \frac{9.81\,\mathrm{m\,s^{-2}}}{10^{-4}\,\mathrm{s^{-1}}\,288.15\,\mathrm{K}}\cdot\frac{10\,\mathrm{K}}{10^6\,\mathrm{m}} = \frac{3.40\,\mathrm{m\,s^{-1}}}{1{,}000\,\mathrm{m}}$. We obtain the level where $\mathbf{v}_g = 0$ by rearranging the above equation to $\Delta z = z_{\mathbf{v}_g=0} - z_{surface}$ where $\mathbf{v}_{g,surface} = 10\,\mathrm{m\,s^{-1}}$. Thus, $z_{\mathbf{v}_g=0} = 10\,\mathrm{m\,s^{-1}}\frac{1{,}000\,\mathrm{m}}{3.40\,\mathrm{m\,s^{-1}}} \approx 2{,}941$ m. Aloft, the geostrophic wind comes from west and increases with height.

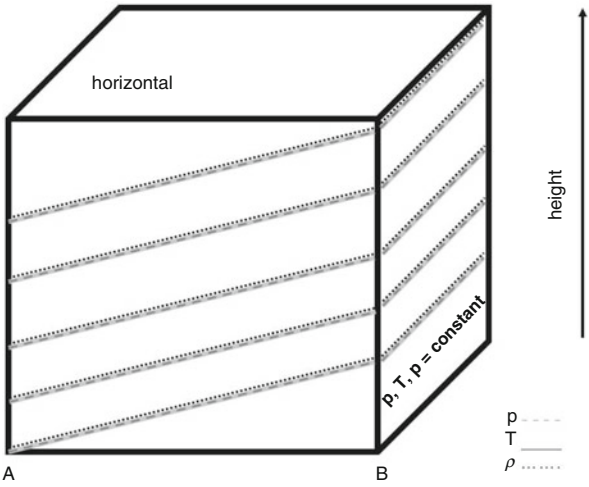

Fig. 6.27 Schematic view of a barotropic atmosphere. Surfaces of constant pressure, p, (*dashed lines*), temperature, T (*solid lines*), and density, ρ (*dotted lines*)

In numerical modeling, the thermal wind equation serves to check analyses of observed wind and temperature fields for consistency. When the geostrophic wind is known at a level, the thermal wind equation can be used to assess the geostrophic wind at any level from the mean temperature field, i.e. the thermal wind equation can be used to initialize mesoscale-β/γ-models.

Example. A west wind of $0.5\,\mathrm{m\,s^{-1}}$ and temperature of $20\,^{\circ}\mathrm{C}$ were measured at a mast in 10 m at a site in 63°N. A wind profiler (Appendix B) provided a wind speed of $17.5\,\mathrm{m\,s^{-1}}$ at 510 m height. What is the temperature 50 km south of the site?

Solution. Rearranging Eq. (6.125) yields $T(50\,\mathrm{km}) = -f\frac{\partial u}{\partial z}\frac{T\Delta y}{g} + T = -\frac{20\,^{\circ}\mathrm{C}\,5{\cdot}10^4\,\mathrm{m}}{9.81\,\mathrm{m\,s^{-2}}}1.299\cdot10^{-4}\,\mathrm{s^{-1}}\frac{(0.5-17.5)\,\mathrm{m\,s^{-1}}}{500\,\mathrm{m}} + 20\,^{\circ}\mathrm{C} \approx 20.5\,^{\circ}\mathrm{C}$

6.4.6.1 Barotropic Atmosphere

In a **barotropic** (*Greek* tropos = direction, barys = heavy) atmosphere, density only depends on pressure. Isobaric surfaces are **isopycnic** (ρ = *constant*) and isothermal surfaces (Fig. 6.27). The gradients of temperature, pressure and density are perpendicular to the surfaces of these quantities and have all the same direction.

Thus, vector products calculated from them are zero (i.e. $\nabla p \times \nabla T = 0$ and $\nabla \rho \times \nabla p = 0$). The thermal wind equation becomes $\frac{\partial v_g}{\partial ln p} = 0$, i.e. the geostrophic wind and direction are independent of height, and no vertical shear of the geostrophic wind exists. The motions of a rotating barotropic air mass or fluid are strongly constrained. A barotropic fluid always follows a barotropic flow, but barotropic flow can exist in a non-barotropic fluid. Tropical cyclones, for instance, build in barotropic environments.

6.4.6.2 Equivalent Barotropic Atmosphere

An **equivalent-barotropic atmosphere** is an idealized atmosphere, characterized by frictionless and adiabatic flow, hydrostatic and quasi-geostrophic equilibrium, in which the vertical shear of the horizontal wind is proportional to the horizontal wind itself. Thus, the wind direction remains constant with height and isotherms and isobaric surfaces are everywhere parallel. The vertically averaged motions can be assumed to be equivalent to those at some intermediate level called the equivalent-barotropic level, typically an isobaric surface (e.g. 500 hPa). At this level, we can describe the behavior of the **equivalent-barotropic model** by just the vorticity equation with a single unknown being the height of the isobaric surface. In an equivalent barotropic atmosphere, a horizontal temperature gradient exists, but the thickness contours are parallel to the height contours. Because of the thickness variation in the direction normal to the height contours, the slope of the pressure surfaces and geostrophic wind speed vary from level to level. According to the thermal wind equation, the vertical wind shear in an equivalent barotropic atmosphere is parallel to the wind itself.

In an equivalent barotropic atmosphere, centers of high and low pressure are centers of positive or negative temperature anomaly. In warm highs and cold lows, the geostrophic wind speed increases with height. The opposite is true for cold highs and warm lows.

6.4.6.3 Baroclinic Atmosphere

In a **baroclinic** atmosphere, density depends on temperature and pressure. The isotherms intersect the height contours (Fig. 6.28). The geostrophic flow has a vertical shear related to the temperature gradient and blows across the isotherms leading to temperature advection. Warm (cold) air advection is flow across isotherms from the relatively warmer (colder) to the relatively colder (warmer) region. Warm (cold) air advection is characterized by counter-clockwise (clockwise) rotation of the geostrophic wind with height.

Baroclinic instability refers to instability that arises from an excessively large meridional temperature gradient and, hence, thermal wind. Because of this instability many extra-tropical cyclones, polar lows and anticyclones develop (Sect. 6.10).

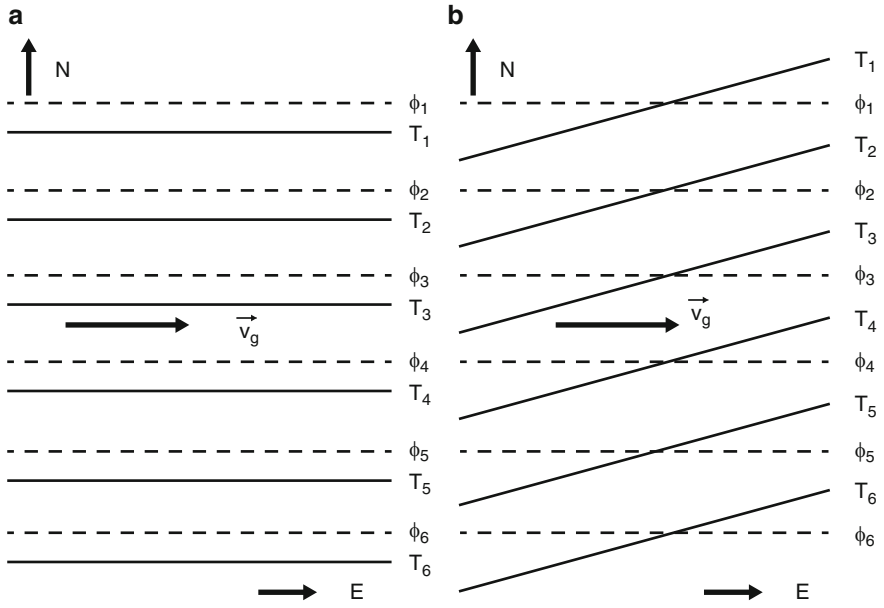

Fig. 6.28 Schematic view of baroclinic atmospheres shown on surfaces of constant pressure with isolines of constant geopotential height, ϕ (*dashed*) and temperature, T (*solid*). Geopotential height and T increase with their index, i.e. $T_2 > T_1$, $\phi_2 > \phi_1$. The *arrows* indicate the geostrophic wind, $\mathbf{v}_g$, blowing parallel to the surfaces of equal geopotential height. (**a**) Equivalent barotropic atmosphere, i.e. a baroclinic field with no horizontal advection of heat. (**b**) Baroclinic field with horizontal advection of heat. Here cold air advection is shown

6.5 Equation of Continuity: Conservation of Total Mass

Let us assume an arbitrarily shaped constant volume. A fluid of density, $\rho(x, y, z, t)$, is passing through this volume at a speed of $\mathbf{v} = (u, v, w, t)$. Both density and speed vary with time, t, and depend on the location, $\mathbf{r} = (x, y, z)$. In x-direction, for instance, the net change in mass depends on the difference of inflow and outflow according to

$$(\rho(x)u(x) - \rho(x + \Delta x)u(x + \Delta x))\Delta y\Delta z \approx -\frac{\partial}{\partial x}(\rho u)\Delta x\Delta y\Delta z = -\frac{\partial}{\partial x}(\rho u)\Delta V, \tag{6.129}$$

where ΔV is the volume. Including the analogous equations for the y- and z-directions and applying the laws of vector analysis lead to $-\nabla \cdot (\rho\mathbf{v})\Delta V$ for the total in- and outflow. This net change must equal the change in mass within the volume $\frac{\partial}{\partial t}(\rho\Delta V)$. As the volume is constant, ΔV cancels out, i.e. the change is independent of the feature of the volume. We obtain the **continuity equation**, or the **mass conservation law**

$$\frac{\partial \rho}{\partial t} + \nabla \cdot (\rho\mathbf{v}) = 0 \tag{6.130}$$

Applying vector calculus yields another often-used form of the continuity equation

$$\frac{d\rho}{dt} = \frac{\partial\rho}{\partial t} + \mathbf{v}\cdot\nabla\rho = -\rho\nabla\cdot\mathbf{v}. \tag{6.131}$$

6.5.1 Incompressible Fluid

For an incompressible fluid ($\frac{\partial\rho}{\partial t} = 0$ and $\nabla\rho = 0$) the continuity equation reduces to

$$\nabla\cdot\mathbf{v} = 0 \tag{6.132}$$

because the specific volume of an individual air parcel is conserved. Incompressible motion implies that the total derivative of density vanishes and $\frac{d\rho}{dt} = 0$. Despite $\frac{d\rho}{dt}$ and $\nabla\cdot\mathbf{v}$ are both zero, density does not have to be uniform everywhere. The vertical density stratification still exists. An air parcel being initially on an isopyncal surface remains on that surface, i.e. isopyncal surfaces are material surfaces under incompressible conditions.

6.5.2 Inert Tracers and Water Vapor

In general, a property χ that is conserved for an individual air parcel, obeys the continuity equation $\frac{d\chi}{dt} = 0$. The mixing ratio of non-reactive trace species far away from their sources, clouds, and the Earth's surface, as well as water-vapor mixing ratio way below saturation and far away from clouds and the Earth's surface move on surfaces of $\chi = constant$.

6.6 Primitive Equations

The atmosphere is a multi-component continuous system, in which transport of momentum, heat and matter as well as diffusion, phase transition processes and chemical reactions may occur (Chaps. 2, 3, 4, and 5). Dissipation of kinetic energy, interaction with electro-magnetic radiation and material exist. In the ABL, turbulent mixing is of importance and the molecular transfer properties are negligible, except at the Earth-atmosphere interface.

The physical and chemical laws derived in the previous chapters provide a set of **macroscopic equations of the molecular system**

- Equation of continuity (conservation of total mass)

$$\frac{\partial\rho}{\partial t} + \nabla\cdot(\rho\mathbf{v}) = 0 \tag{6.133}$$

- First law of thermodynamics (conservation of energy)

$$\frac{\partial(\rho\Theta)}{\partial t} + \nabla\cdot(\rho\mathbf{v}\Theta + \mathbf{J}_\Theta) = S_\Theta \tag{6.134}$$

- Newton's second law for the relative system of the rotating earth (conservation of momentum)

$$\frac{\partial(\rho\mathbf{v})}{\partial t} + \nabla\cdot(\rho\mathbf{v}\mathbf{v} + \mathbf{J}) = -\nabla p - \rho\nabla\Phi - 2\,\rho\,\boldsymbol{\Omega}\times\mathbf{v} \tag{6.135}$$

- Balance equations for dry air (q_0) and water substances ($q_n, n = 1,\ldots,3$ where the subscripts stand for water vapor, $n = 1$, liquid water, $n = 2$, and ice, $n = 3$)[21] (conservation of water; cf. Chap. 3)

$$\frac{\partial(\rho q_n)}{\partial t} + \nabla\cdot(\rho\mathbf{v}q_n + \mathbf{J}_{q_n}) = S_{q_n} \qquad n = 0,\ldots,3 \tag{6.136}$$

- Balance equations for M different chemical species

$$\frac{\partial(\rho\chi_m)}{\partial t} + \nabla\cdot(\rho\mathbf{v}\chi_m + \mathbf{J}_{\chi_m}) = S_{\chi_m} \qquad m = 1,\ldots,M \tag{6.137}$$

- Equation of state[22]

$$p = \rho R_0 T_v \tag{6.138}$$

The contributions of S_Θ include the latent heat released or the heat consumed during phase transition processes, and the divergence or convergence of radiation, where condensation, freezing, deposition, radiative flux convergence, dissipation of kinetic energy by molecular motion, add heat to the system, while evaporation, melting sublimation radiative flux divergence, and dissipation of heat by molecular diffusion consume heat. Furthermore, ∇p is the pressure gradient force, $\rho\nabla\Phi$ the gravity force with $\Phi = gz$ being geopotential height, i.e. the attraction and centrifugal force, and $2\rho\boldsymbol{\Omega}\times\mathbf{v}$ is Coriolis force. Stokes' friction tensor $\mathbf{J}$ is neglected except at the Earth-atmosphere interface. Furthermore, $\mathbf{J}_{q_n}$ and $\mathbf{J}_{\chi_m}$ are the **non-convective**

[21] Here numbers are used to address the different phase of water and dry air as often done in theoretical meteorology to reduce the writing burden.

[22] Herein it is assumed that moist air can be considered as an ideal gas. In the nomenclature introduced above, the computed gas constant for the gas mixture dry air, R_d, is denoted to as R_0, ρ is the density of air, and $T_v = T(1 + 0.61q_1)$ is the virtual temperature, and Θ is the potential temperature using the nomenclature of theoretical meteorology and ABL physics (Chap. 2).

transports. In the case of S_{q_n}, the sources and sinks are the cloud-microphysical processes (Chap. 3), while for S_{χ_m}, they are the chemical reactions and physio-chemical transformation processes (Chap. 5).

Equations (6.133)–(6.137) are **prognostic**, i.e. they provide a change with time. Equation (6.138) is diagnostic, i.e. it provides the state of a variable as a consequence of the other state variables. In Eq. (6.135), the prognostic equation of the vertical wind component can be replaced by the hydrostatic equation (2.7) for large-scale applications (hydrostatic approach).

To apply the primitive equations for numerical modeling and many other application purposes they are usually first converted into a suitable coordinate system. Since the locally formulated macroscopic equations (6.133)–(6.138) are unsuitable to calculate the thermodynamic, dynamic and chemical conditions, they are typically Reynolds averaged. A scale analysis is then applied to the resulting set of equations to simplify the equations. These equations are then discretized and parameterizations are formulated for non-resolvable terms (subgrid-scale processes). Most NWP models use terrain-following coordinates to ensure that model layers do not intercept mountains in complex terrain (Chap. 2).

6.7 Coordinate Transformations

Up to now we chose either appropriate coordinates or Cartesian-height coordinates. Obviously, all physical laws apply generally. A vertical motion given in height coordinates, for example, remains the same in pressure coordinates despite it is given in Pa s^{-1} in the latter and in m s^{-1} in the former. In the following, a first insight into coordinate transformation is given. Exemplarily a coordinate transformation from the Cartesian-height to the Cartesian-pressure system and from the Cartesian to the spherical coordinate system are shown for some of the primitive equations. Of course, the transformation has to be applied to the entire set of equation. The interested reader is referred to literature on modeling for further reading and examples on coordinate transformations.

Since vertical observations (e.g. by radiosondes) are measured in conjunction with pressure, pressure p is a more convenient vertical coordinate than height z for many meteorological applications. Typically, height and pressure surfaces intersect and quantities (e.g. temperature, specific humidity, concentration) vary along surfaces of equal pressure or height. The conversion from Cartesian z to Cartesian p coordinates can be graphically derived as (Fig. 6.29)

$$\frac{q_2 - q_1}{x_2 - x_1} = \frac{q_1 - q_3}{x_2 - x_1} + \left(\frac{p_2 - p_1}{x_2 - x_1}\right)\left(\frac{q_1 - q_2}{p_1 - p_2}\right) \tag{6.139}$$

For $x_2 - x_1 \rightarrow 0$ and $p_1 - p_2 \rightarrow 0$ the differences can be approximated by differentials leading to

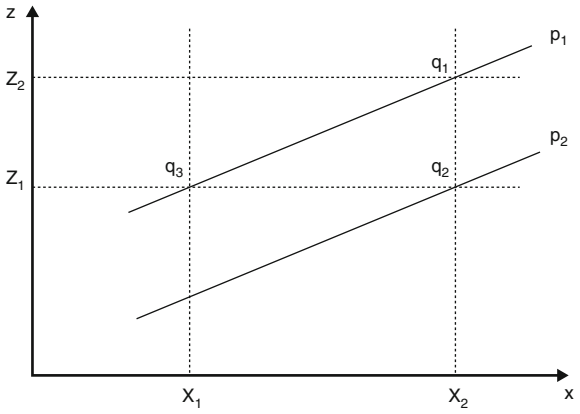

Fig. 6.29 Schematic view of intersection of pressure p and height surfaces z. Specific humidity q varies along each surface of constant pressure

$$(\frac{\partial q}{\partial x})_z = \frac{q_2 - q_3}{x_2 - x_1} \qquad (\frac{\partial q}{\partial x})_p = \frac{q_1 - q_3}{x_2 - x_1} \tag{6.140}$$

$$(\frac{\partial p}{\partial x})_z = \frac{p_2 - p_1}{x_2 - x_1} \qquad (\frac{\partial q}{\partial p})_x = \frac{q_2 - q_1}{p_1 - p_2}. \tag{6.141}$$

Inserting these approximations yields

$$(\frac{\partial q}{\partial x})_z = (\frac{\partial q}{\partial x})_p + (\frac{\partial p}{\partial x})_z (\frac{\partial q}{\partial p})_x \tag{6.142}$$

or in more general form

$$(\frac{\partial}{\partial x})_z = (\frac{\partial}{\partial x})_p + (\frac{\partial p}{\partial x})_z (\frac{\partial}{\partial p})_x \tag{6.143}$$

and with similar considerations for the y-direction we obtain the conversion rule

$$\nabla_z = \nabla_p + \nabla_z(p)\frac{\partial}{\partial p} \tag{6.144}$$

where $\nabla_z = \mathbf{i}(\frac{\partial}{\partial x})_z + \mathbf{j}(\frac{\partial}{\partial y})_z$ and $\nabla_p = \mathbf{i}(\frac{\partial}{\partial x})_p + \mathbf{j}(\frac{\partial}{\partial y})_p$ are the horizontal operators in Cartesian z and Cartesian p coordinates, respectively. Similar consideration for time t yields

$$(\frac{\partial}{\partial t})_z = (\frac{\partial}{\partial t})_p + (\frac{\partial p}{\partial t})_z (\frac{\partial}{\partial p})_t. \tag{6.145}$$

The hydrostatic equation (2.7) and equation of state (2.1) provide

$$g\frac{\partial z}{\partial p}|_{x,y,t} = -\frac{1}{\rho} = -\frac{R_d T}{p}. \tag{6.146}$$

Introducing geopotential height, $\Phi = gz$, results in the hydrostatic equation in pressure coordinates,

$$\frac{\partial \Phi}{\partial p} = -\frac{R_d T}{p} \tag{6.147}$$

Traditionally, the vertical velocity in pressure coordinates is

$$\omega = \frac{dp}{dt} = \frac{\partial p}{\partial t}|_z + (\mathbf{v}\cdot\nabla)p = \frac{\partial p}{\partial t}|_z + (\mathbf{v}_h\cdot\nabla_z)p + w\frac{\partial p}{\partial z}. \tag{6.148}$$

In pressure coordinates, the continuity equation reads

$$\frac{\partial u}{\partial x}|_{y,p,t} + \frac{\partial v}{\partial y}|_{x,p,t} + \frac{\partial \omega}{\partial p}|_{x,y,t} = 0. \tag{6.149}$$

Herein no time derivative of density occurs. The geostrophic wind equations transferred to pressure coordinates read

$$f v_g = \frac{\partial \Phi}{\partial x}\,, \qquad f u_g = -\frac{\partial \Phi}{\partial y}. \tag{6.150}$$

Analogously, we can transfer other equations.

Example. Assume a mesoscale model that uses vertical and horizontal grid increments of 4 km and −10 hPa, respectively. At the west, east, south, and north wall of a grid cell, wind speed is −2, 3, −5, and −2 m s^{-1}, respectively. At the bottom of the grid cell, vertical motion is 0.02 hPa s^{-1}. Calculate the vertical scalar velocity at the top of the grid-cell. What coordinate system is used?

Solution. Pressure coordinates. With $(\frac{\partial u}{\partial x} + \frac{\partial v}{\partial y})_p + \frac{\partial \omega}{\partial p} = 0$ and using the incremental distances (discretization), we yield $\frac{(3-(-2))\,\mathrm{m\,s^{-1}}}{4{,}000\,\mathrm{m}} + \frac{(-2-(-5))\,\mathrm{m\,s^{-1}}}{4{,}000\,\mathrm{m}} + \frac{\omega - 0.02\,\mathrm{hPa\,s^{-1}}}{-10\,\mathrm{hPa}} = 0$ Rearranging provides $\omega = 0.04\,\mathrm{hPa\,s^{-1}}$.

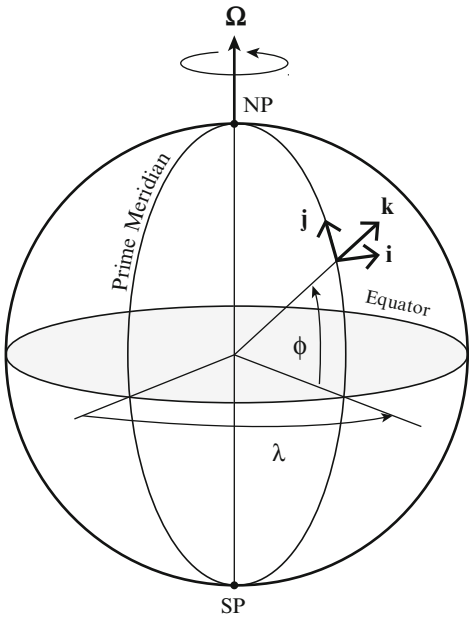

Fig. 6.30 Schematic view of a Cartesian coordinate system on a spherical Earth

6.7.1 Equation of Motion in Spherical Coordinates

Since the Earth is nearly a sphere, its natural coordinates are spherical coordinates, (r, ϕ, λ). Here, r is the distance from the center of the Earth to the point of consideration, ϕ denotes to the geographical latitude, and λ represents geographical longitude (e.g. Fig. 6.30).

By using the unit vectors[23] the transformation from the Cartesian to the spherical coordinate system leads to the identity

$$x = r \cos\phi \cos\lambda \tag{6.151}$$

$$y = r \cos\phi \sin\lambda \tag{6.152}$$

and

$$z = r \sin\phi \tag{6.153}$$

Thus, height, z, is given by $z = r - R$ where R denotes to the radius of the Earth. The physical displacements in the eastward (**zonal**), northward (**meridional**), and upward directions read

[23]The unit vectors in Cartesian $(\mathbf{i}, \mathbf{j}, \mathbf{k})$ and spherical coordinates $(\mathbf{i}_\lambda, \mathbf{j}_\phi, \mathbf{k}_r)$ differ. Only tensors of same rank, and tensors and vectors belonging to the same coordinate systems can be added.

$$dx = r\cos\phi d\lambda \tag{6.154}$$

$$dy = rd\phi \tag{6.155}$$

and

$$dz = dr. \tag{6.156}$$

The physical velocities then read

$$u = \frac{dx}{dt} = r\cos\phi\frac{d\lambda}{dt} = r\cos\phi\dot{\lambda} \tag{6.157}$$

$$v = \frac{dy}{dt} = r\frac{d\phi}{dt} = r\dot{\phi} \tag{6.158}$$

and

$$w = \frac{dz}{dt} = \frac{dr}{dt} = \dot{r}. \tag{6.159}$$

Thus, in spherical coordinates the local velocity vector reads

$$\mathbf{v}|_{spheric} = (r\cos\phi\frac{d\lambda}{dt}, r\frac{d\phi}{dt}, \frac{dr}{dt}) = (r\cos\phi\dot{\lambda}, r\dot{\phi}, \dot{r}) \tag{6.160}$$

where the individual components are expressed now with respect to the Cartesian coordinate system. The gradient operator in spherical coordinates reads

$$\boldsymbol{\nabla}|_{spheric} = (\frac{1}{r\cos\phi}\frac{\partial}{\partial\lambda}, \frac{1}{r}\frac{\partial}{\partial\phi}, \frac{\partial}{\partial r}). \tag{6.161}$$

Substituting these relations into $\boldsymbol{\nabla}\cdot\boldsymbol{v}$ yields

$$\boldsymbol{\nabla}\cdot\boldsymbol{v}|_{spheric} = \frac{1}{r\cos\phi}\frac{\partial u}{\partial\lambda} + \frac{1}{r\cos\phi}\frac{\partial}{\partial\phi}(v\cos\phi) + \frac{\partial w}{\partial r}. \tag{6.162}$$

The total derivative in spherical coordinates is given by

$$\frac{d}{dt} = \frac{\partial}{\partial t} + u\frac{1}{r\cos\phi}\frac{\partial}{\partial\lambda} + v\frac{1}{r}\frac{\partial}{\partial\phi} + w\frac{\partial}{\partial r} \tag{6.163}$$

Inserting these identities in the component form of the Lagrangian version of Eq. (6.55) and neglecting the centripetal forces lead to

$$\frac{du}{dt}|_{spheric} - (2\Omega + \frac{u}{r\cos\phi})(v\sin\phi - w\cos\phi) + \frac{1}{\rho r\cos\phi}\frac{\partial p}{\partial\lambda} = F_{friction,\lambda} \tag{6.164}$$

$$\frac{dv}{dt}|_{spheric} + \frac{wu}{r} + (2\Omega + \frac{u}{r\cos\phi})u\sin\phi + \frac{1}{\rho r}\frac{\partial p}{\partial \phi} = F_{friction,\phi} \tag{6.165}$$

$$\frac{dw}{dt}|_{spheric} - \frac{u^2+v^2}{r} - 2\Omega u\cos\phi + \frac{1}{\rho}\frac{\partial p}{\partial r} + g = F_{friction,r} \tag{6.166}$$

where $F_{friction,\lambda}$, $F_{friction,\phi}$, and $F_{friction,r}$ are the components of the frictional forces along the zonal, meridional and radial direction, respectively. Substituting u, v, and w by their representatives in spherical coordinates provides

$$\frac{dr\cos\phi\dot{\lambda}}{dt}|_{spheric} - (2\Omega + \frac{r\cos\phi\dot{\lambda}}{r\cos\phi})(r\dot{\phi}\sin\phi - \dot{r}\cos\phi) + \frac{1}{\rho r\cos\phi}\frac{\partial p}{\partial\lambda} = F_{friction,\lambda} \tag{6.167}$$

$$\frac{dr\dot{\phi}}{dt}|_{spheric} + \frac{\dot{r}r\cos\phi\dot{\lambda}}{r} + (2\Omega + \frac{r\cos\phi\dot{\lambda}}{r\cos\phi})r\cos\phi\dot{\lambda}\sin\phi + \frac{1}{\rho r}\frac{\partial p}{\partial\phi} = F_{friction,\phi} \tag{6.168}$$

$$\frac{d\dot{r}}{dt}|_{spheric} - \frac{(r\cos\phi\dot{\lambda})^2 + (r\dot{\phi})^2}{r} - 2\Omega r\cos\phi\dot{\lambda}\cos\phi + \frac{1}{\rho}\frac{\partial p}{\partial r} + g = F_{friction,r}. \tag{6.169}$$

In Eqs. (6.164)–(6.166), the distance r is often replaced by the Earth's radius, R. The resulting error is negligible as meteorology considers the atmosphere below 100 km. This layer is small as compared to the mean Earth radius of about 6,371 km. Since except near the poles ($cos\phi \longrightarrow 0$), the zonal wind is usually less than $100\,\mathrm{m\,s^{-1}}$, $\frac{|u|}{Rcos\phi}$ is much smaller than 2Ω. Except near the equator ($sin\phi \longrightarrow 0$), the horizontal velocities are, on average, much greater than the vertical wind velocities so that $|v\sin\phi|$ is much greater than $|w\cos\phi|$.

6.8 Turbulent Motion

As stated above, the locally formulated macroscopic balance and state equations of the molecular, continuous system of the atmosphere given by Eqs. (6.133)–(6.138) are unsuitable to predict the variation of the meteorological quantities in space and time. The following properties are associated with turbulent flows:

1. Turbulence is rotational and dissipative, i.e. mechanical energy is transferred to internal energy. Thus, energy must be supplied to maintain the turbulence
2. Turbulent fluctuations are three-dimensional.
3. Turbulence is stochastic, i.e. the motions are irregular and unpredictable in detail.
4. Turbulence is non-linear. This means that the transfer from one size eddy to another can take place only in a non-linear way.
5. Turbulence is diffusive. This behavior is responsible for the transfer of momentum, energy, and matter.

Therefore, to describe the turbulent flow of the atmosphere in a mathematically adequate manner, we have to define the mean velocity of the turbulent flow as an average value of the true velocity in each point of the atmosphere for a sufficiently large time interval. With the aid of an averaging calculus the variability of the velocity of this turbulent flow is canceled out and the mean velocity of the flowing medium like air or water is a continuously changing function in space and time. The difference between the true and the mean flow velocity that undergoes a characteristically irregular change with respect to turbulence means a fluctuation of velocity with respect to the mean velocity of the turbulent atmospheric flow. Practically, this separation allows addressing the organized fraction, which can be measured, and the stochastic fraction, which cannot be attached. In this sense, Obukhov introduced the measure of observation, i.e. a length that is characteristic for the phenomenon under study. We may also consider it as a macro-scale of turbulence (Chap. 7). Hence, the following model concept of turbulence may be helpful: *Within the atmospheric domain characterized by the measure of observation the fully turbulent flow contains a great number of turbulent elements of different orders of magnitude. In consequence of the large degrees of freedom their flow velocities are arbitrary functions of space and time. Except for large turbulent elements that may significantly be affected by the mean flow the turbulent elements move in a totally chaotic manner within this domain. This can be addressed as a stochastic process.*

The questions that still remain are (1) how to average the governing macroscopic equations in the case of turbulent atmospheric flows, and (2) what are the consequences of such an averaging, not only in the case of atmospheric trace species, but also in the cases of total mass, momentum and various energy forms. In the following subsections we answer these questions.

6.8.1 Reynolds Averaging

Most NWP model formulations rely on **Reynolds**[24] **averaging**. All averaging procedures base on the idea that any instantaneous quantity φ in Eqs. (6.133)–(6.138) can be decomposed in a mean value, $\bar{\varphi}$, and the deviation from that, φ', according to

$$\varphi = \bar{\varphi} + \varphi' \tag{6.170}$$

It is obvious that $\overline{\varphi'} = 0$. The following averaging rules can be applied:

$$\overline{\varphi + \gamma} = \bar{\varphi} + \bar{\gamma}$$

[24] Osborne Reynolds, British physicist, 1842–1912.

$$\overline{\varphi\,\gamma} = \bar{\varphi}\,\bar{\gamma} + \overline{\varphi'\,\gamma'}$$

$$\overline{\alpha\,\varphi} = \alpha\,\bar{\varphi} \qquad \text{with } \alpha = const.$$

$$\bar{\bar{\varphi}} = \bar{\varphi}$$

$$\overline{\frac{\partial\varphi}{\partial t}} = \frac{\partial\bar{\varphi}}{\partial t}$$

$$\overline{\nabla\cdot\varphi} = \nabla\cdot\bar{\varphi}$$

$$\overline{\nabla\varphi} = \nabla\bar{\varphi}$$

$$\overline{\int \varphi\, ds} = \int \bar{\varphi}\, ds.$$

To derive the first-order balance equations for momentum, dry air and water substances, gaseous and particulate trace constituents, various energy forms averaged in the sense of Reynolds, these averaging rules have to be strictly applied. This means, in a first step, we have to substitute the quantities in Eqs. (6.133)–(6.138) by their composites. In a second step, we have to average the resulting ones under consideration of the above rules. Doing so yields a set of equations suitable for the turbulent atmosphere. In these first-order balance equations, the averaged variables are the field quantities to be predicted on a **resolvable scale**. These averaged variables are denoted as scale quantities. The deviations from these averaged quantities, i.e. the turbulent fluctuations, are of **subscale** nature and are not resolved by the scale for which the equations are formulated.

In summary, to derive a set of equations suitable for modeling purposes first the equations are transformed into the coordinate system to be used, then 'averaged' (decomposition plus averaging the macroscopic equations). Finally, scale analysis is applied to simplify the equations by removing terms of negligible contribution.

6.8.2 *Boussinesq-Approximation*

The **Boussinesq**[25] **approximation** is related to **Reynolds**[26] averaging. Here, we demonstrate it by considering of the equation of continuity, and the Navier-Stokes equation

$$\frac{\partial\bar{\rho}}{\partial t} + \nabla\cdot(\bar{\rho}\,\bar{\mathbf{v}} + \underbrace{\overline{\rho'\,\mathbf{v}'}}_{neglected}) = \frac{\partial\bar{\rho}}{\partial t} + \nabla\cdot(\bar{\rho}\,\bar{\mathbf{v}}) = 0 \tag{6.171}$$

[25] Joseph Valentin Boussinesq, French mathematician and physicist, 1842–1929.

[26] Osborne Reynolds, British mathematician and engineer, 1842–1912.

and

$$\frac{\partial(\bar{\rho}\,\bar{\mathbf{v}} + \overbrace{\overline{\rho'\mathbf{v}'}}^{neglected})}{\partial t} + \nabla\cdot\left(\bar{\rho}\,\bar{\mathbf{v}}\,\bar{\mathbf{v}} + \bar{\rho}\,\overline{\mathbf{v}'\mathbf{v}'} + \underbrace{\overline{\rho'\mathbf{v}'}\,\bar{\mathbf{v}} + \bar{\mathbf{v}}\,\overline{\rho'\mathbf{v}'} + \overline{\rho'\mathbf{v}'\mathbf{v}'}}_{neglected} + \bar{\mathbf{J}}\right)$$
$$= -\nabla\bar{p} - \bar{\rho}\,\nabla\phi - 2\,\bar{\rho}\,(\boldsymbol{\Omega}\times\bar{\mathbf{v}}) - \underbrace{2\,\boldsymbol{\Omega}\times\left(\overline{\rho'\mathbf{v}'}\right)}_{neglected} \quad (6.172)$$

We neglect the fluctuations of ϕ and $\boldsymbol{\Omega}$ because they are unimportant for atmospheric turbulence. The term $\bar{\rho}\,\bar{\mathbf{v}}\,\bar{\mathbf{v}}$ is denoted to as the **convective transport** and $\bar{\rho}\,\overline{\mathbf{v}'\,\mathbf{v}'} + \bar{\mathbf{J}}$ is the non-convective transport. Neglecting the terms indicated in Eqs. (6.171) and (6.172) leads to the Boussinesq-approximated equations (of the **Boussinesq fluid**). Obviously, within the framework of the Boussinesq approximation terms containing density fluctuations are neglected except where these density fluctuations are coupled with gravity.

The Boussinesq-approximation is motivated by the fact that compressibility effects in the atmosphere may be neglected except when deep layers are considered. The Boussinesq approximation is equivalent to assuming that $L_z \ll H$ and density can be treated as constant except where it is coupled to gravity in the buoyancy term of the vertical motion equation. The Boussinesq approximation defines the perturbation buoyancy $B' = \frac{g\theta'}{\bar{\theta}}$ and kinematic pressure $\frac{p'}{\bar{\rho}}$ to simplify the set of equations.[27] In particular, the Boussinesq approximation serves to neglect sound waves in meteorological models,[28] which permits larger time steps than would be needed otherwise.

We can write the averaged equation of continuity and the Navier-Stokes equation as

$$\frac{d\,\bar{\rho}}{dt} = -\,\bar{\rho}\,\nabla\cdot\bar{\mathbf{v}} \quad (6.173)$$

and

$$\bar{\rho}\,\frac{d\,\bar{\mathbf{v}}}{dt} + \nabla\cdot\left(\bar{p}\,\mathbf{E} + \bar{\mathbf{J}} + \mathbf{F}\right) = -\,\bar{\rho}\,\nabla\phi - \,2\,\bar{\rho}\,\boldsymbol{\Omega}\times\bar{\mathbf{v}} \quad (6.174)$$

where we used the Boussinesq-approximated Euler operator

$$\frac{d}{dt} = \frac{\partial}{\partial t} + \bar{\mathbf{v}}\cdot\nabla. \quad (6.175)$$

[27] For low Rossby numbers we can extend the Boussinesq approximation to large vertical scales of motion when we use modified pressure and potential density.

[28] Sound waves may not be ignored in meteorological models that aim at investigation of noise annoyance.

The quantity $\mathbf{E}$ is the identity tensor, and $\mathbf{F} = \bar{\rho}\,\overline{\mathbf{v}'\,\mathbf{v}'}$ is also a second-rank tensor called the **Reynolds stress tensor**. It is generated by averaging the term $\overline{\rho\mathbf{v}\,\mathbf{v}} = \bar{\rho}\,\bar{\mathbf{v}}\,\bar{\mathbf{v}} + \bar{\rho}\,\overline{\mathbf{v}'\mathbf{v}'} + \overline{\rho'\mathbf{v}'}\,\bar{\mathbf{v}} + \bar{\mathbf{v}}\,\overline{\rho'\mathbf{v}'} + \overline{\rho'\mathbf{v}'\mathbf{v}'}$, where we neglected the last three terms, which contain the density fluctuations, as illustrated in Eq. (6.172). All other governing equations can be derived and approximated in a similar manner.

For dry air (n = 0), water vapor (n = 1), liquid water (n = 2), and ice (n = 3) we obtain

$$\bar{\rho}\,\frac{d\overline{q_n}}{dt} + \nabla\cdot\left(\overline{\mathbf{J}_{q_n}} + \mathbf{F}_{q_n}\right) = \overline{S_{q_n}} \quad for\ n = 0,1,2,3 \tag{6.176}$$

where $\mathbf{F}_{q_n} = \bar{\rho}\ \overline{\mathbf{v}'\,q_n'}$ is the nth eddy flux density. The mass fractions, $\overline{q_n}$, the macroscopic flux densities,

$$\overline{\mathbf{J}_{q_n}} = \overline{\rho_n\,(\mathbf{v}_n - \mathbf{v})} \cong -\,\bar{\rho}\left(\mathbf{D}_{q_n}\cdot\nabla\overline{q_n} - v_{T,q_n}\,\overline{q_n}\,\delta_{n,j}\,\mathbf{k}\right) \quad for\ j = 2,3$$

the eddy flux densities, $\mathbf{F}_{q_n}$, and the phase transition processes, $\overline{S_{q_n}}$, fulfill the conditions

$$\sum_{n=0}^{3}\overline{q_n} = 1 \quad \Rightarrow \quad \overline{q_0} = 1 - \sum_{n=1}^{3}\overline{q_n}$$

$$\bar{\rho}\,\bar{\mathbf{v}} = \sum_{n=0}^{3}\overline{\rho_n\,\mathbf{v}_n} \quad \Rightarrow \quad \sum_{n=0}^{3}\overline{\mathbf{J}_{q_n}} = 0 \quad \Rightarrow \quad \overline{\mathbf{J}_{q_0}} = -\sum_{n=1}^{3}\overline{\mathbf{J}_{q_n}}$$

$$\sum_{n=0}^{3}\mathbf{F}_{q_n} = 0 \quad \Rightarrow \quad \mathbf{F}_{q_0} = -\sum_{n=1}^{3}\mathbf{F}_{q_n}$$

and

$$\overline{S_{q_0}} = 0 \quad \Rightarrow \quad \sum_{n=1}^{3}\overline{S_{q_n}} = 0 \quad \Rightarrow \quad \overline{S_{q1}} = -\sum_{n=2}^{3}\overline{S_{q_n}}.$$

As this has been discussed already in Chap. 3 here $\mathbf{D}_{q_n}$ is the second-rank tensor containing the molecular diffusion coefficients. This tensor is typically considered as isotropic so that $\mathbf{D}_{q_n} = D_{q_n}\mathbf{E}$. Furthermore, v_{T,q_n} is the terminal settling velocity that serves to parameterize the sedimentation of rain drops, and sufficiently large ice particles (Fig. 3.7; Table 3.1, Eq. (3.28)).

We can derive the balance equation for gaseous and particulate trace constituents in a similar manner, and obtain

$$\bar{\rho}\,\frac{d\overline{\chi_m}}{dt} + \nabla\cdot\left(\overline{\mathbf{J}_{\chi_m}} + \mathbf{F}_{\chi_m}\right) = \overline{S_{\chi_m}} \quad for\ m = 1,\ldots,M \tag{6.177}$$

where the mth eddy flux density is given by $\mathbf{F}_{\chi_m} = \bar{\rho}\ \overline{\mathbf{v}'\ \chi_m{}'}$. Like in case of water substances, the molecular diffusion and sedimentation of matter can be described (e.g. Eqs. (5.161) and (5.162)). To determine the production and depletion of trace species due to chemical reactions, we not only have to consider the reaction rates depending on the mean concentrations of the reactants (Chap. 5), but also segregation effects caused by the fluctuations of the respective concentrations. These segregation effects can reduce the efficiency of chemical reactions taking place within the atmosphere.

The equation for the potential temperature (Eq. (2.41)) reads

$$\left.\begin{aligned} & c_p\,\bar{\rho}\,\bar{\pi}\,\frac{d\bar{\Theta}}{dt} + \nabla\cdot\left(\overline{\mathbf{R}} + \overline{\mathbf{J}_h} + \left\{1 + \sum_{n=1}^{3}\left(\frac{c_{p,n}}{c_{p,0}} - 1\right)\overline{q_n}\right\}\ \bar{\pi}\,\mathbf{H}\right) = \\ & \left\{\left\{1 + \sum_{n=1}^{3}\left(\frac{c_{p,n}}{c_{p,0}} - 1\right)\overline{q_n}\right\}\ \mathbf{H} + c_{p,0}\ \bar{\Theta}\ \sum_{n=1}^{3}\left(\frac{c_{p,n}}{c_{p,0}} - 1\right)\mathbf{F}_{q_n}\right\}\cdot\nabla\bar{\pi} \\ & -\bar{\mathbf{J}} : \nabla\bar{\mathbf{v}} - \overline{\mathbf{J} : \nabla\mathbf{v}'} + \sum_{n=2}^{3}\overline{\lambda_{n1}}\,\overline{S_{q_n}} \end{aligned}\right\}. \qquad (6.178)$$

Here, $\bar{\pi} = \bar{T}/\bar{\Theta}$ is the Exner function, $\bar{\mathbf{R}}$ represents the flux densities of the solar and infrared radiation, $\overline{\mathbf{J}_h} = -\ \bar{\boldsymbol{\lambda}}\cdot\nabla\bar{T}$ is the macroscopic enthalpy flux density, $\mathbf{H} = c_{p,0}\ \bar{\rho}\ \overline{\mathbf{v}'\ \Theta'}$ is the eddy flux density of sensible heat, $\overline{\lambda_{q_2 q_1}}$ is the specific heat of vaporization, $\overline{\lambda_{q_3 q_1}}$ is the specific heat of sublimation, $\overline{S_{q_2}}$ and $\overline{S_{q_3}}$ are the respective phase transition rates of water. Furthermore, $\bar{\boldsymbol{\lambda}}$ is the second-rank tensor containing the heat conductivities. We can express this tensor by $\bar{\boldsymbol{\lambda}} = c_p\ \bar{\rho}\ \overline{\boldsymbol{\alpha}_T}$, where $\overline{\boldsymbol{\alpha}_T} = \overline{\alpha_T}\ \mathbf{E}$ is the second-rank tensor containing the thermal diffusion coefficients. It is typically is considered to be isotropic. Moreover,

$$c_p = \sum_{n=0}^{3} c_{p,n}\ \overline{q_n}$$

is the specific heat at constant pressure, where $c_{p,n}$ are the respective partial specific heats at constant pressure. The condition

$$\left|\sum_{n=1}^{3}\left(\frac{c_{p,n}}{c_{p,0}} - 1\right)\overline{q_n}\right| \ll 1$$

is usually fulfilled because the mean mass fractions $\overline{q_n}$ are small. Thus, we can consider this term as negligible. The direct dissipation, $-\ \bar{\mathbf{J}} : \nabla\bar{\mathbf{v}} > 0$, and the turbulent dissipation, $-\overline{\mathbf{J} : \nabla\mathbf{v}'} > 0$ of kinetic energy can be neglected in this equation. Thus, we approximate Eq. (6.178) by

$$\left.\begin{aligned} & c_p\,\bar{\rho}\,\bar{\pi}\,\frac{d\bar{\Theta}}{dt} + \nabla\cdot\left(\bar{\mathbf{R}} + \overline{\mathbf{J}_h} + \bar{\pi}\,\mathbf{H}\right) = \\ & \left\{\mathbf{H} + c_{p,0}\,\bar{\Theta}\sum_{n=1}^{3}\left(\frac{c_{p,n}}{c_{p,0}} - 1\right)\mathbf{F}_{q_n}\right\}\cdot\nabla\bar{\pi} + \sum_{n=2}^{3}\overline{\lambda_{n1}}\,\overline{S_{q_n}} \end{aligned}\right\}. \tag{6.179}$$

Example. Apply the Boussinesq approximation to the geostrophic wind equation.

Solution. $u \approx u_g = -\frac{\partial\psi}{\partial y}$, $v \approx v_g = \frac{\partial\psi}{\partial x}$, where ψ is the **geostrophic stream function** defined by $\psi = \frac{p'}{f\rho}$. By means of the geostrophic stream-function, we can express the hydrostatic equation as $\rho' = -\frac{f\rho}{g}\frac{\partial\psi}{\partial z}$

6.8.3 Anelastic Approximation

Another approximation is the **anelastic approximation**. Its denotes to the simplified system of equations for deep and shallow atmospheric convection. We can derive these equations under the assumptions that the potential temperature perturbations are negligibly small, and the Brunt-Väisälä frequency (Chap. 2) determines the time scale. The anelastic approximation eliminates all waves with high propagation speed related to rapid adiabatic compression and expansion of the medium. It corresponds to setting the terms that involve the speed of sound c_s^2 to zero in the continuity equation, while keeping the scale height H finite and constant. Consequently, elastic energy is non-existant in the anelastically approximated system. In its anelastically approximated form, the continuity equation reads

$$\nabla\cdot v' - \frac{w'}{H} = 0$$

or alternatively

$$\nabla\cdot(v' e^{\frac{-z}{H}}) = 0.$$

The latter is related to the former when density decays exponentially with height. Another form to express the **anelastic continuity equation** is

$$\nabla\cdot(\overline{\rho}v') = 0.$$

Again, the overbar and prime denote the mean basic state and deviation, respectively. These equations are known as the **deep convection continuity equation**.

We can further simplify the anelastic continuity equation by assuming that the vertical extension of a disturbance L_z is much smaller than the scale height H of the basics state atmosphere $L_z \ll H$, which yields the incompressible or **shallow convection continuity equation**

$$\nabla \cdot v' = 0$$

This approximation means that conservation of mass has become conservation of volume because density is treated as a constant. Note that the basic atmosphere governs the scale height H, while the motion of the fluid controls L_z.

6.8.4 The Closure Problem of Turbulence

The governing equations for macroscopic systems lose information, when we average these equations. Additional terms, so-called turbulent transport phenomena or **subscale transport phenomena**, occur that are **second-order moments** of the structure $\overline{\mathbf{v}'\varphi'}$ of the wind vector $\mathbf{v}$ and any transferable property φ like mass fractions, potential temperature, and wind vector. These turbulent transport phenomena are connected with additional irreversible processes that also contribute to the production of entropy of the system (Chap. 2). Averaging the production or depletion terms due to chemical and phase transition processes yields second moments, too. The number of these unknown quantities exceeds the number of governing equations formulated for a turbulent flow. Thus, the set of equations is under-determined. This fact is called the **closure problem of turbulence**. To close this gap of information, we have to parameterize the turbulent transport phenomena, i.e. we have to relate them to known **s**cale-resolvable quantities. This means that we have to develop parameterizations of the second moments, the cloud- and precipitation processes (Chap. 3), the interaction between surface and atmosphere (Chaps. 3–5), and the calculation of the radiative transfer (Chap. 4).

Using a **gradient approach**, for instance, is one possibility to parameterize of a turbulent atmospheric flux. This method is known as a **first-order closure** in atmospheric numerical modeling. It assumes that the turbulent flux densities (often denoted as fluxes) of momentum, heat, and matter are proportional to the gradient of the related resolvable field quantities. The factors of relation are the turbulent eddy-diffusivity coefficients of momentum, sensible heat, water vapor, and trace constituents. In case of trace constituents, the coefficients are often assumed as being proportional to those of water vapor.

Another method to close the set of equations is to provide predictive (prognostic) equations for the turbulent flux terms by applying Reynolds averaging on the Reynolds-averaged primitive equations. Doing so leads to higher-order unknowns, for which we have to formulate parameterizations (**higher order closure**). This way Mellor and Yamada (1982) formulated a hierarchy of closures. In their hierarchy, a first order closure is a level 1.5 closure, a one-and-a-half-order closure is a level 2.5

closure, etc. In the following, we sketch the principle of first-order and second-order closure, and a combination of both called the one-and-a-half-order closure.

6.8.4.1 First-Order Closure

To close the gap of information in the set of governing equations (6.174), (6.176)–(6.179) we have to parameterize the eddy transport phenomena. This means they have to be derived from the well-known mean quantities. As suggested by Boussinesq and **Schmidt**,[29] the use of flux-gradient relationships of the form

$$\mathbf{F} = \bar{\rho}\,\overline{\mathbf{v}'\,\mathbf{v}'} = -\,\bar{\rho}\,\mathbf{K}_m : \left(\nabla\bar{\mathbf{v}} + (\nabla\bar{\mathbf{v}})^T\right) \tag{6.180}$$

$$\mathbf{H} = c_{p,0}\,\bar{\rho}\,\overline{\mathbf{v}'\,\Theta'} = -\,c_{p,0}\,\bar{\rho}\,\mathbf{K}_h \cdot \nabla\bar{\Theta} \tag{6.181}$$

$$\mathbf{F}_{q_n} = \bar{\rho}\,\overline{\mathbf{v}'\,q_n{}'} = -\,\bar{\rho}\,\mathbf{K}_{q_n} \cdot \nabla\overline{q_n} \quad for\, n = 1, 2, 3 \tag{6.182}$$

and

$$\mathbf{F}_{\chi_m} = \bar{\rho}\,\overline{\mathbf{v}'\,\chi_m{}'} = -\,\bar{\rho}\,\mathbf{K}_{\chi_m} \cdot \nabla\overline{\chi_m} \quad for\, m = 1, \ldots, M. \tag{6.183}$$

is one possibility. This kind of parameterization is called the first-order closure. Here, $\mathbf{K}_m$ is a fourth-rank tensor containing the eddy diffusivities for momentum, where the colon represents the double-scalar product of tensor algebra. This double-scalar product ensures that the Reynolds stress tensor keeps a symmetric second-rank tensor. Furthermore, $\mathbf{K}_h$, $\mathbf{K}_{q_n}$, and $\mathbf{K}_{\chi_m}$ are second-rank tensors containing the eddy diffusivities for sensible heat (subscript h), water substances (subscripts q_n), and trace constituents (subscripts χ_m), respectively. Equations (6.180)–(6.183) suggest that in analogy to the formulation of the macroscopic transport processes as expressed by Newton's law on friction in a viscous flow, **Fourier**[30]'s law on heat conduction, and **Fick**[31]'s law on diffusion, the turbulent flux densities are related to the gradients of the respective mean field quantities $\bar{\mathbf{v}}$, $\bar{\Theta}$, $\overline{q_n}$, and $\overline{\chi_m}$. In contrast to the elements of the respective molecular diffusivity tensors, the elements of the eddy diffusivity tensors depend on the mechanical and thermal properties of the fluid in a turbulent state.

The flux-gradient relationships were empirically introduced into the literature. Here we deduce them on the basis of the thermodynamic theory of irreversible processes (Chap. 2). As postulated by **Herbert**,[32] the processes occurring within

[29] Ernst Heinrich Wilhelm Schmidt, German engineer, 1892–1975.

[30] Jean Baptiste Joseph Fourier, French mathematician and physicist, 1768–1830.

[31] Adolf Eugen Fick, German physician, 1829–1901.

[32] Fritz Herbert, German meteorologist, born 1944.

a micro-turbulent system are, on average, related to a production of entropy and, hence, are subordinated to the thermodynamic evolution and stability criteria. Within such a system, we can parameterize the microturbulent irreversible transports in the sense of the linear **Onsager**[33]-theory by conjugate "forces". Herbert pointed out that for possible anisotropic micro-turbulent transport quantities of different tensorial character may not be related to each other, in accord with the theorem of **Curie**[34] and **Prigogine**.[35]

To fulfil the requirement of an entropy production when parameterizing the turbulent processes, all spatial distributions of mean field quantities, the elements of the eddy diffusivity tensors must always be positive. As pointed out by Herbert, the number of phenomenological coefficients arising, especially the elements of the coefficient tensor of fourth-rank for momentum tensor as well as coefficients of the second-rank tensor for matter and heat, can strongly be reduced by symmetry properties and reasonable assumptions. Doing so yields phenomenological equations that are suitable as flux-gradient relations for micro-turbulent systems like the ABL.

6.8.4.2 Second-Order Closure

We also can close the gap of information by providing additional balance equations for the turbulent transports of momentum, matter, and various energy forms, respectively. This possibility is the second-order closure. Such balance equations, however, have further unknown quantities, especially triple correlation products of the structure $\overline{\mathbf{v}'\,\mathbf{v}'\,\varphi'}$. Here, φ is a transferable property. For these terms we can also derive balance equations. Unfortunately, in these balance equations, terms of fourth-order correlation products occur. To avoid to derive further balance equations for these terms (which again have further unknown correlation products of higher-order), we formulate the unknown terms in the second-order balance equations by lower-order correlation products or their gradients. In the third-order balance equations, we parameterize the fourth-order products by lower-order products by assuming Gaussian probability distributions. Moreover, additional hypotheses like Rotta[36]'s assumption on the tendency-to-isotropy are often used to put the system of first-order and higher-order balance equations in a resolvable state. However, alternative methods like the flux-gradient-relationships require simplifications so that the parameterization of non-available terms of higher-order by known mean quantities and terms of lower-order are required.

[33] Lars Onsager, Norwegian-American physical chemist, 1903–1976.

[34] Pierre Curie, French physicist, 1859–1906.

[35] Ilya Romanovich Prigogine, Belgian physical chemist, 1917–2003.

[36] Julius C. Rotta, German engineer, 1912–2005.

Typically, the second-order balance equations for the turbulent flow are based on Reynolds' averaging and the Boussinesq approximation. To derive, for instance, the second-order balance equation for the momentum, i.e. the balance equation for the Reynolds stress tensor, we need the following steps:

1. The macroscopic balance equation for momentum (Eq. (6.135)) is tensorially multiplied from left with the velocity vector, $\mathbf{v}$, and averaged afterwards. We obtain for a Boussinesq flow:

$$\left.\begin{aligned}
&\frac{\partial}{\partial t}\left\{\bar{\rho}\left(\bar{\mathbf{v}}\,\bar{\mathbf{v}}+\overline{\mathbf{v}'\,\mathbf{v}'}\right)\right\}+\nabla\cdot\left\{\bar{\rho}\left(\bar{\mathbf{v}}\,\bar{\mathbf{v}}\,\bar{\mathbf{v}}+\overline{\mathbf{v}'\,\mathbf{v}'}\,\bar{\mathbf{v}}+\overline{\mathbf{v}'\,\bar{\mathbf{v}}\,\mathbf{v}'}\right.\right.\\
&\left.\left.+\bar{\mathbf{v}}\,\overline{\mathbf{v}'\,\mathbf{v}'}+\overline{\mathbf{v}'\,\mathbf{v}'\,\mathbf{v}'}\right)\right\}=-\left(\nabla\cdot\bar{\mathbf{J}}\right)\,\bar{\mathbf{v}}-\overline{(\nabla\cdot\mathbf{J})\,\mathbf{v}'}\\
&-\bar{\mathbf{v}}\,\nabla\cdot\bar{\mathbf{J}}-\overline{\mathbf{v}'\,\nabla\cdot\mathbf{J}}-(\nabla\bar{p})\,\bar{\mathbf{v}}-\overline{(\nabla p)\,\mathbf{v}'}-\bar{\mathbf{v}}\,\nabla\bar{p}\\
&-\overline{\mathbf{v}'\,\nabla p}-\bar{\rho}\,(\nabla\phi)\,\bar{\mathbf{v}}-\bar{\rho}\,\bar{\mathbf{v}}\,\nabla\phi\\
&-2\,\bar{\rho}\left\{(\boldsymbol{\Omega}\times\bar{\mathbf{v}})\,\bar{\mathbf{v}}+\boldsymbol{\Omega}\times\overline{\mathbf{v}'\,\mathbf{v}'}-\bar{\mathbf{v}}\,(\bar{\mathbf{v}}\times\boldsymbol{\Omega})-\overline{\mathbf{v}'\,\mathbf{v}'}\times\boldsymbol{\Omega}\right\}
\end{aligned}\right\}. \tag{6.184}$$

2. The first-order balance equation for momentum (Eq. (6.172)) is tensorially multiplied from left with the vector of the mean velocity, $\bar{\mathbf{v}}$, providing

$$\left.\begin{aligned}
&\frac{\partial}{\partial t}\left(\bar{\rho}\,\bar{\mathbf{v}}\,\bar{\mathbf{v}}\right)+\nabla\cdot\left(\bar{\rho}\,\bar{\mathbf{v}}\,\bar{\mathbf{v}}\,\bar{\mathbf{v}}\right)=-\left(\nabla\cdot\bar{\mathbf{J}}\right)\,\bar{\mathbf{v}}-\bar{\mathbf{v}}\,\nabla\cdot\bar{\mathbf{J}}\\
&-\left(\nabla\cdot\left(\bar{\rho}\,\overline{\mathbf{v}'\,\mathbf{v}'}\right)\right)\,\bar{\mathbf{v}}-\bar{\mathbf{v}}\,\nabla\cdot\left(\bar{\rho}\,\overline{\mathbf{v}'\,\mathbf{v}'}\right)-(\nabla\bar{p})\,\bar{\mathbf{v}}-\bar{\mathbf{v}}\,\nabla\bar{p}\\
&-\bar{\rho}\,(\nabla\phi)\,\bar{\mathbf{v}}-\bar{\rho}\,\bar{\mathbf{v}}\,\nabla\phi-2\,\bar{\rho}\,\{(\boldsymbol{\Omega}\times\bar{\mathbf{v}})\,\bar{\mathbf{v}}-\bar{\mathbf{v}}\,(\bar{\mathbf{v}}\times\boldsymbol{\Omega})\}
\end{aligned}\right\}. \tag{6.185}$$

Subtracting Eq. (6.185) from Eq. (6.184) and using the identity

$$\nabla\cdot\left(\overline{\mathbf{v}'\,\bar{\mathbf{v}}\,\mathbf{v}'}\right)=(\nabla\bar{\mathbf{v}})^{T}\cdot\overline{\mathbf{v}'\,\mathbf{v}'}+\bar{\mathbf{v}}\,\nabla\cdot\left(\overline{\mathbf{v}'\,\mathbf{v}'}\right)$$

finally yield

$$\left.\begin{aligned}
&\frac{\partial}{\partial t}\left(\bar{\rho}\,\overline{\mathbf{v}'\,\mathbf{v}'}\right)+\nabla\cdot\left\{\bar{\rho}\,\left(\bar{\mathbf{v}}\,\overline{\mathbf{v}'\,\mathbf{v}'}+\overline{\mathbf{v}'\,\mathbf{v}'\,\mathbf{v}'}\right)\right\}=-\,\bar{\rho}\,\overline{\mathbf{v}'\,\mathbf{v}'}\cdot\nabla\bar{\mathbf{v}}\\
&-(\nabla\bar{\mathbf{v}})^{T}\cdot\left(\bar{\rho}\,\overline{\mathbf{v}'\,\mathbf{v}'}\right)-\overline{(\nabla\cdot\mathbf{J})\,\mathbf{v}'}-\overline{\mathbf{v}'\,(\nabla\cdot\mathbf{J})}-\overline{(\nabla p)\,\mathbf{v}'}-\overline{\mathbf{v}'\,\nabla p}\\
&-2\,\bar{\rho}\,\left(\boldsymbol{\Omega}\times\overline{\mathbf{v}'\,\mathbf{v}'}-\overline{\mathbf{v}'\,\mathbf{v}'}\times\boldsymbol{\Omega}\right)
\end{aligned}\right\}. \tag{6.186}$$

Here, the first term on the l.h.s. of this equation is the local temporal change, the second and third terms represent the resolvable and the turbulent exchange of the

Reynolds stress with its environment. Furthermore, the first and second terms of the r.h.s. of this equation are production terms resulting from the kinematic interaction of the Reynolds stress and the gradient of the mean wind vector. The next two terms represent the destruction of Reynolds stress by molecular diffusion effects usually considered as negligible. The fifth and the sixth terms characterize the destruction of Reynolds stress by the interaction between the turbulent flow and pressure gradient forces. They have to be parameterized. The seventh term represents the interaction between the Earth rotation and the Reynolds stress, which we can neglect for averaging intervals less than 1 h or so.

We can derive the second-order balance equations for scalar quantities in a similar manner. In case of trace constituents, for instance, we obtain

$$\left.\begin{aligned} &\frac{\partial}{\partial t}\left(\bar{\rho}\,\overline{\mathbf{v}'\,\chi_m{}'}\right) + \nabla\cdot\left\{\bar{\rho}\,\left(\bar{\mathbf{v}}\,\overline{\mathbf{v}'\,\chi_m{}'} + \overline{\mathbf{v}'\,\mathbf{v}'\,\chi_m{}'}\right)\right\} = \\ &-\bar{\rho}\,\overline{\mathbf{v}'\,\mathbf{v}'}\cdot\nabla\overline{\chi_m} - \bar{\rho}\,\overline{\mathbf{v}'\,\chi_m{}'}\cdot\nabla\bar{\mathbf{v}} - \overline{\chi_m{}'\,\nabla\cdot\mathbf{J}} - \overline{\mathbf{v}'\,\nabla\cdot\mathbf{J}_{\chi_m}} \\ &-\overline{\chi_m{}'\,\nabla p} - 2\,\bar{\rho}\,\boldsymbol{\Omega}\times\left(\overline{\mathbf{v}'\,\chi_m{}'}\right) + \overline{\mathbf{v}'\,S_{\chi_m}} \end{aligned}\right\} \tag{6.187}$$

for $m = 1,\ldots,M$. The terms of this equation have a similar meaning like the corresponding terms of the second-order balance equation for momentum. Thus, the first term on the l.h.s. of this equation is the local temporal change, the second and third terms represent the resolvable and the turbulent exchange of eddy fluxes of trace constituents with its their environment. The first and second terms of the r.h.s. of this equation describe the production of eddy fluxes of trace species due to the kinematic interaction between the eddy fluxes of momentum and trace species on the one hand and the gradients of the mean mass fractions and the mean wind vector on the other hand. The next two terms represent the destruction of eddy fluxes of trace species by molecular diffusion effects, which we can consider as negligible. The fifth term describes the destruction of these eddy fluxes by interaction between the fluctuation of mass fraction and pressure gradient force, which has to be parameterized. Moreover, the seventh term is the interaction between the Earth's rotation and the eddy fluxes of trace species, which we can neglect for averaging intervals less than 1 h or so. The eighth term characterizes the interrelation between the turbulent flow and the production or depletion of trace species due to chemical reactions (Chap. 5).

We can derive the local balance equations for the covariance terms, $\bar{\rho}\,\overline{\chi_m{}'\,\chi_m{}'}$, $\bar{\rho}\,\overline{\chi_m{}'\,\Theta'}$, and $\bar{\rho}\,\overline{\chi_m{}'\,q_n{}'}$ similar to Eq. (6.187), and obtain

$$\left.\begin{aligned} &\frac{\partial}{\partial t}\left(\bar{\rho}\,\overline{\chi_m{}'\,\beta'}\right) + \nabla\cdot\left\{\bar{\rho}\,\left(\bar{\mathbf{v}}\,\overline{\chi_m{}'\,\beta'} + \overline{\mathbf{v}'\,\chi_m{}'\,\beta'}\right)\right\} = -\,\bar{\rho}\,\overline{\mathbf{v}'\,\beta'}\cdot\nabla\overline{\chi_m} \\ &-\bar{\rho}\,\overline{\mathbf{v}'\,\chi_m{}'}\cdot\nabla\bar{\beta} - \overline{\chi_m{}'\,\nabla\cdot\mathbf{J}_\beta} - \overline{\beta'\,\nabla\cdot\mathbf{J}_{\chi_m}} + \overline{\chi_m{}'\,S_\beta} + \overline{\beta'\,S_{\chi_m}} \end{aligned}\right\} \tag{6.188}$$

for $m = 1, \ldots, M$, where β stands for χ_m, Θ, and q_n, respectively. The terms $\overline{\chi_m{}' S_\beta}$ and $\overline{\beta' S_{\chi_m}}$ may be determined similar to $\overline{\mathbf{v}' S_{\chi_m}}$. Replacing χ_m by β in that equation leads to the local balance equation for variance terms for trace constituents, χ_m, potential temperature, Θ, and water substances, q_n, respectively.

As aforementioned, triple correlation terms occur in Eqs. (6.186)–(6.188) for which local balance equations can similarly be derived. These third-order balance equations, of course, contain fourth-order correlation terms. By assuming that the probability distribution of these fourth-order moments corresponds to a Gaussian probability density, we can approximate them as functions of second-moment terms.

To avoid the use of third-order balance equations, all triple correlation terms are usually parameterized by corresponding second-order terms, i.e. by one rank lower than the tensor that is to be parameterized. Recall the flux-gradient relationships discussed above based on similar principles.

The triple correlation term $\overline{\mathbf{v}' \mathbf{v}' \mathbf{v}'} = \overline{u_i' u_j' u_k'}$ for $i = 1, 2, 3$, $j = 1, 2, 3$, and $k = 1, 2, 3$, is a third-rank tensor and symmetric in all three indices. It may be parameterized by

$$\overline{u_i' u_j' u_k'} = -\Lambda \left(\frac{\overline{\mathbf{v}'^2}}{2} \right)^{1/2} \left\{ \frac{\partial}{\partial x_i} \left(\overline{u_j' u_k'} \right) + \frac{\partial}{\partial x_j} \left(\overline{u_i' u_k'} \right) + \frac{\partial}{\partial x_k} \left(\overline{u_i' u_j'} \right) \right\} \tag{6.189}$$

where x_1, x_2, and x_3 represent general coordinates. We can express the terms $\overline{\mathbf{v}' \mathbf{v}' \chi_i{}'}$ and $\overline{\mathbf{v}' \chi_m{}' \beta'}$ similarly by

$$\overline{\mathbf{v}' \mathbf{v}' \chi_i{}'} = -\Lambda \left(\frac{\overline{\mathbf{v}'^2}}{2} \right)^{1/2} \left\{ \nabla \left(\overline{\mathbf{v}' \chi_m{}'} \right) + \left(\nabla \left(\overline{\mathbf{v}' \chi_m{}'} \right) \right)^T \right\} \tag{6.190}$$

and

$$\overline{\mathbf{v}' \chi_m{}' \beta'} = -\Lambda \left(\frac{\overline{\mathbf{v}'^2}}{2} \right)^{1/2} \nabla \left(\overline{\chi_i{}' \beta'} \right). \tag{6.191}$$

We used the kinetic energy per unit mass of the eddying motion, $\overline{\mathbf{v}'^2}/2$, and a characteristic length, Λ in these parameterizations. The length scale may be related to either the scale of the mean motion or the scale of the eddying motion. The latter can be characterized by a **mixing length**. The use of the gradient in these parameterizations is required by the parameterized tensor. The minus sign ensures that turbulent energy is diffused down the gradient. Moreover, $\left(\nabla \left(\overline{\mathbf{v}' \chi_m{}'} \right) \right)^T$ means $\left(\overline{\mathbf{v}' \chi_m{}'} \right) \nabla$, i.e. the nabla operator acts on $\overline{\mathbf{v}' \chi_m{}'}$, but the tensorial product is arranged as shown. The tensor structure on the r.h.s. of Eq. (6.190) ensures the condition of a symmetric second-rank tensor $\overline{\mathbf{v}' \mathbf{v}' \chi_m{}'}$.

To parameterize the pressure gradient terms, we need an expression for the pressure gradient. In accord with the definition of the potential temperature (Eq. (2.41)), we can approximate the pressure gradient by

$$\nabla p = c_{p,0} \left\{ 1 + \sum_{n=1}^{3} \left(\frac{c_{p,n}}{c_{p,0}} - 1 \right) q_n \right\} \rho \, \Theta \, \nabla \pi \tag{6.192}$$

where $\pi = T/\Theta$ is the Exner function. The terms $\overline{(\nabla p)\ \mathbf{v}'}$ and $\overline{\mathbf{v}'\ \nabla p}$, and $\overline{\chi_{m'}\nabla p}$ may, therefore, be parameterized by

$$\left.\begin{aligned} \overline{(\nabla p)\ \mathbf{v}'} = \nabla \bar{\pi} \ \Bigg\{ \Bigg\{ 1 + \sum_{n=1}^{3} \left(\frac{c_{p,n}}{c_{p,0}} - 1 \right) \overline{q_n} \Bigg\} \ \mathbf{H} \\ + c_{p,0}\, \bar{\Theta} \sum_{n=1}^{3} \left(\frac{c_{p,n}}{c_{p,0}} - 1 \right) \mathbf{F}_{q_n} \Bigg\} + \nabla \left(\overline{\mathbf{v}'\, p'} \right) - \delta_1 \end{aligned} \right\} \tag{6.193}$$

$$\left.\begin{aligned} \overline{\mathbf{v}'\nabla p} = \Bigg\{ \Bigg\{ 1 + \sum_{n=1}^{3} \left(\frac{c_{p,n}}{c_{p,0}} - 1 \right) \overline{q_n} \Bigg\} \ \mathbf{H} \\ + c_{p,0}\, \bar{\Theta} \sum_{n=1}^{3} \left(\frac{c_{p,n}}{c_{p,0}} - 1 \right) \mathbf{F}_{q_n} \Bigg\} \ \nabla \bar{\pi} + \left(\nabla \left(\overline{\mathbf{v}'\, p'} \right) \right)^T - \delta_2 \end{aligned} \right\} \tag{6.194}$$

and

$$\left.\begin{aligned} \overline{\chi_{m'}\nabla p} = c_{p,0}\, \bar{\rho} \ \Bigg\{ \Bigg\{ 1 + \sum_{n=1}^{3} \left(\frac{c_{p,n}}{c_{p,0}} - 1 \right) q_n \Bigg\} \ \overline{\chi_{m'}\, \Theta'} \\ + \bar{\Theta} \sum_{n=1}^{3} \left(\frac{c_{p,n}}{c_{p,0}} - 1 \right) \overline{\chi_{m'}\, q_{n'}} \Bigg\} \cdot \nabla \bar{\pi} + \nabla \left(\overline{\chi_{m'}\, p'} \right) - \delta_3 \end{aligned} \right\}. \tag{6.195}$$

The terms δ_1 to δ_3 are usually considered as negligible. The so-called assumption on the **tendency-to-isotropy** is made. Rotta made this assumption to solve this second-order balance equation of momentum. In principle, it is not necessary to describe the interaction between the turbulent flow and the pressure gradient force. Equation (6.195) shows that the covariance terms $\bar{\rho}\,\overline{\chi_{m'}\,\Theta'}$ and $\bar{\rho}\,\overline{\chi_{m'}\,q_{n'}}$ are required to (numerically) solve the balance equation for eddy flux densities of trace constituents.

We can derive the second-order balance equation for the eddy flux densities of water substances and sensible heat similarly like Eqs. (6.186) and (6.187). Herein, we have to consider the interrelation between the turbulent flow and the radiative effects as well as the phase transition rates.

6.8.4.3 One-and-a-Half-Order Closure

The second-order closure principles fulfill all requirements associated with conservation equations, tensor properties, Galilean invariance, and dimensional properties. Even though these principles describe the simplest form of second-order closure, the mathematical-numerical effort for solving such a set of equations is extraordinarily high. Therefore, a combination of first-order, and second-order-closure principles was developed to reduce the mathematical-numerical and computational efforts. This combination is based on the local balance equation of the kinetic energy of the eddying motion, the turbulent kinetic energy abbreviated by TKE. It is called the one-and-a-half-order closure.

The Reynolds stress tensor that occurs in Eq. (6.186) is a symmetric tensor of second-rank. Its first scalar differs by a factor of 2 from the TKE. Since the first scalar of the Reynolds stress tensor is independent of the coordinate system, we can derive the local balance equation for TKE by mathematical reduction of Eq. (6.186) by double scalarly multiplying this equation by the identity tensor $\mathbf{E}$. By using the identity $\overline{\mathbf{v}' \cdot \nabla \cdot \mathbf{J}} = \nabla \cdot \left(\overline{\mathbf{v}' \cdot \mathbf{J}}\right) - \overline{\mathbf{J} : \nabla \mathbf{v}'}$ we obtain after a little algebra

$$\frac{\partial}{\partial t}\left(\bar{\rho}\,\frac{\overline{\mathbf{v}'^2}}{2}\right) + \nabla \cdot \left\{\bar{\rho}\left(\bar{\mathbf{v}}\,\frac{\overline{\mathbf{v}'^2}}{2} + \overline{\mathbf{v}'\,\frac{\mathbf{v}'^2}{2}}\right) + \overline{\mathbf{v}' \cdot \mathbf{J}}\right\} = -\overline{\mathbf{v}' \cdot \nabla p} - \overline{\varepsilon^*} - \mathbf{F} : \nabla \bar{\mathbf{v}} \quad (6.196)$$

where $\overline{\varepsilon^*} = -\overline{\mathbf{J} : \nabla \mathbf{v}'} > 0$ is the turbulent dissipation of kinetic energy into heat. Obviously, the local balance equation for TKE is a second-order equation. In accord with Eqs. (6.193) and (6.194), we obtain for $\overline{\mathbf{v}' \cdot \nabla p}$

$$\overline{\mathbf{v}' \cdot \nabla p} = \left\{ \left\{ 1 + \sum_{n=1}^{3} \left(\frac{c_{p,n}}{c_{p,0}} - 1\right) \overline{q_n} \right\} \mathbf{H} + c_{p,0}\,\bar{\Theta} \sum_{n=1}^{3} \left(\frac{c_{p,n}}{c_{p,0}} - 1\right) \mathbf{F}_{q_n} \right\} \cdot \nabla \bar{\pi} + \nabla \cdot \left(\overline{\mathbf{v}'\, p'}\right) - \delta \Bigg\}. \quad (6.197)$$

The term δ is also considered as negligible. Introducing the **flux Richardson number** defined by

$$Ri_f = \frac{\left\{ \left\{ 1 + \sum_{n=1}^{3} \left(\frac{c_{p,n}}{c_{p,0}} - 1\right) \overline{q_n} \right\} \mathbf{H} + c_{p,0}\,\bar{\Theta} \sum_{n=1}^{3} \left(\frac{c_{p,n}}{c_{p,0}} - 1\right) \mathbf{F}_{q_n} \right\} \cdot \nabla \bar{\pi}}{-\mathbf{F} : \nabla \bar{\mathbf{v}}} \quad (6.198)$$

yields

$$\left.\begin{aligned}\frac{\partial}{\partial t}\left(\bar{\rho}\,\frac{\overline{\mathbf{v}'^2}}{2}\right)+\nabla\cdot\left\{\bar{\rho}\left(\bar{\mathbf{v}}\,\frac{\overline{\mathbf{v}'^2}}{2}+\overline{\mathbf{v}'\,\frac{\mathbf{v}'^2}{2}}\right)+\overline{\mathbf{v}'\,p'}+\overline{\mathbf{v}'\cdot\mathbf{J}}\right\}\\ =-\overline{\varepsilon^*}-\left(1-Ri_f\right)\mathbf{F}:\nabla\bar{\mathbf{v}}\end{aligned}\right\}. \tag{6.199}$$

Herein, we transferred the term $\nabla\cdot\left(\overline{\mathbf{v}'\,p'}\right)$ in Eq. (6.197) to the l.h.s. of Eq. (6.199).

Obviously, the flux Richardson number expresses the relative importance of the two terms of TKE. The ratio of gain ($\overline{\mathbf{v}'\cdot\nabla p}<0$) or loss ($\overline{\mathbf{v}'\cdot\nabla p}>0$) of TKE due to Archimedean effects (Chap. 2) to the production of TKE that arise from the kinematic interrelation between the mean motion and the eddying motion ($-\mathbf{F}:\nabla\bar{\mathbf{v}}>0$). For stable stratification we have

$$Ri_f>0\ if\ \left\{\left\{1+\sum_{n=1}^{3}\left(\frac{c_{p,n}}{c_{p,0}}-1\right)\overline{q_n}\right\}\mathbf{H}+c_{p,0}\,\bar{\Theta}\sum_{n=1}^{3}\left(\frac{c_{p,n}}{c_{p,0}}-1\right)\mathbf{F}_{q_n}\right\}\cdot\nabla\bar{\pi}>0.$$

Unstable stratification is characterized by

$$Ri_f<0\ if\ \left\{\left\{1+\sum_{n=1}^{3}\left(\frac{c_{p,n}}{c_{p,0}}-1\right)\overline{q_n}\right\}\mathbf{H}+c_{p,0}\,\bar{\Theta}\sum_{n=1}^{3}\left(\frac{c_{p,n}}{c_{p,0}}-1\right)\mathbf{F}_{q_n}\right\}\cdot\nabla\bar{\pi}<0.$$

Neutral stratification means that $Ri_f=0$. Observations indicate that turbulence cannot be maintained even at smaller values of $Ri_f=1$. A critical value of $Ri_f=0.25$ is currently accepted. The condition

$$\left|\sum_{n=1}^{3}\left(\frac{c_{p,n}}{c_{p,0}}-1\right)\overline{q_n}\right|\ll 1$$

is usually fulfilled. Thus, we ignore this term in the following.

In Sect. 6.8.4.1, we learned that $\mathbf{K}_m$ is a fourth-rank tensor containing the eddy diffusivities for momentum, and $\mathbf{K}_h$, $\mathbf{K}_{q_n}$, and $\mathbf{K}_{\chi_m}$ are second-rank tensors containing the eddy diffusivities for sensible heat (subscript h), water substances (subscripts q_n), and trace constituents (subscripts χ_m), respectively. Thus, it is rather difficult to derive a general scheme for the one-and-a-half-order closure. Therefore, we only exemplarily present a scheme for horizontally homogeneous conditions. For such conditions, the terms $-\mathbf{F}:\nabla\bar{\mathbf{v}}$ and $\nabla\bar{\pi}$ become

$$- \mathbf{F} : \nabla \bar{\mathbf{v}} = - \bar{\rho}\, \overline{u' w'}\, \frac{\partial \bar{u}}{\partial z} - \bar{\rho}\, \overline{v' w'}\, \frac{\partial \bar{v}}{\partial z} = \boldsymbol{\tau} \cdot \frac{\partial \overline{\mathbf{v}_H}}{\partial z}. \tag{6.200}$$

In accord with the hydrostatic equation (2.7) $\partial \bar{p}/\partial z = - g\, \bar{\rho}$,

$$\frac{\partial \bar{\pi}}{\partial z} = - \frac{g}{c_p\, \bar{\Theta}}. \tag{6.201}$$

Here, $\boldsymbol{\tau} = - \bar{\rho}\, \overline{u' w'}\, \mathbf{i} - \bar{\rho}\, \overline{v' w'}\, \mathbf{j}$ is the **Reynolds stress vector**, $\overline{\mathbf{v}_H} = \bar{u}\, \mathbf{i} + \bar{v}\, \mathbf{j}$ is the mean horizontal wind vector, u, v, and w are the components of the wind vector with respect to the coordinate system sketched in Fig. 6.30, and g is the acceleration of gravity. Thus, for horizontally homogeneous conditions the local balance equation for TKE reads

$$\bar{\rho}\, \frac{\partial}{\partial t} \left(\frac{\overline{\mathbf{v}'^2}}{2} \right) + \frac{\partial}{\partial z} \left(\bar{\rho}\, \overline{w'\, \frac{\mathbf{v}'^2}{2}} + \overline{w'\, p'} + \overline{\mathbf{v}' \cdot \mathbf{J}} \right) = - \overline{\varepsilon^*} + \left(1 - Ri_f \right)\, \boldsymbol{\tau} \cdot \frac{\partial \overline{\mathbf{v}_H}}{\partial z} \tag{6.202}$$

where in case of moist air the corresponding flux Richardson number reads

$$Ri_f = - \frac{g}{c_p\, \bar{\Theta}}\, \frac{H + c_{p,0}\, \bar{\Theta} \left(\frac{c_{p,1}}{c_{p,0}} - 1 \right)\, F_{q_1}}{\boldsymbol{\tau} \cdot \frac{\partial \overline{\mathbf{v}_H}}{\partial z}}. \tag{6.203}$$

Here, $H = c_{p,0}\, \bar{\rho}\, \overline{w' \Theta'}$ and $F_{q_1} = \bar{\rho}\, \overline{w' q_1{}'}$ are the vertical components of the eddy flux densities of sensible heat and water vapor. Now, we can express the thermal stratification of the atmosphere for stable conditions by

$$Ri_f > 0 \quad if \quad H + c_{p,0}\, \bar{\Theta} \left(\frac{c_{p,1}}{c_{p,0}} - 1 \right) F_{q_1} < 0$$

and for unstable stratification by

$$Ri_f < 0 \quad if \quad H + c_{p,0}\, \bar{\Theta} \left(\frac{c_{p,1}}{c_{p,0}} - 1 \right) F_{q_1} > 0.$$

The flux-gradient relationships for momentum (subscript m), sensible heat (subscript h), water substances (subscript q_n), and trace constituents (subscript χ_m) now parameterize the respective eddy fluxes, i.e.

$$\tau_x = - \bar{\rho}\, \overline{u' w'} = \bar{\rho}\, K_m\, \frac{\partial \bar{u}}{\partial z} \qquad \tau_y = - \bar{\rho}\, \overline{v' w'} = \bar{\rho}\, K_m\, \frac{\partial \bar{v}}{\partial z} \tag{6.204}$$

$$H = - c_{p,0}\, \bar{\rho}\, K_h\, \frac{\partial \overline{\Theta}}{\partial z} \tag{6.205}$$

$$F_{q_n} = - \bar{\rho}\, K_{q_n}\, \frac{\partial \overline{q}_n}{\partial z} \tag{6.206}$$

and

$$F_{\chi_m} = -\bar{\rho}\, K_{\chi_m} \frac{\partial \overline{\chi}_m}{\partial z}. \tag{6.207}$$

The quantities K_m, K_h, K_{q_n}, and K_{χ_m} are the corresponding eddy diffusivities with respect to the vertical direction. These quantities essentially depend on the dynamic and thermodynamic state of the ABL and, therefore, notably on height. We can relate them to each other by the turbulent Prandtl number

$$Pr_t = \frac{K_m}{K_h} \tag{6.208}$$

the turbulent **Schmidt number** for water substances and trace constituents,

$$Sc_{t,q_n} = \frac{K_m}{K_{q_n}} \qquad Sc_{t,\chi_m} = \frac{K_m}{K_{\chi_m}} \tag{6.209}$$

and the turbulent **Lewis**[37]**-Semenov** number for water substances and trace constituents,

$$LS_{t,q_n} = \frac{K_h}{K_{q_n}} \qquad LS_{t,\chi_m} = \frac{K_h}{K_{\chi_m}}. \tag{6.210}$$

In ABL models, K_{q_n} and K_{χ_m} are related to that for sensible heat by $K_{\chi_m} = K_{q_n} = K_h$. The use of a common eddy diffusivity for all scalar quantities is based on empirical results that the turbulent transfer of water vapor and sensible heat is similar. It is adopted to other scalar quantities as well.

We can parameterize the vertical component of the TKE eddy flux density by a gradient approach, i.e.

$$\bar{\rho}\, \overline{w' \frac{\mathbf{v}'^2}{2}} = -\bar{\rho}\, K_e \frac{\partial}{\partial z} \left(\overline{\frac{\mathbf{v}'^2}{2}} \right) \tag{6.211}$$

where K_e is customarily related to the eddy diffusivity for momentum, i.e. $K_e = K_m$.

Replacing the covariance terms in Eqs. (6.202) and (6.203) by the corresponding flux-gradient relationships Eqs. (6.204)–(6.206), and (6.211) yields

$$\left.\begin{aligned} \frac{\partial}{\partial t} \left(\overline{\frac{\mathbf{v}'^2}{2}} \right) = &- \frac{1}{\bar{\rho}} \frac{\partial}{\partial z} \left(-\bar{\rho}\, K_m \frac{\partial}{\partial z} \left(\overline{\frac{\mathbf{v}'^2}{2}} \right) + \overline{w'\, p'} + \overline{\mathbf{v}' \cdot \mathbf{J}} \right) \\ &- \frac{\overline{\varepsilon^*}}{\bar{\rho}} + \left(1 - \frac{Ri}{\mathrm{Pr}_t} \right) K_m \left(\frac{\partial \overline{\mathbf{v}}_H}{\partial z} \right)^2 \end{aligned}\right\}. \tag{6.212}$$

[37] Warren Kendall Lewis, American chemical engineer, 1882–1975.

The quantity

$$Ri = \frac{g}{c_p\,\bar{\Theta}}\,\frac{\dfrac{\partial\bar{\Theta}}{\partial z} + c_{p,0}\,\bar{\Theta}\left(\dfrac{c_{p,1}}{c_{p,0}} - 1\right)\dfrac{\partial\overline{q_1}}{\partial z}}{\left(\dfrac{\partial\overline{\mathbf{v}_H}}{\partial z}\right)^2} = Pr_t\,Ri_f \tag{6.213}$$

is the **gradient-Richardson number**.

Obviously, Eq. (6.212) contains four unknown quantities, $\overline{w'\,p'}$, $\overline{\mathbf{v}'\cdot\mathbf{J}}$, $\overline{\varepsilon^*}$, and Pr_t. The term $\overline{\mathbf{v}'\cdot\mathbf{J}}$ can be neglected. Also the pressure term $\overline{w'\,p'}$ can often be ignored in comparison with the transfer of TKE. Nevertheless, two of these four terms have to be parameterized, namely $\overline{\varepsilon^*}$ and Pr_t. The turbulent dissipation ε^* is usually expressed by the **Kolgomorov**[38]**-Obukhov**[39] relation

$$\bar{\varepsilon} = \frac{\overline{\varepsilon^*}}{\bar{\rho}} = \frac{c_e}{\Lambda}\left(\frac{\overline{\mathbf{v}'^2}}{2}\right)^{3/2} \tag{6.214}$$

where $c_e \cong 0.31$ is a constant, $\bar{\varepsilon}$ is the rate of dissipation of turbulent energy per unit mass, and Λ is the mixing length, i.e. a characteristic length scale of turbulent motion. This mixing length Λ has to be specified.

Inserting this equation into Eq. (6.212) yields

$$\left.\begin{aligned}\frac{\partial}{\partial t}\left(\frac{\overline{\mathbf{v}'^2}}{2}\right) = \frac{1}{\bar{\rho}}\,\frac{\partial}{\partial z}\left\{\bar{\rho}\,K_m\,\frac{\partial}{\partial z}\left(\frac{\overline{\mathbf{v}'^2}}{2}\right)\right\} - \frac{c_e}{\Lambda}\left(\frac{\overline{\mathbf{v}'^2}}{2}\right)^{3/2}\\ + \left(1 - \frac{Ri}{Pr_t}\right)K_m\left(\frac{\partial\overline{\mathbf{v}_H}}{\partial z}\right)^2\end{aligned}\right\}. \tag{6.215}$$

This form of the balance equation of TKE has been used in several ABL models. This TKE equation has to be solved numerically.

We can express the eddy diffusivity K_m by the TKE using the Kolmogorov-Prandtl relation

$$K_m = c_m\left(\frac{\overline{\mathbf{v}'^2}}{2}\right)^{1/2}\Lambda \tag{6.216}$$

where c_m is another constant. Combining Eqs. (6.214) and (6.216) yields

$$\bar{\varepsilon} = \frac{\overline{\varepsilon^*}}{\bar{\rho}} = C\,\frac{{K_m}^3}{\Lambda^4}. \tag{6.217}$$

[38] Andrey Nikolaevich Kolmogorov, Russian mathematician, 1903–1984.

[39] Alexander Mikhailovich Obukhov, Russian physicist, 1918–1989.

Here, C is also a constant. We can arbitrarily choose $C = 1$. This equation is the **Heisenberg**[40]**-von Weizsäcker**[41] relation. Inserting the relation into Eq. (6.212) provides

$$\frac{\partial}{\partial t}\left(\frac{\overline{\mathbf{v}'^2}}{2}\right) = \frac{1}{\bar{\rho}}\frac{\partial}{\partial z}\left\{\bar{\rho}\,K_m\,\frac{\partial}{\partial z}\left(\frac{\overline{\mathbf{v}'^2}}{2}\right)\right\} - C\,\frac{{K_m}^3}{\Lambda^4} + \left(1 - \frac{Ri}{Pr_t}\right) K_m \left(\frac{\partial \overline{\mathbf{v}_H}}{\partial z}\right)^2 \Bigg\}. \tag{6.218}$$

For steady-state conditions when ignoring the divergence term, we obtain

$$K_m = \frac{1}{\sqrt{C}}\,\Lambda^2 \left|\frac{\partial \overline{\mathbf{v}_H}}{\partial z}\right| \left(1 - \frac{Ri}{Pr_t}\right)^{1/2}. \tag{6.219}$$

This typical form of the eddy diffusivity for momentum describes that K_m depends on both the wind shear and the thermal stratification characterized by the gradient-Richardson number and the turbulent Prandtl number.

6.8.5 The Atmospheric Boundary Layer

6.8.5.1 Introductory Remarks

As sketched in Fig. 6.31, the ABL is bordered by the Earth's surface (land and water surfaces), called the lower boundary, and the free atmosphere, called the upper boundary. This boundary is usually indicated by a temperature inversion (Chap. 2). The ABL has a typical thickness of about 1 km or so, but spatial, diurnal and seasonal variations exist. Both the ABL and the free atmosphere form the troposphere, in which most of the atmospheric processes occur that are responsible for our weather (Chap. 1). Its top is the tropopause. The troposphere has an averaged thickness of about 11 km. However, spatial, diurnal and seasonal variations occur (Chap. 7).

In the free atmosphere, turbulent friction plays a minor role. In the ABL, however, the dynamic behavior of the air is strongly affected by turbulent friction (molecular friction always exists, but plays only a minor role) mainly generated by wind shear (mechanically generated turbulence) in the vicinity of the Earth's surface. Here usually the strongest wind shear occurs. Beside this mechanically generated turbulence, thermally induced turbulence associated with convection

[40] Werner Karl Heisenberg, German physicist, 1901–1976.

[41] Carl Friedrich von Weizsäcker, German physicist, 1912–2007.

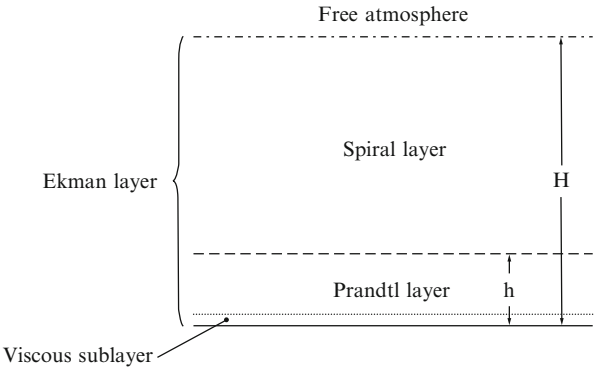

Fig. 6.31 Sketch of the atmospheric boundary layer (ABL) also denoted as the Ekman layer. The Prandtl layer is also called the atmospheric surface layer (ASL) or the constant flux layer. The boundary layer height is denoted by H and the thickness of the Prandtl layer by h. The quantities $\mathbf{v}$, Θ, and q_1 denote the wind vector, the potential temperature, and the specific humidity

especially occurs during daytime (Chaps. 2 and 3). Both forms of turbulence usually coexist. During nighttime, mainly over land, however, mechanically generated turbulence is thermally consumed. We have to consider this consumption when we discuss the physics of the ABL. Following Stull, we define the ABL *as that part of the troposphere that is directly influenced by the presence of the Earth's surface and that responds to surface forcing with a timescale of about an hour or less*. This surface forcing is related to the radiation balance, i.e. the incoming solar and thermal radiation absorbed at the Earth's surface and the outgoing thermal radiation (Chap. 4). Since the latter depends on the surface temperatures of the foliage and the soil, the radiation balance is indirectly affected by frictional drag, evaporation and transpiration (usually gathered to **evapotranspiration**), atmospheric heat transfer and the transfer of heat and water within the soil (Chaps. 4 and 5).

The turbulent nature of the ABL is one of its most conspicuous and important features. As at the top of the ABL, the influence of the Earth's surface vanishes, the turbulent transports of sensible heat and matter and the turbulent friction stress must decrease with height. The latter causes a strong change in wind speed and wind direction that we can qualitatively describe by the Ekman spiral (Fig. 6.33). Therefore, the ABL is called the **Ekman**[42] **layer**.

The lowest layer of the ABL is the **Prandtl**[43] **layer** or atmospheric surface layer (ASL). Its thickness is usually assumed as $h \cong H/10$. This value, however, is not well scrutinized. Two of the most conspicuous and important features of the Prandtl layer are that

[42] Vagn Walfrid Ekman, Swedish oceanographer, 1874–1954.

[43] Ludwig Prandtl, German aeronautical engineer, 1875–1953.

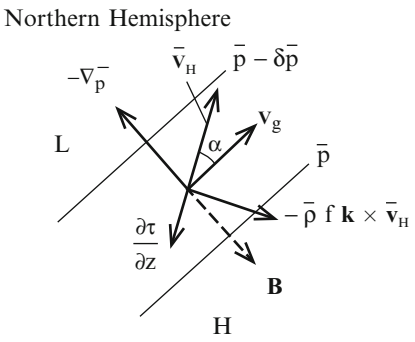

Fig. 6.32 The balance of forces in a mean horizontal flow considered as being in a stationary state (see Eq. (6.221)). The mean horizontal wind vector $\langle \mathbf{v}_H \rangle = \bar{\mathbf{v}}_H$ and the cross-isobar flow angle α are indicated. Also shown is the balance force **B** resulting from the Coriolis force, $-\bar{\rho}\, f\, \mathbf{k} \times \bar{\mathbf{v}}_H$, and the turbulent friction force $\frac{\partial \boldsymbol{\tau}}{\partial z}$

1. The Reynolds stress vector is nearly invariant with height, and
2. Its direction well coincides with that of the vector of the mean horizontal wind speed.

In this layer, the change in wind direction with increasing height is of minor importance. Under the condition of neutral stratification (i.e. atmospheric turbulence is mainly generated mechanically; Chap. 2) a logarithmic wind profile is usually established. As in the Prandtl layer, the vertical components of the turbulent flux densities of sensible heat and water vapor are also nearly invariant with height, this layer is also called the **constant flux layer** (Chap. 5).

In regions of fully developed turbulence, we can neglect molecular transfer effects in comparison with turbulent transfer effects. The same is true for the entire Prandtl layer except for the **viscous sublayer** in the immediately vicinity of the Earth's surface. This layer has a thickness of a few millimeters. In this layer, molecular diffusion controls and limits the transfer of sensible heat and gaseous matter strongly (Chaps. 3 and 5). Whereas momentum is transmitted to the Earth's surface by skin friction and by form drag. Only the former has an analogy in mass and heat transfer by molecular diffusion.

6.8.5.2 Ekman Physics

The Ekman physics deals with a pure horizontal flow that obeys the conditions of horizontal homogeneity and stationary state, where the pressure-gradient force is balanced by the Coriolis force, and the turbulent friction force as illustrated in Fig. 6.32 for the Northern Hemisphere. As the effect of turbulent friction decreases with height, wind speed increases, and simultaneously turns to the right on the Northern Hemisphere by approaching the direction of the geostrophic wind. The change in direction with increasing height is due to the fact that the pressure-gradient force is balanced more and more by the Coriolis force due to the decreasing turbulent friction.

Small-scale eddies can transfer momentum that to some degree is similar to molecular momentum transfer. Therefore, the transport of momentum by small-

scale eddies is often denoted as **eddy diffusion**. The coefficients applied in the description of this transport are the **turbulent diffusion coefficients**. However, this approach has several problems because eddies can be of organized structure, while molecules cannot.

As aforementioned, a vertical gradient of the frictional stress exists. Consequently, there is a horizontal force per unit mass on the large-scale. However, when we assume barotropic conditions so that the geostrophic wind is independent of height, and consider the eddy diffusivity also as height-invariant, we can simplify the equation to a homogeneous differential equation of second order for the ageostrophic wind resulting from friction. The governing equation for a horizontally uniform flow then reads

$$\bar{\rho}\,\frac{\partial\overline{\mathbf{v}_H}}{\partial t} = -\,\bar{\rho}\,f\,\mathbf{k}\times\left(\overline{\mathbf{v}_H}-\mathbf{v}_g\right)+\frac{\partial\boldsymbol{\tau}}{\partial z}. \tag{6.220}$$

This equation corresponds to Eq. (6.174), where we can express the equation of continuity (6.173) by $\nabla\cdot\bar{\mathbf{v}} = 0$ (incompressible fluid), i.e. $\partial\bar{\rho}/\partial t = 0$ and $\nabla\bar{\rho} = 0$. Consequently, the equation of continuity becomes a diagnostic equation. For horizontally homogeneous conditions, this simplified continuity equation leads to $\partial\bar{w}/\partial z = 0$ and, hence, to $\bar{w} = const$. As the wind vector, $\bar{\mathbf{v}}$, vanishes at a rigid surface, this constant must be equal to zero. Over moving boundaries like water surfaces, we have to additionally presuppose that $\bar{w} = 0$.

When we assume steady-state conditions we obtain

$$0 = -\,\bar{\rho}\,f\,\mathbf{k}\times\left(\overline{\mathbf{v}_H}-\mathbf{v}_g\right)+\frac{\partial\boldsymbol{\tau}}{\partial z}. \tag{6.221}$$

As an example of first-order closure of turbulence (Sect. 6.8.4.1), the components of the Reynolds stress vector were parameterized by flux-gradient relationships, i.e.

$$\tau_x = -\,\bar{\rho}\,\overline{u'w'} = \bar{\rho}\,K_m\,\frac{\partial\bar{u}}{\partial z} \qquad\qquad \tau_y = -\,\bar{\rho}\,\overline{v'w'} = \bar{\rho}\,K_m\,\frac{\partial\bar{v}}{\partial z}$$

where K_m is the eddy diffusivity for momentum (Eq. (6.204)). Here, we consider K_m as independent of height. We also consider the mean air density $\bar{\rho}$, and the geostrophic wind vector $\mathbf{v}_g$ as independent of height. Thus,

$$K_m\,\frac{\partial^2\mathbf{v}_a}{\partial z^2} - f\,\mathbf{k}\times\mathbf{v}_a = 0 \tag{6.222}$$

with the ageostrophic wind component $\mathbf{v}_a = \overline{\mathbf{v}_H} - \mathbf{v}_g$ or in Cartesian coordinates

$$K_m\,\frac{\partial^2 u_a}{\partial z^2} + f\,v_a = 0 \qquad\qquad K_m\,\frac{\partial^2 v_a}{\partial z^2} - f\,u_a = 0.$$

These equations are the **Ekman equations**.

Putting the Ekman equations into the complex plane by separating the velocity vectors in real and imaginary parts, multiplying by i (where $i^2 = -1$), lead to a homogeneous differential equation of second order

$$\frac{\partial^2 \Phi}{\partial z^2} - i \, \frac{f}{K_m} \, \Phi = 0 \tag{6.223}$$

where $\Phi = u_a + i \, v_a = \bar{u} - u_g + i \, \left(\bar{v} - v_g\right)$. This type of differential equation requires two boundary conditions. Its general solution reads

$$\Phi = C_1 \, \exp\{a \, (1+i) \, z\} + C_2 \, \exp\{-a \, (1+i) \, z\} .$$

We can determine the parameter a by introducing this general solution into Eq. (6.223). We obtain $a = \sqrt{f/(2 \, K_m)}$. The reciprocal of this parameter has the dimension of a length. Therefore, $L_E = a^{-1}$ is called the **Ekman length**. We have to determine the constants C_1 and C_2 from the boundary conditions given by

$$\Phi = \begin{cases} - \left(u_g + i \, v_g\right) & \text{for z} = 0 \\ 0 & \text{for z} \to \infty \end{cases}$$

i.e. $\bar{u}$ and $\bar{v}$ are equal to zero at the Earth's surface, and $\bar{u} = u_g$ and $\bar{v} = v_g$ when z tends to infinity. These boundary conditions can only be fulfilled when $C_1 = 0$ and $C_2 = - \left(u_g + i \, v_g\right)$. Inserting these expressions into Eq. (6.223) and separately considering the real part and the imaginary part yield

$$\left.\begin{aligned} \bar{u} &= u_g \, \{1 - \exp(-a \, z) \, \cos(a \, z)\} - v_g \, \exp(-a \, z) \, \sin(a \, z) \\ \bar{v} &= v_g \, \{1 - \exp(-a \, z) \, \cos(a \, z)\} + u_g \, \exp(-a \, z) \, \sin(a \, z) \end{aligned}\right\} . \tag{6.224}$$

When we arbitrarily choose $u_g = \left|\mathbf{v}_g\right|$ and $v_g = 0$, we obtain the special solution

$$\left.\begin{aligned} \bar{u} &= u_g \, \{1 - \exp(-a \, z) \, \cos(a \, z)\} \\ \bar{v} &= u_g \, \exp(-a \, z) \, \sin(a \, z) \end{aligned}\right\} \tag{6.225}$$

that is illustrated in Fig. 6.33. The tip of the wind vector described by this equation set traces out a spiral called the Ekman spiral[44]

[44] Originally Ekman derived this relationship for the ocean by using the kinematic viscosity of water instead of the eddy diffusivity for momentum. Ekman also adduced some arguments in favor of using his results to describe the variation of wind speed with height over land. Later, independently of each other, Akerblom in 1908 and Exner in 1912 realized Ekman's idea. Exner was the first who combined both the planetary boundary layers of the ocean, and the atmosphere in a single dynamic system.

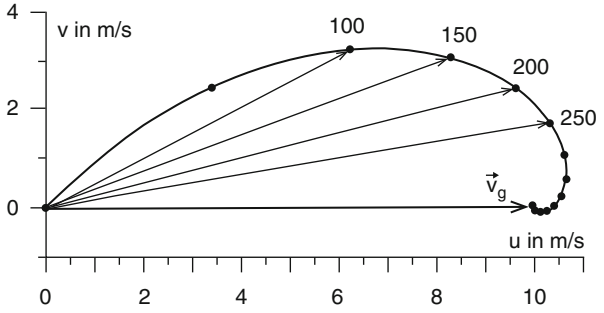

Fig. 6.33 Ekman spiral. Simple model of the increase and change of the horizontal wind with height in the ABL caused by friction. The numbers adjacent to the *wind arrows* give the height in *m* for which these wind vectors are valid. $\mathbf{v}_g$ stands for the geostrophic wind. The *dots* indicate the components of the horizontal wind speed according a 50 m distance of the coordinates (From Kraus (2000))

Table 6.2 Deviation angle of wind in dependence of the surface roughness, geographical latitude, and thermal stability of the atmosphere (From Haltiner and Martin (1957))

	$\varphi = 20°$			$\varphi = 45°$			$\varphi = 70°$		
	Unstable	Neutral	Stable	Unstable	Neutral	Stable	Unstable	Neutral	Stable
Ocean	25°	30°	40°	15°	20°	30°	10°	15°	25°
Smooth land	35°	40°	50°	25°	30°	40°	20°	25°	35°
Medium rough land	40°	45°	55°	30°	35°	45°	25°	30°	40°
Rough land	45°	50°	60°	35°	40°	50°	30°	40°	45°

The angle between the mean horizontal wind vector and the geostrophic wind vector is related to

$$\tan \alpha = \frac{\bar{v}}{\bar{u}} = \frac{\exp(-a\,z)\ \sin(a\,z)}{1 - \exp(-a\,z)\ \cos(a\,z)}. \tag{6.226}$$

When $z = 0$, this equation is indeterminate because $\tan \alpha = 0/0$. However, we can derive a limiting value of $\tan \alpha = 1$ and, hence, $\alpha = 45°$ by using de L'Hôspital's rule when z tends to zero. In reality, the deviation of wind with height due to friction depends on thermal stability, geographic latitude, and the roughness of the surface (Table 6.2; Chaps. 2 and 7).

Since the Ekman spiral is based on first-order-closure principles, we can use Eq. (6.225) to determine the components of the Reynolds stress vector. Thus, we obtain

$$\left.\begin{aligned} \tau_x &= \bar{\rho}\, K_m\, \frac{\partial \bar{u}}{\partial z} = \bar{\rho}\, K_m\, a\, u_g\ \{\sin(a\,z) + \cos(a\,z)\}\ \exp(-a\,z) \\ \tau_y &= \bar{\rho}\, K_m\, \frac{\partial \bar{v}}{\partial z} = \bar{\rho}\, K_m\, a\, u_g\ \{\cos(a\,z) - \sin(a\,z)\}\ \exp(-a\,z) \end{aligned}\right\} \tag{6.227}$$

and for the magnitude of $\boldsymbol{\tau}$ (i.e. $\tau = |\boldsymbol{\tau}|$),

$$\tau = \left({\tau_x}^2 + {\tau_y}^2\right)^{1/2} = \sqrt{2}\ \bar{\rho}\ K_m\ a\ u_g\ \exp\left(-\ a\ z\right).$$

For $z = 0$, we obtain

$$\tau|_{z=0} = \sqrt{2}\ \bar{\rho}\ K_m\ a\ u_g = \bar{\rho}\ u_g\ \sqrt{f\ K_m}. \tag{6.228}$$

Thus, we express the magnitude of the Reynolds stress vector by

$$\tau = \tau|_{z=0}\ \exp\left(-\ a\ z\right).$$

Inserting the **friction velocity** defined by $u_* = +\sqrt{\tau/\bar{\rho}}$ yields

$$u_* = u_{*,0}\ \exp\left(-\ \frac{a\ z}{2}\right)$$

where $u_{*,0} = \left({u_g}^2\ f\ K_m\right)^{1/4}$. Using the definition of the friction velocity and the gradient approach (6.204) provides

$${u_*}^2 = \frac{\tau}{\bar{\rho}} = K_m\ \left|\frac{\partial \overline{\mathbf{v}}_H}{\partial z}\right|. \tag{6.229}$$

We can infer from Eq. (6.224) that the conditions $\bar{u} = u_g$ and $\bar{v} = v_g$ are exactly fulfilled when z tends to infinity. This means that the ABL would tend to infinity. The latter is impracticable because of the finite height of the ABL. Therefore, within the framework of the Ekman physics, we consider the height of the Ekman layer, H_E, as that height where the direction of the horizontal wind vector first coincides with that of the geostrophic wind vector. We can infer this height from Eq. (6.225) by considering $\bar{v} = 0$ for $H_E > 0$. This condition is fulfilled when $\sin\left(a\ H_E\right) = 0$, i.e. when $\pi = a\ H_E$. Thus, we obtain

$$H_E = \pi\ \sqrt{\frac{2\ K_m}{f}}.$$

For $z = H_E$ equation set (6.225) provides $\bar{u} = u_g\ \{1 + \exp\left(-\ \pi\right)\} \cong 1.043\ u_g$, i.e. at this height, the magnitude of the horizontal wind vector exceeds that of the geostrophic wind vector. We call such a wind speed super-geostrophic wind speed. We can derive the height h_{max}, at which the maximum of $|\overline{\mathbf{v}}_H|$ occurs, from the optimum condition $\frac{d}{dz}\ |\overline{\mathbf{v}}_H| = 0$. Then, we obtain $h_{\max} \cong 0.727\ H_E$. For this height equation set (6.225) provides $|\overline{\mathbf{v}}_H| \cong 1.069\ u_g$.

Recall, the increase of wind speed and the change in wind direction with height due to friction depend on geographic latitude, thermal stability, and the roughness of the surface (Table 6.2; Chaps. 2 and 7). Thus, in real situations, numerical solutions

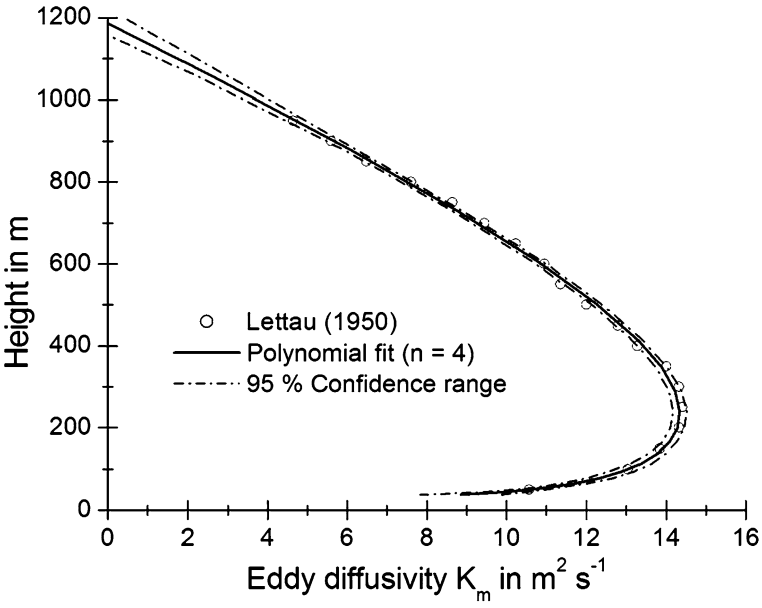

Fig. 6.34 Eddy diffusivity K_m determined by Lettau (1950) on the basis of the Leipzig wind profile

are indispensable because the eddy diffusivity depends on the mechanical and thermal states of the ABL, and, hence, on height. This dependency is illustrated in Fig. 6.34 that is based on Lettau's[45] re-examination of the "Leipzig wind profile", an example of a representative wind distribution in the frictional layer. It is based on Mildner's set of 28 pilot-balloon (Appendix B) observations with two theodolites on October 20, 1931, near Leipzig, Germany. The observations were taken in a uniform "warm" air mass of stable weather conditions with no indication of convectional processes. Lettau's re-examination is based on Eq. (6.221) integrated over the height interval $[0,\ z]$,

$$\boldsymbol{\tau}\,(z) - \boldsymbol{\tau}\,(0) = \int_0^z \bar{\rho}\ f\ \mathbf{k} \times \left(\overline{\mathbf{v}_H} - \mathbf{v}_g\right)\ dz \tag{6.230}$$

and the flux-gradient approach (6.229) in its rearranged form

$$K_m = \frac{\tau}{\bar{\rho}} \left\{ \left(\frac{\partial \bar{u}}{\partial z} \right)^2 + \left(\frac{\partial \bar{v}}{\partial z} \right)^2 \right\}^{-1/2}. \tag{6.231}$$

[45] Heinz Helmut Lettau, German-American meteorologist, 1909–2005.

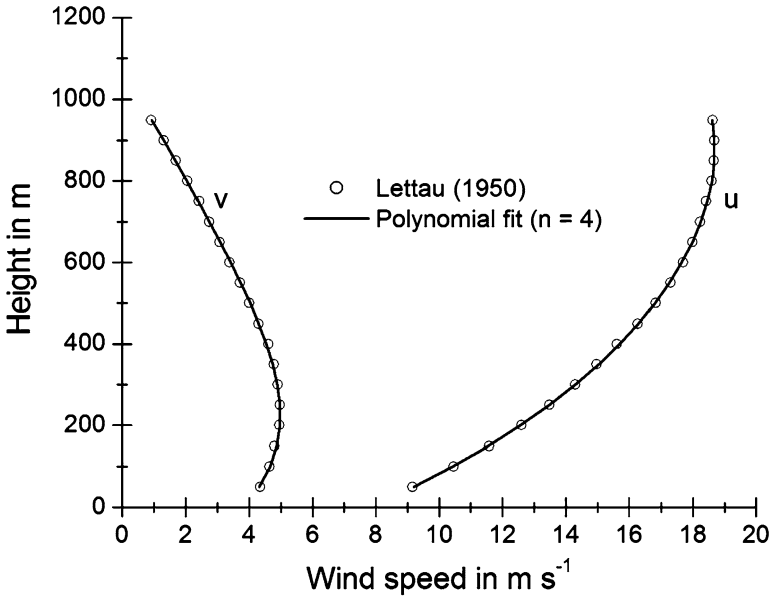

Fig. 6.35 Mildner's Leipzig wind profile (Data taken from Lettau (1950) also fitted by polynomials of fourth-order)

The eddy diffusivity strongly varies with height. This variation can be adequately fitted by a polynomial of fourth-order. The components of the Leipzig wind profile are shown in Fig. 6.35. These components can also be adequately fitted polynomials of fourth-order as well.

Nevertheless, we can apply the results of the Ekman equations to test numerical procedures used in ABL models, and to simply initialize mesoscale numerical models. Such numerical models not only include the local balance equation for momentum (Eq. (6.220)), but also similar equations for water substances and trace constituents, and the prognostic equation for potential temperature (Eqs. (6.176)–(6.179). For horizontally homogeneous conditions as considered in this subsection, these equations read

$$\bar{\rho}\,\frac{\partial \overline{q_n}}{\partial t} + \frac{\partial}{\partial z}\left(\overline{J_{q_n}} + F_{q_n}\right) = \overline{S_{q_n}} \quad for\ n = 1, 2, 3 \tag{6.232}$$

$$\bar{\rho}\,\frac{\partial \overline{\chi_m}}{\partial t} + \frac{\partial}{\partial z}\left(\overline{J_{\chi_m}} + F_{\chi_m}\right) = \overline{S_{\chi_m}} \quad for\ m = 1, \ldots, M \tag{6.233}$$

and

$$c_p\,\bar{\rho}\,\bar{\pi}\,\frac{\partial \bar{\Theta}}{\partial t} + \frac{\partial}{\partial z}\left(\bar{R} + \overline{J_h} + \bar{\pi}\,H\right) = \overline{\varepsilon^*} + \lambda_{q_2 q_1}\,\overline{S_{q_2}} + \lambda_{q_3 q_1}\,\overline{S_{q_3}}. \tag{6.234}$$

In case of particulate matter like water droplets, ice particles, and aerosols the macroscopic fluxes $\overline{J_{q_n}}$ and $\overline{J_{\chi_m}}$ also contain transport by sedimentation. Thus, they cannot generally be ignored. In case of the viscous sublayer, molecular effects have to be considered. The turbulent dissipation of TKE can be ignored in Eq. (6.234) because its small magnitude compared with those of the other terms.

We can only solve the equation set (6.220) and (6.232)–(6.234) numerically. We can parameterize the eddy flux terms τ_x, τ_y, F_{q_n}, F_{χ_m}, and H using gradient approaches (Eqs. (6.204)–(6.207), (Sect. 6.8.4.3)), where the local balance equation for TKE (Eq. (6.215)) serves to determine the eddy diffusivity for momentum, K_m. To specify the mixing length that occurs in Eq. (6.215) we use **Blackadar[46]'s mixing length** for neutral stratification given by

$$\Lambda_B = \frac{\kappa\ (z-d)}{1+\frac{\kappa\,(z-d)}{\lambda_{\max}}}. \tag{6.235}$$

Here, $\kappa \approx 0.4$ is the von Kármán constant, d is the zero-plane displacement that we have to consider in case of landscapes covered by vegetation, and $\lambda_{\max}$ represents the value reached by Λ_B in the free atmosphere. This quantity is related to the magnitude of the geostrophic wind vector and the Coriolis parameter by

$$\lambda_{\max} = 2.7 \cdot 10^{-4}\,\frac{|\mathbf{v}_g|}{f}. \tag{6.236}$$

For small values of $z-d$ Blackadar's mixing length approaches to that of Prandtl given by $\Lambda_P = \kappa(z-d)$. Blackadar's mixing length is also based on Lettau's re-examination of the Leipzig wind profile (Fig. 6.36).

Ekman Pumping

As illustrated by Fig. 6.33, below the height of the Ekman layer, H_E, the horizontal wind vector has a component that is perpendicular to the direction of the geostrophic wind vector and points towards the low pressure. This ageostrophic component is responsible for a cross-isobaric transport of matter (and heat). Since we are interested to outline the effect of this ageostrophic transport of matter, we simply describe it on the basics of the Ekman physics. Thus, we consider the Ekman solution (6.225), i.e. there is no y-component of the geostrophic wind vector. Furthermore, we assume incompressibility, i.e. $\nabla \cdot \bar{\mathbf{v}} = 0$ is fulfilled.

The ageostrophic mass transport per unit area at any level in the ABL is given by $\bar{\rho}\,\bar{v}$. The net mass transport for a column of unit width extending vertically through the entire layer reads

[46] Alfred K. Blackadar, American meteorologist, born 1920.

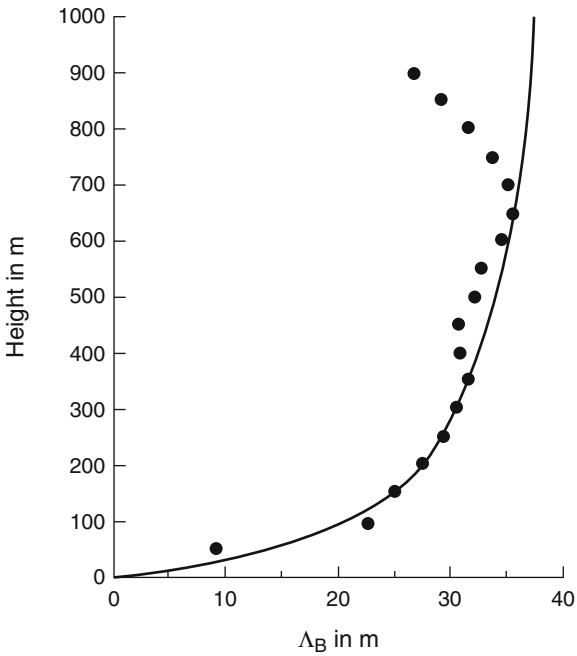

Fig. 6.36 Vertical distribution of the mixing length Λ_B for Lettau's (1950) re-examination of the Leipzig wind profile. The *dots* represent calculated values and the line Eqs. (6.235) and (6.236) (From Blackadar (1962))

$$M = \int_0^{H_E} \bar{\rho}\,\bar{v}\,dz = \int_0^{H_E} \bar{\rho}\,u_g\ \exp(-a\,z)\ \sin(a\,z)\ dz. \tag{6.237}$$

The condition of incompressibility provides

$$\frac{\partial \bar{v}}{\partial y} + \frac{\partial \bar{w}}{\partial z} = 0 \tag{6.238}$$

because $\partial \bar{u}/\partial x = \partial u_g/\partial x\,\{1 - \exp(-a\,z)\,\cos(a\,z)\} = 0$. The integration of this equation over the height interval $[0, H_E]$ yields

$$\bar{w}(H_E) = -\int_0^{H_E} \frac{\partial \bar{v}}{\partial y}\,dz = -\frac{\partial M}{\partial y} \tag{6.239}$$

because $\bar{w}(0) = 0$. From Eq. (6.225) we obtain

$$\frac{\partial \bar{v}}{\partial y} = \frac{\partial u_g}{\partial y}\ \exp(-a\,z)\ \sin(a\,z) \tag{6.240}$$

where we assumed that the derivative $\partial a/\partial y = 0$, i.e. the variation of the Coriolis parameter, and the eddy diffusivity for momentum in y-direction has been neglected so that $\partial f/\partial y = 0$ and $\partial K_m/\partial y = 0$. Inserting Eq. (6.240) into Eq. (6.239) yields

$$\bar{w}\,(H_E) = -\int_0^{H_E} \frac{\partial u_g}{\partial y}\,\exp\,(-\,a\,z)\,\sin\,(a\,z)\;dz$$

$$= -\,\frac{\partial u_g}{\partial y}\,\frac{1+\exp\,(-\,\pi)}{2\,a}. \tag{6.241}$$

Earlier, we derived for the geostrophic vorticity (Eq. (6.84))

$$\xi_g = \frac{\partial v_g}{\partial x} - \frac{\partial u_g}{\partial y}$$

that serves to approximate the vorticity of the wind in the free atmosphere. Since $\partial v_g/\partial x = 0$ we may write

$$\bar{w}\,(H_E) = \xi_g\,\frac{1+\exp\,(-\,\pi)}{2\,a}. \tag{6.242}$$

Because of $\exp\,(-\,\pi) \ll 1$ we can write

$$\bar{w}\,(H_E) = \xi_g\,\sqrt{\frac{K_m}{2\,f}} = \frac{H}{f}\,F_{CE}\,\xi_g \tag{6.243}$$

with

$$F_{CE} = \frac{1}{H\,\sqrt{2}}\,\sqrt{f\;K_m} \tag{6.244}$$

which was introduced by **Charney**[47] and **Eliassen**.[48] The quantity $H = R\,T_0/g \approx 8\,\text{km}$ is the height of the homogeneous atmosphere (Chap. 2), where T_0 is the temperature at the Earth's surface, R is the individual gas constant of moist air, and g is the acceleration of gravity. Note that F_{CE} usually contains $\sin(2\,\alpha)$. However, according to Eq. (6.226), the angle between the mean horizontal wind vector and the geostrophic wind vector is given by $\alpha = 45°$ so that $\sin(2\,\alpha) = 1$. Equation (6.243) represents the linear pumping law of Charney and Eliassen, but the process is often referred to as **Ekman pumping**. When we consider $\xi_g \sim 10^{-5}\,\text{s}^{-1}$, $f \sim 10^{-4}\,\text{s}^{-1}$, and $H_E \sim 1{,}000\,\text{m}$ as appropriate for a typical synoptic-scale system, we obtain a vertical velocity at the height H_e of the order of a few millimeters per second. However, such small values of $\bar{w}\,(H_E)$ are sufficient to affect the lifetime of synoptic systems. Rearranging this expression and considering Eq. (6.228) yield

$$\bar{w}\,(H_E) = \frac{\xi_g}{u_g\,\sqrt{2\,f^2}}\,\frac{\tau_0}{\bar{\rho}}. \tag{6.245}$$

[47] Jule Gregory Charney, Swedish-American meteorologist, 1917–1981.

[48] Arnt Eliassen, Norwegian meteorologist, 1915–2000.

This formula not only reflects the effect of the geostrophic vorticity, but also that of the friction at the Earth's surface. According to Eq. (6.245), surface friction is an effect of some importance for maintaining the vertical circulations in cyclones (Fig. 6.49) and anticyclones. It causes a large-scale vertical motion leading to the decay of high-pressure systems while low-pressure systems are filling up (Fig. 6.51).

Since the geostrophic approximation of the vorticity of the free atmosphere contributes to the mean vertical velocity component at the height H_E, we can reasonably consider the vorticity equation for further description of this secondary circulation. When we ignore that f varies with latitude, we obtain for the vorticity equation

$$\frac{d\xi_A}{dt} = -\xi_A \left(\nabla_H \cdot \overline{\mathbf{v}_H}\right) \tag{6.246}$$

where $\xi_A = \xi + f$. Inserting

$$\frac{\partial \bar{w}}{\partial z} = -\nabla_H \cdot \overline{\mathbf{v}_H} \tag{6.247}$$

into Eq. (6.246) provides

$$\frac{d\xi_A}{dt} = \xi_A \frac{\partial \bar{w}}{\partial z} \tag{6.248}$$

Since $|\xi| \ll |f|$ we can neglect ξ in this equation, and obtain

$$\frac{d\xi_A}{dt} = f \frac{\partial \bar{w}}{\partial z}. \tag{6.249}$$

When we approximate the vorticity of the free atmosphere by the geostrophic vorticity and assume barotropic conditions we obtain that the term $d\xi_A/dt$ is independent of height. Under these conditions, the integration of Eq. (6.249) over the height interval $[H_E, H]$ provides

$$\bar{w}(H) - \bar{w}(H_E) = \frac{1}{f} \frac{d\xi_{A,g}}{dt} (H - H_E) \tag{6.250}$$

where $\xi_{A,g} = \xi_g + f$. Ignoring the spatial variation of ζ_g and assuming that $|\bar{w}(H)| \ll |\bar{w}(H_E)|$ yield

$$\bar{w}(H_E) = -\frac{1}{f} \frac{d\xi_g}{dt} (H - H_E). \tag{6.251}$$

Combining Eqs. (6.243) and (6.251) yields

$$\frac{1}{\xi_g} \frac{d\xi_g}{dt} = -\frac{F_{CE}}{1 - \frac{H_E}{H}}. \tag{6.252}$$

The integration of this equation over the period $[0, t]$ provides

$$\xi_g\,(t) = \xi_g\,(0)\,\exp\left(-\frac{F_{CE}}{1-\frac{H_E}{H}}\,t\right). \tag{6.253}$$

This equation documents that the geostrophic vorticity decreases with time. The e-folding time $t = t_e$ of the decay reads

$$t_e = \frac{1-\frac{H_E}{H}}{F_{CE}}\,. \tag{6.254}$$

For typical values of $H = 8\,\mathrm{km}$, $f = 10^{-4}\,\mathrm{s}^{-1}$, and $K_m = 10\,\mathrm{m}^2\,\mathrm{s}{-}1$, we obtain for the e-folding time $t_e = 3.4$ days. After 7.8 days the geostrophic vorticity is decayed to a value of 10 % of its value at time $t = 0$. This time is in rough agreement with the life cycle of a low-pressure system (Fig. 6.51) and of water vapor in the troposphere (Chap. 1).

6.8.6 Prandtl Layer

6.8.6.1 Constant Flux Approximation

In this subsection, we denote the vertical components of the turbulent flux densities of heat and water vapor as micrometeorological fluxes. The most important prerequisite of the Prandtl layer physics implies that we consider the magnitude of the Reynolds stress vector, $\boldsymbol{\tau}$, and the vertical components of the turbulent flux densities of heat and water vapor as invariant with height. Thus, not only horizontally homogeneous conditions, but also steady-state conditions must be fulfilled, i.e. the local derivatives on the l.h.s. of Eqs. (6.220), (6.232)–(6.234) must be equal to zero. In addition, source or sink terms related to phase transition and chemical processes must be negligible. Consequently, we have to test observational data rigorously to ensure that the height-invariance of these meteorological fluxes can be justified when we want to apply the Prandtl layer relations presented here.

We can express the height-invariance of the meteorological fluxes by $\partial F/\partial z = 0 \Leftrightarrow F = const.$, where F stands for the micrometeorological fluxes of momentum

$$\tau = \bar{\rho}\,\left(\overline{u'\,w'}^2 + \overline{v'\,w'}^2\right)^{\frac{1}{2}} = \bar{\rho}\,{u_*}^2 = const. \tag{6.255}$$

sensible heat,

$$H = c_{p,0}\,\bar{\rho}\,\overline{w'\,\Theta'} = -\,c_{p,0}\,\bar{\rho}\,u_*\,\Theta_* = const. \tag{6.256}$$

water vapor,

$$F_{q_1} = \bar{\rho}\, \overline{w'\, q_1{}'} = -\,\bar{\rho}\, u_*\, q_* = const. \tag{6.257}$$

and long-lived trace gases

$$F_{\chi_m} = \bar{\rho}\, \overline{w'\, \chi_m{}'} = -\,\bar{\rho}\, u_*\, \chi_{m,*} = const.\,, \tag{6.258}$$

respectively. All molecular effects have been neglected in comparison with the corresponding turbulent ones. This neglecting is quite justified in the case of the fully turbulent ASL when sedimentation effects play no role like in case of water vapor and long-lived trace gases (Chaps. 3 and 5). Here, Θ_* is the heat flux temperature or temperature scale, q_* is the water-vapor flux concentration or humidity scale, and $\chi_{m,*}$ is the flux concentration of the mth long-lived trace gas. Note that $\bar{v}$ is arbitrarily chosen as equal to zero. We can justify this choice by arranging the x-axis (and, hence, the y-axis) in such a manner that $\bar{v}$ vanishes. Since we generally exclude the phase transition processes of water substances in this subsection, we only consider water vapor and use, therefore, the notions F_q for the water-vapor flux and q for the specific humidity.

The height-invariance of the micrometeorological fluxes serves to define the thickness of the Prandtl layer. It generally requires that steady-state conditions and the condition of horizontally uniform fields of mean wind speed (i.e. $\bar{w} = 0$), mean temperature, and mean humidity are fulfilled. In addition, net source and sink effects due to phase transition processes are excluded. Even though the condition of height invariance may typically be fulfilled only in a micrometeorological sense (i.e. these micrometeorological fluxes may vary with height across the entire ASL, but not more than 10 % of their values in the immediate vicinity of the surface), it serves as the basis for the constant flux approximation (Chap. 5), on which micrometeorological scaling is based, namely (a) **Monin**[49]**-Obukhov** scaling for forced-convective conditions, and (b) **Prandt-Obukhov-Priestley**[50] scaling for free-convective conditions (Chap. 2), respectively.

Let us estimate the height of the Prandtl layer in case of momentum. The friction stress vector, for instance, is only invariant with height when either $f = 0$ or $\overline{\mathbf{v}_H} = \mathbf{v}_g$. The former is fulfilled at the equator for which $\sin\varphi = 0$, but this is the trivial case. The latter is fulfilled at the top of the Ekman layer, H_E. Below this height, the variation of the friction stress vector with height depends on the ageostrophic wind vector.

Integrating Eq. (6.221) over the height interval $[0,\ z_P]$, where z_P is the top of the Prandtl layer, yields

[49] Andrei Sergeevich Monin, Russian physicist, 1921–2007.

[50] Charles Henry Brian Priestley, British meteorologist, 1915–1998.

$$\boldsymbol{\tau}\,(z_P) - \boldsymbol{\tau}\,(0) = \int_0^{z_P} \bar{\rho}\; f\; \mathbf{k} \times \left(\overline{\mathbf{v}_H} - \mathbf{v}_g\right)\; dz.$$

From this equation we can infer that

$$\left|\left|\boldsymbol{\tau}\,(0)\right| - \left|\boldsymbol{\tau}\,(z_P)\right|\right| \leq \left|\boldsymbol{\tau}\,(0) - \boldsymbol{\tau}\,(z_P)\right| \leq \int_0^{z_P} \bar{\rho}\; \left|f\; \mathbf{k} \times \left(\mathbf{v}_g - \overline{\mathbf{v}_H}\right)\right|\; dz.$$

Because of $\left|f\; \mathbf{k} \times \left(\mathbf{v}_g - \overline{\mathbf{v}_H}\right)\right| = |f|\; \left|\mathbf{v}_g - \overline{\mathbf{v}_H}\right|$ we can express this equation by

$$\left|\left|\boldsymbol{\tau}\,(0)\right| - \left|\boldsymbol{\tau}\,(z_P)\right|\right| \leq \int_0^{z_P} \bar{\rho}\; |f|\; \left|\mathbf{v}_g - \overline{\mathbf{v}_H}\right|\; dz.$$

Apparently, the variation of the magnitude of the friction stress vector with height depends on that of the ageostrophic wind vector. As the condition $|\boldsymbol{\tau}\,(0)| > |\boldsymbol{\tau}\,(z_P)|$ is usually fulfilled, we can write

$$\left|\boldsymbol{\tau}\,(0)\right| - \left|\boldsymbol{\tau}\,(z_P)\right| = \left|\left|\boldsymbol{\tau}\,(0)\right| - \left|\boldsymbol{\tau}\,(z_P)\right|\right|.$$

When we assume that the magnitude of the Reynolds stress vector does not decrease more than 10 % across that height interval $[0, z_P]$ we can define the height of the Prandtl layer in such a sense that we demand

$$\frac{\left|\boldsymbol{\tau}\,(0)\right| - \left|\boldsymbol{\tau}\,(z_P)\right|}{\left|\boldsymbol{\tau}\,(0)\right|} \leq \frac{1}{\left|\boldsymbol{\tau}\,(0)\right|} \int_0^{z_P} \bar{\rho}\; |f|\; \left|\mathbf{v}_g - \overline{\mathbf{v}_H}\right|\; dz \leq 0.1.$$

This decrease corresponds to the relative accuracy with which the Reynolds stress vector can directly be determined by fast-response measurements using, for instance, hot wire (or hot film) and sonic anemometers (Appendix B). Combining formula (6.228) with this condition provides

$$\frac{\left|\boldsymbol{\tau}\,(0)\right| - \left|\boldsymbol{\tau}\,(0)\right|\; \exp\left(-\,a\; z_P\right)}{\left|\boldsymbol{\tau}\,(0)\right|} = 1 - \exp\left(-\,a\; z_P\right) \leq 0.1$$

which is equivalent with $1 \geq \exp\left(-\,a\; z_P\right) \geq 0.9$. Thus, we obtain for the top of the Prandtl layer $z_P \leq -\,\frac{1}{a}\; \ln(0.9) = -\,\frac{H_E}{\pi}\; \ln(0.9) \approx 3.35 \cdot 10^{-2}\; H_E$. Herein, we applied the relationship between the Ekman height and the Ekman length. For typical values of $K_m = 5\ \mathrm{m^2\ s^{-1}}$ and $f = 10^{-4}\ \mathrm{s^{-1}}$, we obtain $H_E \approx 993.5\,\mathrm{m}$, and, hence, $z_P \leq 33.3\,\mathrm{m}$.

The heights of the constant flux layers for momentum, sensible heat and water vapor may differ from each other. Therefore, it is indispensable in field campaigns to measure the meteorological fluxes at different heights directly by covariance techniques (Appendix B) to ensure that the constant flux assumption is justified.

6.8.6.2 Dimensional Analysis

Dimensional analysis is based on a very simple idea. Dimensional analysis is inferred from the fact that physical laws do not depend on arbitrarily chosen basic units of measurements. In recognizing this simple idea, we can conclude that functions that express physical laws must possess a certain fundamental property. From a mathematical point of view, property is called the generalized homogeneity or symmetry. This property allows the number of arguments in these functions to be reduced, thereby simplifying the procedure to obtain them. As **Barenblatt**[51] pointed out, this is the entire content of dimensional analysis – there is nothing more to it.

Let us adopt that, associated with a certain physical problem, we can select a set of characteristic dimensionality quantities, for instance, k variables, parameters or/and constants, $Q_1,\ Q_2, \ldots, Q_k$ that unambiguously and evidently represent the arguments of a mathematical relationship. First, this "law" is unspecified; therefore it is formally employed as a general postulate, commonly referred to as the similarity hypothesis of the problem, which may read[52]

$$F\left(Q_1,\ Q_2, \ldots, Q_k\right) = 0. \tag{6.259}$$

In its implicit representation, Eq. (6.259) declares $k - 1$ free or independent arguments as well as a transformation of the full series of Q_j for $j = 1, \ldots, k$ to a series of p non-dimensional invariants π_i for $i = 1, \ldots, p$ in terms of a factorization by powers. Correspondingly, we can define each π_i-expression by

$$\pi_i = {Q_1}^{x_{1,i}}\ {Q_2}^{x_{2,i}} \ldots {Q_k}^{x_{k,i}} = \prod_{j=1}^{k} {Q_j}^{x_{j,i}} \quad for\ i = 1, \ldots, p. \tag{6.260}$$

It is necessarily linked with the condition of non-dimensionality

$$\dim\ \pi_i = 1 \quad for\ i = 1, \ldots, p \tag{6.261}$$

where $p < k$ is customarily valid.

Next, we assume that the π_i-invariants can have interdependencies of arbitrary forms, and it may exist a corresponding relation

$$\phi\left(\pi_1, \pi_2, \ldots, \pi_p\right) = 0 \tag{6.262}$$

which is to be understood as an alternative similarity hypothesis to Eq. (6.259). In this function, the powers $x_{j,i}$ from Eq. (6.260) are basically unknown numbers.

---

[51] Grigory Isaakovich Barenblatt, Russian mathematician, born 1927.

[52] This procedure was developed by Fritz Herbert (1980, Vorlesung zur Physik der planetarischen Grenzschicht. J.W. Goethe-Universität, Frankfurt/Main, unpublished manuscript). It has been described by Kramm and Herbert (2006b, 2009).

Their determination is the proper problem of **Buckingham**[53]'s π-theorem. When more than one π-invariant exists, i.e. $p > 1$, then we have with Eq. (6.262) the explicit representation

$$\pi_i = \varphi\left(\pi_1, \pi_2, \ldots, \pi_p\right) \tag{6.263}$$

in which we can interpret φ as a universal function within the framework of the similarity hypothesis. Then according to the implicit formulation (6.262), π_i (for any arbitrary $i \in \{1, \ldots, p\}$) is not an argument of that universal function. In the special case of $p = 1$, we merely obtain one π-invariant, that is a non-dimensional universal constant. This special case is expressed by Eq. (6.263) in the singular form

$$\pi = const. \tag{6.264}$$

(or $\varphi = const$). In view to the determination of the powers $x_{j,i}$, we extend our treatment to the concise set of fundamental dimensions, D_n for $n = 1, \ldots, r$ such as length L, time T, mass M, temperature Θ. We consider that any quantity's dimension can be analyzed in terms of the independent D_n by homogeneous power factorization. We can expressed this by

$$\dim\ Q_j = {D_1}^{g_{1,j}}\ {D_2}^{g_{2,j}} \ldots {D_r}^{g_{r,j}} = \prod_{n=1}^{r} {D_n}^{g_{n,j}} \quad for\ j = 1, \ldots, k. \tag{6.265}$$

Here the powers $g_{n,j}$ for $n = 1, \ldots, r$ and $j = 1, \ldots, k$ are known from the relevant quantities Q_j according to the hypothesized similarity condition. Note that $r \leq k$ is valid, where r is the highest number of fundamental dimensions that may occur. In other words: for k relevant quantities Q_j including r fundamental dimensions D_n we obtain $p = k - r$ independent non-dimensional invariants, the π numbers.

Now we can attain a straight-forward development of the analytical framework by introducing Eq. (6.265) together with the factorization by powers from Eq. (6.260) into the condition of non-dimensionality (6.261). In doing so, we obtain this basic law as described in the following detailed representation

$$\dim\ \pi_i = \prod_{j=1}^{k} \left(\prod_{n=1}^{r} {D_n}^{g_{n,j}} \right)^{x_{j,i}} = 1 \quad for\ i = 1, \ldots, p. \tag{6.266}$$

Combining the two factorizations $\prod_j$ and $\prod_n$ in this equation enables us to rewrite this set of conditions in the fully equivalent form

$$\dim\ \pi_i = \prod_{n=1}^{r} {D_n}^{\sum_{j=1}^{k} g_{n,j}\ x_{j,i}} = 1 \quad for\ i = 1, \ldots, p. \tag{6.267}$$

[53] Edgar Buckingham, American physicist, 1867–1940.

For the following conclusion, the latter is more suitable than the former. Indeed, we can immediately infer from the factorizing analysis in dependence on the bases D_n for $n = 1, \ldots, r$ that the set of conditions

$$\sum_{j=1}^{k} g_{n,j}\, x_{j,i} = 0 \quad for\, n = 1, \ldots, r \; and \; i = 1, \ldots, p \tag{6.268}$$

has to hold since each D_n-exponential factor must satisfy due to its mathematical independence, i.e. the condition of non-dimensionality (Eqs. (6.261) and (6.267)), i.e. to be equal to unity. In matrix notation, we can express Eq. (6.268) by

$$\underbrace{\begin{Bmatrix} g_{1,1} & g_{1,2} & \cdots & g_{1,k} \\ g_{2,1} & g_{2,2} & \cdots & g_{2,k} \\ \cdots & \cdots & \cdots & \cdots \\ g_{r,1} & g_{r,2} & \cdots & g_{r,k} \end{Bmatrix}}_{\mathbf{G}=\{g_{r,k}\}} \underbrace{\begin{Bmatrix} x_{1,1} & x_{1,2} & \cdots & x_{1,p} \\ x_{2,1} & x_{2,2} & \cdots & x_{2,p} \\ \cdots & \cdots & \cdots & \cdots \\ x_{k,1} & x_{k,2} & \cdots & x_{k,p} \end{Bmatrix}}_{\mathbf{A}=\{x_{k,p}\}} = \{0\}\,. \tag{6.269}$$

Here $\mathbf{G} = \{g_{r,k}\}$ is the dimensional matrix, and $\mathbf{A} = \{x_{k,p}\}$ is the matrix of powers. The notation $\{0\}$ is an $r \times p$ matrix. Each column of $\mathbf{A}$ is forming solution vectors $\mathbf{x}_i$ for the invariants π_i for $i = 1, \ldots, p$. The set of equations (6.269) serves to determine the powers $x_{j,i}$ for $j = 1, \ldots, k$ and $i = 1, \ldots, p$. Thus, in accord with Eq. (6.269), the homogeneous system of linear equations has for each of these π-invariants the alternative notation

$$\mathbf{G} \cdot \mathbf{x}_i = \mathbf{0} \;\; or \;\; \begin{Bmatrix} g_{1,1} & g_{1,2} & \cdots & g_{1,k} \\ g_{2,1} & g_{2,2} & \cdots & g_{2,k} \\ \cdots & \cdots & \cdots & \cdots \\ g_{r,1} & g_{r,2} & \cdots & g_{r,k} \end{Bmatrix} \begin{Bmatrix} x_{1,i} \\ x_{2,i} \\ \cdots \\ x_{k,i} \end{Bmatrix} = \{0\} \quad for\, i = 1, \ldots, p. \tag{6.270}$$

The rank of the dimensional matrix is equal to the number of fundamental dimensions, r. When the number of dimensional quantities, k, is equal to r, we obtain $p = 0$. In this case, only a trivial solution exists. In the case of $p > 0$, the homogeneous system of linear equations (6.270) is indeterminate. This means more unknowns than equations exist. This fact is true in all instances presented here. Hence, for each of the p non-dimensional π numbers, we have to make a reasonable choice for p of these unknowns, $x_{k,i}$, to turn this equation set into a solvable state. Then we obtain for each π number an inhomogeneous linear equation system that serves to determine the remaining $r = k - p$ unknowns. Thus, the remaining $r \times r$ dimensional matrix $\mathbf{G}_0 = \{g_{r,r}\}$ has the rank r, too. It is the largest square sub-matrix for which the determinant is unequal to zero (i.e., $|g_{r,r}| \neq 0$). Thus, we have

Table 6.3 Table of fundamental dimensions for the example of the logarithmic wind profile

	$z-d$	u_*	$\partial U/\partial z$
Length	1	1	0
Time	0	-1	-1

$$\mathbf{G}_0 \cdot \mathbf{x}_i = \mathbf{B}_i \quad or \quad \begin{Bmatrix} g_{1,1} & g_{1,2} & \cdots & g_{1,r} \\ g_{2,1} & g_{2,2} & \cdots & g_{2,r} \\ \cdots & \cdots & \cdots & \cdots \\ g_{r,1} & g_{r,2} & \cdots & g_{r,r} \end{Bmatrix} \begin{Bmatrix} x_{1,i} \\ x_{2,i} \\ \cdots \\ x_{r,i} \end{Bmatrix} = \begin{Bmatrix} B_{1,i} \\ B_{2,i} \\ \cdots \\ B_{r,i} \end{Bmatrix} \quad for\ i = 1, \ldots, p. \tag{6.271}$$

We can solve this inhomogeneous system of linear equations for $x_{m,i}$ for $m = 1, \ldots, r$ by employing **Cramer**[54]'s rule.

Example: The Logarithmic Wind Profile

Here we follow the above general procedure, and exemplarily present a concrete analysis that leads to the logarithmic wind profile for the neutrally stratified Prandtl layer. In this example, we confine our attention to three basic quantities: $Q_1 = z-d$ is the height difference in m, Q_2 is the height-invariant friction velocity u_* in m s^{-1}, and Q_3 is the shear of the mean horizontal wind speed $\partial U/\partial z$ in s^{-1}, where $U = |\overline{\mathbf{v}_H}|$. In so doing, we set up the similarity hypothesis $F\,(z-d,\ u_*,\ \partial U/\partial z) = 0$. Obviously, only L and T occur as fundamental independent dimensions.

Next, depending on $D_1 = L$ and $D_2 = T$, Eq. (6.267) yields

$$D_1^{\sum_{j=1}^{3} g_{1,j}\, x_{j,i}}\, D_2^{\sum_{j=1}^{3} g_{2,j}\, x_{j,i}} = L^{\,x_{1,i}+x_{2,i}}\, T^{-\,x_{2,i}-x_{3,i}} = 1 \quad for\ i = 1, \ldots, p \tag{6.272}$$

In agreement with formulae (6.268)–(6.270), we have the dimensional matrix

$$\mathbf{G} = \begin{pmatrix} 1 & 1 & 0 \\ 0 & -1 & -1 \end{pmatrix}$$

that is based on the table of fundamental dimensions (Table 6.3).

Thus, the (under-determined) homogeneous equations of solution read

$$\mathbf{G} \cdot \mathbf{x}_i = 0 \quad or \quad \begin{pmatrix} 1 & 1 & 0 \\ 0 & -1 & -1 \end{pmatrix} \begin{pmatrix} x_{1,i} \\ x_{2,i} \\ x_{3,i} \end{pmatrix} = (0) \quad for\ i = 1, \ldots, p \tag{6.273}$$

[54] Gabriel Cramer, Swiss mathematician, 1704–1752.

with which $k = 3$ and $r = 2$ (rank of matrix $\mathbf{G}$) and, consequently, $p = k - r = 1$ are given. This matrix designates a case of one non-dimensional invariant π only. In a free choice, we arbitrarily define $x_{1,1} = 1$ without loss of generality to obtain from Eq. (6.273) the two inhomogeneous equations of solution in accord with Eq. (6.271)

$$\begin{pmatrix} 1 & 0 \\ -1 & -1 \end{pmatrix} \begin{pmatrix} x_{2,1} \\ x_{3,1} \end{pmatrix} = \begin{pmatrix} -1 \\ 0 \end{pmatrix}. \tag{6.274}$$

From this equation, we easily calculate $x_{2,1} = -1$ and $x_{3,1} = 1$. Thus, the full solution vector reads

$$\mathbf{x}_1 = \begin{pmatrix} x_{1,1} \\ x_{2,1} \\ x_{3,1} \end{pmatrix} = \begin{pmatrix} 1 \\ -1 \\ 1 \end{pmatrix}. \tag{6.275}$$

Finally, the elements of this solution vector are to be utilized due to the general context of formulae (6.260), (6.263), and (6.264) to find the desired universal relationship, i.e. the similarity law

$$\pi_1 = (z - d)^1 \, {u_*}^{-1} \left(\frac{\partial U}{\partial z} \right)^1 = \frac{z - d}{u_*} \, \frac{\partial U}{\partial z} = const. \tag{6.276}$$

or in the re-arranged form

$$\frac{\partial U}{\partial z} = \frac{u_*}{\kappa \, (z - d)}. \tag{6.277}$$

Here $\kappa = {\pi_1}^{-1}$ is another non-dimensional universal constant, the von Kármán constant. Furthermore, $\Lambda_P = \kappa \, (z - d)$ is Prandtl's mixing length.

We append to Eq. (6.276) that since π_1 is yet arbitrary. When we choose, for instance, $x_{1,1} = a$, where $a \neq 0$ is an arbitrary real number, we obtain another invariant ${\pi_1}^*$. The relationship between this π invariant and that in Eq. (6.276) is given by $\pi_1 = \sqrt[a]{{\pi_1}^*}$. Therefore, for convenience, we simply choose $x_{1,1} = 1$.

Integrating Eq. (6.277) over the height interval $[z_r, \, z_R]$, where z_r and z_R are the lower and upper boundaries of the fully turbulent part of the Prandtl layer, respectively, yields

$$U(z_R) - U(z_r) = \frac{u_*}{\kappa} \int_{z_r}^{z_R} \frac{dz}{z - d} = \frac{u_*}{\kappa} \ln \frac{z_R - d}{z_r - d}. \tag{6.278}$$

When we assume that $U(z_r)$ extrapolates to zero when z_r tends to $z_r = z_0 + d$ (Fig. 6.37), where z_0 is the roughness length, we can write

$$U(z_R) = \frac{u_*}{\kappa} \ln \frac{z_R - d}{z_0}. \tag{6.279}$$

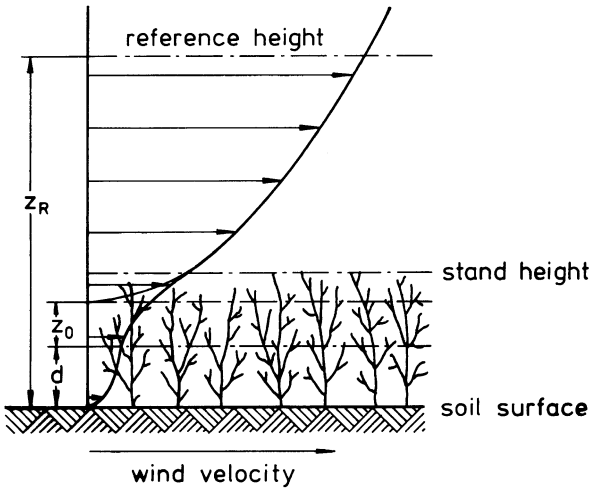

Fig. 6.37 Meaning of the roughness length z_0 and the zero-plane displacement d in the vertical profile of the mean horizontal wind speed over vegetation

This expression is the logarithmic wind profile for (thermally) neutral stratification. Multiplying nominator and denominator of the logarithm in Eq. (6.279) by $u_*\ \nu$, where ν is the kinematic viscosity, and rearranging this equation yield

$$u_R{}^+ = \frac{U\,(z_R)}{u_*} = \frac{1}{\kappa} \ln \frac{u_*\ (z_R - d)}{\nu} - \frac{1}{\kappa} \ln \frac{u_* z_0}{\nu}. \tag{6.280}$$

Over aerodynamically smooth surfaces, we can ignore the zero-plane displacement, d. Thus, when we define the local (or roughness) Reynolds number by

$$\eta = \frac{u_*\ z}{\nu} \tag{6.281}$$

the global Reynolds number by

$$\eta_R = \frac{u_*\ z_R}{\nu} \tag{6.282}$$

and

$$D = -\frac{1}{\kappa} \ln \frac{u_*\ z_0}{\nu} \tag{6.283}$$

we obtain

$$u_R{}^+ = \frac{1}{\kappa} \ln (\eta_R) + D. \tag{6.284}$$

For aerodynamically smooth surfaces, $D \cong 5.5$. Equation (6.284) for the normalized velocity, ${u_R}^+ = U\left(z_R\right)/u_*$, describes the turbulent approximation of Prandtl and **Taylor**[55] for sufficiently large Reynolds numbers.

6.8.6.3 Complete Similarity vs. Incomplete Similarity

Before we derive the similarity hypotheses for the Prandtl layer, we have to discuss the meaning of complete and incomplete similarity. Let us consider the transfer of momentum, sensible heat, and water vapor across the Prandtl layer. The standardized procedure of dimensional analysis (Sect. 6.8.6.2) provides for Monin-Obukhov scaling

$$\frac{z-d}{u_*}\frac{\partial U}{\partial z} = \varphi_m\left(\zeta, \eta, \eta_R, \mathrm{Pr}, Sc_q\right) \tag{6.285}$$

$$\frac{z-d}{\Theta_*}\frac{\partial \bar{\Theta}}{\partial z} = \varphi_h\left(\zeta, \eta, \eta_R, \mathrm{Pr}, Sc_q\right) \tag{6.286}$$

and

$$\frac{z-d}{q_*}\frac{\partial \bar{q}}{\partial z} = \varphi_q\left(\zeta, \eta, \eta_R, \mathrm{Pr}, Sc_q\right). \tag{6.287}$$

Here, $\varphi_m\left(\zeta, \eta, \eta_R, \mathrm{Pr}, Sc_q\right)$, $\varphi_h\left(\zeta, \eta, \eta_R, \mathrm{Pr}, Sc_q\right)$, and $\varphi_q\left(\zeta, \eta, \eta_R, \mathrm{Pr}, Sc_q\right)$ are the local similarity functions or stability functions for momentum, sensible heat, and water vapor, respectively. Furthermore, $\zeta = (z-d)/L$ is the Obukhov number, and L is the Obukhov stability length defined by

$$L = -\frac{c_{p,0}\,\bar{\rho}\,{u_*}^3}{\kappa\,\frac{g}{\bar{\Theta}}\left(H + 0.61\,c_{p,0}\,\bar{\Theta}\,F_q\right)} = \frac{{u_*}^2}{\kappa\,\frac{g}{\bar{\Theta}}\left(\Theta_* + 0.61\,\bar{\Theta}\,q_*\right)} \tag{6.288}$$

where g is the acceleration of gravity, $\bar{\Theta}$ is a mean potential temperature typically chosen as a representative value for the Prandtl layer, and $c_{p,1}/c_{p,0} - 1 \approx 0.61$ (Chap. 2). Furthermore, $Pr = \nu/\alpha_T$ is the Prandtl number, $Sc_q = \nu/D_q$ is the Schmidt number for water vapor, and D_q is the corresponding molecular diffusivity. This kind of scaling assumes complete similarity of the flow in both Reynolds numbers, i.e. the local one, η, and the global one, η_R. The plausibility of such an assumption and, consequently, of neglecting the dependence on η, and η_R is usually argued on the basis of the very large values of both Reynolds numbers above the thin sublayer. We introduced this layer of a few millimeters thickness adjacent to the Earth's surface as the viscous sublayer earlier. The assumption of the

[55] Sir Geoffrey Ingram Taylor, British physicist, 1886–1975.

existence of finite limits of the local similarity functions $\varphi_m(\zeta)$, $\varphi_h(\zeta)$, and $\varphi_m(\zeta)$ as both Reynolds numbers tend to infinity is accepted implicitly. When $\varphi_m(\zeta)$, $\varphi_h(\zeta)$, and $\varphi_m(\zeta)$ tend to finite limits as $\eta \to \infty$ and $\eta_R \to \infty$ in accordance with the assumption of complete similarity, then for sufficiently large η and η_R a universal similarity law, independent of both Reynolds numbers, must hold; and we can consider the local similarity functions for momentum, sensible heat and water vapor,

$$\frac{z-d}{u_*}\frac{\partial U}{\partial z} = \varphi_m\left(\zeta, \mathrm{Pr}, Sc_q\right) \tag{6.289}$$

$$\frac{z-d}{\Theta_*}\frac{\partial \bar{\Theta}}{\partial z} = \varphi_h\left(\zeta, \mathrm{Pr}, Sc_q\right) \tag{6.290}$$

and

$$\frac{z-d}{q_*}\frac{\partial \bar{q}}{\partial z} = \varphi_q\left(\zeta, \mathrm{Pr}, Sc_q\right) \tag{6.291}$$

as universal functions. These functions are the Monin-Obukhov similarity laws. In the case of the fully turbulent Prandtl layer, the dependence of these universal functions on both the Prandtl number, and the Schmidt number for water vapor plays no role.

Already in the case of neutral stratification (Chap. 2), we can detect a weak dependence of these universal functions on both Reynolds numbers. This weak dependence serves to introduce the assumption of incomplete similarity of the flow in the local Reynolds number. This assumption apparently does not contradict experimental data on flows in smooth pipes, etc. Thus, Barenblatt and Monin made a similar assumption for thermally stratified flows in the Prandtl layer.

6.8.6.4 Monin-Obukhov Scaling

Similarity Hypothesis for Momentum

Let us consider the first similarity hypothesis of Monin and Obukhov. It states that the vertical transfer of momentum across the Prandtl layer is only determined by $Q_1 = z - d$, the Obukhov stability length, $Q_2 = L$, the friction velocity, $Q_3 = u_*$, and $Q_4 = \partial U/\partial z$. We can express this similarity hypothesis mathematically by $F(Q_1, Q_2, Q_3, Q_4) = F(z-d, L, u_*, \partial U/\partial z) = 0$. Obviously, the number of dimensional quantities is $k = 4$. The dimensional matrix reads

$$\mathbf{G} = \begin{pmatrix} 1 & 1 & 1 & 0 \\ 0 & 0 & -1 & -1 \end{pmatrix}$$

as we can derive from Table 6.4.

Table 6.4 Table of fundamental dimensions for the example of similarity hypothesis for momentum

	$z-d$	L	u_*	$\partial U/\partial z$
Length	1	1	1	0
Time	0	0	−1	−1

The rank of the dimensional matrix is $r = 2$. We have $p = k - r = 2$ independent π numbers, and, hence, a universal function is established. These facts are true in all instances of flux-gradient relationships presented here. In accord with Eqs. (6.268)–(6.270), we have the (under-determined) homogeneous equations of solution

$$\mathbf{G} \cdot \mathbf{x}_i = 0 \quad or \quad \begin{pmatrix} 1 & 1 & 1 & 0 \\ 0 & 0 & -1 & -1 \end{pmatrix} \begin{pmatrix} x_{1,i} \\ x_{2,i} \\ x_{3,i} \\ x_{4,i} \end{pmatrix} = (0) \quad for\ i = 1, 2. \tag{6.292}$$

Thus, the dimensional π-invariants analysis provides

$$\pi_1 = \frac{z-d}{u_*} \frac{\partial U}{\partial z} = \varphi_m(\pi_2) = \varphi_m(\zeta). \tag{6.293}$$

Here $\pi_2 = (z-d)/L = \zeta$. Apparently, this formula does not contain κ. This result is quite reasonable because the von Kármán constant is a non-dimensional quantity. In case of neutral stratification, κ is related to a π number by $\pi_1 = \varphi_m(0) = \kappa^{-1}$ (Eq. (6.277)). For non-neutral stratification, however, it cannot directly be addressed by a formalized procedure of non-dimensionalization. Following Monin and Obukhov, we put this constant into Eq. (6.293), mainly for historical reasons, and convenience. Thus, the non-dimensional wind shear reads

$$\frac{\kappa\ (z-d)}{u_*} \frac{\partial U}{\partial z} = \Phi_m(\zeta) \tag{6.294}$$

where $\Phi_m(\zeta) = \kappa\ \varphi_m(\zeta)$ is the conventional local similarity function or conventional universal function for momentum. The quantity $\Lambda_P = \kappa\ (z-d)$ in Eq. (6.294) is Prandtl's mixing length of the universal wall law for thermally neutral stratification, i.e. $\Phi_m(0) = 1$.[56] This kind of stratification may prevail either (a) during the transition from stable to unstable stratification and vice versa when steady-state conditions, as required by the constant flux approximation, must not be expected, or (b) under the condition of strong wind shear when thermal effects become of minor importance. Combining Eqs. (6.229) and (6.294) provides

$$K_m = \frac{u_*\ \kappa\ (z-d)}{\Phi_m(\zeta)}. \tag{6.295}$$

[56]This means that replacing $Q_1 = z - d$ in the similarity hypothesis by $Q_1 = \Lambda_P = \kappa\ (z-d)$ would provide the same result.

For neutral stratification, i.e. $\zeta = 0$, we obtain $\Phi_m(0) = 1$. Thus, Eq. (6.295) amounts to $K_m = u_* \kappa (z-d) = u_* \Lambda_P$, and Eq. (6.229) becomes $\partial U/\partial z = u_*/\Lambda_P$ which is identical with Eq. (6.277).

In all instances with more than one π number, we cannot quantify a universal function by the dimensional π-invariants analysis. However, the local similarity function for momentum must be equal to unity when $\zeta = 0$. But for non-neutral conditions, as originally investigated by Monin and Obukhov, it has to be determined empirically or/and theoretically.

Similarity Hypothesis for Sensible Heat

The second similarity hypothesis of Monin and Obukhov states that the vertical transfer of sensible heat across the Prandtl layer is determined by $z-d$, L, Θ_*, and $\partial\bar{\Theta}/\partial z$, expressed by $F\left(z-d, L, \Theta_*, \partial\bar{\Theta}/\partial z\right) = 0$. The dimensional π-invariants analysis provides

$$\pi_1 = \frac{z-d}{\Theta_*}\,\frac{\partial\bar{\Theta}}{\partial z} = \varphi_h(\pi_2) = \varphi_h(\zeta)\,. \tag{6.296}$$

Again, we can put the von Kármán constant into Eq. (6.296) for historical reasons, and convenience. In doing so, the non-dimensional vertical component of the temperature gradient reads

$$\frac{\kappa\,(z-d)}{\Theta_*}\,\frac{\partial\bar{\Theta}}{\partial z} = \Phi_h(\zeta)\,. \tag{6.297}$$

Here $\Phi_h(\zeta) = \kappa\,\varphi_h(\zeta)$ is the conventional local similarity function or conventional universal function for sensible heat. Sometimes, an additional factor, α_h, is introduced into Eq. (6.297),

$$\frac{\alpha_h\,\kappa\,(z-d)}{\Theta_*}\,\frac{\partial\bar{\Theta}}{\partial z} = \alpha_h\,\Phi_h(\zeta) = \Phi_h{}^*(\zeta) \tag{6.298}$$

with $\Phi_h{}^*(\zeta) = \alpha_h\,\Phi_h(\zeta)$. This factor serves to address that the turbulent Prandtl number, Pr_t, differs from unity in case of neutral stratification. Such an additional factor might be used for convenience. But it cannot be justified on the basis of dimensional analysis. Under neutral condition with respect to dry air, the similarity hypothesis is not fulfilled because the vertical component of the temperature gradient, $\partial\bar{\Theta}/\partial z$, is equal to zero. Consequently, formulae (6.296)–(6.298) become unpredictable. Therefore, the similarity function (6.298) is not further considered. Combining Eqs. (6.205) and (6.297) leads to the eddy diffusivity for sensible heat

$$K_h = \frac{u_*\,\kappa\,(z-d)}{\Phi_h(\zeta)} \tag{6.299}$$

and for the turbulent Prandtl number given by Eq. (6.208)

$$Pr_t = \frac{\Phi_h(\zeta)}{\Phi_m(\zeta)}. \tag{6.300}$$

Similarity Hypothesis for Water Vapor

Monin and Obukhov did not consider the vertical transfer of water vapor across the Prandtl layer. But we can deal with this transfer of matter in a similar manner. The water-vapor transfer is only determined by $z-d$, L, the density scale of water vapor, $\rho_{w,*}$ ($\rho_{w,*} = \bar{\rho}\ q_*$), and the vertical component, $\partial\bar{\rho_w}/\partial z$, of the gradient of the mean partial density of water vapor, $\bar{\rho_w} \approx \bar{\rho}\ \bar{q}$, expressed by $F(z-d, L, \rho_{w,*}, \partial\overline{\rho_w}/\partial z) = 0$. We have to use the partial density of water vapor because the specific humidity is a mass fraction, and, hence, a non-dimensional quantity (Chap. 2). The dimensional π-invariants analysis provides

$$\pi_1 = \frac{z-d}{\rho_{w,*}}\ \frac{\partial\overline{\rho_w}}{\partial z} = \varphi_q(\pi_2) = \varphi_q(\zeta). \tag{6.301}$$

Let us assume that the mean air density is height-invariant in the Prandtl layer and define $\Phi_q(\zeta) = \kappa\ \varphi_q(\zeta)$, where $\Phi_q(\zeta)$ is the conventional local similarity function or conventional universal function for water vapor. Then we obtain for the non-dimensional vertical component of the humidity gradient

$$\frac{\kappa\ (z-d)}{q_*}\ \frac{\partial\bar{q}}{\partial z} = \Phi_q(\zeta). \tag{6.302}$$

Combining Eqs. (6.206) and (6.302) provides for the eddy diffusivity for water vapor

$$K_q = \frac{u_*\ \kappa\ (z-d)}{\Phi_q(\zeta)}. \tag{6.303}$$

In case of water vapor, the turbulent Schmidt number, Eq. (6.209), and the turbulent Lewis-Semenov number, Eq. (6.210), read

$$Sc_{t,q} = \frac{\Phi_q(\zeta)}{\Phi_m(\zeta)} \tag{6.304}$$

and

$$LS_{t,q} = \frac{K_q}{K_h} = \frac{\Phi_h(\zeta)}{\Phi_q(\zeta)}, \tag{6.305}$$

respectively.

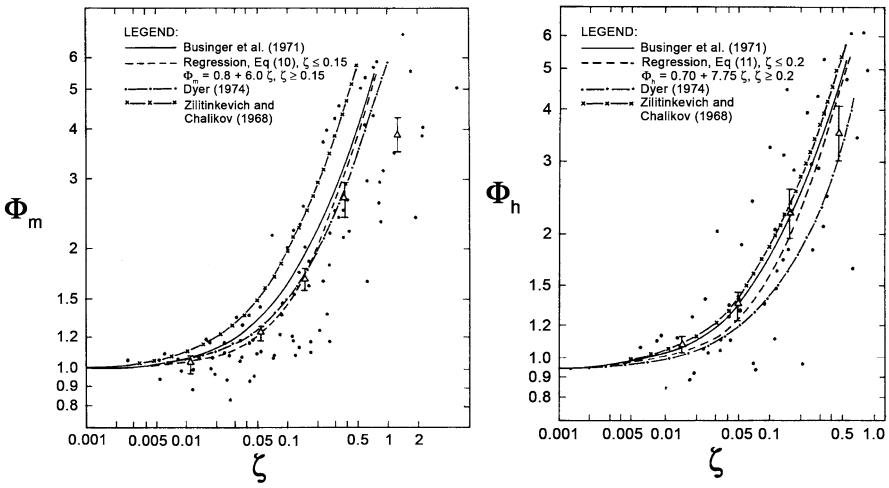

Fig. 6.38 The local similarity functions Φ_m and Φ_h versus the Obukhov number ζ for stable stratification. The *dots* represent Högström's field data (From Högström (1988))

Empirical Φ-Functions for the Transfer of Momentum, Sensible Heat, and Water Vapor

Since the similarity hypotheses of Monin and Obukhov can only serve to show that universal functions may exist, such conventional Φ-functions for the transfer of momentum, sensible heat, and water vapor have to be determined empirically and/or theoretically. Unfortunately, the results of these Φ-functions obtained from sophisticated field campaigns show a considerable scatter (Figs. 6.38 and 6.40).

The empirical results of Zilitinkevich[57] and Chalikov as well as Webb for stable stratification, and Dyer and Hicks for unstable stratification, for instance, may be gathered by

$$\Phi_m(\zeta) = \begin{cases} 1 + \gamma_1 \zeta & for\ \zeta > 0\ \ (stable) \\ 1 & for\ \zeta = 0\ \ (neutral) \\ (1 - \gamma_2 \zeta)^{-1/4} & for\ \zeta < 0\ \ (unstable) \end{cases} \tag{6.306}$$

and

$$\Phi_q(\zeta) = \Phi_h(\zeta) = \begin{cases} \Phi_m(\zeta) & for\ \zeta > 0 \\ 1 & for\ \zeta = 0 \\ {\Phi_m}^2(\zeta) & for\ \zeta < 0 \end{cases} \tag{6.307}$$

[57] Sergej S. Zilitinkevich, Russian-Swedish hydrometeorologist, born 1936.

with $\gamma_1 \cong 5$ and $\gamma_2 \cong 16$. The linear formula $\Phi_m(\zeta) = 1 + \gamma_1\ \zeta$ in Eq. (6.306) was first recommended by Monin and Obukhov for stable stratification (and weakly unstable stratification) and later experimentally determined by Chalikov and Zilitinkevich as well as Businger et al. and others mainly for the stability range $0 \leq \zeta < 1$, but there is a large scatter in case of momentum with some values of $\Phi_m(\zeta)$ for $\zeta > 1$ (Fig. 6.38). The relationship $\Phi_q(\zeta) = \Phi_h(\zeta) = \Phi_m(\zeta)$ first recommended by Webb is often considered for stable stratification.

In 2005, Cheng and Brutsaert suggested the following local similarity functions for stable stratification

$$\Phi_m(\zeta) = 1 + \gamma_3 \left(\frac{\zeta + \zeta^{\gamma_4}\ (1 + \zeta^{\gamma_4})^{\frac{1-\gamma_4}{\gamma_4}}}{\zeta + (1 + \zeta^{\gamma_4})^{\frac{1}{\gamma_4}}} \right) \tag{6.308}$$

and

$$\Phi_h(\zeta) = 1 + \gamma_5 \left(\frac{\zeta + \zeta^{\gamma_6}\ (1 + \zeta^{\gamma_6})^{\frac{1-\gamma_6}{\gamma_6}}}{\zeta + (1 + \zeta^{\gamma_6})^{\frac{1}{\gamma_6}}} \right) \tag{6.309}$$

with $\gamma_3 = 6.1$, $\gamma_4 = 2.5$, $\gamma_5 = 5.3$, and $\gamma_6 = 1.1$. These formulae should cover the entire range of stable stratification. For neutral conditions, i.e. $\zeta = 0$, we obtain $\Phi_h(0) = \Phi_m(0) = 1$. For moderate stable stratification we can approximate both formulae by linear expressions, $\Phi_m(\zeta) \cong 1 + \gamma_3\ \zeta$ and $\Phi_h(\zeta) \cong 1 + \gamma_5\ \zeta$, respectively. For increasing stability, formulae (6.308) and (6.309) tend to $\Phi_m(\zeta) = 1 + \gamma_3$ and $\Phi_h(\zeta) = 1 + \gamma_5$, respectively. Obviously, for the entire range of stable stratification $\Phi_m(\zeta)$ and $\Phi_h(\zeta)$ slightly differ from each other. For higher values of ζ, formulae (6.308) and (6.309) also notably differ from the linear functions given by (6.306) and (6.307) (Fig. 6.39).

We have to consider the results for strongly stable stratification generally with care. As reported by Cheng and Brutsaert, the calculated $\Phi_h(\zeta) - 1$ data points for $\zeta > 2$ were excluded from the analysis because the large scatter suggested either unacceptable error in the measurements or perhaps other unexplained physical effects. They pointed out, a possible reason could be that these data points are already outside the stable surface layer so that Monin-Obukhov similarity, as expressed by Eqs. (6.290) and (6.297), may not be valid.

Obviously, formulae (6.308) and (6.309) lead to logarithmic profiles for neutral and strongly stable conditions. The latter, seems to be awkward because when the magnitude of turbulent fluctuations decreases towards the small values of the quiet regime with increasing stability, the near-surface flow should become mainly laminar. In the case of a pure laminar flow, viscous effects dominate leading to $\partial U/\partial\eta = u_*$, $\partial\bar{\Theta}/\partial\eta = Pr\ \Theta_*$, and $\partial\bar{q}/\partial\eta = Sc_q\ q_*$. Thus, linear profiles have to be expected. The same is true when the respective eddy diffusivities become invariant with height. Such height invariance might be possible when the quiet regime prevails and the magnitude of the turbulent fluctuations is small across the

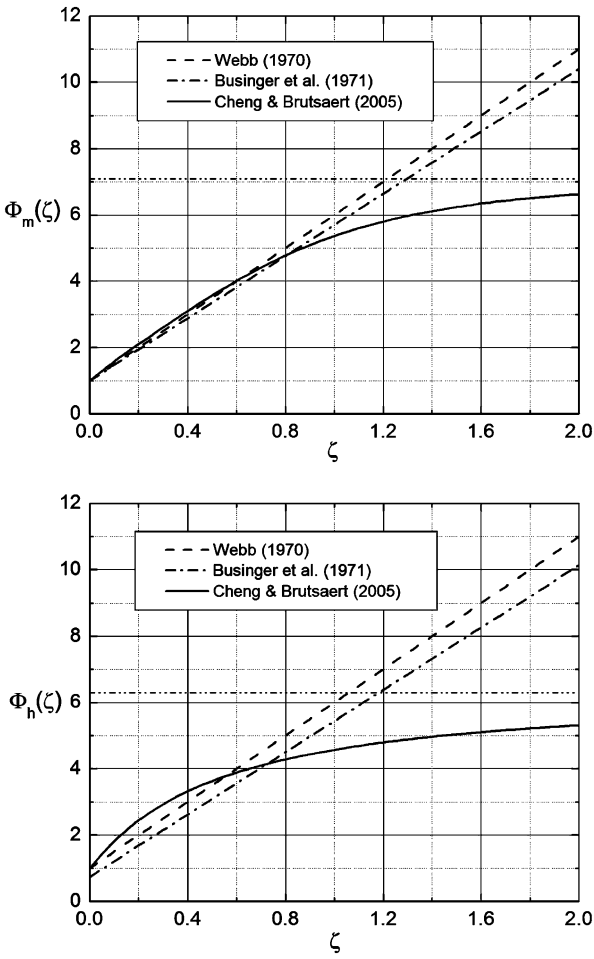

Fig. 6.39 Various local similarity functions Φ_m and Φ_h versus the Obukhov number ζ for stable stratification (From Kramm et al. (2013))

entire Prandtl layer. Thus, we have to assume that Monin-Obukhov similarity is incomplete under strongly stable conditions. If under such conditions the constant flux approximation is no longer valid as debated, for instance, by Webb and others, Monin-Obukhov similarity cannot be expected.

The relationship $\Phi_m(\zeta) = (1 - \gamma_2\,\zeta)^{-1/4}$ in Eq. (6.307) is called the Businger-Dyer-Pandolfo relationship[58] (Fig. 6.40). The relationship $\Phi_h(\zeta) = {\Phi_m}^2(\zeta)$ in Eq. (6.307) for unstable stratification was first suggested by Businger and Pandolfo and eventually proved by Dyer and Hicks for the stability range $-1 \leq \zeta < 0$.

[58]The Businger-Dyer-Pandolfo relationship was later experimentally determined by Dyer and Hicks, Businger et al. and others, where their results mainly cover the stability range $-2 \leq \zeta < 0$.

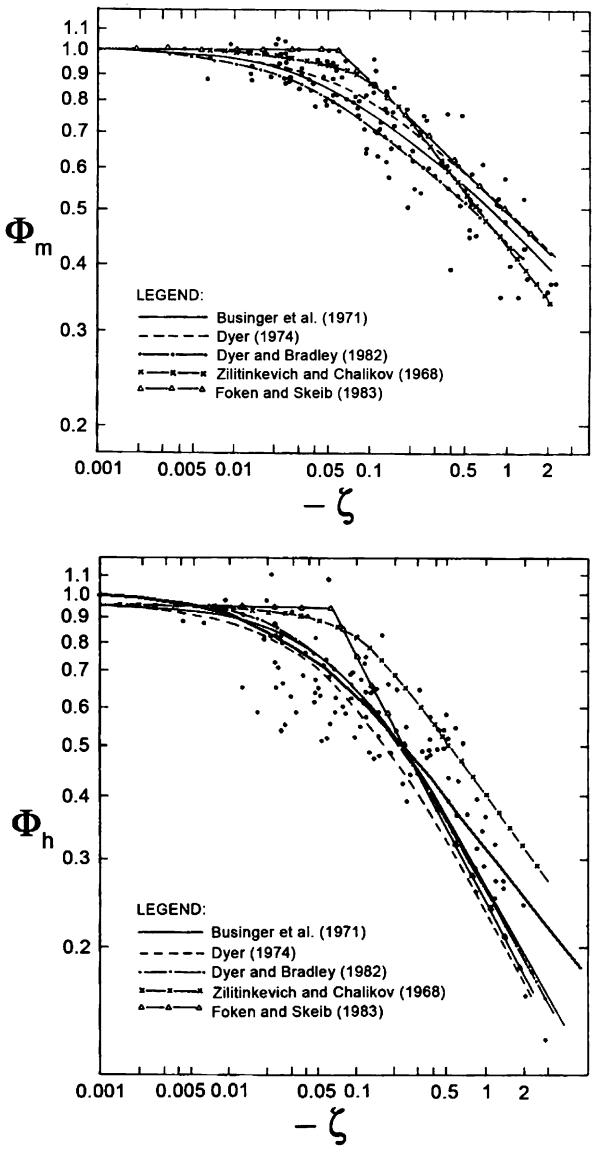

Fig. 6.40 The local similarity functions Φ_m and Φ_h versus the Obukhov number ζ for unstable stratification. The *dots* represent Högström's field data, and the *gray line* on the r.h.s. illustrates Eq. (6.315) (From Högström (1988))

Instead of the Businger-Dyer-Pandolfo relationship for momentum under unstable stratification, we can apply the O'KEYPS formula,[59]

$$\Phi_m{}^4(\zeta) - \gamma_7\,\zeta\,\Phi_m{}^3(\zeta) = 1 \quad for\ \zeta \le 0 \tag{6.310}$$

[59]O'KEYPS stands for the initials of various authors who proposed this formula (Obukhov, Kazansky and Monin, Ellison, Yamamoto, Panofsky, and Sellers).

alternatively. It indicates a $\Phi_m(\zeta) \cong (-\gamma_7\,\zeta)^{-1/3}$ behavior for Obukhov numbers much smaller than zero, for which $\Phi_m(\zeta) \ll -\gamma_7\,\zeta$ becomes valid. The O'KEYPS formula with $\gamma_7 \cong 9$ is experimentally proved for the range $-2 \le \zeta < 0$; Panofsky[60] and Dutton,[61] however, recommended: $\gamma_7 \cong 15$. From a physical point of view, the O'KEYPS formula seems to be preferable over the Businger-Dyer-Pandolfo relationship because the former can be related to the local balance equation for TKE.

In case of steady-state conditions, the local balance equation for TKE (6.202) becomes

$$0 = -\frac{\partial}{\partial z}\left(\bar{\rho}\,\overline{w'\,\frac{\mathbf{v}'^2}{2}} + \overline{w'\,p'}\right) - \overline{\varepsilon^*} + \frac{g}{c_p\,\bar{\Theta}}\left(H + 0.61\,c_{p,0}\,\bar{\Theta}\,F_q\right) + \boldsymbol{\tau}\cdot\frac{\partial\overline{\mathbf{v}_H}}{\partial z}$$

Here, we ignored $\overline{\mathbf{v}'\cdot\mathbf{J}}$. Multiplying this equation with $\Lambda/\left(\bar{\rho}\,{u_*}^3\right)$ yields

$$\begin{aligned} 0 = &-\frac{\Lambda}{\bar{\rho}\,{u_*}^3}\,\frac{\partial}{\partial z}\left(\bar{\rho}\,\overline{w'\,\frac{\mathbf{v}'^2}{2}} + \overline{w'\,p'}\right) - \frac{\Lambda}{{u_*}^3}\,\bar{\varepsilon} \\ &+\frac{\Lambda}{\bar{\rho}\,{u_*}^3}\,\frac{g}{c_p\,\bar{\Theta}}\left(H + 0.61\,c_{p,0}\,\bar{\Theta}\,F_q\right) + \frac{\Lambda}{u_*}\left|\frac{\partial\overline{\mathbf{v}_H}}{\partial z}\right| \end{aligned}$$

Thus, in accord with the definition of the Obukov stability length (Eq. (6.288)), we obtain

$$0 = -\Phi_d(\zeta) + \Phi_m(\zeta) - \zeta - \Phi_\varepsilon(\zeta) \tag{6.311}$$

where

$$\Phi_d(\zeta) = \frac{\Lambda}{\bar{\rho}\,{u_*}^3}\,\frac{\partial}{\partial z}\left(\bar{\rho}\,\overline{w'\,\frac{\mathbf{v}'^2}{2}} + \overline{w'\,p'}\right)$$

$$\Phi_\varepsilon(\zeta) = \frac{\Lambda}{{u_*}^3}\,\bar{\varepsilon}$$

and

$$\Phi_m(\zeta) = \frac{\Lambda}{u_*}\left|\frac{\partial\overline{\mathbf{v}_H}}{\partial z}\right|.$$

[60] Hans A. Panofsky, German-American meteorologist, 1917–1988.

[61] John A. Dutton, American meteorologist.

Here, $\Phi_d(\zeta)$ represents the non-dimensional divergence of both the eddy flux of TKE, $E = \bar{\rho}\,\overline{w'\,\mathbf{v}'^2}/2$, and the eddy flux, $P = \overline{w'\,p'}$, resulting from pressure and vertical wind speed fluctuations. It can be established by the similarity hypothesis $F(\Lambda, L, u_*, \partial(E+P)/\partial z) = 0$. Furthermore, $\Phi_\varepsilon(\zeta)$ is the similarity function for the energy dissipation $\bar{\varepsilon}$. As shown later (Eqs. (6.330) and (6.331)), it is based on the similarity hypothesis $F(\Lambda, L, u_*, \bar{\varepsilon}) = 0$. Here, we can relate it to the Heisenberg-von Weizsäcker law so that we have $\Phi_\varepsilon(\zeta) = {\Phi_m}^{-3}(\zeta)$. Postulating a mixing length for non-neutral conditions by $\Lambda = \Lambda_P\,\Phi_\Lambda(\zeta)$, with which Fortak as well as Herbert and Panhans introduced the similarity function $\Phi_\Lambda(\zeta)$ for improving the treatment of this length scale in dependence on non-neutral conditions leads, therefore, to

$$ {\Phi_m}^4(\zeta) - \left(\frac{\Phi_d(\zeta)}{\zeta} + 1\right)\zeta\,{\Phi_m}^3(\zeta) = {\Phi_\Lambda}^{-4}(\zeta) \tag{6.312} $$

This formula may be valid for both unstable and stable stratification. Under the assumption that $\Lambda = \Lambda_P$, we obtain

$$ {\Phi_m}^4(\zeta) - \left(\frac{\Phi_d(\zeta)}{\zeta} + 1\right)\zeta\,{\Phi_m}^3(\zeta) = 1 \tag{6.313} $$

Comparing this equation with formula (6.310) yields

$$ \gamma_7 = \frac{\Phi_d(\zeta)}{\zeta} + 1 $$

This means that γ_7 is probably not a constant.

Since the O'KEYPS formula is bulky, Carl et al. as well as Gavrilov and Petrov eventually proposed the expression

$$ \Phi_m(\zeta) = (1 - \gamma_8\,\zeta)^{-1/3} \tag{6.314} $$

for the stability range $-10 \le \zeta \le 0$. Here $\gamma_8 \cong 15$ was determined using observations from various locations. This equation reflects the same asymptotic behavior like the O'KEYPS formula, but notably differs from that of the Businger-Dyer-Pandolfo relationship (Fig. 5.4). Kramm et al. proposed the following local similarity function for sensible heat

$$ \Phi_h(\zeta) = (1 - \gamma_9\,\zeta)^{-1/3} \tag{6.315} $$

with $\gamma_9 \cong 35.7$. This formula is illustrated on the r.h.s. of Fig. 6.40 together with those deduced from various field campaigns. Obviously, this local similarity function substantially agrees with Högström's field data for the stability range $-2 < \zeta \le 0$ and tends to the free convective conditions as described by Prandtl-Obukhov-Priestley scaling (Fig. 6.41).

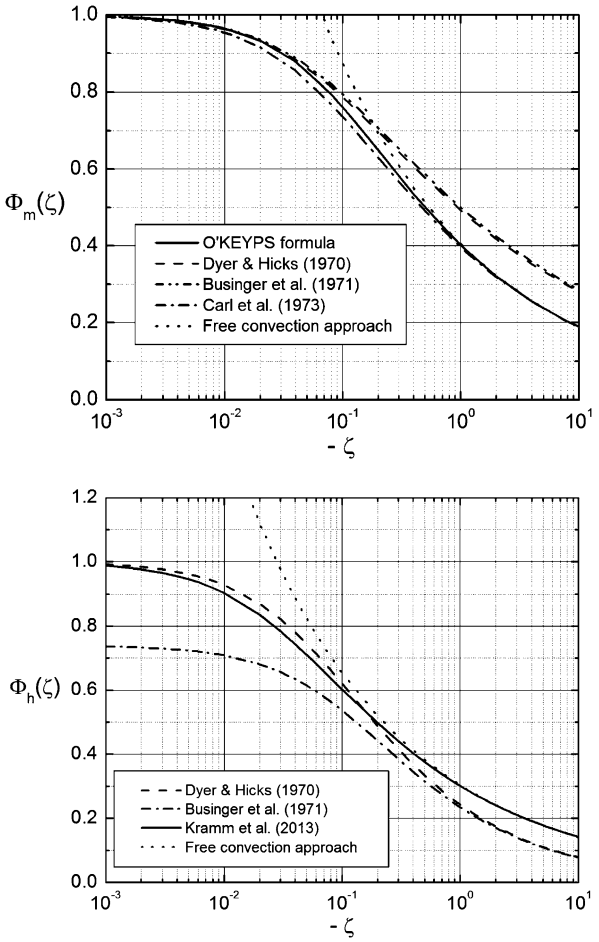

Fig. 6.41 Various local similarity functions Φ_m and Φ_h versus the Obukhov number ζ for unstable stratification (From Kramm et al. (2013))

Expressing the gradient-Richardson number (6.213) by the non-dimensional gradients and assuming that $\Phi_q(\zeta) = \Phi_h(\zeta)$ (formula (6.307)) yield

$$Ri = \frac{\Phi_h(\zeta)}{(\Phi_m(\zeta))^2}\,\zeta. \tag{6.316}$$

Based on Webb's recommendation $\Phi_q(\zeta) = \Phi_h(\zeta) = \Phi_m(\zeta)$ for stable stratification, we obtain

$$Ri = \frac{\zeta}{1+\gamma_1\,\zeta} \quad for\ \zeta > 0. \tag{6.317}$$

Obviously, under such conditions Pr_t is equal or close to unity for stable stratification, i.e. Ri and Ri_f are (nearly) identical. Figure 6.42 illustrates gradient-

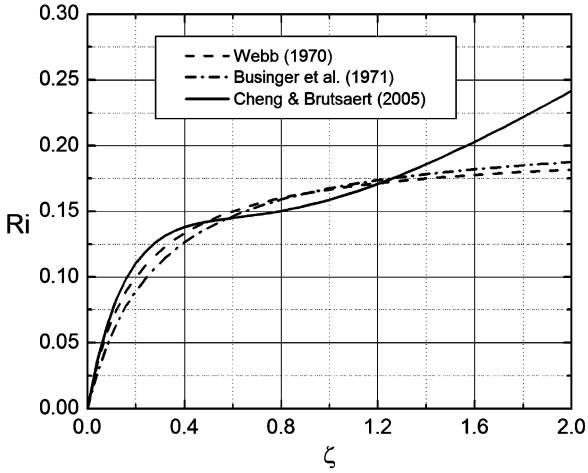

Fig. 6.42 Gradient-Richardson number, Ri, versus the Obkhov number, ζ, for stable stratification, where Ri has been deduced on the basis of formulae (6.306)–(6.309) and (6.316)

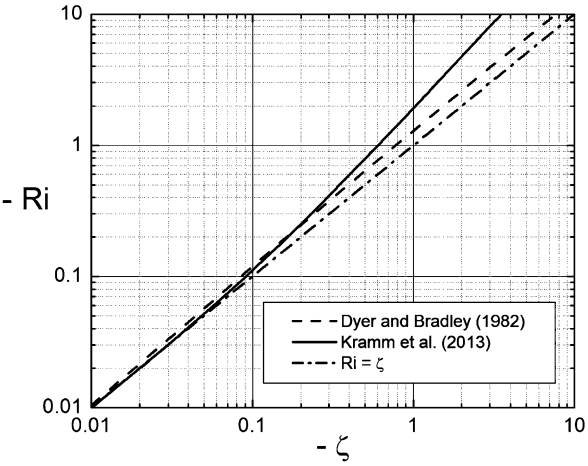

Fig. 6.43 Gradient Richardson number, Ri, versus the Obkhov number, ζ, for unstable stratification, where Ri has been deduced on the basis of formulae (6.314)–(6.316). The one-to-one line represents $Ri = \zeta$ (Eq. (6.318)) (From Kramm et al. (2013))

Richardson numbers for stable stratification that are based on formulae (6.306)–(6.309), and (6.316). Obviously, the gradient-Richardson number that is based on the Φ-functions of Cheng and Brutsaert notably differs from those of Webb and Businger et al.

The Businger-Pandolfo relationship $\Phi_h(\zeta) = {\Phi_m}^2(\zeta)$ for unstable stratification leads to

$$Ri = \zeta \quad for\ \zeta < 0. \tag{6.318}$$

Dyer and Bradley as well as Webb pointed out that small deviations from this identity might occur. Figure 6.43 illustrates gradient-Richardson numbers deduced on the basis of Eqs. (6.314)–(6.316). As suggested by Dyer and Bradley as well as

Webb the condition $|Ri| > |\zeta|$ is fulfilled, but the deviation from the one-to-one line characterized by $Ri = \zeta$ is notably stronger than empirically found, for instance, by Dyer and Bradley.

Variance Relationships

At the beginning of this subsection, we derived flux-gradient relationships on the basis of the dimensional π-invariants analysis. In studies on ASL turbulence, however, we have not only to consider covariance terms that represent the eddy fluxes, but also variance terms. Therefore, we have a strong interest to apply the procedure of non-dimensionalization for determining the various variance terms like $\overline{u'^2}$,$\overline{v'^2}$, $\overline{w'^2}$, $\overline{\Theta'^2}$, and $\overline{q'^2}$. To achieve this goal, we have to replace the vertical gradients in the various similarity hypotheses by the respective variance terms. Thus, in all instances of variance relationships, the number of dimensional quantities is $k = 4$, too. The rank of the various dimensional matrices is $r = 2$. Again, we have $p = k - r = 2$ independent π numbers, i.e. we also can establish universal functions in the cases of variance relationships.

We first consider the variance of the vertical velocity component, $\overline{w'^2}$. Here, the similarity hypothesis reads $F\left(z-d, L, u_*, \overline{w'^2}\right) = 0$. The dimensional π-invariants analysis provides

$$\pi_1 = \frac{\sigma_w}{u_*} = \varphi_w\left(\pi_2\right) = \varphi_w\left(\zeta\right). \tag{6.319}$$

Here $\sigma_w = \left(\overline{w'^2}\right)^{1/2}$ is the standard deviation of the vertical velocity component, σ_w/u_* is the normalized standard deviation, and $\varphi_w\left(\zeta\right)$ is the respective local similarity function or universal function. Since we cannot quantify it by the dimensional π-invariants analysis because two π numbers exist, we have to determine it empirically or/and theoretically. Lumley[62] and Panofsky recommended for both stable and unstable stratification

$$\frac{\sigma_w}{u_*} = \varphi_w\left(\zeta\right) = A_w\left(\Phi_m\left(\zeta\right) - 2.5\,\zeta\right)^{1/3} \tag{6.320}$$

that leads to $\sigma_w/u_* = A_w = 1.3$ for neutral stratification. This formula fits the observation well, but in the case of stable stratification, large scatter occurs. Panofsky et al. eventually recommended for unstable stratification

$$\frac{\sigma_w}{u_*} = \varphi_w\left(\zeta\right) = A_w\left(1 - 3\,\zeta\right)^{1/3} \tag{6.321}$$

that fits observation at smooth sites very well. Since ζ varies with height and u_* is height-invariant, the normalized standard deviation is a function of height, too.

[62] John L. Lumley, American mechanical and aerospace engineer, born 1930.

We can deduce local similarity functions for the normalized standard deviations $\sigma_u/u_* = \left(\overline{u'^2}\right)^{1/2}/u_* = \varphi_u(\zeta)$ and $\sigma_v/u_* = \left(\overline{v'^2}\right)^{1/2}/u_* = \varphi_v(\zeta)$ of the horizontal velocity components u and v in a similar manner. However, $\varphi_u(\zeta)$ and $\varphi_v(\zeta)$ considerably differ from $\varphi_w(\zeta)$. Following Panofsky et al., we can express the normalized standard deviation of the horizontal wind component, σ_U/u_*, by

$$\frac{\sigma_U}{u_*} = \varphi_U(\zeta) = (A_U - B_U\ \zeta_i)^{1/3} \tag{6.322}$$

with $A_U = 12$ and $B_U = 0.5$. Here ζ_i corresponds to the height of the lowest inversion, z_i, considered as the top of the boundary layer. Customarily, the **Deardorff**[63] velocity $w_* = \left(g\ H\ z_i/\left(\Theta_m\ c_p\ \bar{\rho}\right)\right)^{1/3}$ is considered as an appropriate velocity scale in convective-mixed-layer similarity, but not the friction velocity. However, in accord with the definition of the Obukhov stability length, we can relate this velocity to the friction velocity by $w_* = u_*\ \kappa^{-1/3}\ (-\zeta_i)^{1/3}$. As a fixed height z_i is used in this formula, the quantity σ_U/u_* does not vary with height, in complete contrast to σ_w/u_*. This instance of the normalized standard deviation of the horizontal wind component reflects is a weakness of the dimensional π-invariants analysis. It might be that the similarity hypothesis provides an apparently reasonable result, even though it disagrees with the physical behavior because a generalized homogeneity or symmetry is non-existant. Andreas and Hicks, for instance, argued that perhaps, it is time to acknowledge that the similarity hypothesis, on which the derivation of σ_U/u_* is based, violates too many of the assumptions on which Monin-Obukhov scaling relies, and it is time to stop trying to force σ_U/u_* into artificial similarity relations.

For potential temperature variance, $\overline{\Theta'^2}$, the similarity hypothesis reads $F\left(z-d, L, \Theta_*, \overline{\Theta'^2}\right) = 0$. The dimensional π-invariants analysis provides

$$\pi_1 = \frac{\sigma_\Theta}{\Theta_*} = \varphi_\Theta(\pi_2) = \varphi_\Theta(\zeta)\,. \tag{6.323}$$

Here, $\sigma_\Theta = \left(\overline{\Theta'^2}\right)^{1/2}$ is the standard deviation of the potential temperature, σ_Θ/Θ_* is the normalized standard deviation for potential temperature, and $\varphi_\Theta(\zeta)$ is the respective local similarity (or universal) function. Since Θ_* is height-invariant, the standard deviation is a function of height, too. We can express the local similarity function by

$$\varphi_\Theta(\zeta) = \begin{cases} A_\Theta\ (B_\Theta - C_\Theta\ \zeta)^{-1/3} & for\ \zeta < 0 \\ const. & for\ \zeta \geq 0 \end{cases} \tag{6.324}$$

[63] James W. Deardorff, American meteorologist, born 1928.

where A_Θ, B_Θ, and C_Θ are constants. Wyngaard et al., for instance, found for unstable stratification in the range of $-0.7 \leq \zeta < 0$: $A_\Theta = -0.95$, $B_\Theta = 0$, and $C_\Theta = 1$ which closely agree with those of Monji deduced for the range of $-10 \leq \zeta \leq -0.1$. For stable stratification in the range of $0 \leq \zeta \leq 1$, Wyngaard et al. obtained $\varphi_\Theta(\zeta) = 1.8$.

In the case of water vapor, we have to consider the fluctuation of the partial density of water vapor, $\overline{\rho_w{}'^2}$ because the specific humidity is a non-dimensional quantity (Chap. 2). The similarity hypothesis reads $F\left(z-d, L, \rho_{w,*}, \overline{\rho_w{}'^2}\right) = 0$. The dimensional π-invariants analysis gives

$$\frac{\tilde{\sigma}_q}{\rho_{w,*}} \cong \frac{\bar{\rho}\left(\overline{q'^2}\right)^{1/2}}{\bar{\rho}\, q_*} = \frac{\left(\overline{q'^2}\right)^{1/2}}{q_*} = \frac{\sigma_q}{q_*} = \varphi_q(\zeta). \tag{6.325}$$

Here, $\tilde{\sigma}_q = \left(\overline{\rho_w{}'^2}\right)^{1/2}$ is the standard deviation of the partial density of water vapor. We can approximate it by $\tilde{\sigma}_q = \left(\overline{\rho_w{}'^2}\right)^{1/2} \cong \left(\overline{\rho}^2\, \overline{q'^2}\right)^{1/2} = \bar{\rho}\left(\overline{q'^2}\right)^{1/2}$ with $\sigma_q = \left(\overline{q'^2}\right)^{1/2}$, the standard deviation of the specific humidity. The local similarity function, $\varphi_q(\zeta)$, can be considered as a universal function, too. We can express the local similarity function $\varphi_q(\zeta)$ in a similar manner like $\varphi_\Theta(\zeta)$ (Eq. (6.324)). Högström and Smedman-Högström, for instance, postulated for unstable stratification

$$\varphi_q(\zeta) = 1.03\, \zeta^{-1/3}. \tag{6.326}$$

As pointed out by Panofsky and Dutton, it does not significantly differ from the normalized standard deviation recommended by Wyngaard et al. for the potential temperature.

Equations (6.321), (6.324), and (6.326) can be applied to derive the structure parameters (also called the structure constant) ${C_\chi}^2$ (χ stands for w, Θ, and q) that are closely identified with the structure parameter ${C_n}^2$ of the refractive index for acoustic and electromagnetic waves propagating through the atmosphere. Rearranging Eq. (6.324) provides

$$\overline{\Theta'^2} = {\Theta_*}^2\, {\varphi_\Theta}^2(\zeta). \tag{6.327}$$

Dividing this equation by $(z-d)^{2/3}$ yields

$${C_\Theta}^2 = \frac{\overline{\Theta'^2}}{(z-d)^{2/3}} = \frac{{\Theta_*}^2\, {\varphi_\Theta}^2(\zeta)}{(z-d)^{2/3}}. \tag{6.328}$$

The quantity ${C_\Theta}^2$ is the structure parameter for forced-convective conditions, where $z-d$ serves as a characteristic length scale. Combining formulae (6.324) and (6.328) provides for unstable stratification

$$\frac{{C_\Theta}^2 \ (z-d)^{2/3}}{{\Theta_*}^2} = 0.90 \ \zeta^{-2/3}. \tag{6.329}$$

Dissipation of Kinetic Energy

In deriving the local similarity function or universal function for the averaged dissipation of kinetic energy, $\bar{\varepsilon} = \overline{\varepsilon^*}$, we have to replace the vertical gradient of the mean horizontal wind speed, $Q_4 = \partial U/\partial z$, in the similarity hypothesis for momentum by $Q_4 = \bar{\varepsilon}$. Thus, we have $F\,(z-d, L, u_*, \bar{\varepsilon}) = 0$. The dimensional π-invariants analysis provides

$$\pi_1 = \frac{z-d}{{u_*}^3} \ \bar{\varepsilon} = \varphi_\varepsilon\,(\pi_2) = \varphi_\varepsilon\,(\zeta)\,. \tag{6.330}$$

Introducing the von Kármán constant yields

$$\frac{\kappa \ (z-d)}{{u_*}^3} \ \bar{\varepsilon} = \Phi_\varepsilon\,(\zeta)\,. \tag{6.331}$$

We can consider this local similarity function, $\Phi_\varepsilon\,(\zeta) = \kappa \ \varphi_\varepsilon\,(\zeta)$ as a universal function. In case of neutral stratification, for which the similarity hypothesis, $F\,(z-d, u_*, \bar{\varepsilon}) = 0$, seems to be acceptable, κ is related to the π number by $\pi_1 = \phi_\varepsilon\,(0) = \kappa^{-1}$. It follows that $\Phi_\varepsilon\,(0)$ is equal to unity. For thermal stratification, Wyngaard and Coté as well as Kaimal et al. recommended

$$\Phi_\varepsilon\,(\zeta) = \begin{cases} \left(1 + 0.5\ |\zeta|^{2/3}\right)^{3/2} & for\ -2 \le \zeta \le 0 \\ \left(1 + 2.5\ |\zeta|^{3/5}\right)^{3/2} & for\ 0 \le \zeta \le 2. \end{cases} \tag{6.332}$$

Obviously, there is a notable discrepancy between these formulae and the relation $\Phi_\varepsilon\,(\zeta) = {\Phi_m}^{-3}\,(\zeta)$, which is based on the Heisenberg-von Weizsäcker law.

6.8.6.5 Prandtl-Obukhov-Priestley Scaling

Similarity Hypothesis for Sensible Heat

Under free-convective conditions, i.e. $\zeta \ll 0$, the Obukhov stability length is no longer relevant for the vertical profiles of mean values of wind speed, potential temperature, and specific humidity because the vertical transfer of momentum,

sensible heat, and matter is rather independent of the friction velocity u_*. We can express it by

$$\zeta_{fc} = \lim_{u_* \to 0} \frac{z}{L} = -\lim_{u_* \to 0} \kappa \frac{g}{\bar{\Theta}} \frac{H}{c_p \, \bar{\rho} \, {u_*}^3} z \tag{6.333}$$

where the subscript fc indicates free convective conditions.

According to Prandtl, Obukhov, and Priestley, the similarity hypothesis for the free-convective range reads $F\left(z-d, H/\left(c_{p,0}\,\bar{\rho}\right), g/\bar{\Theta}, \partial\bar{\Theta}/\partial z\right) = 0$. In this instance, the number of the dimensional quantities is $k = 4$, too. Now, the rank of the dimensional matrix is $r = 3$. Thus, we obtain $p = k - r = 1$ independent π numbers. The dimensional π-invariants analysis provides

$$\pi_1 = (z-d)^{4/3} \left(\frac{H}{c_{p,0}\,\bar{\rho}}\right)^{-2/3} \left(\frac{g}{\bar{\Theta}}\right)^{1/3} \left(\frac{\partial\bar{\Theta}}{\partial z}\right). \tag{6.334}$$

Rearranging yields finally

$$\frac{\partial\bar{\Theta}}{\partial z} = \pi_1 \left(\frac{H}{c_{p,0}\,\bar{\rho}}\right)^{2/3} \left(\frac{g}{\bar{\Theta}}\right)^{-1/3} (z-d)^{-4/3}. \tag{6.335}$$

The π number is equal to Priestley's constant, C, i.e. $\pi_1 = C \cong -1.03$. The negative sign guarantees a lapse rate in case of free convective conditions for which $H > 0$ is considered. Equation (6.335) is called the $-4/3$ power law. Rearranging this equation in the sense of Monin-Obukhov scaling for dry air (i.e. the influence of water vapor is ignored) leads to

$$\frac{\kappa\ (z-d)}{\Theta_*} \frac{\partial\overline{\Theta}}{\partial z} = -\pi\,\kappa^{4/3}(-\zeta)^{-1/3} = (-35.7\,\zeta)^{-1/3}. \tag{6.336}$$

Obviously, formulae (6.306) and (6.307) with $\Phi_h(\zeta) = {\Phi_m}^2(\zeta) = (1-\gamma\,\zeta)^{-1/2}$ do not converge to the asymptotic solution (6.336) if $\zeta \ll 0$. Furthermore, the O'KEYPS formula (6.310) and the local similarity function (6.314), and formula (6.315) suggest that for unstable stratification the $-1/3$ power law should be valid for both momentum and sensible heat (Fig. 6.41).

Variance Relationship

To derive the variance relationship for free-convective conditions, we have to consider the similarity hypotheses $F\left(z-d, H/\left(c_{p,0}\,\bar{\rho}\right), g/\bar{\Theta}, \overline{\Theta'^2}\right) = 0$. The dimensional π-invariants analysis yields

$$\pi_1 = (z-d)^{1/3} \left(\frac{H}{c_{p,0}\,\bar{\rho}}\right)^{-2/3} \left(\frac{g}{\bar{\Theta}}\right)^{1/3} \left(\overline{\Theta'^2}\right)^{1/2} \tag{6.337}$$

or

$$\left(\overline{\Theta'^2}\right)^{1/2} = \pi_1 \left(\frac{H}{c_{p,0}\,\bar{\rho}}\right)^{2/3} \left(\frac{g}{\bar{\Theta}}\right)^{-1/3} (z-d)^{-1/3}. \tag{6.338}$$

Rearranging this equation in the sense of the Monin-Obukhov similarity hypothesis under consideration of dry air only leads to the asymptotic solution for free-convective conditions

$$\frac{\sigma_\Theta}{\Theta_*} = \frac{\left(\overline{\Theta'^2}\right)^{1/2}}{\Theta_*} = \pi_1\, \kappa^{1/3}\, \zeta^{-1/3}. \tag{6.339}$$

Apparently, any empirical approach should agree with the $\zeta^{-1/3}$ behavior under free-convective conditions. As documented by empirical results, the normalized standard deviation σ_Θ/Θ_* shows a $\zeta^{-1/3}$ behavior for the entire range of unstable stratification.

According to formula (6.338), we obtain for the temperature variance

$$\overline{\Theta'^2} = {\pi_1}^2 \left(\frac{H}{c_{p,0}\,\bar{\rho}}\right)^{4/3} \left(\frac{g}{\bar{\Theta}}\right)^{-2/3} (z-d)^{-2/3}. \tag{6.340}$$

Dividing this equation by $(z-d)^{2/3}$ yields

$${C_\Theta}^2 = \frac{\overline{\Theta'^2}}{(z-d)^{2/3}} = {\pi_1}^2 \left(\frac{H}{c_{p,0}\,\bar{\rho}}\right)^{4/3} \left(\frac{g}{\bar{\Theta}}\right)^{-2/3} (z-d)^{-4/3}. \tag{6.341}$$

Here ${C_\Theta}^2$ is the structure parameter for free-convective conditions. Panofsky and Dutton recommended ${\pi_1}^2 \cong 2.5$ so that the π number amounts to $\pi_1 \cong 1.58$.

6.8.6.6 Profile Relations and Integral Similarity Functions

The gradients of horizontal wind speed, temperature, humidity, and long-lived trace gases like carbon dioxide cannot be measured because of the limited spatial resolution of available sensors (Fig. 6.44). This means that the true flux-gradient relationships and, hence, the local similarity functions, which can also be considered as non-dimensional gradients, are unsuitable for estimating the eddy fluxes of momentum, sensible heat, water vapor, and long-lived trace gases (Chap. 5). Consequently, these eddy fluxes have to be related, at least, to finite differences in the vertical direction of horizontal wind speed, temperature, humidity, and long-lived trace-gases. We can perform this discretization by integrating the non-

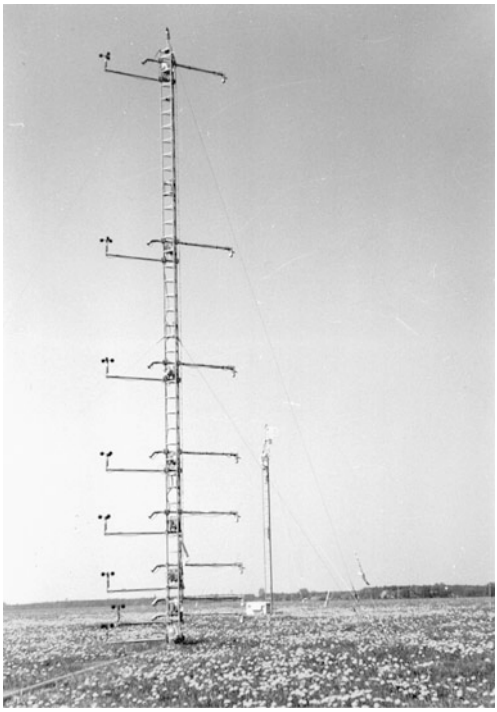

Fig. 6.44 Instrumented masts used in profile measurements (foreground) and eddy covariance measurements (background) at the field research station Melpitz of the Leibniz Institute for Tropospheric Research Leipzig, Germany (Photo courtesy to Spindler who took the photo in 2002)

dimensional gradients over the layer under study, when we consider the constant flux approximations (Sect. 6.8.6.1; Chap. 5). This procedure was already carried out in the case of the logarithmic wind profile for neutral stratification (Eq. (6.278)). The results of such integrations are denoted (vertical) profile functions.

Results from direct measurements of eddy fluxes and corresponding vertical profiles of the mean values of wind speed, temperature, humidity, and long-lived trace gases obtained from concurrent measurements can serve to derive local similarity functions. Profile measurements are customarily carried out using **cup anemometers** and artificially ventilated **psychrometers** (Appendix B), and slow-response infrared H_2O/CO_2 sensors. To perform eddy covariance measurements of momentum, sensible heat, water vapor, and carbon dioxide we have to use fast-response sensors like sonic anemometers/thermometers (measurement rate: $\geq$20 Hz) and infrared open-path H_2O/CO_2 sensors (measurement rate: $\geq$10 Hz) to record fluctuations of wind vector, temperature, humidity, and CO_2 concentrations. For the purpose of evaluation of such local similarity functions, we need quite independent data sets of directly measured eddy fluxes and mean vertical profiles even obtained concurrently. Data sets from field campaigns not considered for deriving such local similarity functions clearly satisfy this requirement.

Integral Similarity Functions

Integrating expression (6.294) for the non-dimensional wind shear, $\Phi_m(\zeta)$, over the height interval $[z_r, z_R]$, where z_r and z_R are the lower and upper boundaries of the fully turbulent part of the Prandtl layer yields

$$U(z_R) - U(z_r) = \frac{u_*}{\kappa} \int_{z_r}^{z_R} \frac{\Phi_m((z-d)/L)}{z-d}\, dz = \frac{u_*}{\kappa} \int_{z_r}^{z_R} \frac{1 - 1 + \Phi_m((z-d)/L)}{z-d}\, dz$$

$$= \frac{u_*}{\kappa} \left(\int_{z_r}^{z_R} \frac{1}{z-d}\, dz - \int_{z_r}^{z_R} \frac{1 - \Phi_m((z-d)/L)}{z-d}\, dz \right)$$

or

$$U(z_R) - U(z_r) = \frac{u_*}{\kappa} \left(\ln \frac{z_R - d}{z_r - d} - \Psi_m(\zeta_R, \zeta_r) \right) \tag{6.342}$$

where

$$\Psi_m(\zeta_R, \zeta_r) = \int_{\zeta_r}^{\zeta_R} \frac{1 - \Phi_m(\zeta)}{\zeta}\, d\zeta \tag{6.343}$$

is called Panofsky's integral similarity function for momentum because Panofsky was the first to derive Eqs. (6.342) and (6.343). We obtain the logarithmic wind profile for neutral stratification (Eq. (6.278)) if $\Phi_m(0) = 1$ and, hence, $\Psi_m(\zeta_R, \zeta_r) = 0$. The integral similarity function is clearly defined by Eq. (6.343), i.e. this definition is independent of the shape of $\Phi_m(\zeta)$.

Similarly, we obtain for the vertical profiles of mean potential temperature, and mean specific humidity

$$\bar{\Theta}(z_R) - \bar{\Theta}(z_r) = \frac{\Theta_*}{\kappa} \left(\ln \frac{z_R - d}{z_r - d} - \Psi_h(\zeta_R, \zeta_r) \right) \tag{6.344}$$

and

$$\bar{q}(z_R) - \bar{q}(z_r) = \frac{q_*}{\kappa} \left(\ln \frac{z_R - d}{z_r - d} - \Psi_q(\zeta_R, \zeta_r) \right). \tag{6.345}$$

Here

$$\Psi_{h,q}(\zeta_R, \zeta_r) = \int_{\zeta_r}^{\zeta_R} \frac{1 - \Phi_{h,q}(\zeta)}{\zeta}\, d\zeta \tag{6.346}$$

represents the integral similarity functions for sensible heat (subscript h) and water vapor (subscript q), respectively.

Inserting formulae (6.306) into Eqs. (6.343) yields

$$\Psi_m(\zeta_R,\ \zeta_r) = \begin{cases} -\gamma_1\ (\zeta_R - \zeta_r) & for\ L > 0 \\ 0 & for\ L \to \infty \\ 2\ln\dfrac{1+y_R}{1+y_r} + \ln\dfrac{1+{y_R}^2}{1+{y_r}^2} - 2\arctan\dfrac{y_R - y_r}{1+y_R\ y_r} & for\ L < 0. \end{cases} . \tag{6.347}$$

Inserting formulae (6.307) into (6.346) provides

$$\Psi_{h,q}(\zeta_R, \zeta_r) = \begin{cases} \Psi_m(\zeta_R, \zeta_r) & for\ L > 0 \\ 0 & for\ L \to \infty \\ 2\ \ln\dfrac{1+{y_R}^2}{1+{y_r}^2} & for\ L < 0. \end{cases} . \tag{6.348}$$

Here, $y_{r,R} = {\Phi_m}^{-1}(\zeta_{r,R}) = (1 - \gamma_2\ \zeta_{r,R})^{1/4}$ is the reciprocal expressions of the local similarity functions for unstable stratification at the two heights z_r and z_R. For $\zeta_r \to 0$ and, hence, $y_r \to 1$, we obtain Paulson's solution for the Businger-Dyer-Pandolfo relationship.

In accord with the integral similarity function for stable stratification (Eq. (6.347)), we obtain the logarithmic-linear wind profile. Because of Webb's recommendation $\Phi_q(\zeta) = \Phi_h(\zeta) = \Phi_m(\zeta)$, the integral similarity functions for sensible heat, and water vapor should be identical with that for momentum. Thus, we would obtain logarithmic-linear profile functions for mean potential temperature and mean specific humidity. Obviously, the linear effect should become more and more important with increasing stability leading to nearly linear profiles for the mean values of wind speed, potential temperature, and specific humidity in case of strongly stable stratification. This, however, is not the case. Inserting the local similarity functions (6.308) and (6.309) into the respective integral similarity functions for momentum yields

$$\Psi_m(\zeta_R, \zeta_r) = -\gamma_3\ \ln\frac{\zeta_R + (1+{\zeta_R}^{\gamma_4})^{\frac{1}{\gamma_4}}}{\zeta_r + (1+{\zeta_r}^{\gamma_4})^{\frac{1}{\gamma_4}}} \tag{6.349}$$

and

$$\Psi_h(\zeta_R, \zeta_r) = -\gamma_5\ \ln\frac{\zeta_R + (1+{\zeta_R}^{\gamma_6})^{\frac{1}{\gamma_6}}}{\zeta_r + (1+{\zeta_r}^{\gamma_6})^{\frac{1}{\gamma_6}}}. \tag{6.350}$$

Figure 6.45 illustrates these different integral similarity functions for stable stratification.

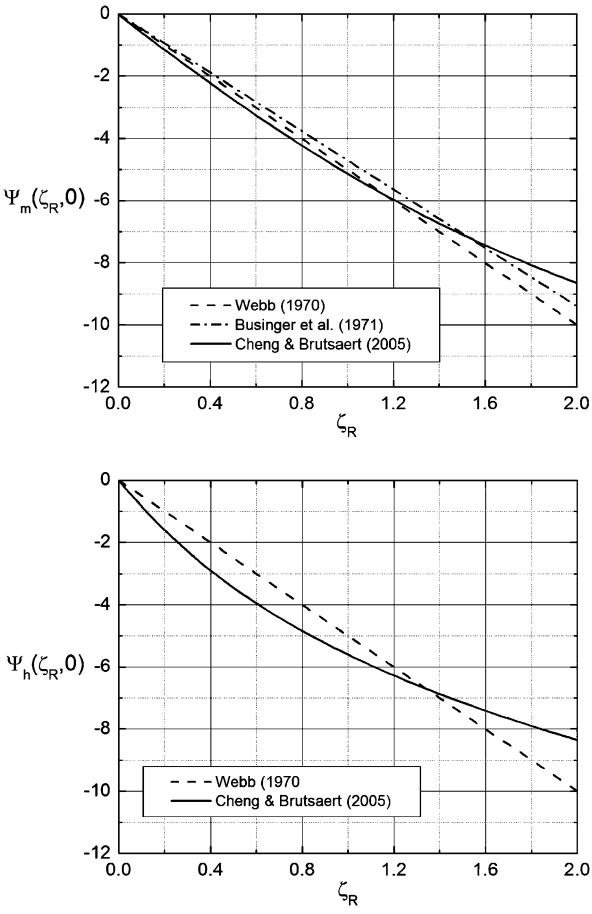

Fig. 6.45 Various forms of the integral similarity functions $\psi_m(\zeta_R, 0)$ and $\psi_h(\zeta_R, 0)$ versus the Obukhov number ζ_R for stable stratification. The references indicate the various local similarity functions (From Kramm et al. (2013))

Inserting the O'KEYPS formula (6.310) into Eq. (6.343) provides

$$\left.\begin{aligned}\Psi_m(\zeta_R,\zeta_r) = {} & \Phi_m(\zeta_r) - \Phi_m(\zeta_R) \\ & + 2\ln\frac{1+\Phi_m(\zeta_R)}{1+\Phi_m(\zeta_r)} + \ln\frac{1+{\Phi_m}^2(\zeta_R)}{1+{\Phi_m}^2(\zeta_r)} \\ & + 2\arctan\frac{\Phi_m(\zeta_R)-\Phi_m(\zeta_r)}{1+\Phi_m(\zeta_R)\,\Phi_m(\zeta_r)} - 3\ln\frac{\Phi_m(\zeta_R)}{\Phi_m(\zeta_r)}\end{aligned}\right\} \text{for } L \le 0 \quad (6.351)$$

with $\Phi_m(\zeta_{r,R})$ provided by the O'KEYPS formula (6.310). Obviously, the solution (6.351) for the O'KEYPS formula is more bulky than that obtained with the Businger-Dyer-Pandolfo relationship (see third row on the r.h.s. of Eq. (6.347)). This bulkiness of the former might be the reason why the latter is more widely used, despite the former has a stronger physical background. For $\zeta_r \to 0$ and, hence, $\Phi_m(\zeta_r) \to 1$, we obtain Paulson's solutions for the O'KEYPS formula.

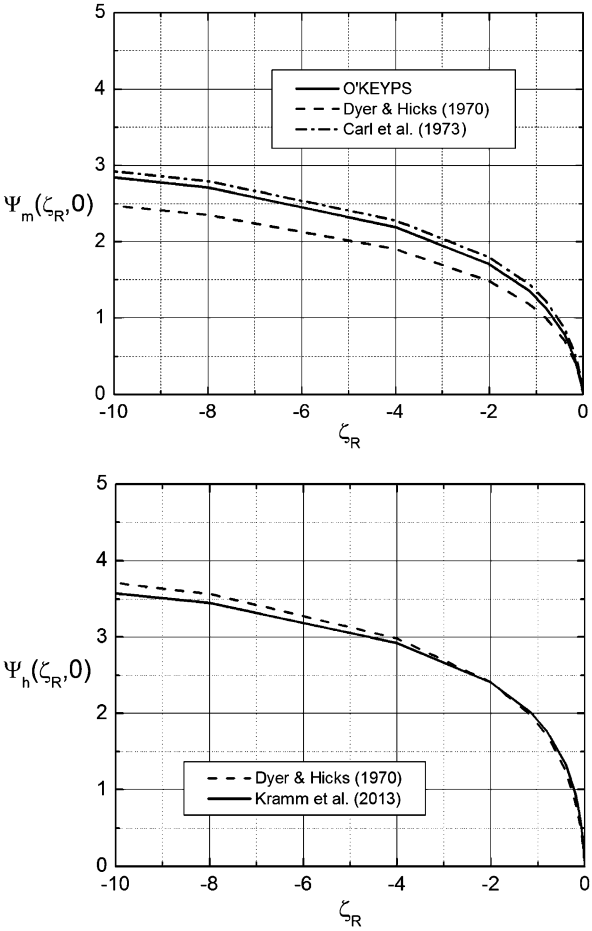

Fig. 6.46 Various forms of the integral similarity functions $\psi_m(\zeta_R, 0)$ and $\psi_h(\zeta_R, 0)$ versus the Obukhov number ζ_R for unstable stratification. The references indicate the various local similarity functions (From Kramm et al. (2013))

Inserting formula (6.314) into Eq. (6.343) provides

$$\Psi_m(\zeta_R, \zeta_r) = \frac{3}{2} \ln \frac{{y_R}^2 + y_R + 1}{{y_r}^2 + y_r + 1} - \sqrt{3} \arctan \frac{x_R - x_r}{1 + x_R\, x_r} \quad for\ L \le 0 \qquad (6.352)$$

with $y_{r,R} = {\Phi_m}^{-1}(\zeta_{r,R}) = (1 - \gamma_8\, \zeta_{r,R})^{1/3}$, the reciprocal expressions of the local similarity functions in the unstable case at the two heights z_r and z_R, and $x_{r,R} = (2\, y_{r,R} + 1)/\sqrt{3}$. It will approach to Lettau's solution if $\zeta_r \to 0$ and, hence, $y_r \to 1$. Figure 6.46 illustrates Eqs. (6.347)–(6.352). As expected, formulae (6.351) and (6.352) only hardly differ when ζ_R tends to Obukhov numbers much smaller than zero, which represent free-convective conditions. Simultaneously, the differences between Eq. (6.347) for unstable stratification and the other two formulae grow continuously.

Similarly, the local similarity function (6.315) leads to

$$\Psi_h(\zeta_R, \zeta_r) = \frac{3}{2} \ln \frac{{y_R}^2 + y_R + 1}{{y_r}^2 + y_r + 1} - \sqrt{3} \arctan \frac{x_R - x_r}{1 + x_R\, x_r} \quad for\ L \le 0 \tag{6.353}$$

with $y_{r,R} = {\Phi_m}^{-1}(\zeta_{r,R}) = (1 - \gamma_9\, \zeta_{r,R})^{1/3}$, the reciprocal expressions of the local similarity functions in the unstable case at the two heights z_r and z_R, and $x_{r,R} = (2\, y_{r,R} + 1)/\sqrt{3}$.

We can use the equation sets (6.342)–(6.353) to determine the scaling quantities u_*, Θ_*, and q_*, and, hence the corresponding fluxes τ, H, and F_{q_1}, as well as the roughness length z_0 (for $z_r = z_0 + d$), and the zero-plane displacement d, from vertical profile measurements of wind speed, potential temperature and specific humidity by least-squares fitting. Figure 6.47 shows typical results of such a procedure for both stable and unstable stratification. Herein, the equation set (6.343)–(6.348) was used. For determining the vertical profiles for the mean values of horizontal wind speed, potential temperature, and specific humidity, and in a further step the respective flux terms, we recommend the following Φ-functions: For stable stratification Eqs. (6.308) and (6.309), and for unstable stratification Eqs. (6.314) and (6.315). Long-lived trace gases may be handled like sensible heat and water vapor if no specific Φ-functions are available.

6.9 Basic Wave Dynamics: Kinematic

Wave denotes a disturbance that travels through space and time. Waves exist in a system, when it obeys dynamic equations in which the spatial changes are coupled with the temporal change. Waves traveling through the atmosphere affect the state variables, stability, and distribution of trace gases. They allow one part of the atmosphere to communicate with another (Chap. 7). The ultimate behavior of any wave is governed by the medium through which the wave propagates momentum and energy and the individual properties of the restoring force responsible for the wave production. Independent of the medium and restoring forces waves can be described by

- Wave frequency ω (real or complex)
- Wave numbers k, l, m
- Phase speed $c = \frac{d\mathbf{v}}{dt}$
- Group velocity c_g
- Dispersion relationship

Any wave propagating at a defined frequency ω has a wavelength λ defined as the distance between repeating features (e.g. troughs, crests). The **frequency** gives the number of repeating events per unit time, and is the ratio of the speed of the wave c to the wavelength $\omega = \frac{c}{\lambda}$. The horizontal and vertical spatial scales, L_x, L_y, L_z of

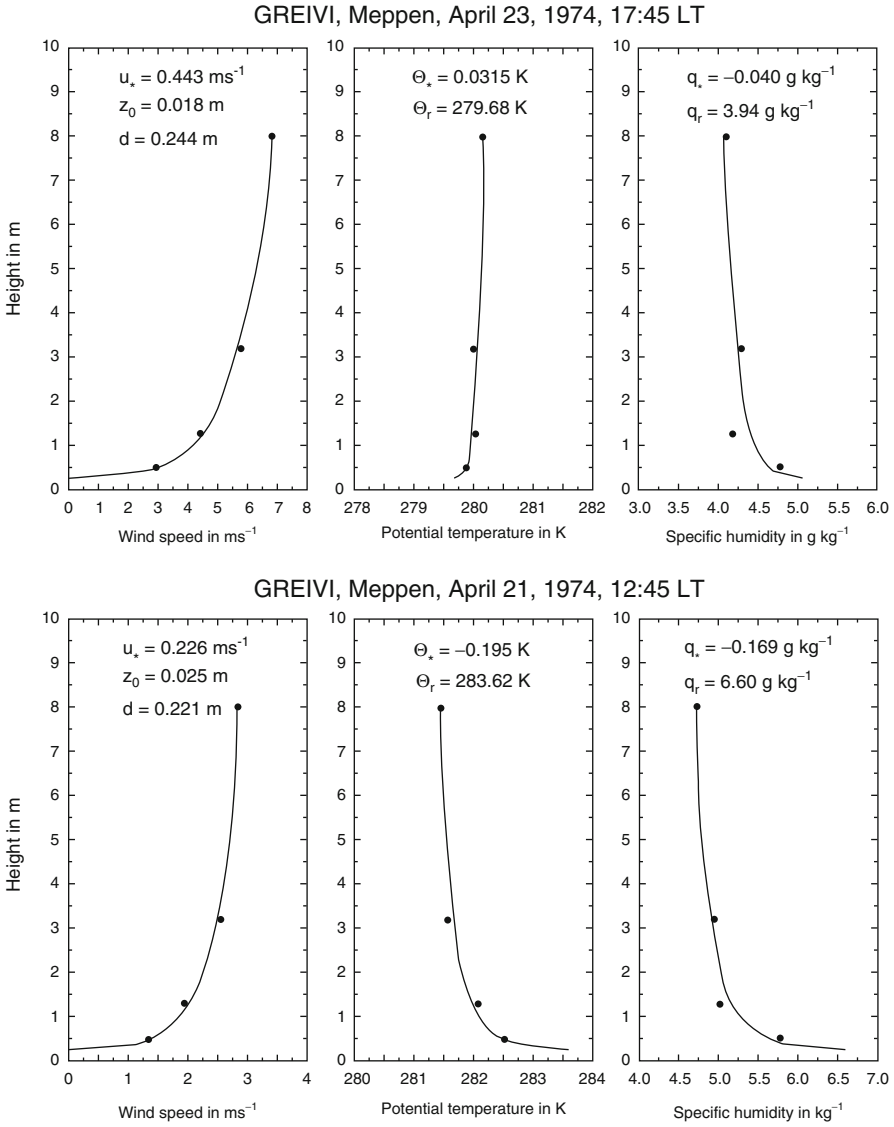

Fig. 6.47 Typical vertical profiles of wind speed, potential temperature, and specific humidity calculated for non-neutral stratification. The *dots* represent the observed values taken from the GREIV I field campaign, and the *solid lines* the calculated profiles using equation set (6.343)–(6.348) (From Kramm and Herbert (2009))

the wave are reciprocally proportional to the wave numbers $k = \frac{2\pi}{L_x}$, $l = \frac{2\pi}{L_y}$, and $m = \frac{2\pi}{L_x}$. Here, the indices x, y, and z denote the west-east, south-north and vertical direction, respectively.

The condition of the system alters periodically according to $\varphi(x, y, z, t) = Re(A \exp(i(kx + ly + mz - \omega t - \alpha)))$. Here Re stands for the real part, A is amplitude, t is time and α is the phase angle that depends on the initial position of the wave. Oscillation is the repeated variation in space with time around an equilibrium state and requires a restoring force (Chap. 2). The amplitude A measures the wave's magnitude of oscillation. Amplitude and phase $kx + ly + mz - \omega t - \alpha$ characterize the wave. For $d(kx + ly + mz - \omega t) = 0$, the wave numbers and frequency are constant in space.

Phase speed c denotes lines of constant phase like wave crest, troughs or any other particular feature of the wave. Phase speeds of a parcel are defined by the ratio of frequency to wave numbers, i.e. $c_{p,x} = \frac{\omega}{k}$, $c_{p,y} = \frac{\omega}{l}$, and $c_{p,z} = \frac{\omega}{m}$. Superposition of waves leads to wave groups that spread with a group velocity c_g.

In the atmosphere, waves are typically very complex due to superposition of wave components of various wavelengths and their nonlinear interaction. Physically dispersion tends to flatten and non-linear effects tend to steepen a wave. Due to this complexity, we often cannot represent waves by a single sinusoidal wave. Nevertheless, we can approximate small-amplitude waves by superposition of wave trains of different wave numbers. For example, we may express a wave in x-direction by a Fourier series of sinusoidal components

$$\varphi(x) = \sum_{n=1}^{\infty} (A_n \sin k_n x + B_n \cos k_n x) \tag{6.354}$$

With the Fourier coefficients

$$A_n = \frac{2}{L} \int_0^L \varphi(x) \sin \frac{2\pi n x}{L} dx \tag{6.355}$$

$$B_n = \frac{2}{L} \int_0^L \varphi(x) \cos \frac{2\pi n x}{L} dx \tag{6.356}$$

The nth Fourier component (nth harmonic of the wave function) φ_n is then given as $A_n \sin k_n x + B_n \cos k_n x$. For an orthogonal relationship we obtain

$$\int_0^L \sin \frac{2\pi n x}{L} \cos \frac{2\pi m x}{L} dx = 0 \qquad \textit{for all } n, m > 0 \tag{6.357}$$

$$\int_0^L \sin \frac{2\pi n x}{L} \sin \frac{2\pi m x}{L} dx = \begin{cases} 0 \text{ for } n \neq m \\ \frac{L}{2} \text{ for } n = m \end{cases}$$

$$\int_0^L \cos \frac{2\pi n x}{L} \cos \frac{2\pi m x}{L} dx = \begin{cases} 0 \text{ for } n \neq m \\ \frac{L}{2} \text{ for } n = m \end{cases}$$

The **dispersion relationship** links the wave frequency and wave number. It is decisive for whether a wave is **dispersive** or **non-dispersive**. Because of the

relationship between phase speed and wave number, a wave composed of a series of Fourier components of different wavelengths may have different phase speeds for each individual component. A wave keeps its initial shape and stays coherent when the phase speed and wave number are independent of each other. Such wave is non-dispersive. When both the frequency $\omega(k, l, m)$ and speed $c(k, l, m)$ are functions of the wave number, dispersion occurs. For a dispersive wave, the velocity of the wave front travels as a function of frequency and the spatial and temporal phase properties of the wave propagation change constantly. Herein waves of shorter wavelength and period travel slower than waves of longer wavelength and period.

For a dissipative,[64] but non-dispersive wave, the wave amplitude decreases and every Fourier component of the wave moves at the same speed, i.e. individual wave groups retain the phase.

By applying scale analysis to the primitive equations based on horizontal scales of motion, we can classify several categories of atmospheric waves

- Sound (acoustic) waves
- Mesoscale waves (e.g. pure gravity waves, inertio-gravity waves, and Kelvin-Helmholtz waves)
- Planetary (Rossby) waves

Each of these waves exhibits multiple flow regimes. The restoring forces differ for the various waves. Sound waves derive their motion from longitudinal expansion and compression. The Coriolis force and the buoyancy force act as restoring force for inertial oscillations and pure gravity waves, respectively. Planetary waves gain their oscillations from meridional variation of the Coriolis force (β-effect). In many NWP models, sound waves are often filtered out as noise because they are of no importance for weather. See the section on the Boussinesq-approximation.

In large-scale dynamics and large-scale NWP, mesoscale waves and sound waves are typically regarded as undesirable noise embedded in the large-scale flow. Typically, they are filtered out in large-scale applications because they can trigger numerical instabilities in operational NWP when the grid increment is not sufficiently small.

Two restoring forces may also work concurrently. Inertio-gravity waves, for instance, move horizontally and vertically at the same time with the buoyancy force and Coriolis force as the restoring mechanisms. Other examples for combined restoring forces are mixed Rossby-gravity waves or mixed acoustic-gravity waves.

Rossby waves are easy to observe by analysis of rawinsonde-derived wind speeds as large-scale meanders of the jet stream, a band of strong wind located around

[64] Dispersion and dissipation are physically different processes. In a dynamical system, dissipation denotes the concept where important mechanisms (e.g. waves, oscillations) lose energy with time because of friction, radiative cooling or turbulence. Energy is converted to heat for which the temperature of the system increases. When a wave loses amplitude, it dissipates.

200 hPa in poleward mid-latitudes. Typically, four to six meanders exist. The wave speed is given by

$$c = u - \frac{\beta}{k^2} \tag{6.358}$$

where c, u, k and β are the wave speed, speed of the mean westerly flow, total wave number and Rossby parameter typically denoted as $\beta = \frac{2\Omega \cos\phi}{R}$. Here, Ω, ϕ, and R are the angular velocity of the Earth rotation, latitude and the radius of the Earth, respectively.

Mesoscale waves can be inferred from microbarographic pressure, thermodynamic soundings, radar echoes, wind profilers, visible and infrared satellite images (Appendix B). We can use such data to forecast mesoscale wave propagation and explain the formation and evolution of a large variety of mesoscale weather phenomena related to the passage of these waves.

Planetary and mesoscale waves play a major role in atmospheric dynamics. The meanders of the planetary waves become very pronounced and can cause formation of cyclones and anticyclones that are responsible for mid-latitude weather patterns. Mesoscale waves transfer energy between large- and small-scale motion, transport momentum and energy vertically and horizontally from one region to the other, generate disturbances like clear air turbulence (CAT) that can affect air safety, trigger hydrodynamic instabilities that cause severe weather and lead to formation of convective storms and clustering of convective cells into a mesoscale convective system.

In the following, we introduce commonly used approximations and discuss their limitations with respect to understanding dynamics of the real, observable systems and circulations. The system may include static (buoyant), shear, symmetric, inertial and baroclinic instabilities. In a structured atmosphere, waves may be reflected, transmitted and over-reflected from certain internal boundaries.

6.9.1 Buoyancy Oscillations

Assume a mean large-scale environment as a reference state (e.g. measurements by rawinsondes) and that potential temperature increases with height. Then any dry-adiabatical displacement of an air parcel from its equilibrium level yields restoring (Chap. 2). Upward (downward) motion leads to negative (positive) buoyancy. When restoring the air parcel may overshoot the equilibrium level followed by an oppositely directed motion. Consequently, in a stable atmosphere, air parcels oscillate vertically around their equilibrium altitude. These motions can be described by air parcel theory (Chap. 2). Parcel theory denotes the analysis of parcels whose pressure

does not deviate from the large-scale environment.[65] In a frictionless Boussinesq flow, the equation of vertical motion and first law of thermodynamics reduce to

$$\frac{dw}{dt} = B \tag{6.359}$$

$$\frac{dB}{dt} = -\frac{wg}{\theta}\frac{\partial \theta}{\partial z} = -wN^2 \tag{6.360}$$

where $B = \frac{g\theta^*}{\theta}$ is the buoyancy force and $N^2 = \frac{g}{\theta}\frac{\partial \theta}{\partial z}$ is the Brunt-Väisälä frequency. Combining yields an equation for undamped harmonic oscillations

$$\frac{d^2w}{dt^2} + wN^2 = 0. \tag{6.361}$$

Thus, the vertical velocity has the form

$$w = \hat{w}e^{i\sqrt{N^2}t} \tag{6.362}$$

where $\hat{w}$ is the complex amplitude. As pointed out in Chap. 2, buoyancy frequency is a primary indicator of stability. Under statically stable conditions, ($N^2 > 0$) and harmonic motions around an equilibrium altitude occur, while under statically unstable conditions ($N^2 < 0$), N is imaginary leading to exponential solutions.

By using the definition for potential temperature and the equation of state, the Brunt-Väisälä frequency (Chap. 2) can be expressed as

$$N^2 = -g\left(\frac{1}{\rho}\frac{\partial \rho}{\partial z} + \frac{g}{c_s^2}\right) \tag{6.363}$$

where g, ρ and c_s are the acceleration of gravity, density and speed of sound, respectively. Obviously, in an incompressible fluid, acoustic waves must be infinite

$$N^2_{incompressible} = -g\left(\frac{1}{\rho}\frac{\partial \rho}{\partial z}\right) > 0. \tag{6.364}$$

This equation has a similar form than $N^2 = -g(\frac{1}{\theta}\frac{\partial \theta}{\partial z})$ that we derived in Chap. 2. Thus, gravity waves can often be examined much easier in incompressible fluids and substituting $-g(\frac{1}{\rho}\frac{\partial \rho}{\partial z})$ by $g(\frac{1}{\theta}\frac{\partial \theta}{\partial z})$ to a compressible fluid that excludes acoustic waves.

[65] Be aware that in principle, zero pressure perturbation contradicts to non-zero buoyancy when mass is conserved.

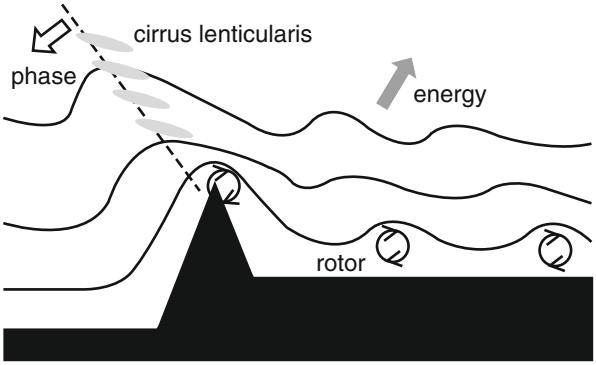

Fig. 6.48 Schematic view of a west-east cross-section illustrating orographic waves for a west wind encountering a north-south orientated mountain range. The westward tilt with altitude indicates upward propagation of wave activity. The ABL may be very turbulent, and rotors may form. At height, the flow may become laminar. Cirrus lenticularis clouds (Chap. 3) form when the LCL is reached

6.9.2 Gravity Waves

Mountain ridges orientated perpendicular to the flow can cause gravity waves. Gravity waves can be detected, for instance, by ground based radar showing the waviness at a fixed location in time (Appendix B). Frequently, lee clouds (Chap. 3) visualize gravity waves caused by a mountain ridge as parallel cloud bands in its downwind region (Fig. 6.48).

As aforementioned, buoyancy means that gravity acts on density anomalies generating wave motions. Assume layers of density ρ_1 and ρ_2 that are in hydrostatic equilibrium with mean thickness of the lower layer being $\overline{h}$. Perturbations yield small changes h'. Thus, $h = h' + \overline{h}$. For simplicity we assume that no variation exists in y-direction and that $\frac{\partial p}{\partial x} = \frac{\partial p}{\partial y} = 0$ in the upper layer. Then the horizontal pressure gradient in x-direction in the lower layer reads $-g\frac{\delta\rho}{\rho'}h'_x$ with $\delta\rho = \rho_1 - \rho_2$. Here the subscripts indicate the perturbation in space (e.g. x for x-direction) or time t i.e. the subscripts x and t stand for $\frac{\partial}{\partial x}$ and $\frac{\partial}{\partial t}$ (e.g. $u'_t = \frac{\partial u}{\partial t}$). For an inviscid fluid under the assumption that the Coriolis effect is nil, we obtain for the linearized, perturbed form of the Boussinesq-approximated equation of motion and continuity equation

$$u'_t + \overline{u}u'_x = -g\frac{\delta\rho}{\rho'}h'_x \qquad with\, u'_x + w'_z = 0 \tag{6.365}$$

At height h, the vertical velocity is $w(h) = h_t + uh_x$. Integration from $z = 0$ to $z = h$ yields

$$h'_t + \overline{u}h'_x + u'_x\overline{h} = 0. \tag{6.366}$$

Inserting leads to

$$(\frac{\partial}{\partial t} + \overline{u}\frac{\partial}{\partial x})h' - \frac{g\overline{h}\delta\rho}{\rho_1}h'_x = 0. \tag{6.367}$$

A potential solution for this equation is

$$h' \approx e^{i(kx-ct)} \tag{6.368}$$

where $c = \overline{u} \pm \sqrt{\frac{g\overline{h}\delta\rho}{\rho_1}}$. There are two solutions meaning the waves are **isotropic**. The perturbation in the thickness of the lower layer propagates in form of a wave with wave number k. It moves at phase speed c as buoyancy restores successfully the fluid to its mean height at a location. The excess mass is transferred to adjacent locations in x-direction. Consequently, a new perturbation is created that requires the buoyancy force to act.

In the atmosphere, gravity waves can propagate vertically as well as horizontally

$$(\frac{\partial}{\partial t} + \overline{u}\frac{\partial}{\partial x})^2(\frac{\partial^2 w'}{\partial x^2} - \frac{\partial^2 w'}{\partial z^2}) + N^2\frac{\partial^2 w'}{\partial x^2} = 0 \tag{6.369}$$

with the solution

$$w' \approx \hat{w}e^{i(kx+mz-\omega t)} \tag{6.370}$$

where $\omega = \overline{u}k \pm Nk\sqrt{k^2+m^2}$ is the frequency of the dispersion. These solutions represent **inertial gravity waves**. Inertial gravity waves transport energy in the direction of the group velocity defined by the vector $(\frac{\partial\omega}{\partial k}, \frac{\partial\omega}{\partial m})$ that is parallel to the phase lines. **Inertial waves** are transverse and restored by the Coriolis force.

Flow over mountains, violent thunderstorms, jet stream shear and solar radiation trigger inertial or gravity waves. Inertial or gravity waves may affect visibility, upper air atmospheric winds, turbulence and chemical composition of the air. Rossby waves, geostrophic currents and geostrophic winds are examples of inertial waves.

6.9.2.1 Long Barotropic Waves: Rossby Waves

Planetary waves or Rossby waves (Fig. 6.49) are long-waves that play a role in the formation of regions of divergence and convergence in the upper troposphere. Along these waves shortwaves may develop and dissipate. The Rossby waves steer the extra-tropical cyclones. Here we have a classical example of planetary and synoptic scale interaction (Fig. 6.49). The number of waves around the globe varies from two to six depending on the synoptic situation. Frequently, we use them to determine a wave number.

The underlying topography governs the mid- and upper tropospheric circulation (Fig. 6.8). The most distinct upper trough over eastern North America, for instance,

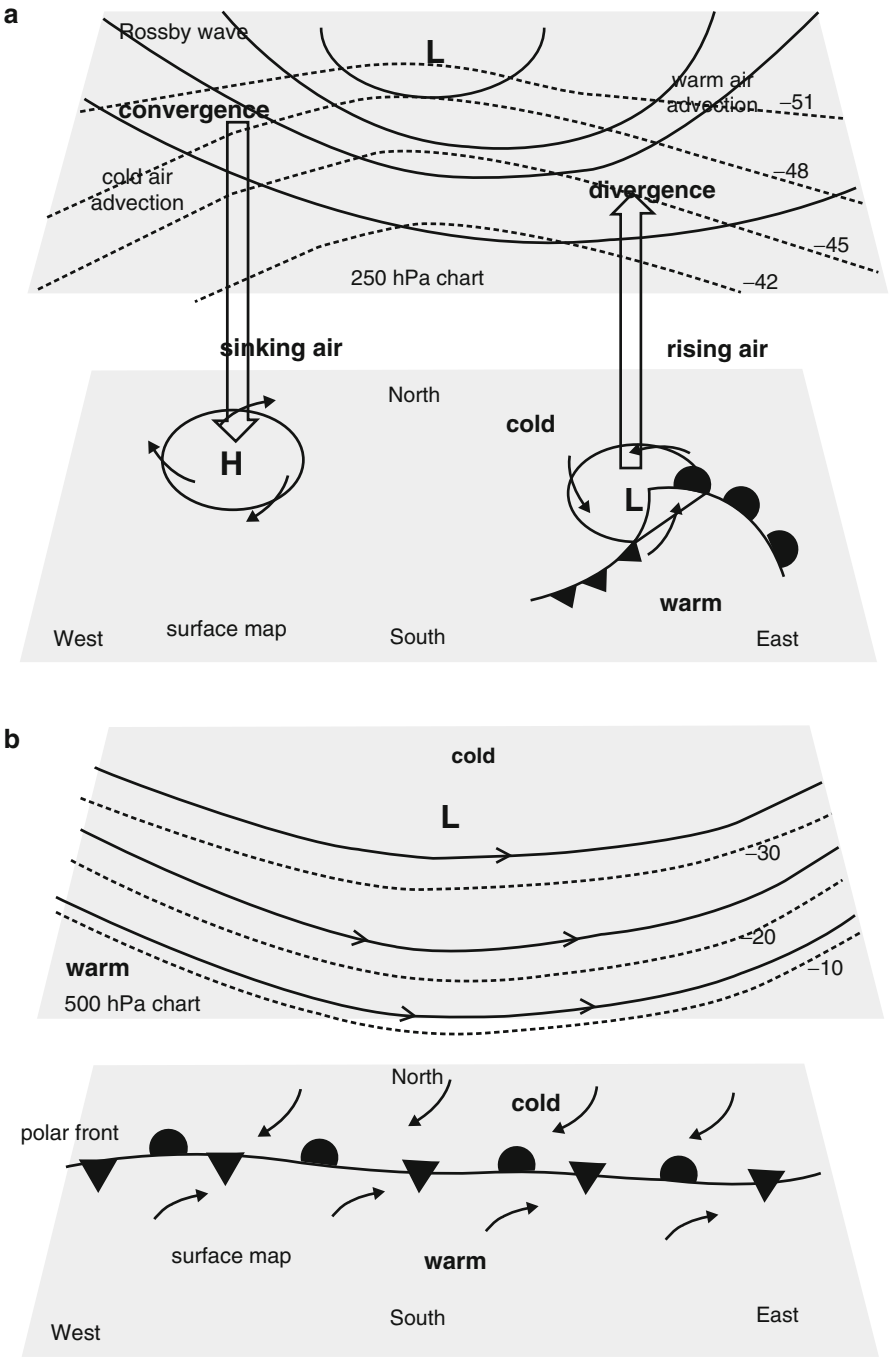

Fig. 6.49 Schematic view of part of a Rossby wave with regions of convergence and divergence at upper levels that are supporting cyclogenesis (*top*), and Rossby wave behavior after dissipation of an extra-tropical cyclone in the Northern Hemisphere

lies in the leeside region of the Rocky Mountains. Large-scale pressure systems resulting from the different heating of water- and land-masses can also influence long-wave development. Most commonly, the upper trough axes are located from the east Canadian Arctic to Florida, Alaska to the Central Pacific, West Siberia to Burma, and Russia to the Black Sea. The dominance of these large-scale wave oscillations in the circulation of the mid- and high-latitudes is related to the increase of Coriolis force pole-wards and the conservation of absolute vorticity.

Example. Assume a geographical latitude of 45° and the circuit of the Earth being 28,300 km and calculate the wavelengths for wave numbers 2–6.

Solution. The wavelengths are 14,100, 9,400, 7,100, 5,700, and 4,700 km.

6.9.2.2 Short Baroclinic Waves: Frontal Cyclones

Shortwaves are superimposed on Rossby waves (Fig. 6.49). These eddies migrate downwind the Rossby waves and undergo their own life cycle as mid-latitude cyclones (see Sect. 6.10.2). The establishing of these shortwaves depends on temperature advection, i.e. the horizontal transport of warm or cold air masses by the wind. Advection occurs on Rossby waves and affects the development of surface cyclones (Fig. 6.49).

The shift in phase of the geopotential-height wave compared to the temperature wave is appreciably smaller for long-waves than for baroclinic waves. This means that long-waves are associated with warm ridges and cold troughs, and heat advection is very small. When a shortwave exists downwind of a Rossby wave trough axis, the divergence is enhanced and the surface low intensifies (Fig. 6.49).

6.9.3 Inertial Oscillations

Planetary waves, geostrophic currents and geostrophic winds are examples of **inertial waves**. Inertial waves are transverse waves. When a horizontal perturbation causes a geostrophic imbalance, the Coriolis force restores the flow to a balanced state.

To describe inertial waves mathematically assume for simplicity unit mass and a mean state geostrophic wind in y-direction with $\overline{v}$ that only depends on x and $\overline{u} = \overline{w} = 0$. Application of parcel theory yields for the dry, inviscid Boussinesq equations for a two-dimensional flow with no variations in y-direction

$$\frac{du}{dt} = f(M - \overline{M}) \tag{6.371}$$

Where $\overline{M} = \overline{v} + fx$ is the absolute momentum of the basic state. Conservation of momentum requires $\frac{dM}{dt} = 0$. Thus, the motion can be described by the harmonic oscillation equation

$$\frac{d^2u}{dt^2} + uf\frac{\partial \overline{M}}{\partial x} = 0 \tag{6.372}$$

with the solution

$$u' \approx \hat{u}e^{i\omega t} \tag{6.373}$$

and the inertial oscillations

$$\omega = \pm\sqrt{f\frac{\partial \overline{M}}{\partial x}} = \pm\sqrt{f(\frac{\partial \overline{v}}{\partial x} + f)}. \tag{6.374}$$

This means that the Coriolis force and horizontal shear of the basic flow absolute momentum determine the frequency of the oscillations. The term in the brackets on the r.h.s of the last equation suggests that the horizontal shear of absolute momentum of the mean basic flow corresponds to the absolute vorticity $\xi_o + f$ where f is the Coriolis parameter.

6.9.4 Inertio-Gravity Waves

When buoyancy and Coriolis force cause vertical and horizontal oscillations concurrently, we obtain **inertio-gravity waves**. We can describe them by the three-dimensional dry adiabatic inviscid Boussinesq equations that are linearized for a motionless hydrostatic basic state. Thus, the equation of motion reads

$$\frac{\partial u'}{\partial t} = -\frac{\partial \Pi''}{\partial x} + fv' \qquad \frac{\partial v'}{\partial t} = -\frac{\partial \Pi'}{\partial y} - fu' \qquad \frac{\partial w'}{\partial t} = -\frac{\partial \Pi'}{\partial z} + B' \tag{6.375}$$

where $\Pi = \frac{\rho^*}{\rho_o}$ and B' is the buoyancy perturbation. The thermodynamic equation reads

$$\frac{\partial B'}{\partial t} = -w'N^2 \tag{6.376}$$

where N is the Brunt-Väisälä frequency. Combination of these equations describes the wave

$$\frac{\partial^2 w'}{\partial z \partial t} + \frac{\partial^2 \Pi'}{\partial z \partial t} + w'N^2 = 0 \tag{6.377}$$

The continuity equation requires $\frac{\partial u'}{\partial x} + \frac{\partial v'}{\partial y} + \frac{\partial w'}{\partial z} = 0$. Solutions for u', v', w', Π' are proportional to $e^{i(kx+ly+mz-\omega t)}$ with

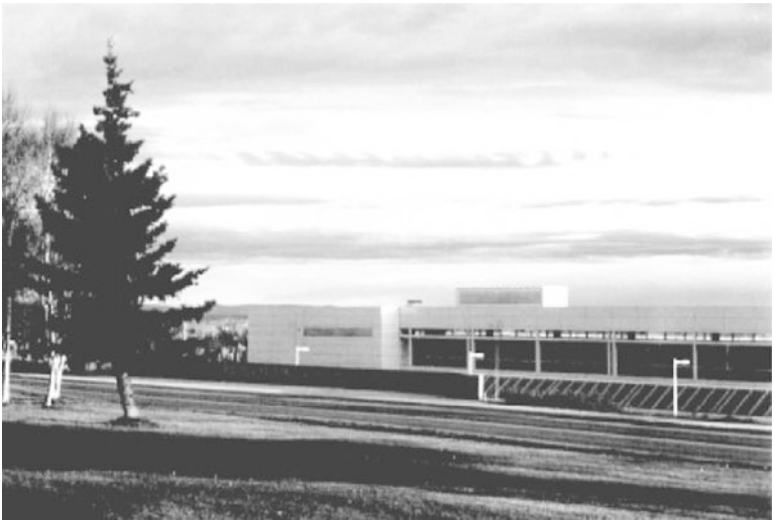

Fig. 6.50 Kelvin-Helmholtz waves over the University of Alaska Fairbanks campus (Photo by Mölders in 2004)

$$\omega^2 = N^2\left(\frac{k^2 + l^2}{k^2 + l^2 + m^2}\right) + f^2\left(\frac{m^2}{k^2 + l^2 + m^2}\right). \tag{6.378}$$

In the case of hydrostatic motions, this solution reduces to

$$\omega^2 = N^2\left(\frac{k^2 + l^2}{m^2}\right) + f^2. \tag{6.379}$$

For a typical basic flow in mid-latitudes with $N \approx 0.01\,\mathrm{s}^{-1}$ and $f \approx 10^{-4}\,\mathrm{s}^{-1}$ the horizontal scale length L of hydrostatic inertial gravity waves is $\approx$100 km.

6.9.5 Kelvin-Helmholtz Instability

Besides the vertical gradient of the horizontal shear of momentum, vertical shear of horizontal wind components is a source of flow instability. Instabilities due to vertical shear of horizontal wind are called **Kelvin-Helmholtz instability**.[66] We discussed them already in Chap. 3 as a mechanism for special cloud types. Kelvin-Helmholtz waves namely become visible when condensation occurs (Fig. 6.50).

[66] Hermann Ludwig Ferdinand von Helmholtz, German physician and physicist, 1821–1894.

Kelvin-Helmholtz waves are quantitatively related to the difference in velocity and density between two overlying fluids. Both layers are irrotational flows, i.e. without vorticity.

Assume an undisturbed horizontal interface between two layers of fluid that flow with mean velocities $\overline{u}_1$ and $\overline{u}_2$. Here the overbar denotes the basic state of the flow and the subscripts 1 and 2 refers to the upper and lower layer. Let the density of these layers be ρ_1 and ρ_2. The interface is a thin layer of strong vorticity, the **vortex shield**. Due to the different velocities of the upper and lower layer the interface consists of discrete small vortices all rotating in the same direction. Up and downward motions cancel out, while horizontal components reinforce the net velocity difference from the top to the bottom of the vortex shield. The sheet is perturbed sinusoidally. Vortex elements interact to produce velocity perturbations along the sheet. Consequently, vorticity increases in front of the wave crest and lessens behind it because the motions beneath the wave crest and trough are opposed. The resulting counter-clockwise rotation lifts the crest and lowers the trough.

For the two layers the hydrostatic equation (2.7) applies

$$\frac{\partial \overline{p}}{\partial z} = \begin{cases} -\rho_1 g \text{ for } z > 0 \\ -\rho_2 g \text{ for } z < 0 \end{cases}$$

with the pressure $p_1 = \overline{p}(z) + p_1'(x, z, t)$ and $p_2 = \overline{p}(z) + p_2'(x, z, t)$. The prime and overbar denote the perturbed and basic mean states, respectively. Let us consider a height h of the interface that is below the equilibrium surface $z = 0$. Integration of the vertical equation of motion from $z = -\infty$ to $z = \infty$ provides three cases

$$(\frac{\partial}{\partial t} + \overline{u}_2 \frac{\partial}{\partial x}) w_2' = -\frac{1}{\rho_2} \frac{\partial p_2'}{\partial z} \tag{6.380}$$

$z < 0$ below the interface,

$$(\frac{\partial}{\partial t} + \overline{u}_1 \frac{\partial}{\partial x}) w_1' = -\frac{1}{\rho_1} \frac{\partial p_1'}{\partial z} + \frac{\rho_2 - \rho_1}{\rho_1 g} \tag{6.381}$$

for $z < 0$ above the interface, and

$$(\frac{\partial}{\partial t} + \overline{u}_1 \frac{\partial}{\partial x}) w_1' = -\frac{1}{\rho_1} \frac{\partial p_1'}{\partial z} \tag{6.382}$$

for $z > 0$ above the interface. The vertical velocity perturbation w' can be expressed by the velocity potential Φ as $w' = \frac{\partial \Phi}{\partial z}$. At the interface, the pressure of the overlying and underlying fluid is the same independent of the location h of the interface, i.e. $p_1(h) = p_2(h)$. Integration and substitution yield

$$\rho_1 (\frac{\partial}{\partial t} + \overline{u}_1 \frac{\partial}{\partial x}) \Phi_1' + (\rho_2 - \rho_1) g h = \rho_2 (\frac{\partial}{\partial t} + \overline{u}_2 \frac{\partial}{\partial x}) \Phi_2'. \tag{6.383}$$

Obviously, for any point of the interface

$$\frac{dh}{dt} = (\frac{\partial}{\partial t} + \overline{u}_1 \frac{\partial}{\partial x})h \tag{6.384}$$

and

$$\frac{dh}{dt} = (\frac{\partial}{\partial t} + \overline{u}_2 \frac{\partial}{\partial x})h \tag{6.385}$$

for the vertical upward and downward motion $-\frac{\partial \Phi_1'}{\partial z} = -\frac{\partial \Phi_2'}{\partial z}$. At $h = z$, this system has the solutions

$$h \approx e^{i(kx-\omega t)} \tag{6.386}$$

$$\Phi_1' \approx e^{i(kx-\omega t)} e^{kz} \tag{6.387}$$

$$\Phi_2' \approx e^{i(kx-\omega t)} e^{-kz} \tag{6.388}$$

where k is positive and

$$\frac{\omega}{k} = \frac{\rho_2 \overline{u}_2 + \rho_1 \overline{u}_1}{\rho_1 + \rho_2} \pm \sqrt{\frac{\rho_1 k(\overline{u}_2 - \overline{u}_1)^2}{(\rho_1 + \rho_2)^2} + \frac{g(\rho_2 - \rho_1)}{k(\rho_1 + \rho_2)}}. \tag{6.389}$$

We can determine the coefficients h, Φ_1' and Φ_2' under the assumption that the magnitude of the velocity at the crest of the disturbance is equal, but opposite in sign to that at the trough. After applying the continuity equation and eliminating all physically unrealistic cases, exponentially growing solutions exist when the term under the square root of the last equation is negative. Such solutions only occur when

$$k > \frac{g(\rho_2^2 - \rho_1^2)}{\rho_1 \rho_2 (\overline{u}_2 - \overline{u}_1)^2} \tag{6.390}$$

for $\rho_2 = \rho_1 + \Delta\rho$ and $\Delta\rho << \rho_1$ the solution simplifies to

$$k > \frac{2g\Delta\rho}{\rho \Delta \overline{u}^2} \tag{6.391}$$

with $\Delta\overline{u} = \overline{u}_2 - \overline{u}_1$. The velocity difference is a measure of vorticity; the greater the vorticity is the stronger the instability it creates. The more the density of the lower layer exceeds that of the upper layer, the greater the buoyancy stability becomes and the more the buckling of the interface between the fluids is suppressed by the restoring buoyancy force. Consequently, for Kelvin-Helmholtz waves (Fig. 6.50) to form the vorticity across the interface must be strong enough to overcome the restoring force. The vertical wind shear destabilizes, the buoyancy stabilizes the flow.

6.10 Frontal Motions

As discussed in Chap. 2, fronts are boundaries between neighboring air masses of different thermal and moisture conditions. Often these fronts represent the boundaries between polar and tropical air masses. The fronts are regarded as comparative narrowing zones of thermal and density discontinuity in air-mass characteristics over an area of about 1,000 km in horizontal extension.

We have to understand this frontal concept as three-dimensional in space with one dimension in time. The fronts are transition zones of about 1 km in thickness. The equilibrium that establishes at a front can be explained by **Bjerknes' circulation theorem**[67]: When isobar density differences exist, a direct circulation occurs. This circulation lifts warm air against the cold air that simultaneously sinks at lower levels and moves towards the warmer air at lower levels. Consequently, the slope of the surface separating the air masses of different temperature decreases. The Coriolis force hinders the air masses to achieve a horizontal layered position as it acts in different directions in the upper and lower part of the front. Circulation acceleration in an indirect sense develops that weakens the direct circulation. In equilibrium, the counteracting motions of the air masses yield a characteristic velocity parallel to the front.

For a front in equilibrium, its slope depends on the shear of the geostrophic wind and the difference in density of the air masses. By starting out with $\frac{dv_N}{dt} = -\frac{1}{\rho}\frac{\partial p}{\partial n} - fv$ we can determine the slope of the front by

$$\tan\alpha = \frac{\frac{\partial p\prime}{\partial n}\frac{\partial p}{\partial n}}{\rho - \rho\prime} \tag{6.392}$$

Substitution and some algebra yield

$$\tan\alpha = \frac{f\overline{T}}{g}\frac{v_g\prime - v_g}{T\prime - T} \tag{6.393}$$

Here $\overline{T}$ is the average temperature of the two air masses. Margules[68] was the first to derive this formula. The stronger the change in wind direction is the steeper the slope becomes, and the greater the change in temperature is, the flatter the slope becomes. Fronts slope gently between 1:25 and 1:300 towards the cold side. The above equation tells us that for $\rho - \rho\prime > 0\,\tan\alpha > 0$ and $v_g > v_g\prime$ meaning cold air moves under the warm air. It also illustrates that temperature discontinuities without wind change mean a horizontal position of the air-mass boundary, i.e. inversion (Chap. 2).

[67] Vilhelm Friman Koren Bjerknes, Norwegian physicist and meteorologist, founder of the modern practice of weather forecasting, 1862–1951.

[68] Max Margules, Austrian mathematician, physicist, and chemist, 1856–1920.

Any frontal area is affected by vertical turbulent mixing between the two air masses. This transition zone is the **frontal surface**.

Example. In mid-latitudes, ahead and behind a front the geostrophic wind speed is 6 and 16 m/s, respectively. As the front passes, temperature increases by 6 K. Average temperature is 20 °C. Determine the slope of the front.

Solution. $\tan\alpha = \frac{10^{-4}\,\mathrm{s}^{-1}\,293.15\,\mathrm{K}}{9.81\,\mathrm{m\,s}^{-2}}\frac{(16-6)\,\mathrm{m\,s}^{-1}}{6\,\mathrm{K}} \approx 0.005$, i.e. the slope is 1:200.

6.10.1 Arctic, Polar and Mediterranean Front, and Jet Stream

There are two major **frontal zones**, the **polar** and **Arctic fronts**.

The polar front is well organized throughout the entire troposphere and lower stratosphere. It separates warm tropospheric and cold stratospheric air on the right and cold tropospheric and warm stratospheric air to the left on the Northern Hemisphere. Its mean slope is 1:100.

The main characteristic of the polar front is its strong baroclinity. The polar front is an active zone of frontogenesis in the Atlantic and Pacific Oceans as well as in the southern ocean mid-latitudes of the Southern Hemisphere. The polar front is the strongest (weakest) during winter (summer) for thermodynamic reasons (Chap. 2). It shifts equator-wards in the Northern Hemisphere in winter due to the seasonal variability in the location of the polar and tropical air masses (Chaps. 2 and 7). As it moves south, relatively colder air flows into the area.

The **jet stream** is a band of air flowing more rapidly than $25.5\,\mathrm{m\,s}^{-1}$ at the tropopause above the polar or Mediterranean front. On average, the jet blows from west to east over the mid-latitudes. On the Northern Hemisphere, usually, the lower part of the jet stream separates the relatively colder polar air to its north from the warmer air to its south. In its upper part, it lies in the stratosphere on its pole-ward side and still in the upper troposphere on its equator-ward side, i.e. it has the warmer air on the pole-ward side.

Air movements associated with the polar front lead to the formation of the polar jet stream. During major cold outbreaks, the polar front moves equator-wards (Figs. 6.51 and 6.49) and so does the polar jet stream in response. In North America, unusually mild conditions in winter and summer go along with the jet stream positioned northward into Canada. Abnormally cold summer or winter conditions result from a jet stream position far south (Chap. 7).

Frequently, the jet stream contains areas of higher wind speeds than the surrounding jet stream. These areas called the **jet streaks** can play a role in storm and precipitation formation. Let us assume that we are in the middle of a jet flowing in a straight line (i.e. no curvatures). Then the area ahead to the left of the jet and the area behind to the right are favorable for storm and precipitation formation as here

jet streaks can occur. Depending on atmospheric conditions, air motions in both of these quadrants tend to increase upward motions. Rising air can lead to a decrease in surface air pressure and to cloud and precipitation formation. In the other quadrants, the air sinks for compensation increasing the surface air pressure below. Sinking of air can dissipate clouds and inhibit storm and precipitation formation.

Despite these favored areas for storm formation, storms also may build in other quadrants as many other factors may play a role. Especially, the curvature of the jet influences storm formation. A curved jet stream results in a flow pattern with large troughs and ridges. As aforementioned (Chap. 2), on the Northern Hemisphere, a cyclonic curvature leads to a counter-clockwise motion, while an anticyclonic curvature creates a clockwise circulation. The opposite is true in the Southern Hemisphere. Generally, a cyclonic curvature favors the formation of low surface pressure and commonly goes along with cloud and precipitation formation. Under anticyclonic curvature, on average, high surface pressure develops and the sky is clear. However, these rules of thumb do not mean that it always rains (is sunny) in the trough (under a ridge). Other factors, such as position of jet streaks, can be superimposed on the effects of curvature, especially, in nearly zonal flow, where the effects of curvature are small.

The **subtropical jet stream** develops during the winter season (Chap. 7). It results from air movements in the Tropics and Subtropics. Like the polar jet stream, the subtropical jet stream can also contribute to the formation of disturbances and storms.

The Arctic front is a distinctive baroclinic zone that separates the ice and snow of the high Arctic regions from the more moderate polar tundra area (Chap. 7). It follows the shores of the Arctic Ocean in both seasons, but travels southwards into North-West America or Siberia as the sea-ice mass grows during polar night. Snow cover also influences the position of the Arctic front. The Arctic front extends to about 1 or 2 km above the surface. The change in temperature going along with the passage of an Arctic front is recognizable, but the relatively shallow front does not provide strong enough updrafts to provide snowfall.

The **Mediterranean front** only occurs in winter when airstreams from Europe and Africa converge over the Mediterranean Sea and lead to frontogenesis.

Another type of air mass boundary is the **dry line**. In contrast to the previously described fronts, air masses separated by a dry line only differ with respect to humidity. Dry lines are associated with serve storms in the Great Plains in spring and summer. Obviously, the surface type plays a role in storm formation.

6.10.2 Extra-Tropical Cyclones

6.10.2.1 Bjerknes Model

Initially low pressure develops along a stationary front on the crest of a wavelike undulation in the shape of a front (Fig. 6.51). This initial process of front formation

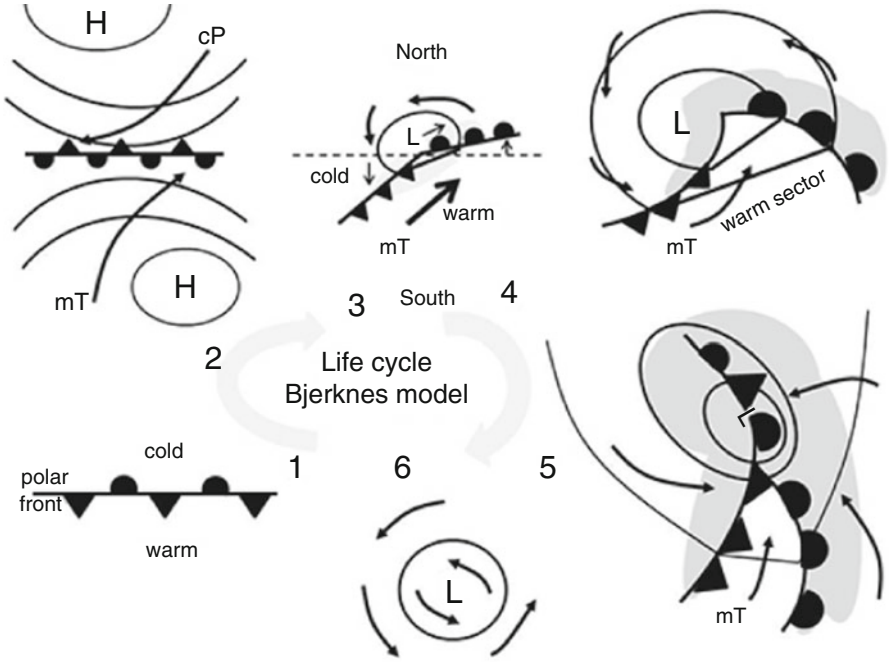

Fig. 6.51 Schematic view of the life cycle of a polar front cyclone according to the Bjerknes model. The letters cP and mT refer to continental polar and maritime tropical air masses (see Chap. 2)

is called the frontogenesis. It commonly occurs in regions of low pressure where air masses of different characteristics converge. A circulation around the low pressure establishes in response to the movement of the frontal zone and deepens the low (Fig. 6.51). This process is called the **cyclogenesis**. In mid-latitude cyclones, the pressure distribution is circular in the larger pole-ward side.

The surface-upper air coupling is an essential feature in the development of wave depressions (Fig. 6.49). The control of the polar front in the evolution of waves or undulations along the boundary between cold and warm air masses is the dynamic origin of wave depression of **extra-tropical cyclones** (Fig. 6.51). For existing fronts to become weaker, the airflow must diverge, which is associated with subsidence of air from upper levels.

The propagation of the low-pressure system towards cold air leads to an **occlusion** (Fig. 6.51). Occlusion indicates the end of the rapid cyclogenesis and is the onset of the mature cyclone. The process of index dissipation is called the **frontolysis**.

A typical mid-latitude cyclone consists of a **warm front**, a **cold front** and eventually an **occluded front**. Pressure decreases between the cold and warm front ahead of it and increases after the cold front passes. This behavior leads to an edge in the isobars at the respective fronts when plotted on surface charts. Form the surface

to the top of the troposphere the frontal surface lays oblique in space and depending on the slope, it affects an area of about 200 km. The line where the frontal surfaces intersect the ground are called the surface (cold, warm, or occluded) front.

A warm front represents the boundary between a colder air mass to which the warmer air mass flows. Warm fronts typically move at about 5 m s^{-1} requiring about 18 h to pass an area and leading to about 6 h of rain in that area. As cold air is typically denser than warm air, it remains close to the ground and forces the lighter warmer air to move upward. The gradual slope of the frontal boundary is about 1:100, on average. The vertical upward motion is largest in the lower troposphere with about 0.1 m s^{-1}. It decreases with increasing height while the Coriolis force shifts the air to the right on the Northern Hemisphere. The upward motion stops at the level where the relative wind becomes parallel to the front.

During a typical warm front passage, we observe the following

- Surface wind increases when the warm front approaches, turns to a front parallel wind, and then decreases.
- Pressure falls rapidly until the passage of the warm front and then keeps constant or only slightly falls.
- Temperature increases when the warm front approaches and stays nearly constant after its passage.
- Dew-point temperature increases when the warm front comes in. In the precipitation area, dew-point temperature increases drastically. After the front passes, dew-point temperature remains constant.
- The frontal slope leads to a gradual development of different cloud types as the air cools adiabatically during ascend. The overrunning air above a warm front is usually stable, which yields wide bands of stratiform-type clouds (Chap. 3). Nevertheless, occasionally unstable rising air may lead to cumuliform clouds. Being an observer at a fixed site the sequence of clouds visible during a warm front passage is cirrus, cirrostratus, altostratus, and nimbostratus in an area of about 200–300 km in horizontal and 6–9 km in vertical extension (Fig. 6.52). This means that the clouds consequently thicken, their bases become lower, and finally the warm front results in a long-lasting, homogeneous, light, but steady (stratiform) precipitation (Chap. 3).

At the warm front, rain falls into the cooler air. The raindrops are warmer than the environmental air, evaporate and frontal fog may form. In winter, when air is cold enough during a warm front passage, rain may freeze and build sleet or solidify on contact with surfaces to build freezing rain (Chap. 3).

A cold front represents the boundary between a warmer air mass to which the colder air mass flows. Cold fronts typically move at about 14 m s^{-1} requiring about 7 h to pass an area and leading to about 2–3 h of showers in that area. A **stationary front** is similar to a cold front structure, but without substantial movement in horizontal direction (<1 km h^{-1} $\approx$ 0.3 m s^{-1}). Cold fronts are about twice as steep as warm fronts, and hence extend less in the horizontal direction (Fig. 6.52). The steep slope yields to vigorous uplifts, convective clouds, and showers (Chap. 3).

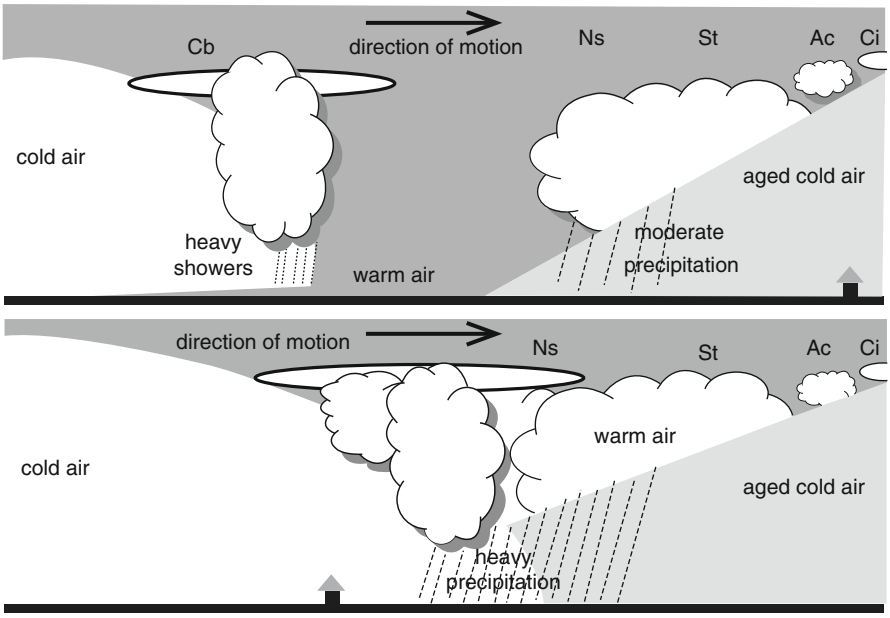

Fig. 6.52 Schematic view of a cross-section through a mid-latitude cyclone prior to occlusion (*top*), and after occlusion in the Northern Hemisphere. The house serves as reference to indicate the propagation of the fronts

We distinguish **slow moving cold fronts** (kata front), and **fast running cold fronts** (cold fronts of second kind; ana front). Visibility decreases (increases) for slow (fast) moving cold fronts (Fig. 6.53). They differ in their steepness with consequences for their lifting, cloud and precipitation formation. Typically, both types of cold fronts have the following characteristics:

- The near-surface winds become gusty before the cold front, and slightly reduce in speed after its passage.
- Pressure decreases before, and depending on the location with respect to the center of the low-pressure system, falls or increases.
- Temperature strongly and dew-point temperature decreases after the passage.
- As a cold front passes, the sequence of clouds is cirrus, cumulus congestus, cumulonimbus, cumulus humilis (Fig. 6.52).
- The resulting precipitation pattern is heterogeneous, convective precipitation with a high precipitation rate (Chap. 3).

Since the cold front moves more rapidly than the warm front, the cold front approaches the warm front and forces the warm air to move upwards (Fig. 6.52). The warm air is cut off from the surface, while at height a warm sector may still exist. The boundary between the relatively warmer cold and the colder air is the occlusion. The occlusion becomes longer and larger as the cyclone ages (Fig. 6.51).

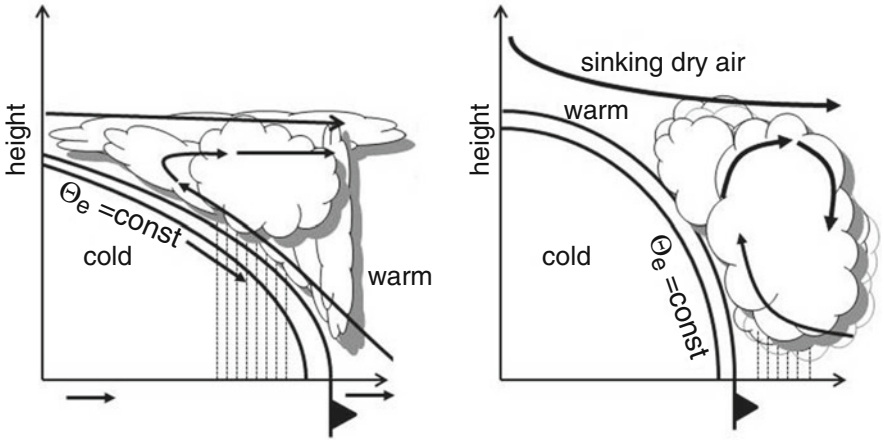

Fig. 6.53 Schematic view of an ana (*left*) and a kata cold front

Eventually the cold front completely overtakes the warm front and the entire system occludes. The warm air lifted aloft cools adiabatically and leads to strong cloud- and precipitation formation (Chaps. 2 and 3).

At the surface, an occluded front appears as the boundary between two cold (polar) air masses, usually with a colder air mass approaching the slightly warmer polar air mass ahead of it. This type is called the **cold type occlusion**, while the opposite case is called the **warm type occlusion**. In British Columbia and the Pacific Northwest, the latter type is most common.

Example. In 12 h a front travels the distance between two cities that are 700 km apart. Calculate the average rate of movement. What type of front is it?

Solution. $v = \frac{700{,}000\,\mathrm{m}}{12 \cdot 3{,}600\,\mathrm{s}} = 16.2\,\mathrm{m\,s^{-1}}$. This front is probably a cold front.

6.10.2.2 Conveyor Belt Theory

The **conveyor belt theory** (Fig. 6.54) adds additional aspects to Bjerknes' front model. It provides more details on how the air moves within the extra-tropical cyclone. The warm conveyor belt describes the flow of warm moist air originating within the warm sector ahead of the cold front. It slopes up above and north of the surface warm front. At the left edge of the conveyor belt, higher density air enters from west and forces a sharp slope to the cold front. Here stratiform precipitation develops north of the warm front along the conveyor belt. Active precipitation north of the warm front is an indicator for further development of the cyclone. A part of the conveyor belt turns to the right (left) in the Northern (Southern) Hemisphere

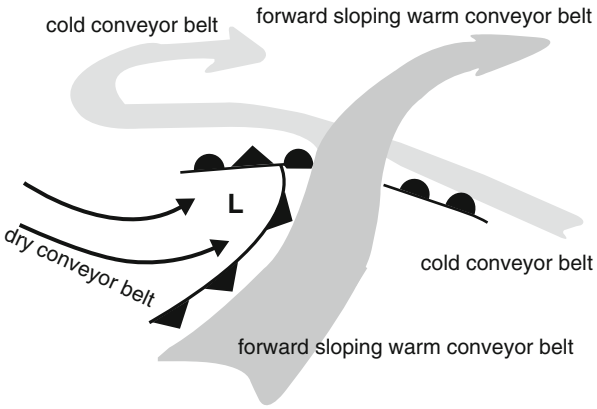

Fig. 6.54 Schematic view of the conveyor belt and the movement of air masses in an extra-tropical cyclone

and aligns with the westerly flow at upper levels. The western part of the conveyor belt wraps around the northwest (southwest) side of the cyclone in the Northern (Southern) Hemisphere. This branch can provide moderate to heavy precipitation. For a cold enough air mass, the precipitation occurs as heavy snow.

The cold conveyor belt originates north of the warm front. In the Northern (Southern) Hemisphere, it flows along a clockwise (counterclockwise) path into the main belt of the westerlies aloft (Chap. 7). Evidence for the existence of the cold conveyor belt is conflicting.

6.10.2.3 Migration of Surface Cyclones Relative to Rossby Waves

An urgent pre-requisite for the development of extra-tropical cyclones is the presence of upper level divergence (Fig. 6.49). When the divergence aloft exceeds the convergence near the surface, the surface low deepens. The optimal position for the development of an extra-tropical cyclone is just beneath the zone of decreasing vorticity aloft. Nevertheless, cyclones travel with the respect to the upper level trough in the same direction, but at about half the speed as the winds in the 700 hPa-level. Thus, the cyclone moves away from the area of maximum divergence and evolves as it migrates. The extra-tropical cyclone undergoes a life cycle of formation, occlusion and dissipation when it approaches the upper level ridge (Figs. 6.51 and 6.49).

6.10.3 Non-wave Depressions

Other kinds of depressions originate from thermal heat lows developing over inland continental areas in summer as well as dynamic or orographic depressions

forming in the lee of high mountain ranges (Chaps. 2 and 7). Lee depressions occur, for instance, in the downwind side of the Italian Alps (Genoa Low), the Rocky Mountains in Alberta, Canada, and the Andes in Patagonia, Argentina (Chaps. 2 and 7). These low depressions can result in violent thunderstorms with destructive hailstones.

6.11 Anticyclones

All anticyclones have the same basic characteristics of subsidence, i.e. sinking of air that warms dry adiabatically due to compression (Chaps. 2 and 7). Consequently, the air is dry and there are hardly clouds. The sinking air spirals downward due to the Coriolis force, and yields strong surface divergence (Fig. 6.49). An anticyclone intensifies when low pressure convergence exists aloft, for instance, in form of a jet stream inflow (Sect. 6.10.1).

The mechanisms for air to start sinking differ. In low latitudes, anticyclones develop from the subtropical jet convergence aloft in conjunction with surface divergence in trade winds or subtropical anticyclones. The moving highs are connected with low-index situations in the westerly, especially on the retarding edge of an upper air trough. The major anticyclones in mid- and high latitudes are mainly blocking highs that developed thermally from cold air subsidence over North America or Eurasia in winter (Chaps. 2 and 7).

6.12 Weather Maps

Weather maps are the result of either observations or NWP. In the following, we briefly discuss various commonly used weather maps. To obtain a complete picture of the worldwide synoptic situation observations are coordinated at 0000, 0600, 1200, 1800 UTC (Universal Time Coordinated,[69] formerly known as Greenwich Mean Time, GMT). Doing so is needed to generate weather maps that cover several time zones, to obtain analysis for GCM and NWP models, and to build reanalysis data and climatologies (Chap. 7). Note that many National Weather Services and non class 1 stations in the US may measure daily accumulated precipitation at different times which needs to be considered when evaluating models or deriving climatologies (Chap. 7, Appendix B).

[69] Sometimes UTC is abbreviated as UT.

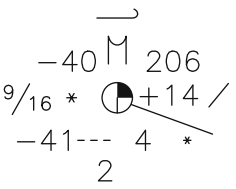

Fig. 6.55 WMO station model. See text for explanation

6.12.1 Surface Maps

Surface maps are based on observations routinely reported by the synoptic weather stations of the worldwide network that usually provide observational data every 6 h at 0000, 0600, 1200, and 1800 UTC . Each station gathers data on high level cloud type, total amount of clouds, wind speed and direction, temperature, visibility, current weather, dew-point temperature, low level cloud type, height of cloud base, part of the sky covered by lowest clouds, type of mid-level clouds, barometric pressure at sea level, amount of change in pressure during the last 3 h, pressure tendency in the last 3 h, indication of pressure being higher or lower than 3 h ago, time of onset or end of precipitation, weather in the last 6 h, precipitation type and amount. The **World Meteorological Organization** (WMO) designed a the standard format for symbolizing weather information on a single weather map (e.g. Fig. 6.55).

Various symbols describe the current weather, type of clouds or precipitation. The circle gives cloud cover in octaves. The wind arrow adjacent to the circle indicates the direction of wind by pointing from where the wind blows. Little vanes on this arrow indicate wind speed in 5 knots (short bar) or 10 knots (long bar), and triangles indicate 50 knots.

The actual distribution of sea-level pressure is of interest for weather forecasting (Chap. 2). A decrease in pressure, for instance, means that a cyclone moves in. Thus, pressure is reduced to sea-level pressure by applying the barometric equation (2.13). Without this reduction, the pressure field would follow more or less the topography (Fig. 2.6).

The sea-level pressure data is shown on surface weather maps as black contour lines with 4 hPa increment. Conventional surface maps show an analysis of the sea-level pressure field together with the position of fronts. Capital letters H and L indicate areas of high and low pressure, respectively. Fronts go along with an abrupt edge in the isobars (Fig. 6.51) and a change in wind direction as wind blows nearly parallel to the isobars (Chap. 2). Moreover, temperature increases (warm front) or drops (cold front) rapidly.

Blue triangles mark cold fronts, while red semicircular symbols indicate warm fronts. Alternating violet triangles and semicircular symbols mark an occlusion. In all cases, the symbols are arranged along a line pointing into the direction of motion.

Alternating semicircular symbols pointing in direction of the cold air and triangles pointing into the direction of the warm air indicate a stationary front. In analyzed surface charts, the precipitation area (fog) is highlighted in green (yellow).

6.12.2 Mid- and Upper Level Maps

As mentioned in Sect. 6.10, the upper level pattern affect the rate of intensification or weakening of surface cyclones and anticyclones, advection as well as precipitation. Due to the three dimensional structure of the atmosphere, a forecaster can analyze the surface synoptic charts more effectively and provide better forecasts when they also consider upper level charts.

Upper level maps are based on radiosonde data or NWP and illustrate the distribution of geopotential height (Fig. 2.5), wind, and temperature on the 850, 700, 500, 250, and 100 hPa pressure surfaces, respectively. At over 800 stations worldwide, radiosonde measurements are performed at least twice a day at 0000 and 1200 UTC.[70] The balloons need about 1 h to ascend to about 30 km above the ground. Data of pressure, temperature, relative humidity are transmitted to the ground station. This data serves to calculate saturation water-vapor pressure, actual water-vapor pressure, specific humidity, and virtual temperature. Radar or Global Positioning System (GPS) is used to track the horizontal displacement of the radiosondes.

The thickness of the atmosphere between two pressure levels (Eq. (2.15)) may be used to interpret advection of heat and moisture (Table 2.1), i.e. the thickness is proportional to the virtual temperature in the lower and mid-troposphere. In the upper troposphere, troughs tend to be filled by positive thickness anomalies, while ridges tend to flatten in the case of negative thickness anomalies. A common forecasting rule of thumb for predicting the rain/snow boundary during a precipitation event is that snow usually falls where the thickness contour of the 1,000 to 500 hPa layer is less than 5,400 m thick, whereas rain usually occurs where this layer is thicker than this (Chap. 2).

Troughs related to surface cyclones are less distinct in higher-level charts. They are displaced upstream relative to their location in the surface chart. Wind speed increases with height at most stations (Chap. 7). On the Northern Hemisphere, the position of the cold front is farther towards the northwest than in the surface map. On the contrary, the warm front is located far north. Frontal zones are less clearly visible in upper level charts than in surface maps.

At 850, 700, and 500 hPa frontal zones appear as well defined zones of packed isotherms accompanied by cyclonal shear of the front parallel geostrophic wind.

[70] The same universal time is needed so that weather maps can be drawn.

Table 6.5 Mean temperatures (in °C) of the polar front

	J	F	M	A	M	J	J	A	S	O	N	D
400 hPa	−40	−42	−40	−38	−36	−33	−31	−30	−32	−34	−38	−39
500 hPa	−29	−31	−29	−27	−24	−22	−20	−19	−20	−22	−26	−28
600 hPa	−21	−21	−20	−18	−15	−13	−11	−10	−11	−14	−18	−19
700 hPa	−13	−13	−12	−10	−8	−6	−3	−3	−4	−7	−10	−11
800 hPa	−9	−8	−6	−4	−1	3	5	5	3	0	−4	−6

Example. The thickness between the 1,000 and 850 hPa level amounts to 1,500 m. Determine whether warm or cold air is advected by using Table 2.1.

Solution. $\overline{T} = \frac{(z_2 - z_2)}{R} \ln \frac{p_1}{p_2} \approx 315.5$ K. Compared to a mean temperature of 295.6 K, the given layer is warmer, i.e. warmer air flows into the area.

6.12.2.1 850 hPa

On the 850 hPa map, solid contours represent the geopotential height and are spaced at 30 m intervals. Geopotential height is labeled in decameters, i.e. a value 120 means a height of 1,200 m. Fronts are detectable by the height-contour lines being closely together. Isotherms are given in a dashed mode and are labeled in °C. The same is true for all higher levels.

The 850 hPa-level resides, on average, at a height of about 1.5 km. At this level, the frontal zone is, on average, between 0 and 4 °C. It is shifted to the cold side with respect to the surface front (Table 6.5).

At the 850 hPa-level, the air is not subject to surface heating, i.e. it does not undergo daily cycles of warming and cooling. Thus, during morning hours the 850-hPa chart provides a good tool to estimate the daily maximum temperature over flat terrain. In mid-latitudes during summer, the maximum surface temperature is about 15 °C higher than the temperature at 850 hPa. In fall and spring (winter), the difference is about 12 °C (9 °C).

6.12.2.2 700 hPa

The 700 hPa-level is located at about 3 km above sea level. The 700 hPa chart has similar features than the 850 hPa chart. At 700 hPa, baroclinity is greater than closer to the surface. Consequently, the frontal zone is found between −4 and −12 °C (Table 6.5). The 700 hPa map is best for observing shortwaves and is particularly valuable to predict the movement of air mass thunderstorms as they usually travel at the same speed as the 700 hPa winds.

Example. In a 700 hPa chart, wind speed is $15\,\mathrm{m\,s^{-1}}$ from 270°. Radar observations show a thunderstorm developing at 50 km west of the radar station. Take the typical lifetime of a thunderstorm (Chap. 3) and its current direction of motion into account for determining whether and if yes, when the thunderstorm will reach the radar station.

Solution. When it travels with the wind in 700 hPa eastwards, the thunderstorm needs $t_{travel} = \frac{50{,}000\,\mathrm{m}}{15\,\mathrm{m\,s^{-1}}} = 3{,}333.3\,\mathrm{s}$ to reach the station. As this time is less than the typical lifetime of a thunderstorm, $1\,\mathrm{h} = 3{,}600\,\mathrm{s}$, it can reach the station.

6.12.2.3 500 hPa

The 500 hPa chart represents the mid-troposphere in about 5.6 km above sea level. Since mean sea-level pressure is approximately 1,000 hPa, about half of the mass of the atmosphere exists below 500 hPa (Chap. 1). Contour lines of geopotential height are drawn at 60 m intervals.

At 500 hPa, winds strengthen and the frontal zones slope towards the cold air. At this level, well-defined frontal zones are seldom, but strong thermal contrasts still exist. Note that throughout the mid- and upper troposphere, isotherms have nearly the same orientation.

Prior to NWP, this chart served for weather forecasting. The **omega high**, for instance, denotes a weather situation under which the upper level pattern are likely to alter slowly over several days. In Europe, it is often accompanied with blocking weather situations.

6.12.2.4 250 and 100 hPa

The 250 hPa-level coincides with the height of the lower, warmer tropopause. At the border of the main circulation cells (Chap. 7), the jet stream is located at the cut in the tropopause, and detectable in 250 hPa charts. As pointed out before, in the pole-ward side of the jet stream, the stratosphere over the colder air is located, while on the equator ward side the upper troposphere of the warmer air mass is found. Consequently, as temperature increases with height in the stratosphere, the warmest air is pole-ward of the jet stream. The circulation pattern is still characterized by a superposition of planetary scale and synoptic scale waves.

The 100 hPa-surface resides in the stratosphere. Wind speed decreases again. The circulation pattern shows planetary features.

Problems

Knowledge and Comprehension

1. What balance has to exist to relate the horizontal temperature gradients to the vertical gradients of the horizontal wind? How are these equations called?
2. A Rossby wave with a wavelength of $7.1 \cdot 10^6$ m was observed. What is the wave number at 45° latitude?
3. To which direction shifts the wind with height on the Southern Hemisphere?
4. How changes friction, wind speed and direction with height?
5. What is the thermal wind?
6. What does the law of Buys-Ballot say?
7. How is the Rossby number defined?
8. What does the geostrophic approximation mean?
9. What is the difference between transport and diffusion?
10. In what direction do high pressure systems rotate on the Southern Hemisphere?
11. Why does the geostrophic wind approximation overestimate the wind speed of a cyclone?
12. When is the geostrophic wind approximation valid?
13. Explain in your own words the difference between an equation in Eulerian and Lagrangian form.
14. What does friction mean for a cyclone (anticyclone)?
15. Name the forces of the Ekman equation and comment on the solution at the equator.
16. Give five examples of atmospheric motions with their typical spatial scales.
17. Why is the quasi-geostrophic approximation not made for low latitudes?
18. What grid resolution (spatial and temporal) would be required to model a cumulus cloud as a system, i.e. ignoring the microphysical processes, cloud droplets, ice crystals, etc.?
19. To capture the diurnal course of air temperature what temporal resolution would you choose and why?
20. Explain why the form $\frac{d\rho}{dt} = -\rho(\nabla \cdot \mathbf{v})$ of the continuity equation cannot be applied for ocean water, and how it has to be modified for ocean water.
21. Why is there usually no or few precipitation in high pressure areas?
22. Why are the mid-latitudes not suitable as air mass source regions?
23. In a 850 hPa chart, temperature is 15 °C above Seattle on July 9 at 1,500 UT. Do you think you can use this chart to predict maximum temperature, T_{max}? Give reasons for your answer.
24. Use the NOAA isentropic backwards trajectory program. Calculate the backward trajectories for a region of your choice for 5 days. Take the satellite images and weather maps of these days and discuss the reliability of the calculated trajectories.

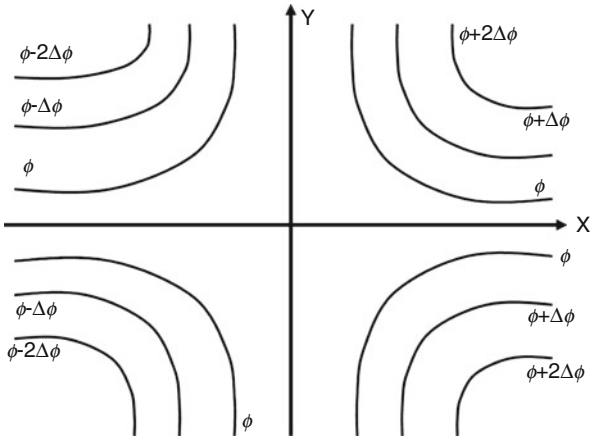

Fig. 6.56 Schematic view of geopotential height surfaces

Application, Analysis, and Evaluation

6.1. Assume a geopotential height and pressure distribution as given in Fig. 6.56. For which x and y values do ridges exist?

6.2. Perform a scale analysis for a tornado. Which forces balance?

6.3. Use the geostrophic wind balance and assume a Coriolis parameter of $10^{-4}\,\mathrm{s}^{-1}$, the horizontal components of the geostrophic wind to be both equal to 10 m/s at a location $x = (0, 0, 0\,\mathrm{km})$ having a surface pressure of 1,013.25 hPa. Give air temperature, and pressure at $y = 100$, 10, and 1 km.

6.4. Assume a wind blowing down a main street of 30 m width. Half the way of the main street there is a 10 m wide alley. At one side of the main street, wind velocity is $20\,\mathrm{m\,s}^{-1}$ and at its end it amounts to $18\,\mathrm{m\,s}^{-1}$. Estimate the velocity in the alley under the assumption of a 2D flow and constant density.

6.5. Calculate the pressure gradient and magnitude of pressure gradient force between Fairbanks and Anchorage (distance, $d = 423\,\mathrm{km}$) if pressure at the respective cities is 1,009 and 1,016 hPa. Assume an air density of $1.2\,\mathrm{kg\,m}^{-3}$.

6.6. Read the station model data.

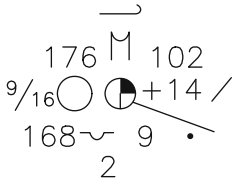

6.7. Calculate the magnitude of Coriolis force acting on an air parcel moving at $8\,\mathrm{m\,s^{-1}}$ at 35° latitude, $27.5\,\mathrm{m\,s^{-1}}$ at 25° latitude, $10\,\mathrm{m\,s^{-1}}$ at 70° latitude. Comment on Coriolis force at the pole, equator, and on your results.

6.8. Determine the horizontal wind speed and direction (in degree) for a wind having a W-E-component of $10\,\mathrm{m\,s^{-1}}$ and a S-N-component of $5\,\mathrm{m\,s^{-1}}$. Hint: Check Appendix A.

6.9. On an island, a concentration decrease of 3 ppm is observed during the last 3 h. On a ship that passes the island westwards, a decrease in concentration of 4 ppm was measured during the last three hours. The ship traveled 50 km during that time. Calculate the change of concentration in W-E-direction for these synoptic conditions.

6.10. Derive the mass-continuity equation for a chemical non-reactive specie of concentration $[\chi]$, here given in the Eulerian form as $\frac{\partial[\chi]}{\partial t} + \nabla \cdot (\mathbf{v}[\chi]) = 0$, by a direct method analogously to that used to derive the continuity equation and convert it to its Lagrangian (material derivative) form by vector manipulation. Hint: Look at Appendix A.

6.11. Perform a scale analysis for the vertical component of the equation of motion for a cumulus cloud. Compare your result with that of a cyclone and discuss the differences.

6.12. In the atmosphere, the vertical pressure gradient depends on density and gravity. Apply scale analysis to derive the relation.

6.13. An air parcel circulates on a surface of equal geopotential height. The rotation is small enough so that variations in latitude and the curvature of the Earth are negligible (inertia motion). Calculate the time needed to complete a full circle (inertia period) for a constant initial velocity. Comment on the direction of rotation of the inertia motion.

6.14. Show that the rotation of the geostrophic wind has only a vertical component and is the relative vorticity or geostrophic vorticity.

6.15. Assume an air parcel that rotates with an absolute vorticity of $0.7 \cdot 10^{-4}\,\mathrm{s^{-1}}$, and that the vorticity of the Earth is $10^{-4}\,\mathrm{s^{-1}}$. Calculate the relative vorticity of the air parcel. Where is this air parcel?

6.16. Derive the thermal wind equation from the hypsometric equation and the geostrophic wind equation.

6.17. Assume a grid cell has dimension $d\lambda = 5°$ and $d\phi = 5°$, centered at 30°N. Calculate the grid-cell extension in x- and y-direction.

6.18. A climate model has a grid increment of $2.8° \times 2.8°$. Determine the horizontal extension of a grid cell located at 58.6°N in both directions for a radius of the Earth

of $R_e = 6{,}371\,\text{km}$. How large an area would be encompassed by 12 grid cells in west-east direction and 6 in south-north direction if 58.6°N is the southern boundary of the area? How many grid cells in west-east direction will be needed to cover an area of approximately the same size for an area with a southern boundary at 27.9°N if the number of grid cells remains the same in south-north direction?

6.19. A typhoon at 20 N has a radial pressure of $40\,\text{hPa}\,10^{-2}\,\text{km}^{-1}$ 60 km apart from its center. Density of air is $1.29\,\text{kg}\,\text{m}^{-3}$. Determine the geostrophic wind and gradient wind speed. Comment on the forces. What balances can you assume? Assume that the tropical cyclone passes an island. Describe the observed wind speed and direction pattern when the cyclone passes the island. Discus the wind speed and direction pattern in the right and left eye-wall counted with respect to the direction of the path.

6.20. Determine the absolute value of the vertical pressure gradient in relation to the absolute value of the horizontal pressure gradient under the assumption that the latter corresponds to a geostrophic wind of $12\,\text{m}\,\text{s}^{-1}$.

6.21. For incompressible air the vertical mean values of $\frac{\partial u}{\partial x}$ and $\frac{\partial v}{\partial y}$ amount $5 \cdot 10^{-5}$ and $0\,\text{s}^{-1}$, respectively. Determine the vertical wind speed at 1,500 m height.

6.22. Use scale analysis to derive the deep convection continuity equation.

6.23. On a surface map, the near-surface geostrophic wind comes from East with $5\,\text{m}\,\text{s}^{-1}$. Inspection of upper level charts indicates that temperature increases at all heights towards the south by $1\,\text{K}\,10^{-2}\,\text{m}^{-1}$, but does not change in west-east direction. Determine the geostrophic wind at 5,000 m for this region.

6.24. On a weather map, pressure decreases from south to north by 5 hPa over 100 km. Determine the geostrophic wind speed and direction.

6.25. From the 200 and 500 hPa charts you derive a mean temperature between these levels of −30°C. How far are these pressure levels apart?

6.26. At the beginning of your hike, you set your altimeter to 400 m. After 5 h the altimeter indicates 2,400 m. During the hike your measurements indicated an air temperature of −1.5, 6 and −14 °C at 400, 900 and 2,400 m, respectively, with a linear behavior between these levels. Correct your altimeter measurement and determine at what elevation you are.

6.27. In two METEOSAT images 15 min apart, the anvil of a cloud cluster increases by 25 %. According to a radiosounding in the same area, air temperatures and dewpoint temperatures indicate super-saturation with respect to ice between 350 and 200 hPa. The visible and IR images indicate that the anvil spreads along the tropopause. From the radiosonde data the virtual temperature is about −43.1 °C at 350 hPa. Determine the mean vertical velocity at this pressure level. Discuss your result.

6.28. Assume a cold front located halfway between two cities that are 200 km apart, and that the density of the warm air ahead and the cold air behind the front are 1.15 and 1.35 kg m^{-3}, respectively. Determine the rate of pressure decrease with height in hPa m^{-1} in a 2 km air column above each city.

6.29. At x, y in the 500 and 850 hPa maps, geopotential heights are 53,955 and 12,029 m^2 s^{-2}, respectively. Virtual temperature is 10 °C at 850 hPa. By using the relative topography as a temperature map determine the virtual temperature at 500 hPa.

6.30. Show that at same latitude the same distance between isohypsic lines corresponds to the same geostrophic wind speed independent of the pressure level of an upper air map.

6.31. Along a front of 1,000 km, potential temperature decreases about 20 K in south-north direction. At the surface, potential temperature is 285 K. Determine the geostrophic wind speed and direction at 10 km height for $f = 10^{-4}\,s^{-1}$. In which direction does the wind blow?

6.32. At a site, average temperature and geostrophic wind before and after the passage of a front are 8 °C, 10 m s^{-1} and 5 °C, 7 m s^{-1}, respectively. Calculate the slope of the front. What type of front is it?

6.33. A front travels 800 km between site A and site B in 17 h. What is the average rate of movement? What type of front is it? The sounding reads 38 °C, $rh = 0.15$, 10 °C, $rh = 0.35$, and −3 °C, $rh = 0.5$ at the surface, 3 and 5 km, height respectively. What is the average environmental lapse rate over this 5 km thick layer? What type of air mass (mT, cP, mP, cT, cA) is advected (see Chap. 2)? When the sounding at a site north of B identifies warm air displaced by the front at 0.7 km, how far away from B would this station be? By the time, the front reaches B, how high would an air plane need to rise above A to reach the overrunning warm air?

6.34. Determine the virtual temperature for an air temperature of 25 °C and saturation vapor pressure of 42 hPa, air pressure of 1,015 hPa, and relative humidity of 50 %. By how much does the use of virtual temperature rather than air temperature affect the calculated air density? What do you conclude from your results?

6.35. Assume a strong surface pressure gradient on the large-scale might consist of a high at 1,025 hPa separated by 800 km from a 995 hPa low. Determine the air pressure gradient and compare it with the pressure gradient between the core of a tornado and the area just outside its funnel of about 100 hPa on a distance of about 500 m. How much greater is the pressure gradient of the tornado? One of the reasons why strong tornadoes are so destructive is that their power, P, increases as the cube of their wind speed, v, according to $P = kv^3$ where k is a constant. An F4 tornado has wind speeds of 92.5 to 116.4 m s^{-1}, while wind speeds range from 32.2 to 50 m s^{-1} for an F1 tornado (Chap. 7). How much faster are the wind speeds of F4 tornadoes? How much higher is the power of an F4 tornado compared to an F1 tornado?

6.36. The westerly speed, c, of a Rossby wave depends on its latitude, its wavelength, λ, and the westerly component of wind speed within the wave, u according to $c = u - 5.8 \cdot 10^{-13} \cos\varphi \cdot \lambda^2$ at 45° latitude. Assume no wind. How much faster and in which direction has a Rossby wave with a wavelength of 6,500 km to travel compared with a Rossby wave of wavelength 3,500 km?

6.37. Determine the slope of the 1,000 hPa surface for a point with a horizontal gradient of sea-level pressure of 6 hPa 10^{-2} km and an air density of 1.29 kg m^{-3}.

6.38. On a weather map, the 500 hPa geopotential height contours are orientated east to west within a small region with a spacing between adjacent (60 m) contours of 300 km. The geopotential height decreases towards the north. Determine the direction and speed of the geostrophic wind. Discuss the result.

6.39. On a surface map, a station located at 43°N reports a wind speed at 10 m height of 10 m s^{-1}. The wind blows across the isobars from high to low pressure at an angle of 20°. Determine the magnitude of the frictional drag force and the horizontal pressure gradient force for an air parcel of unit mass.

References

Material, concepts, ideas and problems of the following books and articles inspired this chapter. These sources are recommended for further reading.

Akerblom, F (1908) Recherches sur les courants les plus bas de l'atmosphere au-dessus de Paris. Nova Acta Regiae Soc Scient Upsalensis Ser 4, 2:1–45

Andreas EL, Hicks BB (2002) Comments on "Critical test of the validity of Monin-Obukhov similarity during convective conditions". J Atmos Sci 59:2605–2607

Andrews DG (2000) Introduction to atmospheric physics. Cambridge University Press, New York, 237pp

Barenblatt GI (1979) Similarity, self-similarity, and intermediate asymptotics. Consultants Bureau, New York/London, 218pp

Barenblatt GI (1994) Scaling phenomena in fluid mechanics. Inaugural lecture delivered before the University of Cambridge, 3 May 1993. Cambridge University Press, Cambridge, 45pp

Barenblatt GI (1996) Similarity, self-similarity, and intermediate asymptotics. Cambridge University Press, Cambridge, 386pp

Barenblatt GI (2003) Scaling. Cambridge University Press, Cambridge, 171pp

Barenblatt GI, Monin AS (1976) Similarity laws for stratified turbulent shear flows. Report of the fourth all-union Congress on theoretical and applied mechanics 41, Naukova, Dumka, Kiev

Barenblatt GI, Monin AS (1979) Similarity laws for stratified turbulent shear flows. Arch Ration Mech Anal 70:307–317

Bernhardt K (1995) Zur Interpretation der Monin-Obuchovschen Länge. Meteorol Z NF 4:81–82

Bernhardt K (1998) "Spin down" versus "Fill in" – zur Abschätzung des Effektes reibungsbedingter Sekundärzirkulationen. Annalen der Meteorologie 37:401

Blackadar AK (1962) The vertical distribution of wind and turbulent exchange in a neutral atmosphere. J Geophys Res 67:3095–3102

Bluestein HB (1992) Synoptic-dynamic meteorology in midlatitudes, vol. I, Oxford University Press, New York, 431pp

Brown RA (1991) Fluid mechanics of the atmosphere. Academic, San Diego, 489pp

Buckingham E (1914) On physically similar systems; illustrations of the use of dimensional equations. Phys Rev 4:345–376
Busch NE (1973) On the mechanics of atmospheric turbulence. In: Haugen DA (ed) Workshop on micrometeorology, Boston. American Meteorological Society, Boston, pp 1–65
Businger JA (1966) Transfer of momentum and heat in the planetary boundary layer. In: Proceedings of the symposium on Arctic heat budget and atmospheric circulation, Lake Arrowhead. The Rand Corporation, pp 305–332
Businger JA (1973) Turbulent transfer in the atmospheric surface layer. In: Haugen DA (ed) Workshop on micrometeorology, Boston. American Meteorological Society, Boston, pp 67–100
Businger JA (1986) Evaluation of the accuracy with which dry deposition can be measured with current micrometeorological techniques. J Appl Meteorol 25:1100–1124
Businger JA, Wyngaard JC, Izumi Y, Bradley EF (1971) Flux-profile relationships in the atmospheric surface layer. J Atmos Sci 28:181–189
Carl DM, Tarbell TC, Panofsky HA (1973) Profiles of wind and temperature from towers over homogeneous terrain. J Atmos Sci 30:788–794
Carlson TN (1998) Mid-latitude weather systems. Braun-Brumfield/A Sheridan Group. American Meteorological Society, Boston, 508pp
Carson DJ, Smith FB (1973) The Leipzig wind profile and the boundary layer wind-stress relationship. Q J R Meteorol Soc 99:171–177
Chalikov DV (1968) O profilja vetra i temperatury v prizemnom sloe atmosfery pri ustojcivoj stratifikacii. Trudy GGO 207:170–173
Charney JG, Eliassen A (1949) A numerical method for predicting the perturbations of the middle latitude westerlies. Tellus 1:38–54
Cheng Y, Brutsaert W (2005) Flux-profile relationships for wind speed and temperature in the stable atmospheric boundary layer. Bound-Layer Meteorol 114:519–538
Droppo JG Jr (1985) Concurrent measurements of ozone dry deposition using eddy correlation and profile flux methods. J Geophys Res 90:2111–2118
Dutton JA (1995) Dynamics of atmospheric motion. Dover, New York, 617pp
Dyer AJ (1974) A review of flux-profile relationships. Bound-Layer Meteorol 7:363–372
Dyer AJ, Bradley EF (1982) An alternative analysis of flux-gradient relationships at the 1976 ITCE. Bound-Layer Meteorol 22:3–19
Dyer AJ, Hicks BB (1970) Flux-gradient relationships in the constant flux layer. Q J R Meteorol Soc 96:715–721
Ekman V (1905) On the influence of the Earth's rotation on ocean-currents. Ark Mat Astron Fys 2:1–52
Eliassen A, Kleinschmidt E Jr (1957) Dynamic meteorology. In: Flügge S (ed) Handbuch der Physik, Bd. XLVIII. Springer, Berlin/Heidelberg/New York, pp 1–154
Ellison TH (1957) Turbulent transport of heat and momentum from an infinite rough plane. J Fluid Mech. 2:456–466
Exner FM (1912) Zur Kenntnis der untersten Winde über Land und Wasser und der durch sie erzeugten Meereströmungen. Annalen der Hydrographie und maritimen Meteorologie 40:226–239
Fleagle RG, Businger JA (1980) An introduction to atmospheric physics. Academic, New York/London/Toronto/Sydney/San Francisco, 432pp
Foken T (2006) 50 years of Monin-Obukhov similarity theory. Bound-Layer Meteorol 119:431–447
Foken T (2008) Micrometeorology (trans: Nappo CJ). Springer, Heidelberg, 350pp
Fortak H (1967) Vorlesungen über theoretische Meteorologie – Kinematik der Atmosphäre. Freie Universität Berlin, Inst f Theor Meteor, 89pp
Fortak H (1969) Berechnung des charakteristischen "Scales" der Turbulenz der bodennahen Grenzschicht aus Windprofilmessungen. Beitr Phys Atmosph 42:245–250
Garratt JR (1994) The atmospheric boundary layer. Cambridge University Press, Cambridge, 316pp

Gavrilov AS, Petrov JS (1981) Ocenka tocnosti opredelenija turbulentych potokov po standartnym gidrometeorologiceskim izmerenijam nad morem. Meteorol i Gidrol 4:52–59
Haltiner GJ, Martin FL (1957) Dynamical and physical meteorology. McGraw-Hill, New York/Toronto/London, 470pp
Hantel M, Mayer D (2006) Skriptum theoretische Meteorologie II. Wiener Meteorologische Schriften, Heft 5, Facultas Verlags- und Buchhandels AG, Wien, 191pp
Hasse L (1983) Introductory meteorology and fluid dynamics. Springer, Dordrecht, pp 1–51
Hasse L, Dobson F (1983) Introductory physics of the atmosphere and ocean. D. Reidel, Dordrecht/Boston/Lancaster/Tokyo, 126pp
Hastenrath S (1996) Climate dynamics of the tropics. Kluwer Academic, Dordrecht/ Boston/London, 488pp
Heisenberg W (1948) Zur statistischen Theorie der Turbulenz. Z Phys 124:628–657
Herbert F (1975) Irreversible Prozesse der Atmosphäre - 3. Teil (Phänomenologische Theorie mikroturbulenter Systeme). Beitr Phys Atmosph 48:1–29
Herbert F, Panhans WG (1979) Theoretical studies of the parameterization of the non-neutral surface boundary layer – part I: governing physical concepts. Bound-Layer Meteorol 16:155–167
Hesselberg T (1926) Die Gesetze der ausgeglichenen atmosphärischen Bewegungen. Beitr Phys fr. Atmosph 12:141–160
Högström U (1967) Turbulent water vapour transfer at different stability conditions. Phys Fluids 10(Suppl):247–254
Högström U (1988) Non-dimensional wind and temperature profiles in the atmospheric surface layer: a re-evaluation. Bound-Layer Meteorol 42:55–78
Högström U, Smedman-Högström AS (1974) Turbulence mechanism at an agricultural site. Bound-Layer Meteorol 7:373–389
Holton JR (1979) An introduction to dynamic meteorology. Academic/New York/San Francisco/ London, 391pp
Holton JR (2004) An introduction to dynamic meteorology. Elsevier/Academic, New York/ San Diego, 535pp
Huntley HE (1952) Dimensional analysis. MacDonald & Co, London, 158pp
Jacobson MZ (1999) Fundamentals of atmospheric modeling. Cambridge University Press, New York, 656pp
Jacobson MZ (2005) Fundamentals of atmospheric modeling. Cambridge University Press, New York, 813pp
Johansson C, Smedman A-S, Högström U, Brasseur JG, Khanna S (2001) Critical test of the validity of Monin-Obukhov similarity during convective conditions. J Atmos Sci 58:1549–1566
Kaimal JC, Finnigan JJ (1994) Atmospheric boundary layer flows. Oxford University Press, New York/Oxford, 289pp
Kaimal JC, Wyngaard JC, Izumi Y, Coté OR (1972) Spectral characteristics of surface layer turbulence. Q J R Meteorol Soc 98:563–589
Kazansky AB, Monin AS (1956) Turbulence in the inversion layer near the surface. Izv Acad Nauk SSSR Ser Geophys 1:79–86
Kondo J, Kanechika O, Yasuda N (1978) Heat and momentum transfer under strong stability in the atmospheric surface layer. J Atmos Sci 35:1012–1021
Kramm G (1989) The estimation of the surface layer parameters from wind velocity, temperature and humidity profiles by least squares methods. Bound-Layer Meteorol 48:315–327
Kramm G, Dlugi R (2006) On the correction of eddy fluxes of water vapour and trace gases. J Calcutta Math Soc 2:29–54
Kramm G, Herbert F (2006a) The structure functions for velocity and temperature fields from the perspective of dimensional scaling. Flow Turbul Combust 76:23–60
Kramm G, Herbert F (2006b) Heuristic derivation of blackbody radiation laws using principles of dimensional analysis. J Calcutta Math Soc 2:1–20
Kramm G, Herbert F (2009) Similarity hypotheses for the atmospheric surface layer expressed by non-dimensional characteristic invariants – a review. Open Atmos Sci J 3:48–79

Kramm G, Meixner FX (2000) On the dispersion of trace species in the atmospheric boundary layer: a re-formulation of the governing equations for the turbulent flow of the compressible atmosphere. Tellus A 52:500–522
Kramm G, Dlugi R, Lenschow DH (1995) A re-evaluation of the Webb correction using density-weighted averages. J Hydrol 166:283–292
Kramm G, Herbert F, Bernhardt K, Müller H, Werle P, Foken T, Richter SH (1996) Stability functions for momentum, heat and water vapour and the vertical transport of TKE and pressure fluctuations estimated from measured vertical profiles of wind speed, temperature, and humidity. Beitr Phys Atmos 69:463–475
Kramm G, Amaya DJ, Foken T, Mölders N (2013) Hans A. Panofsky's integral similarity function – at fifty. Atmos Clim Sci 3:581–594
Kraus H (2000) Die Atmosphäre der Erde. Eine Einführung in die Meteorologie. Vieweg, Braunschweig/Wiesbaden, 470pp
Kraus EB, Businger JA (1994) Atmosphere-ocean interaction. Oxford University Press, New York, 362pp
Kertz W (1969) Einführung in die Geophysik. Band 1. Erdkörper. BI Wissenschaftsverlag, Mannheim/Leipzig/Wien/Zürich, 232pp
Kitaigorodskij SA (1976) Zur Anwendung der Ähnlichkeitstheorie für die Beschreibung der Turbulenz in der bodennahen Schicht der Atmosphäre. Z Meteorologie 26:185–205
Kurz M (1990) Synoptische Meteorologie. Selbstverlag des Deutschen Wetterdienstes, Offenbach
Landau LD, Lifshitz EM (1959) Course of theoretical physics – vol 6 fluid mechanics. Pergamon Press, Oxford/New York/Toronto/Sydney/Paris/Frankfurt, 536pp
Lange H-J (2002) Die Physik des Wetters und des Klimas. Dietrich Reimer Verlag, Berlin, 625pp
Lesieur M (1993) Turbulence in fluids. Kluwer Academic, Dordrecht/Boston/London, 412pp
Lesieur M (1997) Recent approaches in large-eddy simulations of turbulence. In Métais, O, Ferziger J (eds) New tools in turbulence modeling. Springer, Berlin/Heidelberg/New York and Les Éditions de Physique, Les Ulis, pp 1–28
Lettau H (1950) A re-examination of the "Leipzig wind profile" considering some relations between wind and turbulence in the frictional layer. Tellus 2:125–129
Lettau HH (1979) Wind and temperature profile predictions for diabatic surface layers including strong inversion cases. Bound-Layer Meteorol 17:443–464
Lin Y-L (2007) Mesoscale dynamics, Cambridge University Press, Cambridge, 630pp
Lumley JL, Panofsky HA (1964) The structure of atmospheric turbulence. Interscience Publishers (Wiley), New York/London/Sydney, 239pp
Mellor GL, Yamada T (1982) Development of a turbulence closure model for geophysical fluid problems. Rev Geophys 20:851–875
Mildner P (1932) Über Reibung in einer speziellen Luftmasse. Beitr Phys fr Atmos 19:151–158
Möller F (1973a) Einführung in die Meteorologie – Physik der Atmosphäre – Band 1. BI Hochschultaschenbücher, Mannheim, 222pp
Möller F (1973b) Einführung in die Meteorologie – Physik der Atmosphäre – Band 2. BI Hochschultaschenbücher, Mannheim, 221pp
Monin AS, Obukhov AM (1954) Osnovnye zakonomernosti turbulentnogo peremešivanija v prizemnom sloe atmosfery. Trudy Geofiz Inst AN SSSR 24:163–187
Monji N (1973) Budgets of turbulent energy and temperature variance in the transition zone from forced to free convection. J Meteorol Soc Jpn 2:133–145
Obukhov AM (1946/1971) Turbulentnost' v temperaturno-neodnorodnoj atmosphere. Trudy Inst Teoret Geofiz AN SSSR 1. English translation in Bound-Layer Meteorol 2:7–29
Obukhov AM (1958) Über die Energieverteilung im Spektrum einer turbulenten Strömung. In: Goering H (ed) Sammelband zur statistischen Theorie der Turbulenz. Akademie Verlag, Berlin, pp 83–95
Ogura, J, Phillips NA (1962) Scale analysis of deep and shallow convection in the atmosphere. J Atmos Sci 19:173–179
Okamoto M, Webb EK (1970) The temperature fluctuations in stable stratification. Q J R Meteorol Soc 96:591–600

Orlanski I (1975) A rational subdivision of scales for atmospheric processes. Bull Am Meteorol Soc 56:527–530
Pai Mazumder D (2006) On the kinetic energy spectra of turbulence in the thermally stratified atmospheric surface layer. Proc Indian Natl Sci Acad 72:125–133
Pal Arya S (1988) Introduction to micrometeorology. Academic, San Diego, 303pp
Pandolfo J (1966) Wind and temperature profiles for a constant flux boundary layer in lapse conditions with a variable eddy conductivity to eddy viscosity ratio. J Atmos Sci 23:495–502
Panhans WG, Herbert F (1979) Theoretical studies of the parameterization of the non-neutral surface boundary layer – part II: an improved similarity model. Bound-Layer Meteorol 16:169–179
Panofsky HA (1961) An alternative derivation of the diabatic wind profile. Q J R Meteorol Soc 87:109–110
Panofsky HA (1963) Determination of stress from wind and temperature measurements. Q J R Meteorol Soc 89:85–94
Panofsky HA, Dutton JA (1984) Atmospheric turbulence. Wiley, New York/Chichester/Brisbane/Toronto/Singapore, 397pp
Panofsky HA, Tennekes H, Lenschow DH, Wyngaard JC (1977) The characteristics of turbulent components in the surface layer under convective conditions. Bound-Layer Meteorol 11:355–361
Paulson CA (1970) The mathematical representation of wind speed and temperature profiles in the unstable atmospheric surface layer. J Appl Meteorol 9:857–861
Pedlosky J (1979) Geophysical fluid dynamics. Springer, New York, 624pp
Peixto JP, Oort AH (1992) Physics of climate. Springer, New York, 520pp
Pichler H (1984) Dynamik der Atmosphäre. BI Wissenschaftsverlag, Mannheim/Wien/Zürich, 456pp
Pielke RA (1984) Mesoscale meteorological modeling. Academic, London, 612pp
Poulos GS, Burns SP (2003) An evaluation of bulk Ri-based surface layer flux formulas for stable and very stable conditions with intermittent turbulence. J Atmos Sci 60:2523–2537
Prandtl L (1932) Meteorologische Anwendungen der Strömungslehre. Beitr Phys Atmos (Bjerknes-Festband) 19:188–202
Priestley CHB (1959) Turbulent transfer in the lower atmosphere. The University of Chicago Press, Chicago, 130pp
Raupach MR, Antonia RA, Rajagopalan S (1991) Rough-wall turbulent boundary layers. Appl Mech Rev 44:1–25
Ray PS (1986) Mesoscale meteorology and forecasting. Am Meteorol Soc, Boston, 793pp
Reynolds O (1895) On the dynamical theory of incompressible viscous fluids and the determination of the criterion. Philos Trans R Soc 186:123–164
Riegel CA (1999) Fundamentals of atmospheric dynamics and thermodynamics. In: Bridger AFC (ed). World Scientific, Singapore, 496pp
Ross HK, Cooney J, Hinzman M, Smock S, Sellhorst G, Dlugi R, Mölders N, Kramm G (2014) Wind power potential in Interior Alaska from a micrometeorological perspective. Atmos Clim Sci 4:100–121
Salby ML (1996) Atmospheric physics. Academic, San Diego/New York/Boston/London/Sydney/Tokyo/Toronto, 627pp
Schlichting H (1965) Grenzschicht-Theorie. Braun, Karlsruhe, 736pp
Schultz DM (2001) Reexamining the cold conveyor belt. Mon Wea Rev 129:2205–2225
Sellers WD (1962) Simplified derivation of the diabatic wind profile. J Atmos Sci 19:180–181
Shapiro MA, Gronas S (1999) The life cycle of extratropical cyclones. American Meteorological Society, Boston, 359pp
Sommerfeld A (1956) Thermodynamics and statistical mechanic. Lectures on theoretical physics, vol V. Academic, New York, 401pp
Sorbjan Z (1989) Structure of the atmospheric boundary layer. Prentice Hall, Englewood Cliffs, 317pp

Stull RB (1988) An introduction to boundary layer meteorology. Kluwer Academic, Dordrecht/Boston/London, 666pp
Swinbank WC, Dyer AJ (1967) An experimental study in micro-meteorology. Q J R Meteorol Soc 93:494–500
Tillman JE (1972) The indirect determination of stability, heat and momentum fluxes in the atmospheric boundary layer from simple scalar variables during dry unstable conditions. J Appl Meteorol 11:783–792
van Mieghem J (1973) Atmospheric energetics. Clarendon Press, Oxford, 306pp
von Kármán T (1930) Mechanische Ähnlichkeit und Turbulenz. Nachr Ges Wiss Gottingen Math. Phys. Klasse 58:271–286
von Weizsäcker CF (1948) Das Spektrum der Turbulenz bei großen Reynoldsschen Zahlen. Z Phys 124:614–627
Wallace JM, Hobbs PV (1977) Atmospheric science – an introductory survey. Academic, San Diego/New York/Boston/London/Sydney/Tokyo/Toronto, 467pp
Wallace JM, Hobbs PV (2006) Atmospheric science – an introductory survey. Academic, San Diego/New York/Boston/London/Sydney/Tokyo/Toronto, 483pp
Webb EK (1970) Profile relationships: the log-linear range, and extension to strong stability. Q J R Meteorol Soc 96:67–90
Webb EK (1982) Profile relationships in the super adiabatic surface layer. Q J R Meteorol Soc 108:661–688
Wiin-Nielsen A, Defant F, Mörth HT (1978) Compendum of meteorology. WMO no 364, 276pp
Wyngaard JC, Coté OR (1971) The budget of turbulent kinetic energy and temperature variance in the atmospheric surface layer. J Atmos Sci 28:190–201
Wyngaard JC, Coté OR, Izumi Y (1971) Local free convection, similarity and budgets of shear stress and heat flux. J Atmos Sci 28:1171–1182
Yaglom AM (1977) Comments on wind and temperature flux-profile relationships. Bound-Layer Meteorol 11:89–102
Yamamoto G (1959) Theory of turbulent transfer in non-neutral conditions. J Meteorol Soc Jpn 37:60–67
Zdunkowski W, Bott A (2003) Dynamics of the atmosphere. Cambridge University Press, Cambridge, 719pp
Zilitinkevich SS (1966) Effects of humidity stratification on hydrostatic stability. Izv Atmos Ocean Phys 2:655–658
Zilitinkevich SS, Chalikov DV (1968) Opredelenie universal'nych profilej skorosti vetra i temperatury v prizemnom sloe atmosfery. Izv AN SSSR Fiz Atm i Okeana 4:294–302

Chapter 7
Climate and Climatology

Abstract This chapter is a brief introduction to climate and climatology in a sense as it is used in meteorology. It introduces the basic nomenclature used in climate studies and climatology. The chapter provides a brief introduction into basic climate statistics and climate analysis methods and discusses the general circulation in terms of examples of applications. Major large scale and mesoscale features are elucidated from a meteorological point of view as they are part of the regional climate. Furthermore, a brief glimpse on the biogeophysical cycle is provided. Major challenges of climate and Earth system modeling as well as regional climate modeling are pointed out. The chapter also presents the Köppen-Geiger classification that is recently often applied for climate assessment and assessment of climate model simulations.

Keywords Climate analysis methods • Scales in climate • Energy cascade • Scales of climate impacts • Classification of events • Climate classification

This chapter is intended to give a glimpse on climate (*Greek*, klima = slope, zone) and climatology in relation to meteorology, and provides examples of how the processes discussed in the former chapters yield and affect the climate of the various regions on Earth. It is an introductory survey trying to avoid repetition of material already discussed in the previous chapters. Thus, standing alone it is not intended to substitute for a book that is fully devoted to climate and/or climatology.

Classical (atmospheric) climate studies have various goals: Defining the climatology of a region or assessing changes in the climate relative to this climatology. This chapter introduces the components of the climate system, and basic concepts of climate, climate classifications, and climatology and how to derive concepts like the **general circulations** or the typical behavior of cyclones, for instance, by means of statistical methods. The focus is on the physical patterns and their origins caused by the physical and chemical processes discussed before. For a discussion of climate variability and/or change, the interested reader is referred to the respective literature.

N. Mölders and G. Kramm, *Lectures in Meteorology*, Springer Atmospheric Sciences,
DOI 10.1007/978-3-319-02144-7_7,

Table 7.1 Estimates of mass for various Earth system components

Atmosphere	$5.2 \cdot 10^{18}$ kg
Biosphere	$1.8 \cdot 10^{15}$ kg
Cyrosphere	$3.0 \cdot 10^{19}$ kg
Earth	$6.0 \cdot 10^{24}$ kg
Lithosphere	$3.254 \cdot 10^{20}$ kg
Oceans	$1.35 \cdot 10^{21}$ kg

7.1 Climate Analysis Methods

The **climate system** encompasses all gaseous (atmosphere), liquid (oceans, lakes, watersheds, soil water, ground water, cloud-water, rainwater), and solid components (lithosphere, biosphere, cryosphere, cloud snow and ice) of the Earth. These spheres are called **subsystems** (Table 7.1). The climate system results as a complex interaction of physical and chemical processes as the subsystems permanently exchange heat, water, matter, and energy by fluxes from one reservoir to another. It is important to understand that everything is in a reservoir, and in motion at the same time.[1] In this sense, climate research is very interdisciplinary. Even when we restrict us to the atmospheric, i.e. meteorology part, biology, geology, geophysics, oceanography, glaciology, soil sciences, hydrology, and chemistry, are at least important auxiliary disciplines.

To quantify the physiology of the climate system, budgeting is applied (e.g. Fig. 4.23). It considers the phase transition, chemical processes (Chap. 5), conservation of mass and energy in connection with transport (Chaps. 3, 4, 6) to quantify the three-dimensional climate system. As shown in Chaps. 4 and 5, budgeting does not answer the question why the processes evolve as they do; sometimes we even cannot close the budget with our current knowledge. Often simplified estimates are made. However, depending on the assumptions the results may be misleading as is demonstrated in Problem 4.10. Furthermore, it has to be assured that simplifications do not overstretch or violate the applicability of physical laws as demonstrated in the gray box below. Only an allover climate theory could answer this question, and still has to be developed.

Example. For an arbitrary planet, assume a planetary equilibrium temperature, T_p, of $-18\,^\circ$C and a mean natural atmospheric effect of $\Delta T = 33$ K. Any additional atmospheric effect, ΔT_a depends on the relative change of radiatively active gases, $\chi = \frac{(c-\overline{c})}{\overline{c}}$, where c is the concentration of these gases and the overbar indicates the long-year average. Assume that a change in one

(continued)

[1] A drop of water in the reservoir "river", and flows to the sea, or in a cloud and moves with the wind.

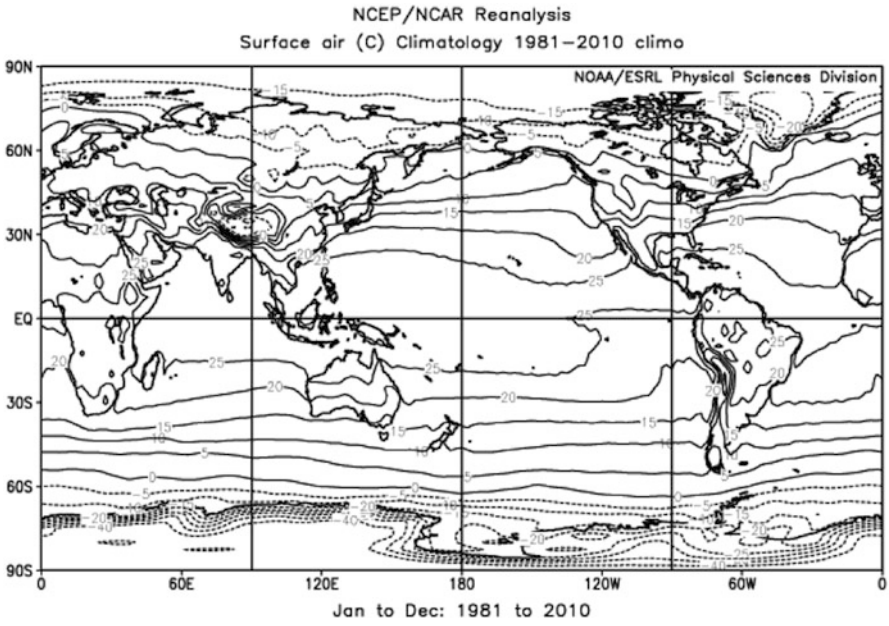

Fig. 7.1 Climate mean annual temperature distribution for the 1981–2010 climate period (Plot bases on National Centers for Environmental Prediction (NCEP) reanalysis data)

(continued)

of the gases provides an atmospheric effect of 2 K. Calculate the intensity of energy for a blackbody planet. How much does the wavelength shift? Explain the simplifications (assumptions) that this simplified model makes.

Solution. $T = T_p + \Delta T + \Delta T_a = (255.15 + 33 + 2)\,\mathrm{K} = 290.15\,\mathrm{K} = 17\,^\circ\mathrm{C}$. Using Wien's law $\lambda_{change} = \frac{2.898}{T} \approx 9.99\,\mu\mathrm{m}$ and $\lambda \approx 10.1\,\mu\mathrm{m}$ means a shift towards shorter wavelengths. Stephan-Boltzmann's law yields $I = \sigma T^4 = 5.67 \cdot 10^{-8}\,\mathrm{W\,m^{-2}\,K^{-4}}(290.15\,\mathrm{K})^4 \approx 402\,\mathrm{W\,m^{-2}}$. However, this law is only valid for local equilibrium locally as it required integration over the adjacent half space (Chap. 4). Another assumption is that the additional gas does not alter the albedo of the planet. However, at the given temperatures, at least water vapor may change phase and hence albedo.

Climate is a characteristic of the climate system defined by the average weather in terms of means, and other statistical quantities (higher order moments) that measure spatial and temporal variability. Typically, observations for a 30 year period define the **normals** used for reference, for instance the 1981–2010 climate normal (Fig. 7.1). The normal can be determined on various time scales, for instance, as a

daily, monthly, seasonal mean temperature, or monthly mean diurnal cycle, as mean over typically 30 years. Figure 7.2 exemplarily shows the 1981–2010 climate normal for boreal winter (DJF) and summer (JJA). Comparison of the two panels illustrates that the land-ocean distribution, distance to the ocean as well as topography have strong impact on the temperature distribution.

While for observations the 30 year climatological means are typically considered to get a reasonable statistic (see World Meteorological Organization and books on statistics for more information), in regional climate modeling often shorter periods are considered as current computational limitations still prohibit long-term high resolution computations under consideration of cloud-aerosol, cloud-radiation, aerosol-chemistry, land-surface-atmosphere, and other regional climate relevant feedbacks. This fact makes the interpretation challenging, despite this procedure in regional climate modeling is state-of-the-art until technological and data processing (random access memory) possibilities drastically improve technologically.

There are various possibilities to assess climate change/variability. The easiest way is to compare two independent climate normals (Fig. 7.1). Another commonly used method is to examine the deviation from the normal, namely the **anomaly** (Fig. 7.3). Often it is of interest how a specific year differs from the current climate normal, or one climate episode differs from the previous one. Climate normals may differ from one 30-year period to the next due to climate multi-decadal variability and/or change. Therefore, when discussing anomalies we have always to provide information, which climate period we considered as reference. To assess a change in climate independent climate periods have to be considered, for instance, the climate-mean temperature distribution of 1951–1980 vs. that of 1981–2010 (Fig. 7.3).

Climate element denotes meteorological or other key quantities that individually and by their interaction with other key quantities characterize climate at different scales (Table 7.2). The term **secondary climate element** refers to two-dimensional field elements like snow-depth, the depth of the atmospheric boundary layer (ABL), albedo, emissivity, the coverage of the Earth by ocean, desert, certain vegetation, snow, ice, or clouds, or the frequency of events like arctic haze, smog, fog, thunderstorms, snow-days, precipitation, wind direction.

Climate phenomenon addresses the appearance of climate-relevant phenomena like the Gulf-stream, an extra-tropical or tropical cyclone, the persistence[2] of marine stratus, föhn, monsoon, precipitation, etc.

Climate mechanism refers to a typical chemical, physical or biological process. A prominent example of climate mechanism is the simplified energy cascade of input of radiation into the Earth-atmosphere system being transferred to reflected solar shortwave and terrestrial long-wave radiation. Another important climate

[2]Persistence is usually also determined to assess the quality of a model forecast. When the forecast is better than persistence and climatology, the model is considered to have forecast skill.

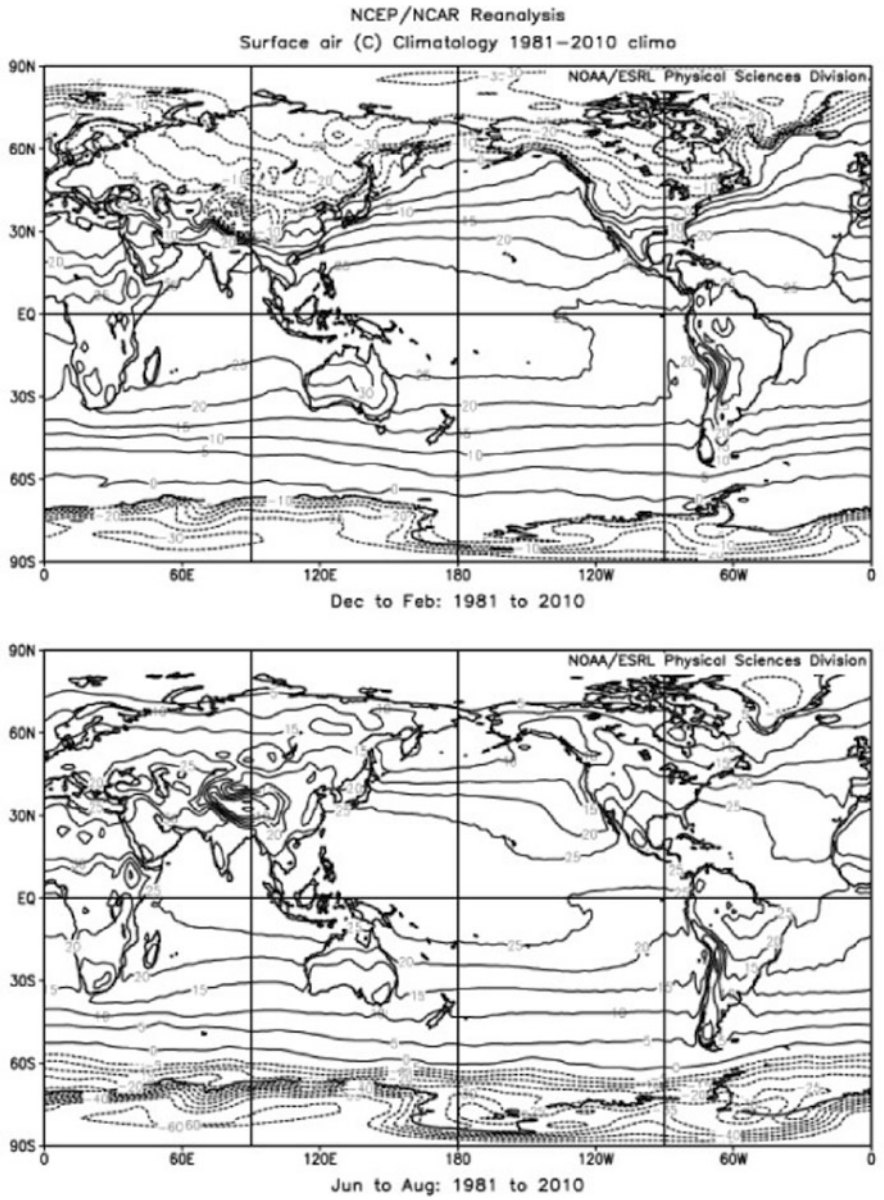

Fig. 7.2 Climate normal of temperature distribution for the 1981–2010 climate for boreal (*top*) and Australia's winter (Plots base on NCEP reanalysis data)

mechanism is the partitioning of incoming solar energy between the fluxes of sensible and latent heat and soil heat flux (Fig. 4.23). Other aspects are the absorption of radiation by trace gases, the emission of methane CH_4 by rice fields, ozone formation and depletion, uptake of CO_2 by vegetation, the radiation budget,

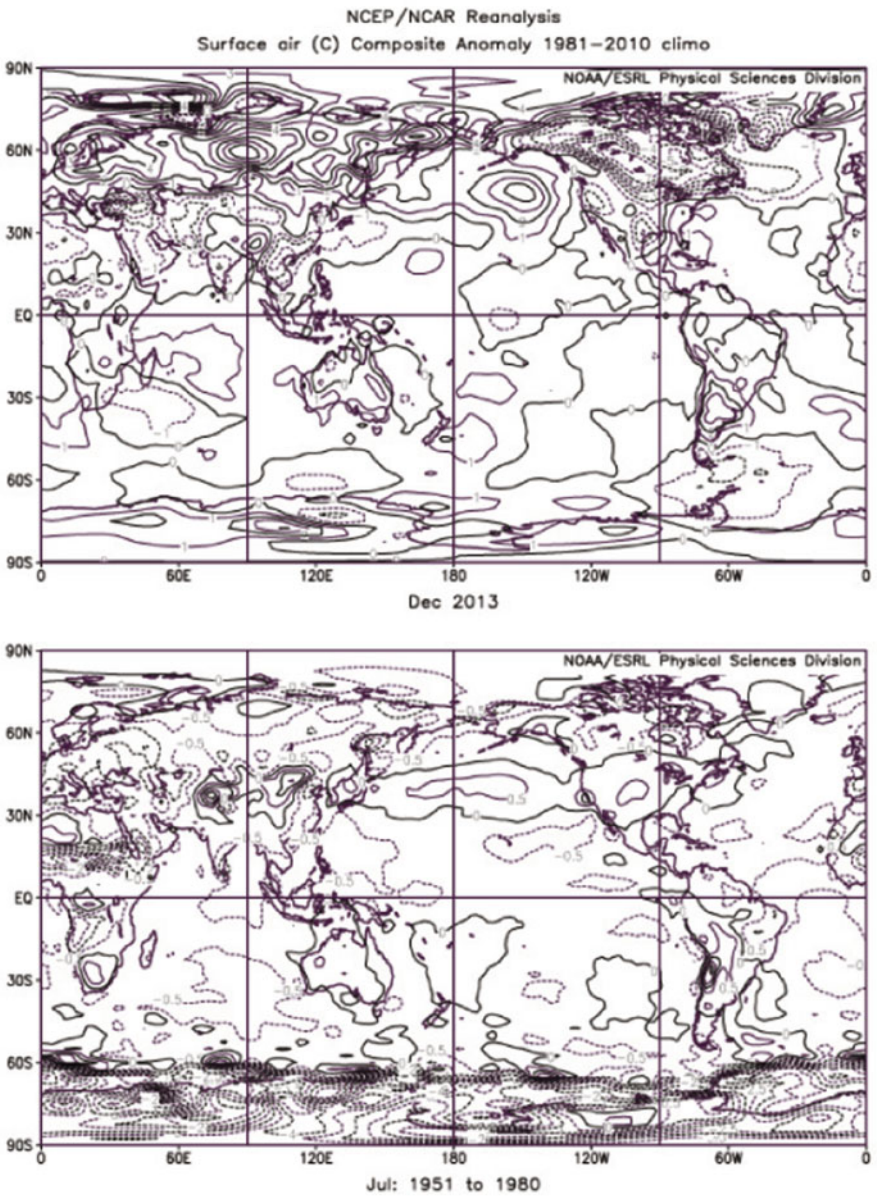

Fig. 7.3 Climate temperature anomalies of the (*top*) December 2013 compared to the 1951–1980 December normal, and July 1951–1980 climate normal compared to the July 1981–2010 climate normal (Plots base on NCEP reanalysis data)

Table 7.2 List of some climate elements

Climate element	Variable of state	Flux quantity	Field quantity	Relative elements
Solar radiation		x	x	Global radiation, direct and diffuse solar radiation, shortwave reflected radiation
Terrestrial radiation		x	x	Long-wave downward radiation, long-wave upward radiation
Radiation balance	x	x		
Temperature	x		x	Air, soil, and water temperature
Humidity	x		x	Specific humidity, relative humidity, water vapor mixing ratio
Soil moisture	x		x	Volumetric water content, plant available water, water potential
Soil ice	x		x	Volumetric ice content, frost depth
Precipitation		x		Hail, snow, graupel, rain, drizzle
Evapotranspiration		x		Potential evapotranspiration
Latent heat flux		x	x	Potential evapotranspiration
Sensible heat flux		x	x	
Ground heat flux		x	x	
Snow heat flux		x	x	
Surface runoff		x		
Pressure	x		x	Geopotential height
Wind	x		x	Wind vector
Friction velocity		x	x	Friction velocity vector
Flow	x		x	Wind vector
Trace gases	x		x	Various liquid, gaseous, and solid species

the water cycle, etc. (Chaps. 4, 5). Figures 5.8–5.11 illustrated the global water, carbon, nitrate, and sulfur cycles. As demonstrated in Fig. 5.8 there also exist cycles on shorter temporal and smaller spatial scales than global or regional.

Climate controls are latitude, longitude, elevation, land-water distribution, geographic position on a continent, mountains and highlands, ocean currents and surface temperatures, prevailing pressure and wind systems (cf. Figs. 7.1, 7.2, 7.6, and 7.9).

7.1.1 Characterization of Climate

To assess climate, climate variability and/or change, we determine, among other things, the mean distribution of first and second order moments, spatial and temporal distributions of minima and maxima, frequency distributions, etc. Often it is advantageous to sort data by meaningful criteria like season, region, along

latitude/longitude, or time of the day, given synoptic situation, etc. Especially on the mesoscale and finer, limitation to events may be required to understand the typical behavior, for instance, of mesoscale dynamics of a supercell.

The term **climate average** or **climate mean** has three different aspects. The **spatial average** of a climate element χ

$$\{\chi\} = \frac{1}{n \cdot m} \sum_{i=1}^{n} \sum_{i=1}^{m} \chi_{i,j} \tag{7.1}$$

serves to investigate climate fluctuation. For instance, we can look at the temporal evolution of its structure (e.g. the mean temperature of a region, and its change during the last 1,000 years). In the above equation, the curled brackets indicate the averaging, the indices n and m give the number of values in west-east and north-south direction. The **zonal** and **meridional average** (*Latin* meri dies = midday) are special cases of spatial averaging. They refer to the averaging along a latitudinal or longitudinal belt, respectively.

The **temporal average**

$$\overline{\chi} = \sum_{i=1}^{n} \frac{\chi}{n} \tag{7.2}$$

of a climate element serves to examine its spatial structure (e.g. regional climate) (Figs. 7.1 and 7.2). Here, the overbar indicates the averaging and n is the number of available measurements in a time series.

Realize that daily mean values may not really be mean values, but determined from the arithmetic means of the observations at 0700 LT, 1400 LT and 2100 LT. In case of air temperature, the mean may also be represented by the arithmetic mean of the records at 0700 LT, 1400 LT and twice the record at 2100 LT. This procedure can be a good approximation, but is not exact.

Example. Use the following hourly values and determine the daily mean temperature based on the hourly values and the two methods used when only the three observations are available. Temperatures were 7.4, 8.2, 7.4, 7, 7.1, 6.5, 6.4, 6.8, 6.8, 6.3, 5.6, 6.1, 6.4, 6.6, 6.6, 6.4, 6.7, 7.2, 6.8, 7.3, 6.7, 7.8, 7.4, and 7.4 °C. Data is LT starting with 0100. The measurement accuracy is ±0.1 K. Discuss the error.

Solution. The mean based on hourly records is 6.9 °C. Based on three data we obtain 6.6, and 6.6 °C, respectively. The value for the last two is only the same due to the rounding rules. The exact values are 6.870833333, 6.566666667, and 6.6, respectively. However, the accuracy of the measurements requires

(continued)

(continued)

cutting the values off after one digit. In this example, the error due to not having high resolved data is small 0.3 K. However, when the weather strongly changes during the day (e.g. frontal passage, thunderstorm, breakup of an inversion) the errors may be much higher than found here.

Spatial and temporal averaging is often applied simultaneously. For instance, averaging over time and all longitudes along latitudes (i.e. in west-east direction) provides zonal means as a function of latitude. Averaging along longitudinal lines or in south-north direction provides a meridional mean.[3] Zonal averages of temperature, for instance, illustrate the temperature contrast along the Earth's longitude. Height-horizontal cross-sections of the zonal averages of wind speed and temperature elucidate the mean position of the polar jet and the different heights of the tropopause in low, mid and high latitudes. Meridional flow leads to extreme weather like heat and cold waves depending on whether the flow is pole ward or equator ward. On the contrary, zonal flow only marginally impacts local weather. Changes in extreme events are of great interest in climate research. Averages of the zonal component of wind speed at 250 hPa help identify the mean position of the jets (Figs. 7.4 and 7.11).

The **ensemble average** looks at a huge amount of different conditions of the climate system and in an ideal case of various climate elements. Scientists gain such ensembles by initializing a climate model with slightly different conditions, using data from different climate models or averaging over data of all observed events of a climate phenomenon (e.g. Föhn, land-sea-breeze, polar low, smog situation, tropical cyclone). Ensemble means serve to define scales of individual climate phenomena and to derive the typical characteristics of a phenomenon. This concept, for instance, allowed the development of the Bjerknes front model (Fig. 6.51) or the theory on tropical cyclones (Fig. 6.23). The Intergovernmental Panel on Climate Change (IPCC), for instance, uses ensembles of data provided by various climate models. The IPCC also uses different scenarios of assumptions how the world will develop in the future, as these aspects bear notable uncertainty.

In general ensemble studies as well as sensitivity studies may increase the confidence in climate model results and provide understanding of uncertainties and sensitivities of the climate system. When using observational data to examine the typical behavior of a climate phenomenon doings so is also generating an ensemble average. However, a lot of thought has to put into such efforts to understand

[3]Recall that for vector fields, the zonal (meridional) component or x-(y-)coordinate is referred to as u (v) (cf. Chap. 6).

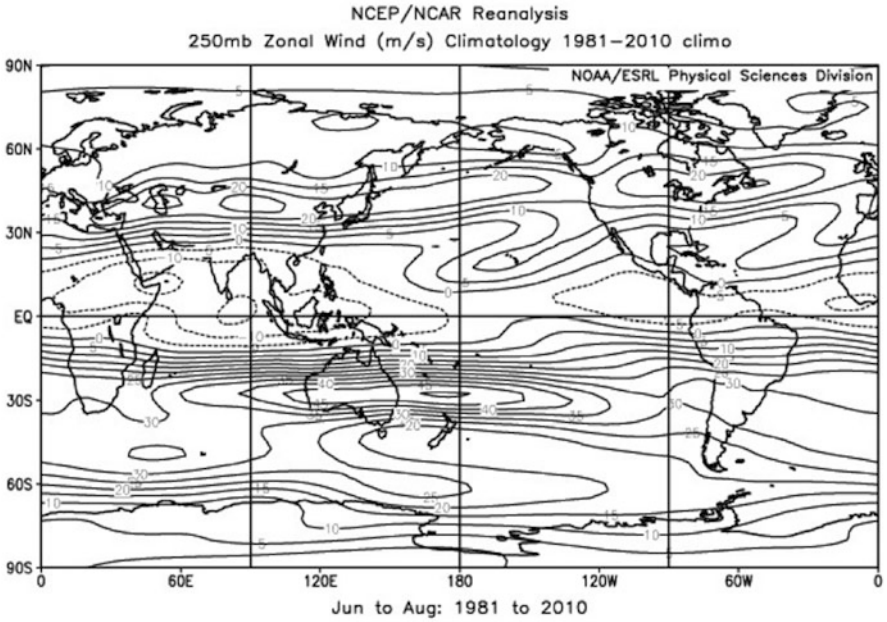

Fig. 7.4 Mean annual wind speed at 250 hPa for the 1981–2010 climate normal (Plot bases on NCEP reanalysis data)

the main processes. Depending on the climate phenomenon to be investigated regional modeling or Large Eddy Simulation (LES) may help in understanding the observations.

The same mean value can be obtained by quite a variety of distributions. Therefore, to identify climate changes, and/or variability – in space and/or time – even when "disguised" by the same mean value, we also have to look at changes in the distribution, i.e. at the moments. A moment quantitatively measures the shape of a dataset. The first moment is the mean of the distribution. The second moment[4] measures the width or variability of the distribution of data points. Most commonly the variance is used

$$Var(\chi_1, \ldots \chi_n) = \frac{1}{n-1} \sum_{i=1}^{n} (\chi_i - \overline{\chi})^2 \tag{7.3}$$

which estimates the mean squared deviation of χ from its mean $\overline{\chi}$. Taking the square root provides the standard deviation $\sigma = \sqrt{Var(\chi_1, \ldots \chi_n)}$. Often the

[4]The second moment is also called second central moment.

mean absolute deviation is used as it is a more robust estimate for the width of the distribution

$$ADev(\chi_1, \ldots \chi_n) = \frac{1}{n}\sum_{i=1}^{n} |\chi_i - \overline{\chi}| \,. \tag{7.4}$$

The third moment of a distribution is its skewness given as

$$Skew(\chi_1, \ldots \chi_n) = \frac{1}{n}\sum_{i=1}^{n} [\frac{\chi_i - \overline{\chi}}{\sigma}]^3 \,. \tag{7.5}$$

As it is obvious from the equation, skewness is a non-dimensional quantity or measure. Positive or negative skewness indicate that the distribution is asymmetrically distributed and has a tail, i.e. there are more positive or negative deviations from the mean. Even when the skewness is zero it still does not mean that the standard deviation describes the skewness of the distribution well. For a normal, i.e. Gaussian distribution the standard deviation is about $\sqrt{15/n}$. Typically in meteorological and consequently in climate application data are non-Gaussian distributed. Typically we believe that the values are skewed when the skewness is much larger than the standard deviation of a Gaussian distribution.

The fourth moment is the kurtosis given by

$$Kurt(\chi_1, \ldots \chi_n) = (\frac{1}{n}\sum_{i=1}^{n} [\frac{\chi_i - \overline{\chi}}{\sigma}]^4) - 3 \tag{7.6}$$

i.e. like skewness a non-dimensional measure. In the case of a normal distribution the "3" makes the kurtosis zero. The kurtosis indicates how flat or peaked the distribution is compared to a normal distribution. A distribution with negative kurtosis is called platylaurti.[5] A positive kurtosis is referred to as leptokurtic.[6] Distributions in-between are called mesokurtic.

Figure 7.5 demonstrates the importance of looking at higher order moments exemplarily by means of two time series of wind data. They have a correlation of 0.82, and both have a mean wind speed of 5.74 m s^{-1}. If the data were Gaussian distributed the standard deviation for these two datasets would be ± 0.07 m s^1. Dataset 1 and 2 have skewnesses of 0.61 and 0.47, respectively. Such skewness is much higher than the estimate for the standard deviation for datasets of this size indicating that the data are not Gaussian distributions. Nevertheless, the standard deviations of dataset 1 and 2 are quite close namely 1.68, and 1.77 m s^{-1}, respectively. This means the width of the two distributions only slightly differs. This means that the wind data distributions differ in shape by about 14 %. Both datasets

[5]The distribution looks like a leaf of bread.

[6]The distribution looks like the Matterhorn.

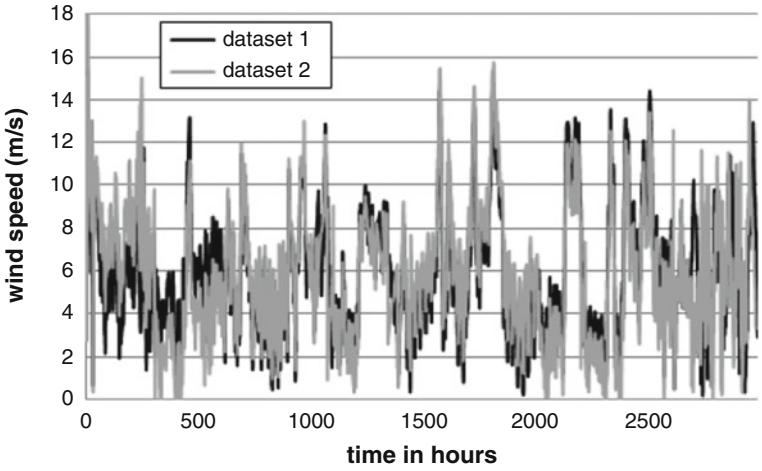

Fig. 7.5 Comparison of mean wind speeds with same mean value

have a positive skewness meaning that the tail towards high wind speed is longer than that for weak winds. Dataset 1 (2) has a kurtosis of 0.01 (−0.06). This means that dataset 1 has a flatter distribution than dataset 2, and that their shapes differ notably.

In the following, we discuss examples of knowledge gained through these averaging methods, and put them into the framework of the previous chapters. Prominent examples of knowledge derived from temporal averaging are the semi-permanent pressure cells, the three circulation cells occurring on each hemisphere, the trade winds, as well as distributions of various meteorological quantities over different time scales.

7.1.1.1 Pressure

Semi-permanent Pressure Cells

Temporal averaging of sea-level pressure reveals a distinct dependency on geographical latitude, especially, on the southern hemisphere that has fewer disturbances by the land-ocean-distribution (Fig. 7.6), among other things. On average, a number of alternating **semi-permanent cells**[7] of high and low pressure covers the Earth (Fig. 7.6). Some of these cells exist for thermal, others for dynamical reasons.

On the Northern Hemisphere, the land-ocean-distribution leads to high (low) pressure over the continents in winter (summer). In the high pressure systems,

[7] Semi-permanent refers to the seasonal change in intensity and position of these cells.

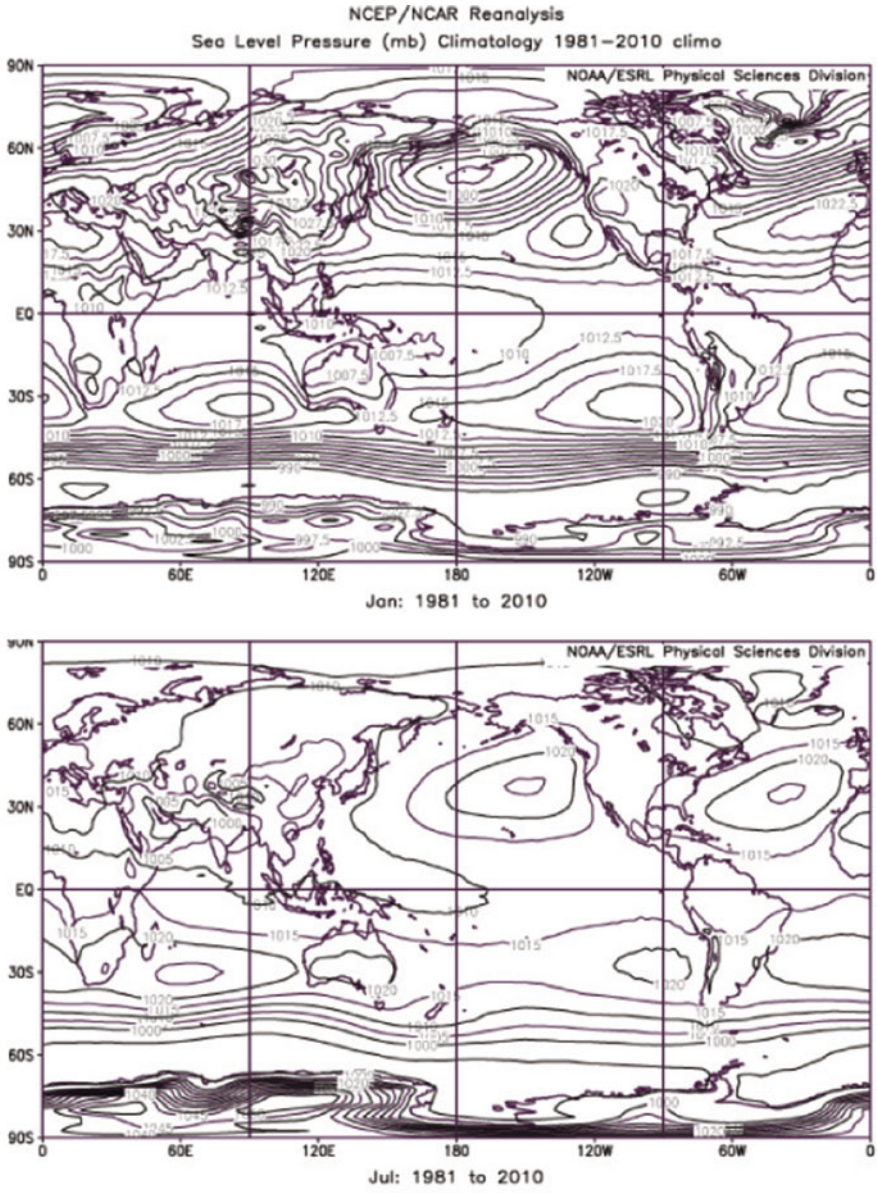

Fig. 7.6 Mean pressure distribution (hPa) in January (*top*) and July for 1981–2010 (Data shown in the plots are NCEP reanalysis)

subsidence (Chap. 2) leads to nearly cloud-free conditions, while in low pressure systems, the lifting leads to cloud and precipitation formation (Chaps. 2, 3, and 6). The differences in pressure distributions over land and ocean, to large degrees, result from the non-equal heating/cooling rates due to the different heat capacities and thermal conductivity of land and water (Chap. 2) as well as the differential insolation (Chap. 4; Fig. 4.10), among other things. On average, relatively flat anticyclones exist at each of the poles.

In winter, the most prominent features are the **Aleutian** and **Island lows** located over the Pacific and Atlantic Ocean, respectively, and the **Siberian high** over Central Asia. In summer, the **Hawaiian** and **Azores high** and **Tibetan low** develop over the Pacific, Atlantic and southern Asia, respectively (Fig. 7.6). The position and strength of these cells change dependent on solar inclination (Fig. 4.8).

Any change of one of these pressure systems is at the cost of the respective other system. For instance, when in winter the Aleutian low strengthens and expands, the Hawaiian high weakens and reduces its size. The opposite is true in summer.

In about 50°N or S, moving extra-tropical cyclones are located. In the satellite data, they are visible by clouds, long-waves, and eddies (Figs. 4.26–4.28). On average, surface pressure is low around the equator in the inner tropical convergence zone (ITCZ, Fig. 7.6).

Rossby Waves, Troughs and Ridges

In Chap. 6, we discussed the formation of Rossby waves. The resulting series of troughs and ridges make up the weather pattern in mid-latitudes. The paths of extra-tropical cyclones are governed by the Rossby waves. The Rossby circulation is a long-wave pattern that becomes visible from temporal averaging. It occurs mainly in the mid- and high latitudes.

North Atlantic Oscillation, North Pacific Oscillation, and Other Circulation Related Indices

The **North Atlantic Oscillation** (NAO), **North Pacific Oscillation** (NPO), and **Southern Oscillation Index** (SOI) indices are examples for temporal averaging, and calculation of anomalies from the long-term mean.

NAO is an inverse pressure variation at the Azores high and Icelandic low. It is associated with temperature anomalies in Europe in relation with the zonal wind pattern over the North Atlantic. NAO is most distinct in winter. NPO is an inverse pressure variation at the North Pacific high and the Aleutian low. NPO goes along with variations in the zonal wind and temperature fields in North America. We will discuss the SOI in detail later in the context of El Niño-Southern Oscillation (ENSO).

Two other important indices in climate research and climatology are the Inter-decadal Pacific Oscillation (IPO) and the Pacific Decadal Oscillation (PDO).[8] PDO refers to the leading Empirical Orthogonal Function (EOF) or principal component of monthly sea-surface temperature anomalies (SSTA) over the Pacific ocean north of 20°N after subtraction of the mean SSTA. Thus, the PDO index is a standardized principle component time series (see books on statistics for further information). Positive (negative) PDO means that the Pacific ocean surface north of 20°N is warmer (cooler) in the eastern (west) Pacific while it is cooler in the West (eastern) Pacific. The PDO shifts phase at inter-decal time scale (20–30 years). The causes of PDO are still subject to research. One of the current hypotheses is that PDO is red noise of the El Niño-Southern Oscillation plus stochastic atmospheric forcing superimposed. Several studies suggest that the PDO is the superimposition of extra-tropical and tropical processes. Obviously, PDO is not a single mode of ocean variability, but several processes of different origin acting dynamically together. On decadal timescales, stochastic atmospheric forcing, teleconnections of ENSO (see Sects. 7.1.3.2 and 7.2.1), and changes in the North Pacific oceanic gyre circulation are contributing to the anomalies. There is also some discussion whether PDO is a response to ENSO.

As the different sea-surface temperatures (SST) have impacts on weather at the seasonal scale and longer, it is desirable to know the PDO. Figure 7.8 exemplarily shows the mean near-surface temperature distribution averaged over years of positive and negative PDO. At inter-annual time scales, we can determine the PDO index by the sum of ENSO related and random variability in the Aleutian low. This procedure serves for help in seasonal forecasts that are of great importance for planning and logistics.

The IPO shows similar SST and sea-surface level pattern, and has a cycle of about 15–30 years. However, it affects the north and south Pacific with an 8–12 year cycle.

Often these indices are used to determine composites of atmospheric means or anomalies for years with positive/negative indices (Figs. 7.7 and 7.8).

7.1.1.2 Wind

Wind pattern are governed by differential heating on all scales (Figs. 4.10, 7.1, 7.6, and 7.11). At meso- and synoptic scale, they are affected by the Coriolis force (Chap. 6).

In the longitudinally averaged zonal wind (east-west), the zonal wind component is about an order of magnitude greater than the meridional wind component at most locations. The strongest zonal winds are the **mesospheric jets** at 60 km height. In mid-latitudes, they reverse between winter westerlies and summer easterlies.

[8] The PDO pattern in the ocean was detected by Steven R. Hare, who performed research on salmon production.

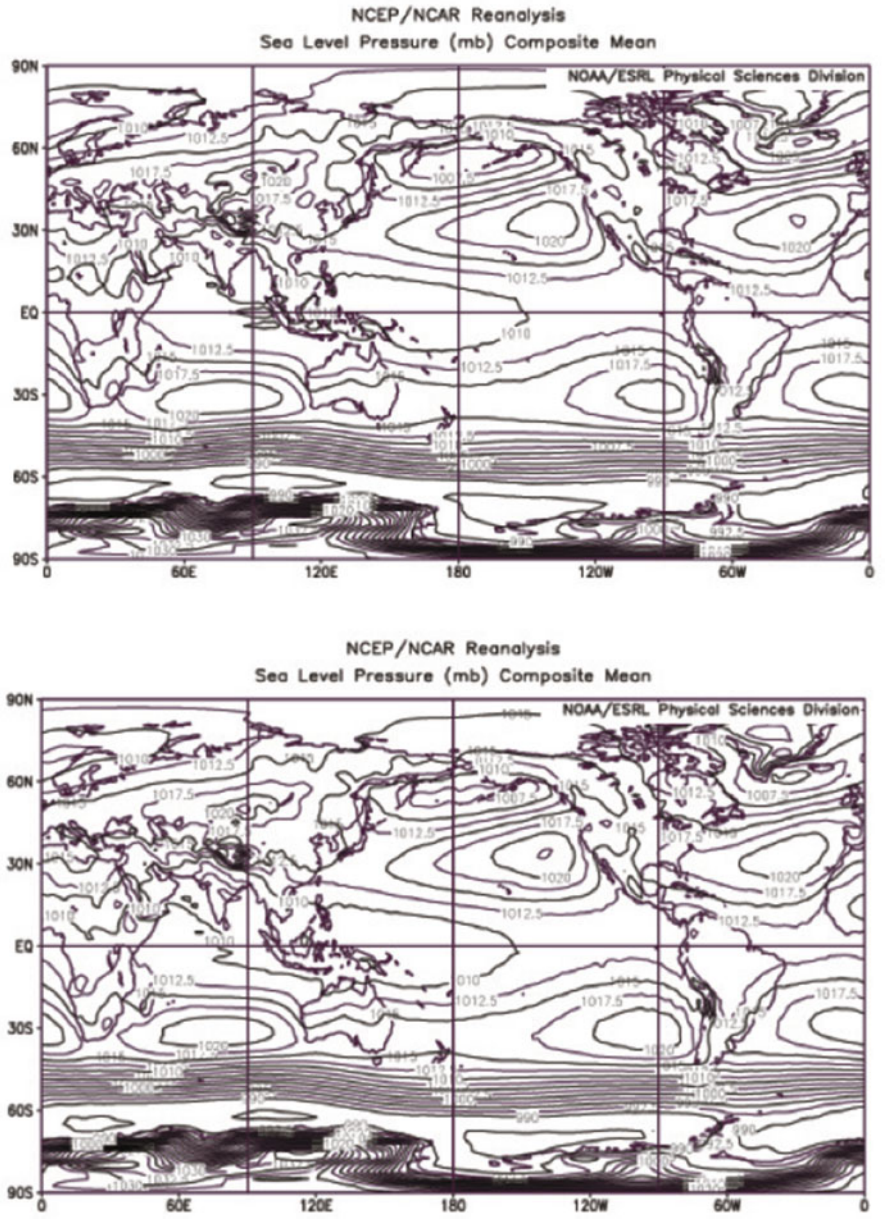

Fig. 7.7 Mean sea-surface pressure distribution (hPa) in years with positive NAO index (*top*) and in years with negative NAO index for 1948–2010 (Plots base on NCEP reanalysis)

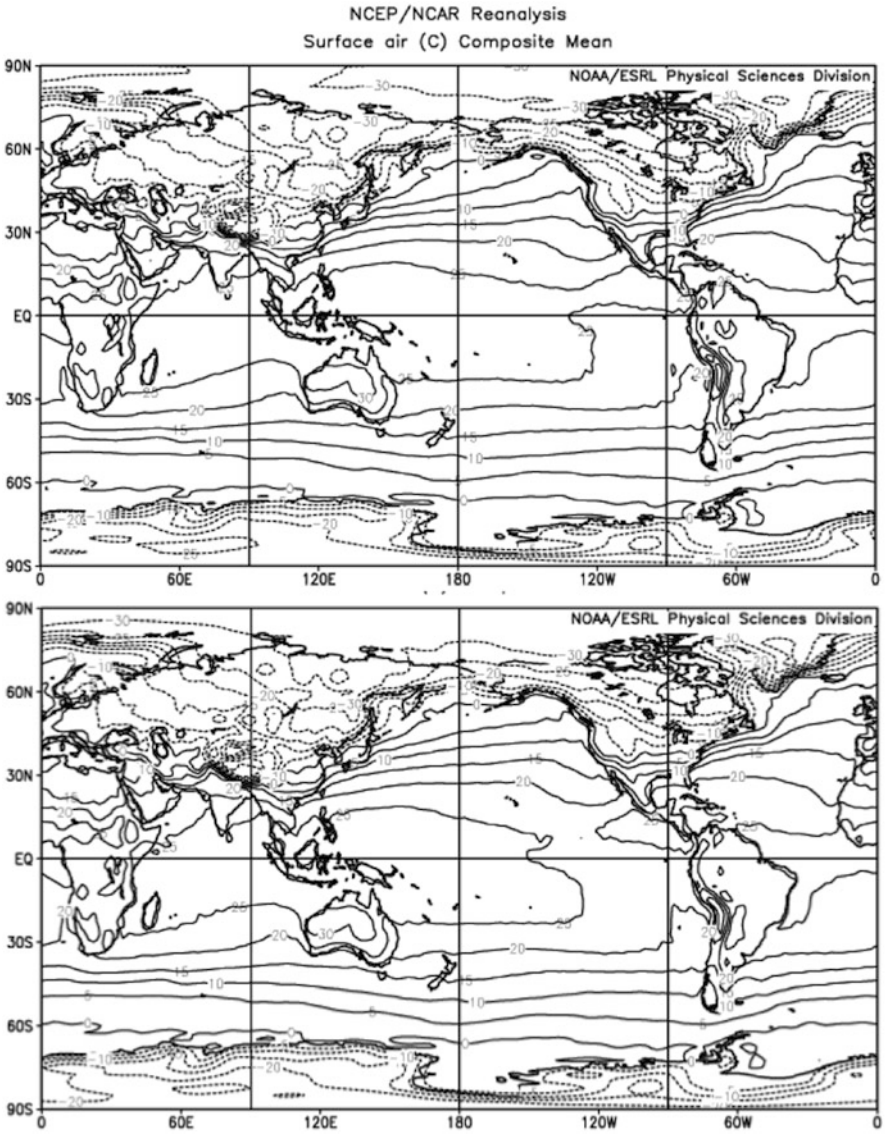

Fig. 7.8 Mean near-surface temperature distribution in years with positive (*top*) and negative PDO index for 1948–2010 (Plots base on NCEP reanalysis)

Hadley, Ferrel and Polar Cells

In a longitude-height cross-section of latitudinal-averaged meridional wind, the Hadley-, Ferrel-, and polar cells become visible. This three-cell circulation pattern is only visible in the long-term average as the land-ocean distribution and topography

modify pressure and wind fields (Figs. 7.6 and 7.9), and, hence, circulation. The general circulation compensates the effects of the geographical differences in radiative heating and is itself driven by them. Ideally, we can describe the general circulation by a **three-cell-model**[9] in each hemisphere (Fig. 7.10), which results from the differential heating (Fig. 4.10) and rotation of the Earth (Chap. 6).

Due to the strong solar heating at the equator, air rises thereby creating a zone of low pressure around the equator called the ITCZ. The prevailing upward motions lead to cloud formation with heavy rain showers, especially in the afternoon. Consequently, a band of cloud clusters exists along the equator (Figs. 4.26 and 4.28), and the ITCZ is the rainiest latitudinal zone on Earth (Fig. 7.15) with many locations having more than 200 rain days per year.

Upon arriving in about 20–30° North or South the air descends toward the surface building the **subtropical highs** (Fig. 7.10). The sinking air warms adiabatically and suppresses cloud formation (Chaps. 2 and 3). Thus, large deserts (e.g. Sahara Desert, Australian Desert, the deserts in the southwestern US and northern Mexico) exist in the Subtropics. In the northern (southern) hemisphere, the pressure-gradient forces direct surface winds to blow from the Subtropics to the Equator, and the weak Coriolis force deflects them to the right (left) (Fig. 7.9; Chap. 6). This superposition of forces causes the **northeast trade winds** (**southeast trade winds**) in the northern (southern) Subtropics. On average, the pressure gradients are light in the subtropical anticyclones, and the winds are shallow[10] (Figs. 7.6 and 7.9). Near the equator, air converges at lower levels forming the ITCZ.

This thermally driven cell is called the **Hadley cell**.[11] Application of the Carnot cycle explains why the circulation is the strongest in winter as then the temperature gradients (Fig. 7.2) are greatest (Chap. 2). Thermally driven cells are **direct circulations**.

Another thermally driven cell is the **polar cell**. Compared to the poles the **sub-polar lows** are warmer yielding low pressure and ascending of air. The extremely cold conditions at the poles result in high surface pressure (Fig. 7.6), and a motion directed equator-ward at lower levels (Fig. 7.9). Thus, air flows from the surface **polar highs** from about 80° to the sub-polar lows in about 60° (Fig. 7.10). On both hemispheres, the polar cell circulation returns from about 60° to about 80° latitude in the upper levels. The Coriolis force deflects the wind and builds a zone of **polar easterlies** in the lower troposphere (Fig. 7.6).

[9]The three cell concept was introduced by the American meteorologist William Ferrel (1817–1891) in 1865.

[10]These areas had large impact on ship traffic in former times. Without wind, the sailing ships were unable to move and sailors often had to throw their live freight (e.g. horses) aboard. For this reason, these regions are called the name **horse latitudes**.

[11]The Hadley cell is named after the British lawyer and hobby meteorologist George Hadley (1685–1768) who proposed a single cell model with a circulation from the equator to the pole in 1735. The Coriolis force is the reason why that cell is ripped apart (Chap. 6).

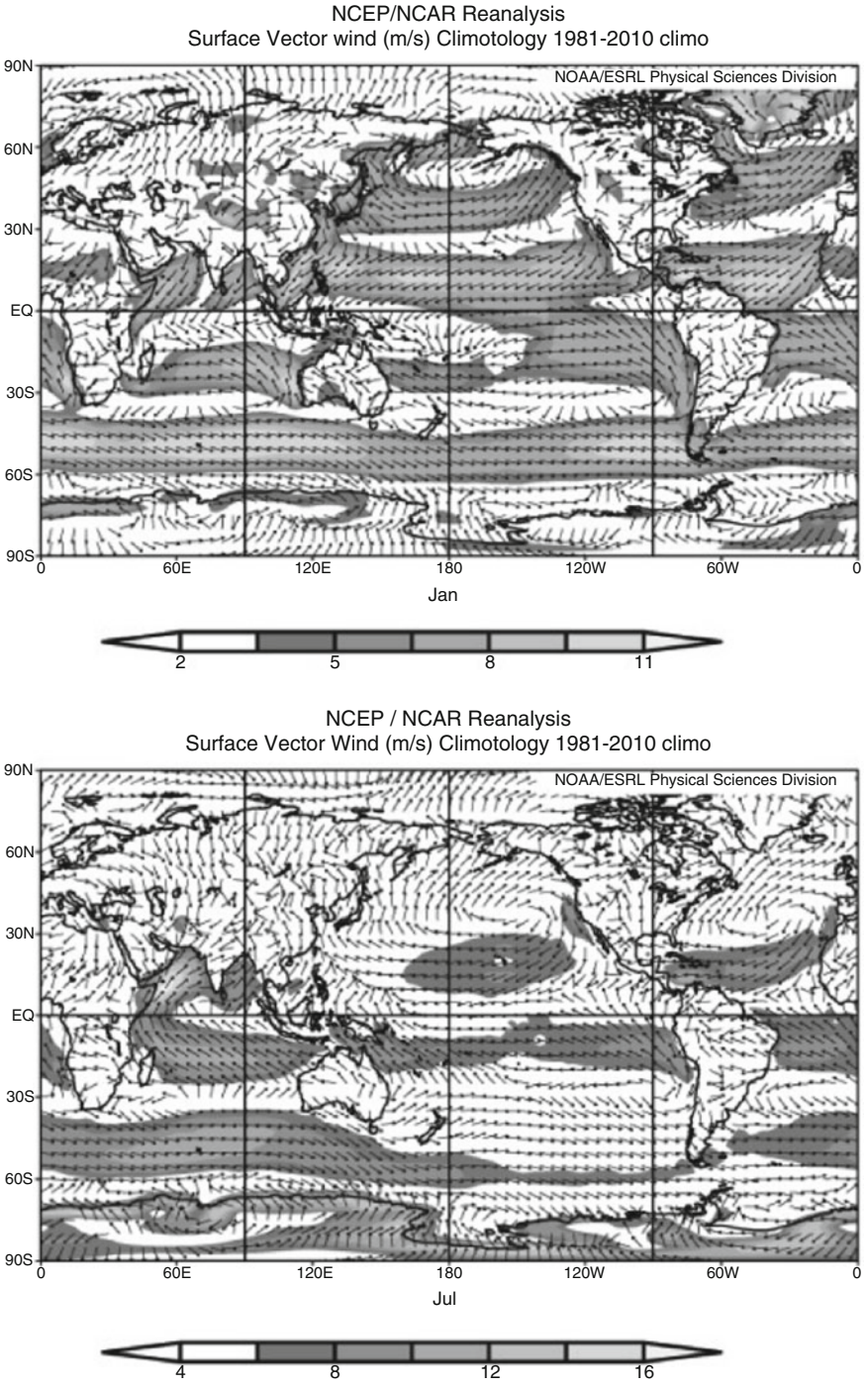

Fig. 7.9 Mean annual surface wind direction and wind speed distribution in January (top) and July for 1981–2010. Data shown in the plots are NCEP reanalysis

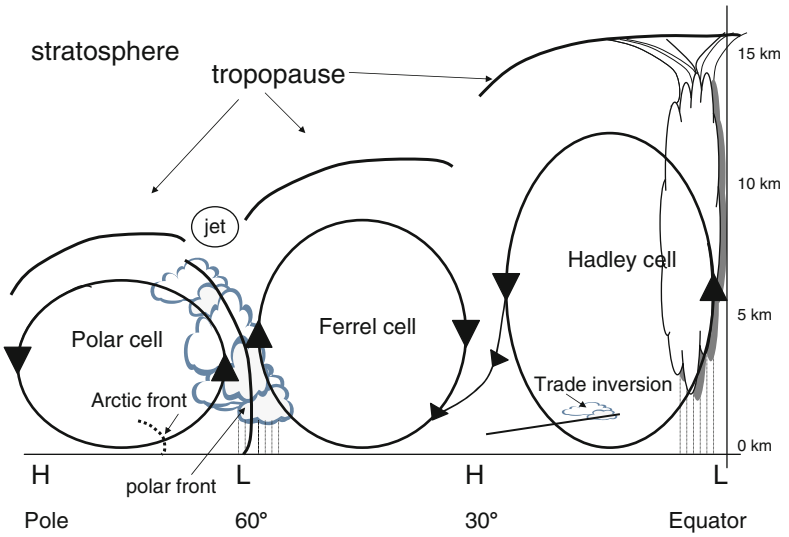

Fig. 7.10 Schematic view of the three-cell circulation concept

On both hemispheres, the **Ferrel cell** is located between the Hadley cell and polar cell. The thermally driven Hadley and polar cells drive the **indirect circulation** of the Ferrel cell (Fig. 7.10). At about 45–60°N, air ascends, travels equator-ward at upper levels to about 30°N latitude, where it sinks (Fig. 7.10), and moves from the subtropics to the sub-polar lows in the lower troposphere. In the southern hemisphere, the Ferrel cell extends from 30°S to 60°S. The Coriolis force again deflects winds to the right (left) yielding to a wind belt called **westerlies** on the Northern (Southern) Hemisphere (Figs. 7.6, 7.9). These zones of westerly winds are called **roaring forties** due to their average location between 40° and 50° latitude.

Due to the cold air of the Polar Regions, the isobaric surfaces slope toward the poles (Chaps. 2 and 6). The higher the isobaric surface slope, the stronger the wind becomes with height (Figs. 6.28 and 7.11). Thus, the predominance of westerly winds in mid-latitudes is a consequence of the temperature gradient from the Equator to the poles on the rotating Earth (Chaps. 2 and 6).

Jet Streams

In Chap. 6, we introduced the thermodynamic and dynamical processes leading to jet streams. In a latitude-height cross-section of longitudinally averaged zonal wind, the westerly jets become visible at about 10 km height in mid-latitudes (Fig. 7.11). The jet stream separates the circulation cells at upper levels. The polar jet is located just south (north) of the polar cell in the northern (southern) hemisphere. The subtropical jets are located just south (north) of the Ferrel cell in the northern (southern) hemisphere. The tropical easterly jet occurs just south of the northern

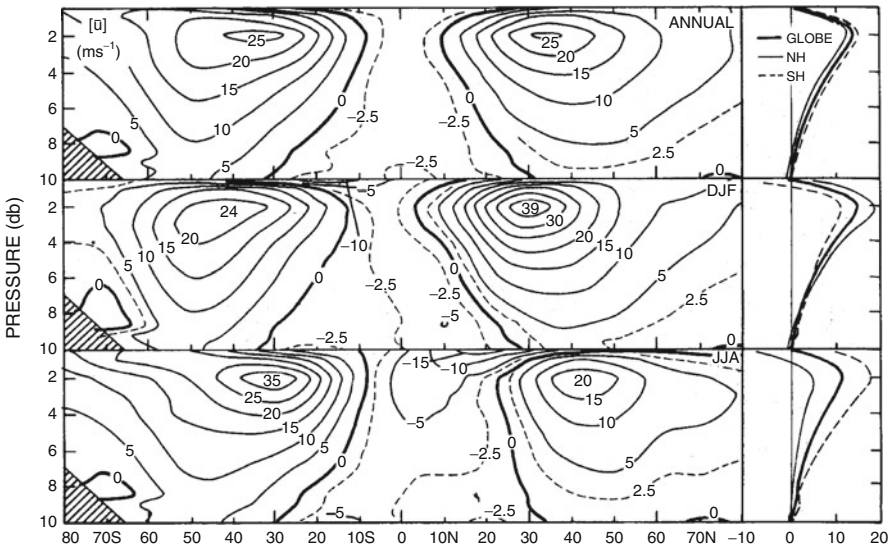

Fig. 7.11 Zonal-mean cross-sections of the zonal wind component ($\mathrm{m\,s^{-1}}$) for annual (*upper*), DJF (*middle*), and JJA (*lower part*) mean conditions. Solid lines give wind speeds from west, dashed lines from the east. Vertical profiles of the hemispheric and global mean values are given on the right (From Peixto and Oort (1992))

Hadley cell. When we recall the thermal wind equations (6.124) and (6.125), we can show that the jet streams exist for thermodynamic and dynamical reasons (see box; Fig. 6.25).

Example. Determine the zonal wind at 250 hPa assuming a mean change of vertical average temperature in south-north direction of $\frac{\partial \hat{T}}{\partial y}$ of $-6.2\,\mathrm{K}\,10^{-3}$ km, a surface pressure of 990 hPa, and a Coriolis parameter of $f = 9.57 \cdot 10^{-5}\,\mathrm{s^{-1}}$.

Solution. In geostrophic and hydrostatic equilibrium, we obtain $f\,u = -\frac{\partial \Phi}{\partial y}$ and $\frac{\partial \Phi}{\partial p} = -\frac{R_d T}{p}$. Differentiating the geostrophic equation with respect to p, and the hydrostatic equation with respect to y eliminates the geopotential Φ, and provides $\frac{\partial (f\,u)}{\partial p} = -\frac{\partial}{\partial p}\frac{\partial \Phi}{\partial y}$ and $\frac{\partial}{\partial y}\frac{\partial \Phi}{\partial p} = -\frac{\partial (\frac{R_d T}{p})}{\partial y}$. Comparison, rearranging and vertical integration between the surface ($p = p_s$, $u = 0\,\mathrm{m\,s^{-1}}$) and 250 hPa yield $\frac{\partial (f\,u)}{\partial p} = \frac{\partial (\frac{R_d T}{p})}{\partial y}$ and $\int_0^{u(p)} du = -\frac{R_d}{f}\int_{p_s}^{p} \frac{dp'}{p'}$. Thus, the horizontal zonal wind component $u(250\,\mathrm{hPa}) = -\frac{R_d}{f}\ln(\frac{p_s}{p})\frac{\partial \hat{T}}{\partial y}$. Inserting the values yield $u(250\,\mathrm{hPa}) \approx 26\,\mathrm{m\,s^{-1}}$.

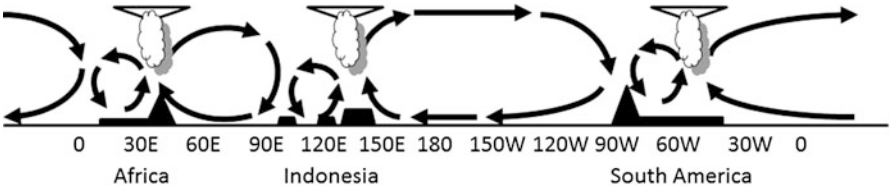

Fig. 7.12 Schematic view of the Walker circulation

7.1.1.3 Walker Circulation

The Walker circulation[12] is an example that it is often important to split the available dataset into smaller chunks, and chose suitable locations to detect a climate process. Walker split his data into four seasonal datasets, and performed the analysis on these seasonal time scales. He also selected wisely, which locations to look at.

While the Walker circulation is hardly visible on the annual mean, it shows notable signals on the seasonal scale. The Walker circulation is a conceptual model of the air flow in the tropical troposphere (Fig. 7.12). It bases on long-term observations, and postulates a closed circulation in the zonal and vertical directions. The Walker circulation is driven by the different heat distribution over land and ocean. The meridional direction of the Hadley circulation discussed above is superimposed.

The Walker circulation is indirectly related to upwelling of cold deep ocean water off the equatorial coasts of South America and Africa. Consequently, in boreal summer, the equatorial SSTs are relatively cool in the eastern Pacific and Atlantic, and western Indian Ocean. The changes in SST are caused by changes of the depth of the thermocline. In boreal summer, the Walker circulation leads to westerly surface winds over the tropical Indian Ocean, and easterly surface winds over the tropical Pacific, and Atlantic.

Besides the sensitivity to changes in SST, the Walker circulation is sensitive to the changing insolation during summer. Recent climate research suggests that deforestation of the tropical rainforests can strongly affect the Hadley and Walker circulations.

Quasi-biannual Oscillation

In the stratosphere, the longitudinally averaged zonal wind shows a strongly semi-annual oscillation at upper levels, and the more irregular **Quasi-Biannual Oscillation** (QBO) $\approx$ 26 months cycle at lower levels (Fig. 7.13). Its easterly and westerly winds are named Krakatoa and Berson, respectively. The wind direction changes gradually from upper to lower layers of the stratosphere. The QBO is initiated in the

[12] Sir Gilbert Thomas Walker (1868–1958; British physicist and statistician) discovered this circulation pattern that by some authors is called Walker cell.

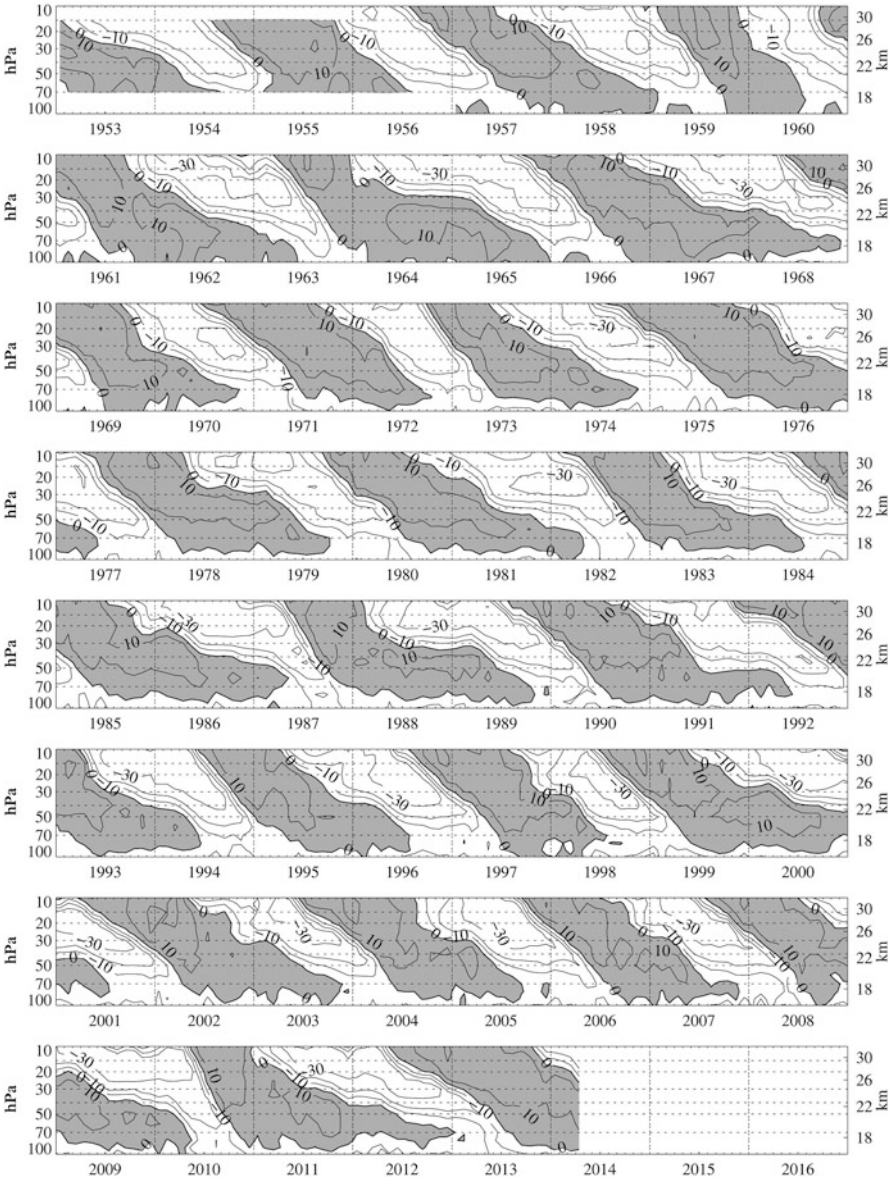

Fig. 7.13 Time-vertical plot of wind in the stratosphere showing the behavior of QBO (Permission by Kunze (2014))

troposphere, as active convection currents hit the tropopause. The resulting vibration is transmitted upward through the stratosphere in the form of waves. Because of these mainly standing vibrations, waves head simultaneously to the east and west. In the presence of a current, the flow selectively absorbs waves propagating in the direction of flow. Waves traveling against the current penetrate it and are transmitted

over a great distance (Chap. 6). Since the waves have momentum in the direction of the phase velocity, they carry reverse momentum opposite to the flow far away when passing through the flow. This momentum finally reverses the flow.

7.1.1.4 Temperature

Chapters 1 and 2 already discussed the vertical temperature distribution. Here we discuss some additional aspects concerning the horizontal variation with height as obtained by temporal averages. The tropopause is considerably higher and colder over the Equator than the poles. In the stratosphere, the air is cold around the Equator and warm at the poles in the summer hemisphere, and a distinct maximum in temperature occurs over the mid-latitudes of the respective winter hemisphere. Over the winter pole, the pole of cold air can vanish by **sudden warming**. This phenomenon can lead to a temperature increase of up to 70 K within a week.

The latitudinal temperature gradient is about twice as steep in the respective winter than summer hemisphere (Fig. 7.1). A huge amount of the latitudinal temperature gradients tends to occur in the narrow bands of the frontal zones that are characterized by strong east-west and north-south temperature differences (Chap. 6). Topography and land-ocean distributions also influence the seasonal and latitudinal temperature distribution (Figs. 7.1 and 7.2). Usually, the central continental areas are much colder (warmer) in winter (summer) than coastal areas of same latitude.

In general, temperature undergoes seasonal variations with higher values in summer than winter. Maximum differences exceed 60 K in high latitudes (Fig. 7.2).

Temperature has a pronounced diurnal course with the lowest temperatures before sunrise. The diurnal temperature range is of the order of 10 K. It can achieve more than 20 K in high-altitude desert regions. The diurnal temperature range is typically smallest over the ocean. It is largest over high altitude desert. In coastal areas or along the shores of large water bodies, the presence of the water leads to a dampening of the diurnal temperature range as compared to the diurnal temperature ranges farther inland.

The differences in the diurnal temperature range over land and water are due to the about twice as high heat capacity of water than soils. Consequently, large water bodies store (release) heat in the warm (cold) season thereby affecting air temperature and moisture in the lower ABL. Thus, in tropical regions, climate is more moderate close to than farther away from water. In mid-latitudes, the release (gain) of energy stored in the water enhances (reduces) the air temperatures. Thus, the climate along the shores has milder winters and cooler summers than farther inland.

Example. The water temperature of a lake was 28 °C at noon. Twenty four hours later it was 30 °C. The lake holds $25 \cdot 10^6$ L of water and has a surface area of 100,000 m^2. On the first day, air temperature was 20 °C at sunrise

(continued)

(continued)

and 35 °C at noon. On the next day, it was 22 °C at sunrise and 42 °C at noon. Make a back of the envelop estimate of the amount of heat that has to be added to heat the water of that lake in 24 h from 28 to 30 °C. Can the diurnal course of air temperature provide that amount of heat? Argue based on mathematical estimates. This box was inspired by the movie Volcano.

Solution. For simplicity we neglect the cooling of the water surface at air temperatures below the water surface temperature, and work with the noon temperatures only. Thus, the heating from the atmosphere is approximated as $Q_{air} = Q_{day2} + Q_{day1}$ with $Q = c_p dT$ we get approximately $1{,}004\,\mathrm{J\,kg^{-1}\,K^{-1}}\,(7\,\mathrm{K} + 14\,\mathrm{K}) = 21{,}084\,\mathrm{J\,kg^{-1}}$. One liter of water is 1 kg. Since we neglected the night time cooling, the heating occurs over 24 h only. Thus, $\frac{dQ}{dt} = \frac{21{,}084\,\mathrm{J\,kg^{-1}}}{84{,}600\,\mathrm{s}} \approx 0.25\,\mathrm{W}$. For a lake surface of $100{,}000\,\mathrm{m^2}$ this means approximately $2.5 \cdot 10^4\,\mathrm{J}$ could be at maximum be provided by the atmosphere. The heat required to heat $25 \cdot 10^6\,\mathrm{L}$ water by 2 K amounts to $\Delta Q = c_w dT = 4{,}200\,\mathrm{J\,kg^{-1}\,K^{-1}} \cdot 2\,\mathrm{K} \cdot 25 \cdot 10^6\,\mathrm{kg} = 2.1 \cdot 10^{11}\,\mathrm{J}$, which is much more than the heat provided by the atmosphere.

In high-latitudes, new sea-ice forms in winter. Thus, long-term changes in sea-ice extend would mean changes in the heat and moisture exchange with the atmosphere and altered diurnal temperature ranges along the coasts of the Arctic Ocean.

In climate modeling like in numerical weather prediction, evaluation of the model performance in reproducing the diurnal and annual ranges of state variables and fluxes is important as the same mean value can be obtained with quite different diurnal and annual cycles.

7.1.1.5 Radiation

Temporal averaging provides the following general distribution of global radiation. As discussed in Chap. 4 radiation depends on latitude and time with a maximum on the respective summer hemisphere (polar day) and no solar radiation at the respective winter pole (polar night). At the equinox, when the length of daylight is the same at all latitudes, insolation is proportional to the cosine of the latitude and zero at both the poles (Fig. 4.10). The ratio of insolation received at the summer to winter solstice amounts to about 5:1 at 50°, 3:1 at 40°, and 2:1 at 30° latitude. The eccentricity of the Earth's orbit yields the slightly asymmetric annual-latitudinal distribution of solar radiation (see Chap. 4).

The global energy balance (Chap. 4) is another example of how meteorological observations of extensive variables (Chap. 2) when averaged in an appropriate way, can provide insight in processes and climate (Fig. 4.23). Figure 7.14 exemplarily shows the 1981–2010 normal of the distribution of outgoing long-wave radiation.

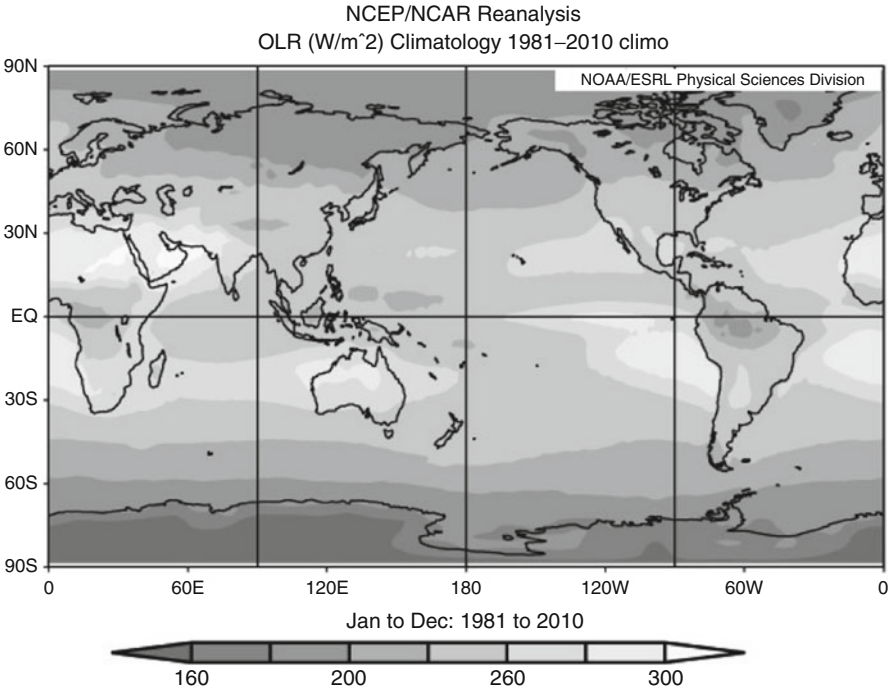

Fig. 7.14 Annual mean of outgoing long-wave radiation for the 1981–2010 normal (Data base on NCEP reanalysis)

We learned in Chap. 4 that clouds reduce incoming radiation. Chapter 3 taught us that different cloud types have different horizontal and/or vertical extend. Thus, different cloud types affect the incoming radiation over differently extended areas. Stratiform clouds, for instance, extend several hundreds of square-kilometers; cumulus clouds affect an area of several square-kilometers depending on geographic location and season. In case of cumulus clouds, the area affected by the cloud shadow is in a certain angle underneath. The cloud shadow intensity, extend and location is a function of cloud-base height, extension (both horizontal and vertical), and solar zenith angle. The reduced insolation in the cloud shadow leads to reduced evapotranspiration, i.e. reduced latent heat fluxes. We already learned in Chap. 4 that clouds affect the surface-energy budget and the partitioning of available radiation energy at the surface in sensible and latent heat (see also section on cloud-albedo feedback in this chapter). For all the above mentioned reasons, in climate variability and/or change research, it is important to look for changes in cloud formation, composition, albedo, distribution, lifetime, type, location, and vertical extent. For a detailed discussion on the climate effects of clouds, greenhouse gases and aerosols on radiation see Chap. 4.

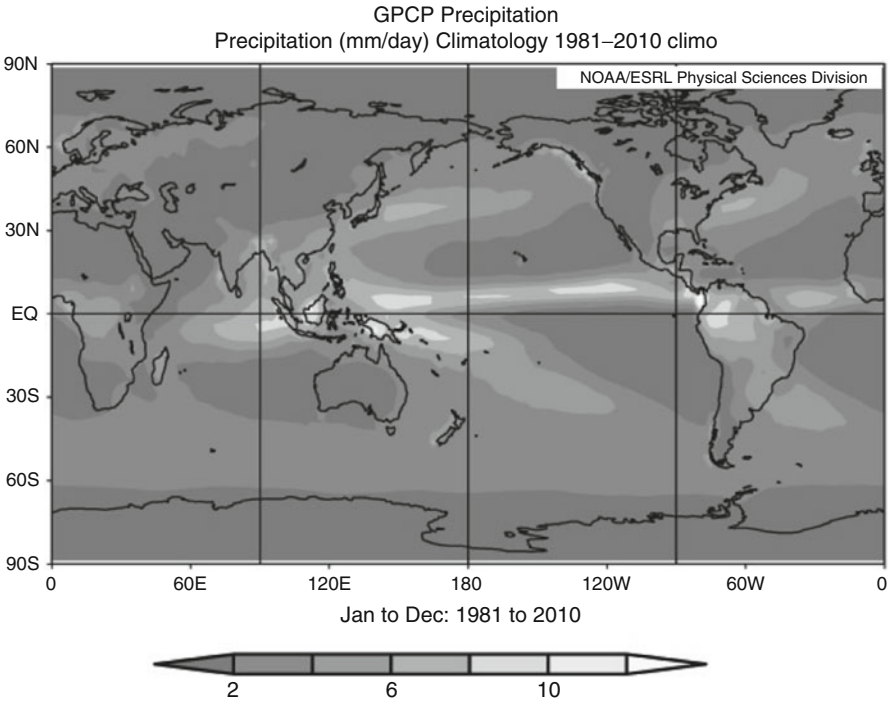

Fig. 7.15 Global distribution of annual-mean precipitation for the 1981–2010 normal (Data are GPCC gridded values based on observations)

7.1.1.6 Humidity, Clouds and Precipitation

We learned in Chaps. 2, 3, and 6 that topography, air temperature, frontal activity, and wind direction in relation to the sources of moisture affect cloud and precipitation formation. Consequently, these factors and the time in the season influence the global distributions of clouds, cloud types, precipitation and precipitation rates (Fig. 7.15). The average general circulation pattern discussed above yields areas of high humidity throughout the entire troposphere and convective cloud systems and cloud clusters in the ITCZ that therefore is easily detectable in satellite data (Figs. 4.26 and 4.28). These regions with strong uplifts of air masses receive high amounts of precipitation (Figs. 7.6 and 7.15). In the trade wind regions, only few clouds, mostly stratocumulus, exist (Figs. 7.9 and 4.26). The global circulation leads to strong sinking air and dry belts (low relative humidity, low precipitation) around 30° coinciding with the main deserts and semi-permanent highs (Fig. 7.6). In the mid-latitude troposphere, humidity is highly variable depending on synoptic situations and clouds are associated with extra-tropical cyclones (Figs. 4.26 and 4.28). In sub-polar and polar areas, tropospheric humidity is low, on average, and polar stratus occurs frequently. Due to their low amount of annual precipitation (Fig. 7.15), the polar regions are also called cold deserts.

In climate change research, it is important to look for changes in cloud formation, composition, albedo, distribution, lifetime, type, and vertical extent. As any life on Earth depends on the availability of water, climate change research strongly focuses on changes in precipitation distribution, amount, seasonality, phase, duration, type, and extremes events. Furthermore, the impacts on runoff and interactions with the energy and trace gas cycles are of great interest (see discussions in Chaps. 5 and 4).

The International Satellite Cloud Climatology Project (ISCCP) had the goal to measure and gather weather satellite radiance measurements to determine the global cloud distribution, cloud properties and their diurnal, seasonal and interannual variations. This dataset is widely used for studying the role of clouds for energy, water and trace-gas cycles as well as global, regional and local climate. The A-train (Chap. 4) enlarged the possibility of determining cloud properties and has given additional insights into the climate impacts of clouds.

When using precipitation data for model evaluation it is important to look for which observational episode they are valid as precipitation data from different data sources may have different observational episodes. Some networks record 0000 UTC to the next day 0000 UTC, other may use local time or even worse the time of their time zone. Thus, daylight saving time may set records off.

Seasonality

For food production, it is important to know the annual cycle of precipitation. In the monsoon-affected areas, distinct dry and wet seasons exist. In mid-latitudes, precipitation occurs more equally throughout the year. In the tropics, there can be two wetter and drier seasons. Due to the shift of the polar front towards higher latitudes, these regions have more precipitation in summer than winter.

Snow

Temporal averaging reveals that the average duration of snow cover depends on latitude and elevation. On average, a gradient of decrease in snowfall exists from the coastal to the inner continental regions, and more snowfall occurs on the windward than leeward side of mountains.

The distribution of snow plays an important role from energetic, hydrological and environmental points of view. For many regions the winter snowpack provides a water storage that is used in summer. Snow can strongly influence the seasonal distribution of runoff by two different mechanisms. The insulating effect of snow holds the heat in the soil (Chap. 4). When soil does not freeze, it keeps its capacity to infiltrate water. Snow stores water on land. Thus, runoff can become very strong during snowmelt. Chemical species that accumulated within the snow are set free rapidly into the ecosystems, leading to a strong short-time acidification of waters.

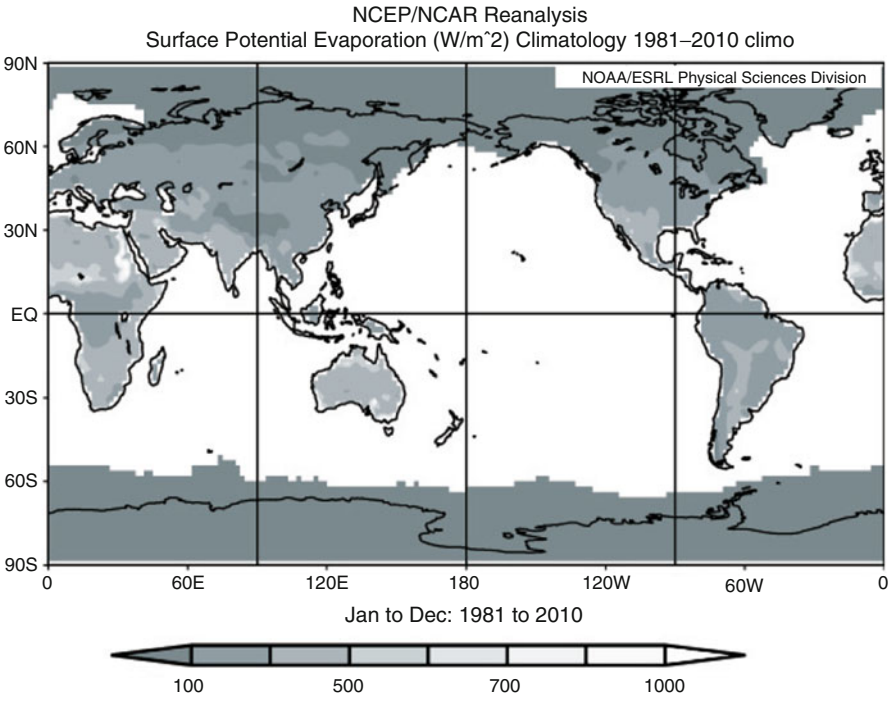

Fig. 7.16 Global distribution of the annual-mean evaporation rate for the 1981–2010 normal (Data used in this plot are NCEP reanalysis)

7.1.1.7 Evapotranspiration

Evapotranspiration, E, encompasses all phase transition processes (from liquid or solid) to water vapor (e.g. evaporation of water from oceans, lakes, rivers, puddles, transpiration of water by plants, interception losses by evaporation or sublimation, sublimation of snow). We can determine global distributions of evapotranspiration in two different ways. Temporal averaging of the components of the surface energy balance, $Q - G_{soil} - H - L_v E = 0$ (Chap. 4) and rearranging can provide the average evapotranspiration. Herein, $Q = R_s \downarrow - R_s \uparrow + R_l \downarrow - R_l \uparrow$, G_{soil}, H, and $L_v E$ are the net radiation, the soil heat flux, the turbulent fluxes of sensible and latent heat, respectively. In the other method, the temporal average differences of precipitation, P, minus runoff, R, give the average evapotranspiration, $E = P - R$ (Fig. 7.16).

Evapotranspiration supplies about 71,000 km^3 water to the atmosphere. Evapotranspiration could be highest at the equator energy wise. However, here relative humidity is already large and hence the uptake is limited. A slight minimum exists over the oceans at the equator due to the calm wind, and the very high relative humidity. Evapotranspiration has minima at the poles as these are cold deserts.

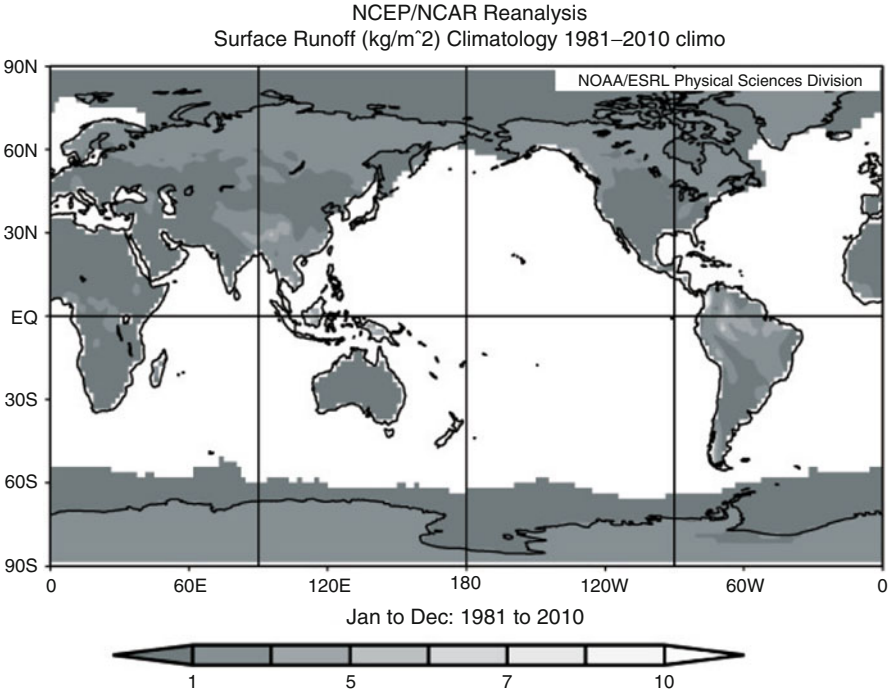

Fig. 7.17 Global distribution of annual runoff rate for the normal 1981–2010 (Plot used NCEP reanalysis data)

Areas of high humidity contribute to the total evapotranspiration on land only by about 3 %. The annual evaporation of water from the oceans amounts to about 11,000 mm and produces about 425,000 km^3 water vapor per year.

7.1.1.8 Runoff

On global average, rivers bring about one third of the precipitation from land to the ocean. On long-term average, runoff is the difference between precipitation and evapotranspiration. Typically, runoff increases as precipitation grows (Figs. 7.15 and 7.17).

Seasonally the distribution of runoff may strongly deviate from that of precipitation because evapotranspiration and storage (e.g. as snow or soil moisture) vary strongly in the annual cycle. In regions that are subject to seasonal snow or in areas with glaciers (*Latin* glacia = ice), runoff has its maximum during snowmelt (e.g. in summer in the Arctic, subarctic, or alpine regions, in spring in low latitudes). In summer, there is a maximum in runoff in the monsoonal regions (e.g. India, Southeast Asia). In fall and winter, maximum runoff correlates with maximum precipitation. Worldwide, Australia has least runoff, Antarctica has least precipitation, and South America has highest runoff and precipitation (Fig. 7.17).

Table 7.3 Characteristic time scales of the climate system

Part of the climate system	Characteristic time scale
Ice sheets	10^4–10^6 year
Ground water	10–10^4 year
Deep ocean	100–1,000 year
Sea-ice	1–10 year
Stratosphere	100 day
Upper oceanic layer	100 day
Upper soil layer	10 day
Lake ice	1–100 day
Troposphere	1–10 day

7.1.2 Scales of Climate Observations and Modeling

Three time scales describe the temporal aspect of climate phenomena. The typical time scale of a phenomenon is the **phenomena time** and the total time of available observations is named **record time** (Table 7.3). The time between two observations is the **sampling time**. The complexity and completeness required for modeling the phenomena increases with phenomena time (Table 7.5). Note that the purpose of most observations was weather forecasting, rather than describing climate or detecting climate change or variability. Thus, these observations may suffer from changes in instrumentation, exposure, measurement techniques, station location, observation times, modifications in the stations immediate vicinity, etc. and required special care in their interpretation.

Numerical studies using the model grid cell values as an artificial "truth" and pulling data at various places that are considered as sites of a network showed that randomly distributed networks with lower number of sites can provide better spatial averages than biased networks with higher number of sites. Biased measurement networks with respect to certain characteristics may save the purpose to make statements about the climatology for these characteristics. However, when applied outside their original purpose strategies have to be developed. For instance, an over 80 year long data series of soil temperature in agriculturally used soils exists for Russia. However, this dataset only considered fertile soils as sites of interest for measurements. Consequently, temporal changes are hard to extend to other soil types as soil moisture and heat fluxes as well as freezing and thawing differ among various soils.

Unfortunately, long time series are hard to find. The time and the costs involved with collecting data over long time and the public and economic pressure for climate adaptations do not permit installation of a climate measurement network. Thus, long timeseries of various kinds that exist have to be used and methods have to be developed to make them meaningful for climate related purposes. Doing so is one of the great challenges regarding climate research. In addition, often long-term data exist on paper and have to be digitized, which is time consuming and pricy as well.

Proxy data from climate-sensitive phenomena, such as tree-rings, ice cores, and pollen in marine sediments are applied for the more distant past. Indicator

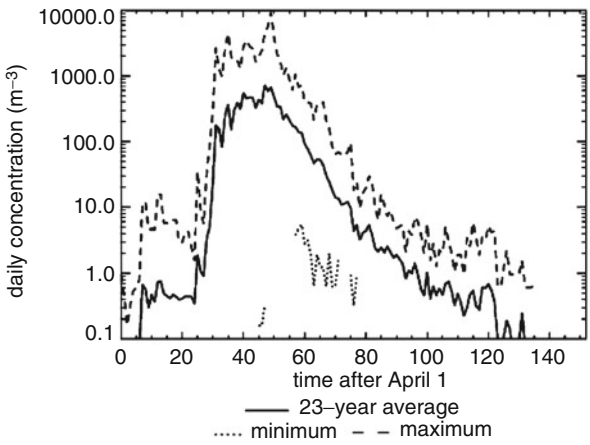

Fig. 7.18 Average birch pollen concentrations as well as maximum and minimum concentrations found on a day in these 23-years of measurements on the University of Alaska Fairbanks campus

or key animals and/or plants, isotopes, chemicals as well as the knowledge on soil- and sediment-formation processes serve to derive paleo-climatic zones. In reconstructing climate, one has to rely on the sum of all available proxies rather than just one proxy.[13] Pollen in peat or wet mud can document the response of vegetation to climate changes (see discussion of Young Dryas).

In the interpretation of proxy data like tree rings, ice cores, pollen in sediments and ice-cores, understanding the current year-to-year variability is an urgent need. Figure 7.18, exemplarily shows a 23-year climatology of birch pollen concentrations. The minimum and maximum birch pollen concentrations on a given day in these 23-years are displayed as well to illustrate the variability. By using half-life time (Chap. 5) of radioactive particles[14] we can date climate keys.

The spatial scale of the phenomena is the **phenomena length**, the total extension of the area covered by observation is named **record length**, and the spatial resolution of the observational sites is called **sampling length**.

7.1.3 Spatial and Temporal Scales of Climate: Scales of Climate Impacts and the Energy Cascade

A fundamental characteristic of climate fluids is their structure. Phenomena at all scales are composed of smaller scale climatic structures. Table 7.4 exemplary lists climate factors relevant on the mesoscale.

[13]Assigning a warm climate to the Arctic because the most similar current mammal to the mammoth is the elephant that lives in a warm climate is an example for that necessity.

[14]The interested reader is referred to textbooks on physics of the C^{14}-method, radio-isotope-method and other methods.

Table 7.4 Some examples of climate factors on the mesoscale scale

Factor	Influencing quantity	Climate impact	Climate phenomenon
Topography	Elevation above sea surface, extension and structure of mountainous regions	Climate elements depend on elevation, special cases with respect to clouds, wind, precipitation	Mountain climate, mountain and valley breezes, föhn
Relief	Elevation above sea surface, slope, azimuth of slope, curvature of slope	Change in temperature, radiation, pressure and wind	Cold air drainage, channelizing effects, mountain wind, topo-climate
Surface	Soil and vegetation type, wetness, albedo, emissivity, roughness, sealing, soil physical and plant physiological parameters	Energy budget, water budget, convection, temperature, internal boundary layers	Land-sea-breeze, coastal or island climate, regional climate
Emission of trace gases	Concentration of primary and secondary trace species, aerosols	Smog, haze, bioclimatic effects, trace species budgets	Climate of valleys, urban climate
Settlement, population density	Heat and water vapor supply to the atmosphere by heating, cooling, exhausts, etc., soil sealing	Water, energy, and trace species budgets, convection, cloudiness, precipitation	Heat island, urban climate

A fluid transports state variables (e.g. heat, moisture, trace gases) thereby transferring energy (Chaps. 2, 4, and 6). Turbulence and convection are effective mechanisms to cascade energy and/or re-distribute the state variables. Turbulence only occurs in fluids and denotes the non-linear interaction between a transported state variables and the vector of momentum flux. These fluxes can act in horizontal and vertical direction on all scales (Chap. 2). Static instability, for instance, leads to rising of warm and sinking of cold air. This process becomes visible in form of clouds when saturation is reached.

In Chap. 6, we introduced scale analysis and assumed typical values that we know from climatology. We learned that atmospheric processes have a spatial extension and structure. As we saw already in the satellite images (Chap. 4), atmospheric processes or systems can occur in various forms like waves, eddies, or convective cells (Chaps. 3, 4, and 6). A low-pressure system, for instance, has a certain horizontal extent and consists of many clouds that again have a certain extent too. The clouds again consist of a huge number of cloud droplets of certain diameters. The low-pressure system, its clouds, and their cloud droplets exist for a typical amount of time that is individual for the system, the clouds, and the droplets. The order of magnitude of the extension is the **spatial scale**.

The **temporal scales** refer to the typical **lifetime** (Table 1.1; see also Chaps. 3, 5, and 6) of an atmospheric system, its subsystems, or processes. Note that the lifetime

does not mean that the same constituents make up the system all the time. As pointed out above everything is in flow and in a reservoir at the same time.

Example. Determine the average time that a parcel that enters a cumulus cloud at the base requires leaving it at the top.

Solution. A cumulus with a typically vertical extent of 1,500 m has a lifetime of 10–30 min and an average vertical updraft velocity of $3\,\mathrm{m\,s^{-1}}$. Thus, an average parcel leaves the cloud after $T_{parcel} = \frac{1{,}500\,\mathrm{m}}{3\,\mathrm{m\,s^{-1}}} = 500\,\mathrm{s}$, i.e. in a shorter time than the lifetime of the cumulus.

In large exchanges, turbulence and convection are organized as cyclones or large waves (macro turbulence, scale 200–2,000 km). On the meso-γ-scale, the exchange occurs as cumulus clouds, wherein again smaller scale turbulence (entrainment, detrainment) is embedded (Chap. 3). Single turbulence elements are distributed stochastically (micro turbulence, scale of eddies cm to m). In this sense, cyclones are not only weather relevant, but also climate relevant due to their transport of energy, heat, and matter.

Like for short-term weather (Chap. 6) the spatial and temporal scales of the climate phenomena go hand in hand due to the inter-dependence of energy on space and time.[15] Consequently, the impact of subsystems on the climate system depends on the time scale. A subsystem is climatically relevant when it contains temporally and spatially variable fluid constituents. On a short-term, for instance, a glacier is solid, while on the long-term it may retreat/progress with implications for surface albedo and local climate.

When we want to model or observe an atmospheric process, we have to ensure a high enough spatial and temporal resolution. As schematically shown in Fig. 7.19 more than three measurements are needed to at least capture the fact of a diurnal temperature cycle. As discussed in a box before, higher resolution provides exacter results when the weather is highly variable. Figure 7.20 schematically elucidates that we need three or more sites to get the different temperature and pressure over land and ocean during a sea-breeze. To be able to interpret the processes a full suite of observations is mandatory. To observe the entire circulation aircraft measurements, wind profilers, etc. are needed. Modeling is a suitable tool as well and/or may be used to support interpretation of observations.

As many mesoscale systems require certain large scale synoptic conditions to be able to form, changes in the large scale circulations are of interest as they impact the frequency of mesoscale systems. These temporal aspects lead to hierarchies in

[15] In other scientific disciplines, for instance, hydrology, the scales are also associated with processes of typical length and time to characterize the typical processes and phenomena. Thus, when working in climate modeling or interdisciplinary research, it is very important to ensure that all participating researchers are on the same plate when scale related words are used.

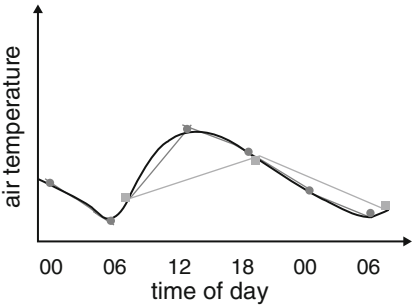

Fig. 7.19 Schematic view on necessity of suitable temporal resolution to capture meteorological climate relevant processes like, for instance, the diurnal temperature range

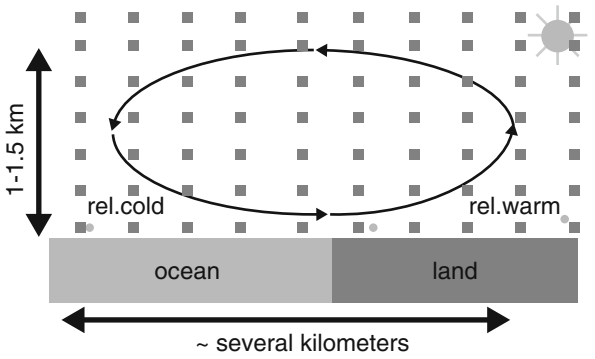

Fig. 7.20 Schematic view on the necessity of suitable spatial resolution to capture locally climate relevant processes like, for instance, the sea breeze

Table 7.5 Hierarchy of numerical models

Purpose	Range of applicability	Treatment of climate subsystems
Weather prediction	$\leq$ 10 day	All components except of the atmosphere are stationary
Short-term climate	$\leq$ 50 year	Ice shields, and continents are stationary, atmosphere, ocean, and sea ice are variable
Long-term climate	$\leq$ 1,000 year	Only the continents are stationary
Geological changes	$\gg$ 1,000 year	Continental drift

modeling of the climate system (Table 7.5). The longer the period of interest, the more complex the model becomes, as more processes that are negligible on the short time scale have to be included on the long time scale. Thus, in Numerical Weather Prediction (NWP), sea-surface temperatures and the extend of glaciers, and/or sea-ice are hold constant over the entire simulation time (5–10 day), while in climate or Earth system modeling, the SSTs and the extend of the glaciers and/or sea-ice are simulated in response to the climate. This means they are treated in a two-way coupled mode. On the long-term, the changes in SSTs, sea-ice and glacier conditions namely response to climate changes, and the climate also changes in response to the cryosphere (area, location, albedo, etc.). Ideally also changes in biomes in response to climate should be considered.

Changes in biome extend may not only affect the water cycle by modified evapotranspiration, but also the energy cycle via altered partitioning of incoming radiation between sensible and latent heat fluxes, and radiative properties, and the trace-gas cycle via altered biogenic emissions, decay of vegetation, fuel for wildfires, pollen, and dust uptake.

In modeling applications, the length of two adjacent grid-cells gives the finest resolution. Thus, a model with a horizontal grid increment of 10 km cannot resolve anything smaller that 20 km. Therefore, the convection (Chap. 3), for instance, has to be parameterized. Any parameterization bases on empirical parameters and/or concepts. Thus, parameterizations induce uncertainty as the sample on which the empirical formulations bases may be biased to certain regions of field campaigns and/or time of the year. Furthermore, any field campaign only covers a comparatively small time compared to a climate period.

We also can determine with which spatial and temporal resolution we regard a system by defining a grid of observational points and times. To resolve the system appropriately, the resolution of this grid must be appreciably finer than that of the entire system. In the case of a low-pressure system with diameter d, for instance, the spatial resolution of the grid should be $d/10$.

We distinguish the

- The magnitude in space and time of an atmospheric process or system, and
- The scale of the consideration.

Compared to the Earth, the systems move slowly and have an internal flow. They change all the time and have a typical **life cycle** that includes typical physical processes in the evolution and dissipation of the system (Fig. 6.51). Imagine, for example, a hurricane running towards the coast of Florida or a thunderstorm approaching from west. All systems have a characteristic velocity, the **scale velocity**, U (see also section on scale analysis in Chap. 6). It can be related to the horizontal extension, L, and the time, T, of the systems by $U = L/T$ (Fig. 6.1). Here T means the time required by the system to pass over the observer. In the case that T is the lifetime, for instance of a convective cloud, then U is the velocity of dissipation defined as the part of L that dissipates within a time.

The spectral temporal and spatial scales of the atmosphere range from 10^{-3} to 10^{7} m for the dissipation eddy of atmospheric turbulence to the magnitude of the Earth's perimeter.[16] The temporal scale reaches from 10^{-3} to 10^{17} s, i.e. from the dissipation of an eddy to the age of the Earth. In meteorology and atmospheric science modeling applications, the often-applied coarse classification of scales is orientated at the spatial scales:

- Macro-scale with $L > 2{,}000$ km
- Meso-scale with $2{,}000\,\text{km} \geq L > 2\,\text{km}$
- Micro-scale with $L \leq 2$ km.

[16] Note that the molecular mean free path amounts to 10^{-7} m.

Table 7.6 Scales as typically used in meteorology. Note that the mesoscale α is often also referred to as synoptic scale, large scale or cyclonic scale. The microscale γ is also known as misoscale

Scale	Range
Planetary scale	Globe
Macro-scale α	$\geq$ 10,000 km
Macro-scale β	2,000–10,000 km
Meso-scale α	200–2,000 km
Meso-scale β	20–200 km
Meso-scale γ	2–20 km
Micro-scale α	200 m–2 km
Micro-scale β	20–200 m
Micro-scale γ	$\leq$ 20 m

These scales[17] are again divided as shown in Table 7.6.

Since climate is the average of weather over a given period, we use the terms micro, meso, macro and global for addressing the scales as introduced in Chap. 6. **Micro-climate** is the climate conditions near the surface over distances of a few meters. Great perturbations to the microclimate can rapidly affect plant life (e.g. a drop in temperature leading to frost). **Meso-climate** is the climate conditions over a few square kilometers (e.g. a town, a valley). **Marco climate** or **regional climate** are the climate conditions for an area of about 1,000 km or greater in one horizontal extension (e.g. Alaska). **Global climate** refers to the climates on Earth.

The concept of the mean lifetime (Table 1.1, Chapters 2, 3, and 5) serves to define the temporal scales of a climate element. For example, a cumulus cloud, the ABL, or ENSO have typical time scales of 10–30 min, 1 day, and 1–2 year, respectively.

The different spatial and temporal aspects of meteorological systems and processes are the origin of the terms of weather, synoptic and climate as discussed above. The spatial and temporal scales are coupled (Fig. 6.1) via the kinetic energy $E_{kin} = \frac{1}{2}\,\mathrm{m\,v^2}$. Speed is distance travelled per time increment. For the atmosphere, they follow a double-logarithmic line along $T \approx L^{\frac{2}{3}}$ where the envelops $T \approx L^{\frac{1}{2}}$ and $T \approx L^2$ correspond to acoustic waves and inner friction of gases, respectively, where T and L again stand for time and length (Fig. 6.1). Knowledge of typical scales is required to choose the adequate grid spacing, domain size, and time steps in atmospheric modeling or for decisions on neglecting processes.

Example. The average amount of water in the Earth's atmosphere is $\approx$12,900 km^3, and the global average precipitation rate is about 577,000 km^3 year^{-1}. Determine the temporal scale of water (in days) in the global atmosphere.

(continued)

[17] Orlanski (1975) came up with the idea to separate the atmospheric processes according to their typical spatial extension and duration.

(continued)

Solution.

$$T = \frac{12{,}900\,\mathrm{km}^3}{577{,}000\,\mathrm{km}^3\,\mathrm{year}^{-1}} = 0.022\,\mathrm{year}\frac{365\,\mathrm{day}}{1\,\mathrm{year}} \approx 8\,\mathrm{day}\ .$$

Many aspects of the Earth system vary on time scales ranging from hours to millennia. The signal-to-noise problem makes detection of climate changes difficult. Climate can change in response to **external** and **internal variations**.

External climate forcing are climate responses to altered external forces and characteristics of the climate system. Such external climate forces can be changes in solar constant due to the variable solar activity, changes in the astronomic constellation Earth-Sun, land-ocean distribution, ocean bottom and land topography due to continental drift, intense meteorite showers or volcanic eruptions (Fig. 7.38; Chap. 4). Here we discuss exemplarily external forcing due to the astronomic variations in the Earth-Sun constellation and volcanic eruptions.

Planet Earth completes one full cycle around its own axis about every 26,000 years. Concurrently, the elliptical orbit rotates slowly. The superposition of these precessions yields a 21,000 year period between the orbit and the astronomic seasons. Furthermore, the obliquity, i.e. the angle between the normal of the orbit plane and the rotational axis of the Earth, oscillates between 22.1° and 24.5° every 41,000 years.[18] These long-term alterations of the Earth orbit parameters are known as the Milankovitch[19] cycles (Figs. 7.21 and 7.22). Climate reconstruction from paleo data suggests that the orbital variations and climate variations correlate well. During the last million years, the 100,000 year cycle provides the strongest climate signal (Quaternary ice-age cycle). However, the eccentricity provides clean variations at periods of 95,000 and 125,000 years.

Many scientists warn about these unresolved frequencies, and state that the data record is too short to resolve them. Many scientists also argue that the available dataset is too small to statistically significantly correlate the variability in climate to eccentricity. The proposed mechanism is as follows. The changes in eccentricity would modify the radiation flux density incident on the Earth, and hence the spatial distribution of the incoming energy. Some paelo-climate models reproduce climate variability in response to these astronomic variations.

An eruption has to inject sulfide compounds in aerosol into the stratosphere to lead to long-term cooling. Stratospheric aerosol reflects solar radiation, and warms the stratosphere by absorbing terrestrial radiation. The ash and droplets obscure the Sun and increase the albedo of the Earth. Less solar radiation reaches the

[18] Currently, the angle amounts 23.44° with decreasing trend.

[19] Milutin Milanković, Serbian mathematician, astronomer, climatologist, and geophysicist, 1879–1958.

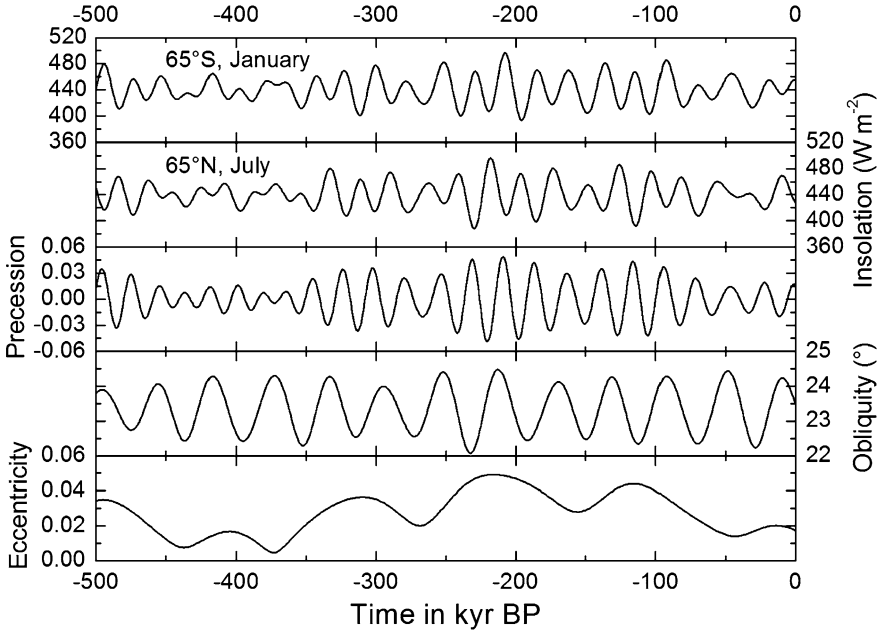

Fig. 7.21 Long-term variations of eccentricity, obliquity, climatic precession (characterized by the climatic precession parameter, $e \sin \varpi$), the mid-month insolation for the latitudes 65°N, July, and 65°S, January, from 500 kyr BP to present (1950 A.D.). A solar constant of $S = 1{,}360$ W m^{-2} was considered (All data stem from Berger and Loutre (1991). From: Kramm and Dlugi (2011))

surface and leads to a cooling of the troposphere. The stratospheric warming and tropospheric cooling modify the circulation in the troposphere and stratosphere. The term **volcanic winter** refers to the reduced temperatures caused by volcanic ash and sulfuric acid droplets in response to a large, explosive eruption. The physical mechanism of the interaction ash-radiation are discussed in Sect. 7.5. For the interaction sulfur dioxide, aerosol formation, and clouds see Chaps. 3 and 5.

The impact of large volcanic eruptions on climate is long documented. Some historians have related the Great Famine of 1315–1317 in Europe to a 5 year volcanic activity in New Zealand. The eruption of Icelandic volcano Laki led to temperature drops in Europe by about 1 K in the following year according to historic documents. Temperature records indicated 2–3 K lower temperatures for about 2–3 years after the 1991 Mount Pinatubo eruption.

Ice cores drilled in the Greenland ice sheet showed that climate changes may often have been quite rapid and large, unrelated with any known external forcing. Abrupt as well as slow climate changes are due to internal variations that occur as components of the climate system influence and interact with the atmosphere. Large-scale changes in vegetation patterns due to deforestation, afforestation, or desertification, for instance, can affect the atmosphere and climate. Other examples are El Niño, La Niña, Southern Oscillation (Sect. 7.2.1). There also exists interaction

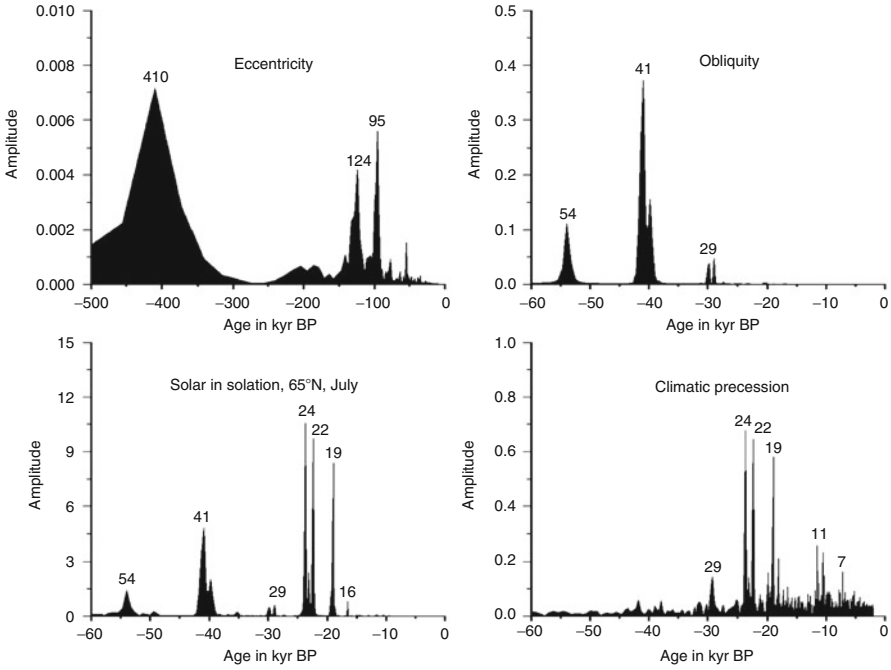

Fig. 7.22 Dominant periods for eccentricity, obliquity, climatic precession, and mid-July insolation at a latitude of 65°N determined by Welch Fast Fourier Transformation using the orbital data of Berger and Loutre (1991). (From: Kramm and Dlugi (2011))

between hurricane formation and strength of the Atlantic conveyer belt. Recall that SST greater than 26.5 °C are one of the six pre-requisites for the possibility of tropical storm formation (Chap. 6).

An example for an abrupt climate change is the Younger Dryas. The Younger Dryas was an about 1,300 year period of cold and dry climate conditions visible in sediment pollen data. It started around 12,800 BP. Many geologists explain the Younger Dryas being caused by the retreat of the American ice sheet. When the ice sheet started draining into the St. Lawrence Stream instead of the Gulf of Mexico, the cold water let to the break-down of the Gulfstream. Thus, Scandinavia was cut off her warm water advection leading to a temporal sudden cooling. The Younger Dryas demonstrates unambiguously that climate can change relatively abruptly. Seemingly, climate sometimes responds in a manner similar to earthquakes where stress builds up over years, leading to sudden abrupt changes, rather than changing in small increments. Therefore it is of great importance to understand climate and its interactions within the Earth system.

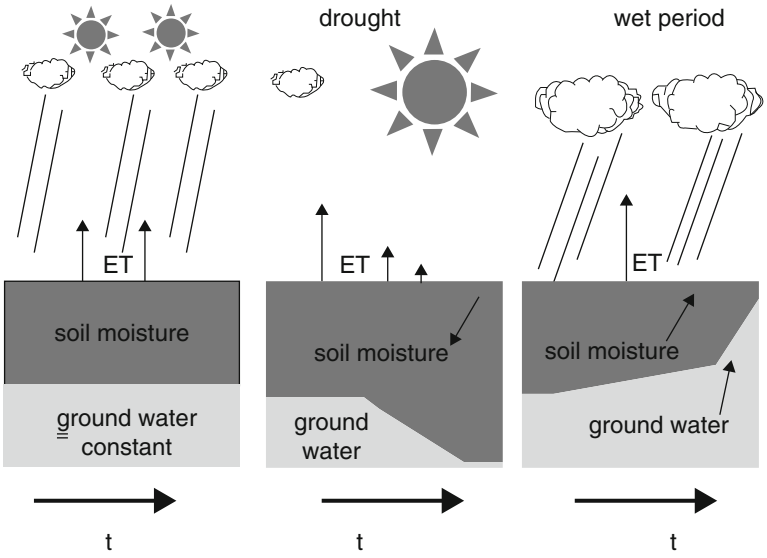

Fig. 7.23 Schematic view of feedback among evapotranspiration, cloud and precipitation formation, and ground water recharge (From: Mölders (2005))

Example. Derive the change of the mean planetary temperature in equilibrium with time assuming that only this temperature depends on time. Comment on an albedo that is independent of temperature.

Solution.

$$\frac{dT_p}{dt} \approx (1 - \alpha(T_p))\frac{S}{4} - \sigma T_p^4 \, .$$

For an albedo that is independent of temperature (constant), an increase in temperature leads to an increase in the second term on the right hand side, for which $\frac{dT_p}{dt}$ must have an acceleration toward the state of equilibrium. The opposite is true for a reduced radiative cooling, but with the right hand side being positive.

7.1.3.1 Feedback Mechanisms

The time-scale relevance is due to **feedback** processes. Feedback refers to the situation in which a part of the outcome of a process serves as input to the next process and subsequently alters the outcome (Fig. 7.23).

In the climate system, feedback can be positive or negative. A **positive feedback** reinforces the original input, i.e. amplifies the outcome of the process. Consequently, small changes can generate increasing and propagating changes that may lead to instability. The **water vapor feedback**, **snow-albedo feedback** or **snow-temperature feedback** are examples of positive feedback loops. A **negative feedback** counteracts the original input and reduces the outcome of the process. Small changes in the input force the system to reduce the changes, and stabilize the system. Various feedback mechanisms are interlinked. Thus, it is often difficult to assess in which direction a change actually will go. Furthermore, it is possible that just marginal differences in involved processes may be decisive in which direction the system develops.

When a climate perturbation decreases (near-)surface temperatures, the area covered by ice and/or snow increases. The latter enlarges the area with high surface albedo. More incoming shortwave radiation is reflected to space leading to cooling of the surface and atmosphere. The comparably cooler conditions can promote more solid precipitation, which reinforces the process. This feedback process is often referred to as snow-temperature, temperature-albedo, or snow-albedo feedback. On the contrary, as snow melts, albedo changes from 0.8 of fresh snow to 0.1 or so of a dark, wet soil (Chap. 4). Emissivity increases from 0.82 or so for (old) snow to 0.95 for wet, dark soil. Since then surface albedo decreases, more of incident solar radiation is absorbed leading to further warming of the near-surface and less snow.

Oceans can release or take up CO_2 as climate warms or cools, respectively (Chap. 5). Being a greenhouse gas, an increase (decrease) of atmospheric CO_2 may lead to further warming (cooling) again altering the equilibrium of aqueous and atmospheric CO_2-concentrations (positive feedback). Note that CO_2 is extremely important for life as vegetation needs it for growth (i.e. food production). Molecular oxygen is a by-product released during photolysis by the plants, but essential for all aerobe beings. The carbon cycle was already discussed in Chap. 5.

A positive feedback establishes for both droughts and wet periods. Under a persistent synoptic situation without advection of clouds and precipitation, soils dry and evapotranspiration becomes low. When the area of reduced evapotranspiration is large enough, the reduced and/or lacking evapotranspiration may lead to reduced or no cloud and precipitation formation leading to further persistence of the drought until moist, precipitation loaded air is advected from outside the region. In regions of flat water tables, the water table plays an important role. It first may feed soil moisture and evapo(transpi)ration until it decouples from soil moisture (Fig. 7.23).

Under synoptic situations with strong precipitation, wet periods can contribute to their persistence. As soon as the sky becomes less cloudy, evaporation from the wet soils and transpiration increase and are not limited by soil moisture deficits. This water supply to the atmosphere yields new cloud and precipitation formation (Fig. 7.23). Flat ground-water tables may contribute to the persistence of wet episodes when they rise. A high water table guarantees enough water available for evapotranspiration for a longer time than for a deep water table.

For most areas of the world, the frequency distribution of soil moisture states shows a bimodal distribution with a wet and dry regime. The peaks are flatter and

less distinct for humid than dry, i.e. arid climates. Arid climates have a large peak in the dry soil regime, and a low peak in the wet soil regime. The driving mechanism that causes the change from one regime to another is still subject to research. Understanding of the soil climate behavior may be also valuable for improved irrigation practices.

Clouds can have both positive and negative feedback effects on local climate (Fig. 7.23). They absorb long-wave radiation thereby warming the surface (positive feedback). However, they also reflect solar radiation thereby cooling the surface (negative feedback). Which of the two feedback processes dominates depends on cloud type, structure, composition, cloud-top height, etc.

The burning of biomass releases CO_2 into the atmosphere and the now more exposed soil provides more aerosols to the atmosphere. The impact of aerosols depends on type and position in the atmosphere (Sect. 7.5). Burning of biomass also changes surface reflectivity and the exchange of the heat and moisture between the soil and atmosphere. All these processes have different impacts on air temperature and at different locations.

The simple model called **Daisyworld** can demonstrate the concept of biotic feedbacks. In Daisyworld, black and white daisies exist that are darker and lighter, respectively, than the bare ground. As in nature, the daisies grow optimally at moderate temperatures. The black daisies absorb more radiation than the white daisies. When the black daisy population increases and covers a greater area, more solar energy is absorbed, and temperature increases. On the contrary, an increase of the white daisy population increases the radiation reflected to space and lowers temperature. The central question is under what conditions, if any, the daisy-population and temperature achieve equilibrium.

7.1.3.2 Teleconnection

In meteorology and climatology, the term **teleconnections** refers to climate anomalies that are related to each other even though they are thousands of kilometers away from each other. The Younger Dryas discussed above is an example of teleconnection. In this case the initial change was the meltwater of the receding American ice sheet draining into the Atlantic, and the atmosphere over Scandinavia was the area being affected. The Gulfstream was the medium through which the connection established.

The most famous examples of teleconnection are related to El Niño-Southern Oscillation (see Section 7.2.1) where droughts occur in many other regions of the world (e.g. southeastern Africa, India, and northeastern South America). As the wave of warm water reaches the western coast of South America during El Niño years, the water travels north and south along the American continent as far as Alaska and the Strait of Magellan thereby affecting the regional climate of the adjacent regions by influencing the high and low pressure pattern around the globe. The increased SST in the eastern Pacific during El Niño years also favor the development of tropical storms. A strong El Niño can lead to a weaker monsoon.

The connection between Southern Oscillation and NAO is negligible, but there is a considerable negative influence on the NPO six month in advance and concurrently (Chaps. 2 and 6).

Recent research has shown that the local climate change caused by land-cover changes may influence the weather and, hence, on the long-term, climate far in their downwind by secondary processes. It has to be understood that any anthropogenically caused land-cover change will persist for a long time. Typically humankind changes land-cover for economic reasons like dams as water reservoirs and for power production, or deforestation for wood harvest and/or agricultural use, just to name a few. Land-cover changes, even when they are of local scale, not only affect the local climate, but also teleconnect to regions far remote from where they occurred. Here the teleconnection can even become the direct forcing as in the above example of the Young Dryas. Large-scale tropical deforestation, for instance, would affect the Hadley and Walker cell circulations. However, as the deforestation persists, the modifications of the Hadley and Walker cells would also mean persistent atmospheric changes.

Climate model simulations suggest that the changes caused by large-scale tropical deforestation would be of similar magnitude like those of the SST anomalies occurring during ENSO events. Climate simulations suggest that deforestation of the South American rainforest would teleconnect to mid-latitudes, and reduce precipitation on global average. The reduced moisture supply over the cleared forest of Amazonia means less moisture advection from the Tropics and lower temperatures in the upper westerlies. The reduced convection weakens the Hadley cell circulation. Consequently, the distribution of upper-level tropical divergence that drives the mid-latitude zonal jet would change (Chap. 6). The atmospheric response over Amazonia would produce low-frequency tropical waves. These waves propagate to the Extra-tropics building the teleconnection. In mid-latitudes, the changes found in response to the assumed tropical deforestation are still statistically significant, even though they are weaker than over Amazonia, and Amazonia's immediate downwind.

Recent climate research on land-cover changes also suggests that the location and degree of land-cover changes as well as the kind of land-cover change determine the atmospheric response. Simulations with artificial landscapes in checker board like pattern brought great insight into the impact of land-cover on the atmosphere. These studies suggested that a critical size must be exceeded for producing coherent responses. When a large region has just one land-cover convection and precipitation occur randomly distributed. Model studies assuming the landscape prior to settlement in the contiguous US and the current land-cover suggest locally notable to significant changes in temperature, precipitation, and wind. The more heterogeneous landscape after the settlement seems also to impact cloud and storm formation.

Let us take the currently ongoing deforestation of Amazonia as another example for impacts of land-cover changes. In Amazonia, deforestation occurs in fishbone type pattern. Radiosonde soundings indicate that over deforested sites the ABL has less Convective Available Potential Energy (CAPE; Chap. 2) and is less unstable than over forest sites. Satellite images indicate coherent cloud pattern of shallow

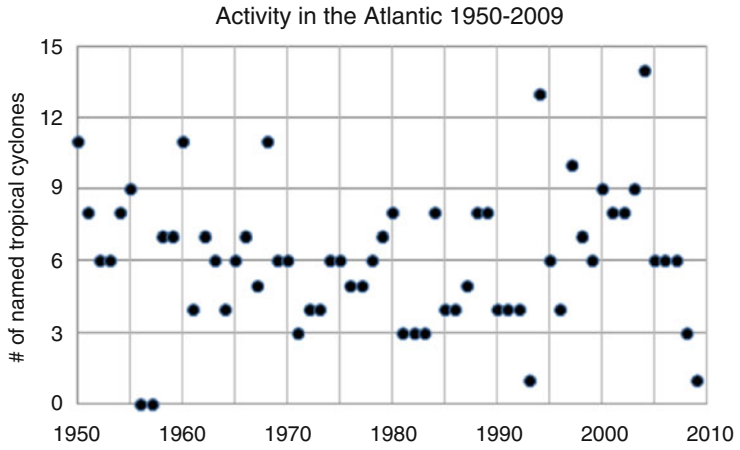

Fig. 7.24 Number of named storms in the Atlantic Ocean in various years

(deep) convection over deforested (forest) areas. These differences in cloud extend can be explained by the differences in sensible and latent heat fluxes at the surface and altered buoyancy (Chaps. 2–4). Regional climate models identified these coherent patterns as non-classical mesoscale circulations. The horizontal extension of deforested areas affects the strength of the non-classical circulation. Modeling studies performed for fire-scars in the boreal forest and land-cover changes in Europe lead to the same conclusion. However, in contrast to ENSO, which is a natural climate event occurring every 3–5 years, any human initiated land-cover changes would persist for a long time meaning that in the next independent climate normal[20] the anomalies become the new normal, i.e. climate. Consequently, recent model development focuses on better describing the biosphere-atmosphere interaction, impacts of anthropogenic land-cover changes as well as land-cover changes in response to climate change.

7.1.4 Classification and Frequency of Events

To put a weather event into the greater climatological picture, weather events are often classified according to their severity, and frequency of occurrence. Typically, a scale is defined where certain criteria, usually associated with the hazard the event causes. All events are categorized and assessed according to this scale. It permits to compare the frequency and climatology of past and actual events (Fig. 7.24), and in climate modeling, of projected events. These scales may differ by national weather services.

[20]The climate period 1951–1980 and 1981–2010 are independent as they do not have temporal overlap.

Table 7.7 Pressure, wind speed, wave height and relative potential of damage of the tropical storms on the Saffir-Simpson-scale

Class	Pressure (hPa)	Maximum wind speed ($m\,s^{-1}$)	Wave height (m)	Relative potential of damage	Typical damages	Example
1	980	33–42	1.0–1.7	1	Minimal	Jerry (1989)
2	965–979	43–49	1.8–2.6	10	Moderate	Bob (1991)
3	945–964	50–58	2.7–3.8	50	Extensive	Gloria (1985)
4	920–944	59–69	3.9–5.6	100	Extreme	Andrew (1992)
5	<920	>69	≥5.6	250	Catastrophic	Mitch (1998)

Table 7.8 Wind speeds of the five categories of Australian tropical cyclones

Category	Maximum wind speed ($m\,s^{-1}$)
1	17–25
2	26–34.5
3	35–45
4	46–62.5
5	>63

The intensity of tropical cyclones, for instance, is categorized in five classes according to the **Saffir-Simpson**-scale (Table 7.7) with category 1 being the less and category 5 being the most intensive tropical storms. The relative potential of damage is normalized to the mean damage of a category 1 tropical storm. The potential of damage increases nonlinearly with the speed of wind. Tropical storms will get names, if they reach an intensity of category 1 on the Saffir-Simpson-scale.

Australian tropical cyclones (in the region between 90°E and 160°E) are classified on another scale (Table 7.8). Here 10-min averages are applied, while the Saffir-Simpson-scale bases on one minute averaged wind speeds. Obviously, in the Australian classification, class 1 still corresponds to a tropical cyclone and class 5 corresponds to category 4 on the Saffir-Simpson-scale (Tables 7.7 and 7.8). In the following, the Saffir-Simpson-scale will be referred to if not indicated otherwise.

Tornadoes are categorized on the Fujita[21] scale[22] (F-Scale). In February 2007, the United States replaced the F-scale with the Enhanced Fujita Scale (EF-scale). Both scales describe the intensity of tornadoes primarily in view of the damage it causes on human construction and vegetation. The F-scale and EF-scale reach from F0 to F5 with F5 being the strongest. The EF-scale is standardized with respect to the damage the tornado causes, for which it is more precise and robust way than the F-scale. The EF-scale classies F0–F5 damage as calibrated by engineers and meteorologists. In the calibration, 28 different types of damage indicators were used to account for the typical strengths and weaknesses of different types of construction.

[21] Tetsuya Theodore "Ted" Fujita, Japanese-American severe storm researcher 1920–1998.

[22] The Fujita scale is often also called Fujita–Pearson scale.

Thus, like for tropical cyclones, when comparing tornadoes in different regions of the Earth or in the US over time, care has also to be taken of differences in scales when discussing climate change/variability.

7.2 General Circulation

We discussed various aspects of the general circulation already when we introduced the climate analysis methods. We found the semi-permanent high pressure systems, the Ferrel-, Hadley-, and polar cells, the Walker circulation, the jet streams, the easterlies and westerlies, the trade wind regions, just to mention a few examples. Therefore, the general circulation is not repeated here. The general circulation is driven by the different insolation of the Earth. For thermodynamic and dynamical reasons the Earth system strives to even these differences out leading to the general circulation pattern elucidated above.

Many interesting climate aspects only become visible as anomalies from the mean conditions. Examples are El Niño-Southern Oscillation, and La Niña, which are large scale climate variabilities. Some aspects of climate only occur on an annual or seasonal scale (e.g. monsoon, precipitation season in the Tropics). Some aspects of climate only occur under certain synoptic scale conditions, but strongly determine the climate of a region. Classical mesoscale circulation systems like land-sea breeze systems, mountain-valley circulation may determine the regional and local climate under weak synoptic scale forcing. Furthermore, non-classical mesoscale circulations like urban heat island and irrigation/vegetation breezes exist that may affect local climate over a limited small area.

Common to these circulation systems is that they are driven by differences in temperatures that cause pressure differences, buoyancy, and finally vorticity, i.e. circulations (Chaps. 2, 3, and 6). Here we discuss some general circulation features not already addressed above as well as classical and non-classical mesoscale circulations. As this chapter is the climate and climatology part of *Lectures in Meteorology*, we focus on the meteorology that makes up climate on the long-term rather than the climate itself and/or its aspects.

While current Global Circulation Models (GCM), climate, and Earth system models are able to capture large scale features (e.g. Ferrel-, Hadley-, and polar cells, the Walker circulation, jet streams, easterlies, westerlies, trade winds, ENSO, monsoons, gravity waves), a resolution around 1° or so is still too coarse to capture many mesoscale features that are part of regional climate. To assess regional climate often regional climate models are applied that are forced with the data of a global model. It is important to realize that mesoscale processes may also impact the large scale. Sea-breezes, for instance, may initiate gravity waves. Such feedbacks from the mesoscale to the large scale can only be considered by two-way coupling which would mean a great burden on computational time, and prohibit multiple ensembles and long simulations.

7.2.1 El Niño-Southern Oscillation

As the example of the tropical cyclone discussed in Chap. 6 showed, high SSTs can serve as a heat source for the atmosphere. They affect the atmosphere through sensible and latent heat fluxes. Such impacts of SST on the atmosphere occur at the synoptic and seasonal scale.

An important SST related natural climate circulation pattern that occurs at a longer than seasonal, but still short-term climate scale is El Niño-Southern Oscillation .

As pointed out above, typically the trade winds have an eastern component meaning they blow westwards across the tropical Pacific (Fig. 7.9). These winds push warm surface water into the west Pacific leading to an about 0.5 m higher sea-surface in the Indonesian waters than at the same latitude in the coastal waters of Ecuador. This situation is the normal, non-El Niño conditions (Fig. 7.25). Under these conditions, SST are about 8 K higher in the west Pacific than they are off the coast of South America where cold deep ocean water wells up (Fig. 7.27). Over the warm water in the west Pacific, air rises, and leads to clouds and precipitation. On the contrary, over the cool ocean water in the east Pacific, the air is relatively dry.

El Niño[23] refers to a short term (a few months to 1 year) climate variation. It is an oscillation of the ocean-atmosphere system in the tropical Pacific that occurs on average every three to five years. In an El Niño year, the trade winds are weaker in the central and western Pacific than normal. Consequently, a depression (elevation) of the thermocline occurs in the eastern (west) Pacific. This ocean-temperature distribution reduces the upwelling of deep ocean water, and yields increased SST in the equatorial Pacific off the South American coast (Fig. 7.25).

Due to the weakened easterly trade winds, the area of warm ocean surface water now travels eastward. As discussed before, the warm ocean water provides a heat source leading to cloud and precipitation formation. The eastward displacement of the high SST region leads to high pressure over the eastern Pacific and droughts in Indonesia and Australia, and finally to low pressure and precipitation in Peru.

Southern Oscillation refers to this atmospheric component of El Niño. We can see this oscillation of the atmosphere in surface air pressure measurements made over the tropical eastern and western Pacific Ocean. The Southern Oscillation Index measures the strength of this atmospheric response. The SOI is calculated from the fluctuations of the difference in the surface pressure between Tahiti and Darwin, Australia. During El Niño events, pressure is below normal over Tahiti and above normal in Darwin, i.e. negative SOI (Fig. 7.26).

The aforementioned change in the location of high and low pressure strongly alters the global atmospheric circulation. Consequently, the weather changes in regions far remote from the tropical Pacific. These changes in weather elsewhere

[23] El Niño is the Spanish word for Christ child. Peruvian fishers introduced this term in the late 1800s to refer to the frequently occurring warming of the ocean around Christmas that caused poor fishing yields.

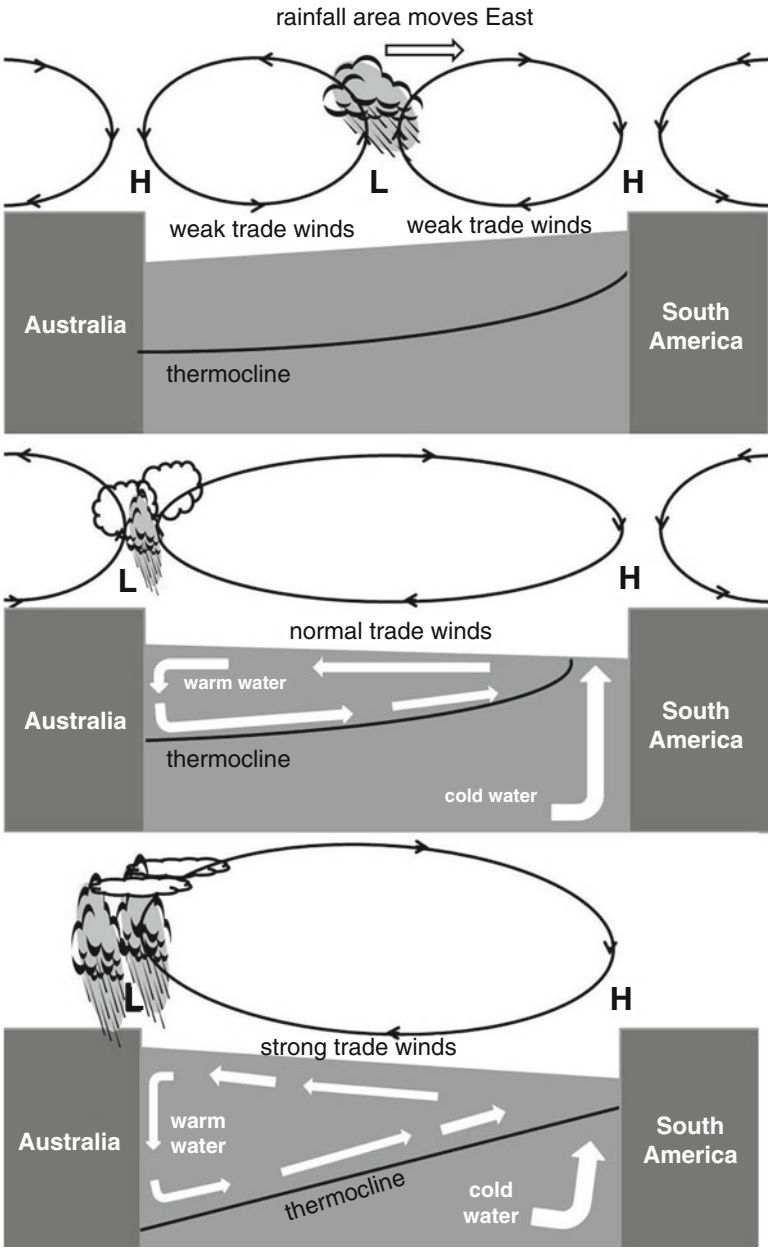

Fig. 7.25 Schematic view of atmospheric and oceanic conditions under El Niño (*top*), normal (*middle*), and La Niña regimes

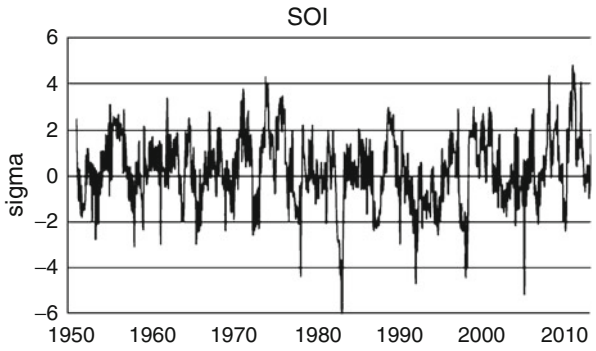

Fig. 7.26 Time series of SOI

in response to due to ENSO are another example for teleconnection. Typically El Niño impacts are most distinct in winter. During El Niño, April to October see warm and very wet weather along the coasts of northern Peru and Ecuador. Further changes are increased rainfall in Peru and the southern US, and droughts in the West Pacific and Australia. Here the droughts are often accompanied by severe wildfires. Since tropical cyclones form in the trade wind region at the equator ward edges of the subtropical highs (Chap. 6), El Niño also affects the tropical storm tracks. East of the dateline, more tropical cyclones form as SST are well above their normal, and the vertical wind shear is reduced. In the tropical Atlantic, however, El Niño decreases the activity of tropical cyclones because it increases the vertical wind shear across that region. During El Niño, winters are colder, and dryer (milder, and wetter) in northern (southern) Europe than normal. In Alaska, winter temperatures are usually above normal, and often mild winter thaw occurs during El Niño winters due to abnormal southerly flow.[24]

El Niño can be detected in SST distribution composites derived from radiometer measurements made on board of satellites and from ocean temperature measurements made from moored buoys. Season climate prediction strives to forecast El Niño events as they have strong ecological, economic and social impacts. The cold upwelling water, for instance, is rich in nutrients and supports marine ecosystems, and, hence, indirectly major fisheries and the related economy. Warmer winters in Alaska, for instance, mean less fuel and wood burning for heating, and less heating costs and air pollution than in normal winters (Fig. 7.27).

Often El Niño is followed by La Niña.[25] While El Niño refers to the warm anomaly of ocean surface water off the coast of Peru, La Niña refers to the cold anomaly (Fig. 7.25), i.e. in a La Niña year, the upper ocean layer is unusually

[24] Alaskans call this warm weather with rain during deep winter the Pineapple Express.

[25] The translation of La Niña is the little girl. Some authors refer to La Niña events as El Viejo, anti-El Niño, cold event or cold episode. In the latter two cases, these authors typically refer to El Niño as a warm event.

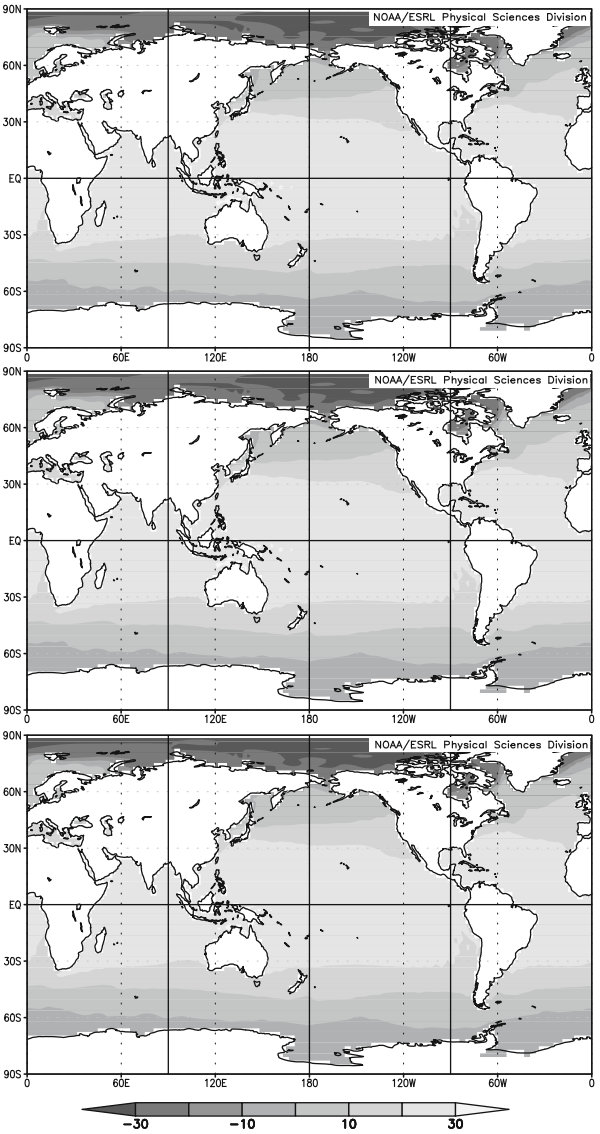

Fig. 7.27 December mean SST anomalies during negative (*top*) and positive (*bottom*) SOI. From the climate normal of SST for 1981–2010 (*middle*)

cold in the equatorial Pacific as compared to normal. La Niña leads to nearly opposite effects than El Niño. La Niña means droughts in the coastal regions of Peru and Chile. Like El Niño events, La Niña events affect the global circulation. Typical changes associated with La Niña are warmer winters than normal in the Southeast US, and cooler than normal winters in the Northwest US. Precipitation is above-normal across northern California, the southern and eastern regions of the Pacific Northwest, northern Rockies, and northern Midwest, while it is below normal in the southwestern and southeastern states. In the Atlantic (Pacific), the frequency of tropical cyclones is above (below) normal. Due to the displacement of the subtropical ridge in the western Pacific, tropical cyclones form more westward. Thus, China sees more landfalls in La Niña years than other years.

The transitional phases at the onset or departure of El Niño (La Niña) often already notably affect global weather. Such episodes are called Trans-Niño and measured by the Trans-Niño index (TNI). In the US, Trans-Niño affects precipitation in the Northwest and means intense tornado activity in Tornado Alley.

7.2.2 Monsoon

The word **monsoon** (*Arabic* mausim = season) originally denoted to the seasonal reversals of the wind direction along the shores of the Indian Ocean, especially in the Arabian Sea. Here, the winds blow from the southwest during one-half of the year (dry winter) and in the opposite direction the other half of the year (wet summer) (Fig. 7.9).

Today, the term monsoon is used in a more general sense for seasonal reversing wind systems driven by land-ocean-atmosphere interaction through the exchange of energy and moisture. The combined effects create the characteristic of monsoon: reversing high winds and precipitation.

The monsoon phenomenon of change in precipitation and wind in the annual cycle occurs in Asia, Australia and Africa and the adjacent seas and oceans. About half of the Tropics can be defined as a monsoon climate (Sect. 7.4). The major monsoon systems are the West African and Asia-Australian monsoons.

All monsoon climates have the same basic physical features:

- Large scale differential heating causes to prevailing winds blowing over long distances.
- Since these circulations occur over horizontally large areas the winds are affected by the Coriolis force that increases with distance from the Equator. The Coriolis force deflects these winds to the right (left) in the northern (southern) hemisphere.
- Ocean and atmosphere interact by storing and releasing energy during phase transition processes.
- Monsoons occur seasonally.

The seasonal winds of the monsoon result from the different absorption of heat by water and land. The high heat capacity of water ($\approx$4,200 J kg^{-1}K^{-1}), and

conduction of water, as well as convection in the upper 50 m of the ocean keeps the SST relatively constant. On the contrary, soils can only conduct absorbed heat to deeper layers or the atmosphere. The relatively lower heat capacity of soils ($\approx$2,500 J kg^{-1}K^{-1} or so) leads to higher variability in soil temperatures as well as to a fast heating up of the soil in the warm months of the year than does the ocean water. Thus, the near-surface air over land heats stronger than the near-surface air over the ocean. Consequently, a large scale horizontal pressure gradient builds up between the land and the ocean with lower pressure over the land than ocean. This pressure pattern yields the wind to blow from the ocean towards the continent. While moving over the ocean air takes up moisture. This moist air rises over the land, and eventually reaches saturation. Clouds form and precipitation occurs. At higher tropospheric levels the air flows back to the ocean and completes the circulation system.

In the cold months, the ocean cools much slower than does the land. Consequently, near-surface air is warmer over the ocean than land. A pressure gradient develops that leads winds to flow from the land to the ocean with and vice versa higher in the troposphere.

The **African monsoon** results from the great seasonal temperature and humidity differences over the equatorial Atlantic and the Sahara desert. Superimposed is the seasonal shift in the ITCZ that results from the annual cycle of insolation (Fig. 4.10). Thus, the African monsoon migrates northward in February and reaches Africa around the boreal summer solstice. Then it moves southward until October. The northward migration of the ITCZ interrupts the northeasterly trade winds (Fig. 7.9) resulting in southwest winds and precipitation in the Sahel and Sudan.

The **Asian monsoon** is often examined as subsystems according to the region they affect. The South Asian monsoon affects the Indian subcontinent and its adjacent land. It occurs from June through September. The monsoon in combination with the orographic effect of the Himalaya causes the **Indian Ocean Monsoon** (IOM) to be the most intense on Earth. Cherapunji (India), for instance, received 26.46 m of rain in the time from August 1860 to July 1861.

The East Asian Monsoon affects Indo-China, South China, Philippines, Korea, Taiwan, and south Japan. Typically, after a period of pre-monsoon rains, the summer monsoon sets on in May and ends in August. It is characterized by a series of dry and wet phases as the rain belt moves northward and then back southward.

The **Australian monsoon** or Indo-Australian monsoon has its rain season from September to February. In boreal winter, it is the main energy source that drives the Hadley cell in this region. This monsoon regime is related to the development of the Siberian High and the change in the insolation when the Sun moves from the Northern to the Southern Hemisphere. Due to the topography of Borneo, the northeasterly trade winds turn to north-westerly to westerly winds towards Australia. Consequently, a cyclonic vortex forms over Borneo. The combined effect of this cyclonic vortex and cold surges from Siberia govern the climate of this region from September to February. Thus, the Australian monsoon stops abruptly rather than gradually. More than 75 % of the annual precipitation of northern Australia occur during these months (Sect. 7.4).

Fig. 7.28 Föhn gap over the Tanana Valley as seen from the University of Alaska, Fairbanks campus. In the background the Alaska Range is seen that caused the Chinook. Chinooks can lead to temperatures above the freezing point even in January in Fairbanks (Photo by Mölders (2004))

7.2.3 Orographically Forced Climate Conditions

The impact of mountain barriers on wind was discussed already in Chaps. 2 and 6. A mountain barrier forces air to flow either around or upward. When air flows around a mountain range cyclones or anticyclones may form in the leeside (e.g. Genoa cyclone, Borneo cyclone). When the flow goes over the mountain top, gravity waves or inertia gravity waves (Chap. 6), and lenticularis clouds may form (Fig. 6.48).

During ascend air expands and cools, which can lead to cloud- and precipitation formation (Chaps. 2, 3). Due to orographic lifting, mountainous regions get more precipitation than lower elevations, and precipitation is less in the leeside of mountain ranges than on the upwind side (Fig. 7.15). When the air lost a huge amount of its moisture load on the upwind side of the mountain range during its ascend, the air descends dry adiabatically on the downwind side. Thus, at the same elevation, air is warmer and drier in the downwind of the mountain range than in its upwind. This type of wind actually responds more to pulling than to gravity (Chap. 6). As the air is actually stable, the air that was vertically displaced due to the mountain barrier tries to go back into its stable position on the leeward side of the mountain range (Chap. 2). These winds are called the **Chinook** in the Rocky Mountains, **Zonda** in the Andes, and **Föhn** in the Northern Alps (Fig. 7.28).

7.3 Regional Climate

In many places on Earth, the distance to large water surfaces, the elevation, topography of the landscape, the land-cover and/or land-use of the landscape strongly affect the regional climate. In various chapters, we already addressed some regional climate features as examples or applications, for instance, orographic lifting, radiation fog, radiative inversions or subsidence inversions. Realize that mesoscale phenomena are going hand in hand with favorable large scale forcing. This means in regional climate dynamics no general overall theory exists. Nevertheless, everything follows the physical laws discussed in previous chapters. Here we briefly present the physics behind the regional climate aspects that are overlain to the general circulation features discussed in the previous sections. For brevity, we restrict the discussion to regional climate aspects not covered in previous chapters.

7.3.1 Classical Mesoscale Circulations

The common climatological features of classical mesoscale circulations are that

- The synoptic scale forcing is weak, i.e. weak synoptic scale pressure gradient and wind,
- They are caused by differential heating,
- Baroclinity forms and initiates vorticity,
- Buoyancy causes the acceleration

Whether or not mesoscale circulations develop depends on insolation, heat absorption, surface characteristics, and synoptic scale flow. However, when the geographic location are suitable mesoscale circulations are part of the regional climate, and therefore discussed here.

Example. Show that buoyancy is an acceleration by applying the material learned in Chaps. 2, and 6, and show by applying scale analysis to the governing equations for a mesoscale-circulation that buoyancy force and the Coriolis force are fundamental for mesoscale circulations.

Solution. The sum of forces is mass times acceleration. With $\rho = m/V$ we obtain for a unit volume of 1 m^3

$$\rho_{ap}\frac{\partial^2 \delta}{\partial t^2} = -\frac{\partial p_{ap}}{\partial z} - \rho_{ap} g \approx \rho_{env} g - \rho_{ap} g = b$$

(continued)

(continued)

with $\frac{\partial^2 \delta}{\partial t^2}, \delta, p, \rho, g, z$, and b being the acceleration, an incremental distance, pressure, density, acceleration of gravity, height, and buoyancy, respectively, and the subscripts ap and env indicating an air parcel and the environment, respectively. With Eq. (2.3)

$$b = g \frac{T_{ap} - T_{env}}{T_{env}}.$$

The first law of thermodynamics and hydrostatic conditions yield

$$\frac{\partial T}{\partial z} = \frac{g}{c_p} = -9.8\,\mathrm{K\,km^{-1}}$$

where c_p is the specific heat capacity at constant pressure. With the definition of potential temperature $\theta = T(\frac{1{,}000}{p})^{\frac{R_d}{c_p}} = \frac{T}{\pi}$ where $\pi = (\frac{1{,}000}{p})^{-\frac{R_d}{c_p}}$ and R_d is the individual gas constant for dry air,

$$b = g \frac{\theta_{ap} - \theta_{env}}{\theta_{env}}.$$

7.3.1.1 Mountain- and Plain Winds and Low Level Jets

Orographically caused wind circulations are quite different from orographically forced ascend and mountain waves (see Chaps. 2 and 6). They require weak large-scale wind and pressure pattern that allow a "decoupling" of the local weather from the synoptic scale flow. Let us first look at an individual mountain range in a plain. During the day, the mountain slope heats up faster than the air in the plain at same height above sea level. Thus, air close to the slope becomes less dense, and hence more buoyant than the air at the same height over the plain. The air over the slope rises and air from the plain flows up the slope. A reverse circulation may develop in the layer above and close the circulation. At night, the mountain slope cools much faster resulting in denser air in its immediate vicinity than the air at same height over the plain. The cold air drains down the slope. Again a reverse flow may develop in the layers above. These circulations are called mountain-plain winds.

Both at day and night, the slope flow is driven by buoyancy. At night, the mountain-wind drains relatively fast in a relatively shallow layer as compared the reverse flow that flows at slower speed in a deeper layer. These winds are katabatic, i.e. cold. On the contrary, descend after orographically forced lifting is adiabatic leading to warming.

Katabatic winds seldom exceed $5\,m\,s^{-1}$, but they can achieve destructive speeds if narrow valleys channel them. In Greenland and Antarctica, katabatic winds can become as strong as $50\,m\,s^{-1}$. At such speeds, they can drive the sea ice away from the coast. Since the adiabatic heating is only slight, the descending air is still very cold when it reaches lower elevations. Thus, the cold air drainage rapidly decreases the ambient air temperature as it speeds downhill.

Katabatic winds also form when a shallow mass of cold, dense air drains from the high elevations of mountains, plateaus, or hills downslope to the valleys or planes below under the influence of gravity. Such cold air drainage often occurs in winter over extensive snow-covered plateaus or mountains. Thus, for areas with suitable terrain, katabatic winds are part of their regional/local climate. In most cases, the synoptic situation triggers the formation of katabatic winds. On the micro-β to γ scale, radiative cooling at night can cause katabatic winds (e.g. cold air drainage from a waste dump). Cyclonic and anticyclonic circulation patterns downwind of the mountain can also force air to flow down the mountain ranges.

Mountains are often involved in the formation of **low level jets** that can reach up to $30\,m\,s^{-1}$. In North America, for instance, the Rocky Mountains cool more than the Great Plains at night. The pressure surfaces drop over the mountains enhancing the southerly geostrophic wind (Chap. 2 and 6). Consequently, in a few hundred-meter above the surface of the Great Plains low level jets form and blow from south on summer nights. The stratification of the near-surface atmosphere is stable because the surface cools (Chaps. 2 and 4). Consequently, vertical mixing is reduced. At a height of a few hundred meters, the winds are no longer forced to slow down to mix with the slower near-surface winds.

In several regions, strong interaction between mesoscale and synoptic scale occurs that makes huge impact on the climate of these regions. Over these regions, large-scale wind pattern are strongly influenced by the underlain topography, and land-water distribution leading to the major regional wind phenomena. The **Bora**, for instance, is a wind system that occurs during winter when a high pressure system containing polar air exists over the snow-covered Balkans. Then air can flow katabatically through the valleys of the Dinaric Alps toward the warm Adriatic Sea. These northeasterly Bora winds can achieve storm strength. Interaction of high pressure over the Balkan with low pressure in the Ionian Sea can also generate Bora. Since Bora is a combination of a fall wind and a land breeze (Sect. 7.3.1.3), it is weakest in the afternoon and strongest near dawn.

Another famous wind system related to synoptic scale and mesoscale interaction is the **Mistral**. A Mistral is a northwesterly katabatic wind that descends downslope the snow-covered Alps into the Rhone Valley, and along the adjacent Mediterranean Coast eventually extending as far south as the Strait of Sicily. Mistral events often occur as a fast moving cold front or trough approaches the Alps parallel to their extension, in winter or spring. The cold front becomes quasi-stationary over the northern Alps. The large scale flow splits and the cold air flows around the western and eastern edge of the Alps. The topographic situation leads to the Mistral in the west and Bora in the east. In the Gulf of Genoa a lee cyclone may form.

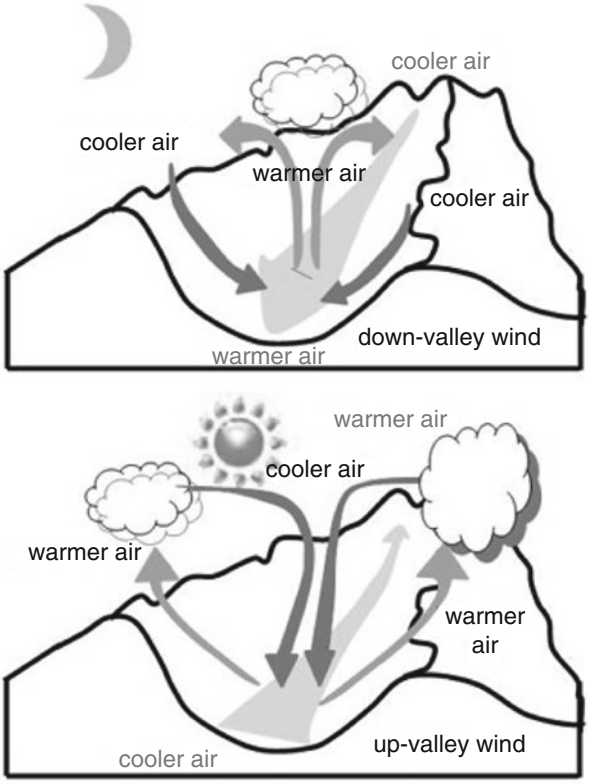

Fig. 7.29 Schematic view of mountain and valley circulations

7.3.1.2 Slope, Mountain- and Valley Winds

Now assume a situation of a valley (Fig. 7.29). The mountain slopes heat stronger during the day than the air at the same height in the valley. Again the differential heating leads to buoyancy that drives the flow close to the mountain slopes. Again warm air moves up the slope at day, down at night. When the meteorological conditions are suitable, cumuliform convection may form over the mountain tops at day. When at day an inversion exists, the air moves along the inversion towards the valley, sinks over the valley, and a circulation may form.

Down-slope winds affect a relative small layer and are relatively strong as compared to the reverse circulation that occurs over a thicker layer and flows comparatively slower. The cold air drainage may build a surface inversion in the valley. Under suitable meteorological conditions, fog layers starting at the mountain slope may form that eventually may cover large parts or even the entire valley, while clear skies exist above (Fig. 3.23). Note that down-slope flows may also leave the slope.

In addition to the wind circulation along the slopes, a circulation orientated along the valley floor may form. In such case, air flows down the valley during night and up the valley during day (Fig. 7.29). Valley winds are closed circulations. These circulations are caused by the temperature gradient that is greater in the air column within the valley than the air column in the plain at same elevation. Thus, horizontal pressure gradients form with lower (higher) pressure at same height above sea-level in the valley at day (night) than in the plain. The valley circulation aims at removing the horizontal pressure gradient that built up hydrostatically between the valley and the plain.

The valley wind circulation and the slope wind circulation exist at the same time. Thus, the wind vectors are superimposed leading to a slight modification of the direction of the slope winds. Snow-cover and/or moist soil inhibit valley-wind circulations.

7.3.1.3 Land and Sea Breezes

Under suitable synoptic conditions (edge of a high pressure system), **land-sea-breeze systems** develop at the coast or shores of large lakes because of differential heating. Recall that the heat capacity of land is much lower than that of water. As the Sun rises and warms the surface, the air becomes warmer over land than water. As cool air is heavier and denser than warm air (Chap. 2), a buoyancy difference develops resulting in a surface wind from water to land (Chap. 6). Light off-shore wind would maximize the convergence and produce a sharp sea-breeze front. The front moves inland and the air warms from below. Thus, the front weakens, while at the same time, the Coriolis force deflects the wind direction. The differential heating causes the baroclinity that results in vorticity (Chap. 6). At 1–2 km height, the air moves from land to water replacing the air. The Coriolis force affects the wind field and turns the vorticity. This circulation is known as sea-breeze and is part of the regional climate in many coastal regions and along the shores of large lakes.

At night, the land and its overlying air cool quicker than the water and its overlying air. Consequently, an opposite directed wind circulation develops leading to a surface wind blowing from land to water. In general, the greater the inland air and water temperatures differ, the higher is the chance for a land-breeze developing and the stronger it will be. The Coriolis force affects the wind field and turns the vorticity, and wind to an alongshore direction. Thus, we have to examine the vertical, horizontal and velocity scale. The height and velocity scale follow the atmospheric boundary layer height.

It is important to understand that land-breezes are not the opposite of sea-breezes. Typically daytime heating is about the same as nighttime cooling. The land-breeze circulation is weaker than the sea-breeze circulation because air is more stable at nighttime than at daytime. In general, heating near the Earth's surface weakens stratification and encourages vertical motion. Instability strengthens a circulation, while any low-level inversion weakens it. At night, the cooling produces only a shallow change in the temperature gradient. Thus, the land breeze flow is shallower

than the sea-breeze flow. Shallow flow and stable stratification yield friction. Thus, the land-breeze is much more retarded than the sea-breeze. The less stable stratified air during day means that the sea-breeze can affect a deep layer for which friction is not as notable as in the land-breeze.

In the Tropics, the diurnal wind reversals can penetrate about 100 km and more inland due to the lack or low Coriolis force. In mid- and high-latitudes, land- and sea-breezes have typical extentions of 10–20 km. Here, the major controlling factors presumably are the Coriolis effect and horizontal the buoyancy gradient (Chaps. 2 and 6). In the Arctic, when the ocean along the coast is open, sea-breezes may develop in summer. According to mesoscale model simulations, the sea-breeze weakens or breaks down during the long white summer nights, but does not reverse. Lakes with 20 km or more in horizontal extend may produce lake breezes of similar strength than sea-breezes.

In mid-latitudes, land- and sea-breezes are most common in spring and summer and may be part of the coastal climate regime. At the density interface of sea-breezes, the shear instabilities may form Kelvin-Helmholtz waves (Fig. 6.50). Sea-breezes may also initiate inertia-gravity waves (Chap. 6). Sea-breezes suppress convection behind front, but precipitation along the front may occur. The leading edge of sea or land-breezes is an air mass boundary with a strong wind shift.

Example. In the previous box, we proved that buoyancy is an acceleration. Now apply the material learned in Chaps. 2 and 6, and show by applying scale analysis to the governing equations for a sea-breeze that the buoyancy force and Coriolis force are the fundamental forces that govern this mesoscale system. Neglect friction and molecular diffusion for simplicity.

Solution.

$$\frac{\partial u}{\partial t} + u\frac{\partial u}{\partial x} + v\frac{\partial u}{\partial y} + w\frac{\partial u}{\partial z} - fv + \frac{1}{\rho}\frac{\partial p}{\partial x} = 0$$

$$\frac{\partial v}{\partial t} + u\frac{\partial v}{\partial x} + v\frac{\partial v}{\partial y} + w\frac{\partial v}{\partial z} + fu + \frac{1}{\rho}\frac{\partial p}{\partial y} = 0$$

$$\frac{\partial w}{\partial t} + u\frac{\partial w}{\partial x} + v\frac{\partial w}{\partial y} + w\frac{\partial w}{\partial z} = 0\,.$$

Sea-breezes only build under synoptic conditions with low horizontal pressure gradient $\approx 10^4$ Pa in the area of the coast-line. Thus, $U < 10\,\mathrm{m\,s^{-1}}$. The Coriolis parameter f is about $\approx 10^4\,\mathrm{s^{-1}}$. The horizontal and vertical extend of the system are $\approx 10^4$ m, $L_z \approx 10^3$ m, while those of the synoptic scale are $L \approx 10^6$, and 10^5 m, respectively. The time scale is about half a day $\approx 10^5$ s. In

(continued)

(continued)

the following, U, V, and W are the horizontal and vertical wind components, respectively. We can estimate for $f\,v = 2\,\Omega\,v\,\sin\varphi$ and $-f\,u = 2\,\Omega\,u\sin\varphi$

$$f\,V \approx f\,U \approx 10^{-4}\,\mathrm{s}^{-1}\,10\,\mathrm{m\,s}^{-1} \approx 10^{-3}\,\mathrm{m\,s}^{-2}$$

$$\frac{\partial u}{\partial t} \approx \frac{U}{T} < \frac{10^{1}\,\mathrm{m\,s}^{-1}}{10^{5}\,\mathrm{s}} \approx 10^{-4}\,\mathrm{m\,s}^{-2}$$

$$u\frac{\partial u}{\partial x} + v\frac{\partial u}{\partial y} \approx \frac{U^2}{L} < \frac{10^{2}\,\mathrm{m}^2\,\mathrm{s}^{-2}}{10^{6}\,\mathrm{m}} \approx 10^{-4}\,\mathrm{m\,s}^{-2}$$

$$w\frac{\partial u}{\partial z} < 10^{-4}\,\mathrm{m\,s}^{-2}\,.$$

This result leaves $w\frac{\partial u}{\partial z} \approx \frac{UW}{L}$ as balancing term for the Coriolis force term. The vertical velocity is related to buoyancy. Analogously, we can estimate the y-component that are of same order of magnitude.

$$w\frac{\partial w}{\partial z} \approx \frac{W^2}{L_z} < \frac{10^{2}\,\mathrm{m}^2\,\mathrm{s}^{-2}}{10^{3}\,\mathrm{m}} \approx 10^{-3}\,\mathrm{m\,s}^{-2}$$

With $w = \frac{\partial z}{\partial t}$ we can write $w\frac{\partial w}{\partial z} = \frac{\partial z}{\partial t}\frac{\partial w}{\partial z} = \frac{\partial w}{\partial t} := b = g\frac{\theta_{ao}-\theta_{env}}{\theta_{env}}$.
Thus, scale analysis and combination with the results of the previous box show that the remaining terms are the buoyancy force and the Coriolis force.

7.3.2 Non-classical Mesoscale Circulations

7.3.2.1 Urban Wind Circulation and Heat Island Effect

Urban areas can also modify the wind field. High buildings along paved streets create the urban canyon and trap incoming heat energy. Only a small amount of long-wave heat is re-radiated back out. The sealed surface and urban canyons result in high turbulent fluxes of sensible heat. Due to the high thermal diffusivity of the soil and low heat-capacity of settlements, urban surfaces heat more intensely than cultivated land during the day. Exhausts from cars, industries, fuel combustion, and air conditioners also heat the air, and an urban heat island forms. The as compared to rural land increased buoyancy leads to upward motion (Chap. 2), and potentially more clouds downwind of the city (Chap. 3). Air blowing over a city experiences strong turbulence due to the high roughness, for which vertical mixing increases

(Chap. 6). For continuity reasons, the lifted air is replaced by moist air moving in from adjacent rural land. Consequently, due to the strong lifting of moist air, the air reaches higher levels over the city as compared to the rural area and may achieve saturation. Combustion, plants, and cooling towers may add moisture to the urban atmosphere. Clouds and precipitation may form in the lee of the city. Release of precursor gases may yield to gas-to-particle conversion, and hence increased number of cloud condensation nuclei (CCN) and ice nuclei (IN). Furthermore, particles may be also emitted directly. The increased number of CCNs may lead to smaller droplets and may suppress precipitation (Chap. 3). Depending on the size distribution and amount of urban aerosols, precipitation may decrease or increase in the downwind region.

Although the sealed ground of an urban area provides less water vapor to the atmosphere, exhausts of industry and cooling towers may be significant sources of moisture, which also can be critical for precipitation in the downwind region. The topography around or within an urban area has a large influence on the wind field and distribution of air pollutants as due to differential heating anabatic and katabatic winds may be established.

7.3.2.2 Irrigation and Vegetation Breezes

In irrigated areas, the soil is moister and cooler than the non-irrigated, dry surrounding land. Consequently, when these irrigated areas are large enough, a thermally driven circulation pattern analogously to a land-sea-breeze develops. Such circulation pattern are called vegetation-breeze and can strongly affect local trace-gas concentration.

Example. Determine the speed of air flowing over adjacent dry and warm steppe and irrigated wet and cool areas. Assume a density of air of $1.17\,\mathrm{kg\,m^{-3}}$ and temperatures of 30 and 29 °C over the steppe and the irrigated areas in 30°N. These values were measured 20 km apart from each other.

Solution. The pressure over the steppe and irrigated area are $1.29 \cdot 287 \cdot 303.15\,\mathrm{Pa} = 101{,}795\,\mathrm{Pa}$, and $1.16 \cdot 287 \cdot 302.15\,\mathrm{Pa} = 101{,}459\,\mathrm{Pa}$, $v = \frac{1}{fg}\frac{\partial p}{\partial x}$ $= \frac{1\mathrm{s}^3}{3.645 \cdot 10^{-4} 9.81\mathrm{m}} \frac{(101{,}795 - 101{,}459)\,\mathrm{Pa}}{20{,}000\,\mathrm{m}} = 5.21\,\mathrm{m\,s^{-1}}$.

7.3.2.3 Fire Scars

Fire-weather situations (e.g., droughts) may lead to wildfires that ensure the natural successive development of landscapes in many regions on Earth. The modification

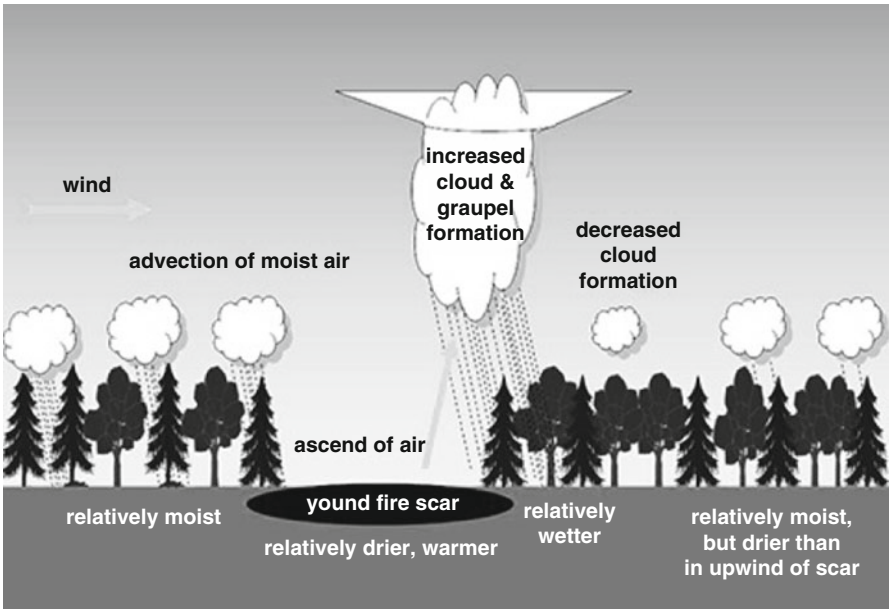

Fig. 7.30 Schematic view of impact of young wildfire scars on local precipitation formation (After Mölders and Karmm (2007))

of the landscape by huge wildfires impact at least local climate until the former vegetation will be totally re-established. This change is due to the other dynamic (roughness length), radiative (albedo, emissivity), vegetative (vegetation type and fraction, stomata resistance), thermal (soil heating, thawing of permafrost), and hydrological (water loss due to the fire) surface characteristics of the fire scar and subsequent re-growth as compared to the original vegetation (Fig. 7.30).

Fire scars from moderate and strong burns can be distinguished from each other in Advanced Very High Resolution Radiometer (AVHRR) imagery for more than a decade after the fire event. In the Canadian boreal forest, for instance, fire scars were up to 6 K warmer than the adjacent unharmed forest. These differences in skin temperature yield to a different thermal and hydrological regime of the soils as compared to the soils in the non-burned environment. Aircraft measurements showed that sensible heat fluxes into the atmosphere are about 10–20 % over young fire scars as compared to those in their environment, while latent heat fluxes are slightly smaller. These differences in sensible and latent heat fluxes increase the Bowen ratio (= sensible heat flux/latent heat flux) by about 50 %. The changes in Bowen ratio evolve with time back to the Bowen ratio of their environment as the original vegetation is fully reestablished.

Modeling studies suggest that in boreal forest, for instance, young fire scars may alter summer cloud and precipitation formation. Over large scars sensible heat fluxes into the atmosphere and air temperatures increase by up to 225 $W\,m^{-2}$, and

3 K. Scars exceeding 600 and 800 km^2 in extension significantly (at the 90 % or higher confidence level according to statistical tests) alter the partitioning of net radiation between sensible and latent heat fluxes, respectively. Scars greater than 600 km^2 already cause enough buoyancy to produce pattern of enhanced cloud and precipitation particles in their immediate downwind, and areas of reduced cloud and precipitation particles in their farther downwind. The enhanced buoyancy of scars covering more than 1,600 km^2 even leads to statistically significant changes in upward transport of air. These changes yield to a more heterogeneous precipitation distribution with similar regional means, but locally increased extremes in dryness and precipitation rates. Figure 7.31 illustrates the processes schematically.

The wildfire scar induced increased buoyancy allows air parcels to reach higher layers than in the undisturbed landscape (Fig. 7.30). The comparatively lower temperatures at these levels shift the cloud and precipitation formation process towards the cold path. Due to the Findeisen-Bergeron process (Chap. 3) precipitation formation becomes more efficient, and precipitation rates increase in the downwind of the scar. Consequently, the precipitation pattern changes as an appreciable amount of the atmospheric water load has been removed from the atmosphere earlier in the downwind of the scar as compared to the original landscape (Fig. 7.31). On days with weak synoptic forcing ($|v| < 5\,m\,s^{-1}$ or so), large fire scars may develop an reverse wind at the top of the ABL when inversions are present. This air then sinks in the upwind of the scar closing the circulation.

7.4 Climate Classification

Climate maps illustrate the characteristic climates of the Earth (Fig. 7.32). To derive climate maps characteristic climates have to be defined by means of air temperatures, precipitation, and energy budget. Here exemplarily the classification by Köppen[26] and Geiger[27] is discussed as it is simple, easy to handle, and frequently used to assess climate model performance and results (Fig. 7.32). The Köppen-Geiger classification addresses climate by three letters according to the main climate (Table 7.9) given by the first letter, precipitation under consideration of its annual sum and seasonal distribution (Table 7.10) given by the second letter, and air temperature at 2 m height (Table 7.11) given by the third letter. The letter k denotes to the *German* word kalt = cold.

[26] Wladimir Peter Köppen, German climatologist and ecologist, 1846–1940.

[27] Rudolf Geiger, German climatologist, 1894–1981.

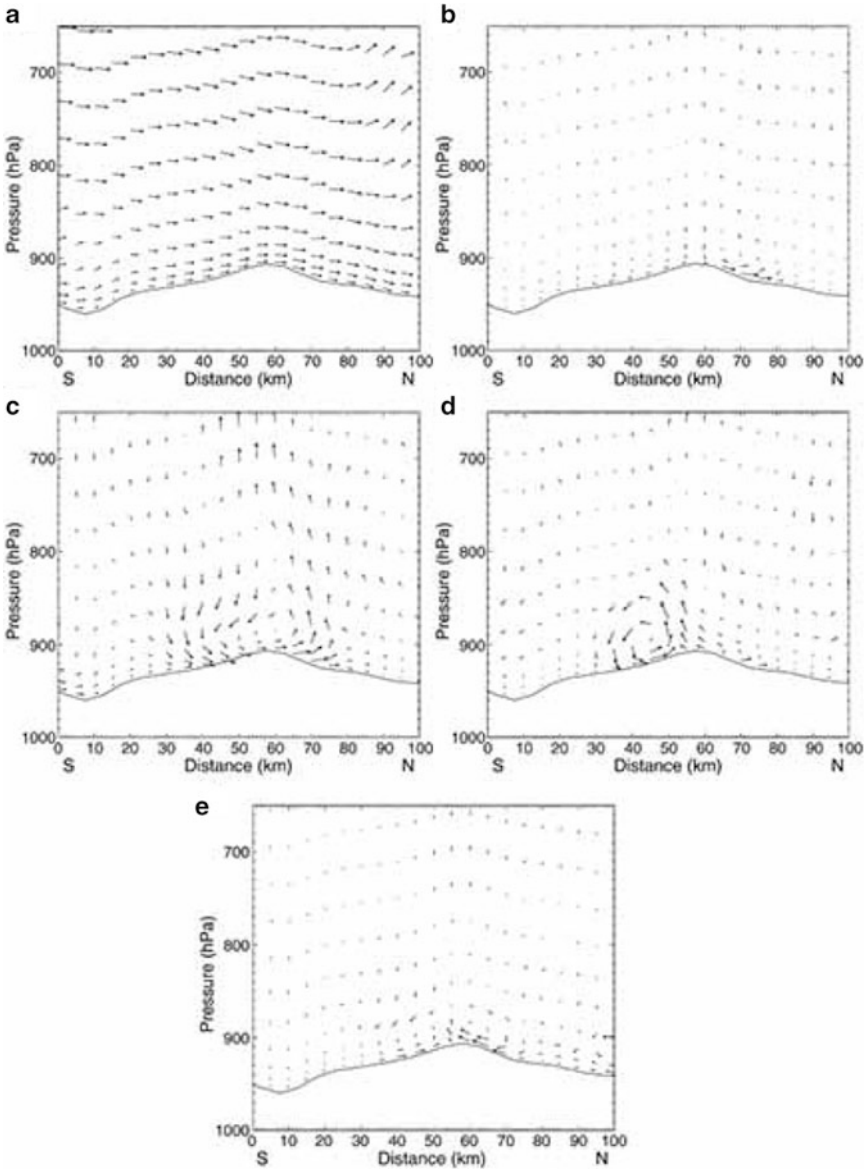

Fig. 7.31 South–north cross section over a fire scar as obtained from a model simulation. (**a**) Wind vectors as obtained by a simulation without consideration of the fire scar for July 20 1400 UTC (0500 LT), max. horizontal and vertical vector component 7.3 m s^{-1}, 89 Pa s^{-1}. Differences of wind vectors with minus without fire scar considerations for (**b**) 1400 UTC (0500 LT), max. horizontal and vertical vector component 0.5 m s^{-1}, 5 Pa s^{-1}, (**c**) 2000 UTC (1100 LT), max. horizontal and vertical vector component 0.2 m s^{-1}, 8 Pa s^{-1}, (**d**) on July 21 0200 UTC (July 20 1700 LT), max. horizontal and vertical vector component 0.3 m s^{-1}, 9 Pa s^{-1}, and (**e**) July 21 0600 UTC (July 20 2100 LT), max. horizontal and vertical vector component 0.4 m s^{-1}, 8 Pa s^{-1}. Note that the synoptic scale vector field remains nearly constant with time. The scar is located between 25 and 75 km (After Mölders and Karmm (2007))

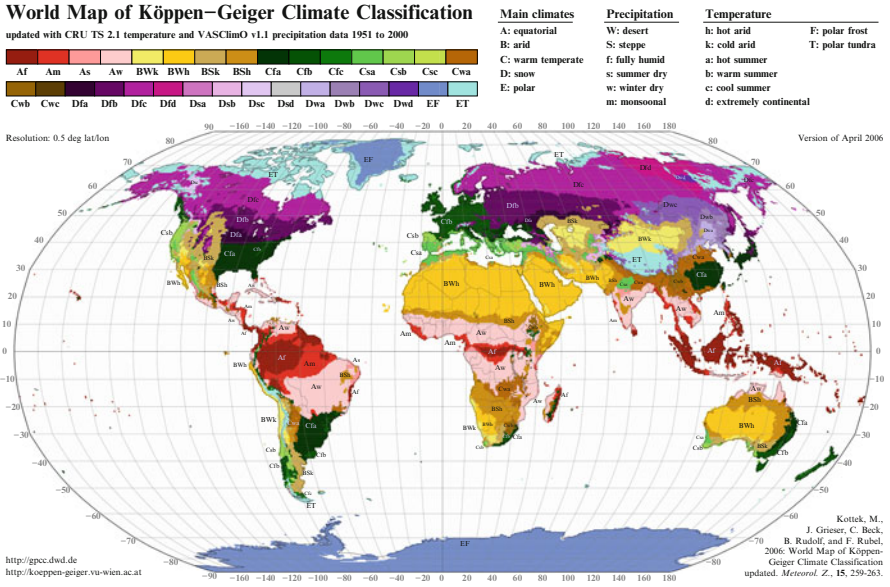

Fig. 7.32 Climate classification after Köppen and Geiger (From Kottek et al. (2006))

Table 7.9 Letters characterizing the main climates

	Climate
A	Tropical climates
B	Arid climate (dry)
C	Warm moderate climate (mild)
D	Snow climate (severe mid-latitudes)
E	Glacial climate (polar)
H	Highland

The reasonable combinations of the first and third letters provide the thermal definition of the 11 **climate regions**. Herein, the second letter plays no role.

Thus, these temperature thresholds[28] indirectly include important boundaries for habitats of vegetation. The −3 °C-isotherm of the lowest monthly mean is regarded as the boundary between maritime and continental climates. Forest only exists where the monthly mean temperature is at least 10 °C. The annual mean temperature required to grow palms is 18 °C.

The letters S and W indicate differences with respect to moisture conditions. When $\overline{T_a}$ is the annual mean temperature in degree Celsius and P is the annual accumulated precipitation in cm we obtain the following classification

[28] −38 °C is the freezing point of mercury.

Table 7.10 Letters characterizing precipitation under consideration of the annual sum and seasonal distribution

	Further distinction of climate	Comments
S	Steppe	Semi-dry
W	Desert climate	Dry
f	Humid	All month have enough precipitation for vegetation
m	Monsoon	Tropical forest despite of dry season, short dry season
s		Dry season in summer on the respective hemisphere
w		Dry season in winter on the respective hemisphere

Table 7.11 Letters characterizing air temperature at 2 m height. Here, $\overline{T_m}$ and $\overline{T_a}$ denote to the long-annual monthly mean and annual mean air temperature, respectively

a	Hot summer	Maximum $\overline{T_m} \geq 22\,^{\circ}\mathrm{C}$
b	Warm summer	Maximum $\overline{T_m} < 22\,^{\circ}\mathrm{C}$, 4 months maximum $\overline{T_m} \geq 10\,^{\circ}\mathrm{C}$
c	Cool summer	Less than 4 months with maximum $\overline{T_m} \geq 10\,^{\circ}\mathrm{C}$
d	Cool summer, extremely continental severe winter	Less than 4 months with maximum $\overline{T_m} \geq 10\,^{\circ}\mathrm{C}$ and lowest $\overline{T_m} \leq -38\,^{\circ}\mathrm{C}$
h	Hot dry climate	$\overline{T_a} \geq 18\,^{\circ}\mathrm{C}$ (only for B)
k	Cold dry climate	$\overline{T_a} < 18\,^{\circ}\mathrm{C}$ (only for B)

The threshold for temperature is chosen to be 14 °C higher in summer because of the then much higher evapotranspiration than in winter. This value leads to positive values of $\overline{T_a} + 14\,^{\circ}\mathrm{C}$ even for very cold dry climates (e.g. Yakutsk with an annual mean temperature of −13 °C).

7.4.1 Tropical Climates

The seasonal change in the position of the Hadley cell dominates all three **tropical climates**.

7.4.1.1 Tropical Wet Climate (Af)

Tropical wet climate has significant rainfall year round. The ever-present surface moisture shifts the partitioning of the incoming solar energy more to the latent than to the sensible heat flux. Evaporation is favored over a rise in surface temperature (Fig. 7.33). The clouds inhibit heating of the air at day and cooling at night leading to a less distinct diurnal course as compared to desert climate. Unlike most climates, the diurnal course of temperature (about 10 K) exceeds the annual. Tropical wet climate exists in the Amazon Basin, over western equatorial Africa,

A		All $\overline{T_a} \geq 18\,^{\circ}\mathrm{C}$	The third letters play no role as the thermal conditions vary only slightly between summer and winter
B	h		$\overline{T_a} \geq 18\,^{\circ}\mathrm{C}$
B	c		$\overline{T_a} < 18\,^{\circ}\mathrm{C}$
C	a	$-3\,^{\circ}\mathrm{C} < \overline{T_m} < 18\,^{\circ}\mathrm{C}$	Maximum $\overline{T_m} \geq 22\,^{\circ}\mathrm{C}$
C	b	$-3\,^{\circ}\mathrm{C} < \overline{T_m} < 18\,^{\circ}\mathrm{C}$	Maximum $\overline{T_m} < 22\,^{\circ}\mathrm{C}$, 4 months maximum $\overline{T_m} \geq 10\,^{\circ}\mathrm{C}$
C	c	$-3\,^{\circ}\mathrm{C} < \overline{T_m} < 18\,^{\circ}\mathrm{C}$	Maximum $\overline{T_m} \geq 22\,^{\circ}\mathrm{C}$, less than 4 months with maximum $\overline{T_m} \geq 10\,^{\circ}\mathrm{C}$
D	a	Lowest $\overline{T_m} \leq -3\,^{\circ}\mathrm{C}$ Maximum $\overline{T_m} \geq 10\,^{\circ}\mathrm{C}$	Maximum $\overline{T_m} \geq 22\,^{\circ}\mathrm{C}$
D	b	Lowest $\overline{T_m} \leq -3\,^{\circ}\mathrm{C}$ Maximum $\overline{T_m} \geq 10\,^{\circ}\mathrm{C}$	Maximum $\overline{T_m} < 22\,^{\circ}\mathrm{C}$, 4 months maximum $\overline{T_m} \geq 10\,^{\circ}\mathrm{C}$
D	c	Lowest $\overline{T_m} \leq -3\,^{\circ}\mathrm{C}$ Maximum $\overline{T_m} \geq 10\,^{\circ}\mathrm{C}$	Maximum$\overline{T_m} \geq 22\,^{\circ}\mathrm{C}$, less than 4 months with maximum $\overline{T_m} \geq 10\,^{\circ}\mathrm{C}$
E		Maximum $\overline{T_m} < 10\,^{\circ}\mathrm{C}$	
S	$\overline{T_a} < P < 2\overline{T_a}$	Precipitation in winter	
S	$(\overline{T_a} + 14) < P < 2(\overline{T_a} + 14)$	Precipitation in summer	
W	$P \leq \overline{T_a}$	Precipitation in winter	
W	$P \leq (\overline{T_a} + 14)$	Precipitation in summer	

and the islands of the East Indies. Singapore (Malaysia), Colombo (Sri Lanka), Palembang (Indonesia) or Sao Louis (Brazil) are examples of wet tropical climate.

7.4.1.2 Tropical Monsoon Climate (Am)

Monsoon climate[29] has one to three months of relative dryness, but receives enough precipitation so that vegetation has not to adapt to seasonal droughts (Fig. 7.33). Every variation in monthly average temperature is related to the timing of precipitation. Typically, the warmest month is prior to the onset of the main precipitation season (Fig. 7.33). Monsoon climate exists near the eastern Bay of Bengal, in northeastern South America, southwest India, and the Philippines. Typical examples for monsoon climate are Monrovia (Liberia), Cairns (Australia), or Miami (USA).

[29]Note that the designation of monsoonal climate is not synonymous with the locations subject to the reversal of winds discussed earlier in this chapter.

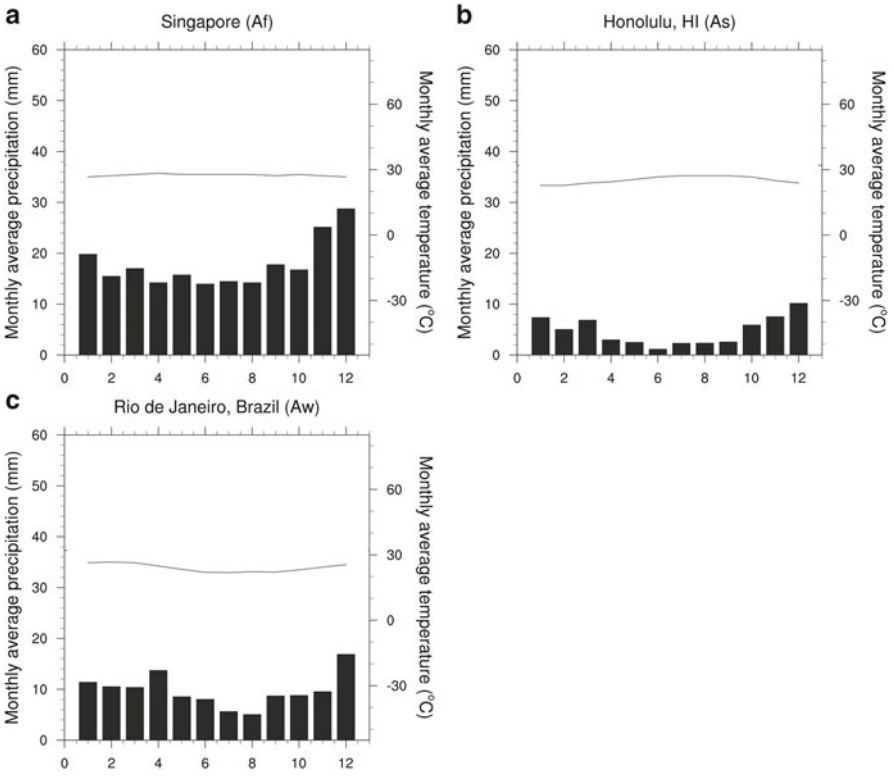

Fig. 7.33 Climate diagrams showing examples of three different types of the A climate, Af wet throughout the year, As short dry season, and Aw extended dry season and greater annual temperature range than the other stations

7.4.1.3 Tropical Wet and Dry Climate (Aw)

Tropical wet and dry climate[30] has a distinct dry season that is due to the movement of the ITCZ. In the annual course, monthly mean temperatures vary more strongly than in other tropical climates, but the variation is low as compared to most other climates (Fig. 7.33). Diurnal variations can be large. Representatives for tropical wet and dry climate are Calcutta, Mumbai (India), Bangkok (Thailand), Acapulco (Mexico), Port Darvin (Australia), Caracas (Venezuela), or Bamako (Mali).

[30]Some authors use As instead of Aw when the dry season occurs during summer like, for instance, in Hawaii (USA), Mombasa (Kenya) or Trincomalee (Sri Lanka).

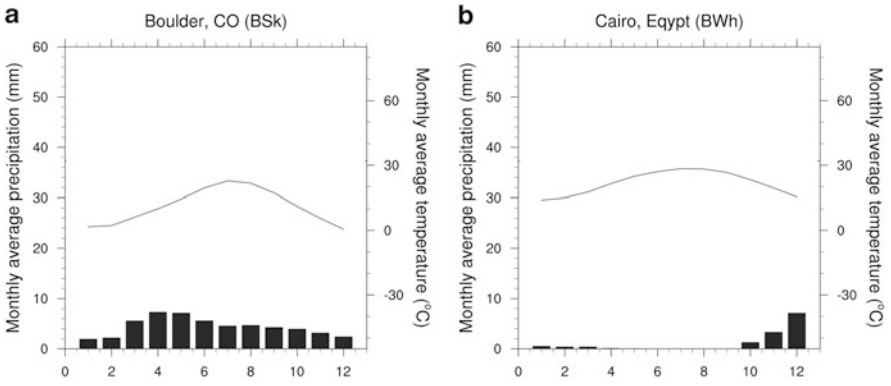

Fig. 7.34 Climate diagrams showing examples of the B climate for (**a**) a cold semi-arid steppe climate and (**b**) a hot arid desert climate

7.4.2 Dry Arid and Semi-arid Climates

The smaller the annual precipitation, the more irregular and unpredictable it is.

7.4.2.1 Subtropical Deserts Climate (BWh)

The most extensive deserts exist in the subtropical regions in the western part of the continents. **Subtropical deserts climate** is associated with the sinking path of the Hadley cell. Summer precipitation mainly results from local convective activity. Winter precipitation results from extra-tropical cyclones. Daytime temperatures can be extremely high. The low humidity and clear sky lead to strong nocturnal cooling. The amplitude of the diurnal and annual temperature course is great (Fig. 7.34). Representatives for subtropical desert climate are Phoenix (Arizona), Alice Springs (Australia) or Cairo (Egypt).

7.4.2.2 Subtropical Steppe Climate (BSh)

The **subtropical steppe climate** commonly borders the subtropical deserts. It is famous for its aridity, high year-to-year variations in precipitation, distinct seasonality of precipitation, extreme summer temperatures, and large annual and daily temperature ranges (Fig. 7.34). Typical examples for a subtropical steppe climate are Monterrey (Mexico) or Normanton (Australia).

7.4.2.3 Mid-latitude Desert Climate (BWk)

The **mid-latitude desert climate** results from the continental location or being downwind of major orographic barriers that cut off humidity from the ocean. Diurnal and annual temperature ranges are great (Fig. 7.34), but nocturnal cooling is less than in subtropical desert climate. Due to its higher amount of precipitation and lower potential evapotranspiration, mid-latitude desert climate is more humid than subtropical desert climate. The western US or the areas around the Caspian Sea or north of the Himalayas are examples for mid-latitude desert climate. Las Vegas (Nevada) or Kuqa (China) are prominent examples.

7.4.2.4 Mid-latitude Steppe Climate (BSk)

Temperature characteristics of the **mid-latitude steppe climate** are like those of the mid-latitude desert climate. The main difference is the precipitation amount, which is usually about 500 mm year^{-1} (Fig. 7.34). This climate accounts for most of the arid areas of western North America. Boulder (Colorado) or Semey (Kazakhstan) are representatives for a mid-latitude steppe climate.

7.4.3 Mild Mid-latitude Climates

The term mild refers to winter temperatures.

7.4.3.1 Mediterranean Climate (Csa, Csb)

Mediterranean climate has a distinct summer dry season and a concentration of precipitation in winter. Summer precipitation is of convective type, winter precipitation stems from extra-tropical cyclones. Summer temperatures range from mild to hot (Fig. 7.35). Typical examples for Mediterranean climate are Tel Aviv (Israel), Seville (Spain), Los Angeles (USA), Santiago (Chile), Lisbon (Portugal), Perth (Australia), Capetown (South Africa) or Nice (France).

7.4.3.2 Humid Subtropical Climate (Cfa, Cwa)

Humid subtropical climate regions receive abundant precipitation (about 750–2,500 mm year^{-1}). This climate provides a distinct tropical feeling in its long summers. In winter, temperatures are usually cooler than in Mediterranean climate (Fig. 7.35). Humid subtropical climate exists in lower mid-latitudes of eastern North

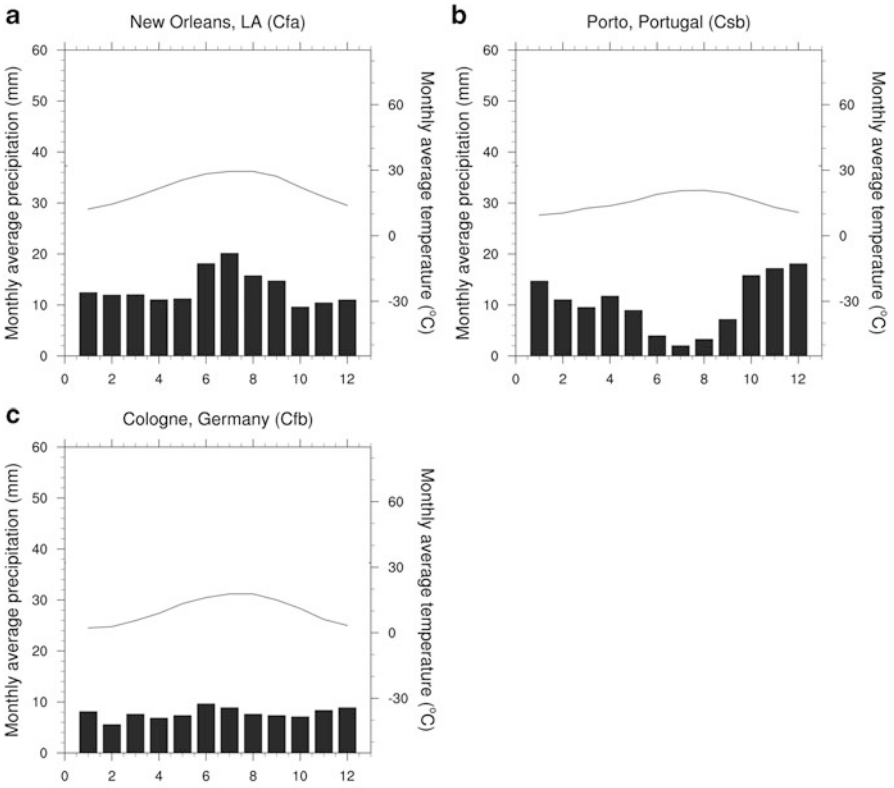

Fig. 7.35 Climate diagrams showing examples of three different types of the C climate

America, South America and Asia. Typical examples for humid subtropical climate are São Paulo (Brazil), Dallas (Texas), Guangzhou (China) or Brisbane (Australia).

7.4.3.3 Marine Temperate or Oceanic Climate (Cfb, Cfc, Cwb, Cwc)

Both summers and winters are mild under marine west coast climate. Summers face no extremely high temperatures. Low clouds keep daytime temperatures low and provide drizzle or light rain to coastal regions. In this climate, the annual temperature amplitude is small (Fig. 7.35). Typical examples of marine west coast climates are Sitka (Alaska), Auckland (New Zealand), or London (Great Britain). Cwb and Cwc are temperate highland climates in the Tropics with ocean to the west. Examples are Juliaca (Peru) or Copacabana (Bolivia).

7.4.4 Severe Mid-latitude Climates

Severe mid-latitude climates receive precipitation throughout the year. In many cases, summer precipitation exceeds winter precipitation. Summer precipitation results from convection or extra-tropical cyclones, while winter precipitation is almost exclusively from cyclonic activity.

7.4.4.1 Humid Continental Climate (Dfa, Dfb, Dwa, Dwb, Dsa, Dsb)

Summers are warm and often hot under **humid continental climate**. The mean annual precipitation amounts between 500 and 1,000 mm year^{-1}. Areas in the eastern part of the continents in mid-latitudes often have this climate. Chicago (USA), Stockholm (Sweden), Minsk (Belarus), Kiev (Ukraine), New York (USA), Montreal (Quebec), Moscow (Russia) or Shenyang (China) are examples.

7.4.4.2 Subarctic or Boreal Climates (Dfc, Dfd, Dwc, Dwd, Dsc, Dsd)

Subarctic climate covers the northernmost extent of the mid-latitude severe climate with most of Alaska and Canada. Summer temperatures are slightly lower than in the adjacent humid continental areas. In winter, temperatures can be extremely low (Fig. 7.36). Locally temperatures remain below freezing for seven months. Precipitation is higher in summer, mostly due to the more pole-ward position of the storm tracks than in winter. Annual precipitation ranges from 120 to 500 mm year^{-1}. When continental subarctic climate occurs with extreme severe winter (coldest month temperature lower than −38 °C) we speak of Dfd, Dwd or Dsd climate. Dawson (Yukon) is an example for subarctic climate.

7.4.5 Polar Climates

Polar climate types exist at latitudes higher than 70°. They have average temperatures below 10 °C in all months of the year. Examples are Mount Fuji (Japan), Jotunheimen (Norway) or Mt. Washington (USA).

7.4.5.1 Tundra Climate (ET)

Tundra climate is characterized by severe winters (low Sun), strong radiative cooling at the surface, low temperatures, and strong stability in winters (Chaps. 2 and 4). All these factors inhibit precipitation. In summer, temperatures are mild due to the long daylight. Permafrost occurs frequently. The annual temperature range is large, while the daily temperature range is low (Fig. 7.37). Spitsbergen (Norway) and Barrow (Alaska) are examples for tundra climate.

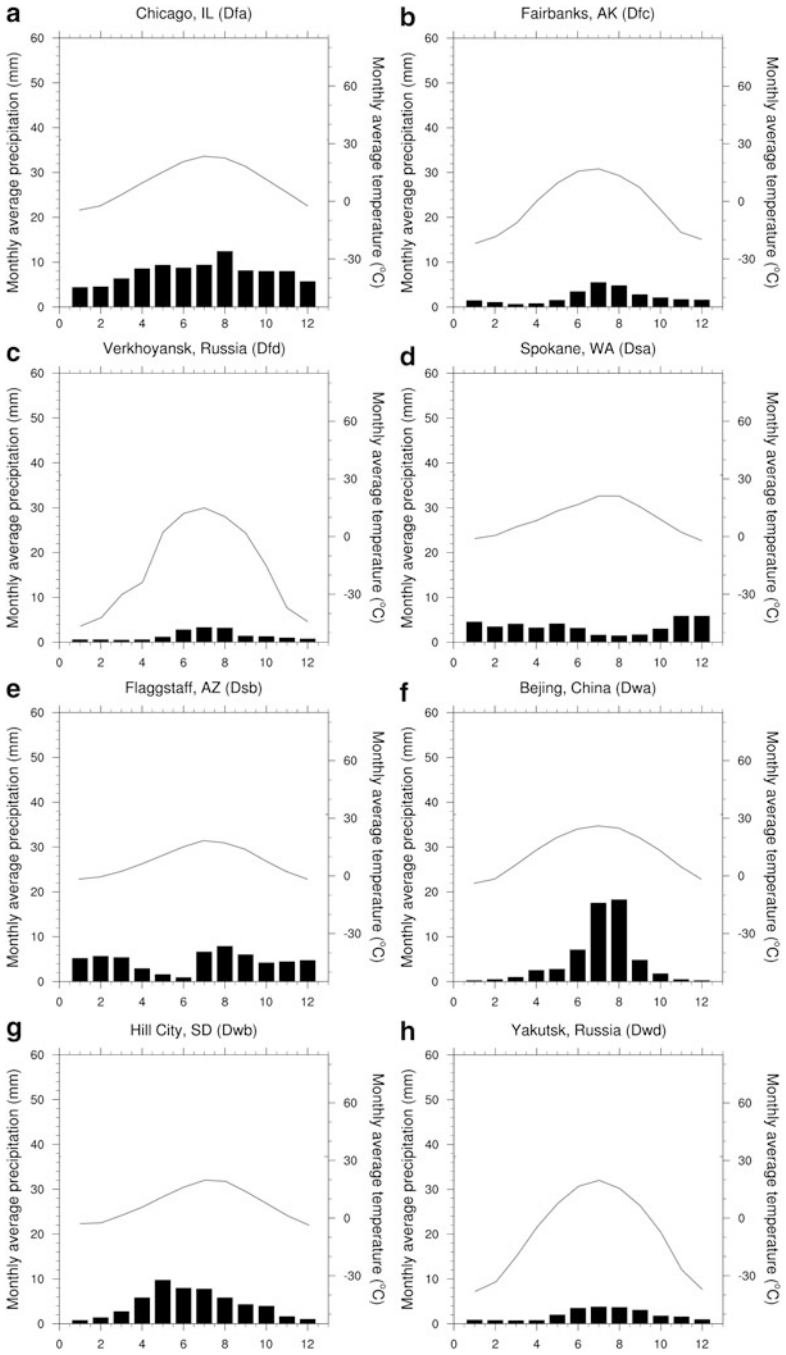

Fig. 7.36 Climate diagrams showing examples of different types of the D climate

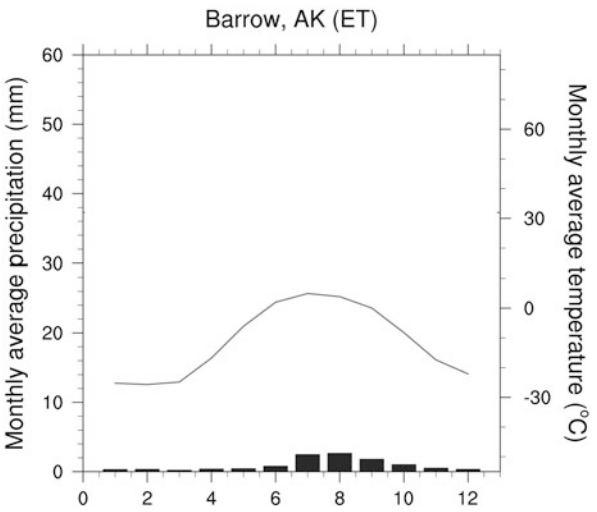

Fig. 7.37 Climate diagram showing an example of the E climate

7.4.5.2 Ice Cap Climate (EF)

Polar ice cap climate refers to the interior Greenland and Antarctica. The mean temperatures of the warmest month do not exceed the melting point. All precipitation falls as snow and accumulates on the ice (Fig. 7.37). Sublimation is low. Little America (Antarctica) and Eismitte (Greenland) are examples of ice cap climates.

7.4.5.3 Highland Climate (H)

The **highland climate** category is unique as this climate is governed by altitude, rather than geographic location. Precipitation type and intensity vary spatially over the highlands depending on windward or rain-shadow side. Elevation determines the fraction of precipitation falling in liquid or solid form and temperature. Mount Kilimanjaro (Tanzania) is an example of highland climate.

Example. Determine the climate of a site in the Southern Hemisphere where the record high and low temperatures are 37 and 16 °C, respectively, and the monthly average temperatures, average temperature ranges, and monthly average precipitation are

(continued)

(continued)

	J	F	M	A	M	J	J	A	S	O	N	D
T ($°C$)	25	25	25	26	26	26	26	26	26	26	26	26
ΔT ($°C$)	8	8	7	8	8	9	9	9	10	10	11	9
P (mm)	318	358	358	320	259	170	150	112	89	84	66	155

Solution. The climate is monotonous. The average monthly temperatures vary less than 3 °C and the monthly and annual average temperature is 26 °C. The annual temperature range is about 1 °C. The annual mean temperature and marginal temperature range indicate a tropical climate (A). Most precipitation falls in summer, and no distinct dry season (f) exists. It is humid year round. Thus, the climate can be categorized as Af.

7.5 Aerosols and Climate

The sources and mean distributions of the major atmospheric trace gases (Fig. 1.4) have been discussed already in Chaps. 1, 3, and 5, for which this material is not repeated here. In Chaps. 1 and 5, we learned that aerosols have natural and anthropogenic sources, and can build in the atmosphere from precursor gases by gas-to-particle conversion. We learned in Chap. 4 that many gases absorb in certain ranges of the spectrum. Thus, remote sensing brought huge insights of the global distributions of many trace gases and the aerosol optical depth.

As pointed out in Chap. 4, energetically relevant trace gases, i.e. the so-called greenhouse gases, and aerosols are climate-relevant. This means that changes in their concentrations can affect climate to various degrees. Some of these gases are naturally in the atmosphere, some are anthropogenically caused or the concentrations are elevated due to anthropogenic emissions. As pointed out above aerosols from volcanic eruptions (Fig. 7.38) can strongly affect climate. Therefore, climate scientists are not only interested in the mean spatial distributions and annual cycle of GHG and aerosols, but also in changes therein. In Chap. 1, we discussed already the trends in CO_2 concentrations (Fig. 1.3).

We learned in Chap. 3 that a shift of the particle spectrum towards larger particles, and/or lower number of cloud condensation and/or ice nuclei accelerate the onset of precipitation. The opposite occurs for a shift towards smaller particles and/or increased numbers of CCN/IN. Under saturated conditions hygroscopic aerosols compete for excess water vapor. Consequently, more cloud droplets, and/or ice crystals form, but they are smaller in size compared to situations with few CCN/IN. The reduced sizes mean decreased likelihood for growth by collection (Chap. 3). Hence precipitation-formation becomes less efficient, and cloud lifetimes increase. Furthermore, cloud albedo increases (Fig. 3.4) with radiative feedbacks, changes in the vertical temperature and moisture profiles, and finally changes in

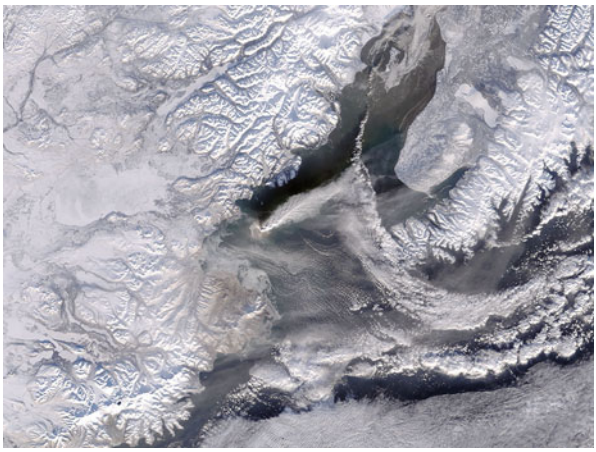

Fig. 7.38 Aerosol cloud from the Augustine, Alaska 2006 eruption moving into the Cook Inlet (Retrieved 2006. Reproduced with the permission of University of Alaska Fairbanks, Geographic Information Network of Alaska, www.gina.alaska.edu)

the surface-energy budget as consequences. An enhanced cloud albedo affects the photolysis rates with consequences for the gas-phase chemistry below, within and above clouds, i.e. the profiles of atmospheric constituents (Fig. 5.12; Chaps. 4 and 5). The radiative properties of cloud ice and cloud water differ tremendously over wide ranges of the spectrum (Chap. 4). This fact is another reason to be interested in trends of the distributions of precursor gases and aerosols.

The Cloud-Aerosol Lidar and Infrared Pathfinder Satellite Observation (CALIPSO) satellite serves to collect data on cloud phase and aerosol vertical profiles (Chap. 4) among other things for these reasons.

All these radiative, thermodynamic, dynamic and physiochemical effects contribute to changes of the total thermal energy within the atmospheric air column. We learned that many precursor gases stem, at least to a certain part, from anthropogenic emissions (Chaps. 1 and 5). Thus, any regulatory action can potentially affect at least local climate.

Hydroscopic aerosols can serve as CCN or IN (Chap. 3). Changes in the precursor gas distribution and/or amount affect gas-to-particle formation and, hence the number and spectra of CCN and/or IN. The same applies to changes in emission of hygroscopic aerosols. Here we discuss the consequences under the aspect of climate.

A direct aerosol effect on the atmosphere stems from their absorbing and scattering radiation in various ranges of the spectrum. In the troposphere, huge aerosol concentrations from anthropogenic and/or natural emissions compete for excess water vapor under saturated conditions. Consequently, more, but smaller cloud droplets build, and cloud lifetime increases. Under current climate, clouds are typically IN limited. Under (ice-)saturated conditions, an increase of the number of IN would enhance the ice-particle concentrations and ice-particle sizes would decrease when all other factors remained the same. When locally huge natural and/or anthropogenic emissions of IN occur under (ice-)saturated conditions, **over-seeding** may occur. Thus, the ice-particle concentrations and cloud lifetime increase, but ice-particle sizes decrease. In comparison to thermodynamically and dynamically

similar clouds, the cloud may glacify in a relatively narrow layer. However, small cloud-droplets and ice-crystals mean no, or at least reduced coalescence and riming, which is known as the **riming-indirect effect**. Consequently, precipitation formation becomes less efficient. The opposite is true for a decrease in the IN number.

In mixed phase clouds, the **glaciation indirect aerosol effect** may enhance the efficiency of precipitation formation via the Bergeron-Findeisen-Wegener process (Chap. 3) when locally additional IN are available. The lower saturation vapor pressure over ice than water yields ice crystals growths at the cost of cloud droplets (Chap. 3). Cloud-droplet size decreases and freezing is delayed. The changes in the vertical pattern of release of latent heat and consumption of heat alter the vertical temperature profile, with consequences for stability, vertical motions, the total thermal energy within the cloud, and buoyancy. Meteorologists speak of microphysics-dynamics interaction.

Emission of particles suitable as CCN/IN into a cloud means small droplets and/or ice crystals, and an increase in cloud albedo (Fig. 3.4). This phenomenon is known as the **Twomey effect**. Climate researchers denote to the increased cloud albedo and cloud lifetime as **indirect aerosol effects**.

The term **semi-direct aerosol effect** relates to absorption of solar radiation. This process can yield evaporation and/or sublimation of liquid and solid cloud particles. Thus, any change in aerosol amount, no matter whether caused naturally or anthropogenically, modifies clouds and/or optical thickness. However, the modifications of the atmospheric conditions affect net surface solar radiation, and the surface-energy budget below the cloud (Chap. 4). This process is called the **surface-energy budget effect**. It is important to realize that any changes in the aerosol distribution have consequences for the semi-direct aerosol effects.

In the stratosphere, aerosols scatter some of the incoming solar radiation back to space leading to surface cooling. In the upper troposphere, aerosols may enhance high-level cloudiness and cloud lifetime with impacts on the radiation budget. On the local scale, tropospheric aerosols may lead to surface cooling during daylight by reflecting sunlight to space, while their downward infrared emission may warm the surface at night. This **aerosol infrared effect** may enhance air temperatures potentially resulting in evaporation and/or sublimation of cloud particles. Note that the infrared effect exists both at day and night. However, it is much stronger in the absence of solar radiation.

On the local scale, deposition of soot on snow or ice reduces the surface albedo, and increases near-surface air temperatures. On contrary, aerosol deposition on vegetation may increase albedo, and hence reduce near-surface air temperatures.

Research also suggests that the location (latitude, longitude, height) of high aerosol concentrations may influence atmospheric dynamics. Various climate and mesoscale studies suggest that the various feedback mechanisms make the polar regions very sensitive to even slight changes in aerosol concentrations. Changes in surface albedo due to aerosol deposition, for instance, may alter the contrasts between adjacent surfaces with consequences for (non-) classical mesoscale circulations, and local scale processes. Aerosols residing in the Arctic stratosphere (e.g. from aircrafts, volcanic eruptions, troposphere-stratosphere exchange), for

instance, absorb radiation leading to warming. The latter can alter the zonal winds. Given the general three cells circulation pattern (Fig. 7.10), the mid and low latitude regions are affected on long-term. In the Tropics, high stratospheric aerosol concentrations (e.g. from biomass burning) may affect the heating as well, and hence the tropospheric general circulation.

The very complex interactions between aerosols, weather, and climate are far beyond being completely understood. Recent research suggest that some buffering processes might exist that compensate between various cloud responses to aerosols. Numerical modeling studies suggest that the number of CCNs may affect funnel formation in super-cells. Recent studies showed that aerosols can induce invigoration of deep convective clouds. This mechanism may transport large amounts of small ice particles to the anvil of these clouds. Thus, the anvils extend over a larger area than without aerosols. These larger anvils are higher, colder than the cloud tops were otherwise and, hence, emit less thermal radiation to space. This fact can lead to warming in the layers below. The smaller ice particles in response to aerosols from pollution have lower fall speeds than would occur when ice crystal formation were IN-limited. When many IN are present the ice crystals' growth is slower and hence the ice crystals' fall-speeds. Thus, the anvils do not only extend larger, but also exist longer in polluted than clean thunderstorm clouds. Obviously, the relative magnitudes of the processes determine the net effect. These buffering mechanisms are referred to as **aerosol cloud-mediated effects**.

The microphysical processes by which hydrophilic aerosols affect droplet growth and how droplets coalesce to produce raindrops are well understood (Chap. 3). The impact of turbulence (Chap. 6) on these processes is still subject to research. Ice crystal formation processes and their interaction with liquid droplets are hard to examine due to the small size of IN and the limited ability to measure IN activation. Unfortunately, these microscale aerosol and cloud processes, and hence cloud properties have large impacts through all scales. This means that aerosols may influence the cloud organization.

Obviously, the aforementioned aerosol-induced reduced cloud-droplet size triggers other processes leading to radiative perturbation. Another question of large concern is what the processes would look like with just natural aerosols being present or under pre-industrial conditions. Such a reference level would be incredibly valuable to better quantitatively understand cloud-aerosol-radiation interactions. It also would be useful to distinguish between, and quantify natural and anthropogenic forcing effects.

Current satellite missions serve to gather data on aerosols at-large (i.e. without specification) as well as cloud and precipitation properties. The goal of the CALIPSO mission, for instance, is to gather data to gain more insight into aerosol-cloud distributions, and to collect data for better aerosol-cloud-radiation interaction parameterizations in climate models. The most interesting region from a cloud formation point of view is the cloud base. Unfortunately, in the case of thick clouds the lidar signal may be already attenuated here. Thus, concurrent lidar measurements from below are required to gain information on aerosol nucleation.

The radiometers to be flown on the next generation of satellites will overcome of these limitations. EarthCare is one of these satellites expected to be launched in 2015. EarthCare will carry a 355 nm lidar to measure vertical profiles of aerosol types and concentrations. The Doppler cloud radar (see Appendix B) on board of EarthCare will concurrently observe (cloud) vertical motions. This experimental setup allows investigation of the relationship between vertical aerosol concentrations and vertical growth of clouds along the path of the sub-satellite point. In an ideal world, it would be nice to fly instruments that provide multispectral, multi-angle polametric data of cloud properties at a high resolution ($\approx$10 m). Large-Eddy simulation models with embedded cloud microphysics and line-by-line radiation models then could be developed and evaluated by means of this data and be used to test and develop parameterization of cloud-aerosol-radiation interaction in climate and Earth system models.

7.6 Biogeophysical Cycle

We learned in Chap. 5 that we can divide the global biogeophysical cycle into the hydrological cycle, various gaseous cycles, biogeochemical cycle, sedimentary cycle, and the energy cycle. These cycles are strongly linked with each other (Figs. 4.23, 5.8, 5.9, 5.10, and 5.11). For brevity we restrict the discussion of biogeophysical cycles to aspects that we have not yet discussed, and refer the reader to Chap. 4 for a discussion of the energy cycle, Chaps. 2–5 for the atmospheric part of the hydrological cycle, trace-gas cycle, and Chap. 5 for a brief discussion of the biogeochemical cycle.

At the Earth-atmosphere interface, biogeophysical processes regulate the fluxes of momentum, water, trace gases, particles, and heat. Surface properties like heat capacity, heat conductivity, shielding factor, maximum evaporative conductivity, heterogeneity, albedo (Chap. 4), roughness length (Chap. 6), etc. namely affect the fluxes of energy, momentum and matter. Recall that albedo determines the fraction of solar radiation reflected back to space. This means the albedo of the Earth's surface affects net radiation (Chap. 4). We also learned that surface characteristics govern the partitioning of incoming energy between sensible and latent heat (Chap. 4), the momentum fluxes, the uptake/release of trace gases (Chap. 5) as well as the possibility for dust to become airborne (Chap. 6). In micrometeorology, the partitioning of energy into sensible and latent heat-fluxes is often characterized by the **Bowen ratio**. In climatology, changes in microclimate are often expressed in terms of changes in Bowen ratio.

The surface fluxes modify the state variables. The state variables, however, themselves affect the fluxes and modify them. Thus, the microclimate close to the surface is strongly related to the surface conditions. Different surface conditions not only yield different surface energy budgets, but also different fluxes of momentum and matter (moisture, trace gases, particles). The atmospheric composition, buoyancy, and momentum have consequences for the dynamic, thermodynamic and chemical

state of the air column above. The composition, for instance, affects the availability of CCN and IN as well as the formation thereof by gas-to-particle conversion, and hence cloud and precipitation formation with feedbacks the energy, water and trace gas cycles. The momentum fluxes affect vertical mixing, ABL structure, and moist static energy. These factors are important for whether or not trace-gases and aerosols reach the upper atmosphere and become subject to long-range transport. As these processes are decisive for the vertical profiles of GHG, they link back to the energy cycle. We learned in the previous chapters that the related processes are often strongly non-linear. Furthermore, non-linear feedback mechanisms may occur.

Biogeophysical processes also explain why the simple zero-dimensional approach of the energy balance model (Problem 4.4) failed to describe our expectation that an increase in albedo decreases temperature (temperature-albedo feedback). One important aspect that was neglected in the solution of that problem is that albedo also affects the surface moist static energy flux. The magnitudes, with which surface parameters influence the energy, matter, and momentum fluxes, differ strongly. Relative stomata conductance and surface roughness explain most of the variability of the surface sensible heat fluxes. Roughness length strongly affects the momentum fluxes and vertical mixing, and the structure of the ABL as well as the precipitation distribution in its down-stream. Observations as well as modeling studies, for instance, indicate that fronts propagate slower over large conurbations and small mountain barriers than they do over rural and/or flat areas (Chaps. 2 and 6).

The local weather determines the length of the vegetation season, onset of green-up, leaf coloring, and actual uptake of CO_2 for photosynthesis. The vegetation growth and health depends on temperature, photosynthetic available radiation, concentrations of CO_2 and harmful pollutants, as well as soil water, soil nutrients, and toxics from atmospheric deposition. Plant available water strongly depends on precipitation. However, it is important to have the right amount of plant available at the right time. Any land-cover changes, no matter whether they occur in response to climate changes or whether they are anthropogenically caused, modify the exchanges of matter, heat, and momentum at the surface-atmosphere interface. Consequently, the temperature-, moisture-, wind-, trace-gas- and aerosol profiles change.

A warmer climate means changes in the water cycle, and the efficiency of the precipitation-formation process. Many GCM simulations have suggested precipitation increases of less than 4 % per degree Kelvin warming. However, according to the slope of the Clausius-Clapeyron equation (2.71), we would expect about 6.5 % increase of precipitation per degree Kelvin increase in temperature. A major reason for this difference between the simulated and theoretically derived magnitude is the energy-limitation of evaporation.

Biogeophysical feedbacks can enhance or diminish climate changes. Most studies suggest that land-cover changes may impact the atmosphere in a similar way as they do today also under warmer climate conditions. Biogeophysical feedback mechanisms may initiate land-cover changes and increases of GHG. Climate variability and/or change affect the length of the growing season, the water amount and time of water availability, the amplitude of the diurnal and annual

temperature cycle, and at high latitudes or high elevation, the active layer depth in permafrost regions. These factors constrain biota. Along the borders of climate zones (Sect. 7.4), slight changes in temperature and/or precipitation may permit a vegetation specie to invade and/or extinguish another from the region. Thus, a major research field is to find affordable and reasonable ways to cope with varying/changing climatic conditions. Any ecological or anthropogenic response to climate variability/change affect the biogeophysical feedbacks and hence again climate.

The Daisyworld model, discussed above, was developed with the intension to better understand the feedbacks between biogeophysical effects and anthropogenic climate change. Recent research even suggests that these feedbacks may differ from one region to the other. These studies suggest that it is important to realistically simulate the biogeochemical and biogeophysical processes in climate models. Such a description of the complex biogeophysical and biogeochemical feedbacks requires Earth System models. Therefore, the climate community started efforts on coupling climate models with dynamic vegetation and chemistry models. However, such Earth System models have huge computational and storage demands, for which the number of potential studies may be very limited unless the computer technical progress is tremendously. Thus, current Earth system models widely vary in their degree of complexity depending on the research questions to be addressed with them. It is not surprising that the results obtained by them differ widely as well. Nevertheless, these studies provide valuable insight in the Earth system and unambiguously document the climate relevance of biogeophysical and biogeochemical processes.

In describing the biogeochemical and biogeophysical processes realistically, another challenge is to design plausible future emission scenarios. A big key issue is the population growth, the economic development (globalization vs. regional/national), prosperity/poverty of the population, land-use changes to accommodate water needs, food and bio-fuel production, development of technology, kind of transportation, way of life (megacities vs. rural), energy demands, use and productions. Due to these uncertainties various different scenarios are constructed. The simulations performed with them, of course, provide different answers on how climate might change. These answers are nevertheless meaningful as they provide an envelope of potential climate changes, and increase our understanding of the climate and Earth system.

We must be aware that any climate assessment and/or adaptation modeling performed with data from a climate or Earth system model will unavoidably propagate the uncertainty, and has its own uncertainty as well. When scientists started coupling ocean and atmospheric models, the first simulations showed strong drifts of the simulated climate. The reason was as simple as the parameterizations were adapted to SST from climatology. These SST, however, stem from measurements and, of course, were subject to observational uncertainty. Both the atmospheric and the ocean models used this data, as lower and upper boundary condition, respectively. Both types of models, of course, were evaluated and improved by measurements, i.e. the parameters and parameterizations were optimized for the models as they were.

When coupling the models these parameters and parameterizations were not entirely appropriate (as they indirectly corrected for errors in SST observations), and had to be revised and improved.

Another example is driving hydrological models with data from NWP models. When the NWP model predicts the precipitation in the wrong catchment the runoff may be quite different. Too strong/weak precipitation affects the flood-wave height and propagation, soil moisture, evapotranspiration, as well as ground-water recharge. Since NWP models use the soil moisture and temperature distribution of the previous simulation as initial conditions for the next forecast, and (simulated) precipitation is usually higher over mountains than the valleys, convective clouds and precipitation form in the wrong places. This initial data problem in NWP is one reason why driving or coupling a hydrological model with NWP data provides worse results than driving hydrological models with data from rain gauges and/or estimates from radar observations.

Other uncertainty in climate modeling results from soil and vegetation parameters (e.g. albedo, emissivity, stomata resistance, porosity, pore-size distribution index, vegetation fraction, shielding factor, leaf and stem area index, photosynthesis active radiation). While in nature such quantities vary hugely even on a square-meter, and furthermore with time, in any model, the parameterization require fixed single values. Various sensitivity studies show that surface fluxes, and near-surface temperatures, for instance, strongly vary with the choice of these quantities. Therefore, minimizing uncertainty and assessment of the magnitude of uncertainty are hot research topics in climate research.

It is obvious that evaluation of Earth system models will be an even greater challenge than the evaluation of climate models. A major difficulty in the evaluation of any model is that any measurement is a point observation, while models simulate area-averaged and volume-averaged quantities (Chap. 6). Furthermore, any observation includes the signal of the local conditions, while the models strongly simplify or parameterize them. Thus, the modeled values are subject to systematic errors. Initialization of the models is another major challenge, for which often ensemble simulations are run. Furthermore, any observation is subject to measurement errors. An Earth system model would require long time series not only of meteorological, oceanic, cryospheric, and hydrological data, but also soil, vegetation, aerosol, and chemical constituent data. The latter would be needed for the soil, water and atmosphere.

Problems

Knowledge and Comprehension

1. Name five different circulation systems and describe them briefly (not more than two sentences for each).

2. Assume that all land masses would form a continuous belt around the equator. How would such a land-water distribution affect the general circulation? Now assume that a continuous belt of landmass follows a longitudinal belt. Would this affect the circulation in the same way?
3. Why do tropical cyclones not form at latitudes less than 5° from the equator?
4. What wind speed must the sustained surface winds have at least to constitute a typhoon?
5. Compare the mean distribution of pressure and the air-mass source regions (Figs. 2.19 and 7.6). What do you conclude from these figures for weather and climate? Use your knowledge from the previous chapters to give a physical explanation.
6. At what time of the year are sea-breezes the strongest, and at what time land breezes? With you answer in mind provide arguments why it would be incorrect to speak of the land breeze as the "reverse" of the sea-breeze.
7. Discuss how the general circulation would look if the Earth would (a) rotate at same speed, but in the other direction, and (b) roll along its axis along the planetary plane with the axis always pointing to the Sun.

Analysis and Application

7.1. Assume that in the first 300 m of an ocean, temperature increased by 3 K over the last century. By how much must air temperature increase to be the source for the increase in ocean temperature?

7.2. At 2 m height, air temperature was 6 and 9 °C at a rural site and in town, respectively. The dew-point temperatures were −6 °C in the rural area and −5 °C in town. Determine the difference in cloud-base height and explain the differences in dew-point temperatures. On another day in winter, air and dew-point temperature were 5 °C, −2 °C and 3 °C, −5 °C at the rural site and in town, respectively. Discuss the situation for this case and explain under which conditions a city may have a lower temperature than the adjacent rural area.

7.3. In the Tropics, surface pressure, relative humidity and air temperature at the ground ($z_T = 0$ km) are 998 hPa, 65 % and 27 °C, respectively. Let T and E be the subscripts for Tropics and extra-tropics. Assume tropical air parcels ascend from the surface to the tropopause located at 16 km. From there they are transported north or southward in a thin layer of same temperature ($T_T(z = 15\,\text{km}) = T_E(z = 15\,\text{km})$). In the extra-tropics, the air parcels descend to the ground ($z_E = 0$ km). The saturated lapse rate is $0.65\,\text{K}\,10^{-2}\,\text{m}^{-1}$. Determine the dew-point temperature at the surface, cloud-base height for the Tropics, and the temperature at the tropopause and at the ground in the extra-tropics. If your answer is right for the surface air temperature in the extra-tropics, it will have an unreasonably value. Explain what the mechanism leads to the much lower near-surface temperature than actually

observed in the subtropical highs. Now assume a cooling of $2\,\mathrm{K\,day^{-1}}$. When the surface temperature in the extra-tropics is 310 K, how long does it take the air from ascending in the Tropics moving pole wards, descending and moving back to the Tropics?

7.4. Revisit the gray boxes in Chap. 2 and apply typical values for the Tropics, mid-latitudes, and Polar Regions. Then re-do the calculations for these regions, but with 2 K increased temperature values. Compare and discuss your results. What do you conclude from this mathematical experiment?

7.5. During[31] the ice age, the snow line was located at 4.5 km at about 570 hPa in the Tropics. Today the snow line is around 5.3 km and 500 hPa and near-surface air temperature is 26 °C. Determine the recent environmental lapse rate and use the dry adiabatic lapse rate to calculate the temperature at the snow line. Determine the heating rate required for condensation. At the snow line, saturation pressure is 6.11 hPa. Calculate the mixing ratio assuming an average relative humidity of 65 %. Calculate the relative humidity at the surface. Perform exactly the same calculations for the ice age for a near-surface air temperature of 25 °C in the Tropics. Discuss the water-vapor amount in the atmosphere. Comment on whether the atmosphere was drier or wetter during the ice age than today.

7.6. By simplifying assumptions and applying the principles of conservation of energy and momentum, we can approximate the speed of a density current or temperature difference and the depth of the two fluids as $v_{front} - v_{env} = k\sqrt{g\,H_c(\frac{T_w - T_c}{T_w})}$ where v_{front}, v_{env}, k, g, H_c, T_c, and T_w are the speed of the front of a mesoscale circulation, speed of ambient wind, a dimensionless constant (≈ 1), the acceleration of gravity, the depth of the cold air, and the temperature of the cold and warm air, respectively. Make reasonable assumptions about air temperature for summer and assume a temperature difference of 5 K, and a height of 1 km. Examine the critical conditions under which conditions a circulation could form. Discuss your results with your classmates.

7.7. The upper limit of intensity that a mature tropical cyclone can reach can be estimated by the Carnot cycle as heat is converted to mechanic energy (wind). Consider the ocean as an infinite reservoir of heat at $T_{ocean} = 28\,^{\circ}\mathrm{C}$. At the top of the troposphere, $T_{top} = -75\,^{\circ}\mathrm{C}$. Determine the maximal energy that the tropical cyclone could take. Assume that above the ocean, the relative humidity is equal to 0.8 and surface pressure is 900 hPa. Determine the maximal heat that can be released from the ocean. Determine the available energy for the Carnot cycle. Calculate the maximum wind speed of the tropical cyclone under the assumption that the ratio of the transfer coefficients of heat and friction is equal to 1. Note that there is one main difference. In the atmosphere, the amount of heat is a function of temperature and humidity. For simplicity, do not consider the dependency on humidity.

[31] This estimate was first made by Wallace Broeckner, a well known climatologist and oceanographer, in 1997.

7.8. Get the meteorological surface observation data of a site close to your home town (MESONET is fine for this exercise). Determine the monthly mean values for the various quantities using the available data. If the data allow calculate monthly mean diurnal cycles. For all means determine the higher moments. Analyze the extremes. Discuss the climate of your region in terms of climate phenomena, extremes, frequency of rain days/snow days, means and moments as well as regional and large scale regimes that govern the local climate of your hometown. Compare your local climate report and analysis with those of your classmates. Exchange experiences of local climate with them.

References

Material, concepts, ideas and problems of the following books and articles inspired this chapter. These sources are recommended for further reading.The interested reader is also referred to the various books and journals on climate change and variability as well as the IPCC-reports.

ARCUS (2001) Arctic Research Consortium of the United States. http://www.arcus.org/annual_meetings/arctic_forum_archive/2001/forum2001.pdf. Retrieved 2001

Baumgartner A, Reichel E (1975) World water balance: mean annual global, continental and maritime precipitation, evaporation and runoff. Elsevier, Amsterdam, 348pp

Beck C, Grieser J, Rudolf B (2005) A new monthly precipitation climatology for the global land areas for the period 1951 to 2000. Climate status report 2004, 181–190, German Weather Service, Offenbach. Reprint available at http://gpcc.dwd.de

Berger A, Loutre MF (1991) Insolation values for the climate of the last 10 million years. Quat Sci Rev 10:297–317

Broeckner WS (1997) Thermohaline circulation, the achilles heel of our climate system: will man-made CO_2 upset the current balance? Science 278:1582–1588

Canfield DE (2014) Oxygen – A four billion year history. Princeton University Press, Princeton and Oxford, 196pp

Dingman SL (1994) Physical hydrology. Macmillan, New York/Oxford/Singapore/Sydney, 557pp

Essenwanger OM (2001) Classification of climates, world survey of climatology 1C, General climatology. Elsevier, Amsterdam, 102pp

Etling D, Hantel M, Kraus H, Schönwiese C-D (1987) Climatology. Landolt-Börnstein: numerical data and functional relationships in science and technology. New series/geophysics, vol 4. Berlin/Heidelberg/New York/London/Paris/Tokyo, 199pp

Hastenrath S (1996) Climate dynamics of the tropics. Kluwer Academic, Dordrecht/Boston/London, 488pp

Foken T (2014) Micrometeorology (trans. Nappo CJ). Springer, Heidelberg, 350pp

Gregory KJ, Walling DE (1973) Drainage basin form and process: a geomorphological approach. Wiley, Chicago, 456pp

Hantel M (1997) Klimatologie. In: Bergmann-Schaefer: Lehrbuch der Experimentalphysik, Bd. 7, Erde und Planeten. de Gruyter, Berlin, pp 311–426

Hupfer P, Kuttler W (2006) Witterung und Klima – Eine Einführung in die Meteorologie und Klimatologie. Teubner Verlag, Wiesbaden, 554pp

Jaeger L (1976) Monatskarten des Niederschlags für die ganze Erde. Berichte des Deutschen Wetterdienstes, Offenbach a. M., No. 139, Bd., 18, 38pp

Keeling CD, Whorf TP (1998) Atmospheric CO_2 concentrations – Mauna Loa Observatory, Hawaii, 1958 $\approx$ 1997. ORNL NDP-001, Oak Ridge Natl. Lab., Oak Ridge

Köppen W, Geiger R (1930) Handbuch der Klimatologie. Band I Das geographische System der Klimate. Bornträger Verlag, Berlin
Kottek M, Grieser J, Beck C, Rudolf B, Rubel F (2006) World map of the Köppen-Geiger climate classification updated. Meteorol Zeitschr 15:259–263
Kramer E, Hupfer P, Chmielewski F-M (1989) Das Klima von Berlin. Akademie Verlag, Berlin, 288pp
Kramm G, Dlugi R (2011) Scrutinizing the atmospheric greenhouse effect and its climatic impact. Nat Sci 3:971–998
Kraus H (2000) Die Atmosphäre der Erde. Eine Einführung in die Meteorologie. Vieweg, Braunschweig, Wiesbaden, 470pp
Labitzke KG, van Loon H (1999) The stratosphere, history and relevance. Springer, Heidelberg, 179pp
Liljequist GH, Cehak K (1979) Allgemeine Meteorologie. Friedrich Vieweg und Sohn, Braunschweig, 396pp
Marquardt C (1998) Die tropische QBO und dynamische Prozesse in der Stratosphäre. PhD Thesis, Met. Abh. FU-Berlin, Serie A, Band 9/Heft 4, Verlag Dietrich Reimer Berlin, Berlin, 260pp
Mölders N (2005) Feedbacks at the hydrometeorological interface. In: Bronstert A, Carrera J, Kabat P, Lütkemeier S (eds) Couppled models for the hyrological cycle. Springer, Heidelberg, pp 193–214
Mölders N (2012) Land-use and land-cover changes – impact on climate and air quality. Atmospheric and oceanographic sciences library 44. Springer, Dordrecht. doi:10.1007/978-94-007-1527-1 3
Mölders N, Kramm G (2007) Influence of wildfire induced land-cover changes on clouds and precipitation in Interior Alaska – a case study. Atmos Res 84:142–168
Naujokat B (1986) An update of the observed quasi-biennial oscillation of the stratospheric winds over the tropics. J Atmos Sci 43:1873–1877
NCEP reanalysis data (2014). http://www.esrl.noaa.gov/psd/cgi-bin/data/composites/comp.pl
Neelin JD (2010) Climate change and climate modeling. Cambridge University Press, Cambridge/New York, 304pp
Orlanski I (1975) A rational subdivision of scales for atmospheric processes. Bull Am Meteorol Soc 56:527–530
PaiMazumder D, Mölders N (2009) Theoretical assessment of uncertainty in regional averages due to network density and design. J Appl Meteor Clim 48:1643–1666
Peixto JP, Oort AH (1992) Physics of climate. Springer, New York, 520pp
Robock A (2000) Volcanic eruptions and climate. Rev Geophys 38:191–219
Rohli RV, Vega A (2008) Climatology. Jones and Bartlett, Sudbury, 432pp
Rosenfeld D, Sherwood S, Wood R, Donner L (2014) Climate effects of aerosol-cloud interactions. Science 24:379–380
Trenberth KE (1992) Climate modeling. Cambridge University Press, Cambridge, 788pp
van Andel TH (1995) New views of an old planet. Cambridge University Press, Cambridge, 439pp
von Storch H, Zwiers FW (1999) Statistical analysis in climate research. Cambridge University Press, Cambridge, 484pp
Walsh JE (1984) Snow cover and atmospheric variability: changes in the snow covering the earth's surface affect both daily weather and long-term climate. Am Sci 72:50–57
Washington WM, Parkinson CL (2005) Introduction to three-dimensional climate modeling. University Science Books, Sausalito, 353pp
Weickmann H (1963) A realistic appraisel of weather control. J Appl Math Phys 14:528–543
Weischet W (1994) Eine Einführung in die allgemeine Klimatologie. Teubner Verlag, Stuttgart, 276pp
World Meteorological Organization (2014) Climate. http://www.wmo.int/pages/themes/climate/index_en.php

Appendix A
Simple Mathematical Concepts for Meteorology

A.1 Kinematics of a Fluid

Let $\mathbf{r}(t) = (x(t), y(t), z(t))$ be the trajectory of an air parcel. It is determined by the coordinates of the air parcel and the motion field $\mathbf{v}(\mathbf{r}, t)$. For a fixed initial location the vector $d\mathbf{r} = (dx, dy, dz)$ describes the incremental displacement of the air parcel during the time interval dt. In general, the velocity is defined as change of position per time given by $\mathbf{v} = \frac{d\mathbf{r}}{dt}$ with the components $\mathbf{v} = (u, v, w) = (\frac{dx}{dt}, \frac{dy}{dt}, \frac{dz}{dt})$. At any time the velocity field defines the **streamlines** that are everywhere tangential to $\mathbf{v}(\mathbf{r}, t)$.

A.2 The Material Derivative

Acceleration is defined as the change in velocity per time. The acceleration in x-direction, for instance, is given by

$$\frac{d^2x}{dt^2} = \frac{\partial u}{\partial x}\frac{dx}{dt} + \frac{\partial u}{\partial y}\frac{dy}{dt} + \frac{\partial u}{\partial z}\frac{dz}{dt} + \frac{\partial u}{\partial t} \tag{A.1}$$

By applying the definition of velocity at a fixed location (e.g. $u = \frac{\partial x}{\partial t}$), the above equation can be written as

$$\frac{d^2x}{dt^2} = \frac{\partial u}{\partial t} + u\frac{\partial u}{\partial x} + v\frac{\partial u}{\partial y} + w\frac{\partial u}{\partial z}. \tag{A.2}$$

Using the definitions of the **nabla-operator**,

$$\nabla = \left(\frac{\partial}{\partial x}, \frac{\partial}{\partial y}, \frac{\partial}{\partial z}\right) \tag{A.3}$$

N. Mölders and G. Kramm, *Lectures in Meteorology*, Springer Atmospheric Sciences,
DOI 10.1007/978-3-319-02144-7, © Springer International Publishing Switzerland 2014

and a vector, $\mathbf{v} = (u, v, w)$, yields

$$\frac{d^2x}{d\,t^2} = \frac{\partial u}{\partial t} + \mathbf{v} \cdot \nabla u \Longleftrightarrow \frac{d\,u}{dt}. \tag{A.4}$$

The term $\nabla \cdot \mathbf{v}$ is a **scalar product**.

Analogously, the y- and z-components of acceleration can be derived. In vector form, acceleration reads

$$\mathbf{a} = \frac{d^2\mathbf{r}}{dt^2} = \frac{\partial \mathbf{v}}{\partial t} + (\mathbf{v} \cdot \nabla)\mathbf{v} = \frac{d\,\mathbf{v}}{dt}. \tag{A.5}$$

The identity (Euler operator)

$$\frac{d}{dt} = \frac{\partial}{\partial t} + \mathbf{v} \cdot \nabla \tag{A.6}$$

is the **material derivative** or **substantial derivative**.

In contrast to the rate of change at a fixed location, $\frac{\partial}{\partial t}$, (local derivation), the material derivative represents the rate of change with respect to time following the motion. The term $(\mathbf{v} \cdot \nabla)\mathbf{v}$ contributes to the material derivative nonlinearly. Therefore, the behavior of the atmosphere is difficult to forecast as nonlinear systems behave chaotically.

Example. Assume a cold air mass flows down from an ice cap.[1] Determine the wind speed the air mass will reach at the bottom a minute later if its acceleration is $0.5\,\mathrm{m\,s^{-2}}$.

Solution. Acceleration is given by $\mathbf{a} = \frac{d\mathbf{v}}{dt}$ where t is time and $\mathbf{v}$ is velocity. Rearranging and inserting the values yields $\mathbf{v} = \frac{0.5\,\mathrm{m\,s^{-2}}}{60\,\mathrm{s}} = 30\,\mathrm{m\,s^{-1}}$.

A.2.1 Divergence and Convergence

Sometimes only the horizontal components of the wind field are of interest and the following identity can describe the horizontal divergence[2]

$$\nabla \cdot \mathbf{v_H} = \frac{\partial u}{\partial x} + \frac{\partial v}{\partial y}. \tag{A.7}$$

[2]In many books $div\mathbf{v_H}$ is used to indicate the divergence.

A divergence of the horizontal wind field, for example, will exist if u increases with x and v grows with y, or if u increases with x and v decreases with y, but the net-effect $\frac{\partial u}{\partial x} + \frac{\partial v}{\partial y}$ being positive. Imagine that the divergence of $\mathbf{v}$ is accompanied by a change in mass. In our example, this would mean a loss of mass. A convergence would mean the opposite.

Example. Assume winds, $\mathbf{v} = (5, 3, 0)$, $\mathbf{v} = (5, -3, 0)$, $\mathbf{v} = (3, -5, 0)$, and all with a specific mixing ratio of $10\,\mathrm{g\,kg^{-1}}$ moving over a distance of 2 km. Is there moisture convergence or divergence?

Solution. As the vertical wind component is zero and wind speed remains constant with time, the moisture flow is given by $(\frac{\partial u}{\partial x} + \frac{\partial v}{\partial y})q = (\frac{5\,\mathrm{m\,s^{-1}}}{2{,}000\,\mathrm{m}} + \frac{3\,\mathrm{m\,s^{-1}}}{2{,}000\,\mathrm{m}})10\,\mathrm{g\,kg^{-1}} \approx 0.04\,\mathrm{g\,kg^{-1}\,s^{-1}}$, $0.01\,\mathrm{g\,kg^{-1}\,s^{-1}}$, and $-0.01\,\mathrm{g\,kg^{-1}\,s^{-1}}$ for $\mathbf{v} = (5, 3, 0)$, $\mathbf{v} = (5, -3, 0)$ and $\mathbf{v} = (3, -5, 0)$, respectively. The positive values mean moisture divergence, the negative value moisture convergence.

A.3 Rotation

Another frequent form of motion is rotation,[3] which can be mathematically expressed by using the definition of the nabla-operator and the unit vectors

$$\nabla \times \mathbf{v} = \zeta\mathbf{i} + \eta\mathbf{j} + \xi\mathbf{k} \tag{A.8}$$

with

$$\zeta = \frac{\partial w}{\partial y} - \frac{\partial v}{\partial z} \tag{A.9}$$

$$\eta = \frac{\partial u}{\partial z} - \frac{\partial w}{\partial x} \tag{A.10}$$

$$\xi = \frac{\partial v}{\partial x} - \frac{\partial u}{\partial y}. \tag{A.11}$$

Tornados and tropical storms are examples where rotation becomes important.

[3] Many books use $rot\,\mathbf{v}$ or $curl\,\mathbf{v}$ instead of $\nabla \times \mathbf{v}$.

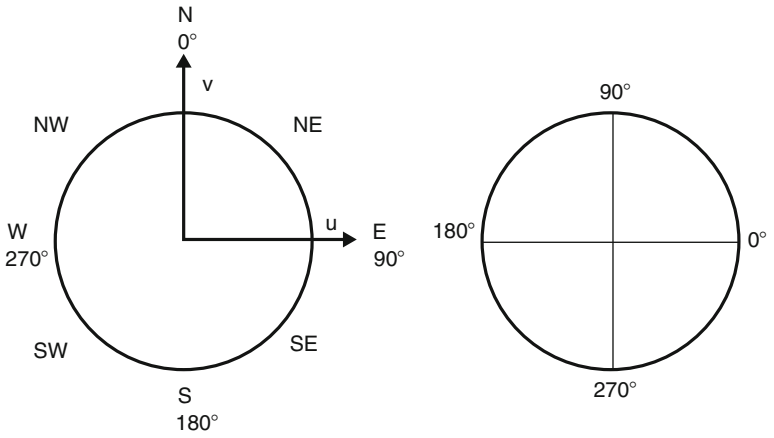

Fig. A.1 Schematic view of wind directions in degrees (*left*) and counting of degrees in geometry (*right*) for comparison

Example. Calculate the rotation of a dust devil with 0.05, 0.08, and 2 m in extension in x-, y- and z-direction and a of a wind vector, $\mathbf{v} = (5, 6, 2)\,\mathrm{m\,s^{-1}}$ in x, y and z direction.

Solution. $\nabla \times \mathbf{v} = (\frac{2}{0.8} - \frac{6}{2}, \frac{5}{2} - \frac{2}{0.05}, \frac{6}{0.05} - \frac{5}{0.08})$.

A.4 Scalar Quantities

Scalar quantities (e.g. density, pressure, temperature, etc.) are only defined by an amount, while **vectors** are quantities that are defined by an amount and a direction. In this sense, we distinguish between wind speed (the amount) and wind direction when taking about wind velocity (the vector). To indicate a vector bold letters, underlining, or an arrow above are used.

In Cartesian coordinates, the x-axis points to the east, the y-axis points to the north (Fig. A.1), and the z-axis points upwards (against gravity) according to the traditional definition in meteorology (Chap. 6). The components of the **wind vector** may be expressed by u, v, and w.

By use of the azimuth angle λ and the zenith angle φ we obtain

$$u = |\mathbf{v}| \sin\varphi cos\lambda \qquad v = |\mathbf{v}| \sin\varphi \sin\lambda \qquad w = |\mathbf{v}| \cos\varphi \tag{A.12}$$

By using the components the wind vector can be expressed by

$$\mathbf{v} = u\mathbf{i} + v\mathbf{j} + w\mathbf{k} \tag{A.13}$$

where **i**, **j**, and **k** are the **unit vectors** given by

$$\mathbf{i} = (1, 0, 0), \tag{A.14}$$

$$\mathbf{j} = (0, 1, 0), \tag{A.15}$$

$$\mathbf{k} = (0, 0, 1). \tag{A.16}$$

In this notation, wind speed reads

$$|\mathbf{v}| = \sqrt{u^2 + v^2 + w^2} \tag{A.17}$$

A.5 Changes of Field Quantities with the Field Coordinates

Partial differentials describe changes in direction of one field coordinate only. Let us assume an arbitrary property α of an air parcel. We can write for its individual displacement in one direction at constant other directions

$$\frac{\partial \alpha}{\partial x}|_{y,z,t}, \tag{A.18}$$

$$\frac{\partial \alpha}{\partial y}|_{x,z,t}, \tag{A.19}$$

$$\frac{\partial \alpha}{\partial z}|_{x,y,t}, \tag{A.20}$$

$$\frac{\partial \alpha}{\partial t}|_{x,y,z}. \tag{A.21}$$

These derivations are called **local derivations** or **local changes** because only one coordinate varies while the other keep being constant.

Continuous observation of the concentration of an inert trace gas at a station provides a function $C(x, y, z, t)$ where x, y, z are constant and t changes. The associated registration provides $\frac{\partial C}{\partial t}$.

An example of a change in space coordinate is the temperature profile provided by a radiosonde on a calm day, and without temporal change in temperature.[4] These measurements deliver $T(z)$ and $\frac{\partial T}{\partial z}$.

A velocity $\mathbf{v} = \frac{d\mathbf{r}}{dt}$ with $\mathbf{r} = x\mathbf{i} + y\mathbf{j} + z\mathbf{k}$ describes the motion of a particle

$$\mathbf{v} = \frac{d\mathbf{r}}{dt} = \frac{dx}{dt}\mathbf{i} + \frac{dy}{dt}\mathbf{j} + \frac{dz}{dt}\mathbf{k} \tag{A.22}$$

where $\frac{dx}{dt} = u$, $\frac{dx}{dt} = v$, and $\frac{dz}{dt} = w$.

[4] In nature, radiosondes usually drift.

Another question is how the characteristics α of a parcel will change with time without holding the coordinates constant if the parcel moves. It is the change of α that a moving particles experiences or that we would find if one traveled on the particle. This change is called **individual change** or derivation and the differential is denoted to as individual or **total derivation** (or differential).

Regarding the change of the characteristic α of a particle on its way from a point $P_1(x, y, z, t)$ to a point $P_2(x + dx, y + dy, z + dz, t + dt)$ shows the relationship between the partial and the total differential

$$d\alpha = \frac{\partial \alpha}{\partial t}|_{x,y,z} dt + \frac{\partial \alpha}{\partial x}|_{y,z,t} dx + \frac{\partial \alpha}{\partial y}|_{x,z,t} dy + \frac{\partial \alpha}{\partial z}|_{x,y,t} dz \tag{A.23}$$

Using the components of the wind vector and rearranging results in

$$\frac{d\alpha}{dt} = \frac{\partial \alpha}{\partial t} + u\frac{\partial \alpha}{\partial x} + v\frac{\partial \alpha}{\partial y} + w\frac{\partial \alpha}{\partial z} = \frac{\partial \alpha}{\partial t} + \underbrace{\mathbf{v} \cdot \nabla \alpha}_{convective\ changes} \tag{A.24}$$

where $\nabla = \frac{\partial}{\partial x} + \frac{\partial}{\partial y} + \frac{\partial}{\partial z}$. The above equation means that the total differential $\frac{d\alpha}{dt}$ consist of the local differential $\frac{\partial \alpha}{\partial t}$ and the velocity components related (convective) changes of α.

When at a place the field quantity does not change with time $\frac{\partial \alpha}{\partial t} = 0$, the field quantity behaves stationary.[5] The change on a particle path is called **Lagrangian** and looks at $\frac{d\alpha}{dt}$, while the change at a fixed place is named **Eulerian** and looks at $\frac{\partial \alpha}{\partial t}$.

[5]Think of a sink that is filled and the water keeps on running. The access water will run out at the second outlet and the water level keeps the same. Although the water is in motion all the time the system is in a stationary state.

Appendix B
Meteorological Measurements

This appendix gives a very brief glimps on how meteorological quantities are measured and the typical range of magnitude. This appendix is more thought as a help for the student to develop a feeling for assessment of whether calculated values fall into the right ballpark and for uncertainty in observations than being a complete survey. The interested reader is referred to specific literature on meteorological measurements, and the devices mentioned here. See the reference section for some suggestions.

B.1 Temperature Measurements

In Chap. 1, temperature was defined as the thermal condition of a medium. The zeroth law of thermodynamics (Chap. 2) introduced temperature as a state variable, and defines how to determine temperature, namely by establishing thermodynamic equilibrium between the system and sensor.

The second law of thermodynamics provides a definition of temperature independent of the properties of the material. A reversibly performed cycle process yields $\frac{\Delta q_1}{T_1} = \frac{\Delta q_2}{T_2} \Rightarrow \frac{\Delta q_1}{\Delta q_2} = \frac{T_1}{T_2} = \frac{T_2+\Delta T}{T_2}$. When ΔT is fixed (e.g. in steps of degree Celsius on the Celsius scale) and T_2 is chosen as the freezing point of water, the ratio $\Delta q_1/\Delta q_2$ determines the value of the absolute temperature T_2. The absolute temperature scale defined by the second law of thermodynamics is the same as that deduced earlier from the equation of state and kinetic theory of heat. This means it provides the absolute zero point of the scale to measure temperature.

Thermometers measure temperature either electrically or mechanically (Fig. B.1). They make use of the change in characteristics of materials in response to a temperature change, i.e. an expansion or altered resistance.

N. Mölders and G. Kramm, *Lectures in Meteorology*, Springer Atmospheric Sciences,
DOI 10.1007/978-3-319-02144-7, © Springer International Publishing Switzerland 2014

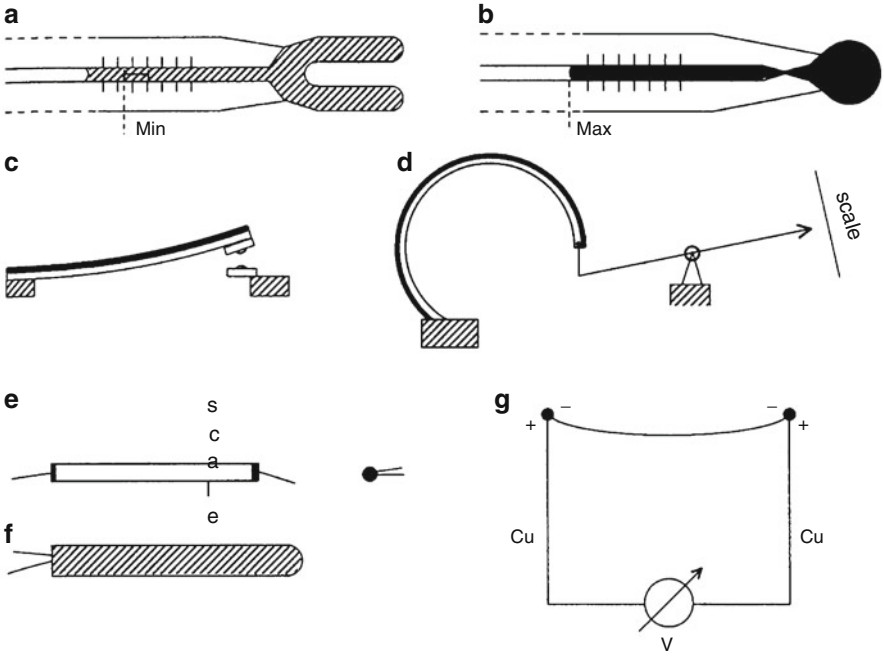

Fig. B.1 Schematic view of various thermometer types (**a**) minimum thermometer, (**b**) maximum thermometer, (**c**) bimetal thermometer serving as a contact element, (**d**) bimetal thermometer with scale, (**e**) thermistor, (**f**) platin wire glas thermometer, (**g**) thermo-element (From Kraus 2000)

B.1.1 Mechanical Thermometers

The basic equation for temperature-dependent volume expansion is $V(T) = V_0 (1 + \gamma T)$ where T is the temperature in °C, V_0 stands for the volume at 0 °C, and γ is the expansion coefficient. As the expansion coefficient depends on the respective material, different materials (e.g. liquids, gaseous, solid) require other scaling. The expansion coefficient of mercury,[1] for instance, is $18 \cdot 10^{-5}\,\mathrm{K}^{-1}$.

B.1.2 Liquid-in-Glass Thermometer

The liquid-in-glass thermometer was developed in the late 1600s. When temperature increases, the molecules of the liquid become more active. Thus, the liquid expanses, and rises in the capillary. This movement is calibrated against an established scale.

[1]The expansion of mercury with temperature means that pressure measurements carried out with a mercury barometer have to be temperature corrected.

Sometimes the highest and lowest temperatures are of interest. A **maximum thermometer** contains mercury and has a narrowed passage called the constriction in the bore of the glass tube just above the bulb. When temperature increases the mercury expanses and passes the constriction. As temperature falls, the constriction prevents the mercury from returning into the bulb. Thus, the mercury stays at highest temperature reached between two resets. Shaking easily resets the thermometer to air temperature. Maximum thermometers are applied, for instance, for determining daily maximum temperature or measuring fever.

A **minimum thermometer** contains a liquid of low density (e.g. alcohol), and a small dumbbell-shaped index at the top of the liquid. When temperature falls, the surface tension of the meniscus moves the index towards the bulb. As temperature rises, the liquid flows past the index remaining the index at the lowest point of temperature reached since the last reset of the thermometer. Since the index is subject to gravity and tilting resets the thermometer, a minimum thermometer has always to be installed horizontally. Minimum thermometers serve to determine the lowest temperature during a given period (e.g. year, season, month, day).

B.1.3 Gas Thermometer

By using the equation of state the change in pressure of a gas can be related to the change in temperature by $\Delta p = \frac{mR}{V}\Delta T = \frac{p_0}{T_0}\Delta T$ or $\frac{\Delta p}{p_0} = \frac{\Delta T}{T_0}$.

B.1.4 Bimetal Thermometer

A **thermograph** is an instrument that measures temperature continuously. It uses that the curvature of a bimetal plate varies with temperature. The curvature of the bimetal strip can be applied to move a pen that writes on a calibrated chart, which is located on a clock-driven rotating drum. Thermographs do not reach the accuracy of mercury thermometers. Therefore, one has to check and correct thermograph records routinely by comparing them with an accurate, similarly exposed thermometer.

B.1.5 Electrical Thermometer: Thermo-elements

A **thermistor** is a thermally sensitive resistor whose resistance to current flow increases as temperature decreases. The current drives a meter that displays the flow of current or that is calibrated in degrees temperature. Thermistors are rapid temperature sensors to capture quick temperature changes, for instance, on weather balloons.

For most thermistors that are semi-conductors the relationship between temperature, T, and resistance, R, follows $R = A\exp(\frac{b}{T})$ with $A = \frac{1}{R}\frac{dR}{dT} = -\frac{b}{T^2}$ where A and b are constants. For Platin-thermistors the relationship is $R = R_0(1 + \alpha T)$ with $\alpha = \frac{1}{R_0}\frac{dR}{dT} \approx 4 \cdot 10^{-3}\,\mathrm{K}^{-1}$ and T in °C. The main disadvantage of a thermistor is its non-linear characteristic.

B.1.6 Radio Acoustic Sounding System and Sodars

The **Radio Acoustic Sounding System** (RASS) transmits a strong, short acoustic tune vertically upwards. This sound travels as a compression wave with the speed of sound, v_{sound}, upwards in the atmosphere. Since sound propagation depends on the virtual temperature (Sect. 2.67), profiles of temperature can be calculated for the received return signal as $T_v = (M/cR^*)v_{sound}^2$, where M is the molecular weight, c is specific heat, and R^* is the universal gas constant. The RASS measures the acoustic speed $v_{RASS} = (v_{sound} + w)$, where w are vertical motions. Thus, vertical air motion can cause measurement errors. To correct this error most RASS systems measure the sound and vertical air speed concurrently. Some RASS apply this correction in real time.

SOnic Detection and Ranging (**sodar**) applies a similar principle and can provide measurements of temperatures in the lower atmospheric boundary layer.

B.1.7 Temperature Scales

In the US, the public give the temperature in degrees Fahrenheit[2] defined by Fahrenheit in 1714. He put the lowest temperature reached by a mixture of salt, water and ice to 0 °F and the temperature of a human body to 96 °F.[3] On this scale, the freezing point of water is at 32 °F and the boiling point of water at 212 °F.

Scientists use the Celsius scale[4] or the absolute temperature scale often denoted as Kelvin scale. On the Celsius scale, the freezing point of water is at 0 °C and the boiling point of water is at 100 °C. The Celsius-Fahrenheit relationship is given by

$$^\circ\mathrm{F} = (1.8 \cdot {}^\circ\mathrm{C}) + 32, \tag{B.1}$$

$$^\circ\mathrm{C} = \frac{^\circ\mathrm{F} - 32}{1.8}. \tag{B.2}$$

[2]Gabriel Daniel Fahrenheit German physicist 1686–1736

[3]Later human's body temperature was found to be at 98.6 °F.

[4]The Celsius scale was defined by the Swedish astronomer and biologist Anders Celsius (1701–1744).

Many scientific questions require the absolute temperature scale. It is similar to the Celsius scale in so far as the steps in degree are the same, but the melting point is set at 273.15 K and the boiling point of water is equal to 373.15 K. The reason is that the zero point of temperature is set to the point where all motion of the molecules is absolute zero (Chap. 2). No negative temperatures occur on the Kelvin scale. The relationship between the Celsius and Kelvin scale is $T\,in\,°C = T\,in\,K - 273.15$ or $T\,in\,K = 273.15 + T\,in\,°C$.

On the seldom used Reaumir-scale,[5] the melting and boiling points of water are at 0 and 80 °R, respectively.

B.1.8 Extreme Values

The lowest temperature measured in the USA was −62.1 °C at Prospect Creek (Alaska) on 23 January 1971. The coldest summer average temperature of the USA was found at Barrow (Alaska) with 2.2 °C in the time from 1941 to 1970. The world's highest annual mean temperature was reported to be 34.4 °C at Dallol, Ethiopia.

B.1.9 Instrument Shelter

The accuracy of a temperature reading depends not only on the design of the instrument and its quality, but also on the place of the instrument. A thermometer absorbs more radiation than the air in its surrounding (Chap. 4). Therefore, it must be installed away from exposure to direct sunlight and heat sources in an area where the air is able to freely move around the thermometer. The ideal place is an instrument shelter (Fig. B.2), a white box located in 2 m above grass far away from all other obstacles that affect the free wind flow. The shelter guarantees free movement of air while protecting the instrument from direct sunlight. The shelter is orientated as shown in Fig. B.2.

B.2 Measuring Humidity

For near-surface observations humidity is typically observed at 2 m height. An instrument to measure humidity are called a **hygrometer** (*Greek* hygros = moist). Out of the variety of devices to measure humidity here only the most common ones are introduced briefly.

[5]The Reaumir-scale is named after the French physicist and biologist Rene Antoine Ferchault de Reaumir (1683–1757)

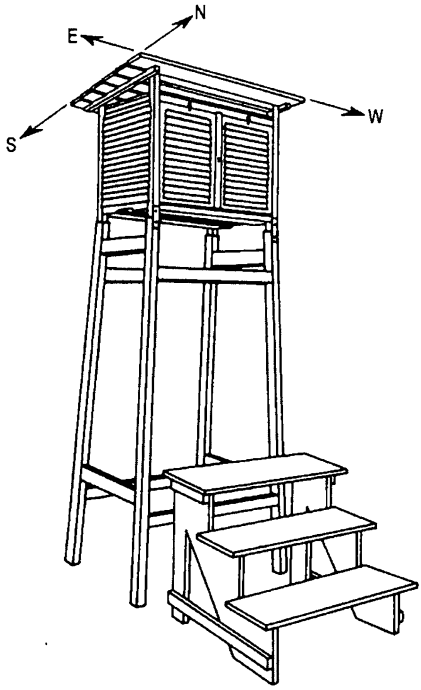

Fig. B.2 Schematic view of an instrument shelter as used in the German Weather Service (From Hupfer and Kuttler 2006)

B.2.1 Psychrometer

The psychrometer (*Greek* psychros = cool, cold) is a simple device consisting of two ventilated thermometers installed close to each other. For one of them, called the **wet (bulb) thermometer**, a moist tissue covers the sensor. Distilled water is provided to the tissue automatically.

The wet thermometer measures the **wet temperature**, T_m; the dry thermometer measures air temperature, T_a. At subsaturation, water evaporates proportional to the humidity conditions of the ambient air. The evaporative cooling causes the mercury column of the wet bulb thermometer to drop. The dry bulb thermometer shows the actual air temperature. The wet blub thermometer provides the dewpoint temperature. The temperature difference between the dry and wet thermometer reading gives the psychrometric depression. By using the dewpoint temperature, we can calculate the actual water-vapor pressure of the air and relative humidity. There also exist tables and online humidity calculators for easy conversion.

In general, the radiation, $R_s^{\downarrow}$, turbulent exchange of energy, between the surface and the air (H, L_vE) and the heat conduction from the surface of the thermometer towards its interior, G, should balance, i.e. $R_s^{\downarrow} - G - H - L_vE = 0$. The quantities

H and L_vE can be expressed by difference approaches using the temperatures observed at the wet and dry thermometer and the saturated (moist) and actual air specific mixing ratios $H = \alpha(T_m - T_a)$ and $L_vE = \frac{\alpha}{c_p} L_v(q_s - q) = \frac{0.622 L_v}{p c_p} \alpha(e_s - e)$. Herein, the term $A := \frac{p c_p}{0.622 L_v}$ is called the **psychrometer constant**, and L_v is the latent heat of vaporization. The energy balance equation can be written as

$$R_s^{\downarrow} - G + \alpha((T_m - T_a) + \frac{1}{A}(e - e_s)) = 0 \,, \tag{B.3}$$

$$\frac{A}{\alpha}(R_s^{\downarrow} - G) + A(T_a - T_m) + e - e_s = 0 \,. \tag{B.4}$$

Rearranging leads to the equation of a real psychrometer

$$e = e_s - A(T_a - T_m) - \frac{A}{\alpha}(R_s^{\downarrow} - G) \,. \tag{B.5}$$

The last term on the right hand side requires additional measurements as G is proportional to $\frac{\partial T_m}{\partial t}$ and $R_s^{\downarrow} \approx 0$ because of the use of the instrument shelter. Ventilating and protecting the thermometers from radiation ensures that this term can be hold negligibly small. For conditions close to $L_vE = -G$ the **ideal psychrometer equation** can be applied

$$e = e_s - A(T_a - T_m) \tag{B.6}$$

i.e. the water vapor pressure can be gained by measuring the wet and dry temperatures.

Since the latent heat of condensation/sublimation and the specific heat capacity at constant pressure slightly depend on temperature (Chap. 2), the psychrometer constant does so too. At $p = 1{,}013.25\,\text{hPa}$, it amounts $0.654\,\text{hPa}\,\text{K}^{-1}$ and $0.578\,\text{hPa}\,\text{K}^{-1}$ for a wet and a frozen tissue, respectively. Due to the different saturation pressures over water and ice, ice may grow on the tissue. Thereby the release of latent heat warms the thermometer, and the wet thermometer can even become warmer than the environment (0.35 K at maximum). This effect has to be considered when determining vapor pressure. Due to the complicate form of the vapor-pressure curve (Sect. 2.8.3), this consideration has to be made iteratively.

Another possibility to determine humidity is the Assmann aspirator psychrometer (Fig. B.3). It measures the air temperature and the humidity by two identical mercury thermometers. The wet bulb thermometer is enclosed in a wick, and has to be moistened prior to use of the instrument. The thermometers are arranged in a parallel position both in their own tube. The bulbs are protected from radiation

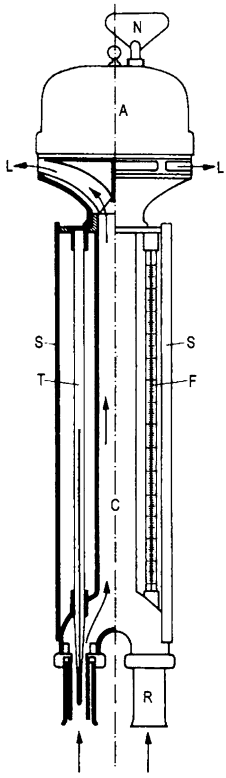

Fig. B.3 Schematic view of an aspiration psychometer. The letters T, F, N, A, L, S, R, and C denote to the dry thermometer, the wet thermometer, screw to wind up the clock, aspirator, vents, radiation protection, double sided air intake pipe, that surrounds both thermometers (not shown on the *left*) and the connection pipe to the aspirator (From Hupfer and Kuttler 2006)

by polished radiation shields. The principle is the same as for the wet and dry thermometer discussed above. While in a shelter the wind serves for ventilation (or not), an Assmann aspiration psychometer ventilates both thermometer bulbs during the measurements with an average speed of $3\,\mathrm{m\,s^{-1}}$.

Example. Psychrometer measurements showed 15.8 and 26.8 °C at the wet and dry thermometers. Determine the relative humidity and mixing ratio assuming an air and saturated water vapor pressure of 1,013.25 and 17.9214 hPa, respectively.

Solution. With 1,013.25 hPa $A = 0.654\,\mathrm{hPa\,K^{-1}}$ and the psychrometer equation $e_{air} = 17.9214\,\mathrm{hPa} - 0.654\,\mathrm{hPa\,K^{-1}}(26.8 - 15.8)\,K = 10.727\,\mathrm{hPa}$. With $rh = \frac{e_{air}}{e_s} = \frac{10.7274\,\mathrm{hPa}}{17.9214\,\mathrm{hPa}} \approx 0.3051$, $RH = 30.51\,\%$ and $r = 0.622\frac{e_{air}}{p - e_{air}} = 0.622\frac{10.727\,\mathrm{hPa}}{1{,}013.25 - 10.727\,\mathrm{hPa}} = 0.0066554\,\mathrm{kg^{kg-1}}$.

B.2.2 Hair Hygrometer

Hair hygrometers base on the effect of hygroscopy and exist since the fifteenth century. In 1783, de Saussure[6] developed a measuring device for humidity using human hair as a sensor.[7] Hair like a bunch of other organic materials is hygroscopic and takes up water vapor to be in equilibrium with its environment.[8] Hair takes up water vapor from the air and increases non-linearly by about 2.5 % for a humidity increasing from 0 to 100 %. Ventilation ensures that the hair has the same temperature than the air because relative humidity depends on temperature (Chap. 2). Due to hysteresis effects, the error in measuring relative humidity by a hygrometer may be 3 %.

B.2.3 Optical Hygrometer

Optical hygrometers measure the absorption bands of water vapor (see Chap. 4 for the physical details). The Lyman-Alpha-hygrometer, for instance, uses the Lyman-α-radiation in the ultra-violet spectral range. Here, the absorption coefficient of water vapor exceeds that of other atmospheric gases by several orders of magnitude.

B.2.4 Extreme Values

The world's highest humidity observed was a dew point of 34 °C at Sharjah in Saudi Arabia in July of the years 1962–1966. The world's highest average afternoon dew point was found in Assab, Ethiopia (28.9 °C) in June.

B.3 Pressure Measurements

There are three different types of **barometers** (*Greek* barys = heavy) for pressure measurements.

---

[6] Horace Benedict de Saussure Swiss natural scientist 1740–1799.

[7] This type of hair hygrometer served to measure relative humidity in the network of *Societas Meteorologica Palatina* an organization that did meteorological observation in the area of Baden-Württemberg (south-west Germany).

[8] The sensitivity of hair to air humidity can be easily observed with curly hair that looks more curly when it is wet and more straight when it is dry.

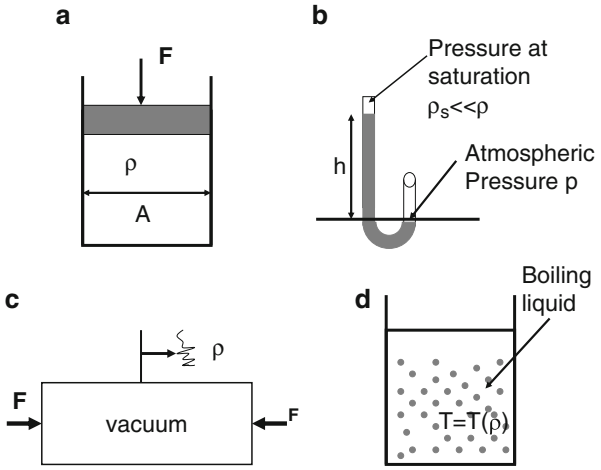

Fig. B.4 Schematic views of the (**a**) principle, and some devices to measure pressure: (**b**) liquid barometer, (**c**) aneroid barometer, and (**d**) hypsometer

B.3.1 Liquid Barometer

A liquid barometer is a half-open transparent straight or U-shaped pipe typically filled with mercury or alcohol. The pipe is upside down in a reservoir of the liquid without allowing the liquid to leave the pipe (Fig. B.4). The result is a small vacuum in the upper part of the pipe. The position of the liquid in the column is in equilibrium with the atmospheric pressure experienced by the liquid in the reservoir. The position changes in response to air pressure. After putting a scale on the pipe, pressure can be determined by $p = \rho g h$, where h is the observed height of the column, and ρ is the density of the liquid. At normal pressure, $T = 0\,°\mathrm{C}$, and normal gravity acceleration, the height of the column amounts to 0.760 and 10.33 m for mercury ($\rho_{Hg} = 13{,}595\,\mathrm{kg\,m^{-3}}$) and water ($\rho_{H_2O} = 1{,}000\,\mathrm{kg\,m^{-3}}$), respectively.

Example. A mercury barometer was calibrated at 20 °C in Pa. At 40 °C the reading is 1,025 hPa. Assume that the glass and scale material expand negligibly. Consider that heat expands materials, and determine the real pressure. Comment on the real pressure.

Solution. At calibration temperature of 20 °C the pressure $p_1 = 102{,}500\,\mathrm{Pa}$ requires a mercury height h_1. Thus, the label 102,500 Pa is set. At $p_1 = h_1\rho_1 g$, the density of mercury is ρ_1 at 20 °C. At 40 °C the changed density ρ_2 is in equilibrium with p_2. Thus, $p_2 = h_1\rho_2 g$. Consequently, $p_2/p_1 =$

(continued)

(continued)

$\rho_2/\rho_1 = v_1/v_2$. After rearranging and inserting the expansion factor $v = v_0(1+\gamma\vartheta)$ one obtains $p_2 = p_1(1+\gamma\vartheta_1)/(1+\gamma\vartheta_2) = 102{,}500\,\text{Pa}(1+182.2\cdot 10^{-6}\,\text{m}^3\,\text{m}^{-3}\,\text{K}^{-1}20\,°\text{C})/(1+182.2\cdot 10^{-6}\,\text{m}^3\,\text{m}^{-3}\,\text{K}^{-1}40\,°\text{C}) = 102{,}129\,\text{Pa}$. The real pressure is lower than the measured value because the density of mercury decreased in response to the heating.

B.3.2 Aneroid Barometer

The aneroid barometer applies a partially evacuated metal chamber that compresses/expanses as pressure increases/decreases (Fig. B.4). The chamber can be easily connected with a recording mechanism and the resulting instrument is called the barograph. Barographs are often used to record flight altitude in aircrafts, or mountain climbing.

B.3.3 Boiling Barometer

The principle of a boiling barometer is to determine air pressure by direct measuring the boiling temperature (Fig. B.4). The saturation pressure curve (Sect. 2.7) provides the temperature at which the phase transition from the liquid to the gaseous phase occurs.[9] For each air pressure less than that of the liquid, there exists a fixed boiling temperature (e.g. at $p = 1{,}013.25\,\text{hPa}$, $T = 100\,°\text{C}$, or at $p = 700\,\text{hPa}$, $T = 90\,°\text{C}$).[10]

B.3.4 Typical Values and Extremes

Typical horizontal pressure distributions are discussed in Chap. 7. Strong low-pressure systems typically have sea-level pressures ranging between 980 and 990 hPa. Sea level pressures of strong high-pressure systems typically range around 1,040 hPa.

[9]Pressure chambers are required to prevent the human blood to boil when flying at extreme altitudes.

[10]The pressure dependence of the boiling point explains why freshly brewed coffee tastes better at sea-surface level than at 1 mile height, e.g. Denver.

The highest sea-level pressure reported amounted to 1,084 hPa at Agata, Sibiria on 31 December 1968. The highest sea level pressure reported in the United States of America was 1,064 hPa at Miles City, Montana in December 1983. The lowest sea level pressure reported was 870 hPa during typhoon Tip in October 1979. In extra-tropical cyclones, minima of about 915 hPa have been observed, for instance, in the Island cyclones 915 hPa on 15 December 1986, and 912 hPa on 10 January 1993. America's highest sea-level air pressure was observed as 1,067.7 hPa at Northway, Alaska on 31 January 1989.

For weather forecasting, the change of pressure is important as it indicates whether a cyclone or anticyclone is approaching (Chap. 6). The former is associated with clouds and precipitation, while the latter is usually related to cloud dissipation. One of the strongest rates of decrease in pressure was observed in the eye of typhoon Irma east of the Philippines. Here, pressure decreased by 97 hPa within 24.5 h from 981 to 884 hPa.

B.4 Measuring Wind

A system always tries to achieve a state of equilibrium, i.e. to remove difference in pressure, density, and/or temperature. Thus, air moves from high to low pressure areas (Chap. 6), and wind speed is the velocity at which the air travels. In the SI-system, the unit of wind speed is $\mathrm{m\,s^{-1}}$.

B.4.1 Vane and Anemometer

Two different sensors are required to measure wind. For near-surface wind observations the wind speed is typically measured at 10 m height. A wind vane measures wind direction. The design of the instrument makes it to always point into the wind. The dial gives the direction either as N, NE, E, SE, S, SW, W, NW or as degrees on the compass rose from 360° in the north, 90° for the east, 180° for the south, and 270° for the west. No wind (calm) is denoted by 0° in synoptic meteorology. Be aware that the counting of the wind direction differs from that in geometry (Appendix A).

Wind speed is often determined with a cup anemometer (Fig. B.5). The wind speed is read from a dial similar to the speedometer in a car. The principle of an anemometer relies on the difference in built up pressure of the concave and convex side of the cups directed to the wind. The concave cup catches wind, while the wind flows around the convex cup. Consequently, the anemometer starts to rotate. The convex cup turns towards the wind, while the wind pushes the concave cup. When u is the rotation velocity of the cups and v is the wind speed, the flow speed at the cups is $v + u$ for the convex and $v - u$ for the concave cup. When v_R is the relative speed

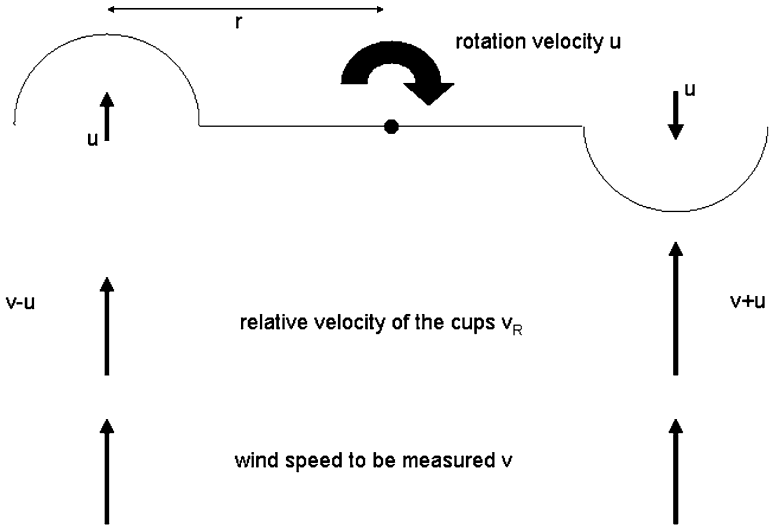

Fig. B.5 Schematic view of a horizontal cross section of a cup anemometer consisting of two cups to illustrate the relation between wind speed and rotation velocity (From Kraus 2000)

of a respective cup, the pressure is given by $\frac{1}{2}C\rho v_R^2$. The resistance coefficients C_1 and C_2 are about 1.3 and 0.3 s m^{-1} for the concave and convex cup, respectively.

Multiplying the pressure felt on the surface cross-section, A, of the cups and the half distance r between the cups provides the momentum. The equilibrium of the momentum is given by

$$\frac{1}{2}C_1\rho(v-u)^2Ar = \frac{1}{2}C_2\rho(v+u)^2Ar \tag{B.7}$$

or after some algebra

$$\frac{(v+u)}{v-u} = \pm(\frac{C_1}{C_2})^{\frac{1}{2}} = \pm q\ . \tag{B.8}$$

Only the positive sign makes sense in atmospheric science because of $v > u$. We obtain $v = ku$ with $k = \frac{q+1}{q-1}$. This derivation shows that the horizontal wind speed v can be determined by a linear function of the rotation velocity u and that v is about the threefold of u. It also demonstrates that the instrument is independent from wind direction.

Example. Calculate the wind speed for a rotation velocity of 5 m s^{-1}.

Solution. $q = \sqrt{\frac{1.3}{0.3}}$, $k = \frac{q+1}{q-1} = 2.85$. The wind speed is 14.25 m s^{-1}.

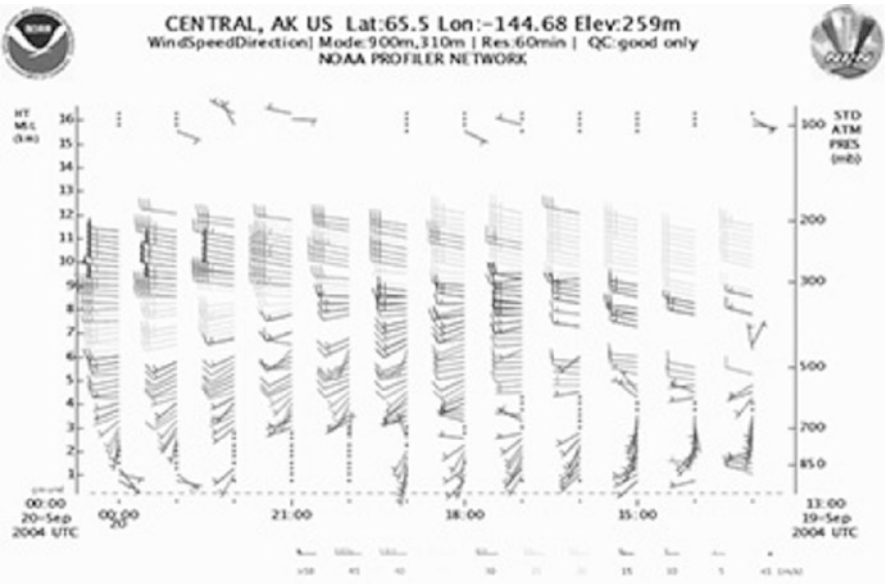

Fig. B.6 Temporal evolution of vertical wind profiles measured in Alaska (From NOAA Profiler Network. Retrieved 2004)

B.4.2 Wind Profiler, Radar, and Sodar

During the last three decades, Doppler radars (RAdio Detection And Ranging) were developed to probe the atmosphere. The speed and direction of wind are derived as function of height from the return signal of the transmitted radio-waves produced by turbulence in the clear air. The wind profiler sends out sequences of high power pulses in the vertical and in oblique directions, i.e. it remotely senses the wind field. These **wind profilers** are operationally applied for measuring the echo intensity and the wind profile up to about 30 km height with high spatial (30–1,500 m) and temporal (≈6 min) resolution (Fig. B.6), i.e. they reach higher than rawinsondes or radiosondes. The received return signals are analyzed to calculate the radial velocity and turbulence intensity. To determine wind speed and direction observations have to be made from at least three directions.

The maximum height, wind-profiler radar can reach, mainly depends on the operating frequency. Unfortunately, wind profilers need bandwidths in the electromagnetic spectrum already taken by cellular phones, two-way-radios, radio- and TV stations. Since the echo-producing processes exist only at certain frequencies, the operating frequency cannot be chosen entirely free. To monitor wind up to 5, 16, and 30 km, a wind profiler requires frequencies at about 1,000 MHz (above the cellular phone range), 400 MHz (television range), and 50 MHz (above the shortwave radio range). Wind profiler can be run unmanned under nearly all weather conditions

and have low operational costs. In contrast to wind measurements obtained from rawinsondes, wind profilers measure the wind directly above the site. Often wind profilers are operated in conjunction with RASS. Data from wind profilers can support predictions of the wind field and transport of plumes or air pollutants.

Velocity images serve to indicate regions of strong marcobursts or the speed of cold fronts. Typically the public never sees velocity images. Base velocity images represent the motion at a 0.5° angle elevation scan. Doppler radar only "sees" the motion directly toward or away from its location, i.e. the radial velocity along the direction of the beam. This means that the radial velocity is always less than the actual wind except when the wind moves directly towards (away) from the radar (Fig. B.7).[11] The motion away (towards) the radar are color-coded in red (green). Weather forecasters estimate the wind direction using this transition zone, i.e. the boundary between motion away and towards the radar. From the radar, the approximate wind direction is perpendicular to the transition line. The 0.5° radar beam displays lower wind speeds closer to the radar's location (e.g. at point 1 in Fig. B.7) as the return signal stems from regions closer to the ground where friction is larger than farther away at higher elevation (e.g. points 2, and 3 in Fig. B.7). Consequently, the wind direction has an angle toward the region of of lowest pressure. At point 3, we can see that the wind direction starts to diverge clockwise at the top of the storm due to outflow (Chap. 6).

Sodars work in a similar way as RASS. They emit accoustic waves and measure the Doppler shifted frequency to determine the 3D-wind field. Sodars collect data in lower layers than wind profilers.

B.4.3 Typical Values and Extremes

The average vertical component of the wind vector is usually about a factor of 10^3–10^4 smaller than its horizontal components. Typical values are of the order of 0.001 and $10\,\mathrm{m\,s^{-1}}$ for the vertical and horizontal component, respectively. In thunderstorms, updrafts locally exceed $10\,\mathrm{m\,s^{-1}}$.

[11] NOAA Profiler Network Real-time Data Display Disclaimer. This data and/or display products as well as their documentation are in the public domain and are furnished "as is." This data is research data and was collected with the intent of using it for meteorological research. The United States government, its instrumentalities, officers, employees, and agents make no warranties, express or implied, as to the accuracy, quality, usefulness of the data, products, and/or documentation for any purpose. They cannot be held responsible for any circumstances resulting from their use, unavailability, or possible inaccuracy. NWS may make data and/or display products available in World Meteorological Organization (WMO), NWS, or other standard formats which may change at any time. NWS reserves the right to suspend or discontinue this service, or portions thereof, at any time. Permission to use, copy, and distribute this data is hereby granted, provided that the entire disclaimer notice appears in all copies.

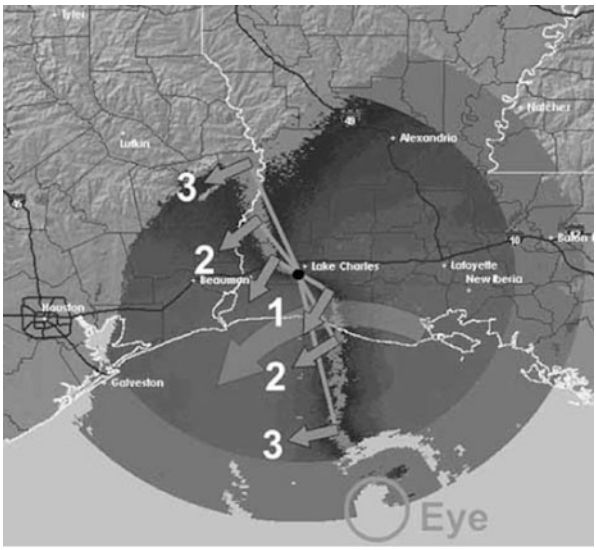

Fig. B.7 Radial velocity image of hurricane Rita in September 2005 as obtained by the radar located SW of Lake Charles. The eye of the storm, the motion of the storm, and wind direction with transition zones for three different elevations are superimposed. The outer ring indicates the region where the radar is unable to determine the radial velocity (From: http://forecast.weather.gov/jetstream/doppler/images/lch_basevel2.jpg (2014))

The world highest 5-min average wind speed was $303\,\mathrm{km\,h^{-1}} = 84.17\,\mathrm{m\,s^{-1}}$, measured at Mount Washington, NH, on 12 April 1934. At the same place, the highest wind speed within a month ($113\,\mathrm{km\,h^{-1}} = 31.39\,\mathrm{m\,s^{-1}}$ in February 1939) and the highest mean wind speed ($206\,\mathrm{km\,h^{-1}} = 57.22\,\mathrm{m\,s^{-1}}$ on 11 and 12 April 1934) for 24 h were reported. At Mount Washington, the highest average annual wind speed and the highest surface wind observed were $56\,\mathrm{km\,h^{-1}}$ ($15.55\,\mathrm{m\,s^{-1}}$) and $372\,\mathrm{km\,h^{-1}}$ ($103\,\mathrm{m\,s^{-1}}$).

The critical wind speed a tropical cyclone has to exceed to become a hurricane or typhoon is $17\,\mathrm{m\,s^{-1}}$.

B.5 Measuring Precipitation

An accurate determination of precipitation is essential for quantitative hydrological analysis and management decisions (e.g. prediction of floods, water resource management, construction of dikes, irrigation, etc.). It is of relevance how exact point measurements can be interpolated onto an area and how representative they are for that area. Errors in point measurements amount to 5–15 % on the long-term, but for individual thunderstorms they may be up to 75 %.

B.5.1 Precipitation Gauge

Nearly every state on Earth uses its own type of precipitation gauges. The members of WMO, however, agreed upon having at least one station that operates in

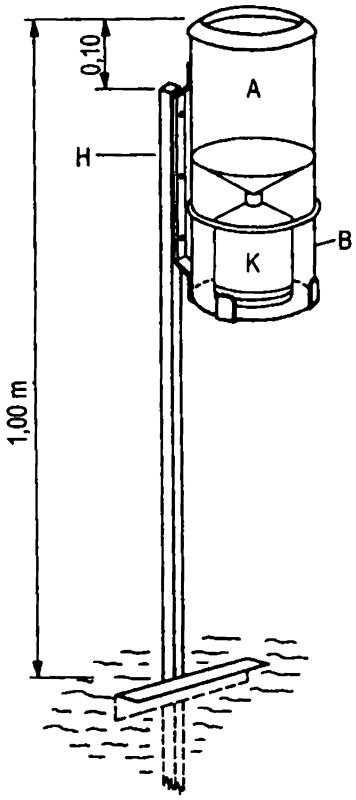

Fig. B.8 Schematic view of a Hellmann precipitation gauge. The letters H, A, K, and B indicate the post, collection device, collection can, and the holder (From: Hupfer and Kuttler 2006)

addition one reference station (IRPG; **interime reference precipitation gauge**) to homogenize the precipitation observations of the national network with those of the world (Fig. B.8).

Non-permanent recording precipitation gauges consist of a collecting cylinder. Often precipitation gauges have a windshield to minimize catch deficiencies by dynamic effects. To prevent loss from splashing, deep gauges or outward sloping walls are preferable. When the gauges are at the ground, in-splashing can be prevented by placing the gauge in a shallow excavation in which the upper soil is replaced by an egg-crate structure (Fig. B.9).

Optical precipitation gauges are more accurate than collecting cylinders, especially for solid precipitation. Precipitation rate is proportional to the flow of the beam between an IR-diode and a sensor. Optical precipitation gauges avoid problems due to splashing, wind, evaporation, and mechanic errors.

Precipitation gauges should be at least so far away from high obstacles (e.g. buildings, trees, etc.) that their uppermost edge is below 45° for a line from the gauge to the object.

Fig. B.9 Rain gauge with opening at ground level surrounded by an egg-crate structure to prevent in-splashing and errors due to aerodynamic effects (Photo by N. Mölders 2000)

B.5.1.1 Accuracy

Sources of errors are splashing and evaporation of already collected water. Putting oil onto the collected water or directly moving the collected water into a closed container may reduce errors by evaporation. Errors by eddies can be reduced by windshields. These systematic errors may amount to up to $-30\,\%$ of the precipitation. The error can be determined in labs. On average, eddies contribute to 2–10 % of the error, the wetting effect is of same amount. Up to 4 % error result from evaporation, while splashing contributes 1–2 %. In the case of snow, eddies and wind-blow cause errors of 10–50 %. Snow is more difficult to measure than rain, because it can be easily blown out of the gauge or eddies may hinder the snow to enter the gauge at all. The catch deficiency depends on wind speed and may exceed 30 % of the snow amount. Furthermore, snow first has to be melted to determine the water equivalent.

An important factor for accuracy is also the size of the gauge. It should not be larger than 300 mm in diameter as it is not suitable for snow, variations by manufacturing become too evident, adhesion effects and evaporation are no longer negligible otherwise.

Errors in annual precipitation result from the fact that **traces** of precipitation ($P < 0.1\,\mathrm{mm\,day^{-1}}$)[12] are not recorded. Doing so may cause an underestimate of 5–15 %. For example, on average, 10 % of the summer precipitation in Alaska are less than 0.25 mm and neglected. This amount may be one third of the annual precipitation. For individual events, the error may be up to 75 %. In general, the accurarcy in precipitation measurements decreases with increasing wind speed due

[12] In Europe, a trace is less than $0.1\,\mathrm{mm\,day^{-1}}$, while in the U.S. a trace is less than $0.1\,\mathrm{in.\,day^{-1}}$.

to aerodynamic effects caused by gauges. Hydrometeors may be hindered to enter the cylinder causing a catch deficit.

In the case of solid precipitation, this catch deficit be appreciable. Snow pillows are more suitable for measuring solid precipitation. Solid precipitation is also often estimated by measuring snow height and multiplying the value by 0.1 assuming that the density of snow is $100\,\mathrm{kg\,m^{-3}}$. However, as discussed in Chap. 3 the density of snow and ice crystals is highly variable and may be lower or higher than this value.

Frequently occult precipitation (Chap. 5) is not measured. Measuring occult precipitation requires special equipment. Scavenging of water from clouds may be hydrologically significant at high elevation and in arid areas. Errors in global precipitation estimates due to scavenging may be about 30 % of the annual precipitation. For instance, in the forests of Oregon, occult precipitation amounts $800\,\mathrm{mm\,year^{-1}}$ which corresponds to about 30 % of the annual precipitation. At elevations higher than 1,200 m in the New England States, occult precipitation amounts to $450\,\mathrm{mm\,year^{-1}}$ (20 % of the annual precipitation) and in the mountains of New Mexico, it is about 20–30 $\mathrm{mm\,year^{-1}}$. Ripe contributes to 38–50 $\mathrm{mm\,year^{-1}}$ to the annual precipitation in the Casacade Mountains of Washington.

In different countries, the readings are made at different times, which has to be considered in preparing regional distributions of precipitation for climatologies (Chap. 7) and model evaluation purposes. If a thunderstorm, for instance, occurs on the last day of a month, this may lead to differences in the monthly averages.

In long-term recordings, changes in the environment (e.g. growth of trees, building of houses, etc.) may cause inconsistent time series. Time series have to be checked for such inconsistencies and eventually be corrected before drawing conclusions on altered temporal behavior. Time series can be examined for homogeneity by successive summing up the accumulated annual precipitation of the station with probable changes in the environment and an unchanged station close by and comparing their behavior for the same time range. Changes result in a different trend of the curve and may be corrected by multiplying the values of the altered time series from the onset of change onwards with the ratio of the slopes before and after the change. Usually a time series is considered as inconsistent when a jump occurs that exists for more than 5 years and/or is statistically significant. Note that multiple changes may also be caused by climate change (Chap. 7). Thus, time series should be only homogenized if there is a proven change in the environment.

B.5.2 Radar Reflectivity

Atmospheric radars measure the backscatter of pulses of microwave radiation ($1\,\mathrm{cm} < \lambda < 30\,\mathrm{cm}$) emitted by the radar itself. The most frequently used wavelengths are the 3-, 5-, and 10 cm-band named X-band, C-band, and S-band, respectively. Out of these, the S-band is the most suitable for detection of precipitation; however, it needs a huge antenna (about 8 m in diameter) for which the other bands are favored on mobile platforms (e.g. ships, aircrafts). Shorter wavelengths

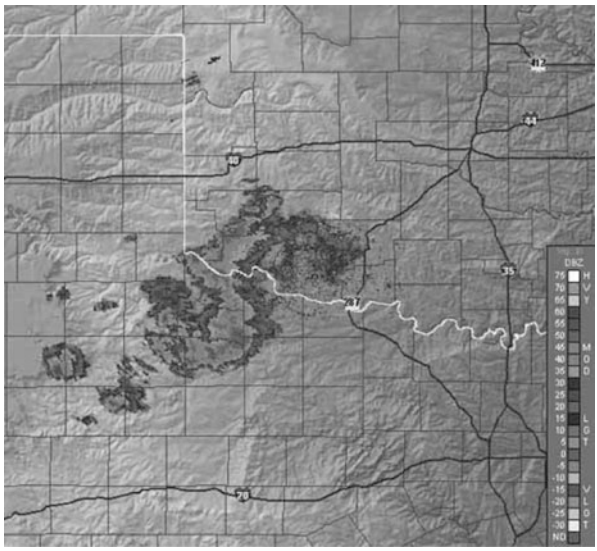

Fig. B.10 Reflectivity image from the Doppler radar in Frederick, Oklahoma (From: http://forecast.weather.gov/jetstream/doppler/images/fdr_baserefl.jpg (2014))

(1 mm $< \lambda <$ 8 mm) are applied to examine cloud particles. Wavelength of 75 cm or 6 m serve to measure atmospheric turbulence and vertical wind profiles, respectively.

The transmitter/receiver unit of radar can slowly rotate around and move vertically up and down. Thus, nearly the entire half-sphere around the radar can be observed to a distance of about 50 km or so. Mountains, high obstacles etc. may act as masks behind which the radar cannot sense.

By measuring the return time and strength of the returned signal, profiles can be taken illustrating how much precipitation is occurring at what distance from the radar. The closer the precipitation or cloud system is to the radar the more rapidly the signal returns. Typically scans are made at 0.5° angle.

Composite images base on scans at various altitudes during each volume scan. They are advantageous in mountainous terrain as the usual 0.5° scan may not be high enough to reach areas behind the mountains. The greatest echo intensity (reflectivity) from any altitude angle serve to make the composits to display the highest reflectivity in all sampled radar echoes.

Figure B.10 shows an example of a base reflectivity image from a Doppler radar. The radar is in the center of the image. The reflectivities are color coded and give the magnitude of energy that returned to the radar. The data gained can be monitored and stored continuously.

Hail is a good reflector of energy. Hail of about 2 cm in diameter leads to reflectivities of 60–65 dBZ. However, this value does not mean that severe weather will occur. Light rain produces reflectivities of about 20 dBZ. By using radar reflectivity, Z, the amount of precipitation, R, can be estimated from empirical formula of the type

$$Z = aR^b \tag{B.9}$$

Table B.1 Z-R-relationships found for various precipitation types

$Z-R$-relationship	Precipitation type	Reference
$140R^{1.5}$	Drizzle	Joss et al. (1970)
$250R^{1.5}$	Large scale precipitation	Joss et al. (1970)
$200R^{1.6}$	Stratiform type precipitation	Marshall and Palmer (1948)
$31R^{1.71}$	Orographic rain	Blanchard (1953)
$500R^{1.5}$	Rain from a thunderstorm	Joss et al. (1970)
$486R^{1.37}$	Rain from a thunderstorm	Jones (1956)
$2000R^{2}$	Aggregated snowflakes	Gunn and Marshall (1958)
$1780R^{2.21}$	Snowflakes	Sekhan and Srivastava (1970)

Table B.2 Typical values of radar reflectivity for various atmospheric particles

(dB)	Precipitation particle
−30–0	Hardly detectable precipitation
≈ 0–10	Drizzle, slight rain
≈ 10–30	Moderate rain, heavy snowfall
≈ 30–45	Melting snow
≈ 30–60	Moderate to heavy rain
≈ 60–70	Hail

where a and b are (site dependent) parameters (Table B.1; see also Chap. 3). The precipitation gained by this Z-R-relation serves, in particular, as input in hydrological models to get a first guess for various applications as there are management of dams, estimation of stream flow, flood of a river, etc.

The type of precipitation (Table B.2) can also be derived from radar data. The movement of a cloud or precipitating system can be interpolated in the future. Thunderstorm clouds, for instance, move with the wind at the 700 hPa level. Forecaster speak of the radar getting "hot" ("cold") when a stronger (weaker) than normal storm occurs.

B.6 Measuring Radiation

The simplest instrument to measure solar radiation is the sunshine autograph. It consists of a glass sphere that focuses the sun beam and causes a burn trace on special paper. When the Sun is covered by clouds, the burn trace is interrupted. This way the hours of sunshine can be registered.

All meteorological instruments for measuring radiation use a black area that absorbs or emits radiation. Several instruments may be used for measuring the intensity of radiation:

1. Devices that measure the direct radiation normal to the sun beam (pyrheliometer), and

Table B.3 Some changes in weather features typically associated with the advection of various cloud types

Cloud type advected	Change in weather in the next hour
Cirrus	Cooling
Cumulonimbus	Cooling, squall lines, increase in wind, heavy precipitation, hail probable
Cumulus	Alternation of insolation and shadow, showers possible, updrafts, improvement of air quality
Warm frontal system	Warming, later long-lasting slight to moderate precipitation, decrease in pressure
Cold frontal system	Cooling, showers, increase in pressure

2. Devices that measure the global radiation, $R_s^{\downarrow}$, onto a horizontal surface (pyranometer). Protecting this device from direct solar radiation allows for measuring the diffuse radiation. Switching the device downward allows for measuring the reflected upward shortwave radiation, $R_s^{\uparrow} = \alpha R_s^{\downarrow}$. A device that combined the upward and downward measurement is called an albedometer.

According to the measuring principle, three kinds of instruments are distinguished:

1. The absorbed radiation energy is transferred to heat and the temperature of the device increases. This increase serves as a measure for the uptake of heat or the heat uptake for melting or sublimation. These devices require no calibration.
2. Instruments where the measuring body is in thermal equilibrium with the uptake of heat by radiation and the release of heat to the environment bases on the difference in temperature measured. They require calibration.
3. The heating of the measuring body is compared with the heating of an artificially heated body of same construction.

B.6.1 Satellite Images

In synoptic meteorology, satellite imagery serves for now-casting (Chaps. 4 and 6). In a short-term prediction for a selected site, the satellite movie, which is a sequence of consequently scanned satellite images, is looked at. The weather (wo)man interpolates the movement of the cloud system in time (e.g. 1 h). By knowing the typical weather associated with the various types of clouds he can nowcast weather of the next hour(s) by assuming that the cloud system does not change its speed and direction of motion (Table B.3). Various authors derived regional specific relationships between satellite borne radiometer data and surface precipitation to assess precipitation over the oceans or in unmonitored areas.

Table B.4 lists a scheme of how to interpret satellite data. Besides the visible and IR imagery of geostationary satellites (Figs. 4.26 and 4.28), data from other

Table B.4 Scheme for interpretation of IR and visible imagery. Note that all statements refer to inverted data in the case of IR imagery

Visible	IR	Feature	Temperature	Scene
Dark	Dark	Homogeneous	Warm	Land/ocean
White	Relatively dark	Homogeneous	Relatively warm	Sea ice
White	White	Structured	Cold	Clouds
White	White	Homogeneous	Cold	Snow/ice
Bright	Bright	Structured	Warm	Low clouds
Dark	White	Feathered	Cold	Thin cirrus
White	White	Structured	Cold	Deep convection
White	Bright	Point-pattern, organized	Relatively warm	Cumulus

Table B.5 Major regions of the electromagnetic spectrum and applicability for remote sensing

Region	Wavelength	Applicability in remote sensing
Gamma ray	<0.03 nm	Entirely absorbed by the atmosphere, useless for remote sensing
X-ray	0.03–30 nm	Entirely absorbed by the atmosphere useless for remote sensing
Ultraviolet	0.03–0.4 μm	$0.03 < \lambda < 0.3$ μm absorbed by ozone
Photographic ultraviolet	0.3–0.4 μm	Available for remote sensing
Visible	0.4–0.7 μm	Remote sensing of clouds, surface characteristics
Infrared	0.7–100 μm	Temperature, clouds, surface characteristics
Reflected infrared	0.7–3.0 μm	Remote sensing of water clouds, distinction between water and ice clouds
Near infrared	0.7–0.9 μm	Remote sensing, vegetation, clouds, ice
Thermal infrared	3.0–14 μm	
Microwave	0.1–100 cm	Clouds, and precipitation, longer wavelengths of this band pass through clouds, fog, and rain
Radio waves	>100 cm	Normally not used for remote sensing

satellites (e.g. NOAA-AVHRR) can be used. Table B.5 lists the applicability of the various wavelength ranges. For further discussion see Chap. 4.

In regions of sparse synoptic observations, satellite imagery serves as the primary basis to locate the major features on the surface map.

B.7 Profile Measurements

As discussed in Chap. 2, radiosondes (*German, French* sonde = probe) allow to carry out profile measurements of wind, speed and direction, temperature, dewpoint temperature, and pressure, and when they reach high altitudes cosmic rays. They are equipped with GPS or radio direction finder, and a transmitor to send the observed

Fig. B.11 Tetherballoon with sonde (Photo by N. Mölders 1987)

state variables to a receiver at the ground station. A rawinsonde only measures wind speed and direction. Ozonsondes are radiosondes that measure ozone.

Typically these sondes are deployed via latex or rubber balloons. Depending on the weight of the sonde and the desired altitude to be reached by the balloon the balloons are either filled with helium or hydrogen. Occassionally radiosondes or dropsondes are released from aircraft.

Over 800 radiosonde launch sites exist worldwide. Radiosondes take about 45 min to be prepared and should be anchored outside the preparation hangar for the temperature devices to adjust to the ambient air temperature prior to their release at 0000 UT and 1200 UT. Additional typical launch times are 0600 UTC and 1800 UTC. The coordinated launch allows for obtaining an initial analysis of the atmospheric state that is required to initialize global (weather forecast) models.

Tether balloons (Fig. B.11) are another possibility to take vertical profile measurements up to about 500 m. These balloons are anchored on a robe that allows to wind the balloon up and down to take profiles. The shape of the balloon ensures that the sonde is held in the same position with respect to the wind. Typically they fly sondes that allow for temperature, humidity and wind measurements.

Pilot balloons carry sensors and drift with the wind at a given pressure level. They are often used to expore the atmospheric boundary layer (Chap. 6).

B.8 Measuring Aerosols and Trace Gases

When performing air quality measurements it is important to have power supply by battery, from the electricity grid, or solar power. Diesel generators or wind energy would impact the measured concentrations. When measuring voltaile carbon compounds it is also important to be aware not to use any perfumed products and/or wear perfumed clothes when going into the field as they may affect the measurements.

An often applied method to measure the cloud condensation nuclei or ice nuclei concentrations is to draw a known volume of air into a container and cool it until a cloud forms. In expansion chambers, cooling is produced by compressing the air and suddenly expanding it. In mixing chambers, the air is cooled by refrigeration. The number of cloud droplets (ice crystals) occurring in the chamber are determined by illuminating a certain volume of the chamber. Ice crystals can be collected on a super-cooled sugar or soap solution, photographed and counted.

Various radiometers in limb scanning mode can provide vertical profiles of species provided they measure in a range suitable to detect the species (Chap. 4).

B.8.1 Dry Deposition Measurements

Most dry deposition data of nitrogen compounds are based on enclosure and micrometeorological techniques (Chap. 6). This data is only representative for a spot of up to a square meter and of limited meaning. Micrometeorological measurements provide flux data representative for areas of several hectares that can be used for model evaluation.

Most micrometeorological techniques are indirect methods (e.g. Bowen ratio and aerodynamic profile techniques, inferential methods). The disjunct true eddy accumulation (DEA) flux measurements serves to measure α-pine fluxes, and the relaxed eddy accumulation (REA) method measures carbon dioxide and biogenic hydrocarbon fluxes. The interpretation of this data requires model assumptions, which also have to be evaluated so that this data cannot directly be used for evaluation of air quality models. Direct evaluation of simulated dry deposition fluxes requires fluxes directly measured by eddy covariance or true conditional sampling (eddy accumulation). Since many trace constituents cannot be measured fast enough to apply eddy covariance techniques, the conditional sampling method that does not require fast-response chemical sensors seems to be an alternative. However, considerable efforts have to be undertaken to develop a conditional sampling system for measuring eddy fluxes of trace species under field conditions. Therefore, an adequate conditional sampling system is still required. Directly measured dry deposition fluxes of highly reactive trace gases exist only for a few trace species and are still scarce. Consequently, for most trace species directly measured flux data is unavailable for model evaluation.

Air quality networks that measure wet depositions typically provide data on nitrate, ammonium and organic nitrogen, methyl, and total mercury.

B.9 Runoff

Lysimeter (Fig. B.12) are soil filled tanks with an outlet at the bottom. They are implemented in such way that their top is at the same level than the surrounding soil so they have the same environmental conditions. They also have the same vegetation as their surroundings. The precipitation (input) is typically measured somewhere in the field nearby by a device as shown in Fig. B.9. A lysimeter can be used to just determine the groundwater recharge (runoff from the lysimeter) caused by the precipitation or the evapotranspiration via the difference of precipitation and runoff. Many lysimeter are mounted on scales. Such lysimeter allow to determine the soil water content when the weight of the dry soil and soil at saturation is known. Typically in maritime mid-latitude soils are saturated in October. The weight of the dry soil typically is determined by weighting the oven-dry soil.

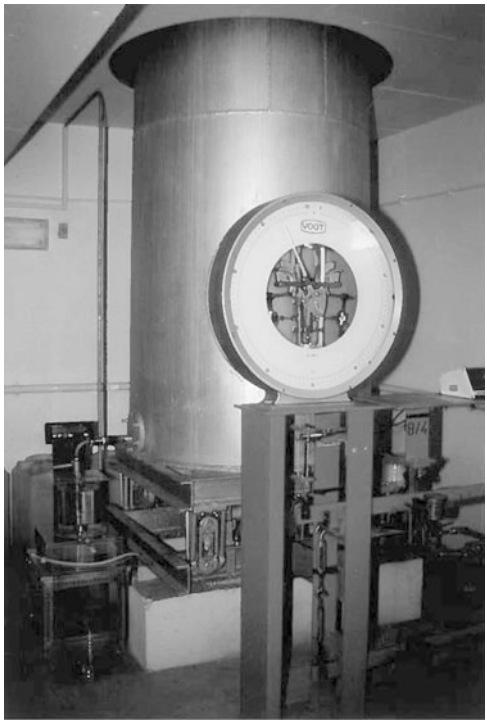

Fig. B.12 Lysimeter with weight station (Photo by N. Mölders 1999)

References

Material, concepts, ideas and problems of the following books and articles inspired this chapter. These sources are recommended for further reading.

Andrews DG (2000) Introduction to atmospheric physics. Cambridge University Press, New York, 237pp

Angevine WM, Ecklund WL (1994) Errors in radio acoustic sounding of temperature. J Atmos Ocean Technol 11:837–842

Battan L (1973) Radar = observation of the atmosphere. University of Chicago Press, Chicago, 324pp

Blanchard DC (1953) Raindrop size-distribution in Hawaiian rains. J Meteorol 10:457–473

Bradley S (2006) Atmospheric accoustic remote sensing. CRC/Taylor and Francis, London/New York, 271pp

Brock FV, Richardson SJ (2001) Meteorological measurement systems. Oxford University Press, Oxford, 306pp

Dingman SL (1994) Physical hydrology. Macmillan Publishing Company, New York/Oxford/ Singapore/Sydney, 557pp

Foken T (2014) Micrometeorology (translated by Nappo, C.J.). Springer, Heidelberg, 350pp

Gunn KLS, Marshall JS (1958) The distribution with size of aggregate snowflakes. J Atmos Sci 15:452–461

Hupfer P, Kuttler W (2006) Witterung und Klima - Eine Einführung in die Meteorologie und Klimatologie. Teubner Verlag, Wiesbaden, 554pp

Jones DMA (1956) Rainfall drop size-distribution and radar reflectivity. Defense Technical Information Center

Joss J, Schram K, Thams JC, Waldvogel A (1970) On the quantitative determination of precipitation by a radar. No. Wissenschaftliche Mitteilung-63. Osservatorio Ticinese della Centrale Meteorologica Svizzeria Locarno-Monti, pp 1–37

Joss J, Waldvogel A (1990) Precipitation measurement and hydrology. In: Atlas D (ed) Radar in meteorology. American Meteorological Society, Boston, pp 577–606

Kessler E (1983) Instruments and techniques for thunderstorm obsevation and analysis. University of Oklahoma Press, Norman/London, 268pp

Kidder SQ, Vonder Haar TH (1995) Satellite meteorology. Academic, San Diego, 466pp

Kramm G (1995) Zum Austausch von Ozon und reaktiven Stickstoffverbindungen zwischen Atmosphäre und Biosphäre. Maraun-Verlag, Frankfurt, 268pp

Kramm G, Dlugi R, Dollard GJ, Foken T, Mölders N, Müller H, Seiler W, Sievering H (1995) On the dry deposition of ozone and reactive nitrogen compounds. Atmos Environ 29:3209–3231

Kramm G, Beier N, Foken T, Müller H, Schröder P, Seiler W (1996) A SVAT scheme for NO, NO_2, and O_3 – model description and test results. Meteorol Atmos Phys 61:89–106

Kraus H (2000) Die Atmosphäre der Erde. Eine Einführung in die Meteorologie. Vieweg, Braunschweig, Wiesbaden, 470pp

Marshall JS, Palmer WK (1948) The distribution of raindrops with size. J Meteorol 5:165–166

Marshall JS, Hitschfeld W, Gunn KLS (1958) Advances in radar weather. Adv Geophys 2:1–56

Mölders N (2011/2012) Land-use and land-cover changes – impact on climate and air quality. Atmospheric and oceanographic sciences library, vol 44. Springer. doi:10.1007/978-94-007-1527-1 3

Möller F (1973a) Einführung in die Meteorologie - Physik der Atmosphäre - Band 1. BI Hochschultaschenbücher, Mannheim, 222pp

Möller F (1973b) Einführung in die Meteorologie - Physik der Atmosphäre - Band 2. BI Hochschultaschenbücher, Mannheim, 223pp

Raghaven S (2003) Radar meteorology. Springer, Berlin/Heidelberg, 549pp

Sekhon KS, Srivastava RC (1970) Snow size spectra and radar reflectivity. J Atmos Sci 27:299–307

Srivastava GP (2009) Surface meteorological instruments and measurement practices. Atlantic Publishers and Distributors, New Dehli, 429pp
Wallace JM, Hobbs PV (1977) Atmospheric science – an introductory survey. Academic, San Diego/New York/Boston/London/Sydney/Tokyo/Toronto, 467pp
Wallace JM, Hobbs PV (2006) Atmospheric science – an introductory survey. Academic, San Diego/New York/Boston/London/Sydney/Tokyo/Toronto, 483pp

Solutions

Answers to Selected Problems of Chap. 2

2.1 $M_{moist} = (1-X)(M_{N_2}\frac{p_{N_2}}{p} + M_{O_2}\frac{p_{O_2}}{p} + M_{Ar}\frac{p_{Ar}}{p} + M_{CO_2}\frac{p_{CO_2}}{p}) + XM_{HO_2}\frac{p_{HO_2}}{p}$, $M_{moist} = (1-X)\cdot((28.013\cdot 0.7808 + 31.999\cdot 0.2095 + 39.948\cdot 0.0093 + 44.010\cdot 0.0004) + 18.02\cdot X)\cdot 10^{-3}\,\mathrm{kg\,mol^{-1}}$. With $X = 4\,\% = 0.04$, $M_{moist} = 28.5272\cdot 10^{-3}\,\mathrm{kg\,mol^{-1}}$, $X = 1\,\%$, $M_{moist} = 28.856\cdot 10^{-3}\,\mathrm{kg\,mol^{-1}}$, $R_{1\,\%} = 291.5\,\mathrm{J\,kg^{-1}\,K^{-1}}$, $R_{4\,\%} = 288.1\,\mathrm{J\,kg^{-1}\,K^{-1}}$

2.2 $M_{Mars} = \sum_{i=1}^{k}\frac{p_i}{p}M_i = (3\cdot 10^{-4}18 + 2.8\cdot 10^{-6}20 + 0.95\cdot 44 + 0.027\cdot 28 + 0.0013\cdot 32 + 7\cdot 10^{-4}28 + 0.016\cdot 40)\,\mathrm{g\,mol^{-1}} \approx 43\,\mathrm{g\,mol^{-1}}$, $R_{Mars} = \frac{R^*}{M} = 0.19\,\mathrm{J\,kg^{-1}\,K^{-1}}$, $\rho = 14\,\mathrm{kg\,m^{-3}}$

2.3 $n = \frac{p}{kT} = \frac{101{,}325\,\mathrm{Nm^{-2}}}{1.3806\cdot 10^{-23}\,\mathrm{J\,K^{-1}}288\,\mathrm{K}} \approx 2.55\cdot 10^{25}\,\mathrm{m^3}$, i.e. there are enough molecules to define temperature in a statistical sense, i.e. macroscopic way

2.4 $p = p_0\exp(-\frac{g(z-z_0)}{RT}) = p_0\exp(-\frac{g(z-z_0)}{\frac{R^*}{M\cdot T}}) = \sum_{i=1}^{n}p_{0,i}\exp(-\frac{g(z-z_0)}{R^*M_iT})$. Thus, for any inert trace gas i, $p_i = p_{0,i}\exp(-\frac{g(z-z_0)}{R_iT})$

2.5 $M_d = M(N_2)\frac{p(N_2)}{p} + M(O_2)\frac{p(O_2)}{p} + M(A)\frac{p(A)}{p} + M(CO_2)\frac{p(CO_2)}{p}$, $M_d = (28.013\cdot 0.7808 + 31.999\cdot 0.2095 + 39.948\cdot 0.0093 + 44.010\cdot 0.0004)\cdot 10^{-3}\,\mathrm{kg\,mol^{-1}} = 28.965\cdot 10^{-3}\,\mathrm{kg\,mol^{-1}}$, $R_d = \frac{R}{M_d} = 8.3144\,\mathrm{J\,mol^{-1}\,K^{-1}}/28.965\cdot 10^{-3}\,\mathrm{kg\,mol^{-1}} = 287\,\mathrm{J\,kg^{-1}K^{-1}}$, $M_w(= 18.016\,\mathrm{kg})$, $R_v = \frac{R^*}{M_w} = 461\,\mathrm{J\,K^{-1}\,kg^{-1}}$

2.6 At 1,013 hPa, $V/N_A = \frac{R^*T}{p}$. $V/N_A = 2.2414\cdot 10^{-4}\,\mathrm{m^3\,mol^{-1}}$, $1\,\mathrm{m^3} = 1001$, $1\,\mathrm{mol} = 22.4\,\mathrm{l}$, $\frac{1{,}000\,\mathrm{L}}{22.4\,\mathrm{L\,mol^{-1}}} = 44.6\,\mathrm{mol}$, using $6.022\cdot 10^{23}$ molecules $\mathrm{mol^{-1}}$ provides $2.69\cdot 10^{25}$ molecules

2.7 $m_{ozone} = \frac{3\cdot M_{ozone}}{N_A}$, $m_{ozone} = \frac{3\cdot 16\cdot 10^{-3}\,\mathrm{kg\,mol^{-1}}}{6.022\cdot 10^{23}\,\mathrm{mol^{-1}}}$, $m_{ozone} \approx 7.971\cdot 10^{-26}\,\mathrm{kg}$, $E_{kin} = \frac{1}{2}mv^2 = \frac{1}{2}7.971\cdot 10^{-26}\,\mathrm{kg}(5\,\mathrm{m\,s^{-1}})^2 \approx 9.963\cdot 10^{-25}\,\mathrm{J}$

N. Mölders and G. Kramm, *Lectures in Meteorology*, Springer Atmospheric Sciences,
DOI 10.1007/978-3-319-02144-7, © Springer International Publishing Switzerland 2014

2.8 $p = \sum_{i=1}^{n} p_i + e$, $p = \rho_d R_d T + \rho_v R_v T$, $p = \rho_{air,X} T((1-X)R_d + XR_v)$, $\rho_{air,X} = \frac{p}{T((1-X)R_d + XR_v)}$, $\rho_{air,1\,\%} = 1.197\,\mathrm{kg\,m^{-3}}$, $\rho_{air,4\,\%} = 1.176\,\mathrm{kg\,m^{-3}}$. Moist air is lighter than drier air at same p, T

2.10 Boyle-Mariotte's law: $pV = const$ at $T = const$, $pV = N_A R^* T$. As long as $T = const$, $pV = const$

2.11 Gay-Lussac's law: $pV = p_0 V_0(1 + a\theta)$, $pV = N_A R^* T = N_A R^*(b + \theta)$, $pV = N_A R^* b + N_A R^* \theta$, $pV = p_0 V_0 + N_A R^* b\theta / b$, $pV = p_0 V_0 + p_0 V_0 \theta / b$, $pV = p_0 V_0 + p_0 V_0 a\theta$, $pV = p_0 V_0(1 + a\theta)$

2.13 $p_i = \frac{m_i T R^*}{M_i V} = \frac{0.0062\,\mathrm{kg}\,294.15\,\mathrm{K}\,8.3144\,\mathrm{J\,K^{-1}\,mol^{-1}}}{44.01 \cdot 10^{-3}\,\mathrm{kg\,mol^{-1}\,m^{-3}}} = 11\,\mathrm{Pa}$

2.16 $dp = \beta p_0 dT = \frac{1}{273.15\,\mathrm{K}} 1{,}013.25\,\mathrm{hPa}\,60\,\mathrm{K} = 222.57\,\mathrm{hPa}$, $p = \rho R_d T$, $dp = d(\rho R_d T) = R_d T d\rho + \rho R_d dT = 0 + 1.29\,\mathrm{kg\,m^{-3}} 287\,\mathrm{J\,kg^{-1}} 60\,\mathrm{K} = 222.14\,\mathrm{hPa}$. The pressure does not raise this much because there is exchange which the environment.

2.17 $d\Phi = gdz = -\alpha dp$, $dq = dh - \alpha dp$, $dh = c_p dT$, $D\Phi = gdz = dq - dh$, $dq = dh + d\Phi = c_p dT + d\Phi = d(c_p T + d\Phi)$

2.19 $z_{755\,\mathrm{hPa}} = H \ln(\frac{p_0}{755}) = 8.23\,\mathrm{km}\ \ln(\frac{1{,}024}{755}) \approx 2.438\,\mathrm{km}$

2.21 Isotherm atmosphere: $\rho(z) = \rho_0 \exp(-z/H)$. Density is a function of all trace species and the troposphere is well mixed for inert gases, i.e. $c(z) = c_0 \exp(-z/H)$. The height z is successively equal to H, $2H$, $3H$, etc. Thus, $\frac{c(z)}{c_0}$ is proportional to $\exp(-1)$, $\exp(-2)$, $\exp(-3)$, etc., i.e. the concentration decreases by a factor $e(= 2.718)$ for each increase in height z above the surface.

2.25 $\frac{dp}{dz} = -\rho g = -\frac{pg}{R_d T}$, $\int_{p_0}^{p} \frac{dp}{p} = \ln(\frac{p}{p_0}) = -\int_0^Z \frac{g}{R_d T} dz$, $T = T_0 - \gamma z$, $\frac{p}{p_0} = (1 - \gamma \frac{z}{T_0})^{(\frac{g}{\gamma R_d})}$, for $T = T_0 = const$ and $z_0 \le z \le Z$, $\frac{p}{p_0} = \exp(-g(Z - z_0)/(R_d T_c))$

2.26 Assume unit mass: $ds = c_p \frac{dT}{T} - \frac{V}{T} dp$, $ds = c_p \frac{dT}{T} - R \frac{dp}{p} = (-c_p \cdot 0.04 + 287 \cdot 0.06)\,\mathrm{J} \approx 57\,\mathrm{J}$

2.27 No change in the macroscopic potential or kinetic energy occurs because the center of mass remains in place. The pressure remains the same as well. According to the first law of thermodynamics, for a unit mass $\delta Q = dU + pdV$. For finite changes of the air parcel $\Delta Q = 10^7\,\mathrm{J}$, $p\Delta V = 70{,}000\,\mathrm{Pa} \cdot 22\,\mathrm{m^3} = 0.154 \cdot 10^7\,\mathrm{J}$, $\Delta U = \Delta Q - p\Delta V = 10^7 - 0.154 \cdot 10^7\,\mathrm{J} = 8.46 \cdot 10^6\,\mathrm{J}$. When air molecules exert no force on each other, internal energy is their kinetic energy, i.e. air temperature. An energy of $m\ c_p \Delta T$ is required to increase the temperature by ΔT. Consequently, $\Delta U = m c_p \Delta T$ or $\Delta T = \frac{\Delta U}{m c_p}$. $\Delta T = 1.2\,\mathrm{K}$

2.28 $u = c_v dT$, $\frac{-30\,\mathrm{J\,kg^{-1}\,K^{-1}}}{717\,\mathrm{J\,kg^{-1}}} - 273\,\mathrm{K}$, $\theta = 268.8\,\mathrm{K}$

2.29 $\theta(400\,\mathrm{hPa}) = 300\,\mathrm{K}$, $\theta(600\,\mathrm{hPa}) = 260\,\mathrm{K}$

2.30 $c_v dT + pdv = \delta q$, $c_p dT - vdp = \delta q$, $c_v dT + pdv = 0$, $c_p dT - vdp = 0$

2.34 $Q = -mL_f$, $Q = -0.333 \cdot 10^6 \cdot 10^{-4}\,\mathrm{J} = -33.3\,\mathrm{J}$, $W = \int_{cloud-water}^{ice} pdV = p(V_{ice} - V_{cloudwater})$, $V = \frac{m}{\rho}$, $V_{ice} = \frac{10^{-4}\,\mathrm{kg}}{916\,\mathrm{kg\,m^{-3}}} = 1.09 \cdot 10^{-7}\,\mathrm{m^3}$, $V_{cloudwater} = \frac{10^{-4}}{1{,}000\,\mathrm{kg}} = 10^{-7}\,\mathrm{m^3}$, $W = 70{,}000(1.09 - 1)10^{-7}\,\mathrm{J} = 6.3 \cdot 10^{-3}\,\mathrm{J}$, $\Delta U = Q - W \approx 33.3\,\mathrm{J}$, counteract

2.35 Assume unit mass. $\Delta s_{env} = 0$, $\Delta w = \Delta q = 0$, $\Delta s_{tot} = \Delta s_{sys} + \Delta s_{env} = \Delta s_{gas}$, $\delta u = 0$ (Joule's law). The gas passes isothermally from its initial state to its final state, i.e. $\Delta T = 0$, $\delta s_{gas} = \int_1^2 \frac{dq_{rev}}{T}$, for an ideal gas $\frac{dq_{rev}}{T} = c_p \frac{dT}{T} - R\frac{dp}{p}$, $\Delta s_{gas} = c_p \int_1^2 \frac{dT}{T} - R\int_1^2 \frac{dp}{p} = c_p \ln\frac{T_2}{T_1} - R\ln\frac{p_2}{p_1}$. Isothermal means $T_1 = T_2$ and the ideal gas equation reduces to Boyle's law, i.e. $\frac{p_1}{v_1} = \frac{p_2}{v_2}$, $\Delta s_{gas} = -R\ln(\frac{p_2}{p_1}) = -R\ln(\frac{v_2}{v_1}) = R\ln(\frac{v_1}{v_2})$, $\Delta s_{tot} = R\ln(\frac{v_1}{v_2})$. Due to the second law of thermodynamics $R\ln(\frac{v_1}{v_2}) > 0$, $v_1 > v_2$, i.e. the gas spontaneously expands. If the opposite were true, $\Delta s_{tot} < 0$, which would violate the second law of thermodynamics. Entropy can only decrease in open systems when entropy is exported

2.36 $c_p T\frac{d\Theta}{\theta} = c_p dT + g dz$, $\frac{1}{\theta}\frac{d\theta}{dz} = \frac{1}{T}(\frac{dT}{dz} + \frac{g}{c_p}) = \frac{1}{T}(\Gamma_d - \Gamma)$, for $\frac{d\theta}{dz} > 0$, $\Gamma < \Gamma_d$, i.e. positive static stability

2.37 $-\frac{dT}{dz} = \frac{g}{c_p}$

2.43 $T(p) = \theta(\frac{p}{p_0})^\kappa = T_0(\frac{p}{p_0})^\kappa$, $T(750\,\mathrm{hPa}) \approx 260.7\,\mathrm{K}$, $T(500\,\mathrm{hPa}) \approx 232.1\,\mathrm{K}$, $\Delta T \approx 22.4\,\mathrm{K}$ and $\approx 50.9\,\mathrm{K}$, respectively. This is about $10\,\mathrm{K10^{-2}\,hPa^{-1}}$, i.e. a nonlinear decrease with height z

2.46 $RH = 100\frac{e}{e_s}$, $e_s = 6.112\exp(17.5043(-10)/(241.3 - 10)) = 2.868\,\mathrm{hPa}$, $e_{60} = 0.6 \cdot 2.868\,\mathrm{hPa} = 1.72\,\mathrm{hPa}$, $e_{90} = 2.5812\,\mathrm{hPa}$, $\Gamma_d = \frac{0.98\,\mathrm{K}}{100\,\mathrm{m}}$, $\frac{dT_d}{dz} = \frac{0.172\,\mathrm{K}}{100\,\mathrm{m}}$. Fog forms when saturation is reached, i.e. $T_{fog} = T_{initial} - \Gamma_d \Delta z = (T_{wet,initial} - T_d)\Delta z$, $z = \frac{T_{initial} - T_{wet,initial}}{\Gamma_d - \frac{dT_d}{dz}}$, $T_{wet,initial} = 241.3\frac{\ln(e_s)\ln 6.112}{17.5043 - \ln(e_s) + \ln 6.112}$, $T_{60} = 0.1\,^\circ\mathrm{C}$, $T_{90} = -0.1\,^\circ\mathrm{C}$

2.47 $r = 0.622\frac{e}{p-e}$, $e = 24\,\mathrm{hPa}$, $T_d = 20.5\,^\circ\mathrm{C}$

2.48 $p = \rho_d R_d T + \rho_v R_v T$, $\rho_m = \rho_d + \rho_v$

2.49 $RH = 100\frac{e}{e_s}$, $e(14\,^\circ\mathrm{C}) = e(25\,^\circ\mathrm{C})$, $e = \frac{60}{100}$, $RH(25\,^\circ\mathrm{C}) = 100\frac{0.6}{e_s} = 30\,\%$

2.50 Non-adiabatic, non-isenthalpic process $dh = c_p dT + l_v dr$, $dh \approx \frac{dH}{m_d}$ where r is the saturation mixing ratio. For an isobaric process $dh = \delta q$, $r \approx frac\epsilon pde_{sw}$, $dr = \frac{\epsilon}{p}\frac{l_v e_{sw}}{R_v T^2}dT$, $\delta q = (c_p + \frac{\epsilon l_v^2 e_{sw}}{pR_v T^2})dT$. Since the integration of $e_{sw}(T)$ is difficult, assume that $e_{sw}/T^2 \approx const$ for small temperature changes. Thus, for $T = 283.15\,\mathrm{K}$, $e_{sw} = 12.16\,\mathrm{hPa}$, $l_v = 2.5 \cdot 10^6\,\mathrm{J\,kg^{-1}}$, $\delta q = -12 \cdot 10^3\,\mathrm{J\,kg^{-1}}$, $\Delta T = -5.3\,\mathrm{K}$ and the final temperature is $4.7\,^\circ\mathrm{C}$. For the decrease in water-vapor pressure $\delta q = c_p dT + \frac{l_v \epsilon}{p} de_{sw}$. By assuming small differences we can go to differentials and obtain $\Delta e_{sw} = -4.3\,\mathrm{hPa}$

2.51 $rh = \frac{e}{e_s} \approx \frac{0.622e(p-e_s)}{0.622(p-e)e_s} = \frac{r}{r_s}$, $r_s = 0.00263\,\mathrm{kg\,kg^{-1}}$, $RH = \frac{0.00138}{0.00263}100\,\% \approx 52\,\%$

2.52 $T_v = T(1 + 0.61q)$, $q_s = 0.622\frac{e_s}{p-0.378e_s}$, $e_s = 6.1078\exp(\frac{17.1\delta}{235+\delta})$, $e_s(25) = 31.62\,\mathrm{hPa}$, $e_s(0) = 6.178\,\mathrm{hPa}$, $q_s(25) = 0.01964\,\mathrm{kg\,kg^{-1}}$, $q_s(0) = 0.003758\,\mathrm{kg\,kg^{-1}}$, $T_v(25) \approx 301.7\,\mathrm{K}$, $T_v(0) \approx 273.8\,\mathrm{K}$, $\Delta T_{virtual}(25) \approx 2.6\,\mathrm{K}$, $\Delta T_{virtual}(0) \approx 0.6\,\mathrm{K}$

2.54 $\Delta z = \frac{R_d\overline{T_v}}{g}\ln(\frac{p_1}{p_2})$, $\Delta z = \frac{287\,\mathrm{J\,kg^{-1}K^{-1}}233.15\,\mathrm{K}}{9.81\,\mathrm{m\,s^{-2}}}\ln(\frac{1{,}000\,\mathrm{hPa}}{500\,\mathrm{hPa}}) \approx 4{,}728\,\mathrm{m}$

2.56 $20\,^\circ\mathrm{C} - 9.8\,^\circ\mathrm{C\,km^{-1}}z = -10\,^\circ\mathrm{C} - 6z$, $20\,^\circ\mathrm{C} - 9.8\,^\circ\mathrm{C\,km^{-1}}z = -10\,^\circ\mathrm{C} + z$, $z = \frac{(20+10)\,^\circ\mathrm{C}}{(9.8-6)\,^\circ\mathrm{C\,km^{-1}}} = 7.895\,\mathrm{km}$, $z = \frac{(20+10)\,^\circ\mathrm{C}}{(1+9.8)\,^\circ\mathrm{C\,km^{-1}}} = 2.778\,\mathrm{km}$

2.59 $T_{10\,\mathrm{km}} = T_0 - \frac{\partial T}{\partial z}10{,}000\,\mathrm{m} = -55\,^\circ\mathrm{C}$

2.62 $\overline{T_v} = \frac{1}{R_d}\frac{\Phi_{500\,\mathrm{hPa}}-\Phi_{850\,\mathrm{hPa}}}{\ln p_{850\,\mathrm{hPa}}-\ln p_{500\,\mathrm{hPa}}} = \frac{(53{,}955-12{,}029)\,\mathrm{m^2\,s^{-2}}}{287(11.35-10.8)\,\mathrm{K^{-1}\,m^2\,s^{-2}}} = 265.6\,\mathrm{K}$, $T_{500\,\mathrm{hPa}} = 2\overline{T_v} - T_{850\,\mathrm{hPa}} \approx -25\,^\circ\mathrm{C}$

2.63 As these highs are usually associated with dry air, moisture effects can be neglected and the gas constant for dry air can be used. $\rho_{Yukon} = \frac{p}{R_d T} = \frac{106{,}000\,\mathrm{Pa}}{287\,\mathrm{J\,K^{-1}}233.15\,\mathrm{K}} = 1.584\,\mathrm{kg\,m^{-3}}$, $\rho_{Arizona} = \frac{100{,}000\,\mathrm{Pa}}{287\,\mathrm{J\,K^{-1}}313.15\,\mathrm{K}} = 1.113\,\mathrm{kg\,m^{-3}}$

2.64 $\Delta z = \frac{287\,\mathrm{J\,K^{-1}}273.15\,\mathrm{K}}{9.81\,\mathrm{m\,s^{-2}}}\ln(\frac{100{,}000\,\mathrm{Pa}}{50{,}000\,\mathrm{Pa}}) = 5{,}539.1\,\mathrm{m}$, $\overline{T} = \frac{\Delta z g}{R_d\ln(\frac{p_1}{p_2})} = 266.3\,\mathrm{K} \approx -6.9\,^\circ\mathrm{C}$, rain

2.65 $\frac{r_s}{dp} \approx \frac{d}{dp}(\frac{\epsilon e_s}{p}) \approx \epsilon(\frac{1}{p}\frac{de_s}{dp} - e_s\frac{1}{p^2}) \approx \epsilon(\frac{1}{p}\frac{de_s}{dT}\frac{dT}{dp} - e_s\frac{1}{p^2}) \approx \frac{\epsilon e_s}{p}(\frac{1}{e_s}\frac{de_s}{dT}\frac{dT}{dp} - \frac{1}{p}) \approx r_s(\frac{1}{e_s}\frac{de_s}{dT}\frac{dT}{dp} - \frac{1}{p})$. With the Clausius-Clapeyron equation, first law of thermodynamics and equation of state: $\frac{dr_s}{dp} = r_s(\frac{L}{R_v T^2}\frac{R_d T}{c_p p} - \frac{1}{p}) \approx \frac{r_s}{p}(\frac{\epsilon L}{c_p T} - 1)$. Thus, for any typical atmospheric temperature values $\frac{dr_s}{dp} > 0$, i.e. saturation mixing ratio always decreases during adiabatic pressure reduction. The pressure can be reduced adiabatically until the saturation-mixing ratio is reached. Any further reduction leads to condensation.

2.69 Outside: $-15\,^\circ\mathrm{C}$, 1.92, 1.92 hPa, 100 %. Inside: 21 °C, 1.92, 24.82 hPa, ≈ 8 %, difference 92 %

Answers to Selected Problems of Chap. 3

3.2 Once a droplet reaches its terminal velocity, the drag force equals the gravity force $kv^2 4\pi r^2 = \rho\frac{4}{3}\pi r^3 g$, $v_T^2 = \frac{\rho\frac{4}{3}\pi r^3 g}{k4\pi r^2} = \frac{g}{3}\frac{\rho}{k}r$, $v_T = c\sqrt{r}$ where $c = \sqrt{\frac{g}{3}\frac{\rho}{k}}$ is another constant. As the droplet radius increases terminal velocity increases non-linearly.

3.12 $\frac{(22-10)\,^\circ\mathrm{C}}{2{,}000\,\mathrm{m}} = 0.6\,^\circ\mathrm{C}10^{-2}\,\mathrm{m}^{-1}$, absolutely stable, $T_{b,2\,\mathrm{km}} = T_{b,0\,\mathrm{km}} - \Gamma_s \Delta z = 22\,^\circ\mathrm{C} - \frac{0.5\,^\circ\mathrm{C}}{100\,\mathrm{m}} 2{,}000\,\mathrm{m} = 12\,^\circ\mathrm{C}$, $T_{t,4\,\mathrm{km}} = T_{t,2\,\mathrm{km}} - \Gamma_d \Delta z = 10\,^\circ\mathrm{C} - \frac{1\,^\circ\mathrm{C}}{100\,\mathrm{m}} 2{,}000\,\mathrm{m} = -10\,^\circ\mathrm{C}$, temperature gradient: $1.1\,^\circ\mathrm{C}10^{-2}\,\mathrm{m}^{-1}$, absolutely unstable. Forced convection, accelerating ascend, thunderstorms

Answers to Selected Problems of Chap. 4

4.1 $F_s = \frac{R_p}{R_{es} F_p}$, $F_{Dec} = 1{,}361 \cdot 1.034\,\mathrm{W\,m^2} = 1{,}411\mathrm{W\,m^2}$, $F_{Jul} = 1{,}361 \cdot 0.967\,\mathrm{W\,m^2}$, difference $\approx 7\,\%$

4.2 $E = \sigma T^4$, $E_{Earth} = 5.67 \cdot 10^{-8}\,\mathrm{W\,m^{-2}\,K^{-4}} \cdot (255\,\mathrm{K})^4 = 239.7\,\mathrm{W\,m^{-2}}$, $E_{Sun} = 73{,}483{,}200\,\mathrm{W\,m^{-2}}$, $\frac{T_{Sun}}{T_{Earth}} \approx 23.529$. The Sun is about 24 times warmer than the Earth. $\frac{E_{Sun}}{E_{Earth}} = 306{,}563.2$. The ratio of the temperatures to the fourth, 306,488, equals the ratio of the emitted energy within the error of truncation. $\lambda = \frac{2{,}989}{T} \longrightarrow T = \frac{2{,}898}{\lambda} = \frac{2{,}898\,\mu\mathrm{m\,K}}{0.5\,\mu\mathrm{m}} = 5{,}800\,\mathrm{K}$, $\lambda = \frac{2{,}898}{T_{Sun}} = \frac{2{,}898\,\mu\mathrm{m\,K}}{6{,}000\,\mathrm{K}} = 0.483\,\mu\mathrm{m}$. The wavelength shifts towards larger wavelength when the temperature of the Sun would be lower than it is. $\lambda = \frac{2{,}898\,\mu\mathrm{m\,K}}{(475+273)\,\mathrm{K}} = 3.88\,\mu\mathrm{m}$, $\lambda = \frac{2{,}898\,\mu\mathrm{m\,K}}{255\,\mathrm{K}} = 11.37\,\mu\mathrm{m}$, $\lambda_{Sun} < \lambda_{Venus} < \lambda_{Earth}$

4.4 $I = S(1-\alpha)$, $R_{out} = R_{in}$, $R_{out} = \sigma T_p^4 A$ where A is the area of the system. $T_p = (\frac{S(1-\alpha)}{\sigma A})^{1/4}$. Assuming typical albedo values for forest and desert $T_p = (\frac{1.74 \cdot 10^{17}\,\mathrm{W}(1-\alpha)}{5.67 \cdot 10^{-8}\,\mathrm{W\,m^{-2}\,K^4} 5.1 \cdot 10^{14}\,\mathrm{m^2}})^{1/4}$, $T_{p,\alpha=0.1} = 271.3\,\mathrm{K}$, $T_{p,\alpha=0.3} = 254.8\,\mathrm{K}$, $T_{p,\alpha=0.35} = 250.1\,\mathrm{K}$. This result means that a forest planet would have a higher planetary temperature than a desert planet or than the planetary temperature obtained for the average albedo based on recent land-use. This result is in contrast to observations made where forest was deforested and replaced by deserts. Consequently, other processes must exist that also affect temperature.

4.6 $E_{BB} = \sigma T^4$, $E_{GB} = \epsilon \sigma T^4$, $T_{BB} = (\frac{400\,\mathrm{W\,m^{-2}}}{5.67 \cdot 10^{-8}\,\mathrm{W\,m^{-2}\,K^{-4}}})^{1/4} = 289.8\,\mathrm{K}$, $T_{GB} = (\frac{400\,\mathrm{W\,m^{-2}}}{0.9 \cdot 5.67 \cdot 10^{-8}\,\mathrm{W\,m^{-2}\,K^{-4}}})^{1/4} = 297.5\,\mathrm{K}$. The gray-body must have a higher temperature to have the same intensity of radiation. For $\epsilon = 0.9$, $2.4\,\%$

4.7 $E = \sigma T^4 = 5.67 \cdot 10^{-8}\,\mathrm{W\,m^{-2}K^{-4}(255\,K)^4} \approx 239\,\mathrm{W\,m^{-2}}$, $\lambda_{max} = \frac{2{,}898\,\mu\mathrm{m\,K}}{T} = \frac{2{,}898\,\mu\mathrm{m\,K}}{255\,\mathrm{K}} \approx 11.36\,\mu\mathrm{m}$, IR

4.8 $E = \sigma T^4$, $E_{Barrow} = 5.67 \cdot 10^{-8}\,\mathrm{W\,m^{-2}\,K^{-4}((273.15 - 27)K)^4} = 208.2\,\mathrm{W\,m^{-2}}$, $E_{warm} = 5.67 \cdot 10^{-8}\,\mathrm{W\,m^{-2}\,K^{-4}((273.15 - 27 + 10)\,K)^4} = 244.1\,\mathrm{W\,m^{-2}}$, $\frac{E_{Barrow}}{E_{warm}} \approx 1.15$, i.e. the intensity of radiation increases by $15\,\%$.

4.10 $T_p = \frac{S(1-\alpha)}{\sigma A} = (6.0172 \cdot 10^9 (1-\alpha))^{0.25}\,\mathrm{K}$, $T_p(\alpha = 0.15) = 267.4\,\mathrm{K}$, $T_p(\alpha = 0.6) = 221.5\,\mathrm{K}$, $T_p(\alpha = 0.3) = 254.7\,\mathrm{K}$, $\frac{T_{p,\alpha=0.3}}{T_{p,\alpha=0.6}} \approx 1.15$, $\frac{T_{p,\alpha=0.3}}{T_{p,\alpha=0.15}} \approx 0.95$,

$\frac{T_{p,\alpha=0.15}}{T_{p,\alpha=0.3}} \approx 1.04$, i.e. non-linear decrease in temperature for increasing albedo, but nature shows that this is not necessarily the case

4.12 5,794 K, 6,101 K

4.18 $E_{absorbed} = a1{,}380\,\mathrm{W\,m^{-2}} = E_{emitted} = \epsilon\sigma T^4$. Kirchhoff's law $a = \epsilon$, $T = (\frac{1{,}380}{\sigma})^{0.25}\,\mathrm{K} = 395\,\mathrm{K}$. The assumed surface temperature is lower than the radiative equilibrium for which net radiation is downward directed $E_{net} = a1{,}380 - \epsilon\sigma T^4 435\,\mathrm{W\,m^{-2}} = 435\,\mathrm{W\,m^{-2}}$, use inverse square law.

Answers to Selected Problems of Chap. 5

5.2 $\approx 0.7\,d$. The calculation provides an upper limit. Additional processes exist that remove HNO_3 from the layer are physio-chemical processes, transport, diffusion, thermal or light decomposition. Sources are chemical reaction of precursor gases, e.g. H_2O and NO_2, emissions.

5.3 At 20 °C, $k_2 = 51.4\,\mathrm{ppm^{-1}\,s^{-1}} \approx 0.0514\,\mathrm{ppb\,s^{-1}}$. No other reactions or emissions mean the system is in steady-state, i.e. $[O_3] = \frac{j[NO_2]}{k_2[NO]} = 19.8\,\mathrm{ppb}$

5.4 $T_R = \frac{m}{F}$. The total mass of ammonia is given by the partial fraction times the mass of the stable's air, $m = 2{\cdot}10^{-8}{\cdot}10^3\,\mathrm{kg} = 2{\cdot}10^{-5}\,\mathrm{kg}$, $\frac{2{\cdot}10^{-5}}{7{\cdot}10^{-5}}\,d = 0.29\,d = 6.9\,\mathrm{h}$

5.5 Transport is $19.9 \cdot 10^9 \cdot 0.033\,\mathrm{kg}$ and $21.3 \cdot 10^9 \cdot 0.445\,\mathrm{kg}$ for SO_2 and NO, respectively. $\frac{21.3{\cdot}10^9{\cdot}0.445\,\mathrm{kg}}{19.9{\cdot}10^9{\cdot}0.033\,\mathrm{kg}} \approx 14.43$, i.e. 14:1.

5.7 $p = N_A kT$, $N_A = \frac{102{,}500\,\mathrm{Pa}}{1{,}381{\cdot}10^{-23}\,\mathrm{J\,K^{-1}\,molecules248.15\,K}} = 2.991 \cdot 10^{25}\,\mathrm{molecules\,m^{-3}}$ as the volume occupied by gases at same T, p is proportional to the number of molecules in the gas. With $SO_2 = 360\,\mathrm{ppb}$, $360 \cdot 10^{-9} 2.991 \cdot 10^{25}\,\mathrm{molecules\,m^{-3}} = 1{,}076.76 \cdot 10^{13}\,\mathrm{molecules\,m^{-3}} = 1.07676 \cdot 10^{10}\,\mathrm{molecules\,m^{-3}}$

5.8 $\overline{F}(\lambda_i) = \frac{\overline{I}(\lambda_i)}{\Delta\lambda}$, $j = \sum_i \overline{\sigma}(\lambda_i, T)\overline{\phi}(\lambda_i, T)\overline{I}(\lambda_i)$, layer 1: $j = 6.2 \cdot 10^{-23}\,\mathrm{m^2}\,0.75{\cdot}4.6{\cdot}10^{19}\,\mathrm{m^{-2}\,s^{-1}} = 2.139{\cdot}10^{-3}\,\mathrm{s^{-1}}$, Layer 2: $j = 6.2{\cdot}10^{-23}\,\mathrm{m^2}\,0.75{\cdot}1.3 \cdot 10^{18}\,\mathrm{m^{-2}\,s^{-1}} = 6.045 \cdot 10^{-5}\,\mathrm{s^{-1}}$

5.9 $[NO_2]/[NO] = \frac{\chi_{NO_2}}{\chi_{NO}}$ with the triad $NO - NO_2 - O_3$, $[O_3] = \frac{j[NO_2]}{k_1[NO]} = 1.118 \cdot 10^{18}\,\mathrm{molecules\,m^{-3}}$, $n = \frac{p}{k_b T} = 2.1 \cdot 10^{25}\,\mathrm{molecules\,m^{-3}}$, $\chi_{O_3} = \frac{[O_3]}{n} \approx 53.1\,\mathrm{ppb}$

5.10
$NO_2 + h\nu \rightarrow NO + O$
$O_3 + NO \rightarrow NO_2 + O_2$
$O + O_2 + M \rightarrow O_3 + M$
$O_3 + OH \rightarrow O_2 + HO_2$
net reaction: $HO_2 + h\nu + O_3 + OH \rightarrow H_2O_2 + 2O_2$, ozone depletion
$NO_2 + h\nu \rightarrow^{j} NO + O$
$O_3 + NO \rightarrow^{k_1} NO_2 + O_2$

$O + O_2 + M \rightarrow^{k_2} O_3 + M$
$O_3 + OH \rightarrow^{k_3} O_2 + HO_2$
$HO_2 + O_3 \rightarrow^{k_4} 2O_2 + OH$
net reaction: $2O_3 \rightarrow 3O_2$
The net reaction chain permits twice the depletion of ozone than in the previous part. The changes are
$\frac{d[NO_2]}{dt} = -j[NO_2] + k_1[O_3][NO]$
$\frac{d[NO]}{dt} = j[NO_2] - k_1[NO][O_3]$
$\frac{d[O]}{dt} = j[NO_2] - k_2[O][O_2][M]$
$\frac{d[O_3]}{dt} = -k_1[O_3][NO] + k_2[O][O_2][M] - k_3[O_3][OH] - k_k[HO_2][O_3]$
$\frac{d[OH]}{dt} = -k_3[O_3][OH]$
$\frac{d[HO_2]}{dt} = k_3[O_3][OH] - k_4[HO_2][O_3]$

5.11 $NO + HO_2 \rightarrow^{k_1} NO_2 + OH$
$NO_2 + h\nu \rightarrow^{j} NO + O$
$O_3 + NO \rightarrow^{k_2} NO_2 + O_2$
$O + O_2 + M \rightarrow^{k_3} O_3 + M$
net reaction: $HO_2 + NO + h\nu \rightarrow OH + NO_2$
$\frac{d[NO]}{dt} = -k_1[NO][HO_2] + j[NO_2] - k_2[O_3][NO]$
$\frac{d[HO_2]}{dt} = -k_1[NO][HO_2]$
$\frac{d[NO_2]}{dt} = k_1[NO][HO_2] - j[NO_2] + k_2[O_3][NO]$
$\frac{d[OH]}{dt} = k_1[NO][HO_2]$
$\frac{d[O_3]}{dt} = -k_2[O_3][NO] + k_3[O_2][O][M]$
Steady-state: $\frac{d[O_3]}{dt} = 0$
$[O_3] = -\frac{j[NO_2]}{k_2[NO]}$

5.14 One CH_4 produces two NO_2. Net reaction of all seven eqs.: $CH_4 + 2OH + CO + CH_3CHO + 2O_2 + 2NO \longrightarrow H + CO_2 + H_2O + CH_3CO + 2NO_2 + HCHO$
$\frac{d[CH_4]}{dt} = -k_1[OH][CH_4]$
$\frac{d[CO_2]}{dt} = k_2[OH][CO]$
$\frac{d[NO]}{dt} = -k_5[CH_3O_2][NO] - k_7[HO_2][NO]$
$\frac{d[NO_2]}{dt} = k_5[CH_3O_2] + k_7[HO_2][NO] = -\frac{d[NO]}{dt}$
When ozone is present add (substract) $-k_8[O_3][NO][NO_2]$ to (from) $\frac{d[NO]}{dt}$ ($\frac{d[NO_2]}{dt}$)
The presence of methane provides a path of net oxidation of nitric oxide without use of ozone, which is not the case in the pseudo-equilibrium situation described by the triad $NO - NO_2 - O_3$.

5.15 At steady state: $\frac{d[O^{1D}]}{dt} = j_1[O_3] - k_1[O^{1D}][M] - k_2[O^{1D}][H_2O] = 0$. Thus, $[O^{1D}] = \frac{j_1[O_3]}{k_1[M]+k_2[H_2O]} \approx \frac{j_1[O_3]}{k_1[M]}$. The change in odd oxygen reads $\frac{d([HO]+[HO_2])}{dt} = 2k_2[O^{1D}][H_2O] - 2k_6[HO][HO_2]$. Since the reactions k_4 and k_5 are much quicker than those of k_2 and k_6 the former determine the concentrations of odd oxygen. Under these conditions, steady state means $k_4[HO][O_3] \approx k_5[HO_2][O_3]$ or $\frac{[HO_2]}{[HO]} \approx \frac{k_4}{k_5}$, $2.8 \cdot 10^{14}$ molecules m^{-3}

5.16 $[HNO_3]_{total} = \frac{p_{HNO_3}}{RT} + ([HNO_3(aq)] + [NO_3^-])\, LWC$

$[HNO_3(aq)] = k_{HNO_3} p_{HNO_3}$

$K_{dis} = \frac{[H^+][NO_3^-]}{[HNO_3(aq)]}$

where K_{dis} is the dissosciation equilibrium. Solving for the concentrations yields

$[HNO_3(aq)] = \frac{k_{HNO_3} RT}{1+LWC\, k_{HNO_3} RT} [HNO_3]_{total}$

$[NO_3^-] = \frac{K_{dis}}{[H^+]} \frac{k_{HNO_3} RT}{1+LWC\, k_{HNO_3} RT} [HNO_3]_{total}$

5.17 Pure water: $pH = 7$, acidity of 10^{-7}, normal rainwater: $pH = 5.6$ acidity of $10^{-5.6}$. Thus, normal rainwater is 25 times more acidic than pure water. In the Northeast, rainwater is 39.8 times more acid than in some western parts of the US.

5.18 $pH = 5 = -\log_{10}[H^+]$, $[H^+] = 10^{-pH}$, $[H^+] = 10^{-5}\,\mathrm{mol\,L^{-1}}$, $K_w = [H^+][OH^-] = 10^{-14}\,\mathrm{mol\,L^{-1}}$, $[OH^-] = 10^{-14}/10^{-5} = 10^{-9}\,\mathrm{mol\,L^{-1}}$, $[H^+] = 10^{-5} \cdot 10^{-1}\,\mathrm{L} = 10^{-6}\,\mathrm{mol}$, $[OH^-] = 10^{-9} \cdot 10^{-1}\,\mathrm{L} = 10^{-10}\,\mathrm{mol}$. By use of the Avogardo number, the number of H^+ (or OH^-) ions per mole of ions $[H^+] = 10^{-6} \cdot 6.023 \cdot 10^{23} = 6.023 \cdot 10^{17}$ and $[OH^-] = 10^{-10} \cdot 6.023 \cdot 10^{23} = 6.023 \cdot 10^{13}$ ions

5.19 $CO_2(g) + H_2O \rightleftharpoons CO_2(aq) \rightarrow H_2CO_3$
$H_2CO_3 \rightleftharpoons H^+ + HCO_3^-$
$395.1\,\mathrm{ppm} = 0.3951 \cdot 10^{-5}\mathrm{M}$, $K = 4.16 \cdot 10^{-7} = [H^+][HCO_3^-]/[H_2CO_3]$, $[H_2CO_3] = 0.3951 \cdot 10^{-5}\mathrm{M}$, $[H^+] = [HCO_3^-]$, $4.16 \cdot 10^{-7} = [H^+]^2/0.3951 \cdot 10^{-5}$, $[H^+]^2 \approx 1.64 \cdot 10^{-12}$, $pH = -\log_{10}([H^+]) = 5.9$

Answers to Selected Problems of Chap. 6

6.1 $y = x$, $y = -x$, for $x > 0$

6.4 Only the flows at the entrances and outlets of the streets have to be considered, i.e. $v_1 A_1 + v_2 A_2 + v_3 A_3 = 0$, $-20\,\mathrm{m\,s^{-1}} 30\,\mathrm{m} \cdot H + 18\,\mathrm{m\,s^{-1}} 30\,\mathrm{m} \cdot H + v_3 10\,\mathrm{m} \cdot H = 0$, $v_3 = \frac{30\,\mathrm{m}(20-18)\,\mathrm{m\,s^{-1}}}{10\,\mathrm{m}} = 6\,\mathrm{m\,s^{-1}}$

6.5 $\frac{p(A)-p(F)}{d} = \frac{(1{,}016-1{,}009)\,\mathrm{hPa}}{423\,\mathrm{km}} = 0.00165\,\mathrm{Pa\,m^{-1}}$, $F = \frac{1}{1.2\,\mathrm{kg\,m^{-3}}} \frac{700\,\mathrm{Pa}}{423{,}000\,\mathrm{m}} \approx 1.4 \cdot 10^{-1}\,\mathrm{m\,s^{-2}}$

6.7 $F = vf = v2\Omega \sin\varphi$, $F = 8\,\mathrm{m\,s^{-1}}\, 2 \cdot 7.29 \cdot 10^{-5}\,\mathrm{s^{-1}} \sin 35° = 6.69 \cdot 10^{-4}\,\mathrm{m\,s^{-2}}$, $\frac{F}{2\Omega \sin\varphi} = \frac{6.69 \cdot 10^{-4}\,\mathrm{m\,s^{-2}}}{2 \cdot 7.29 \cdot 10^{-5}\,\mathrm{s^{-1}} \sin 65°} = 5.06\,\mathrm{m\,s^{-1}}$. Wind speed must slow down by $2.94\,\mathrm{m\,s^{-1}}$. Pole: $v = 4.59\,\mathrm{m\,s^{-1}}$.

6.8 $u = 10\,\mathrm{m/s}$, $v = 5\,\mathrm{m/s}$, $|\mathbf{v}| = \sqrt{u^2 + v^2} = \sqrt{(100 + 25)\,\mathrm{m^2/s^2}} = \sqrt{125}\,\mathrm{m\,s^{-1}} = 11.18\,\mathrm{m\,s^{-1}}$, 247.5°

6.9 $\frac{d\chi}{dt} = \frac{\partial\chi}{\partial t} + \mathbf{v}\cdot\nabla\chi$. There are no components in y- and z-direction: $\frac{d\chi}{dt} = \frac{\partial\chi}{\partial t} + u\frac{\partial\chi}{\partial x}$. Ship travels towards the west: $u = -50\,\mathrm{km}\,(3\,\mathrm{h})^{-1} = -16.666\,\mathrm{km\,h^{-1}}$, $\frac{\partial\chi}{\partial x} = (\frac{d\chi}{dt} - \frac{\partial\chi}{\partial t})\frac{1}{u} = (-4\,\mathrm{ppm}\,(3\,\mathrm{h})^{-1} - (-3\,\mathrm{ppm}\,(3\,\mathrm{h})^{-1})\frac{1}{-16.666\,\mathrm{km\,h^{-1}}} = -1.3\,\mathrm{ppm\,km^{-1}}$

6.10 A concentration $[\chi]$ is passing through an arbitrarily shaped constant volume at $\mathbf{v} = (u, v, w)$. Both the concentration and speed change with time, t, and depend on the location, $\mathbf{r}$. The difference of inflow and outflow gives the net change in concentration $([\chi](x)u(x) - [\chi](x+\Delta x)u(x+\Delta x))\Delta y\Delta z \approx -\frac{\partial}{\partial x}([\chi]u)\Delta x\Delta y\Delta z = -\frac{\partial}{\partial x}([\chi]u)\Delta V$, where ΔV is the volume. The equations in y- and z-direction look accordingly. Including the analogous equations for the y- and z-direction and vector analysis yields $-\nabla\cdot([\chi]\mathbf{v})\Delta V$. This net change must be equal to the change in mass within the constant volume $\frac{\partial}{\partial t}([\chi]\Delta V)$. As $V = const$, ΔV cancels out, $\frac{\partial[\chi]}{\partial t} + \nabla\cdot([\chi]\mathbf{v}) = 0$, $\frac{\partial[\chi]}{\partial t} + \mathbf{v}\cdot\nabla[\chi] + [\chi]\nabla\cdot\mathbf{v} = 0$. The Eulerian form of the mass-continuity equation can be converted to its Lagrangian form using $\frac{\partial[\chi]}{\partial t} + v\cdot\nabla[\chi] = \frac{d[\chi]}{dt}$, $\frac{d[\chi]}{dt} + [\chi]\nabla\cdot v = 0$

6.13 As the Coriolis force is perpendicular to the wind vector, the wind speed remains constant. $\frac{v^2}{R} = 2\Omega v\sin\varphi$ where R is the radius of the trajectory of the air parcel. The time required for a complete inertia cycle can be derived from the relationship between velocity and the length of the path given by $2\pi R$, i.e. $v = \frac{2\pi R}{t}$, $v = 2\Omega\sin\varphi R$, $t = \frac{2\pi R}{v} = \frac{2\pi R}{2\Omega\sin\varphi R} = \frac{\pi}{\Omega\sin\varphi} = \frac{1d}{2\sin\varphi}$. The inertia period is 12 h at the poles and about 1 day at 30° latitude. The inertia motion is anticyclonic (cyclonic) in the Northern (Southern) Hemisphere.

6.14 $\nabla\times\mathbf{v}_g = \frac{1}{f}(\nabla\Phi\cdot\nabla)\mathbf{k} - \frac{1}{f}\nabla\Phi(\nabla\cdot\mathbf{k}) - \frac{1}{f}(\mathbf{k}\cdot\nabla)\nabla\Phi = \frac{1}{f}\mathbf{k}(\nabla^2\Phi)$. The first three terms vanish. The last term remains and has only a vertical component. Projection to $\mathbf{k}$ yields $\nabla\times\mathbf{v}_g = (\frac{1}{f}\nabla^2\Phi)\mathbf{k} = \zeta_g\mathbf{k} = \boldsymbol{\zeta}_g = \boldsymbol{\zeta}$ where ζ is the 3D-vector of the relative vorticity.

6.15 $\nabla\times\mathbf{v} + 2\Omega$, $\nabla\times\mathbf{v} = 0.7\cdot10^{-4}\,\mathrm{s^{-1}} - 10^{-4}\,\mathrm{s^{-1}} = -0.3\cdot10^{-4}\,\mathrm{s^{-1}}$, negative relative vorticity means southern hemisphere

6.18 $dx = R_e\cos\varphi d\lambda = 162\,\mathrm{km}$, $dy = R_e d\varphi = 6{,}371\cdot\frac{\pi}{180°} = 311\,\mathrm{km}$. The area is $2.7\cdot10^6\,\mathrm{km^2}$ and reaches to 75.4°. Here, the grid cell width is 78.4 km. Thus, the northern border is 942 km. Adding the length of the northern and southern borders and dividing by two yields the approximate mean area width of 1,444.5 km for the grid cells and an approximate area of $2.69\cdot10^6\,\mathrm{km^2}$. At 27.9°, the grid cell width is 275 km. The northern boundary is at 44.7 °N. Here, the grid cell has a width of 221.3 km. Thus, the mean width of a grid cell is 248 km. To cover a distance of about 1,444.5 km we need about six grid cells

6.27 The vertical wind component is zero at the tropoause. $\rho = \frac{P}{R_d T_v} = 0.53\,\mathrm{kg\,M^{-3}}$. $\nabla\cdot\mathbf{v} = \frac{1}{A}\frac{dA}{dt} = \frac{0.25}{900\,\mathrm{s}} = 2.78\cdot10^{-4}\,\mathrm{s^{-1}}$, $\frac{d\omega}{dp} = -\nabla\cdot\mathbf{v}$, $\omega_{350} = \omega_{200} - (\nabla\cdot\mathbf{v})(350 - 200\,\mathrm{hPa}) = 0 - 2.78\cdot10^{-4}\,\mathrm{s^{-1}}250\,\mathrm{hPa} = -6.94\cdot10^{-2}\,\mathrm{hPa\,s^{-1}}$. The anvil

averaged vertical velocity can be estimated as $w = -\frac{\omega}{\rho \mathbf{g}} = \frac{6.94\,\mathrm{Pa\,s^{-1}}}{9.81\,\mathrm{m\,s^{-2}} 0.53\,\mathrm{kg\,m^{-3}}} \approx 1.33\,\mathrm{m\,s^{-1}}$. Locally the updraft may be much stronger or weaker

6.28 $p_{A,2\,\mathrm{km}} = p_0 - \rho g h = (101{,}325 - 1.35 \cdot 9.81 \cdot 2{,}000)\,\mathrm{Pa} = 748.38\,\mathrm{hP}$, $p_{B,2\,\mathrm{km}} = p_0 - \rho g h = (101{,}325 - 1.15 \cdot 9.81 \cdot 2{,}000)\,\mathrm{Pa} = 787.62\,\mathrm{hP}$, $\frac{dp}{dz} = -0.132\,\mathrm{hPa/m}$, $\frac{dp}{dz} = -0.113\,\mathrm{hPa\,m^{-1}}$ for the warm and cold air, respectively. The horizontal gradient at 2 km is $\frac{dp}{dx} = (787.62 - 748.38)/200{,}000\,\mathrm{hPa\,m^{-1}} = 0.1962\,\mathrm{Pa\,km^{-1}}$

6.29 $\overline{T_v} = \frac{1}{R_d} \frac{\Phi_{500\,\mathrm{hPa}} - \Phi_{850\,\mathrm{hPa}}}{\ln p_{850\,\mathrm{hPa}} - \ln p_{500\,\mathrm{hPa}}} = \frac{(53{,}955 - 12{,}029)\,\mathrm{m^2\,s^{-2}}}{287(11.35 - 10.8)\,\mathrm{K^{-1}\,m^2\,s^{-2}}} = 265.6\,\mathrm{K}$, $T_{500\,\mathrm{hPa}} = 2\overline{T_v} - T_{850\,\mathrm{hPa}} = 248.06\,\mathrm{K} \approx -25\,^\circ\mathrm{C}$

6.30 $\mathbf{v_g} = \frac{1}{f}\mathbf{k} \cdot \nabla_p \Phi = \frac{\mathbf{g}}{f}\mathbf{k} \cdot \nabla_p z$. In Cartesian-pressure coordinates, $\nabla_p = \frac{\partial}{\partial x} + \frac{\partial}{\partial y}$ are on the same pressure surface ($p = const$). Consequently, the geostrophic wind is independent of density in this coordinate system and only depends on f and the gradient of geoptential height

6.31 $\frac{\partial u_g}{\partial z} = -\frac{g}{f\theta_0}\frac{\partial \theta}{\partial y} = \frac{9.81\,\mathrm{m\,s^{-2}} \cdot 20\,\mathrm{K}}{10^{-4}\,\mathrm{s^{-1}} 285\,\mathrm{K} 1{,}000{,}000\,\mathrm{m}} = 0.00688\,\mathrm{s^{-1}}$, $u_g(10\,\mathrm{km}) = 68.84\,\mathrm{m\,s^{-1}}$, west to east

6.33 $v = \frac{800{,}000\,\mathrm{m}}{17 \cdot 3{,}600\,\mathrm{s}} = 13.07\,\mathrm{m\,s^{-1}}$, probably a cold front because of its speed and duration of 7.7 h over 360 km distance, $\Gamma = 0.9\,\mathrm{K10^{-2}\,m^{-1}}$, i.e. close to the dry adiabatic lapse rate, cP. The typical slope is 1:200. Dividing the distance by 200 gives the height of the warm air to be at 4.025 km in A when it is visible at B. Using the same slope, but searching for the distance leads to a distance of 120 km for the site

6.34 $e = 20\,\mathrm{hPa}$, $q = 0.622 \frac{20}{1{,}010 - 20 \cdot 0.378}\,\mathrm{kg\,kg^{-1}} = 0.0124\,\mathrm{kg\,kg^{-1}}$, $T_v = 300(1 + 0.61 \cdot 0.0124)\,K = 30.7\,^\circ\mathrm{C}$, $p = \rho R_d T$, $\rho(T_v) = \frac{101{,}000\,\mathrm{Pa}}{287\,\mathrm{J\,K^{-1}}\,303.9\,\mathrm{K^{-1}}} = 1.158\,\mathrm{kg\,m^{-3}}$, $\rho(T) = \frac{101{,}000\,\mathrm{Pa}}{287\,\mathrm{J\,K^{-1}} 300.2\,\mathrm{K}} = 1.17\,\mathrm{kg\,m^{-3}}$, $\frac{\rho(T)}{\rho(T_v)} = 1.01$. The use of virtual temperature rather than air temperature affects the calculated air density by 1 %. At same temperature and pressure, moist air is actually lighter than dry air

6.35 $F_{pressure} = -\frac{1}{\rho}\frac{dp}{dx}$, $0.00375\,\mathrm{m\,s^{-2}}$ for the large scale pressure system, $20\,\mathrm{m\,s^{-2}}$ for the tornado. Comparing the ranges of wind speeds yields 2.3–2.9 times higher wind speeds in an F4 than in an F1 tornado. With $P = kv^3$, the power increase can be determined according to $\frac{P_{F4}}{P_{F1}} = \frac{{v_{F4}}^3}{{v_{F1}}^3}$. Taking into account the given range of wind speed the power is between 12.6 and 23.7 times higher in an F4 than in an F1 tornado

6.36 $\frac{6{,}500^2}{3{,}500^2} \approx 3.45$. When the wavelength increases, the velocity becomes twice as fast. The wave travels westward

6.37 $F_{pressure} = -\frac{1}{\rho}\frac{\partial p}{\partial n} = \frac{600\,\mathrm{Pa}}{1.29\,\mathrm{kg\,m^{-3}} 10^5\,\mathrm{m}} = 4.7 \cdot 10^{-3}\,\mathrm{m\,s^{-2}}$, $F_{pressure} = -g\frac{\partial z}{\partial n}$, $\frac{\partial z}{\partial n} = 4.741 \cdot 10^4 \approx 0.4741\,\mathrm{m\,km^{-1}}$

Answers to Selected Problems of Chap. 7

7.1 $\Delta E_m = c_m m_m \Delta T_m$, $\Delta E_w = \Delta E_a$, $\Delta T_a = \frac{c_w m_w \Delta T_w}{c_a m_a}$

7.2 $z_{LCL,rural} = 1{,}485\,\mathrm{m}$, $z_{LCL,town} = 1{,}733\,\mathrm{m}$, $\Delta z = 248\,\mathrm{m}$. The difference in dew-point temperatures is small, but the difference between dew-point temperature and temperature differ strongly over the rural and town area. It is larger for the town, for which the cloud base (LCL) is higher over the town than rural area. In the second case, this difference is less, but cloud base again will be higher over the town than rural area. The small temperature difference is most likely due to frontal passage. Under these conditions, local effects play only a marginal role.

7.7 $E_1 = \frac{T_0 - T_l}{T_0} = \frac{301.15 - 197.15\,\mathrm{K}}{301.15\,\mathrm{K}} \approx 0.223$. The source of heat is the evaporation of water from the ocean. The amount of water evaporated is proportional to the amount of water that can be taken up by the atmosphere. Thus, evaporation can take place as long as the air is unsaturated. Consequently, the amount of heat is proportional to the dry air above the water surface and the maximal amount of heat that can be taken up is given by $L_v q_s (1 - rh)$, $q_s = 0.622 \frac{e_s}{p - e_s}$, $e_s(28\,^\circ\mathrm{C}) = 37.793\,\mathrm{hPa}$, $E_2 = 0.622\,\mathrm{J\,kg^{-1}\,K^-\,J^{-1}\,kg\,K}\frac{37.793\,\mathrm{hPa}}{(900 - 37.793)\,\mathrm{hPa}} \approx 0.0273\,\mathrm{kg\,kg^{-1}} = 2.5 \cdot 10^6 \cdot 0.0273 \cdot (1 - 0.8)\,\mathrm{J} = 13{,}650\,\mathrm{J}$. Multiplication of this maximal import of heat, E_2, and the amount of heat that can be converted to mechanic energy, E_1, yields the maximal energy available $E = \frac{T_0 - T_l}{T_0} L_v q_s (1 - rh) = 0.223 \cdot 13{,}650\,\mathrm{J} = 304\,\mathrm{J}$. The maximal intensity of a tropical cyclone is usually measured by its wind speed. The maximum wind speed can be estimated by knowing how the energy is used. An appropriate assumption is that most of the energy is required to overcome the turbulent dissipation of the very turbulent layer above the ocean. The rate with which the energy enters the Carnot cycle above the ocean is given by $C_h v E$ where C_h is the transfer coefficient of heat, v is the respective wind speed close to the surface of the ocean. At the surface, the rate of dissipation of mechanic energy is given by $C_d v^3$, where C_d is the friction coefficient. In equilibrium, the input energy has to be equal to the output energy, i.e. $C_h v E = C_d v^3$, $v_{max} = \sqrt{\frac{C_h}{C_d} E}$. When we know the transfer coefficient, we are able to determine the maximal wind speed of the assumed tropical cyclone. In good approximation, the relation of the transfer coefficient of heat to that of friction can be assumed to be equal to 1. Then, $v_{max} = 17.45\,\mathrm{m\,s}$

Index

Some additional help for navigating the book

N. Mölders and G. Kramm, *Lectures in Meteorology*, Springer Atmospheric Sciences,
DOI 10.1007/978-3-319-02144-7, © Springer International Publishing Switzerland 2014